

# **MECHANICS OF CRACK GROWTH**

*Proceedings of the  
Eighth National Symposium  
on Fracture Mechanics*

 **STP 590**

**AMERICAN SOCIETY FOR TESTING AND MATERIALS**

# MECHANICS OF CRACK GROWTH

Proceedings of the  
Eighth National Symposium  
on Fracture Mechanics

A symposium sponsored by  
Committee E-24 on  
Fracture Testing of Metals,  
AMERICAN SOCIETY FOR  
TESTING AND MATERIALS  
Brown University,  
Providence, R. I., 26-28 Aug. 1974

ASTM SPECIAL TECHNICAL PUBLICATION 590  
J. R. Rice and P. C. Paris,  
symposium co-chairmen

List price \$45.25  
04-590000-30



AMERICAN SOCIETY FOR TESTING AND MATERIALS  
1916 Race Street, Philadelphia, Pa. 19103

© by AMERICAN SOCIETY FOR TESTING AND MATERIALS 1976  
Library of Congress Catalog Card Number: 75-18413

NOTE

The Society is not responsible, as a body,  
for the statements and opinions  
advanced in this publication.

## Dedication

*This volume is dedicated with profound appreciation to the memory of the late Donald P. Wisdom, ASTM Staff Liaison Officer to Committee E-24 from 1971 until his untimely decease in September 1974. His good-natured guidance and helpfulness were particularly appreciated by the Committee's Officers and Members. He helped to organize and attended the symposium.*

*May he rest in peace.*

## **Foreword**

This publication, *Mechanics of Crack Growth*, contains papers presented at the Eighth National Symposium on Fracture Mechanics which was held at Brown University, Providence, R. I., 26-28 Aug. 1974. The symposium was sponsored by Committee E-24 on Fracture Testing of Metals of the American Society for Testing and Materials. J. R. Rice and P. C. Paris, Brown University, presided as symposium co-chairmen.

## **Related ASTM Publications**

**Resistance to Plane-Stress Fracture (R-Curve Behavior) of A572 Structural Steel, STP 591 (1976), \$5.25, 04-591000-30**

**Fracture Analysis, STP 560 (1974), \$22.75, 04-560000-30**

**Fracture Toughness and Slow-Stable Cracking, STP 559 (1974), \$25.25, 04-559000-30**

**Fatigue and Fracture Toughness—Cryogenic Behavior, STP 556 (1974), \$20.25, 04-556000-30**

## **A Note of Appreciation to Reviewers**

This publication is made possible by the authors and, also, the unheralded efforts of the reviewers. This body of technical experts whose dedication, sacrifice of time and effort, and collective wisdom in reviewing the papers must be acknowledged. The quality level of ASTM publications is a direct function of their respected opinions. On behalf of ASTM we acknowledge with appreciation their contribution.

*ASTM Committee on Publications*

## **Editorial Staff**

Jane B. Wheeler, *Managing Editor*  
Helen M. Hoersch, *Associate Editor*  
Charlotte E. Wilson, *Senior Assistant Editor*  
Ellen J. McGlinchey, *Assistant Editor*

# Contents

|   |     |
|---|-----|
| <b>Introduction</b>   | 1   |
| <b>J-Integral Estimates for Strain Hardening Materials in Antiplane Shear</b>   |     |
| Using Fully Plastic Solutions—C. F. SHIH  | 3   |
| Fully Plastic Problem for Antiplane Shear   | 4   |
| Estimation Procedures for Two Strain-Hardening Laws   | 9   |
| An Assessment of the Proposed Estimation Procedures   | 14  |
| Conclusion  | 18  |
| <b>Single Specimen Tests for <math>J_{Ic}</math> Determination—G. A. CLARKE, W. R. ANDREWS, P. C. PARIS, AND D. W. SCHMIDT</b>  | 27  |
| Theoretical Considerations  | 28  |
| Material  | 32  |
| Test Procedures   | 32  |
| Results   | 34  |
| Discussion  | 37  |
| Conclusions   | 42  |
| <b>Elastic Plastic (<math>J_{Ic}</math>) Fracture Toughness Values: Their Experimental Determination and Comparison with Conventional Linear Elastic (<math>K_{Ic}</math>) Fracture Toughness Values for Five Materials—W. A. LOGSDON</b> | 43  |
| Materials and Specimens   | 45  |
| Experimental Procedure  | 46  |
| Results and Discussion  | 49  |
| Conclusions   | 58  |
| <b>Application of the J-Integral to the Initiation of Crack Extension in a Titanium 6Al-4V Alloy—G. R. YODER AND C. A. GRIFFIS</b>  | 61  |
| Experimentation   | 63  |
| Results and Discussion  | 67  |
| Summary   | 79  |
| <b>Fatigue Crack Growth During Gross Plasticity and the J-Integral—N. E. DOWLING AND J. A. BEGLEY</b>   | 82  |
| Preliminary   | 82  |
| Experimental Techniques   | 88  |
| Test Results  | 94  |
| Discussion  | 97  |
| Conclusions   | 101 |
| Recommendations   | 101 |
| <b>A Simple Method for Measuring Tearing Energy of Nicked Rubber Strips—H. L. OH</b>  | 104 |
| Existing Methods for Measuring Tearing Energy   | 105 |
| J-Integral Method for Measuring Tearing Energy  | 109 |
| Experimental Implementation on the Simple Extension Specimen  | 111 |
| Concluding Remarks  | 113 |

|   |     |
|---|-----|
| <b>A Study of Plane Stress Fracture in the Large-Scale Plastic Yielding Regime—</b>           |     |
| G. E. TARDIFF, JR., B. A. KUHN, AND L. A. HELDT   | 115 |
| Experimental Details  | 116 |
| Results and Discussion  | 119 |
| Conclusions   | 125 |
| <br>  |     |
| <b>A Fracture Mechanics Approach to Creep Crack Growth—J. D. LANDRES</b>                      |     |
| AND J. A. BEGLEY  | 128 |
| C*-Parameter  | 130 |
| Experimental Technique  | 133 |
| Results   | 138 |
| Discussion  | 145 |
| Conclusions   | 147 |
| <br>  |     |
| <b>Creep Cracking in 2219-T851 Plate at Elevated Temperatures—J. G.</b>                       |     |
| KAUFMAN, K. O. BOGARDUS, D. A. MAUNEY, AND R. C. MALCOLM                                      | 149 |
| Object  | 151 |
| Material  | 151 |
| Procedure   | 151 |
| Results   | 153 |
| Discussion of Results   | 156 |
| Summary   | 165 |
| <br>  |     |
| <b>Investigation of R-Curve Using Comparative Tests with Center-Cracked-</b>                  |     |
| <b>Tension and Crack-Line-Wedge-Loaded Specimens—D. Y. WANG</b>                               |     |
| AND D. E. MCCABE  | 169 |
| Validity of Plane Stress Fracture Toughness, $K_{Ic}$   | 170 |
| Program and Procedure   | 171 |
| Results and Discussion  | 173 |
| Prediction of CCT Panel Instability   | 175 |
| General Observations  | 181 |
| Specimen Size Limitations   | 183 |
| Conclusions   | 185 |
| <br>  |     |
| <b>Ductility, Fracture Resistance, and R-Curves—VCLKER WEISS AND</b>                          |     |
| MUKULESH SENGUPTA   | 194 |
| Foundations of the Model  | 195 |
| Thickness Effect  | 201 |
| R-Curves  | 203 |
| <br>  |     |
| <b>What R-Curves Can Tell Us About Specimen Size Effects in the <math>K_{Ic}</math> Test—</b> |     |
| R. L. LAKE  | 208 |
| Material  | 209 |
| Procedure   | 209 |
| Results and Discussion  | 211 |
| Conclusions   | 218 |
| <br>  |     |
| <b>Effect of Specimen Size on Fracture Toughness of a Titanium Alloy—</b>                     |     |
| D. MUNZ, K. H. GALDA, AND F. LINK   | 219 |
| Characteristic Values of Fracture Mechanics   | 220 |
| Effect of Thickness on $K_{Ic}$   | 222 |
| Procedure   | 225 |
| Results   | 226 |
| Discussion  | 230 |
| Conclusions   | 232 |
| <br>  |     |
| <b>Resistance to Plane-Stress Fracture (R-Curve Behavior) of A572 Structural</b>              |     |
| <b>Steel—S. R. NOVAK</b>  | 235 |
| Summary   | 236 |

|  |     |
|--|-----|
| <b>Running Ductile Fracture in a Pressurized Line Pipe—L. B. FREUND,<br/>D. M. PARKS, AND J. R. RICE</b>   | 243 |
| Deformation Field  | 245 |
| Distribution of Applied Pressure   | 248 |
| Equation of Motion for the Pipe Wall   | 249 |
| Rigid-Perfect Plastic Model  | 251 |
| Linear Pressure Decay  | 257 |
| Effects of Wall Inertia  | 259 |
| Concluding Discussion  | 260 |
| <b>Mixed-Mode Fracture of Shear Panels—A Finite Element Analysis—S. T.<br/>CHIU AND A. F. LIU</b>  | 263 |
| Shear Panel Finite Element Model   | 265 |
| Mixed-Mode Fracture Criteria   | 268 |
| Results and Discussion   | 269 |
| Conclusions  | 279 |
| <b>A Finite-Element Analysis of Fatigue Crack Closure—J. D. NEWMAN, JR.</b>  | 281 |
| Finite-Element Analysis  | 283 |
| Application of the Finite-Element Analysis to Cyclic Crack Extension   | 288 |
| Concluding Remarks   | 300 |
| <b>A Preliminary Study of Fatigue Crack Retardation Using Laser Interferometry to Measure Crack Surface Displacements—W. N. SHARPE, JR.,<br/>AND A. F. GRANDT, JR.</b> | 302 |
| Experimental Procedure   | 304 |
| Crack Displacement Profiles and Opening Load Determination   | 306 |
| Overload Experiments   | 313 |
| Concluding Remarks   | 316 |
| <b>Effect of Stress Ratio and Overload Ratio on Fatigue Crack Delay and Arrest Behavior Due to Single Peak Overloads—M. K. HIMMELEIN<br/>AND B. M. HILLBERRY</b>       | 321 |
| Experimental Procedure   | 323 |
| Test Procedure   | 324 |
| Results  | 325 |
| Conclusion   | 329 |
| <b>Predicting Fatigue Crack Retardation Following a Single Overload Using a Modified Wheeler Model—T. D. GRAY AND J. P. GALLAGHER</b>                                  | 331 |
| Model Development  | 333 |
| Data Correlation   | 338 |
| Summary  | 344 |
| <b>Cyclic Crack Growth Analysis for Notched Structures at Elevated Temperatures—R. M. GAMBLE AND P. C. PARIS</b>   | 345 |
| Nature of the Problem  | 346 |
| Initial Cyclic Crack Growth Predictions for Turbine Disks  | 349 |
| Cyclic Crack Growth from Notches—A General Method  | 360 |
| Further Discussion   | 364 |
| Conclusions  | 366 |
| <b>Practical Method for Calculating Stress-Intensity Factors Through Weight Functions—R. LABBENS, A. PELLISSIER-TANOR, AND J. HELIOT</b>                               | 368 |
| Existence of an Influence Function   | 368 |
| Relationship Between the Influence Function and the Compliance   | 370 |
| Weight Function  | 371 |

|   |     |
|---|-----|
| Calculation of the Crack Opening Displacement in a Dugdale Model  | 373 |
| Calculation of Weight Functions by Finite Element   | 373 |
| Checking the Method   | 375 |
| Weight Functions for Plane and Cylindrical Problems   | 377 |
| Comparison with Another Method  | 380 |
| Conclusion  | 383 |
| <b>Stress Intensity Factor Solutions for Continuous Surface Flaws in Reactor Pressure Vessels—C. B. BUCHALET AND W. H. BAMFORD</b>                    | 385 |
| Method  | 387 |
| Stress Intensity Factor Solutions   | 390 |
| Conclusion  | 400 |
| <b>Residual Life Estimates for Structures with Partial Thickness Cracks—P. M. BESUNER</b>   | 403 |
| Residual Life Prediction Procedure  | 406 |
| An Influence Function Theory for the Computation of $\bar{K}_i$   | 410 |
| Stress Intensity Factor and Residual Lifetime Computations for the Two DOF Buried Ellipse   | 414 |
| Summary and Conclusions   | 418 |
| <b>Application of Fracture Mechanics to the Calculation of Deflections in Stepped Structural Elements—J. I. BLUHM</b>                                 | 420 |
| Concept   | 422 |
| Illustration  | 425 |
| Conclusion  | 428 |
| <b>Stress Intensity Factors for Through and Part-Through Cracks Originating at Fastener Holes—R. C. SHAH</b>  | 429 |
| Formulation of Procedure  | 431 |
| Verification of Procedure   | 433 |
| Application of Procedure  | 437 |
| Estimation of SIF's for Quarter-Elliptical Cracks in a Plate  | 453 |
| Discussion  | 454 |
| Conclusions   | 455 |
| <b>Stress Intensity Factors for Deep Cracks Emanating from the Corner Formed by a Hole Intersecting a Plate Surface—J. J. MCGOWAN AND C. W. SMITH</b> | 460 |
| Analytical Considerations   | 462 |
| Experiments   | 464 |
| Analytical Comparisons  | 470 |
| Problems Characterization and Conclusions   | 471 |
| <b>Stress Intensity Factor of a Corner Crack—A. S. KOBAYASHI AND A. N. ENETANYA</b>   | 477 |
| Method of Approach  | 478 |
| Quarter-Elliptical Crack Within a Quarter-Infinite Solid  | 488 |
| Discussion  | 491 |

## Introduction

---

The content of this book continues to present the state of the art in "Fracture Mechanics Applications and Research" as exemplified by earlier symposium volumes, that is, ASTM Special Technical Publications 513 and 514 (1972), 536 (1973), and 559 and 560 (1974). The themes of fracture mechanics analysis which continue to be dominant interests in this book are applications to elastic-plastic fracture through J-integral methods, instability and material property analysis through R-curve methods, fatigue crack growth phenomena and life estimation, creep cracking analysis, and applications of fracture mechanics to particular engineering problems in fracture control.

The success of the Eighth National Symposium, as evidenced by the papers in this volume, is largely due, not only to the authors, but also to the many people associated with ASTM Committee E-24 who contribute enormously of their efforts toward assisting the symposium each year. Moreover, the effective assistance of Jane Wheeler and (the late) Donald Wisdom of the ASTM staff, as well as the crucial on-site coordination and assistance of John McLaughry, Director of Special Programs at Brown University, are especially cited as having been essential to the final result of producing this book.

*J. R. Rice*, professor

*P. C. Paris*, visiting professor

Brown University, Providence, R. I.  
02912; symposium co-chairmen.

C. F. Shih<sup>1</sup>

## J-Integral Estimates for Strain Hardening Materials in Antiplane Shear Using Fully Plastic Solution

---

**REFERENCE:** Shih, C. F., “J-Integral Estimates for Strain Hardening Materials in Antiplane Shear Using Fully Plastic Solution,” *Mechanics of Crack Growth, ASTM STP 590*, American Society for Testing and Materials, 1976, pp. 3-26.

**ABSTRACT:** General procedures are proposed which utilize the elastic and the fully plastic solutions to interpolate behavior from the small-scale yielding range to the fully plastic range. The relations between the J-integral, load point displacement, crack opening displacement, and the applied load thus developed, are applicable to test configurations and cracked bodies in general. To assess the accuracy of the estimated relationships, a detailed numerical investigation, which employs an accurate finite element approach, is carried out for a particular configuration under antiplane shear. The results obtained from the full numerical calculations, for values of the applied load well into the fully plastic range, are in excellent agreement with the estimated results.

**KEY WORDS:** crack propagation, elastic properties, plastic properties, plastic deformation, stresses, strains, shear properties

In recent experiments, Begley and Landes [*I*]<sup>2</sup> have demonstrated the potential of the J-integral as a fracture initiation criterion in the large-scale yielding range. In this paper some relatively simple approximate formulas are proposed for estimating the relations between the path-independent integral, *J*, the applied stress, the load point displacement, and the crack opening displacement for cracked bodies of strain hardening elastic-plastic materials. The formulas make use of results from the elastic solutions and the fully plastic solutions to interpolate from the small-scale yielding range to the fully plastic range. The approximate interpolation

<sup>1</sup> Research fellow in applied mechanics, Division of Engineering and Applied Physics, Harvard University, Cambridge, Mass. 02138. Presently with Corporate Research and Development, General Electric Company, Schenectady, N. Y. 12345.

<sup>2</sup> The italic numbers in brackets refer to the list of references appended to this paper.

procedure is similar in a number of respects to that suggested by Bucci et al [2] for elastic-perfect plastic materials. The formulas apply to the fracture analysis of cracked bodies as well as the analysis of test specimens which sustain large-scale plasticity prior to fracture.

In the first part of the paper, the fully plastic solution to the problem of an edge crack in a finite width slab under antiplane shear is presented. Then the general estimation procedure to predict the relationships between  $J$ , the load point displacement, the applied stress, etc., in the large-scale yielding range is introduced. Finally a detailed assessment of the accuracy of the method is made. A particular configuration under antiplane shear is chosen for this assessment. Estimated predictions are compared to the full numerical calculations for materials characterized by two different stress-strain relations, the Ramberg-Osgood relation, and the piecewise power hardening relation.

### Fully Plastic Problem for Antiplane Shear

A discussion of fully plastic crack problems of the type considered here has been given by Goldman and Hutchinson [3]. In this paper attention is restricted to a small strain formulation of plasticity in antiplane shear. In simple shear the pure power hardening law is

$$\gamma/\gamma_0 = \alpha(\tau/\tau_0)^n \quad (1)$$

where  $\alpha$  is a dimensionless constant and  $\gamma_0$  and  $\tau_0$  are reference values of the strain and stress. The generalization of Eq 1 based on the  $J_2$  deformation theory of plasticity gives

$$\gamma_\beta/\gamma_0 = \alpha(\tau_e/\tau_0)^{n-1} \tau_\beta/\tau_0 (\beta = 1, 2) \quad (2)$$

where

$$\begin{aligned} \gamma_\beta &= \gamma_{\beta 3}, \\ \tau_\beta &= \tau_{\beta 3}, \text{ and,} \\ \tau_e^2 &= \tau_1^2 + \tau_2^2. \end{aligned}$$

The plane of the crack is taken to lie in the  $x_2 = 0$  plane with its edge along the  $x_3$  axis as shown in the insert in Fig. 1. The crack has length  $a$  and the width of the slab is  $b$ . The body is subjected to a remotely applied shear stress  $\tau_2 = \tau^\infty$  (at  $h = \infty$ ) and the edges  $x_1 = -a$  and  $x_1 = b - a$  are traction free. By symmetry this problem is equivalent to the center-cracked slab with crack length  $2a$  and width  $2b$  subjected to the same loading.

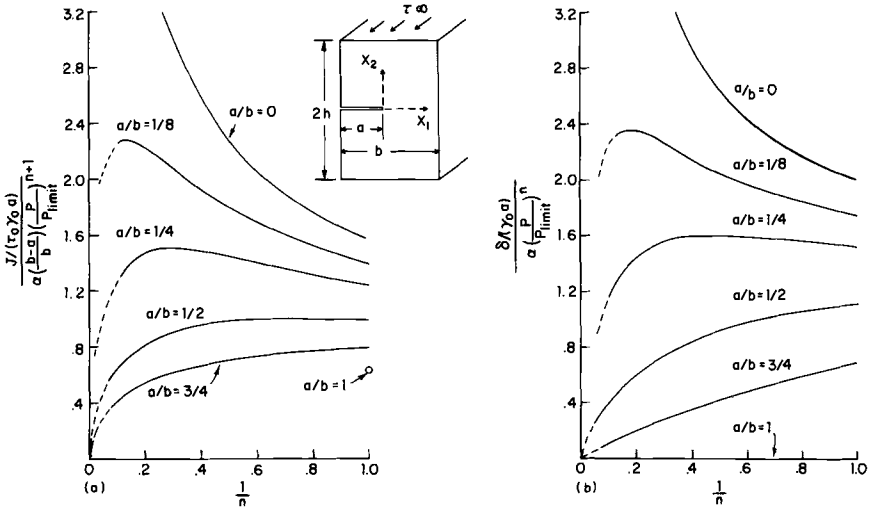


FIG. 1—Curves of  $J$  and  $\delta$  normalized with respect to the applied load  $P$ . Dotted lines are extrapolations. The results corresponding to  $a/b = 0$  are taken from Ref 7.

Within the context of a deformation theory of plasticity, the path-independent integral,  $J$ , is defined by [4,5]

$$J = \int_{\Gamma} (W dx_2 + \mathbf{T} \times \frac{\partial \mathbf{u}}{\partial x_1} ds) \quad (3)$$

where

- $W$  = strain energy density,
- $\Gamma$  = any contour in the  $x_1, x_2$  plane which encircles the crack tip,
- $\mathbf{T}$  = traction acting on  $\Gamma$ , and
- $\mathbf{u}$  = displacement vector.

Another quantity which will be examined in detail is the crack opening displacement at the edge of the slab denoted by  $\delta$ . This is defined as

$$\delta = w(x_1 = -a, x_2 = 0^+) - w(x_1 = -a, x_2 = 0^-) \quad (4)$$

where  $w(x_1, x_2)$  is the displacement in the  $x_3$  direction.

As discussed in Ref 3, the solution to a traction boundary value problem based on Eq 2 has the simple functional form

$$\begin{aligned} \tau_{\beta}/\tau_0 &= (\tau^{\infty}/\tau_0) \hat{\tau}_{\beta}(x_1/a, x_2/a, a/b, n) \\ \gamma_{\beta}/\gamma_0 &= \alpha (\tau^{\infty}/\tau_0)^n \hat{\gamma}_{\beta}(x_1/a, x_2/a, a/b, n) \\ w/(\gamma_0 a) &= \alpha (\tau^{\infty}/\tau_0)^n \hat{w}(x_1/a, x_2/a, a/b, n) \end{aligned} \quad (5)$$

## 6 MECHANICS OF CRACK GROWTH

Furthermore, for the J-integral and the crack opening displacement,  $\delta$

$$J = \alpha \tau_0 \gamma_0 a (\tau_\infty / \tau_0)^{n+1} \hat{J}(a/b, n) \quad (6a)$$

$$\delta = \alpha \gamma_0 a (\tau_\infty / \tau_0)^n \hat{\delta}(a/b, n) \quad (6b)$$

where the quantities topped by (^) are dimensionless functions. It may be noted that the functional form of Eq 6b also applies to other displacement-like quantities, notably the residual load-point displacement which will be defined later. The character of the solution to the field quantities, as expressed by Eq 5, demonstrates that this solution is valid for both  $J_2$  deformation and  $J_2$  flow theory as long as the applied stress is increased monotonically.

Define  $P$  to be the total shear load per unit thickness carried by the slab, that is

$$P = \tau^\infty b \quad (7)$$

and denote by  $P_{\text{limit}}$  the limit load for a perfectly plastic slab ( $n = \infty$ ), that is

$$P_{\text{limit}} = \tau_0 (b - a) \quad (8)$$

A convenient normalization of  $J$  for tabulation purposes based on Eq 6a is in Ref 3

$$\frac{J / (\tau_0 \gamma_0 a)}{\alpha \left( \frac{b - a}{b} \right) \left( \frac{P}{P_{\text{limit}}} \right)^{n+1}} = f_1(a/b, n) \quad (9)$$

Similarly, a suitable normalization of  $\delta$  is

$$\frac{\delta / (\gamma_0 a)}{\alpha \left( \frac{P}{P_{\text{limit}}} \right)^n} = f_2(a/b, n) \quad (10)$$

Values of  $f_1$  and  $f_2$  were calculated using an accurate finite element method which is discussed briefly in the Appendix. These values are given in Table 1 and are presented graphically in Fig. 1 in the form of plots of  $f_1$  and  $f_2$  as a function of  $1/n$  for several values of  $a/b$ .<sup>3</sup>

<sup>3</sup> The specimen configuration with  $h/b = 3$  was used in all the finite element calculations. For purposes of numerical crack analyses, this configuration may be regarded as a slab of finite width and infinite height.

TABLE 1—Values of  $f_1$  to  $f_5$ .<sup>a</sup>

| a/b \ n                     |       | n      |        |        |        |        |        |        |        |        |
|-----------------------------|-------|--------|--------|--------|--------|--------|--------|--------|--------|--------|
|                             |       | 1      | 1.5    | 2      | 3      | 5      | 7      | 10     | 15     | 20     |
| $\frac{a}{b} = 0$           | $f_1$ | 1.5708 | 1.9389 | 2.2709 | 2.8638 | 3.8654 | ...    | 5.7878 | ...    | 8.5240 |
|                             | $f_2$ | 2.0000 | 2.3338 | 2.6444 | 3.2090 | 4.1748 | ...    | 6.0445 | ...    | 8.7267 |
|                             | $f_3$ | 0.3927 | 0.4722 | 0.5281 | 0.6050 | 0.6957 | ...    | 0.7999 | ...    | 0.8765 |
|                             | $f_4$ | 0.0    | 0.0    | 0.0    | 0.0    | 0.0    | 0.0    | 0.0    | 0.0    | 0.0    |
|                             | $f_5$ | 0.0    | 0.0    | 0.0    | 0.0    | 0.0    | 0.0    | 0.0    | 0.0    | 0.0    |
| $\frac{a}{b} = \frac{1}{8}$ | $f_1$ | 1.3899 | 1.6206 | 1.7916 | 2.0232 | 2.2301 | 2.2855 | 2.2214 |        |        |
|                             | $f_2$ | 1.7465 | 1.9221 | 2.0544 | 2.2266 | 2.3544 | 2.3442 | 2.2404 |        |        |
|                             | $f_3$ | 0.3987 | 0.4772 | 0.5324 | 0.6088 | 0.6984 | 0.7553 | 0.8036 |        |        |
|                             | $f_4$ | 0.1717 | 0.2489 | 0.3289 | 0.4895 | 0.7843 | 1.0216 | 1.2665 |        |        |
|                             | $f_5$ | 0.0983 | 0.1295 | 0.1601 | 0.2198 | 0.3331 | 0.4358 | 0.5653 |        |        |
| $\frac{a}{b} = \frac{1}{4}$ | $f_1$ | 1.2423 | 1.3744 | 1.4467 | 1.5065 | 1.4795 | 1.3892 | 1.2670 |        |        |
|                             | $f_2$ | 1.5268 | 1.5820 | 1.6017 | 1.5813 | 1.4532 | 1.3113 | 1.2163 |        |        |
|                             | $f_3$ | 0.3997 | 0.4799 | 0.5353 | 0.6133 | 0.7086 | 0.7644 | 0.8211 |        |        |
|                             | $f_4$ | 0.3002 | 0.4076 | 0.5060 | 0.6706 | 0.8779 | 0.9658 | 1.0541 |        |        |
|                             | $f_5$ | 0.1966 | 0.2577 | 0.3159 | 0.4241 | 0.6041 | 0.7365 | 0.8666 |        |        |
| $\frac{a}{b} = \frac{1}{2}$ | $f_1$ | 1.0006 | 1.0044 | 0.9836 | 0.9250 | 0.8148 | 0.7316 | 0.6350 | 0.5310 | 0.4668 |
|                             | $f_2$ | 1.1116 | 1.0176 | 0.9281 | 0.7798 | 0.5899 | 0.4824 | 0.3893 | 0.3042 | 0.2598 |
|                             | $f_3$ | 0.4049 | 0.4878 | 0.5501 | 0.6444 | 0.7675 | 0.8416 | 0.8963 | 0.9448 | 0.9609 |
|                             | $f_4$ | 0.4381 | 0.5128 | 0.5561 | 0.5830 | 0.5373 | 0.4687 | 0.3875 | 0.3042 | 0.2598 |
|                             | $f_5$ | 0.3942 | 0.5040 | 0.5992 | 0.7477 | 0.9109 | 0.9716 | 0.9954 | 0.9998 | 1.0000 |
| $\frac{a}{b} = \frac{3}{4}$ | $f_1$ | 0.8046 | 0.7502 | 0.7035 | 0.6329 | 0.5414 | 0.4803 | 0.4121 |        |        |
|                             | $f_2$ | 0.6818 | 0.5258 | 0.4220 | 0.3020 | 0.2026 | 0.1606 | 0.1272 |        |        |
|                             | $f_3$ | 0.4327 | 0.5475 | 0.6415 | 0.7808 | 0.9194 | 0.9707 | 0.9956 |        |        |
|                             | $f_4$ | 0.4049 | 0.3843 | 0.3501 | 0.2836 | 0.2014 | 0.1607 | 0.1272 |        |        |
|                             | $f_5$ | 0.5939 | 0.7310 | 0.8295 | 0.9389 | 0.9942 | 1.0000 | 1.0000 |        |        |

<sup>a</sup> The results corresponding to  $a/b = 0$  are taken from Ref 7.

For the linear elastic case ( $n = 1$ ) the solution is known exactly for all  $a/b$  [6], for the finite crack in an infinitely wide slab ( $a/b = 0$ ) analytical solutions have been obtained for the complete range of  $n$  by Amazigo [7]. The curves corresponding to  $a/b = 0$  have been taken from this reference. In the present numerical calculations,  $f_1$  and  $f_2$  have been obtained for values of the strain hardening exponent up to  $n = 10$  ( $n = 20$  for case of  $a/b = 1/2$ ). The sections of the curves indicated by dashed lines are extrapolations.

The relation between  $J$  and the crack opening displacement,  $\delta$ , can be obtained by eliminating  $P/P_{\text{limit}}$  from Eqs 9 and 10 with the result

$$\frac{J/(\tau_0 \gamma_0 a)}{\alpha^{-1/n} (\delta/\gamma_0 a)^{(n+1)/n}} = f_3(a/b, n) \quad (11)$$

where  $f_3$  involves  $f_1$  and  $f_2$  and is also given in Table 1. This relationship, Eq 11, is shown in Fig. 2. It may be noted that in the limit of perfect plasticity ( $n \rightarrow \infty$ )  $J = \tau_0 \delta$  for all  $a/b$ .

## 8 MECHANICS OF CRACK GROWTH

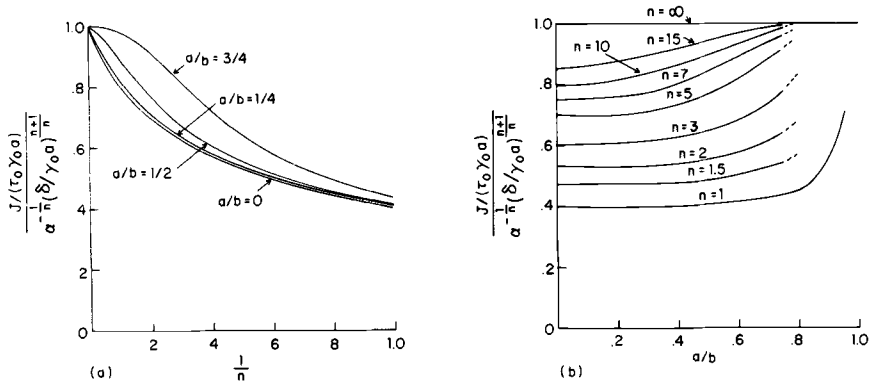


FIG. 2—Curves of  $J$  normalized with respect to  $\delta$ . In Fig. 2a the curve for  $a/b = 1/8$  is not shown since it practically coincides with the curve for  $a/b = 0$ .

We will later want to estimate the load point displacement of a slab of finite height. For this purpose let  $\Delta$  be the load point displacement of a slab of height  $2h$  where the stress is applied at  $x_2 = \pm h$  according to  $\tau_2 = \tau^\infty$ , as shown in the insert in Fig. 1, that is

$$\Delta(h) = \frac{1}{b} \int_{-a}^{b-a} [w(x_1, h) - w(x_1, -h)] dx_1 \quad (12)$$

For finite values of  $n$ ,  $\Delta \rightarrow \infty$  as  $h \rightarrow \infty$  with all other quantities remaining constant. For an uncracked slab of height  $2h$ ,  $\Delta$  is given by  $2h\gamma^\infty$  where  $\gamma^\infty/\gamma_0 = \alpha(\tau^\infty/\tau_0)^n$ . Define a residual load point displacement for the cracked body according to the well defined limit

$$\Delta_c = \lim_{h \rightarrow \infty} [\Delta(h) - 2h\gamma^\infty] \quad (13)$$

For purposes of fracture analyses of cracked bodies, the load point displacement for a slab of finite height,  $2h$ , is approximated very accurately by

$$\Delta(h) = \Delta_c + 2h\gamma^\infty \quad (14)$$

as long as  $h/b$  is greater than about 2. Values of  $f_4$  are tabulated in Table 1 where  $f_4$  is defined by

$$\frac{\Delta_c/(\gamma_0 a)}{\alpha(P/P_{\text{limit}})^n} = f_4(a/b, n) \quad (15)$$

Using Eqs 10 and 15, it can be seen that

$$\Delta_c/\delta = f_3(a/b, n) \quad (16)$$

where  $f_3 = f_4/f_2$  is given in Table 1 and is plotted in Fig. 3. Note that in the limit of perfect plasticity ( $n \rightarrow \infty$ ),  $\Delta_c = \Delta = \delta$  for all  $a/b$ .

### Estimation Procedures for Two Strain-Hardening Laws

In this section simple procedures to estimate large-scale yielding behavior utilizing only the linear elastic and the fully plastic solutions are proposed. These procedures are valid for cracked bodies subjected to in plane or out of plane loadings. However, in this paper they will be illustrated in the context of the antiplane shear problem. The accuracy of these procedures will be assessed in the next section.

First we introduce the estimation procedure for a material governed by the stress-strain law due to Ramberg and Osgood which for pure shear takes the form

$$\gamma/\gamma_0 = \tau/\tau_0 + \alpha(\tau/\tau_0)^n \quad (17)$$

To motivate our proposal, consider an infinitely wide slab of height  $2h$  with a semi-infinite slit as shown in Fig. 4a. The clamped boundaries are given constant shearing displacements, that is,  $w(x_1, h) = w_0$  and  $w(x_1, -h) = -w_0$ . For this problem  $J$  can be calculated exactly [4]. Let the shear stress,  $\tau_2$ , far ahead of the crack be denoted by  $\tau^\infty$ , then  $J$  is given by

$$J/(2h\tau_0\gamma_0) = \frac{1}{2}(\tau^\infty/\tau_0)^2 + \alpha\left(\frac{n}{n+1}\right)(\tau^\infty/\tau_0)^{n+1} \quad (18)$$

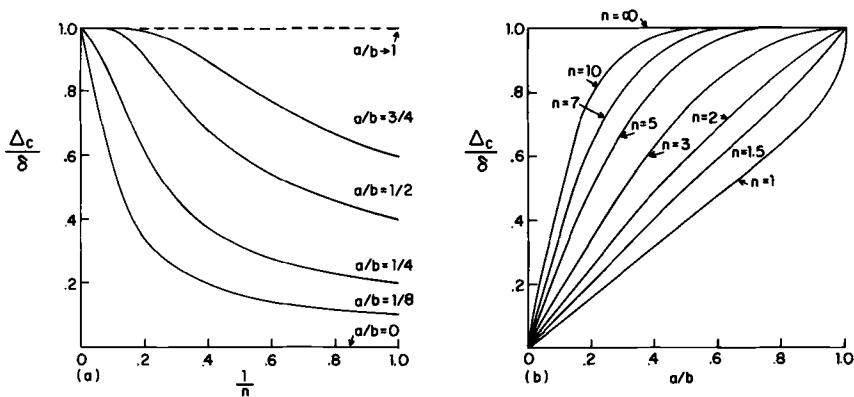


FIG. 3—Ratio of the residual load point displacement to the crack opening displacement.

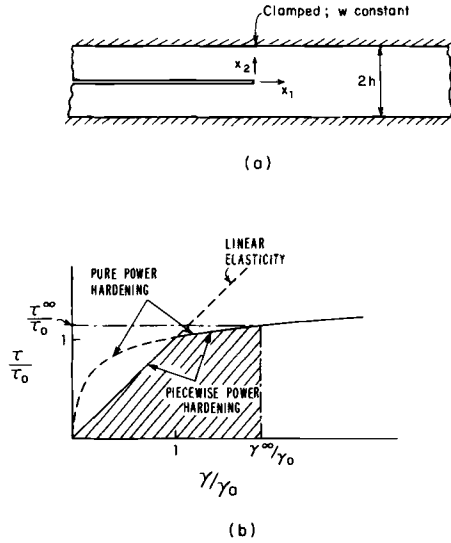


FIG. 4—(a) Infinitely wide slab with semi-infinite slit, (b) stress-strain curves for pure shear.

Note also that the solution to the fully plastic problem for the configuration of Fig. 4a is (using the notation of Eq 6a) of the form

$$J = 2h\alpha\tau_0\gamma_0(\tau^\infty/\tau_0)^{n+1}\bar{f}_1(n) \tag{19}$$

where for this problem  $\bar{f}_1(n) = n/(n + 1)$ . Furthermore, in the case of antiplane shear, Eq 19 holds without modification for the value of  $J$  corresponding to linear elasticity ( $n = 1$ ).<sup>4</sup> Thus, in terms of the dimensionless number  $\bar{f}_1(n)$ , the solution, Eq 18, for the infinitely wide slab may be rewritten as

$$J/(2h\tau_0\gamma_0) = (\tau^\infty/\tau_0)^2\bar{f}_1(n = 1) + \alpha(\tau^\infty/\tau_0)^{n+1}\bar{f}_1(n) \tag{20}$$

Guided by Eq 20, an obvious candidate for approximating the relation between  $J$  and  $P$  for the slab of width  $b$  and crack length  $a$  is

$$\frac{J}{\tau_0\gamma_0a[(b - a)/b]} = \left(\frac{P}{P_{\text{limit}}}\right)^2 f_1(a/b, n = 1) + \alpha\left(\frac{P}{P_{\text{limit}}}\right)^{n+1} f_1(a/b, n) \tag{21}$$

<sup>4</sup> In plane strain problems,  $f_1(n = 1)$  is a function of Poisson's ratio.

where  $f_1(a/b, n)$  was defined in Eq 9 and recall  $P = \tau^\infty b$  and  $P_{\text{limit}} = \tau_0(b - a)$ . Note that for sufficiently small values of  $P/P_{\text{limit}}$ , Eq 21 reduces to the well-known linear elastic solution while for large  $P/P_{\text{limit}}$  Eq 21 approaches the fully plastic prediction, as it should.

To obtain a more refined approximate relationship, we follow Bucci et al [2] and modify the linear elastic contribution using Irwin's idea of a plastically adjusted crack length. For example, for an elastic-perfect plastic material ( $n = \infty$ ) the second term in Eq 21 makes no contribution for  $P/P_{\text{limit}} < 1$ . But it is known that the linear elastic prediction starts to noticeably underestimate the actual value of  $J$  when  $P$  exceeds  $0.5 P_{\text{limit}}$ . To account for this discrepancy in an approximate manner, we replace Eq 21 by

$$\frac{J}{\tau_0 \gamma_0 a [(b - a)/b]} = \left( \frac{P}{P_{\text{limit}}} \right)^2 \chi f_1(a_{\text{eff}}/b, n = 1) + \alpha \left( \frac{P}{P_{\text{limit}}} \right)^{n+1} f_1(a/b, n) \quad (22)^5$$

where

$$a_{\text{eff}} = a + r_y \quad (23a)$$

and

$$\chi = \left( \frac{a_{\text{eff}}}{a} \right) \left( \frac{b - a}{b - a_{\text{eff}}} \right) \quad (23b)$$

The adjustment to the crack length for strain hardening material is given by

$$r_y = \frac{1}{2\pi} \left( \frac{n - 1}{n + 1} \right) \left( \frac{K_{\text{III}}}{\tau_0} \right)^2 \quad (24)$$

where  $K_{\text{III}}$  is the elastic stress intensity factor, and the introduction of  $(n - 1)/(n + 1)$  takes into account strain hardening in a manner consistent with the small-scale yielding antiplane shear solutions [5]. In Irwin's original proposal, the value of  $K_{\text{III}}$  in Eq 24 is a function of  $a_{\text{eff}}$ , thus, Eq 24 gives an implicit relation for  $r_y$ . To simplify the approximation procedure, we follow Bucci et al [2] and calculate  $K_{\text{III}}$  based on the original crack length  $a$ . For the present crack problem,  $K_{\text{III}}$  can be related to  $f_1(a/b, 1)$  but it may be more conveniently expressed by the exact formula

$$K_{\text{III}} = \frac{P}{b} \sqrt{\pi a} \sqrt{\frac{2b}{\pi a} \tan \frac{\pi a}{2b}} \quad (25)$$

<sup>5</sup> In the original report, Harvard University Report DEAP S-10, the factor  $\chi$  should appear in the Eqs 22, 26, 27, 31, 32, and 33, as indicated in this paper. The calculations in that report were performed with this additional factor.

From Eqs 23, 24, and 25 we have the simplest explicit adjustment to the elastic solution. The differences in the adjusted elastic solution due to the two slightly different definitions for  $a_{\text{eff}}$  are rather small, at least in this particular application. In the application of Eq 22,  $a_{\text{eff}}$  is calculated according to Eqs 23a, 24, and 25 for  $P \leq P_{\text{limit}}$ . For  $P > P_{\text{limit}}$ ,  $a_{\text{eff}}$  is taken to be the value associated with  $P = P_{\text{limit}}$ . Note that  $P_{\text{limit}}$  is calculated from Eq 8 based on the actual crack length.

Following the same line of reasoning, formulas for estimating the crack opening displacement and the residual load point displacement for the Ramberg-Osgood material are

$$\frac{\delta}{(\gamma_0 a)} = \left( \frac{P}{P_{\text{limit}}} \right) \chi f_2(a_{\text{eff}}/b, n = 1) + \alpha \left( \frac{P}{P_{\text{limit}}} \right)^n f_2(a/b, n) \quad (26)$$

and

$$\frac{\Delta_c}{(\gamma_0 a)} = \left( \frac{P}{P_{\text{limit}}} \right) \chi f_4(a_{\text{eff}}/b, n = 1) + \alpha \left( \frac{P}{P_{\text{limit}}} \right)^n f_4(a/b, n) \quad (27)$$

where  $a_{\text{eff}}$  is calculated according to the same prescription just given.

Next, consider the piecewise power hardening law which in pure shear is given by

$$\begin{aligned} \gamma/\gamma_0 &= \tau/\tau_0 \quad \text{for } \tau \leq \tau_0 \\ \gamma/\gamma_0 &= (\tau/\tau_0)^n \quad \text{for } \tau > \tau_0 \end{aligned} \quad (28)$$

According to Eq 28, the exact result for  $J$ , for the infinitely wide slab of Fig. 4a, is given in terms of the stress far ahead of the crack,  $\tau^\infty$ , by

$$\begin{aligned} J/(2h\tau_0\gamma_0) &= (\tau^\infty/\tau_0)^2/2 \quad \text{for } \tau^\infty \leq \tau_0 \\ &= 1/2 + [n/(n+1)] [(\tau^\infty/\tau_0)^{n+1} - 1] \quad \text{for } \tau^\infty > \tau_0 \end{aligned} \quad (29)$$

The right hand side of Eq 29 is just the shaded area under the stress-strain curve in Fig. 4b. In terms of the elastic and fully plastic solutions (see Eqs 19 and 20), Eq 29 may be rewritten as

$$\begin{aligned} J/(2h\tau_0\gamma_0) &= (\tau^\infty/\tau_0)^2 \bar{f}_1(n = 1) \quad \text{for } \tau^\infty \leq \tau_0 \\ &= \bar{f}_1(n = 1) + [(\tau^\infty/\tau_0)^{n+1} - 1] \bar{f}_1(n) \quad \text{for } \tau^\infty > \tau_0 \end{aligned} \quad (30)$$

where again  $\bar{f}_1(n) = n/(n+1)$ . The straightforward generalization, suggested by Eq 30, to the finite width slab is

$$\frac{J}{\tau_0 \gamma_0 a [(b-a)/b]} = \left( \frac{P}{P_{\text{limit}}} \right)^2 \chi f_1(a_{\text{eff}}/b, n = 1) \quad \text{for } P \leq P_{\text{limit}} \quad (31a)$$

$$= \chi f_1(a_{\text{eff}}/b, n = 1) + \left[ \left( \frac{P}{P_{\text{limit}}} \right)^{n+1} - 1 \right] f_1(a/b, n) \quad \text{for } P > P_{\text{limit}} \quad (31b)$$

where  $a_{\text{eff}}$  in Eq 31a is given by Eq 23 and where  $a_{\text{eff}}$  in Eq 31b is taken as the value associated with  $P = P_{\text{limit}}$ . Similarly, we propose the following formulas for estimating the crack opening displacement and the residual load point displacement for the piecewise power hardening material

$$\frac{\delta}{\gamma_0 a} = \left( \frac{P}{P_{\text{limit}}} \right) \chi f_2(a_{\text{eff}}/b, n = 1) \quad \text{for } P \leq P_{\text{limit}} \quad (32a)$$

$$= \chi f_2(a_{\text{eff}}/b, n = 1) + \left[ \left( \frac{P}{P_{\text{limit}}} \right)^n - 1 \right] f_2(a/b, n) \quad \text{for } P > P_{\text{limit}} \quad (32b)$$

and

$$\frac{\Delta_c}{\gamma_0 a} = \left( \frac{P}{P_{\text{limit}}} \right) \chi f_4(a_{\text{eff}}/b, n = 1) \quad \text{for } P \leq P_{\text{limit}} \quad (33a)$$

$$= \chi f_4(a_{\text{eff}}/b, n = 1) + \left[ \left( \frac{P}{P_{\text{limit}}} \right)^n - 1 \right] f_4(a/b, n) \quad \text{for } P > P_{\text{limit}} \quad (33b)$$

A quantity frequently measured in fracture toughness tests is the load point displacement. As mentioned earlier, this displacement may be estimated by using the simple formula

$$\Delta(h) = \Delta_c + 2h\gamma^\infty \quad (14)$$

where  $2h$  is the distance between the load points. For a Ramberg-Osgood material,  $\gamma^\infty$  and  $\Delta_c$  in Eq 14 are given by Eqs 17 and 27; for piecewise power hardening, they are given by Eqs 28 and 33. As long as  $h/b \geq 2$ , Eq 14 should be an excellent approximation to the load point displacement.

Thus far, expressions for  $J$ ,  $\delta$ ,  $\Delta_c$ , and  $\Delta$  have been given in terms of the load parameter  $P$ . The relationships between  $J$  and  $\delta$  and  $J$  and  $\Delta$  may be obtained by simply eliminating (numerically)  $P$  from the earlier expressions. Of particular interest is the relation of  $J$  to  $\Delta$ . Bucci et al [2]

proposed a procedure to approximate this relationship for an elastic-perfect plastic material. Adopting an approach similar to Ref 2, Rice et al [8] obtained analytical expressions for  $J$  in terms of  $\Delta$  and  $P$  based on elastic-plastic material behavior for several deeply notched configurations. In the nonhardening limit, the two procedures proposed in this section are equivalent to the procedure presented elsewhere [8].<sup>6</sup>

### An Assessment of the Proposed Estimation Procedures

For this assessment we have chosen the edge crack configuration with  $a/b = 1/2$  and  $h/b = 2$  subject to a uniform out of plane shear  $\tau^\infty$  (see insert in Fig. 1). Boundary value problems associated with this configuration, for material behavior governed by the stress-strain characterizations, Eqs 17 and 28, considered previously and generalized using  $J_2$  deformation theory, were solved by the finite element method. A brief description of the numerical calculations is given in the Appendix.

First we consider the boundary value problem associated with the Ramberg-Osgood characterization. Accurate numerical solutions corresponding to high ( $n = 3$ ) and ( $n = 10$ ) strain hardening were obtained for values of the applied load,  $P$ , well into the large-scale yielding range. In the stress-strain curve Eq 17,  $\alpha$  is taken to be  $3/7$ , which is the same choice made by Ramberg and Osgood for their tensile stress-strain relation. At each load level, the quantities  $J$ ,  $\delta$ , and  $\Delta$  are computed. These are tabulated in Table 2 for values of  $P$  ranging from  $0.6P_{\text{limit}}$  to  $2P_{\text{limit}}$ . The corresponding estimated values due to the proposed formulas for the Ramberg-Osgood material are given in Table 3. A comparison of the calculated and estimated values, for both cases of high- and low-strain hardening, reveals that they are in excellent agreement. The relationships between  $J$  and  $P$ ,  $\Delta$  and  $P$ , and  $J$  and  $\Delta$  are plotted in Figs. 5 to 7. The latter relationship is obtained by numerically eliminating  $P$  from the first two relationships.

In these figures, the linear elastic solution (without plasticity adjustment) and the fully plastic solution are given by Curves 1 and 2, respectively. The rigid-perfect plastic curve is included to illustrate the influence of strain hardening. Curve 3 (dotted line) represents the estimated results due to the proposed Eqs 22, 27, and 14. The results from the full numerical calculations are given by Curve 4.<sup>7</sup>

These same relationships for the piecewise power hardening material,

<sup>6</sup> In Ref 2, the perfect plastic portion of the  $J - \Delta$  relationship parallels the rigid-perfect plastic solution and is tangent to the plastically adjusted elastic solution. In the procedure of Rice et al and in ours, the perfect plastic portion also parallels the rigid-perfect plastic solution, but it intersects the plastically adjusted elastic solution at values of  $J$  and  $\Delta$  associated with the attainment of limit load.

<sup>7</sup> When Curves 3 and 4 are too close to be identified separately in the figures, they are shown by a single curve.

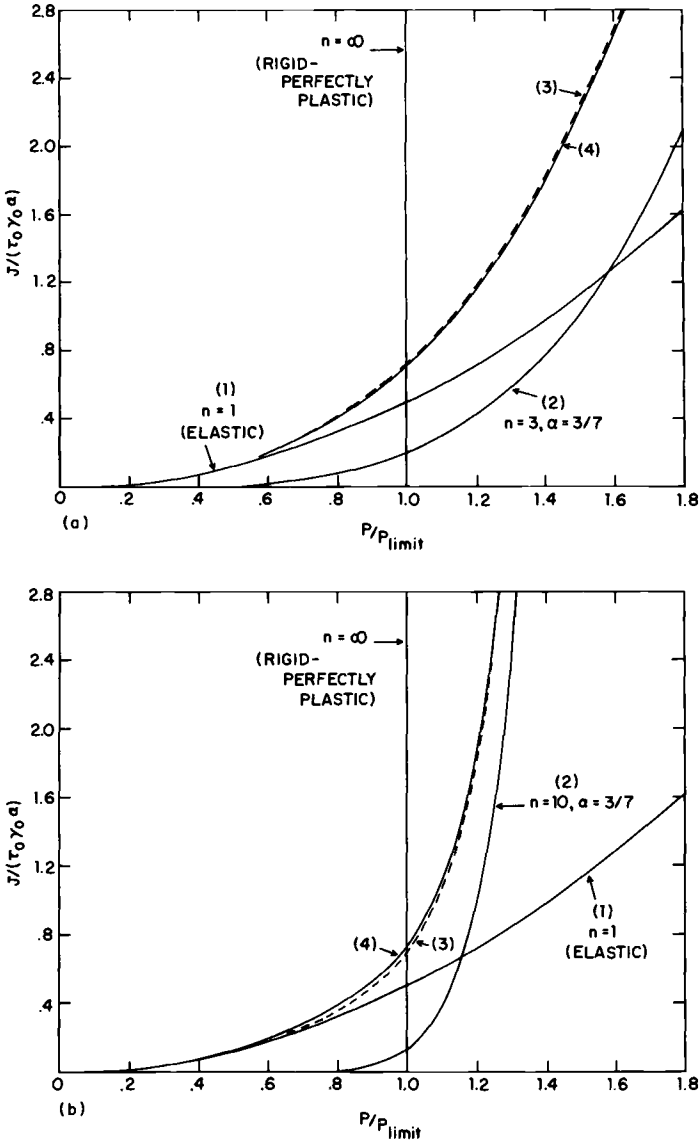
TABLE 2—Results from full numerical calculations for Ramberg-Osgood material.

| $n$      | $P/P_{\text{limit}}$   | $J/(\tau_0\gamma_0\alpha)$ | $\delta/(\gamma_0\alpha)$ | $\Delta/(\gamma_0\alpha)$ |         |
|----------|------------------------|----------------------------|---------------------------|---------------------------|---------|
| $n = 3$  | 0.60                   | 0.2095                     | 0.7507                    | 2.80                      |         |
|          | 0.80                   | 0.4120                     | 1.087                     | 3.913                     |         |
|          | 1.00                   | 0.720                      | 1.490                     | 5.143                     |         |
|          | 1.20                   | 1.166                      | 1.974                     | 6.535                     |         |
|          | 1.40                   | 1.794                      | 2.554                     | 8.124                     |         |
|          | $\alpha = \frac{3}{7}$ | 1.60                       | 2.652                     | 3.247                     | 9.941   |
|          |                        | 1.80                       | 3.800                     | 4.068                     | 12.02   |
|          |                        | 2.00                       | 5.294                     | 5.033                     | 14.39   |
| 0.60     |                        | 0.1965                     | 0.7135                    | 2.6969                    |         |
| $n = 10$ | 0.80                   | 0.3830                     | 1.0210                    | 3.6510                    |         |
|          | 1.00                   | 0.7310                     | 1.4680                    | 4.7379                    |         |
|          | 1.10                   | 1.100                      | 1.8681                    | 5.4616                    |         |
|          | 1.20                   | 1.845                      | 2.5967                    | 6.5226                    |         |
|          | $\alpha = \frac{3}{7}$ | 1.25                       | 2.490                     | 3.1814                    | 7.2787  |
|          |                        | 1.30                       | 3.410                     | 3.9917                    | 8.2653  |
|          |                        | 1.35                       | 4.751                     | 4.1108                    | 9.5668  |
|          |                        | 1.40                       | 6.652                     | 6.6469                    | 11.2933 |

Eq 28, are plotted in Figs. 8 to 10. An examination of the plots of  $J$  as a function of  $P$  and the  $\Delta$  as a function of  $P$  shows that in the immediate vicinity of  $P$  equal to  $P_{\text{limit}}$ , the estimated values of  $J$  and of  $\Delta$  may differ from the calculated values by as much as 15 percent. At higher load levels, these discrepancies diminish. Despite these differences, the estimated and calculated curves of  $J$  as a function of  $\Delta$  are in good agreement over the entire range of loading considered, for both cases of high- and low-strain hardening. This is particularly significant since it is from this

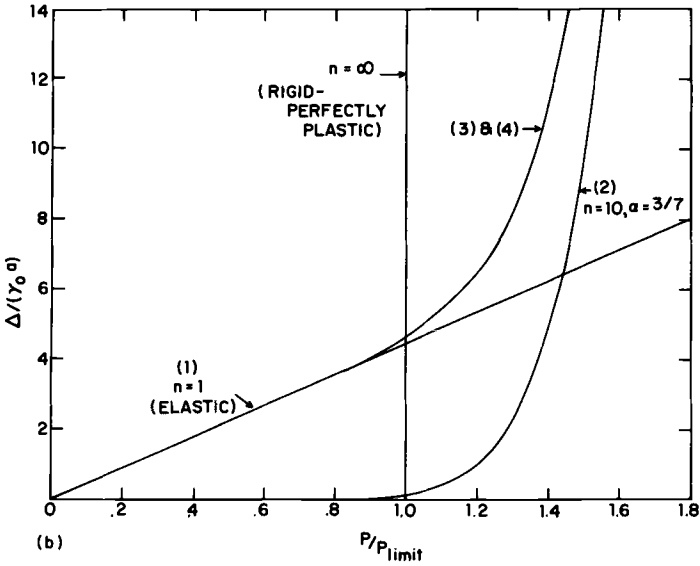
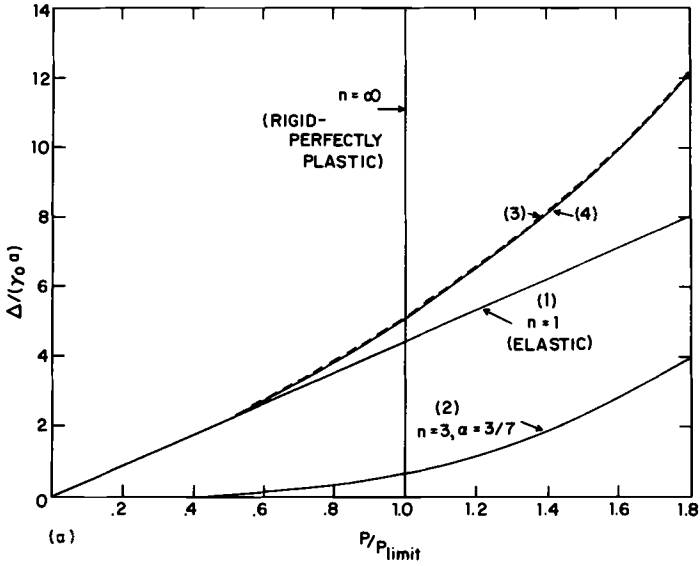
TABLE 3—Estimated results using Eqs 22, 26, and 27 for Ramberg-Osgood material.

| $n$      | $P/P_{\text{limit}}$   | $J/(\tau_0\gamma_0\alpha)$ | $\delta/(\gamma_0\alpha)$ | $\Delta/(\gamma_0\alpha)$ |        |
|----------|------------------------|----------------------------|---------------------------|---------------------------|--------|
| $n = 3$  | 0.60                   | 0.211                      | 0.770                     | 2.829                     |        |
|          | 0.80                   | 0.417                      | 1.128                     | 3.943                     |        |
|          | 1.00                   | 0.738                      | 1.573                     | 5.205                     |        |
|          | 1.20                   | 1.188                      | 2.064                     | 6.604                     |        |
|          | 1.40                   | 1.819                      | 2.651                     | 8.198                     |        |
|          | $\alpha = \frac{3}{7}$ | 1.60                       | 2.681                     | 3.350                     | 10.021 |
|          |                        | 1.80                       | 3.830                     | 4.178                     | 12.104 |
|          |                        | 2.00                       | 5.331                     | 5.151                     | 14.480 |
| 0.60     |                        | 0.189                      | 0.715                     | 2.695                     |        |
| $n = 10$ | 0.80                   | 0.358                      | 1.013                     | 3.642                     |        |
|          | 1.00                   | 0.702                      | 1.484                     | 4.755                     |        |
|          | 1.10                   | 1.075                      | 1.881                     | 5.484                     |        |
|          | 1.20                   | 1.832                      | 2.613                     | 6.552                     |        |
|          | $\alpha = \frac{3}{7}$ | 1.25                       | 2.479                     | 3.200                     | 7.310  |
|          |                        | 1.30                       | 3.411                     | 4.012                     | 8.297  |
|          |                        | 1.35                       | 4.750                     | 5.132                     | 9.597  |
|          |                        | 1.40                       | 6.658                     | 6.669                     | 11.321 |



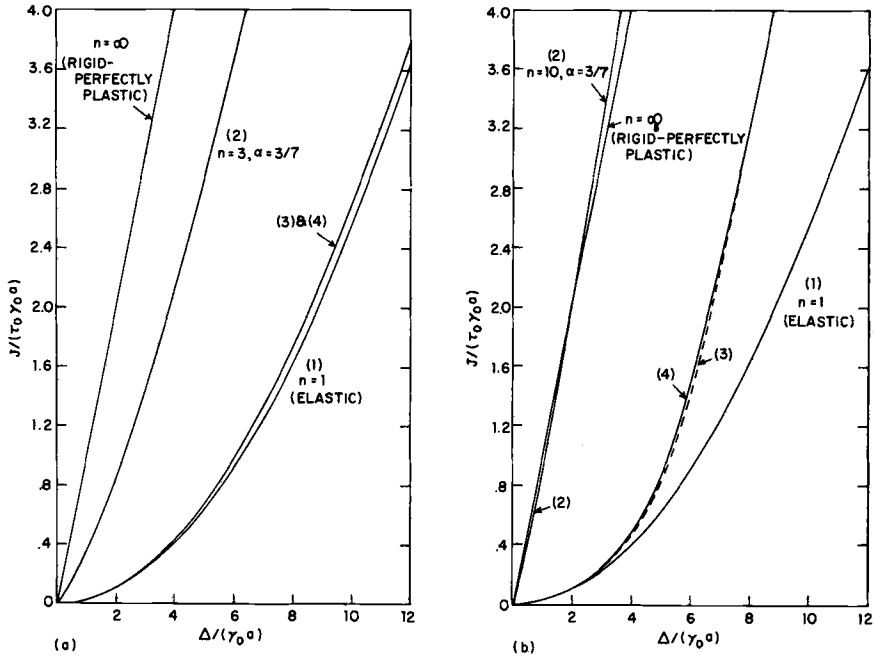
- (1) Linear elastic solution.
- (2) Fully plastic solution for pure power hardening material.
- (3) Predictions based on plastically adjusted elastic and fully plastic solutions.
- (4) Results from the full numerical solution for a Ramberg-Osgood material.

FIG. 5—Curves of  $J$  as a function of  $P$  for (a) high-strain hardening ( $n = 3$ ), (b) low-strain hardening ( $n = 10$ ).



- (1) Linear elastic solution.
- (2) Fully plastic solution for pure power hardening material.
- (3) Predictions based on plastically adjusted elastic and fully plastic solutions.
- (4) Results from the full numerical solution for a Ramberg-Osgood material.

FIG. 6—Curves of  $\Delta$  as a function of  $P$  for (a) high-strain hardening ( $n = 3$ ), (b) low-strain hardening ( $n = 10$ ).



- (1) Linear elastic solution.
- (2) Fully plastic solution for pure power hardening material.
- (3) Predictions based on plastically adjusted elastic and fully plastic solution.
- (4) Results from the full numerical solution for a Ramberg-Osgood material.

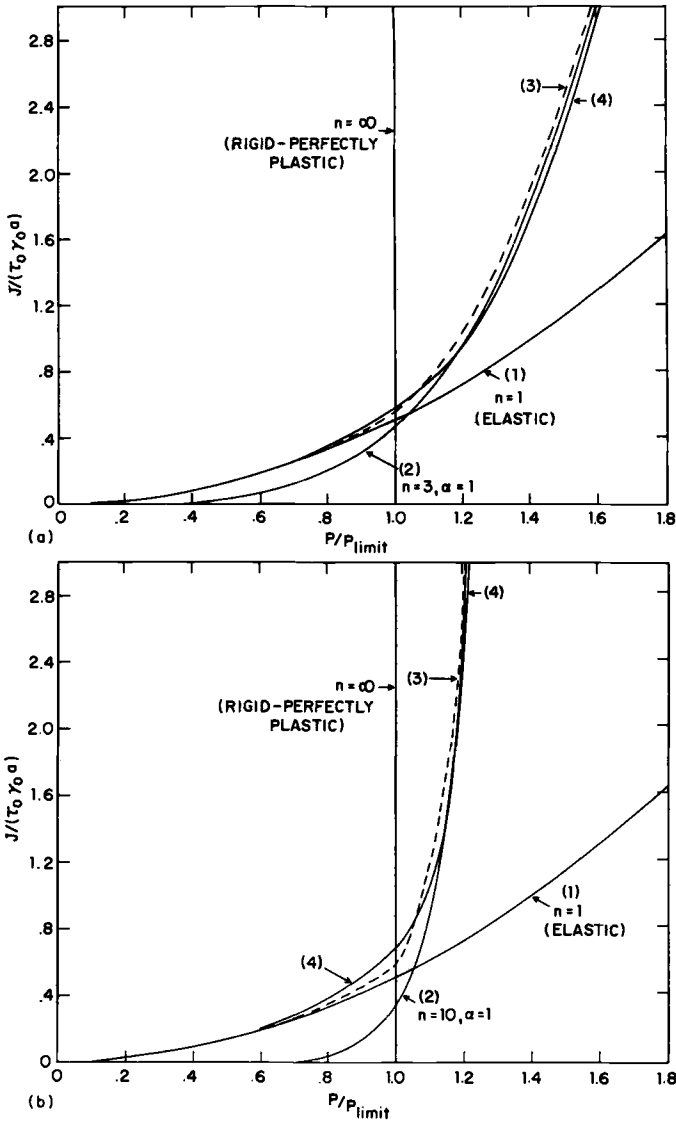
FIG. 7—Curves of  $J$  as a function of  $\Delta$  for (a) high-strain hardening ( $n = 3$ ), (b) low-strain hardening ( $n = 10$ ).

relationship that the critical value of  $J$  is obtained usually in fracture toughness tests. The calculated and estimated values of  $J$ ,  $\delta$ , and  $\Delta$  for values of  $P$  ranging from  $0.6 P_{limit}$  to  $2 P_{limit}$  are tabulated in Tables 4 and 5, respectively.

The relationship between  $J$  and  $\delta$  is also of some interest [9]. Again this relationship is constructed easily since both  $J$  and  $\delta$  are known in terms of the applied load  $P$ . The estimated relationships between  $J$  and  $\delta$  for the two material characterizations (Ramberg-Osgood and piecewise power hardening relations) are in excellent agreement with the results obtained from the detailed finite element calculations as can be verified from the tables.

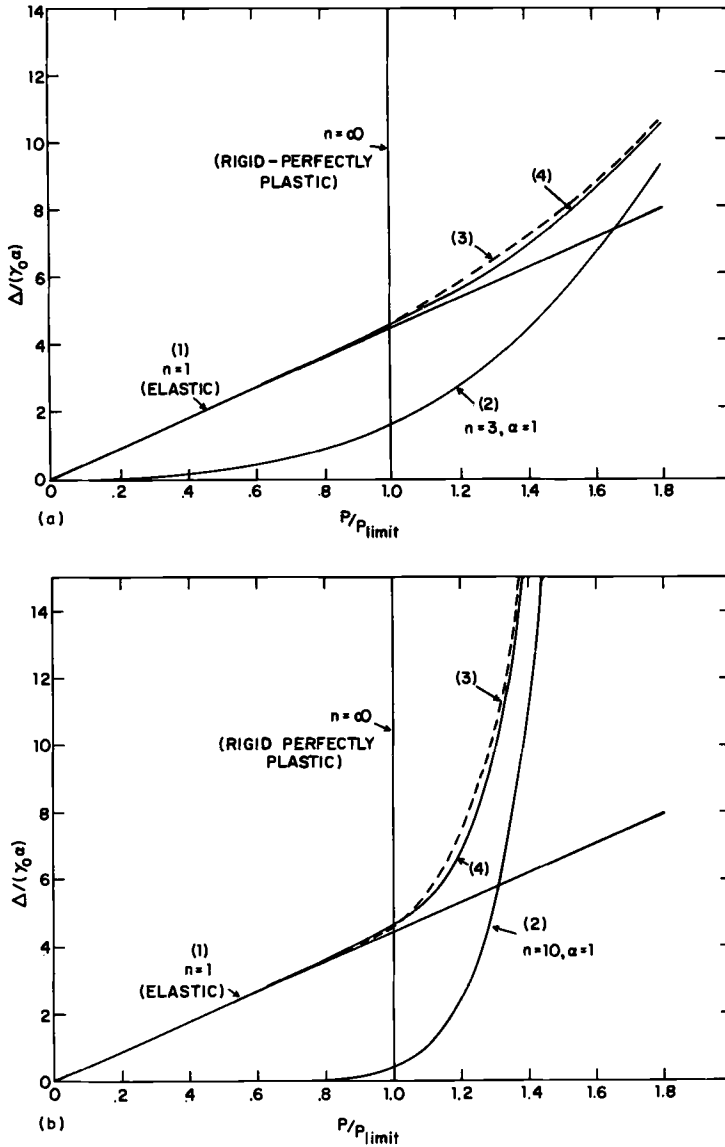
### Conclusion

The results that have been presented thus far demonstrate that reasonably accurate approximate relationships among  $J$ ,  $\delta$ ,  $\Delta$ , and  $P$ , which take into account strain hardening, may be constructed from the adjusted



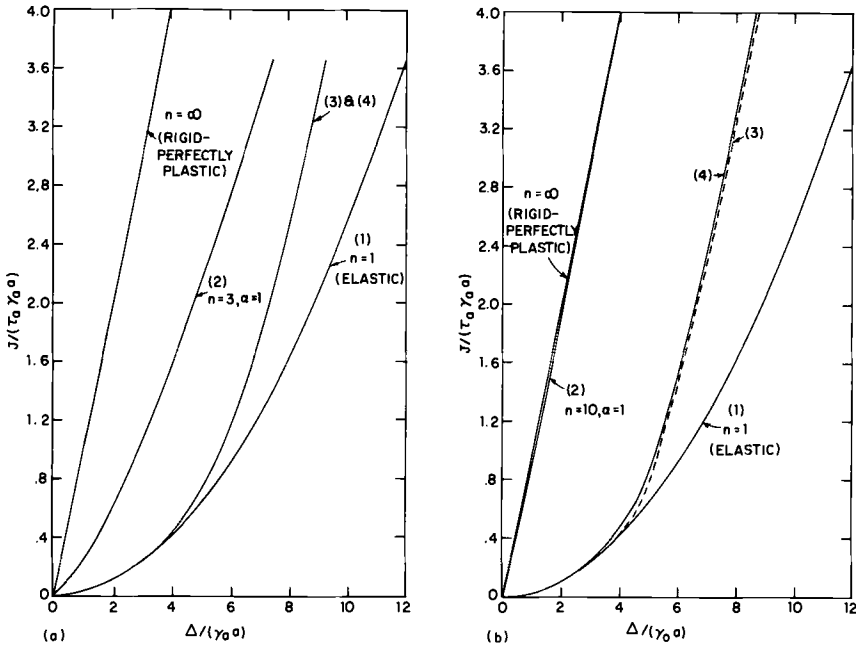
- (1) Linear elastic solution.
- (2) Fully plastic solution for pure power hardening material.
- (3) Predictions based on plastically adjusted elastic and fully plastic solutions.
- (4) Results from the full numerical solution for a piecewise power hardening material.

FIG. 8—Curves of  $J$  as a function of  $P$  for (a) high-strain hardening ( $n = 3$ ), (b) low-strain hardening ( $n = 10$ ).



- (1) Linear elastic solution.
- (2) Fully plastic solution for pure power hardening material.
- (3) Predictions based on plastically adjusted elastic and fully plastic solutions.
- (4) Results from the full numerical solution for a piecewise power hardening material.

FIG. 9—Curves of  $\Delta$  as a function of  $P$  for (a) high-strain hardening ( $n = 3$ ), (b) low-strain hardening ( $n = 10$ ).



- (1) Linear elastic solution.
- (2) Fully plastic solution for pure power hardening material.
- (3) Predictions based on plastically adjusted elastic and fully plastic solutions.
- (4) Results from the full numerical solution for a piecewise power hardening material.

FIG. 10—Curves of  $J$  as a function of  $\Delta$  for (a) high-strain hardening ( $n = 3$ ), (b) low-strain hardening ( $n = 10$ ).

elastic and fully plastic solutions. They also reveal that these relationships can be quite sensitive to the degree of strain hardening.

To illustrate the last statement, relationships between  $J$  and  $\Delta$ , obtained from the full numerical calculations, are plotted in Fig. 11a for the Ramberg-Osgood characterization and in Fig. 11b for the piecewise power hardening characterization. In these figures Curve 1 represents the linear elastic solution, Curves 2 and 3 are the relationships obtained from the finite element calculations corresponding to high- ( $n = 3$ ) and low- ( $n = 10$ ) strain hardening materials, respectively. The rigid-perfect plastic solution (from limit analysis) is given by the straight line through the origin. The relation of  $J$  to  $\Delta$  for an elastic-perfect plastic material is given by Curve 4. This curve parallels the rigid-perfect plastic solution for  $P > P_{\text{limit}}$  and intersects the adjusted elastic curve at the point corresponding to the attainment of the limit load, according to the estimation procedure [8]. As mentioned earlier, this curve is also the limit of our estimated solution for  $n \rightarrow \infty$ .

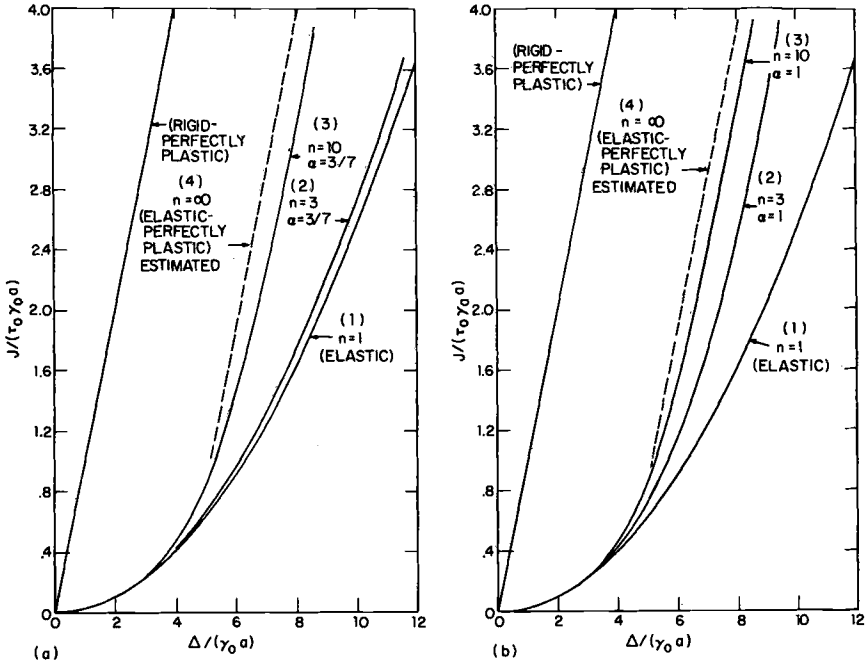
TABLE 4—Results from full numerical calculations for piecewise power hardening material.

| $n$          | $P/P_{\text{limit}}$ | $J/(\tau_0\gamma_0a)$ | $\delta/(\gamma_0a)$ | $\Delta/(\gamma_0a)$ |
|--------------|----------------------|-----------------------|----------------------|----------------------|
| $n = 3$      | 0.60                 | 0.190                 | 0.6928               | 2.561                |
|              | 0.80                 | 0.350                 | 0.9541               | 3.598                |
|              | 1.00                 | 0.581                 | 1.250                | 4.541                |
|              | 1.20                 | 0.936                 | 1.623                | 5.555                |
|              | 1.40                 | 1.680                 | 2.272                | 6.854                |
| $\alpha = 1$ | 1.60                 | 2.905                 | 3.226                | 8.473                |
|              | 1.80                 | 4.720                 | 4.520                | 10.460               |
|              | 2.00                 | 7.280                 | 6.197                | 12.924               |
|              | 0.60                 | 0.196                 | 0.7107               | 2.6945               |
| $n = 10$     | 0.80                 | 0.375                 | 1.0045               | 3.6355               |
|              | 1.00                 | 0.669                 | 1.3850               | 4.6493               |
|              | 1.10                 | 1.000                 | 1.7573               | 5.3330               |
|              | 1.20                 | 2.270                 | 3.0146               | 6.9064               |
| $\alpha = 1$ | 1.25                 | 3.600                 | 4.1710               | 8.2231               |
|              | 1.30                 | 5.550                 | 5.8593               | 10.074               |
|              | 1.35                 | 8.480                 | 8.2662               | 12.6436              |
|              | 1.40                 | 12.707                | 11.6477              | 16.1903              |

For both stress-strain characterizations, Figs. 11a and b clearly show that at the same value of the load point displacement, the value of  $J$  for a low-hardening material ( $n = 10$ ), may differ from the elastic-perfect plastic estimate by as much as 20 percent. Furthermore, a comparison between Figs. 11a and b shows that the curve for  $n = 3$  for a Ramberg-Osgood characterization differs considerably from the curve for  $n = 3$  for

TABLE 5—Estimated results using Eqs 31, 32, and 33 for piecewise power hardening material.

| $n$          | $P/P_{\text{limit}}$ | $J/(\tau_0\gamma_0a)$ | $\delta/(\gamma_0a)$ | $\Delta/(\gamma_0a)$ |
|--------------|----------------------|-----------------------|----------------------|----------------------|
| $n = 3$      | 0.60                 | 0.185                 | 0.698                | 2.682                |
|              | 0.80                 | 0.336                 | 0.957                | 3.595                |
|              | 1.00                 | 0.540                 | 1.239                | 4.526                |
|              | 1.20                 | 1.036                 | 1.806                | 5.751                |
|              | 1.40                 | 1.854                 | 2.598                | 7.143                |
| $\alpha = 1$ | 1.60                 | 3.108                 | 3.653                | 8.731                |
|              | 1.80                 | 4.932                 | 5.006                | 10.543               |
|              | 2.00                 | 7.477                 | 6.697                | 12.607               |
|              | 0.60                 | 0.188                 | 0.714                | 2.694                |
| $n = 10$     | 0.80                 | 0.347                 | 0.995                | 3.624                |
|              | 1.00                 | 0.565                 | 1.317                | 4.586                |
|              | 1.10                 | 1.158                 | 1.937                | 5.603                |
|              | 1.20                 | 2.622                 | 3.338                | 7.398                |
| $\alpha = 1$ | 1.25                 | 3.969                 | 4.553                | 8.807                |
|              | 1.30                 | 5.977                 | 6.294                | 10.740               |
|              | 1.35                 | 8.926                 | 8.755                | 13.389               |
|              | 1.40                 | 13.197                | 12.188               | 17.007               |



- (1) Linear elastic solution.
- (2) Strain hardening solution for  $n = 3$ .
- (3) Strain hardening solution for  $n = 10$ .
- (4) Estimated elastic-perfect plastic solution.

FIG. 11—Curves of  $J$  as a function of  $\Delta$  for (a) Ramberg-Osgood characterization (b) piecewise power hardening characterization.

the piecewise power hardening relation. Nevertheless, the curves for  $n = 10$  for the two material characterizations are reasonably close to each other.

Finally, note that in the estimation schemes presented, we have made use of Irwin's plasticity corrections to adjust the elastic contribution to the estimated solution in the range between the small-scale yielding and the fully plastic state. If more accurate plasticity corrections are available for this intermediate range, the relationships among  $J$ ,  $\delta$ ,  $\Delta$ , and  $P$  may be estimated to greater accuracy, particularly in the case of the piecewise power hardening characterization. Despite the simplicity of the estimation schemes discussed in this paper, the investigation has shown that large-scale yielding behavior in antiplane shear as measured by the parameters  $J$ ,  $\delta$ ,  $\Delta$ , and  $P$  may be predicted fairly accurately for a broad range of elastic-plastic materials.

The procedures just proposed can be applied without essential modifications to inplane problems. Of course this will entail use of the analogous

elastic and fully plastic solutions for the plane problem in question. At the writing of this paper, only solutions for the fully plastic center cracked strip under plane strain are yet available [3]. It can be hoped that the accuracy achieved by the simple estimation procedure in the antiplane shear problem discussed here will continue to hold for plane problems, although this remains an open question. This question, as well as the solution to additional fully plastic plane problems, will be left for future work.

### *Acknowledgment*

This work was supported in part by the Air Force Office of Scientific Research under Grant AFOSR-73-2476, in part by the Advanced Research Projects Agency under Contract DAHC 15-73-G-16, and by the Division of Engineering and Applied Physics, Harvard University. The author is greatly indebted to Professor J. W. Hutchinson for suggesting the problem and for contributing numerous ideas throughout the investigation. The estimation procedures, presented in the paper, are the outcome of several discussions with him. In addition the author wishes to thank Dr. N. L. Goldman for reading the manuscript and suggesting several improvements in the presentation.

## APPENDIX

Descriptions of an accurate finite element method, which embeds the dominant singularity solution of the near-tip through the use of a singular tip element, have been given elsewhere [3,10,11]. Typically the singular element has a radius of  $0.02a$ . The region between the tip element and the boundary is represented by conventional elements. For this analysis we have chosen to work with quadrilateral "elements" that are formed from four constant strain triangular elements. The common node of the four triangular elements (or the midnode of the quadrilateral) is removed by static condensation. This results in considerable savings in computer storage and in the total number of matrix operations associated with the solution of the system of algebraic equations. We will restrict our attention, in this appendix, to several computational details pertinent to this investigation.

For fully plastic crack problems of the type described by Eq 28 the material is fully nonlinear and incompressible. In plane strain situations, enforcement of the incompressibility constraint complicates the numerical procedure. In antiplane shear this difficulty does not arise; nevertheless, the problem is still fully nonlinear. To avoid the comparatively large stiffness terms that may arise from elements that are virtually stress free, the pure power hardening law is slightly modified to allow a linear relationship between the stress and strain, for stresses less than  $\tau_c$  where  $\tau_c/\tau_0$  is much less than unity.

The finite element discretization of the nonlinear boundary value problem results in a system of nonlinear equations. We briefly discuss Newton's method for solving the nonlinear system of equations.

$$A(w)w = b \quad (34)$$

At the  $i^{\text{th}}$  iterate, Newton's method gives

$$\Delta w_i = \left[ A(w_i) + \frac{\partial A(w)}{\partial w} \Big|_{w_i} w_i \right]^{-1} (b - A(w_i)w_i) \quad (35)$$

where

$$w_{i+1} = w_i + \Delta w_i$$

The second term of the Jacobian involves the derivatives of  $A$ . It is precisely this term that is responsible for the second order convergence attainable with Newton's method. If this term is absent, the resulting iterative process is only first order convergent.

For the pure power hardening law, Eq 2, and the Ramberg-Osgood relation Eq 17, the derivatives  $\partial A/\partial w$  are continuous for all values of  $w$ . In this case, the iterative process as given by Eq 35 is second order convergent. Assuming that matrix,  $A$ , is fairly well conditioned and a good initial estimate of the solution is available, the initial solution will converge very rapidly to the actual solution. The initial solution may be obtained by the process of parameter tracking. Thus, the solution to the  $n = 1$  case can be used as the initial estimate to the  $n = 3$  case, the  $n = 3$  solution as the initial estimate to the  $n = 5$  case and so on.

The derivatives  $\partial A/\partial w = (\partial A/\partial y/\partial w)$ , associated with the piecewise power hardening relation is given by Eq 28, are discontinuous at  $\tau_e = \tau_0$  (or  $\gamma_e = \gamma_0$ ). Then the iterative process described by Eq 35 is numerically unstable for this class of problems. In this case, linear iteration will work; however, the convergence is only of first order. To "smooth" the abrupt change in  $\partial A/\partial w$  at  $\gamma_e = \gamma_0$  ( $\partial A/\partial w = 0$  for  $\gamma_e < \gamma_0$ ) every  $\partial A/\partial w$  term generated during the formation of the element stiffness matrix is multiplied by the factor

$$f = \left[ \left( \frac{\gamma_e}{\gamma_0} \right)^m - 1 \right] / \left( \frac{\gamma_e}{\gamma_0} \right)^m \quad \text{for } \gamma_e \geq \gamma_0$$

It may be noted that  $f$  approaches unity for  $\gamma_e \gg \gamma_0$ , and  $f \rightarrow 0$  as  $\gamma_e \rightarrow \gamma_0$ . In the present calculations  $m$  was taken to be 4. With the preceding modification, the rate of convergence is not quite second order but definitely better than the convergence rate associated with linear iterations.

The quantity of primary interest in this paper is the J-integral. As discussed elsewhere [3,10,11],  $J$  may be obtained from the formula

$$J = \alpha \tau_0 \gamma_0 K_\sigma K_\epsilon I_n = \alpha \tau_0 \gamma_0 K_\epsilon^{(n+1)/n} I_n \quad (36)$$

where  $K_\sigma$  and  $K_\epsilon$  are the plastic stress and strain intensity factors and  $I_n$  is a numerical constant. The finite element approach which embeds the dominant singularity solution allows  $K_\sigma$  and  $K_\epsilon$  to be computed directly. Thus  $J$  associated with a particular crack problem may be obtained rather easily from Eq 36.

Alternatively,  $J$  may be obtained by computing the integral given by Eq 3 along a contour,  $\Gamma$ , which encircles the crack tip. An accurate technique for this purpose is discussed in Ref 11. Briefly, the contour,  $\Gamma$ , passes through selected midnodes of the quadrilateral "elements"; the quantities (stresses and displacement gradients) associated with a particular midnode are obtained by averaging the quantities associated with the four triangular elements that comprise the quadrilateral. The values of the J-integral, so computed for different contours throughout the body are in excellent agreement. Specifically, the values of  $J$

computed on various contours differed by less than 1 percent for the pure power hardening and Ramberg-Osgood characterizations. For the piecewise power hardening relation, where there is a distinct yield stress (also note that at yield stress, the slope of the stress-strain curve is discontinuous),  $J$ 's computed for contours away from the elastic-plastic boundary differed by less than 3 percent. For contours close to or intersecting the elastic-plastic boundary the differences may reach 10 percent for low-strain hardening materials ( $n \geq 10$ ); this is consistent with the averaging technique used in the computations [11].

A comparison of the values of  $J$ , obtained from Eq 36 and from the latter technique, reveals that they are in good agreement for high-strain hardening materials. For low-strain hardening materials ( $n \geq 10$ ), they may differ by as much as 15 percent for levels of applied stress well into the fully plastic range. Since at low-strain hardening, the values of  $J$  computed by the latter technique for different contours throughout the cracked configuration are within 1 percent of the average value, we conclude that  $J$  obtained from Eq 36 is inaccurate at high levels of applied stress for low-strain hardening materials.

## References

- [1] Begley, J. A. and Landes, J. D. in *Fracture Toughness, Proceedings of the 1971 National Symposium on Fracture Mechanics, Part II, ASTM STP 514*, American Society for Testing and Materials, 1972, pp. 1-23, pp. 24-39.
- [2] Bucci, R. J., Paris, P. C., Landes, J. D., and Rice, J. R. in *Fracture Toughness, Proceedings of the 1971 National Symposium on Fracture Mechanics, Part II, ASTM STP 514*, American Society for Testing and Materials, 1972, pp. 40-69.
- [3] Goldman, N. L. and Hutchinson, J. W., "Fully Plastic Crack Problems: The Center-Cracked Strip under Plane Strain," Report DEAP S-7, Harvard University, Cambridge, Mass., Feb. 1974.
- [4] Rice, J. R., *Journal of Applied Mechanics, Transactions, American Society of Mechanical Engineers*, Vol. 35, 1968, pp. 379-386.
- [5] Rice, J. R. in *Fracture*, Vol. 2, H. Liebowitz, Ed., Academic Press, New York, 1968, pp. 191-311.
- [6] Tada, H., Paris, P. C., and Irwin, G. R., *The Stress Analysis of Cracks Handbook*, Del Research Corporation, Hellertown, Pa., 1973.
- [7] Amazigo, J. C., "Fully Plastic Crack in an Infinite Body Under Anti-Plane Shear," Report DEAP S-6, Harvard University, Cambridge, Mass., Dec. 1973.
- [8] Rice, J. R., Paris, P. C., and Merkle, J. G. in *Progress in Flaw Growth and Fracture Toughness Testing, ASTM STP 536*, American Society for Testing and Materials, 1973, pp. 231-245.
- [9] Wells, A. A., *Engineering Fracture Mechanics*, Vol. 1, No. 3, 1969, pp. 399-410.
- [10] Hilton, P. D. and Hutchinson, J. W., *Engineering Fracture Mechanics*, Vol. 3, No. 4, 1971, pp. 435-451.
- [11] Shih, C. F., "Elastic-Plastic Analysis of Combined Mode Crack Problems," Ph.D. thesis, Harvard University, Cambridge, Mass., Oct. 1973.

G. A. Clarke,<sup>1</sup> W. R. Andrews,<sup>1</sup> P. C. Paris,<sup>2</sup> and D. W. Schmidt<sup>3</sup>

## Single Specimen Tests for $J_{Ic}$ Determination

---

**REFERENCE:** Clarke, G. A., Andrews, W. R., Paris, P. C., and Schmidt, D. W., "Single Specimen Tests for  $J_{Ic}$  Determination," *Mechanics of Crack Growth*, ASTM STP 590, American Society for Testing and Materials, 1976, pp. 27–42.

**ABSTRACT:** A  $J_{Ic}$  test procedure using a single deeply cracked specimen is proposed. The crack extension is measured by partially unloading the specimen to determine the elastic compliance.  $J_{Ic}$  tests were made using ASTM A469 steel. Compact specimens from 1/2T to 5T were tested. No size effect was found. Results from two independent laboratories are presented and are in agreement. The errors due to simple formulation of  $J_I$  calculation, periodic partial unloading, and simplified analysis for the extension of deep cracks in compact specimens are explored. The measurement point of crack extension for establishing  $J_{Ic}$  is discussed. The results indicate that a practical and effective single specimen test procedure has been developed.

**KEY WORDS:** crack propagation, fracture tests, fracture properties, tests, steels, plastic properties, elastic properties, elastic deformation, fracture strength

The elastic-plastic stress-strain response of cracked structures has been characterized by Rice [1,2]<sup>4</sup> and Hutchinson [3], and the crack tip region response described in terms of a path independent integral termed  $J_I$ . Begley and Landes noted that  $J_I$  is a field quantity similar to the stress intensity factor,  $K_I$  [4]. Accordingly they formulated a fracture criterion around  $J_I$  in a fashion similar to that normally done with  $K_I$ . They used Rice's [2] definition that the J-integral (referred to as  $J_I$  in the remainder of the report) is related to the rate of change in area under the load versus

<sup>1</sup> Stress analysis engineer and materials test engineer, respectively, General Electric Company, Schenectady, N. Y. 12345.

<sup>2</sup> Chairman and chief executive officer, Del Research Corporation, Hellertown, Pa. 18055, and visiting professor of engineering, Brown University, Providence, R. I. 02912.

<sup>3</sup> Engineer, Del Research Corporation, Hellertown, Pa. 18055.

<sup>4</sup> The italic numbers in brackets refer to the list of references appended to this paper.

load-point-deflection curve with respect to change in crack length. Fracture toughness as defined through  $J_I$  was termed  $J_{Ic}$  for plane strain crack tip constraint.

Since  $J_I$  is analyzed based on the deformation theory of plasticity, significant unloading cannot be permitted without serious questions. Because of this, Begley and Landes [5] chose to use a  $J_{Ic}$  test procedure involving the use of multiple specimens. They suggested measuring the crack extension in each of the several identical specimens after marking the crack depth at various values of load-point displacement, and breaking open each specimen to measure the marked crack length. The marking may be made, for example, by heat tinting the crack surface after unloading the specimen. This procedure normally has required four to six specimens to obtain a single value of  $J_{Ic}$ .

To overcome the use of multiple specimens, a  $J_{Ic}$  test procedure using a single deeply cracked compact specimen is proposed. The crack extension is measured during repeated partial unloading of the specimen using linear elastic compliance calculations. Justification will be given as to why this unloading does not seriously affect the results considering the previously mentioned limitation in deformation theory of plasticity.

A number of tests to determine  $J_{Ic}$  were made using ASTM A469 steel. The extent of crack growth selected as a measurement point criterion for  $J_{Ic}$  is discussed. Various criteria are compared.

Compact specimens of sizes ranging from 1/2 to 5 in. thick were tested and the results compared. The 5-in.-thick specimens were tested according to ASTM Test for Plane Strain Fracture Toughness of Metallic Materials (E 399) at  $-10$ ,  $5$ ,  $32$ , and  $75^\circ\text{F}$ .  $J_{Ic}$  test temperatures ranged from  $5$  to  $250^\circ\text{F}$ . Results were obtained from two independent laboratories.

## Theoretical Considerations

### *Accuracy of $J_I$ Calculation*

Rice et al [6] showed that a simple formula for  $J_I$  is

$$J_I = \frac{2A}{B(w - a)} \quad (1)$$

where bending loading is applied to a specimen deeply cracked compared to the width  $w$ ;  $A$  is the area under the load versus load-point-displacement curve;  $B$  is the specimen thickness; and  $a$  is the crack depth.

The applicability of Eq 1 to the compact specimen can be demonstrated. To do this, it is noted that for essentially elastic loading

$$J_I = G_I \quad (2)$$

where  $G_1$  is the elastic strain energy release rate. Equation 2 is a necessary condition for the formula to be used. Available elastic analyses will be used to show that this condition is satisfied and, therefore, demonstrate the applicability of Eq 1.

Srawley and Gross [7] gave the results of a boundary collocation K-calibration for the compact specimen. They gave a table of  $f(a/w)$  in which

$$f(a/w) = \frac{K_1 B (w - a)^{3/2}}{P(2w + a)} \quad (3)$$

where  $P$  is the load. The tabulation of  $f(a/w)$  will be used to compare with values in the same form as Eq 3 resulting when Eq 1 is employed. The latter values will be termed  $\bar{f}(a/w)$ . Assuming Eq 2 holds and using  $P \times \delta = 2A$ , Eq 1 becomes

$$G_1 = \frac{P \times \delta}{B(w - a)} \quad (4)$$

where  $\delta$  is the load line displacement and  $(w - a)$  is the remaining ligament.  $G_1$  is related to  $K_1$  for plane strain deformation through

$$K_1^2 = \frac{G_1 E}{(1 - \nu^2)} \quad (5)$$

where  $E$  is young's modulus and  $\nu$  is Poisson's ratio. Substitution of Eq 4 into Eq 5 and in turn into Eq 3 yields the following expression for  $\bar{f}(a/w)$

$$\bar{f}(a/w) = \left[ \frac{cEB}{(1 - \nu^2)} \right]^{1/2} \times \frac{(w - a)}{(2w + a)} \quad (6)$$

In this expression,  $c$  is the compliance defined at the load line

$$c = \frac{\delta}{P} \quad (7)$$

The elastic compliance at the load line has been given by Tada et al [8] as

$$c = \frac{V_2(a/w) \times (1 - \nu^2)}{E \times B} \quad (8)$$

TABLE 1—The functions  $f(a/w)$  and  $\bar{f}(a/w)$ , Eqs 3 and 9 comparing the accuracy of Eq 1 to elastic collocation results.

| $a/w$ | $f(a/w)$ | $\bar{f}(a/w)$ | $\bar{f}/f$ |
|-------|----------|----------------|-------------|
| 0.4   | 1.419    | 1.21           | 0.85        |
| 0.5   | 1.364    | 1.23           | 0.90        |
| 0.6   | 1.326    | 1.24           | 0.94        |
| 0.7   | 1.312    | 1.23           | 0.94        |
| 0.8   | 1.311    | 1.24           | 0.945       |
| 0.9   | 1.311    | 1.26           | 0.965       |
| 1.0   | 1.311    | 1.32           | 1.008       |

Substituting Eq 8 into Eq 6 gives the desired expression for  $f(a/w)$

$$f(a/w) = V_2(a/w)^{1/2} \times \frac{w - a}{2w + a} \quad (9)$$

A comparison of  $f(a/w)$  with  $\bar{f}(a/w)$  is given in Table 1. Note that in the range of  $(a/w)$  from 0.6 to 0.8, the ratio of  $\bar{f}(a/w)$  to  $f(a/w)$  is constant, and that  $\bar{f}$  (and thus  $K_1$  calculated from Eqs 1 and 5) is about 6 percent low. This is considered an acceptable error and hence, Eq 1 is considered verified for the compact specimen loaded in the essentially elastic range. The error in the plastic range is also expected to be small.

#### Calculation of Crack Extension

A simple formula can be obtained relating the crack extension to the change in elastic compliance of the compact specimen. For the deeply crack specimen, the applied load may be considered to be a moment  $M$  applied to the remaining ligament of length  $(w - a)$ . The angular rotation of the applied moment

$$\theta = \frac{16}{E \times B} \times \frac{M}{(w - a)^2} \quad (10)$$

The compliance then is

$$\frac{\theta}{M} = c = \frac{16}{EB} \times \frac{1}{(w - a)^2} \quad (11)$$

The derivative

$$dc = \frac{-32}{EB} \times \frac{d(w - a)}{(w - a)^3} \quad (12)$$

Dividing Eq 12 by Eq 11 gives

$$\frac{dc}{c} = \frac{2da}{(w-a)}$$

or rearranging<sup>5</sup>

$$da = \frac{(w-a)}{2} \times \frac{dc}{c} \quad (13)$$

An alternate derivation for the foregoing result may be obtained from analysis of the compact specimen using the compliance relation of Tada et al [8].

That result is

$$da = \frac{w-a}{2} \times \frac{dc}{c} \times g(a/w) \quad (14)$$

The values for  $g(a/w)$  are given in Table 2, and they indicate that Eq 13 will over estimate the crack extension by about 10 percent for  $0.6 \leq (a/w) \leq 0.8$ .

#### *Experimental Errors Due to Unloading*

As mentioned earlier, the theoretical concept of  $J_I$  does not permit "significant" unloading. The experimental expedient of unloading to measure the elastic compliance must be, therefore, shown to not materially affect the experimental fracture toughness results. For that reason tests were performed with and without unloading and results compared. This can also be demonstrated further through physical reasoning by showing that the unloading crack tip plastic zone size remains small compared to the process zone size [9],  $Z_p$ , existing at the time unloading is initiated

$$Z_p \approx J_I / \sigma_y \quad (15)$$

TABLE 2—Factors  $g(a/w)$  for the crack extension Eq 15.

| $a/w$ | $g(a/w)$ |
|-------|----------|
| 0.5   | 0.808    |
| 0.6   | 0.872    |
| 0.7   | 0.891    |
| 0.8   | 0.906    |
| 0.9   | 0.934    |
| 1.0   | 1.000    |

<sup>5</sup> An analogous equation can be derived for load changes at limit load.

where  $\sigma_y$  is the yield stress. Also the unloading plastic size,  $r_y$ , is approximately

$$r_y = \frac{1}{6\pi} \left( \frac{K_I}{2\sigma_y} \right)^2 \quad (16)$$

where  $K_I$  is calculated for the unloading only.

The criterion then for limiting unloading will be established as

$$\frac{r_y}{Z_p} \leq \alpha \quad (17)$$

where  $\alpha$  is to be a number much less than 1.0

A suitable value for  $\alpha$  may be selected at about 0.01. For 10 percent unloading in our tests of 1T compact specimens a typical value for  $\alpha$  is 0.002. Further assurance that unloading will not affect results may be obtained by realizing that the extent of unloading was not as large as the loading prescribed for precracking specimens by ASTM Method E 399. We were assured then that 10 percent unloading would not materially affect the results.

### Material

The material tested was a steel similar to that specified by ASTM A469. The mill analysis is shown in Table 3. This steel was procured as a 22-in.-diameter round forging in a quenched and tempered (1100°F) condition. The mechanical properties of this material at various temperatures are shown in Table 4. The temperatures span the range used for  $J_{Ic}$  testing. The Charpy impact properties taken from a depth of 4 1/2 to 5 in. below the quenched surface are shown in Table 5.

All  $J_{Ic}$  specimens were of the compact design. The size of the specimens tested range from 1/2T to 5T. The compact specimens were all taken from the forged cylinder with the crack propagation planes either radial or up to 45 deg to the radial plane. All the crack tips were located at 4 to 9 in. from the axis of the forging.

### Test Procedures

The linear elastic fracture toughness ( $K_{Ic}$ ) of this material was determined using 5T specimens according to ASTM Method E 399 at  $-10^\circ\text{F}$  and  $+5^\circ\text{F}$ .

TABLE 3—Chemical analysis of test material.

| Element | C    | Mn   | P     | S     | Si   | Ni   | Cr   | V    | Mo   |
|---------|------|------|-------|-------|------|------|------|------|------|
| %       | 0.22 | 0.31 | 0.011 | 0.012 | 0.23 | 3.63 | 0.07 | 0.11 | 0.27 |

TABLE 4—Mechanical properties of specimens (0.505-in. round tension specimens).

| Temperature              | +5°F    | 75°F    | 175°F   |
|--------------------------|---------|---------|---------|
| 0.2% yield strength, psi | 93 000  | 88 800  | 85 000  |
| Tensile strength, psi    | 109 000 | 103 000 | 101 000 |
| Elevation in 2 in., %    | 24.0    | 22.5    | 23.0    |
| Reduction of area, %     | 58.3    | 60.6    | 59.8    |
| Fracture stress, psi     | 194 200 | 195 200 | 184 100 |

For the test temperatures 32 and 75°F, values of fracture toughness are estimated based on  $K_{Ic}$  values (both occurred at abrupt failure points). The fracture toughness values are shown in Table 6.

For the J-integral testing, the compact specimens were modified to permit measurement of load-line displacements. Specimens of 1/2T, 1T, and 2T sizes (Fig. 1) were used in this test program.

Fatigue precracking was accomplished at peak loads less than 1/2 the expected limit load [10]. The crack lengths were extended by fatigue precracking to obtain crack lengths to-specimen-width ratios ( $a/w$ ) from 0.70 to 0.80.

The specimens were loaded under ram position control in a closed loop electrohydraulic test machine. The heating of the specimens was accomplished by wrapping resistance heating tapes around the specimen and insulating with glass wool insulation. Cooling was accomplished by allowing liquid nitrogen vapor to pass through a chamber surrounding the specimen. The temperature was controlled to within  $\pm 5^\circ\text{F}$ .

All load and displacement signals were recorded on an  $x$ - $y$  plotter and were normally stored in digital form in the core memory of a PDP-8 computer. The testing procedures fell in two categories, (1) no-unloading and (2) unloading. For those specimens in (1) the load displacement points were stored in digital form so that curves could be easily reproduced and the  $J_I$  value quickly calculated. For those tests with unloading (2), a linear signal was subtracted from the displacement signal; the result was plotted versus load. The subtracted signal was proportional to the load and the

TABLE 5—Charpy V-notch impact properties of specimens.<sup>a</sup>

| Temperature, °F | Absorbed Energy, ft·lb | Fibrous Appearance, % |
|-----------------|------------------------|-----------------------|
| 25              | 32.5                   | 40                    |
| 50              | 40.0                   | 48                    |
| 75              | 49                     | 60                    |
| 125             | 72.5                   | 87                    |
| 175             | 87                     | 100                   |

<sup>a</sup> 50 percent fracture appearance transition temperature (FATT) = 50°F.

TABLE 6—ASTM fracture toughness tests ASTM Designation E 399 5T compact specimens.

| Test Temperature, °F | $P_Q$ , lb | Average Crack Length, in. | Load Deflection Curve Types | $K_Q$ , psi · (in.) <sup>1/2</sup> |
|----------------------|------------|---------------------------|-----------------------------|------------------------------------|
| -10                  | 188 000    | 4.668                     | III                         | 103 000                            |
| 5                    | 187 000    | 4.675                     | III                         | 103 000                            |
| 32                   | 262 000    | 4.595                     | III                         | 142 000                            |
| 75                   | 325 000    | 4.662                     | III                         | 180 000                            |

constant of proportionality was equal to the initial elastic compliance of the specimen. A typical load displacement curve is shown in Fig. 2. A plot with the elastic compliance signal subtracted is shown in Fig. 3.

The test procedure for category (2) tests called for unloading 10 to 20 times. The unloading lines remained vertical until crack propagation took place at which time the lines changed slope proportionally to the change in compliance of the specimen. This measurement technique is capable of detecting crack length changes of less than 0.001 in.

The unloading was accomplished with a ramp command signal which allowed loading and unloading at equal rates. The load was never reduced by more than 10 percent of the calculated limit load.

The foregoing testing system was duplicated in all of its essential features in a second laboratory. A limited number of tests were performed on the second system. These results are included and identified as being from a second laboratory.

The calculated value of  $J_1$  at various points is given by Eq 1 and the change in crack length by Eq 13. Values of the compliance changes were taken from the load-inelastic displacement record just described.

## Results

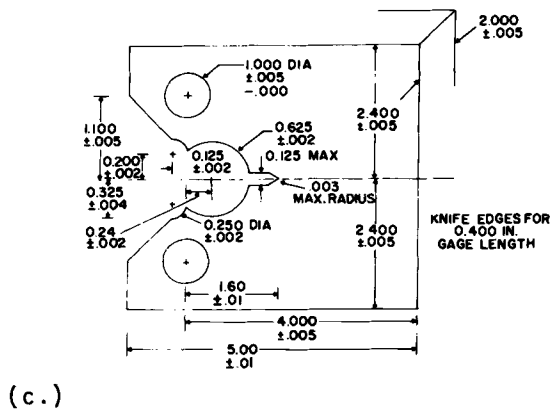
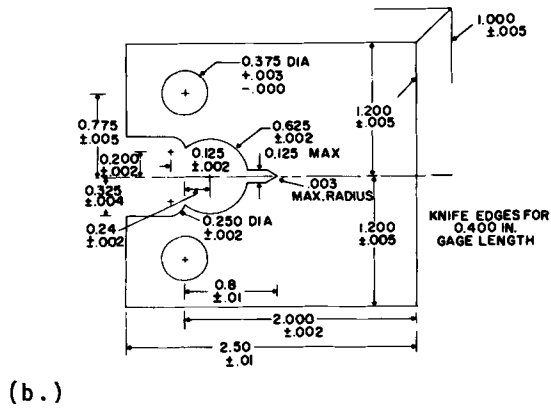
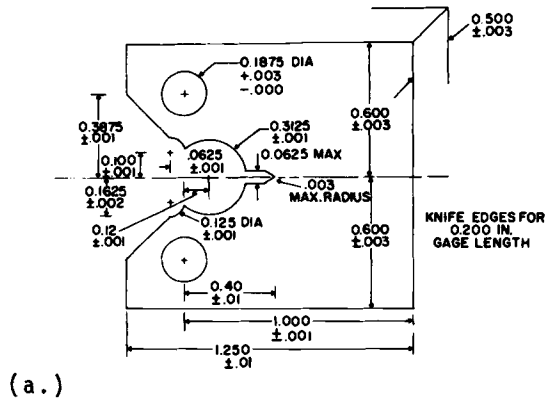
The results of calculating the  $J_{1c}$  values from the crack extension data, using the various criteria described next, are shown in Table 7. The codes for the various columns are as follows: In column 1 the first digit of each row is the specimen size (that is, 1/2 means 1/2T specimen size), whereas the second and third digits are the location number and the serial number, respectively. Results of tests from the second laboratory are those designated as "1-3-X" in Table 7. In column 2 the test temperature is given in °F. In column 3 the procedure category is identified as described in the Test Procedures. In columns 4 through 7 the subscripts on the critical stress intensity factor,  $K$ , are as follows

FLD = first load drop,

$J/2\sigma_y$  = intersection point of the  $\Delta a = J/2\sigma_y$  line with the  $J_1$  versus  $\Delta a$  curve,

FG = first measurable crack extension, and

SF = specimen failure (fast fracture or separation).



- (a) 1/2T size.
- (b) 1T size.
- (c) 2T size.

FIG. 1—Specimen design.

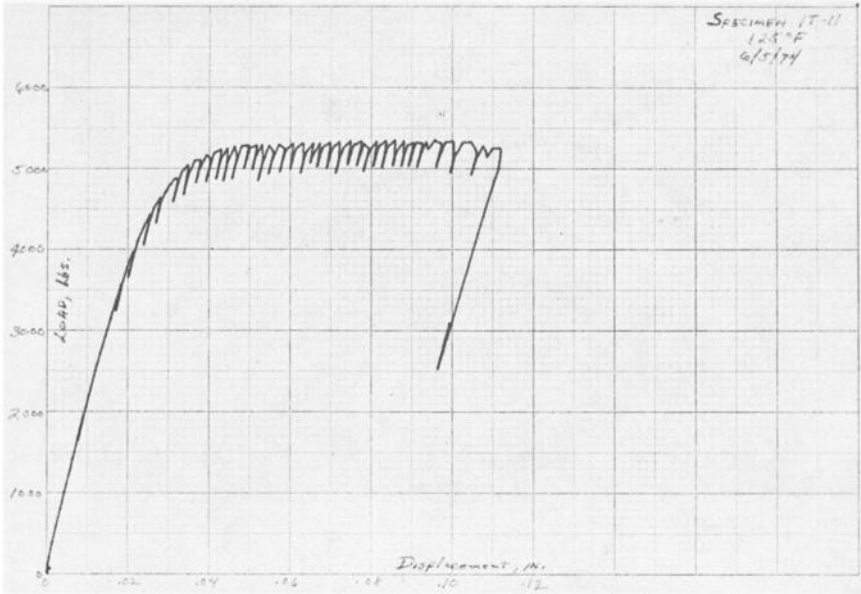


FIG. 2.—Typical load deflection curve.

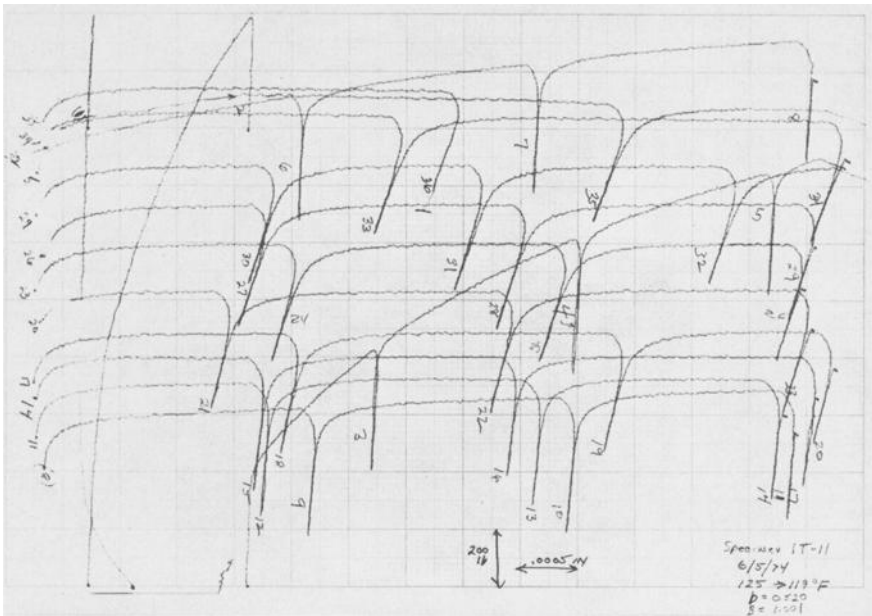


FIG. 3—Typical load versus inelastic displacement diagram.

In columns 8 and 9 the values under  $b$  and  $P_{\max}$  are the remaining ligament ( $w - a$ ) and the maximum load in each test.

All fracture results in Table 7 are expressed in terms of  $K_I$  ( $\text{ksi} \cdot (\text{in.})^{1/2}$ ) which is related to  $J_I$  in the elastic range by Eqs 2 and 5.

Curves and their scatterbands of  $K_I$  versus temperature are shown in Fig. 4 for the various  $J_{Ic}$  criteria.

Crack growth resistance data,  $J_I$  versus  $\Delta a$ , are shown for some specimens tested with unloading at 175°F in Fig. 5.

The fracture toughness values obtained with 5T specimens are plotted versus test temperature in Fig. 6.

### Discussion

Once Begley and Landes [4,5] showed that the J-integral has promise as a failure criterion, a great deal of interest was generated in  $J_{Ic}$  testing because of the obvious advantages of reduced specimen size and reduced specimen cost. It soon became apparent that standards were necessary to define the point at which the value of  $J_I$  was considered critical, that is,  $J_{Ic}$ . As these standards are not yet defined, a number of options are still open to discussion. Following are just a few of the criteria commonly used in defining a point on the  $J_I$  versus  $\Delta a$  curve considered  $J_{Ic}$ .

#### *Criterion 1*

Using the crack extension equivalent to  $J_I/(2\sigma_y)$  or the crack opening stretch (COS) [6].

#### *Criterion 2*

Using the first load drop found in the load-displacement record and calculating the value of  $J_I$  corresponding to this point.

#### *Criterion 3*

Using the value of  $J_I$  calculated at the point of first measurable crack extension.

#### *Criterion 4*

Using the value of  $J_I$  calculated at the specimen failure point (fast fracture or specimen separation).

In recent  $J_{Ic}$  testing by Begley and Landes [5], they have shown a good correspondence between  $J_{Ic}$  values obtained through Criterion 1 and valid  $K_{Ic}$  values. The procedure used by Begley and Landes requires four to six specimens to measure  $J_{Ic}$ .

The object of our test program was to develop a procedure for the determination of  $J_{Ic}$  from a single specimen test. A method of determining unloading slopes was used to calculate the crack extension at any load

TABLE 7—Results of  $J_{IC}$  Test in terms of  $K_{IC}$ .

| Specimen  | Temperature, °F | Unloading | $K_{I,0.2}$ ,<br>ksi·(in.) <sup>1/2</sup> | $K_{I,0.5}$ ,<br>ksi·(in.) <sup>1/2</sup> | $K_{I,0.7}$ ,<br>ksi·(in.) <sup>1/2</sup> | $K_{IC}$ ,<br>ksi·(in.) <sup>1/2</sup> | $K_{SF}$ ,<br>ksi·(in.) <sup>1/2</sup> | $b$ ,<br>in. | $P_{max}$ ,<br>lb |
|-----------|-----------------|-----------|---|---|---|--|--|--------------|-------------------|
| 1/2-21-1  | 5               | no        | 106                                       | ...                                       | ...                                       | ...                                    | 106                                    | 0.243        | 1055              |
| 1/2-21-2  | 5               | no        | 105                                       | ...                                       | ...                                       | ...                                    | 105                                    | 0.240        | 1162              |
| 1/2-21-3  | 5               | no        | 102                                       | ...                                       | ...                                       | ...                                    | 102                                    | 0.255        | 1317              |
| 1/2-21-4  | 5               | no        | 61 <sup>a</sup>                           | ...                                       | ...                                       | ...                                    | 122                                    | 0.239        | 950               |
| 1/2-21-6  | 5               | no        | 109                                       | ...                                       | ...                                       | ...                                    | 155 <sup>a</sup>                       | 0.258        | 1250              |
| 1/2-21-7  | 5               | no        | 111                                       | ...                                       | ...                                       | ...                                    | 111                                    | 0.254        | 1312              |
| 1/2-21-8  | 5               | no        | 123                                       | ...                                       | ...                                       | ...                                    | 123                                    | 0.247        | 1250              |
| 1/2-21-9  | 5               | no        | 72  | ...                                       | ...                                       | ...                                    | 72                                     | 0.257        | 1170              |
| 1/2-21-11 | 5               | no        | 112                                       | ...                                       | ...                                       | ...                                    | 112                                    | 0.290        | 1695              |
| 1/2-21-12 | 5               | no        | 99  | ...                                       | ...                                       | ...                                    | 99                                     | 0.279        | 1555              |
| 1/2-21-13 | 5               | no        | 85  | ...                                       | ...                                       | ...                                    | 85                                     | 0.277        | 1532              |
| 1/2-21-14 | 5               | no        | 96  | ...                                       | ...                                       | ...                                    | 96                                     | 0.285        | 1582              |
| 1/2-23-2  | 5               | no        | 146                                       | ...                                       | ...                                       | ...                                    | 146                                    | 0.253        | 1295              |
| 1/2-23-3  | 5               | no        | 104                                       | ...                                       | ...                                       | ...                                    | 104                                    | 0.225        | 975               |
| 1/2-23-4  | 5               | no        | 130                                       | ...                                       | ...                                       | ...                                    | 130                                    | 0.241        | 1425              |
| 1/2-23-6  | 5               | yes       | 118                                       | ...                                       | ...                                       | ...                                    | 118                                    | 0.251        | 1325              |
| 1/2-23-8  | 5               | yes       | 123                                       | ...                                       | ...                                       | ...                                    | 123                                    | 0.240        | 1160              |
| 1/2-23-1  | 75              | yes       | 146                                       | ...                                       | ...                                       | ...                                    | 146                                    | 0.225        | 1000              |
| 1/2-23-5  | 75              | no        | 172                                       | ...                                       | ...                                       | ...                                    | 196                                    | 0.219        | 1037              |
| 1/2-23-7  | 75              | yes       | 184                                       | ...                                       | ...                                       | ...                                    | 184                                    | 0.260        | 1413              |
| 1-22-1    | 75              | no        | 176                                       | ...                                       | ...                                       | ...                                    | 234                                    | 0.442        | 4040              |
| 1-22-2    | 75              | no        | 217                                       | ...                                       | ...                                       | ...                                    | 217                                    | 0.548        | 6450              |
| 1-22-4    | 75              | yes       | 213                                       | ...                                       | ...                                       | ...                                    | 213                                    | 0.501        | 5100              |
| 1-35-5    | 75              | yes       | 146                                       | ...                                       | ...                                       | ...                                    | 146                                    | 0.476        | 4550              |
| 1-35-6    | 75              | yes       | 147                                       | ...                                       | ...                                       | ...                                    | 147                                    | 0.510        | 4750              |
| 1-35-7    | 75              | yes       | 184                                       | ...                                       | ...                                       | ...                                    | 185                                    | 0.516        | 5300              |
| 1-35-8    | 75              | no        | 152                                       | ...                                       | ...                                       | ...                                    | 152                                    | 0.503        | 4800              |
| 1-11-3    | 100             | no        | 167                                       | ...                                       | ...                                       | ...                                    | >260 <sup>b</sup>                      | 0.575        | 4660              |
| 1-11-5    | 100             | yes       | 203                                       | ...                                       | ...                                       | ...                                    | 203                                    | 0.484        | 4550              |
| 1-11-7    | 100             | yes       | 196                                       | ...                                       | ...                                       | ...                                    | 160                                    | 0.579        | 6500              |
| 1-11-8    | 100             | yes       | 197                                       | ...                                       | ...                                       | ...                                    | 156                                    | 0.584        | 6620              |
| 1/2-21-10 | 125             | yes       | 177                                       | ...                                       | ...                                       | ...                                    | 132                                    | 0.234        | 1175              |
| 1/2-21-16 | 125             | yes       | 188                                       | ...                                       | ...                                       | ...                                    | >284                                   | 0.224        | 1000              |
| 1-11-1    | 125             | yes       | 196                                       | ...                                       | ...                                       | ...                                    | 126                                    | 0.480        | 4480              |
| 1-11-2    | 125             | yes       | 173                                       | ...                                       | ...                                       | ...                                    | 167                                    | 0.476        | 4250              |
| 1-11-6    | 125             | no        | 165                                       | ...                                       | ...                                       | ...                                    | 151                                    | 0.565        | 5225              |
| 1-12-5    | 125             | yes       | 209                                       | ...                                       | ...                                       | ...                                    | >291                                   | 0.476        | 4450              |
|           |                 |           | 189                                       | ...                                       | ...                                       | ...                                    | 209                                    | 0.476        | 4450              |

|                                    |     |     |     |     |     |      |       |       |
|------------------------------------|-----|-----|-----|-----|-----|------|-------|-------|
| 1-31-2                             | 125 | yes | 197 | 256 | 232 | 324  | 0.476 | 4370  |
| 1-31-3                             | 125 | yes | 211 | 192 | 144 | 241  | 0.460 | 4020  |
| 1-31-4                             | 125 | yes | 204 | 167 | 144 | >265 | 0.488 | 4106  |
| 1-21-1                             | 150 | yes | 204 | 197 | 122 | >313 | 0.482 | 4325  |
| 1-12-4                             | 150 | no  | 151 | ... | ... | >274 | 0.625 | 4450  |
| 1/2-21-5                           | 175 | yes | 167 | 164 | 122 | >321 | 0.249 | 1175  |
| 1/2-21-15                          | 175 | yes | 182 | 189 | 109 | >253 | 0.237 | 1110  |
| 1-12-2                             | 175 | yes | 184 | 155 | 94  | >331 | 0.532 | 5230  |
| 1-12-3                             | 175 | yes | 198 | 169 | 136 | >312 | 0.495 | 4625  |
| 1-12-6                             | 175 | no  | 175 | ... | ... | >316 | 0.575 | 5000  |
| 1-31-1                             | 175 | yes | 169 | 176 | 156 | >304 | 0.484 | 4440  |
| 2-5-1                              | 175 | yes | 256 | 221 | 154 | >314 | 0.996 | 18620 |
| 2-5-2                              | 175 | yes | 232 | 192 | 150 | >350 | 0.997 | 18600 |
| 1-12-7                             | 250 | yes | 190 | 197 | 166 | >326 | 0.583 | 6250  |
| 1-12-8                             | 250 | yes | 191 | 171 | 154 | >338 | 0.597 | 6550  |
| (1/2-1)-14-1 <sup>e</sup>          | 175 | yes | 185 | 192 | 140 | ...  | 0.260 | 612   |
| (1/2-1)-14-2                       | 175 | yes | 177 | 190 | 137 | ...  | 0.254 | 584   |
| (1/2-2)-14-1 <sup>e</sup>          | 175 | yes | 170 | 150 | 125 | ...  | 0.252 | 268   |
| (1/2-2)-14-2                       | 175 | yes | 174 | 188 | 138 | ...  | 0.246 | 269   |
| Additional Data, Second Laboratory |     |     |     |     |     |      |       |       |
| 1-3-1                              | 75  | yes | 117 | ... | 117 | ...  | 0.518 | 4850  |
| 1-3-5                              | 75  | yes | 191 | 155 | 145 | 215  | 0.547 | 5595  |
| 1-3-8                              | 75  | yes | 214 | 194 | 170 | 214  | 0.531 | 5630  |
| 1-3-10                             | 75  | yes | 244 | 175 | 175 | 244  | 0.533 | 5580  |
| 1-3-12                             | 75  | yes | 200 | 173 | 155 | 227  | 0.530 | 5713  |
| 1-3-2                              | 125 | yes | 212 | 205 | 172 | ...  | 0.534 | 5560  |
| 1-3-4                              | 125 | yes | 207 | ... | 140 | ...  | 0.525 | 5520  |
| 1-3-9                              | 125 | yes | 203 | 210 | 160 | ...  | 0.569 | 5700  |
| 1-3-11                             | 125 | yes | 240 | 110 | 164 | 240  | 0.520 | 5090  |
| 1-3-7                              | 150 | yes | 210 | 141 | 134 | ...  | 0.536 | 5470  |

<sup>a</sup> Possible interpretation problem.  
<sup>b</sup> > Exceeded instrumental range at value indicated.  
<sup>c</sup> Data not obtained.  
<sup>d</sup> 1/2 thickness, IT profile geometry.  
<sup>e</sup> 1/2 in. thickness 2T profile geometry.

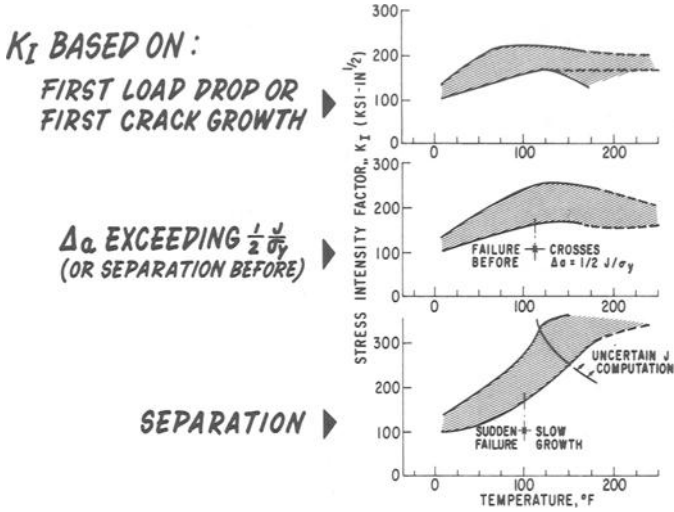


FIG. 4—Scatterbands for the  $J_{Ic}$  criteria.

pont. By noting the slope change, as seen in Fig. 3, and calculating the change in compliance from this new slope, the crack extension,  $\Delta a$ , can be calculated from Eq 13.  $J_I$  values may be calculated from Eq 1 corresponding to the load necessary for a crack extension,  $\Delta a$ . A typical plot of  $J_I$  versus  $\Delta a$  is shown in Fig. 5.

Now let us refer to Fig. 4 and compare the various criteria for determining  $J_{Ic}$ . It was necessary to raise the temperature of the specimens so that slow crack extension could be detected before the onset of

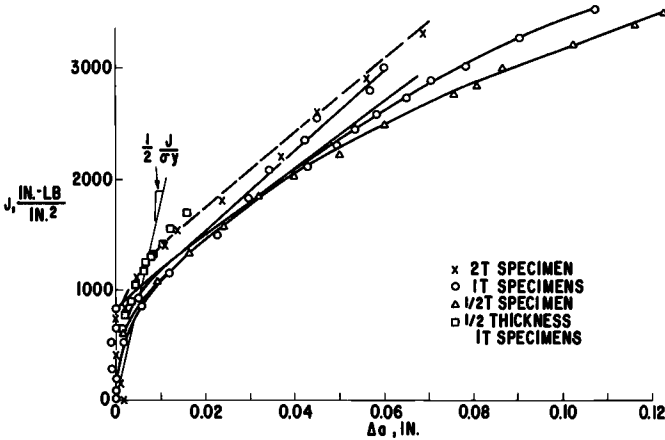


FIG. 5—Crack growth resistance curves for tests at 175°F.

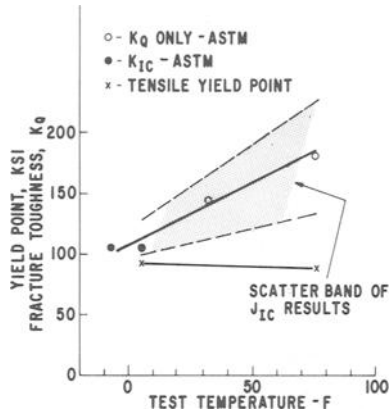


FIG. 6—ASTM fracture toughness, A469 Steel, 5T compact specimens.

rapid crack growth. At temperatures below 100°F, rapid fracture occurred before any sign of slow crack growth. It appears, therefore, that all the criteria are applicable below this temperature. The  $J_{IC}$  values measured, using all of the foregoing criteria, are essentially the same for temperatures below 100°F.

By heating the specimens to temperatures of 100°F and above, all four of the criteria can be applied to the  $J_I$  versus  $\Delta a$  curve to determine  $J_{IC}$ . The values obtained using each of the criteria will be different, however. The scatterbands of the results  $K_I$  versus temperature for the various fracture criteria, in Fig. 4, shows at higher temperatures, the divergence in results. The divergence is greatest for the criterion which depends on final failure or separation of the specimen.

The final separation or failure of the specimen criterion shows an ever increasing  $K_I$  value for higher temperatures, whereas all the other criteria show a leveling off trend of the  $K_I$  values at higher temperatures. This difference between the results of Criterion 4 and the other criteria is due to the slow crack extensions that occur; we would expect higher  $K_I$  values due to the force necessary to drive the crack and also due to the breakdown of the relationship, Eq 1, used to calculate  $J_I$ .

Specimen size effects only appear at large crack extension values as seen in Fig. 5. To eliminate the effect of specimen size, a short crack extension criterion should be used such as (a) first measurable crack extension or (b) intersection of the  $J_I$  versus  $\Delta a$  curve with the  $\Delta a = J_I/2\sigma_y$  line.

There are two findings worth noting in Fig. 5 which differ somewhat with the findings of Begley and Landes.

1. The initial slopes of the  $J_I$  versus  $\Delta a$  curves are vertical rather than on the line  $\Delta a = J_I/2\sigma_y$ .

2. The crack extension curves are linear beyond the intersection of the  $J_I$  versus  $\Delta a$  and the  $\Delta a = J_I/2\sigma_y$  line.

Work is continuing on both the testing of compact specimens and on testing three- and four-point bend bars.

### Conclusions

1.  $J_{Ic}$  testing using a single specimen to determine a  $J_I$  versus  $\Delta a$  curve has been successfully executed and duplicated in two independent laboratories. Good agreement in results was achieved.

2. The practice of measuring compliance changes to determine crack extension in a  $J_{Ic}$  test has been shown to be sensitive and practical in both laboratories.

3. The simple formulations for relating  $J_I$  to the area under load-deflection curve, Eq 1 and for relating crack extension to compliance change, Eq 13 have been shown to be sufficiently accurate for testing purposes for deeply cracked compact specimens.

4. Effects on results due to unloading are negligible when unloading is limited to less than 10 percent of the limit load.

5. The measurement point for determining  $J_{Ic}$  should be limited to short crack extensions. A suggested value is  $\Delta a = J_I/2\sigma_y$ .

6. No effects of specimen size and geometry on  $J_{Ic}$  were found for the range of specimens tested providing the  $J_{Ic}$  criterion is limited to short crack extension.

7. The results indicate that a practical and effective single specimen test procedure has been developed.

### References

- [1] Rice, J. R., *Journal of Applied Mechanics, Transactions, American Society of Mechanical Engineers*, Vol. 35, June 1968, pp. 379-386.
- [2] Rice, J. R., *Journal of the Mechanics and Physics of Solids*, Vol. 16, 1968, pp. 1-12.
- [3] Hutchinson, J. W., *Journal of the Mechanics and Physics of Solids*, Vol. 16, 1968, pp. 13-31.
- [4] Begley, J. A. and Landes, J. D. in *Fracture Toughness, Proceedings of the 1971 National Symposium on Fracture Mechanics, Part II, ASTM STP 514*, American Society for Testing and Materials, 1972, pp. 1-20.
- [5] Begley, J. A. and Landes, J. P., "Tentative  $J_{Ic}$  Test Method," presented to the ASTM Committee E-24.01 on the Fracture of Metals, 31 Oct. 1973, Philadelphia, Pa.
- [6] Rice, J. R., Paris, P. C., and Merkle, J. G. in *Progress in Flaw Growth and Fracture Toughness Testing, ASTM STP 536*, American Society for Testing and Materials, 1973, pp. 231-245.
- [7] Srawley, J. E. and Gross, B., Compendium, *Engineering Fracture Mechanics*, Vol. 14, 1972, pp. 587-589.
- [8] Tada, H., Paris, P., and Irwin, G., *The Stress Analysis Handbook*, Del Research Corp., Hellertown, Pa. 1973.
- [9] Paris, P. C. written discussion to Ref 4, p. 21.
- [10] Green, A. P. and Hundy, B. B., *Journal of the Mechanics and Physics of Solids*, Vol. 4, 1956, pp. 128-144.

W. A. Logsdon<sup>1</sup>

## Elastic Plastic ( $J_{Ic}$ ) Fracture Toughness Values: Their Experimental Determination and Comparison with Conventional Linear Elastic ( $K_{Ic}$ ) Fracture Toughness Values for Five Materials

---

**REFERENCE:** Logsdon, W. A., "Elastic Plastic ( $J_{Ic}$ ) Fracture Toughness Values: Their Experimental Determination and Comparison with Conventional Linear Elastic ( $K_{Ic}$ ) Fracture Toughness Values for Five Materials," *Mechanics of Crack Growth*, ASTM STP 590, American Society for Testing and Materials, 1976, pp. 43-60.

**ABSTRACT:** Good agreement was found between elastic plastic ( $J_{Ic}$ ) and previously developed conventional linear elastic ( $K_{Ic}$ ) critical fracture toughness values for five materials. The materials investigated included four rotor forging steels (ASTM A471 Ni-Cr-Mo-V, ASTM A469 Ni-Mo-V, ASTM A470 Cr-Mo-V, and AISI 403 modified 12Cr) plus an ASTM A217 21/4Cr-1Mo cast steel. A resistance curve test technique recently developed by Landes and Begley was employed to obtain the  $J_{Ic}$  fracture toughness values. Elastic plastic fracture toughness tests were performed with 1-in.-thick compact tension specimens at a minimum of three temperatures per material, the highest temperature being that where upper shelf fracture toughness behavior was first expected. The fine agreement between the elastic plastic and linear elastic critical fracture toughness values for this class of steels further supports the realization that the elastic plastic  $J_{Ic}$  fracture criterion, based largely on the path independent J-integral proposed by Rice, extends the concepts of linear elastic fracture mechanics into the elastic plastic fracture regime. Thus, it is now possible to obtain critical fracture toughness values with small specimens over a wide range of temperatures for tough materials.

**KEY WORDS:** crack propagation, fracture strength, mechanical properties, steels, fracture tests, stress analysis

Problems are often encountered in applying linear elastic fracture mechanics to the lower-strength, higher-toughness materials commonly

<sup>1</sup> Research engineer, Mechanics Department, Westinghouse Research Laboratories, Westinghouse Electric Corporation, Pittsburgh, Pa. 15235.

used for many structural applications. In order to meet the requirement of essential elastic behavior, structures of interest must be very large. Linear elastic fracture toughness specimens become massive (even though the maximum temperatures for valid test results based on the ASTM Test for Plane-Strain Fracture Toughness of Metallic Materials (E 399-72) are often as much as 400 to 500°F below service operating temperatures), and critical crack sizes at elastic stress levels are large enough to be of little practical concern. More often the practical problem concerns relatively small defects adjacent to stress concentration sites where the extent of plasticity rules out the use of linear elastic fracture mechanics. Consequently, Begley and Landes developed an elastic plastic  $J_{Ic}$  fracture criterion to provide a direct extension of fracture mechanics into the elastic plastic fracture regime [1,2].<sup>2</sup>

The purpose of this investigation was to determine experimentally elastic plastic  $J_{Ic}$  fracture toughness results and compare them with conventional linear elastic  $K_{Ic}$  fracture toughness results obtained previously according to ASTM Method E 399-72. Four rotor forging steels (ASTM A471 Ni-Cr-Mo-V, ASTM A469 Ni-Mo-V, ASTM A470 Cr-Mo-V, and AISI 403 modified 12Cr) plus an ASTM A217 21/4Cr-1Mo cast steel were the materials investigated.

A resistance curve test technique developed by Landes and Begley was employed to obtain the  $J_{Ic}$  fracture toughness values [4]. Elastic plastic fracture toughness tests were conducted at a minimum of three temperatures per material with the highest temperature being that where upper shelf fracture toughness behavior was first expected. One inch thick compact tension specimens were utilized for all the elastic plastic fracture toughness tests.

Keep in mind, linear elastic fracture mechanics technology provides a one parameter fracture criterion for a limited class of problems; those of cracked bodies with small-scale yielding where the crack tip plastic region is at least an order of magnitude smaller than the physical dimensions of the component. Clearly, it would be very desirable to have a fracture criterion which, by direct extension of the concepts of linear elastic fracture mechanics technology, could enable us to predict fracture in structures in cases of both large- as well as small-scale plasticity. The elastic plastic  $J_{Ic}$  fracture criterion, based largely on the path independent energy line integral  $J$  developed by Rice [3], has been proposed to satisfy the foregoing objectives.

As advanced by Begley and Landes [1], the physical significance of  $J$  for elastic plastic materials is that it is a measure of the characteristic crack tip elastic plastic field. As such  $J$  can be viewed as a single parameter characterization of the crack tip elastic plastic field, obviously

<sup>2</sup> The italic numbers in brackets refer to the list of references appended to this paper.

very similar to the role of  $K$  relative to linear elastic fracture mechanics. This is possible from the description of the strain hardening plastic crack tip singularity given by Hutchinson [5] and Rice plus Rosengren [6]. In fact, McClintock has shown that by combining  $J$  with the Hutchinson, Rice, and Rosengren crack tip model the near tip values of stress and strain can be expressed as a function of  $J$  [7]. This is directly analogous to the stress field equations of linear elastic fracture mechanics. In addition, for linear elastic behavior the  $J$ -integral is identical to  $G$ , the energy release rate per unit crack extension [1,8]. Therefore, the  $J_{Ic}$  fracture criterion for the linear elastic case is identical to the  $K_{Ic}$  fracture criterion. Consequently, the similarities between the  $J_{Ic}$  and  $K_{Ic}$  fracture criterion become apparent. Hopefully, the fine agreement found between the linear elastic and elastic plastic critical fracture toughness values for the class of steels investigated will further support the  $J_{Ic}$  elastic plastic fracture criterion as a direct extension of linear elastic fracture mechanics technology which can enable us to predict fracture in structures in cases of both large- as well as small-scale plasticity.

### Materials and Specimens

The materials tested include four rotor forging steels (ASTM A471 Ni-Cr-Mo-V, ASTM A469 Ni-Mo-V, ASTM A470 Cr-Mo-V, and AISI 403 modified 12Cr) plus an ASTM A217 21/4Cr-1Mo cast steel [9-13]. The chemical compositions and room temperature (except where noted) mechanical properties of these five materials are presented in Tables 1 and 2, respectively. The room temperature yield strengths of these steels ranged from 60.7 ksi for the ASTM A217 21/4Cr-1Mo cast steel to 135.0 ksi for the ASTM A471 Ni-Cr-Mo-V rotor forging steel. Therefore, all these materials could be considered medium strength steels.

One inch thick compact tension specimens were used to generate the fracture toughness data. In all cases, the elastic plastic fracture toughness specimens were removed from the corresponding fractured large-scale linear elastic fracture toughness specimens. Concerning the four rotor

TABLE 1—Chemical compositions of four rotor steels (ASTM A471 Ni-Cr-Mo-V, ASTM A469 Ni-Mo-V, ASTM A470 Cr-Mo-V, and AISI 403 modified 12Cr) plus an ASTM A217 21/4Cr-1Mo cast steel.

| Material   | Chemical Compositions, weight percent |      |       |       |      |      |       |      |      |       |       |
|------------|---------------------------------------|------|-------|-------|------|------|-------|------|------|-------|-------|
|            | C                                     | Mn   | P     | S     | Si   | Ni   | Cr    | Mo   | V    | Sn    | Sb    |
| Ni-Cr-Mo-V | 0.28                                  | 0.29 | 0.010 | 0.008 | 0.20 | 3.80 | 1.76  | 0.49 | 0.14 | 0.019 | 0.001 |
| Ni-Mo-V    | 0.25                                  | 0.66 | 0.008 | 0.012 | 0.23 | 2.92 | 0.25  | 0.43 | 0.09 | ...   | ...   |
| Cr-Mo-V    | 0.30                                  | 0.82 | 0.006 | 0.010 | 0.32 | 0.15 | 1.02  | 1.12 | 0.25 | ...   | ...   |
| 12Cr       | 0.13                                  | 0.57 | 0.009 | 0.006 | 0.33 | 1.60 | 12.32 | 0.55 | ...  | ...   | ...   |
| 21/4Cr-1Mo | 0.15                                  | 0.53 | 0.016 | 0.015 | 0.25 | ...  | 2.33  | 0.98 | ...  | ...   | ...   |

TABLE 2—Mechanical properties (75°F except where noted) of four rotor steels (ASTM A471 Ni-Cr-Mo-V, ASTM A469 Ni-Mo-V, ASTM A470 Cr-Mo-V and AISI 403 modified 12Cr) plus an ASTM A217 21/4Cr-1Mo cast steel.

| Material   | Mechanical Properties    |                        |                      |               |                     |                       |
|------------|--------------------------|------------------------|----------------------|---------------|---------------------|-----------------------|
|            | 0.2% Yield Strength, ksi | Ultimate Strength, ksi | Reduction in Area, % | Elongation, % | Energy Level, ft·lb | FATT, <sup>a</sup> °F |
| Ni-Cr-Mo-V | 135.0                    | 148.3                  | 56.7                 | 16.6          | 25                  | 110                   |
| Ni-Mo-V    | 85.5                     | 104.5                  | 62.5                 | 21.8          | 19                  | 145                   |
| Cr-Mo-V    | 90.8                     | 113.7                  | 46.9                 | 17.1          | 6                   | 215                   |
| 12Cr       | 98.9                     | 119.1                  | 48.5                 | 16.8          | 42                  | 68                    |
| 21/4Cr-1Mo | 60.7                     | 83.1                   | 42.8                 | 17.6          | 82                  | 12                    |

<sup>a</sup> FATT = fracture appearance transition temperature.

forging steels, test specimen orientation within the various rotor forgings (for both the  $J_{1c}$  and  $K_{1c}$  fracture toughness specimens) placed the specimen notch directions as near radial as possible.

Figure 1 illustrates the compact tension specimen geometry. Note that these specimens were modified so displacements could be measured at the specimen centerline of loading. Prior to conducting fracture toughness tests, the compact tension specimen starter notches were extended to fatigue crack severity. In order to avoid introducing any bias to the test results, the amount of crack tip plasticity created during fatigue precracking was limited to amounts significantly less than those anticipated in the subsequent fracture toughness tests. For all compact tension specimens involved in this program, a fatigue stress intensity ( $K_f$ ) of 25 ksi√in. accomplished precrack initiation, while fatigue stress intensities of 20 and 15 ksi√in. generated the initial and final crack extensions, respectively. Precrack lengths were controlled to produce a “deep notch” specimen,  $a/w = 0.6$ , where  $a$  is the crack length measured from the specimen centerline of loading and  $w$  is the specimen width (2.0 in. for a 1-in.-thick compact tension specimen, see Fig. 1).

### Experimental Procedure

Fracture toughness tests were conducted at a minimum of three temperatures per material. The first series of tests was performed normally at a temperature 50 to 75°F above the maximum temperature of valid fracture toughness results per the ASTM Method E 399-72 generated with 1-in.-thick compact tension specimens. A second series of tests was conducted at the temperature where zero percent brittle fracture first occurred in the Charpy V-notch impact test results. Upper shelf fracture toughness values are generally observed first at this temperature. The final test temperature was taken approximately midway between the above two



where

$A$  = area under the load-displacement curve taken at the displacement of interest,

$B$  = specimen thickness, and

$b$  = remaining uncracked ligament

was utilized to obtain  $J$  values. The critical value of  $J(J_{Ic})$  was obtained by extrapolating the resistance curve backward to the point of zero crack extension due to actual material separation. Note that critical elastic plastic fracture toughness values ( $J_{Ic}$ ) are based on crack initiation, not on an absolute value of crack extension as is the case for linear elastic fracture toughness values ( $K_{Ic}$ ). Finally, corresponding  $K_{Ic}$  values were calculated from the relationship between elastic plastic and linear elastic fracture mechanics parameters [1,8]

$$J_{Ic} = G_{Ic} = \frac{1 - \nu^2}{E} K_{Ic}^2$$

where

$\nu$  = Poisson's ratio and

$E$  = Young's modulus.

As an alternative to the resistance curve test technique, if the test temperature is low enough that the fracture toughness specimens experience a 100 percent cleavage fracture upon failure, the testing procedure is modified to: (a) test one specimen to failure by 100 percent cleavage; (b) load a second specimen to a centerline of loading displacement one or two mils less than that experienced by the failed specimen, unload the second specimen and mark the crack; and (c) if, as expected, the second specimen experiences no crack growth, the  $J$  value obtained from the first specimen is termed  $J_{Ic}$  and a full resistance curve is not necessary. This procedure was utilized to obtain  $J_{Ic}$  values at a minimum of one test temperature relative to each of the five materials investigated.

Finally, Landes and Begley have proposed a size requirement which must be met by an elastic plastic fracture toughness test specimen to assure valid fracture toughness results [4]. This size requirement is stated analytically as

$$a, B, b, \geq 25 \frac{J}{\sigma_f}$$

and has been adhered to in the present work.

## Results and Discussion

$J$  resistance curves relative to ASTM A471 Ni-Cr-Mo-V, ASTM A469 Ni-Mo-V, ASTM A470 Cr-Mo-V, and AISI 403 modified 12Cr rotor forging steels plus ASTM A217 21/4Cr-1Mo cast steel are presented in Figs. 2 through 6, respectively. Those temperatures where the fracture toughness test specimens experienced a 100 percent cleavage fracture upon failure (full resistance curve was not necessary) are revealed in Table 3. To provide a visual illustration, the specimens which comprise the 300°F resistance curve relative to AISI 403 modified 12Cr rotor steel (Fig. 5) are arranged in order of decreasing crack extension in Fig. 7. Note how the heat tinting procedure for marking the cracks makes the crack extension experienced by each of the specimens easily visible.

The fracture toughness (both  $K_{Ic}$  and  $J_{Ic}$ ) versus temperature results relative to Ni-Cr-Mo-V, Ni-Mo-V, Cr-Mo-V, and modified 12Cr rotor forging steels plus 21/4Cr-1Mo cast steel are illustrated in Figs. 8 through 12. In all cases, the solid lines through the linear elastic fracture toughness test results were drawn before the elastic plastic test results were added to these figures. Good agreement was obtained between the linear elastic ( $K_{Ic}$ ) and elastic plastic ( $J_{Ic}$ ) fracture toughness results for all five materials at all test temperatures. In a few cases, this may not be obvious. Apparent inconsistencies between linear elastic and elastic plastic fracture toughness results occurred in three instances; ASTM A471 Ni-Cr-Mo-V rotor forging steel at 150 and 250°F plus ASTM A217 21/4Cr-1Mo cast steel at -150°F. To help explain the first two apparent inconsistencies an "equivalent fracture toughness" (defined subsequently) was added to two of the fracture toughness temperature relationships (note Figs. 8 and 11).

Concerning the ASTM A471 Ni-Cr-Mo-V rotor forging steel (Fig. 8), the elastic plastic fracture toughness values at 150 and 250°F are considerably lower than the linear elastic fracture toughness results. Note that unlike the other four materials, this is the only material where valid linear elastic fracture toughness values are available at upper shelf temperatures. In fact, upper shelf linear elastic  $K_{Ic}$  behavior for low to intermediate strength steels was first observed on this rotor steel [9]. Recall that linear elastic fracture toughness values are based on 2 percent effective crack growth (that is, including the effect of plastic zone formation). Therefore, at 150°F, where 6-in.-thick compact tension specimens produced the valid fracture toughness results per ASTM Method E 399-72, fracture toughness was based on approximately 0.120 in. crack growth. Recall, the corresponding elastic plastic fracture toughness value was based on crack initiation (zero crack growth due to actual material separation). Observing the 150°F Ni-Cr-Mo-V resistance curve (Fig. 2), note for 0.120 in. crack growth  $J$  equals 990 lb/in. The corresponding value of linear elastic fracture toughness (termed the equivalent

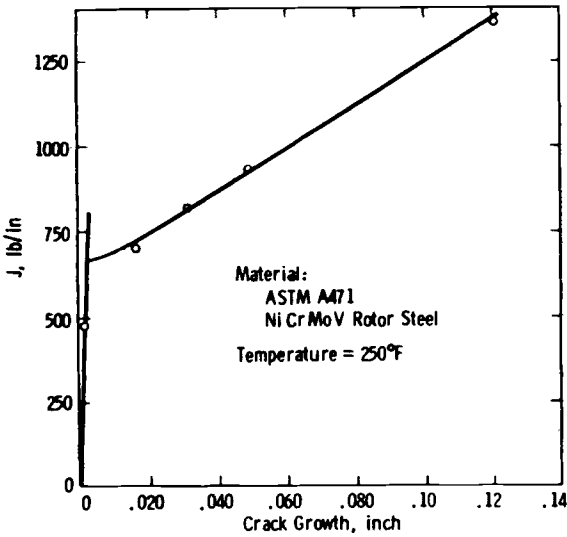
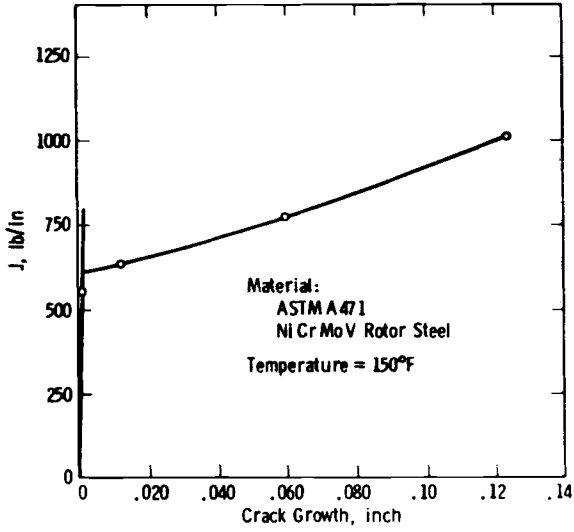


FIG. 2—J resistance curves for an ASTM A471 Ni-Cr-Mo-V rotor steel at temperatures of 150 and 250°F.

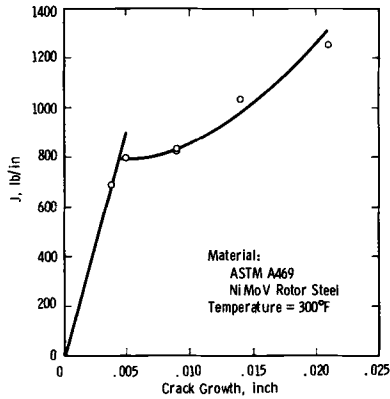


FIG. 3—J resistance curve for an ASTM A469 Ni-Mo-V rotor steel at a temperature of 300°F.

fracture toughness, EFT) equals  $180 \text{ ksi}\sqrt{\text{in.}}$ , which checks with the linear elastic fracture toughness value predicted in Fig. 8.

It should be pointed up that the equivalent fracture toughness (EFT) was utilized only as a means to relate the linear elastic and elastic plastic fracture toughness values and to demonstrate that the resistance curve test method for predicting elastic plastic fracture toughness provides in effect a “lower limit” fracture toughness value at elevated (approaching a material’s upper shelf) temperatures. The EFT was not employed to substantiate linear elastic versus elastic plastic critical fracture toughness values or vice versa. As has been documented [4], the EFT can vary

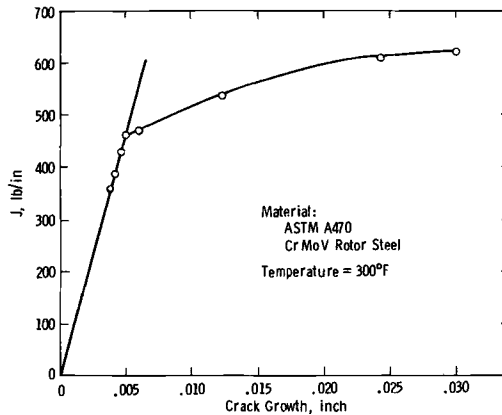


FIG. 4—J resistance curve for an ASTM A470 Cr-Mo-V rotor steel at a temperature of 300°F.

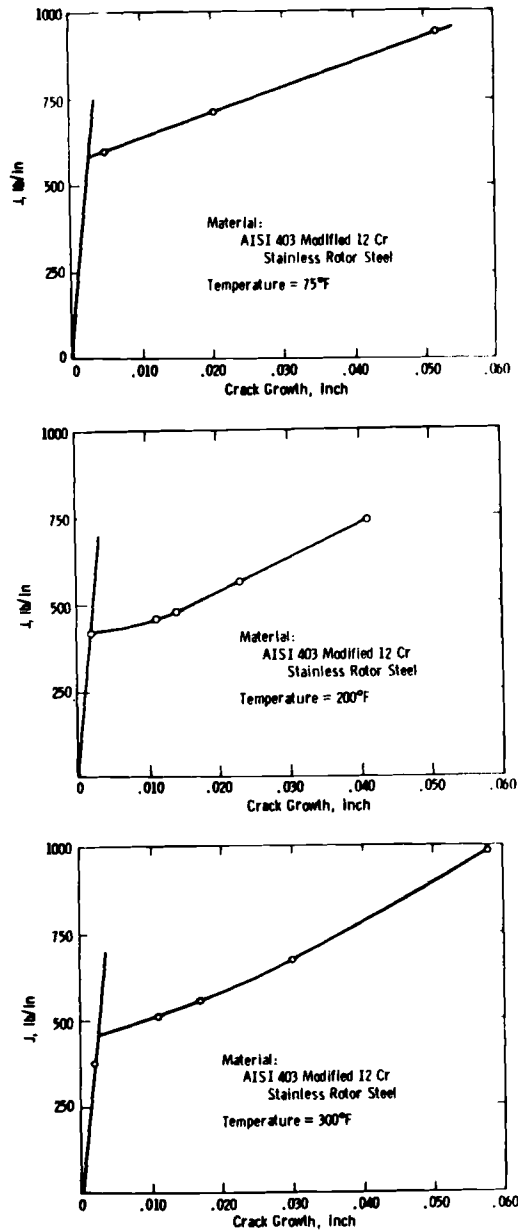


FIG. 5—J resistance curves for an AISI 403 modified 12Cr stainless rotor steel at temperatures of 75, 200, and 300°F.

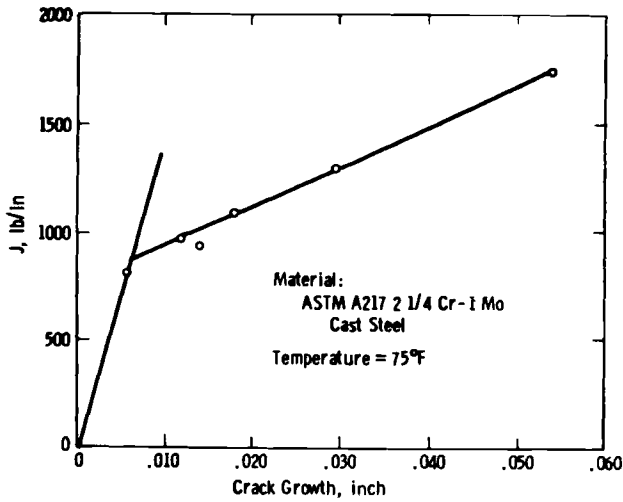
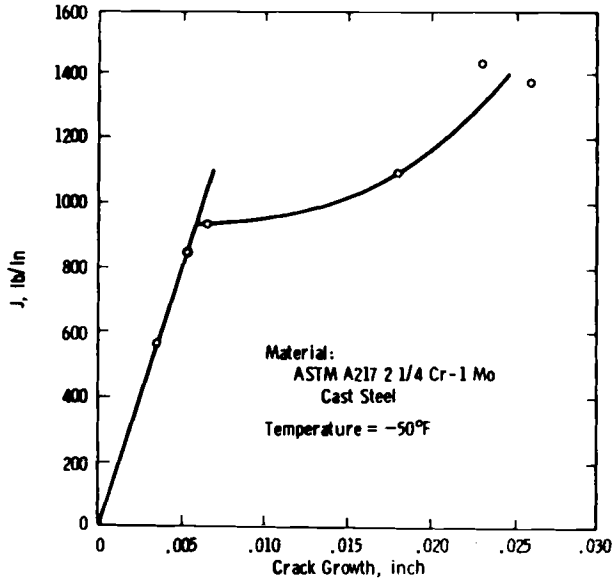


FIG. 6—J resistance curves for an ASTM A217 2¼Cr-1Mo cast steel at temperatures of -50 and 75°F.

TABLE 3—Temperatures where the specimens experienced 100 percent cleavage fractures and a full resistance curve was not necessary.

| Material   | Test Temperature, °F |
|------------|----------------------|
| Ni-Cr-Mo-V | 75                   |
| Ni-Mo-V    | 75, 150              |
| Cr-Mo-V    | 75, 200              |
| 12Cr       | 0                    |
| 21/4Cr-1Mo | -150                 |

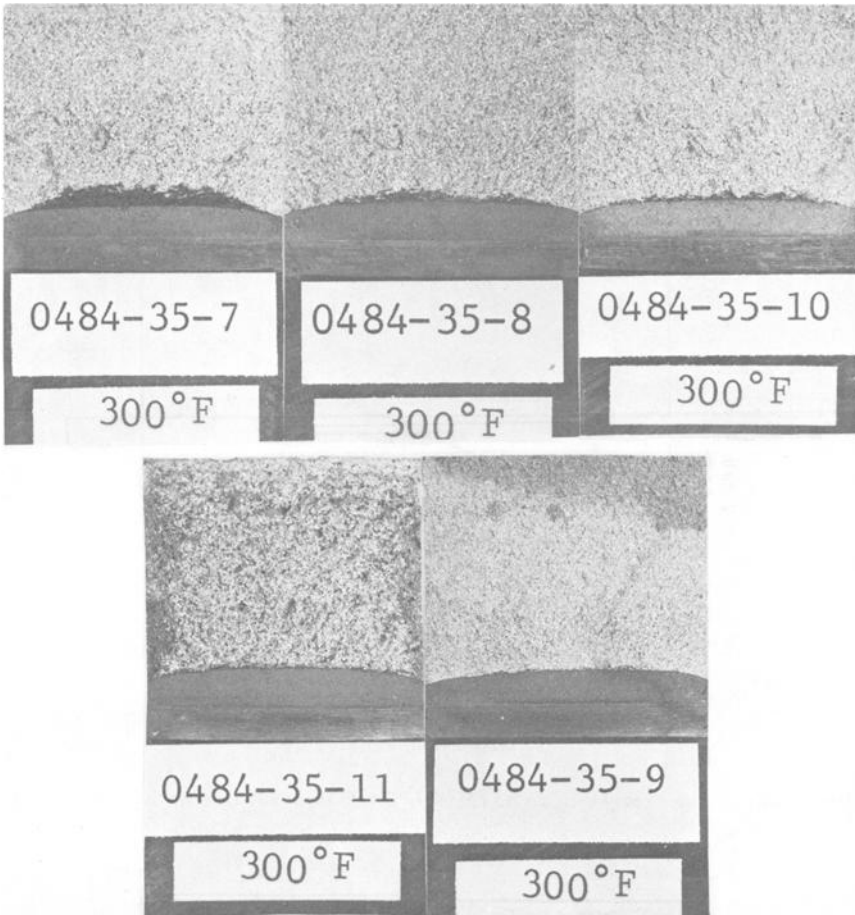


FIG. 7—Fracture surfaces of AISI 403 modified 12Cr rotor steel specimens tested at 300°F arranged in order of decreasing crack extension.

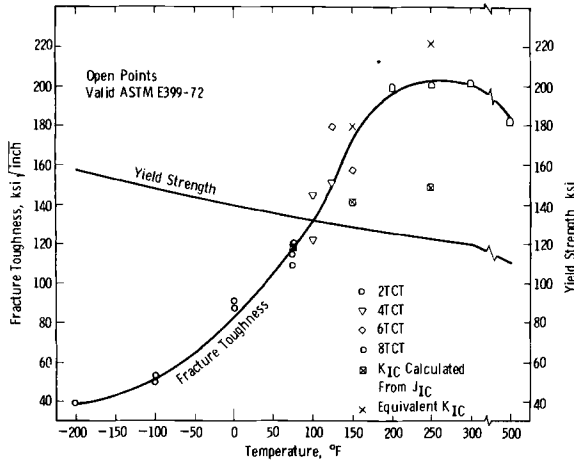


FIG. 8—Temperature dependence of yield strength and fracture toughness for an ASTM A471 Ni-Cr-Mo-V rotor steel.

enormously depending on the arbitrary selection of specimen geometry used to determine a resistance curve (especially for materials which produce steeply rising resistance curves with increasing crack growth) and is, therefore, not a single valued function of crack growth. It is the author's opinion, however, that the EFT provides the only effective means of relating linear elastic and elastic plastic fracture toughness values which would otherwise be unrelatable due to the different crack extension values which define their critical measurement points.

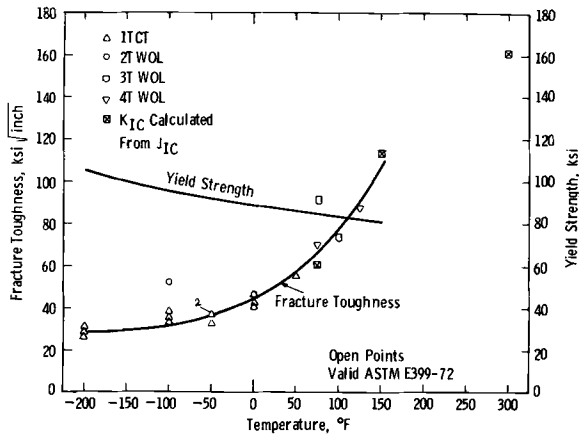


FIG. 9—Temperature dependence of yield strength and fracture toughness for an ASTM A469 Ni-Mo-V rotor steel.

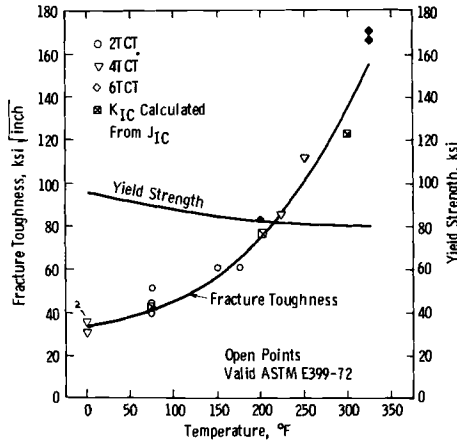


FIG. 10—Temperature dependence of yield strength and fracture toughness for an ASTM A470 Cr-Mo-V rotor steel.

Observing the fracture toughness values for ASTM A471 Ni-Cr-Mo-V rotor forging steel at 250°F, although 8-in.-thick compact tension specimens were utilized at this temperature, 7-in.-thick specimens would be adequate to obtain valid fracture toughness results per ASTM Method E 399-72. Therefore, valid fracture toughness values at 250°F would be based on 0.140 in. crack growth. The 250°F Ni-Cr-Mo-V resistance curve (Fig. 2) extrapolated to 0.140 in. crack growth yields a  $J$  value of 1500 lb/in. The corresponding EFT equals  $221.3 \text{ ksi}\sqrt{\text{in.}}$ , which is moderately

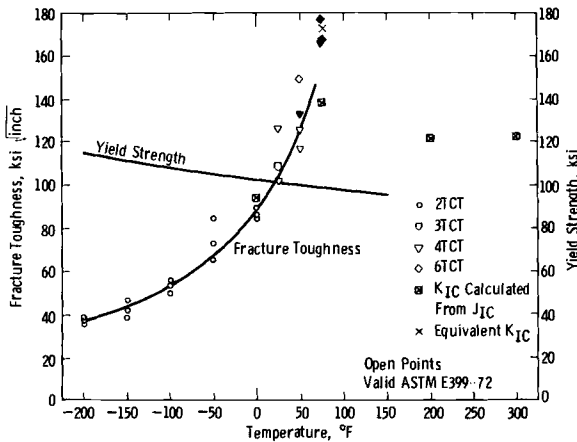


FIG. 11—Temperature dependence of yield strength and fracture toughness for an AISI 403 modified 12Cr stainless rotor steel.

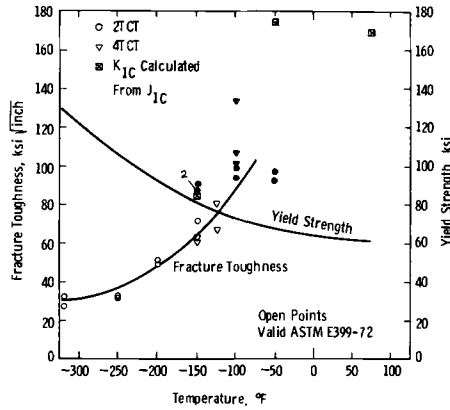


FIG. 12—Temperature dependence of yield strength and fracture toughness for an ASTM A217 2 $\frac{1}{4}$ Cr-1Mo cast steel.

higher than the value of linear elastic fracture toughness predicted in Fig. 8.

An additional instance where the equivalent fracture toughness was utilized to clarify an elastic plastic fracture toughness result occurs for AISI 403 modified 12Cr stainless rotor steel at 75°F. For this 12Cr stainless rotor steel, where linear elastic fracture toughness data, although invalid per ASTM Method E 399-72, was available at 75°F, the EFT was based on 0.050 in. crack growth. Since  $J_{1c}$  is based on crack initiation, the author's feeling is that reasonable estimates of  $J$  are best calculated out to a maximum of 5 percent crack growth (based on 1-in.-thick elastic plastic fracture toughness specimens), when no valid linear elastic fracture toughness data are available for comparison purposes.

Regarding the ASTM A217 2 $\frac{1}{4}$ Cr-1Mo cast steel (Fig. 12), the elastic plastic fracture toughness value at -150°F is higher than the corresponding valid linear elastic fracture toughness results. Recall that this material experienced a 100 percent cleavage fracture at this temperature and a full resistance curve was not necessary. This higher fracture toughness value is logical considering the property variability of the cast steel and the relative sampling size of  $J_{1c}$  and  $K_{1c}$  specimens. Where a 1-in.-thick specimen was employed for the elastic plastic test, 2- and 4-in.-thick specimens were utilized for the linear elastic fracture toughness tests. The crack tip leading edge thus sampled two or four times the property controlling near tip volume of the 1-in.-thick elastic plastic specimens. In general, smaller specimens will more likely be entirely composed of tough material while larger specimens will more likely contain a low toughness region and thus exhibit a relatively low  $K_{1c}$  or  $J_{1c}$  value. As shown by the data for 2 $\frac{1}{4}$ Cr-1Mo cast steel at -150°F, the larger the specimen the

lower the fracture toughness. The tendency for  $J_{Ic}$  values to lie somewhat above the  $K_{Ic}$  curve at low temperatures (where 100 percent cleavage fractures occur and a full resistance curve is not necessary) is interpreted as a Weibull type phenomenon rather than an intrinsic effect of specimen size on toughness.

Therefore, with each of the three apparent inconsistencies explained, the fine agreement between elastic plastic ( $J_{Ic}$ ) and linear elastic ( $K_{Ic}$ ) critical fracture toughness values for all five materials at all test temperatures becomes clear.

### Conclusions

The development and success of an elastic plastic fracture criterion which directly extends the concepts of linear elastic fracture mechanics into the elastic plastic fracture regime will result in both immediate and far reaching consequences.

Naturally, foremost is the ability to predict failures in cases of large-scale yielding. Providing the critical elastic plastic fracture toughness ( $J_{Ic}$ ) of a particular material is known and an elastic plastic analysis (which describes  $J$  as a function of the loading parameter and crack size) is available for a specific structure of interest manufactured from this same material, it is now possible to prevent failures by observing appropriate precautions which will ensure that the applied level of  $J$  in the structure never exceeds  $J_{Ic}$ .

Several less obvious benefits also originate from the development and success of an elastic plastic fracture criterion. First is the tremendous savings in both material and machining costs relative to the compact tension specimen sizes required for  $J_{Ic}$  as opposed to  $K_{Ic}$  fracture toughness tests. For the five materials investigated, 1-in.-thick compact tension specimens adequately produced valid upper shelf elastic plastic  $J_{Ic}$  fracture toughness values. At the identical temperatures, compact tension specimens up to 8-in.-thick were required to obtain valid linear elastic  $K_{Ic}$  fracture toughness test results. Thus, it is now possible to obtain critical fracture toughness values with small specimens over a wide range of temperatures for tough materials.

Secondly, the maximum temperature for valid linear elastic  $K_{Ic}$  fracture toughness results for this class of steels (even with massive specimens) is normally less than 300°F. Naturally, the actual service operating temperatures experienced by many structural components are often several hundred Fahrenheit degrees higher. When performing a fracture mechanics analysis, some of the procedures presently employed to obtain the operating temperature fracture toughness values are to: (a) extrapolate the fracture toughness temperature curve to the operating temperatures of interest, (b) estimate the fracture toughness by utilizing one of the correlations developed between fracture toughness and Charpy V-notch

impact properties [15], or (c) simply use the maximum valid fracture toughness value available. With the development and success of the elastic plastic fracture criterion, however, it is now possible to obtain actual fracture toughness values at specific service operating temperatures with small compact tension specimens. Thus, increased confidence can be placed in the fracture mechanics analysis techniques utilized to predict the critical flaw sizes required to cause failure of specific structural components.

A final important and far reaching outcome of the elastic plastic fracture criterion and the small-scale specimens now required to obtain valid fracture toughness results concerns the future possibility that lower limits of fracture toughness relative to specific temperatures (possibly the actual intended service operating temperature) be included in material specifications and acceptance standards. This is presently the case for tensile and Charpy impact properties. With the small specimens now required for fracture toughness tests, ample material is generally available to manufacture the necessary fracture toughness specimens from core bars, etc. Therefore, at least for this class of steels, a giant step forward toward increased product integrity and structural reliability may now be possible by requiring that specific minimum fracture toughness standards be satisfied as an integral part of the material specifications and acceptance standards.

#### *Acknowledgments*

This work is based in full on an M. S. thesis submitted by the author in partial fulfillment of the requirements for the degree of Master of Science in Mechanical Engineering at the University of Pittsburgh. The author gratefully acknowledges Doctors T. C. Woo, M. J. Doyle, and J. G. Wagner at the University of Pittsburgh for their advice and review of the work.

The author is also particularly indebted to Doctors J. A. Begley and J. D. Landes of the Westinghouse Research Laboratories for their helpful suggestions and review of the work and to W. H. Pryle and A. R. Petrush, also of the Westinghouse Research Laboratories, for their contributions to the experimental phases of the program. The material, specimens, and test equipment were provided by the Westinghouse Research Laboratories through the Fracture Mechanics Section, under the direction of E. T. Wessel.

#### **References**

- [1] Begley, J. A. and Landes, J. D. in *Fracture Toughness, Proceedings of the 1971 National Symposium on Fracture Mechanics, Part II, ASTM STP 514*, American Society for Testing and Materials, 1972, pp. 1-20.
- [2] Landes, J. D. and Begley, J. A. in *Fracture Toughness, Proceedings of the 1971 National Symposium on Fracture Mechanics, Part II, ASTM STP 514*, American Society for Testing and Materials, 1972, pp. 24-39.

- [3] Rice, J. R., *Journal of Applied Mechanics, Transactions, American Society of Mechanical Engineers*, Vol. 35, Series E, June 1968, pp. 379-386.
- [4] Landes, J. D. and Begley, J. A. in *Fracture Analysis, Proceedings of the 1973 National Symposium on Fracture Mechanics, Part II, ASTM STP 560*, American Society for Testing and Materials, 1974, pp. 170-186.
- [5] Hutchinson, J. W., *Journal of the Mechanics and Physics of Solids*, Vol. 16, 1968, pp. 13-31.
- [6] Rice, J. R. and Rosengren, G. F., *Journal of the Mechanics and Physics of Solids*, Vol. 16, 1968, pp. 1-12.
- [7] McClintock, F. A. in *Fracture; An Advanced Treatise*, Vol. 3, H. Liebowitz, Ed., Academic Press, New York, 1971, Chapter 2.
- [8] Begley, J. A., Landes, J. D. and Wessel, E. T., "Fracture Mechanics, A Practical Tool for Preventing Failures," presented at the Third International Conference on Fracture, Munich, Germany, April 1973.
- [9] Begley, J. A. and Toolin, P. R., "Fracture Toughness and Fatigue Crack Growth Rate Properties of a NiCrMoV Steel Sensitive to Temper Embrittlement," presented at the Fourth National Symposium on Fracture Mechanics, Carnegie-Mellon University, Pittsburgh, Pa., Aug. 1970.
- [10] Greenberg, H. D., Wessel, E. T., Clark, W. G., Jr. and Pryle, W. H., "Critical Flaw Sizes for Brittle Fracture of Large Turbine Generator Rotor Forgings," presented at the Fifth International Forgemaster Meeting, Turin, Italy, May 1970.
- [11] Madeyski, A., Logsdon, W. A., and Breneman, C. B., Jr., "Correlation of Ultrasonic Tests, Material Evaluation and Spin Test Results for a CrMoV Turbine Rotor Forging," presented at the International Forging Conference, Paris, France, 20-25 April 1975.
- [12] Logsdon, W. A., *Engineering Fracture Mechanics*, Vol. 7, No. 1, March 1975.
- [13] Logsdon, W. A. and Pryle, W. H., "Fracture Toughness and Fatigue Crack Growth Rate Properties of ASTM A217 GR WC-9 21/4Cr-1Mo Cast Steel," unpublished Westinghouse Research data, 1972.
- [14] Rice, J. R., Paris, P. C. and Merkle, J. G. in *Progress in Flaw Growth and Fracture Toughness Testing, ASTM STP 536*, American Society for Testing and Materials, 1973, pp. 231-245.
- [15] Begley, J. A. and Logsdon, W. A., "Correlation of Fracture Toughness and Charpy Properties for Rotor Steels," unpublished Westinghouse Research data, 1971.

G. R. Yoder<sup>1</sup> and C. A. Griffis<sup>1</sup>

## Application of the J-Integral to the Initiation of Crack Extension in a Titanium 6A1-4V Alloy

---

**REFERENCE:** Yoder, G. R. and Griffis, C. A., "Application of the J-Integral to the Initiation of Crack Extension in a Titanium 6A1-4V Alloy," *Mechanics of Crack Growth, ASTM STP 590*, American Society for Testing and Materials, 1976, pp. 61-81.

**ABSTRACT:** Tests were conducted to determine  $J_{1c}$  from resistance curves of  $J$  versus crack extension, obtained from fatigue-precracked specimens of a titanium 6A1-4V alloy. Specimens of various geometries were employed, all in three-point bending. Crack extensions were delineated by heat tinting.

Results obtained with  $J$  computed from the equation,  $J = 2A/Bb$ , are compared to those obtained with the compliance technique, using the plane-stress solutions of Bucci et al.  $J_{1c}$  results are compared with a valid  $K_{1c}$  value for this material.

The range of ratios of crack length to specimen width ( $a/W$ ) is explored over which the equation  $J = 2A/Bb$  applies. The decrease in crack extension at experimental limit load ( $\Delta a_{P_{max}} \rightarrow \Delta a_c$ ) is examined as the ratio of specimen thickness to uncracked ligament ( $B/b$ ) is increased. Variation in  $J_{1c}$  from specimens cut from different positions through the plate thickness is also examined.

**KEY WORDS:** crack propagation, fractures (materials), elastic-plastic fracture, mechanical properties, crack extension, titanium alloys, compliance calibration, fracture initiation

A growing body of experimental evidence [1-5]<sup>2</sup> supports the critical value of Rice's J-integral [6,7],  $J_{1c}$ , as a criterion for the initiation of crack extension in elastic-plastic fracture. Recent J-integral studies demonstrate success with an unload/heat-tint, resistance-curve technique to determine  $J_{1c}$  in steel [3], titanium [4], and aluminum [5] alloys. The purpose of this

<sup>1</sup> Metallurgists, Strength of Metals Branch, Engineering Materials Division, Naval Research Laboratory, Washington, D. C. 20375.

<sup>2</sup> The italic numbers in brackets refer to the list of references appended to this paper.

paper is to present in the open literature the first J-integral studies of a titanium alloy.

In this work, eight different types of fatigue-precracked, three-point bend specimens have been tested. For several of these, resistance curves of  $J$  versus crack extension ( $\Delta a$ ) have been obtained by heat tinting multiple specimens of a given type which have been unloaded from different points on the respective diagram of load ( $P$ ) versus load point displacement ( $\delta$ ). For purposes of comparison, evaluation of the J-integral has been made by two methods: (1) the Begley and Landes compliance calibration technique [1,2], using the plane-stress plastic-zone-size corrected solutions of Bucci et al [8] which simulate well the experimental  $P$  versus  $\delta$  traces obtained from the precracked specimens, and (2) the approximation equation proposed independently by Rice et al [9] and Srawley [10]

$$J = \frac{2A}{Bb} \quad (1)$$

where

$A$  = area under the  $P$  versus  $\delta$  curve at the point of interest,

$B$  = specimen thickness, and

$b$  = uncracked ligament.

To define the point of initiation of crack extension,  $\Delta a_c$ , and hence  $J_{Ic}$ , it is necessary to select a criterion, perhaps somewhat arbitrarily at this point. The one used in this work was proposed recently by Paris [11], namely, that  $\Delta a_c$  be defined by the largest amount of actual crack extension (1 percent) permitted in the smallest allowable  $K_{Ic}$  specimen

$$\Delta a_c = 0.025 \frac{EJ_{Ic}}{\sigma_{ys}^2(1 - \nu^2)} \quad (2)$$

where

$E$  = Young's modulus,

$\sigma_{ys}$  = uniaxial yield strength, and

$\nu$  = Poisson's ratio.

Values of  $J_{Ic}$  obtained in this study are compared to a valid  $K_{Ic}$  value for this alloy via

$$J_{Ic} = G_{Ic} = \frac{K_{Ic}^2(1 - \nu^2)}{E} \quad (3)$$

where material constants  $G_{Ic}$  and  $K_{Ic}$  are critical values of the crack extension force and stress-intensity factor, respectively.

The specimen type of least thickness is used to examine for possible variation in  $J_{Ic}$  as a function of position through the plate thickness. In another series of tests, the range of ratios of crack length to specimen width ( $a/W$ ) is explored over which Eq 1 holds.

**Experimentation**

*Material and Specimens*

All specimens were cut from a 1-in.-thick plate of mill-annealed Ti-6Al-4V alloy with the chemical composition and mechanical properties given in Table 1. Light photomicrographs in Fig. 1a reveal a microstructure consisting of elongated primary  $\alpha$  grains dispersed in an  $\alpha$ - $\beta$  Widmanstätten (basketweave) matrix. Extensive crossrolling is evident from these micrographs and seems to be reflected in the tensile properties, determined with standard 0.505-in.-diameter specimens. The yield strength in both the longitudinal (L) and transverse (T) directions is 124 ksi; Young's modulus is  $18.55 \times 10^3$  ksi in the T direction. The mode of

TABLE 1—Alloy composition and mechanical properties.  
Chemical Composition, (weight percent)

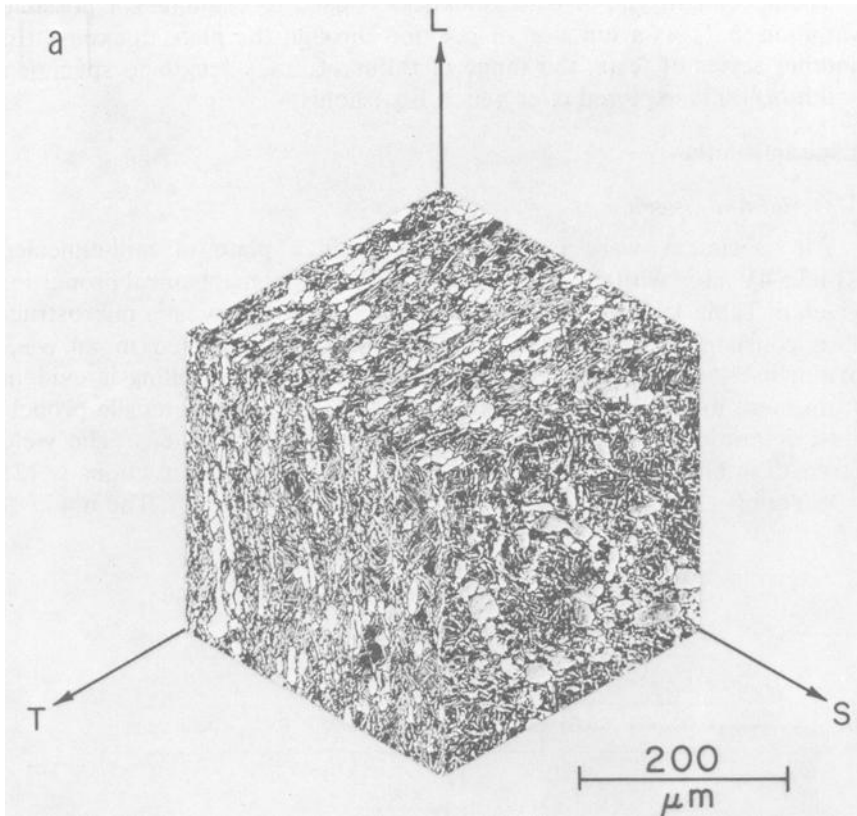
| Al  | V   | Fe   | C     | N     | H     | O    | Ti      |
|-----|-----|------|-------|-------|-------|------|---------|
| 6.0 | 4.1 | 0.05 | 0.023 | 0.008 | 0.005 | 0.06 | balance |

Tensile Properties

| 0.2% Offset Yield Strength        |       | Tensile Strength |       | Reduction of Area, % | Elongation, %     | Young's Modulus   |       |
|-----------------------------------|-------|------------------|-------|----------------------|-------------------|-------------------|-------|
| ksi                               | MPa   | ksi              | MPa   |                      |                   | $\times 10^3$ ksi | GPa   |
| <i>Transverse Direction (T)</i>   |       |                  |       |                      |                   |                   |       |
| 124.4                             | 868.3 | 133.8            | 933.9 | 39.5                 | 13.5 (in 2 in.)   | 18.55             | 129.5 |
| <i>Longitudinal Direction (L)</i> |       |                  |       |                      |                   |                   |       |
| 124.1                             | 866.2 | 130.5            | 910.9 | 39.5                 | 16.5 (in 1.4 in.) | 18.56             | 129.5 |

Stress Intensity Factor Data

| Specimen Type | $P_{max}/P_Q$ | $K_Q, \text{ksi}\sqrt{\text{in.}}$ | $2.5$                               | $K_Q = \bar{K}_{Ic}$ |
|---------------|---------------|------------------------------------|-------------------------------------|----------------------|
|               |               |                                    | $(K_Q/\sigma_{ys})^2 < B, a, W - a$ |                      |
| A (a)         | 1.12          |                                    |                                     | no                   |
| (b)           | 1.09          | 59.7                               | yes                                 | yes                  |
| (c)           | 1.11          |                                    |                                     | no                   |
| C (a)         | 1.23          |                                    |                                     | no                   |

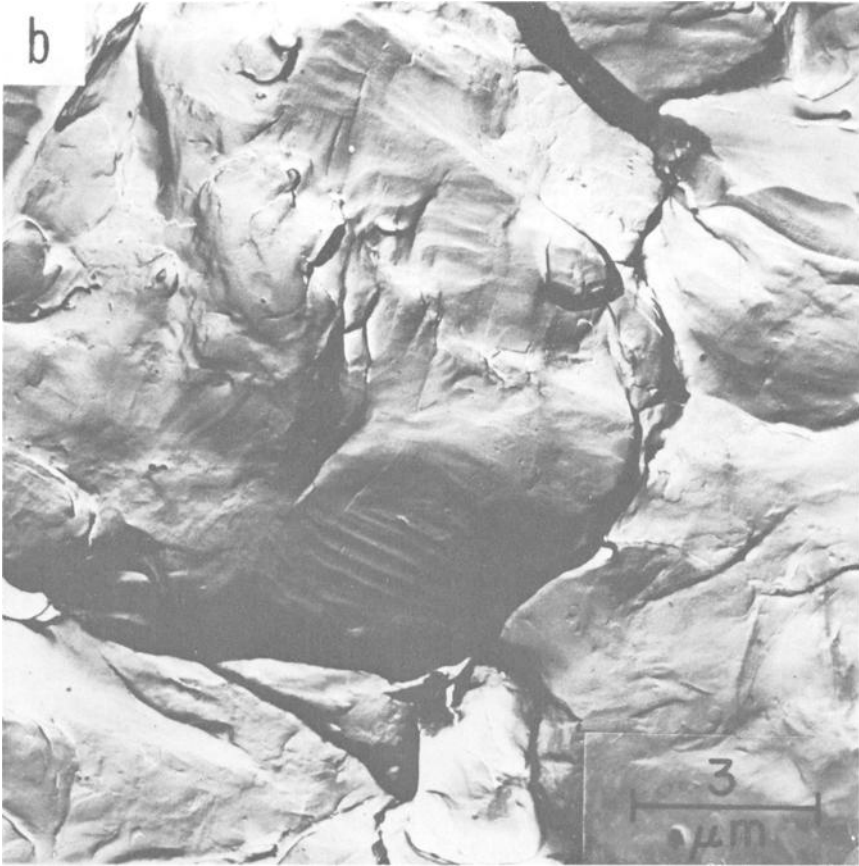


(a) Light photomicrographs of microstructure; etched with Kroll's reagent.

FIG. 1—Definition of alloy microstructure and mode of crack extension.

crack extension in this alloy is microvoid coalescence, as illustrated by the replica electron micrograph of Fig. 1*b*.

Cross sectional geometries of the eight types of three-point bend specimens used, Types A through H, are presented in Fig. 2 with a list of dimensions. Thicknesses ( $B$ ) range from 0.250 to 1.000 in., widths from 0.658 to 1.500 in.,  $a_0/W$  ratios from 0.313 to 0.745 and  $B/b$  ratios from 0.61 to 2.99. All specimen types, with one exception, were machined from the plate midthickness, that is, with equal amounts of metal removed from the plate surfaces relative to the  $B$  dimension. In the case of Type E, subscripts are used to designate position of the specimen relative to plate thickness, that is,  $E_c$  from the center or plate midthickness versus  $E_s$  cut from as near the plate surface as possible. All specimens were fatigue precracked at levels of stress-intensity factor permitted by ASTM Test for Plane-Strain Fracture Toughness of Metallic Materials (E 399-72), with



(b) Replica electron fractograph of dimpled rupture.

FIG. 1—(Continued).

crack orientations all in the TL direction. These specimen types exhibited, to varying degrees, loading behavior characteristic of the lower end of the elastic-plastic regime. That is, all exhibited limit loads which were substantially less than those expected for the fully plastic state, which may be approximated for three-point bending by [8,12]

$$P_L = 1.456 \sigma_{ts} \frac{B}{S} (W - a)^2 \quad (4)$$

where

$\sigma_{ts}$  = uniaxial tensile strength and  
 $S$  = span length.

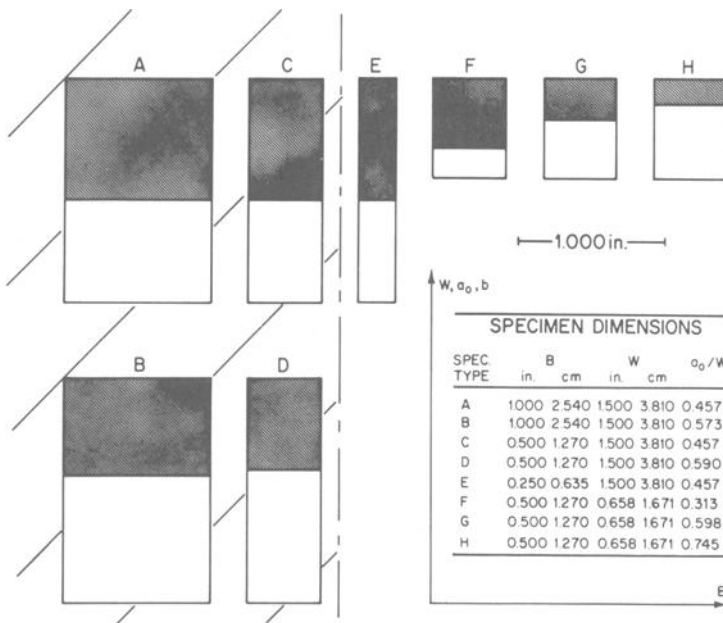


FIG. 2.—Cross-sectional views of specimen types and list of dimensions. Shaded portion of cross section indicates ligament  $b \times B$ .

Moreover, behavior of the specimen type with the most highly constrained crack (Type A) appeared to be only marginally “invalid” with respect to ASTM Method E 399-72, as only one specimen of three of this type examined for  $K_Q$  provided a valid  $K_{Ic}$  value of 59.7 ksi $\sqrt{\text{in.}}$ , as noted in the stress-intensity factor data of Table 1.

### Test Procedure

All specimen types were tested in the fixture shown in Fig. 3a. A clip gage was used to measure  $\delta$  as illustrated; a supplementary gage can be seen to span the crack mouth opening in accord with ASTM Method E 399-72. The span between rollers was  $S = 5.975$  in. All tests were conducted in room-temperature air.

To determine the point on a  $P$  versus  $\delta$  diagram at which crack extension initiated, multiple specimens of a given type were loaded to various points on the respective  $P$  versus  $\delta$  diagram (anywhere from the incidence of nonlinearity to maximum load), followed by complete unloading, as illustrated in Fig. 3b for specimens of Type C. Specimens were then heat tinted in a circulating-air furnace at 600°F (589 K) for 2 h and broken open for examination. Crack extensions corresponding to the points of unloading in Fig. 3b are shown in the photograph of Fig. 3c. Initial

fatigue-precrack length was measured according to ASTM Method E 399-72, as was the crack extension delineated by heat tinting, that is, the amount of crack extension was taken as an average of that measured at the quarterpoints of specimen thickness. Inasmuch as the initiation of crack extension is a heterogeneous nucleation process, this is admittedly an arbitrary measure of crack extension and, therefore, should be kept in mind as a potential source of scatter in results. Uncertainty in individual measurements is  $\approx \pm 0.001$  in.

In one of the ways used to evaluate the J-integral, the Begley and Landes technique was used to obtain a compliance calibration from  $P$  versus  $\delta$  diagrams generated for several  $a/W$  ratios from plane stress plastic zone size corrected solutions of Bucci et al. These  $P$  versus  $\delta$  traces were integrated graphically using the trapezoidal rule, with increments of 0.005-in. displacement. These solutions simulate well the experimental  $P$  versus  $\delta$  traces obtained from the precracked specimens, as illustrated in Fig. 4 for specimen Types A through D; notable deviations at some of the greatest displacements are attributable to crack extension in the precracked specimens. In using Eq 1 to evaluate the J-integral, it is appropriate to note that  $A$  has been taken to be area under the actual experimental  $P$  versus  $\delta$  trace, minus the component owing to the test fixture, in accord with the Srawley formulation.

## Results and Discussion

### *Comparison of Resistance-Curve Data*

Resistance-curve data of  $J$  versus  $\Delta a$  for specimen Types A through D are presented in Figs. 5a and b, for which  $J$  was evaluated from the compliance calibration technique and Eq 1, respectively. Curves sketched for each specimen type in Fig. 5a are shown as solid lines in Fig. 5c for comparison with the respective dashed curves from Fig. 5b. At lower values of  $\Delta a$ , the scatter in data defined by the solid lines overlaps quite well that from the dashed lines, although near  $\Delta a = 0$  there is a tendency toward slightly lower  $J$  values as calculated from Eq 1. On the other hand, at the higher values of  $\Delta a$ , the dashed curves indicate notably greater  $J$  values, as maximum load ( $P_{\max}$ ) is approached, than do the respective solid lines, particularly for specimen Types C and D. This may be a reflection of Landes and Begley's prediction that  $J$  values computed by Eq 1 would be overestimated, particularly at greater  $\Delta a$ , owing to the influence of crack growth effects on  $A$  [3]. By comparison, the compliance technique would not be expected to so overestimate  $J$ .

To infer levels of  $J_{1c}$  from Figs. 5a and b,  $\Delta a_c$  can be estimated from Eq 2 to be approximately  $6 \times 10^{-3}$  in., by using the mean extrapolated value of  $J$  for  $\Delta a = 0$  in Fig 5, or from the value of  $K_{1c}$  noted earlier. From Fig. 5a, it follows that  $J_{1c} = 188$  to  $235$  in·lb/in.<sup>2</sup> or  $211 \pm 24$  in·lb/in.<sup>2</sup>; this

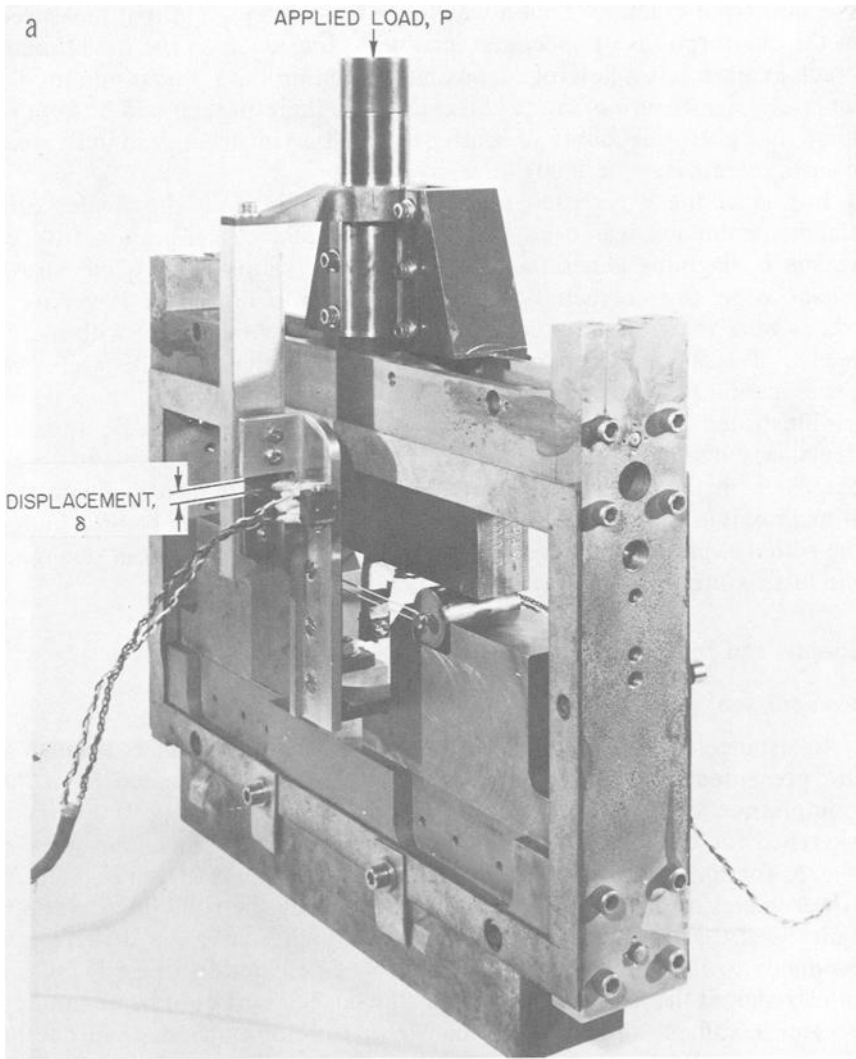


FIG. 3—Test procedure: multiple specimens of each type were loaded in three-point bend test fixture shown in (a) to various points on respective  $P$  versus  $\delta$  diagram as shown in (b); then they were unloaded and heat tinted to reveal crack extensions as shown in (c). Case illustrated is for specimen Type C, with individual specimen numbers identified in (b) and (c).

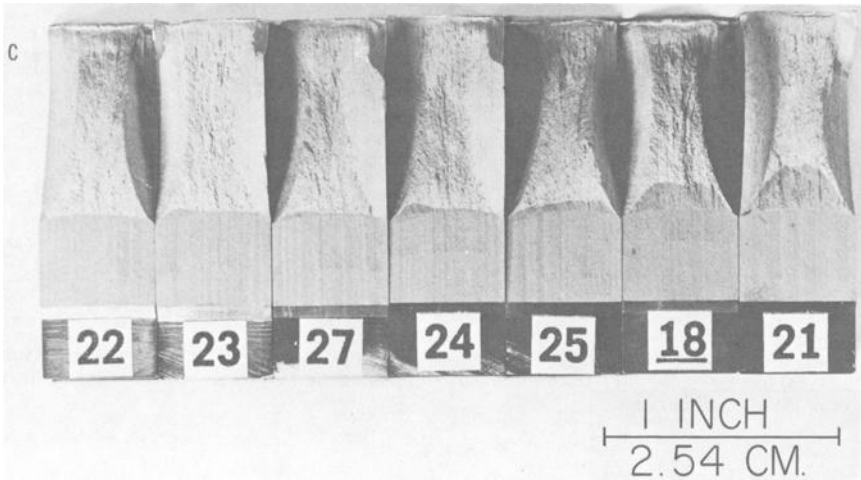
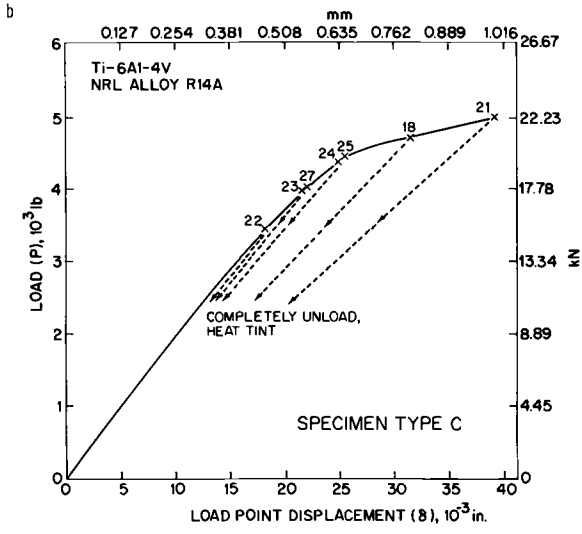


FIG. 3—(Continued).

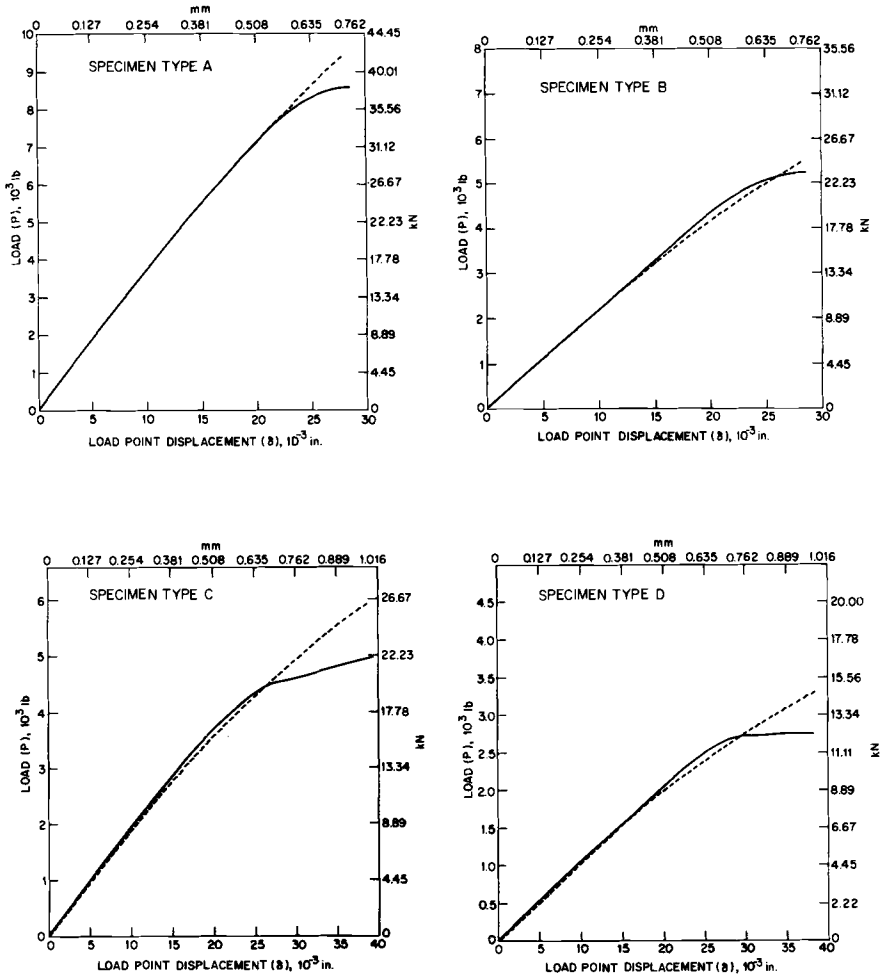


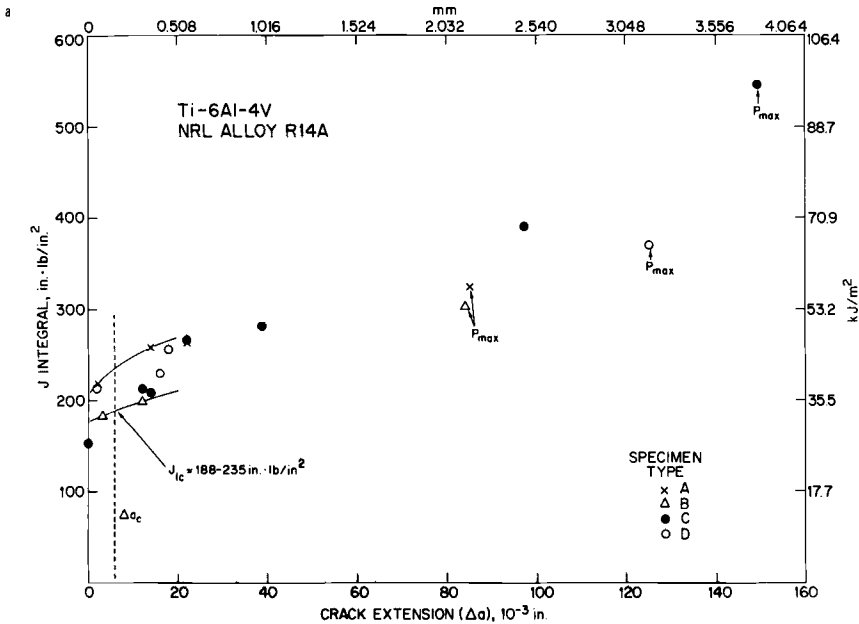
FIG. 4—Comparison of  $P$  versus  $\delta$  diagrams obtained from precracked specimens (solid curves) to those generated from plane-stress plastic-zone-size corrected solutions of Bucci et al [8] (dashed curves).

compares with  $J_{Ic} = 158$  to  $209$  in·lb/in.<sup>2</sup> or  $184 \pm 26$  in·lb/in.<sup>2</sup> inferred from Fig. 5*b*. This amounts to a variation in  $J_{Ic}$  of  $< \pm 12$  percent from Fig. 5*a* and  $< \pm 15$  percent from Fig. 5*b*. These correspond to variations in  $K_{Ic}$  of  $< \pm 6$  percent and  $< \pm 7$  percent, respectively. This is substantially less variation than might well be found in  $K_{Ic}$  testing of mill-annealed titanium alloy plates [13]. The question as to which of the two mean values,  $J_{Ic} = 184$  or  $211$  in·lb/in.<sup>2</sup>, is the more accurate is a moot point. The value of  $K_{Ic}$  cited in Table 1 translates to  $J_{Ic} = 170$  or  $192$  in·lb/in.<sup>2</sup>, depending on whether the factor  $(1 - \nu^2)$  should be included or not in Eq 3 [14,15]. Moreover it can be argued that the quoted  $K_{Ic}$  value may be in fact lower than the average value for the plate material, inasmuch as two out of three  $K_Q$  tests failed to provide a valid  $K_{Ic}$  determination.

*Specimen-Size Analysis*

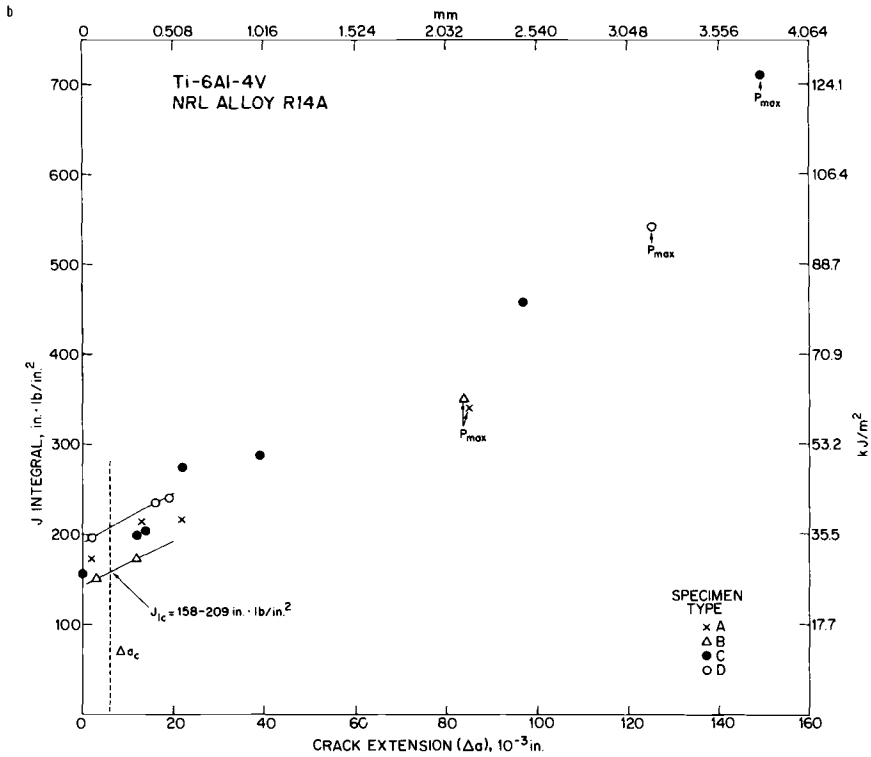
It has been estimated that “legal”  $J_{Ic}$  determinations can be obtained with specimens of limiting dimensions [3,16]

$$a, B, b > \alpha \frac{J_{Ic}}{\sigma_{flow}} \tag{5}$$



(a) Data for  $J$  evaluated by compliance calibration technique.

FIG. 5—Resistance curves of  $J$  versus  $\Delta a$  for specimen Types A through D, from which  $J_{Ic}$  is defined at  $\Delta a_c$ .



(b) Data for  $J$  evaluated from  $J = 2A/Bb$ .

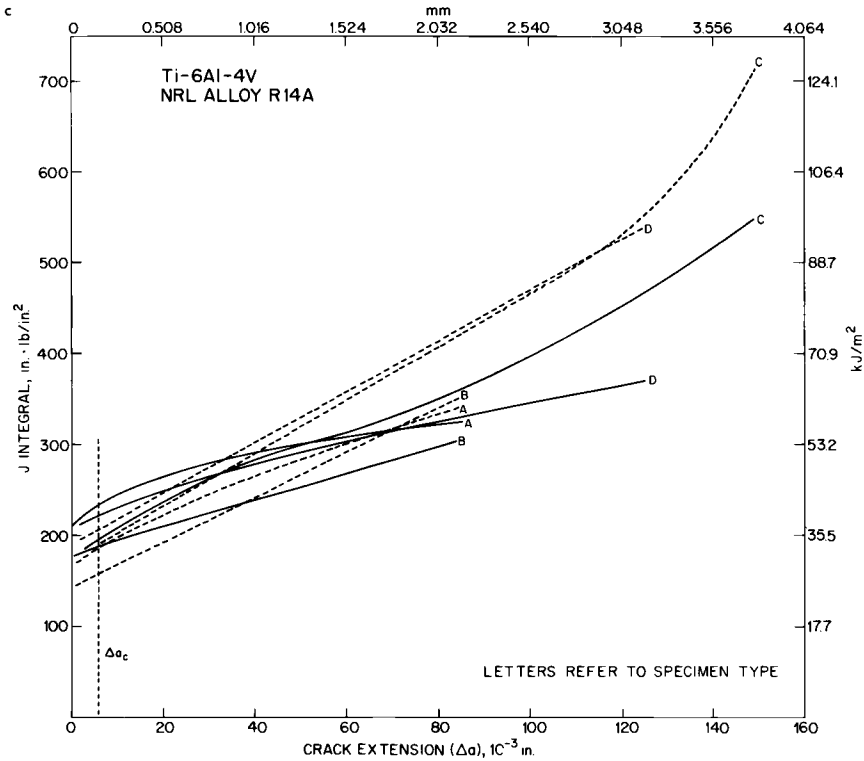
FIG. 5—(Continued).

with  $\alpha = 50$  and  $\sigma_{flow}$  taken as the mean of  $\sigma_{ys}$  and  $\sigma_{ts}$ . For a level of  $J_{1c} = 195 \text{ in}\cdot\text{lb}/\text{in}^2$ , this means for the present alloy that  $a$ ,  $B$ , and  $b$  must exceed about 0.08 in. This value is exceeded by the respective dimensions of all specimens, Types A through H.

*Variation of  $J_{1c}$  with Position Through the Plate Thickness*

Specimens  $E_c$  and  $E_s$  were unloaded at displacements near the initiation point and heat tinted. Results are plotted in Fig. 6a relative to the data scatterband obtained near initiation in Fig. 5a, for specimen Types A through D with  $J$  evaluated by the compliance method. A substantial difference in  $J$  values is evident between the two specimens: for  $\Delta a = 12$  and 13 mils, respectively, specimen  $E_c$  exhibits a level of  $J = 256 \text{ in}\cdot\text{lb}/\text{in}^2$ , whereas  $J = 159 \text{ in}\cdot\text{lb}/\text{in}^2$  for specimen  $E_s$ .

As might be expected, replica electron fractographs of actual heat-tinted crack extension reveal significantly larger dimples in the region of greater toughness, namely, the plate midthickness, Fig. 6b, than appear in



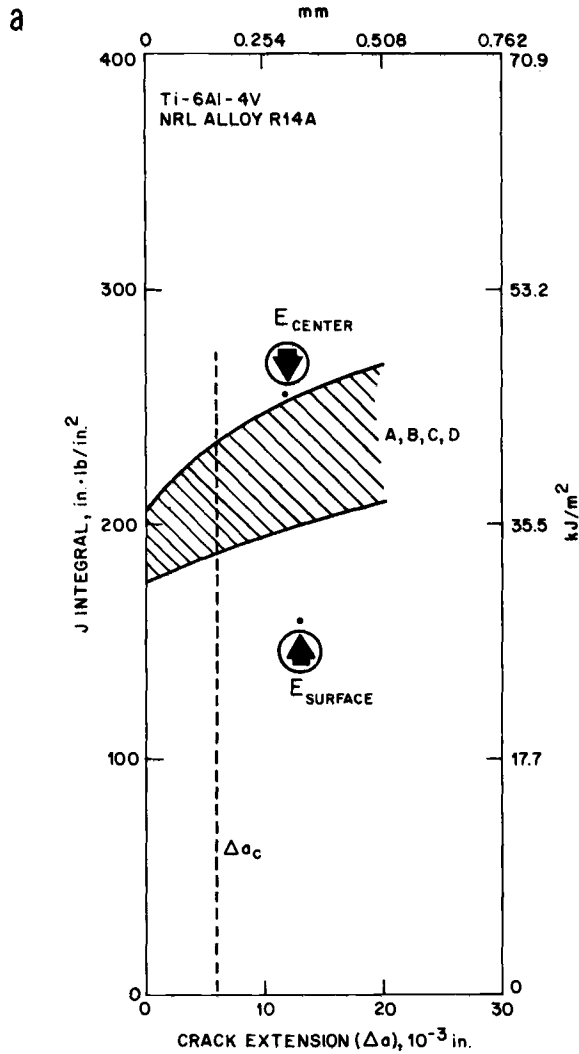
(c) Comparison of resistance curves from data in Figs. 5a and b, solid and dashed curves, respectively.

FIG. 5—(Continued).

the region near the plate surface, Fig. 6c. (Note that heat tinting has done little to obscure fractographic features in this alloy). Though the microstructure of this alloy is relatively uniform for a mill-annealed plate of Ti-6Al-4V, the primary  $\alpha$ -phase was somewhat greater in percentage and more elongated in shape at the plate midthickness; the grain size of the  $\alpha$ - $\beta$  Widmanstätten matrix was also somewhat finer there than near the surface. On the other hand, Rockwell C hardness measurements (HRC) made through the plate thickness showed little variation. On the face normal to the L direction, HRC varied from  $\sim 31$  at the center to  $\sim 32$  at the surface; however, on the face normal to the T-direction, HRC was higher in the center ( $\sim 33.5$ ) than near the surface ( $\sim 32.0$ ).

*Effect of a/W and B/b Ratios on  $J_{1c}$  Determination*

Specimen Types F, G, and H were tested to explore the range of a/W ratios for which J may be calculated via Eq 1; Srawley [10] has suggested



- (a) J-integral data evaluated by compliance calibration technique and plotted relative to data for specimen Types A through D near initiation.
- (b) Replica electron fractograph of crack extension at plate midthickness after heat tinting.
- (c) Replica electron fractograph of crack extension near plate surface after heat tinting.

FIG. 6—Differential in toughness between plate midthickness region and region near plate surface, as revealed from specimens  $E_c$  and  $E_s$ , respectively. Dimple size is notably larger in region corresponding to position of  $E_c$  than that of  $E_s$ , shown in (b) and (c) respectively.

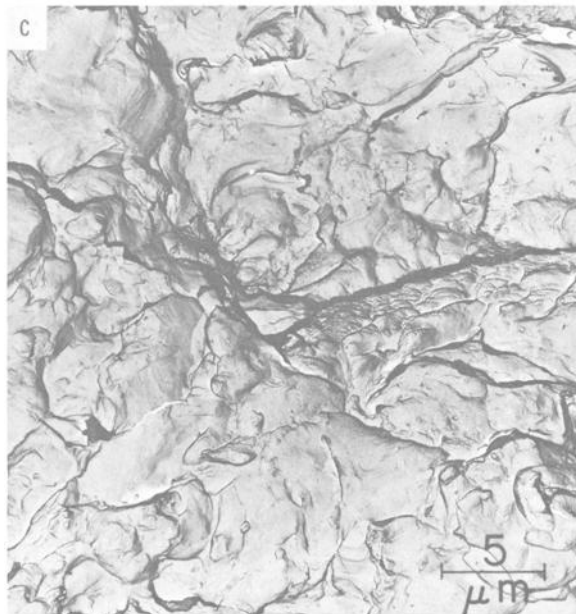
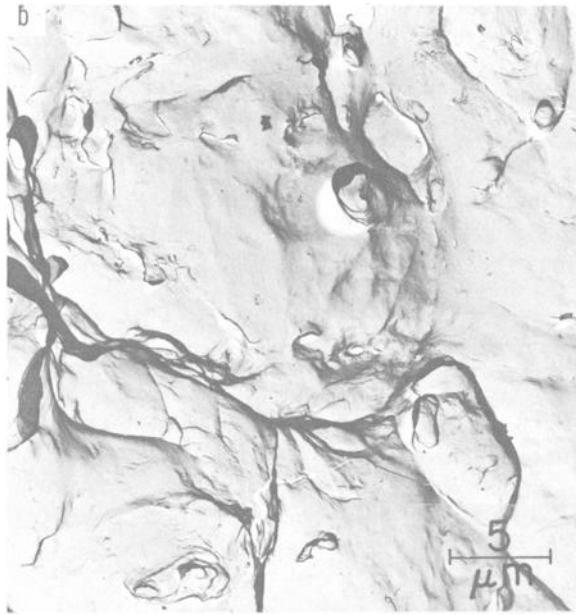


FIG. 6—(Continued).

that the range should extend from 0.2 to 0.95. Specimens of these three types were unloaded near the initiation point and heat tinted. Results are plotted in Fig. 7 relative to the data scatterband obtained near initiation in Fig. 5b for specimen Types A through D. For specimen Type F ( $a/W = 0.313$ ), the  $J$  value calculated from Eq 1 is obviously too high, namely, 306 in·lb/in.<sup>2</sup> at  $\Delta a = 3$  mils. Though for specimen Type G ( $a/W = 0.598$ ) the  $J$  value appears reasonable, that for specimen Type H is obviously too low with  $J = 148$  in·lb/in.<sup>2</sup> at  $\Delta a = 13$  mils.

In view of the derivation of Eq 1 by Rice et al, the result for specimen Type F might not be unexpected; however, for a deeply cracked specimen such as Type H, it is. From Table 2, which summarizes  $J_{Ic}$  data obtained via Eq 1 for the different specimen types, it is evident that specimen Type H has the smallest dimension  $b$  (0.167 in.). Though this dimension is about twice the limiting value of 0.08 in. suggested by  $\alpha = 50$  in Eq 5, perhaps this limiting value is too low for the present case; that is, maybe  $\alpha \approx 100$  or greater. It is pertinent to note that for the case of bend bars of a rotor steel, Landes and Begley [2] noted a decrease in apparent  $J_{Ic}$  for a specimen with  $b < 50 J_{Ic}/\sigma_{flow}$ . Similarly for the case of specimen Type F, it is possible that specimen size limitation could be a factor in the result, since Type F has the smallest dimension  $a$  of all types examined, namely, 0.206 in.

In the interest of developing a single specimen test for  $J_{Ic}$ , as opposed to the multiple specimens required by the unload/heat-tint, resistance-curve technique, Corten has proposed [17] that  $J_{Ic}$  can be obtained from a single specimen if  $B/b \geq 2$  and if  $P_{max}/P_L \geq 0.85$ ; that is, under these conditions, it is proposed that  $\Delta a_{Pmax} \rightarrow \Delta a_c$ . For each specimen type listed in Table 2, the  $B/b$  ratio is given as well as the experimentally observed  $P_{max}$ , the ratio  $P_{max}/P_L$ , and the value of  $J$  corresponding to  $P_{max}$ , namely  $J_{Pmax}$ . Also included are values of crack extension found at  $P_{max}$ ,  $\Delta a_{Pmax}$ , for comparison with  $\Delta a$  near the initiation point,  $\Delta a_c$ . In Fig. 8,  $\Delta a_c$ ,  $J_{Pmax}$  and  $P_{max}/P_L$  are plotted versus  $B/b$ . It is evident that none of the specimen types exhibit  $P_{max}/P_L \geq 0.85$ , as they range from a low of 0.40 for Type A to a high of 0.56 for Type H. However, it is readily apparent that  $\Delta a_{Pmax}$  is an inverse function of  $B/b$ , with  $\Delta a_{Pmax}$  ranging from a high of 0.149 in. at the lowest  $B/b = 0.61$ , to a low of  $\Delta a = 0.013$  in. at the highest  $B/b = 2.99$ . Values of  $J_{Pmax}$  vary similarly with  $B/b$ . Though these trends support Corten's basic idea, unfortunately it may be difficult to design "legal"  $J_{Ic}$  specimens of this alloy to attain  $P_{max}/P_L \geq 0.85$ . Comparison of Types D and G, specimens of equal  $B$  and  $a/W \approx 0.6$ , shows that reduction of  $W$  from 1.5 to 0.66 in. led to an increase of  $P_{max}/P_L$  from 0.45 to only 0.55; however,  $W$  could not be so reduced much further if the size limitation on  $a$  and  $b$  is indeed  $\approx 0.2$  in. for this alloy (that is, if  $\alpha = 100$  in Eq 5).

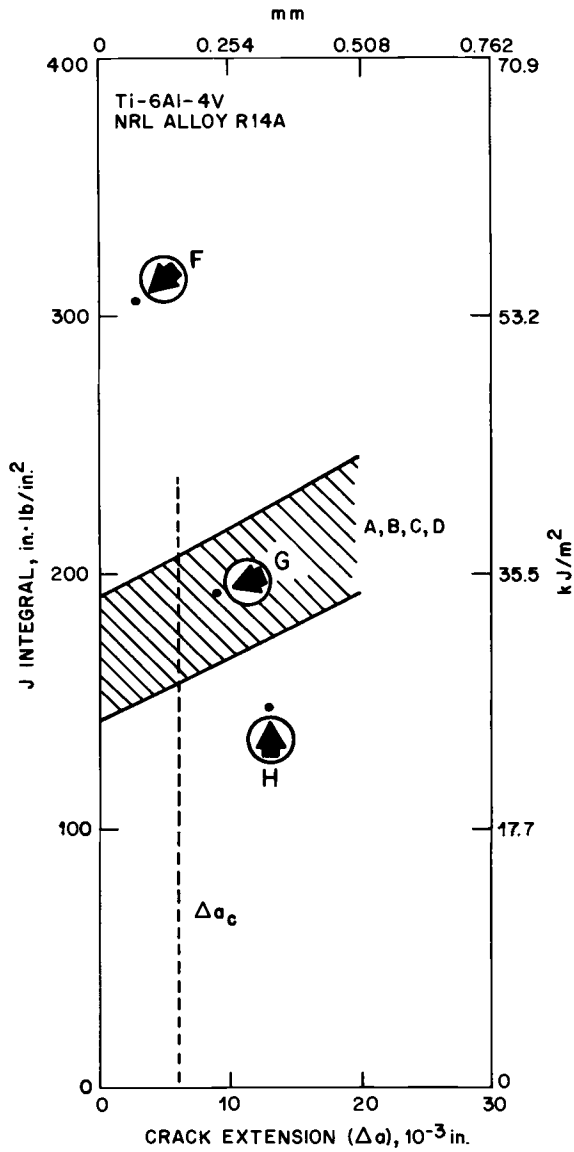


FIG. 7—Data of  $J$  versus  $\Delta a$  for specimen Types F through H, with  $J$  computed from  $J = 2A/Bb$  and plotted relative to data for specimen Types A through D near initiation.

TABLE 2—Summary of J-integral data for the various specimen types, with J evaluated from  $J = 2A/Bb$ .

| Specimen Type | $a_0/W$ (nominal) | $J_{Ic}$ (approximate), in. lb/in. <sup>2</sup> | $\Delta a_c$ (approximate), 10 <sup>-3</sup> in. | $\Delta a_{max}$ , 10 <sup>-3</sup> in. | $P_{max}$ , lb | $P_{max}/P_L$ | $b$ , in. | $B/b$ | $J_{Ic,max}$ , in. lb/in. <sup>2</sup> |
|---------------|-------------------|---|--|---|----------------|---------------|-----------|-------|--|
| A             | 0.457             | 186   | 6  | 85                                      | 8600           | 0.40          | 0.815     | 1.23  | 341                                    |
| B             | 0.573             | 158   | 6  | 84                                      | 5585           | 0.44          | 0.640     | 1.56  | 351                                    |
| C             | 0.457             | 190   | 6  | 149                                     | 4975           | 0.46          | 0.815     | 0.61  | 711                                    |
| D             | 0.590             | 206   | 6  | 125                                     | 2790           | 0.45          | 0.615     | 0.81  | 542                                    |
| F             | 0.313             | 306   | 3  | 81                                      | 1548           | 0.47          | 0.452     | 1.11  | 472                                    |
| G             | 0.598             | 192   | 9  | <45                                     | 623            | 0.55          | 0.265     | 1.89  | <274                                   |
| H             | 0.745             | 148   | 13   | 13                                      | 257            | 0.56          | 0.167     | 2.99  | 148                                    |

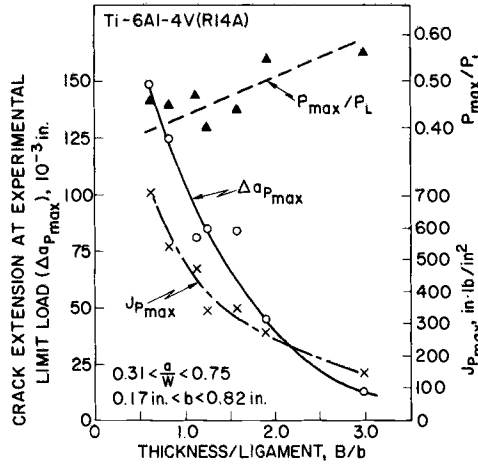


FIG. 8—Influence of thickness to ligament ratio (B/b) on crack extension at experimental limit load ( $\Delta a_{p_{max}}$ ),  $J_{p_{max}}$  and  $P_{max}/P_L$ .

**Summary**

Tests were conducted to determine  $J_{Ic}$  from resistance curves of  $J$  versus crack extension obtained from fatigue-precracked specimens of a titanium 6Al-4V alloy. Three-point bend specimens of eight geometries were employed, with crack extensions delineated by heat tinting. Findings from this work include:

1. Over the range  $a/W = 0.45$  to  $0.60$ , the determination of  $J_{Ic}$  obtained with  $J$  computed from the equation  $J = 2A/Bb$  agrees quite well with that obtained by evaluating  $J$  via the compliance calibration technique; moreover, these determinations of  $J_{Ic}$  are in good agreement with a valid  $K_{Ic}$  value for this alloy.

2. At the greater crack extensions, as experimental limit load is approached, resistance curves obtained with  $J$  computed as  $J = 2A/Bb$  are notably higher than those obtained with  $J$  evaluated by the compliance method.

3. In exploring the range of  $a/W$  over which the equation  $J = 2A/Bb$  is applicable, erratic results were obtained at ratios of  $0.31$  and  $0.75$ . Though the former might be interpreted to be outside the range of applicability, the latter may imply that the specimen size limitation defined by  $a$ ,  $B$ ,  $b > \alpha(J_{Ic}/\sigma_{flow})$  was violated at a surprisingly high level of  $\alpha \approx 100$ . Further work is suggested to determine whether  $\alpha$  might indeed be this high for titanium alloys in general.

4. Significant variation in  $J_{Ic}$  was found from specimens machined from different positions through the plate thickness. This finding has serious implications regarding any future standard method for  $J_{Ic}$  testing: If  $J_{Ic}$

results obtained from relatively small, thin specimens are to be used to estimate toughness of a thick plate from which they are cut, such specimens should be made at multiple positions through the plate thickness. If the variance of  $J_{Ic}$  with position exceeds some specified percentage, the estimate for the thick plate should not be legal, at least until some rational averaging procedure is adopted.

5. Crack extension at maximum load was found to vary inversely with  $B/b$ . For  $B/b$  ratios ranging from 0.61 to 2.99,  $\Delta a_{p_{max}}$  decreased from 0.149 to 0.013 in. Values of  $J_{p_{max}}$  similarly decreased with increasing  $B/b$  ratio.

### Acknowledgments

The authors gratefully acknowledge the very able technical assistance of S. J. McKaye and the financial support of the Office of Naval Research. Special thanks are extended to Drs. G. R. Irwin and F. J. Loss for stimulating discussions during the evolution of this work and to S. M. McCoy and J. N. Robinson for the electron fractographs.

### References

- [1] Begley, J. A. and Landes, J. D. in *Fracture Toughness, Proceedings of the 1971 National Symposium on Fracture Mechanics, Part II, ASTM STP 514*, American Society for Testing and Materials, 1972, pp. 1-20.
- [2] Landes, J. D. and Begley, J. A. in *Fracture Toughness, Proceedings of the 1971 National Symposium on Fracture Mechanics, Part II, ASTM STP 514*, American Society for Testing and Materials, 1972, pp. 24-39.
- [3] Landes, J. D. and Begley, J. A. in *Fracture Analysis, Proceedings of the 1973 National Symposium on Fracture Mechanics, Part II, ASTM STP 560*, American Society for Testing and Materials, 1974, pp. 170-186.
- [4] Yoder, G. R. and Griffis, C. A., "J Integral and the Initiation of Crack Extension in a Titanium Alloy," NRL Report 7662, Naval Research Laboratory, 26 Feb. 1974.
- [5] Griffis, C. A. and Yoder, G. R., "Application of the J Integral to Crack Initiation in a 2024-T351 Aluminum Alloy," NRL Report 7676, Naval Research Laboratory, 3 April 1974.
- [6] Rice, J. R., *Transactions, American Society of Mechanical Engineers, Series E, Journal of Applied Mechanics*, Vol. 35, 1968, pp. 379-386.
- [7] Rice, J. R. in *Fracture*, Vol. II, H. Liebowitz, Ed., Academic Press, New York, 1968, Chapter 3, pp. 191-311.
- [8] Bucci, R. J., Paris, P. C., Landes, J. D., and Rice, J. R. in *Fracture Toughness, Proceedings of the 1971 National Symposium on Fracture Mechanics, Part II, ASTM STP 514*, American Society for Testing Materials, 1972, pp. 40-69.
- [9] Rice, J. R., Paris, P. C., and Merkle, J. G. in *Progress in Flaw Growth and Fracture Toughness Testing, ASTM STP 536*, American Society for Testing and Materials, 1973, pp. 231-245.
- [10] Srawley, J. E., "On the Rice J Integral Concept in Fracture Mechanics," lecture notes, NASA—Lewis Research Center, Cleveland, Ohio, July 1972; see also footnote 6 on p. 235 in Ref 9.
- [11] Paris, P. C., discussion presented at meeting of J-Integral Task Group (No. TG-E24.01-09), Committee E-24 on Fracture Testing of Metals, American Society for Testing and Materials, 10 Oct. 1973, Carnegie-Mellon University, Pittsburgh, Pa.
- [12] Green, A. P. and Hundy, B. B., *Journal of the Mechanics and Physics of Solids*, Vol. 4, 1956, pp. 128-144.

- [13] Goode, R. J., Strength of Metals Branch, Engineering Materials Division, Naval Research Laboratory, personal communication, 1973.
- [14] Irwin, G. R., written discussion to Ref 1, pp. 22-23.
- [15] Srawley, J. E. in *Fracture*, Vol. IV, H. Liebowitz, Ed., Academic Press, New York, 1969, Chapter 2, pp. 45-68.
- [16] Paris, P. C., written discussion to Ref 1, pp. 21-22.
- [17] Corten, H. T., discussion presented at meeting of J-Integral Task Group (No. TG-E24.01.09), Committee E 24 on Fracture Testing of Metals, American Society for Testing and Materials, 10 Oct. 1973 in Pittsburgh, Pa. and 5 March 1974 in Atlanta, Ga.

*N. E. Dowling<sup>1</sup> and J. A. Begley<sup>1</sup>*

## **Fatigue Crack Growth During Gross Plasticity and the J-Integral**

---

**REFERENCE:** Dowling, N. E. and Begley, J. A., “**Fatigue Crack Growth During Gross Plasticity and the J-Integral,**” *Mechanics of Crack Growth, ASTM STP 590*, American Society for Testing and Materials, 1976, pp. 82–103.

**ABSTRACT:** An attempt is made to apply the J-integral concept as an elastic-plastic criterion for fatigue crack growth. Compact tension fracture specimens of A533B steel are subjected to gross cyclic plastic deformations, and fatigue crack growth rates up to 0.01 in./cycle are obtained. The results show correlation with J-integral values estimated from load versus deflection hysteresis loops. Also, agreement is obtained with the extrapolation of linear elastic fatigue crack growth rate data.

**KEY WORDS:** fatigue (materials), cracking (fracturing), crack propagation, plastic deformation, cyclic loads

Fatigue crack growth rates during gross plasticity are experimentally investigated, and the test results are interpreted in terms of the J-integral concept. The possibility of predicting fatigue crack growth rates under elastic-plastic conditions in a manner analogous to the linear elastic fracture mechanics approach to fatigue is considered. It is hoped that the results of this preliminary study will stimulate expanded discussion and research on elastic-plastic fatigue cracking behavior.

### **Preliminary**

In this section, the limitations of linear elastic fracture mechanics and the need for more general criteria are first considered. Next, the J-integral concept as employed in static fracture toughness testing is discussed. Finally, some comments are made concerning the relationship between fracture mechanics criteria and fatigue crack growth rate.

<sup>1</sup> Senior engineers, Mechanics Department, Westinghouse Research Laboratories, Pittsburgh, Pa. 15235.

### *Limitations of Linear Elastic Fracture Mechanics*

Linear elastic fracture mechanics is based on the analytical result that the elastic stresses surrounding a crack tip are distributed in a manner that is independent of applied load or geometry [1,2].<sup>2</sup> The intensity of the stress field surrounding a crack tip may thus be uniquely described in terms of the applied load and member geometry. Hence, stress intensity factors, which are functions of applied load, component dimensions, and crack length, are employed [1,2]. The resistance of metals to both static fracture [3] and fatigue cracking [4] are commonly expressed in terms of stress intensity factors.

As the mathematical equations used to define stress intensity factors are based on linear elastic behavior, important limitations on the use of linear elastic fracture mechanics arise when materials capable of plastic deformation, such as engineering metals, are considered. With reference to Fig. 1a, linear elastic fracture mechanics is not valid unless the region of plasticity surrounding the crack tip,  $r_y$ , is small compared to both the crack length,  $a$ , and the remaining ligament of uncracked material,  $b$ . If the plastic zone is not small, plasticity effects are significant, and stress intensities determined by the methods of linear elastic fracture mechanics have no meaning. In such cases, more general criteria capable of handling plasticity effects are needed.

For a small crack in a region of plasticity associated with a notch, as in Fig. 1b, linear elastic fracture mechanics is also invalid. Consider a crack length,  $a$ , which is of the same order of size or smaller than the notch root radius,  $\rho$ . The local stress concentrating effect of the notch is significant, but this effect cannot be evaluated by linear elastic analysis due to the fact that the plastic zone,  $r_y$ , is not small compared to other significant dimensions,  $\rho$  and  $a$ . Linear elastic fracture mechanics is valid for configurations similar to Fig. 1b after the crack grows to a length that is

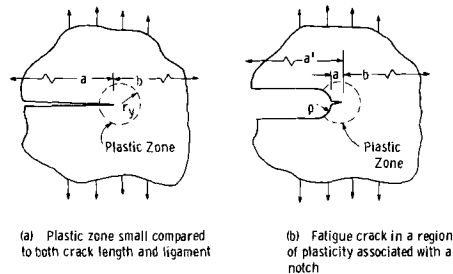


FIG. 1—Relative dimensions governing the applicability of linear elastic fracture mechanics.

<sup>2</sup> The italic numbers in brackets refer to the list of references appended to this paper.

large compared to the root radius of the notch, and then only if the crack tip plastic zone is small compared to both the remaining ligament,  $b$ , and the effective crack length,  $a'$ , which includes the notch length.

The behavior of small cracks near notches, as in Fig. 1*b*, is of major practical importance. It is not generally feasible to design engineering structures or machines so that localized plasticity does not occur at regions of stress concentration. Fatigue crack initiation usually occurs at such locations and can be predicted based on the local elastic-plastic notch strains [5-8]. However, the available fracture mechanics procedures cannot predict growth rates for such cracks until they have grown out of the region of plasticity associated with the notch. Thus, a significant portion of the fatigue life for many practical problems cannot be predicted with currently available technology. The problem of small cracks near plastically deformed notches is difficult due to its geometric complexity. Some approximations may be made [9], but additional analytical and experimental work will be necessary before fatigue problems of this nature can be handled effectively. Fatigue test results for plastically loaded cracked members of simpler geometry, such as standard fracture mechanics specimens, will contribute to an understanding of this problem and, in the future, can be expected to aid in its solution.

*J-Integral Concept*

The mathematical basis of the J-integral concept in terms of nonlinear elasticity is described in Ref 10. Values of  $J$  may be determined from load versus deflection curves as indicated in Fig. 2*a*. At a given deflection,  $\delta_0$ ,

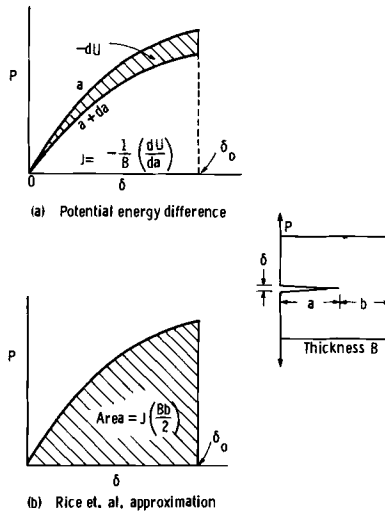


FIG. 2—Determination of  $J$  from load versus deflection curves.

the potential energy change,  $dU$ , caused by a small increase in the crack length,  $da$ , is related to  $J$  as follows

$$J = -\frac{1}{B} \left( \frac{dU}{da} \right) \quad (1)$$

where  $B$  is the specimen thickness. Deflections,  $\delta$ , are measured coincident with the applied load vector.

Load versus deflection curves for several different crack lengths may be used with Eq 1 to determine empirical relations between  $J$  and deflection at various values of crack length [11,12]. The procedure employed is similar to the compliance method [13] of determining the linear elastic strain energy release rate,  $G$ . In fact, if the specimen behaves in a linear elastic manner, that is, if the load deflection lines in Fig. 2a are straight, then  $J$  reduces [10] to  $G$ , which is in turn simply related [2] to the stress intensity,  $K$ .

$$J = G = \frac{K^2}{E} \quad (2)^3$$

For elastic-plastic materials, the quantity  $U$  in Eq 1 cannot be interpreted as the potential energy, rather it is the elastic-plastic work necessary to deflect the specimen. In this case,  $J$  loses its physical interpretation in terms of the potential energy available for crack extension, but it retains physical significance as a measure of the intensity of the characteristic crack tip strain field [11]. Note that this latter interpretation of  $J$  is similar in philosophy to the stress intensity concept,  $K$ , which gives the intensity of the linear elastic stress field surrounding the crack tip. This crack tip strain field interpretation of  $J$  accounts for its success as a geometry independent static fracture toughness criterion for engineering metals under elastic-plastic conditions [11,12,14].

The mathematical developments leading to the J-integral concept imply, for elastic-plastic materials, that the concept is valid where deformation theory of plasticity is valid [10]. As deformation theory of plasticity cannot directly account for the plasticity effects observed on unloading, there is some question concerning the applicability of the J-integral concept to cyclic loading. The most relevant unanswered question is the following: Does the J-integral concept have meaning

<sup>3</sup> If the specimen thickness is sufficient to cause a condition of plane strain, the elastic modulus,  $E$ , employed in Eq 2 should be replaced by  $E/(1 - \nu^2)$ , where  $\nu$  is Poisson's ratio [2]. As this correction causes a change of only about 10 percent, it is not of great importance.

relative to the changes that occur in the crack tip stress and strain fields during the loading half of one fatigue cycle?

As the limitations of the J-integral concept are not definitely known, the concept may have more general applicability than can be mathematically verified at this time. Thus, laboratory experiments which probe the limitations of the J-integral concept are appropriate. It is in this spirit that an attempt will be made in this investigation to apply  $J$  to cyclic loading.

It is somewhat inconvenient to apply Eq 1 to elastic-plastic materials as test results from several specimens are needed in the compliance procedure employed [11,12]. Fortunately, an approximation is available which allows  $J$  values to be determined from a single load versus deflection curve [15]. This approximation, which is valid only for deeply notched compact tension and bend bar specimens, is illustrated in Fig. 2b. The approximate  $J$  value at a given deflection is simply related to the area under the load versus deflection curve

$$J = \frac{2}{Bb} \int_0^{\delta_0} Pd\delta \quad (3)$$

Compact tension specimens are employed in this investigation and cyclic  $J$  values are determined in a manner related to Eq 3.

#### *Criteria for Fatigue Crack Growth*

The relationship between stress intensity and fatigue crack growth rate obtained from linear elastic fracture mechanics is shown schematically in Fig. 3. At intermediate values of stress intensity range,  $\Delta K$ , a straight line is usually obtained on a log-log plot of  $\Delta K$  versus cyclic crack growth rate,  $da/dN$ . The following relationship [4,16] results

$$da/dN = C(\Delta K)^n \quad (4)$$

where  $C$  and  $n$  are constants for a given material and stress ratio ( $K_{\min}/K_{\max}$ ).<sup>4</sup> At low values of  $\Delta K$ , crack growth rates fall off rapidly, and there appears to be, for a given material and stress ratio, a threshold value of  $\Delta K$  below which fatigue cracks will not grow [17,18].

It is significant that fatigue crack growth rates of magnitudes corresponding to the linear and threshold regions of the  $da/dN$  versus  $\Delta K$  curve occur for small cracks where plasticity precludes the use of linear elastic fracture mechanics. This is the case for surface cracks in a uniform cyclic plastic strain field, as during low-cycle fatigue tests after crack initiation,

<sup>4</sup> The constants  $C$  and  $n$  are also affected by temperature and chemical environment, and these latter factors result in frequency effects. Environmental factors are beyond the scope of this paper.

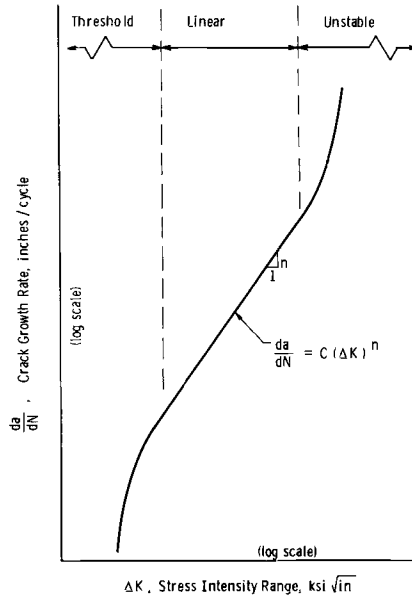


FIG. 3—Relationship between fatigue crack growth rate and stress intensity.

and is also the case for small cracks growing in regions of cyclic plasticity associated with notches. Criteria for fatigue crack growth which account for plasticity effects, and which could be used in place of  $\Delta K$  where it does not apply, are needed.

As indicated in Fig. 3, unstable behavior occurs at high  $\Delta K$  values and results in a rapid increase in the crack growth rate just prior to complete failure of the specimen. There are two possible causes of this behavior. First, the increasing crack length during constant load testing causes the peak stress intensity to reach the fracture toughness of the material, and the unstable behavior is related to the early stages of brittle fracture [19,20]. And second, the growing crack reduces the uncracked area of the specimen sufficiently for the peak load to cause fully plastic limit load behavior. The first possibility is operative for high-strength, low-toughness metals [19,20], where the specimen sizes normally used for fatigue crack growth rate testing behave in a linear elastic manner at  $K$  levels equal to the fracture toughness. The second possibility, plastic limit load behavior, is probably common for ductile metals, particularly if the fracture toughness is high.

Where plastic limit load behavior causes unstable crack growth,  $\Delta K$  values have no meaning as the limitations of linear elastic fracture mechanics have been exceeded. In other words, the apparent effect is not real but is related to the fact that the  $\Delta K$  values determined are not

appropriate criteria for fatigue crack growth due to plasticity effects. The interesting possibility is raised that straight line  $da/dN$  versus  $\Delta K$  behavior for ductile metals can be observed at higher  $\Delta K$  levels by testing larger specimens. Conversely, unstable behavior is expected at lower  $\Delta K$  values for smaller specimens. This is due to the fact that the extent of plastic deformation depends, to a first approximation, on only the stress intensity level and the flow strength of the material<sup>5</sup> and, therefore, becomes smaller relative to the specimen size if the specimen size is increased [21]. Note that this is the same size effect that necessitates the minimum specimen size requirement in  $K_{Ic}$  testing. (See ASTM Test for Plane-Strain Fracture Toughness of Metallic Materials, E 399-73.)

In this investigation, fracture mechanics specimens are subjected to gross plastic deformations, and fatigue crack growth rates are measured. The test results are interpreted in terms of the J-integral concept. There has been limited previous work by others [22-24] on fatigue crack growth during plastic deformation. However, no criterion having general applicability has been developed, nor has any attempt been previously made to apply the J-integral concept to fatigue crack growth.

The remainder of this paper is first concerned with describing the laboratory techniques and data reduction procedures employed. Next, the test results are presented. Following discussion of the test results, conclusions are drawn and recommendations for related future work are made.

## Experimental Techniques

### *Material, Specimens, and Laboratory Tests*

The material tested was A533B pressure vessel steel having a yield strength of 70 ksi and a Charpy fracture appearance transition temperature (FATT) of 95°F. Specimens having the dimensions shown in Fig. 4 were machined from this material. These specimens were identical to the ASTM standard compact tension specimen (ASTM Method E 399-73) except that modifications were made to accommodate clip gages. Specifically, the machined slot was widened at the front of the specimen, and knife edges were machined under the centers of the loading pin holes. An ASTM standard double cantilever clip gage (ASTM Method E 399-73) was attached to these knife edges and was used for measuring deflections along the loading line. Also, four pairs of shallow threaded holes were machined in one side of the specimens. These were used to attach knife edges for a second clip gage that was employed to measure displacements across the crack tip. This second clip gage was moved as the crack grew so that it was always attached at the pair of holes closest to the crack tip.

<sup>5</sup> For small-scale plasticity, the plastic zone size is estimated [21] to be  $r_p = (K/\sigma_y)^2/2\pi$ .



load control, plastic limit load behavior in the uncracked ligament of the specimen causes the mean deflection to increase in an unstable manner. This behavior is related to the cycle dependent creep, or ratcheting, phenomenon observed in uncracked axially loaded specimens [25,26]. Unstable deformation behavior under load control causes the crack growth rate to increase rapidly, and little data can be obtained before failure of the specimen. Under deflection control, the mean load relaxes [27] toward zero and the crack growth rate decreases. As it cannot be assured that crack growth delay effects [28] caused by the decreasing severity of the loading do not affect the data, simple deflection control is also disadvantageous.

The difficulties with simple load or deflection control were avoided by controlling the deflection to a sloping line on a load versus deflection plot as indicated in Fig. 6. In other words, as the load dropped due to the increasing crack length, the deflection limit was increased. Intercept values for the sloping line used in each test, such as *S* and *D* in Fig. 6, were chosen so that the crack growth rate gradually increased with elapsed cycles. Typical crack length versus cycles data are shown in Figs. 7 and 8. The specific choices of *S* and *D* used were based on experience obtained during preliminary tests.

Deflection control to a sloping line as in Fig. 6 was achieved automatically by means of an analog control circuit. The control circuit employed is described in detail in Ref 29, and general discussion on limit control using an analog computer with closed loop mechanical testing equipment is given in Ref 30.

A limited number of tests were also conducted under load control to a

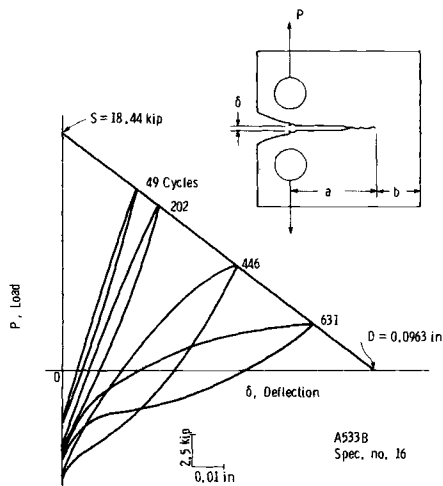


FIG. 6—Load versus deflection hysteresis loops during deflection control to a sloping line.

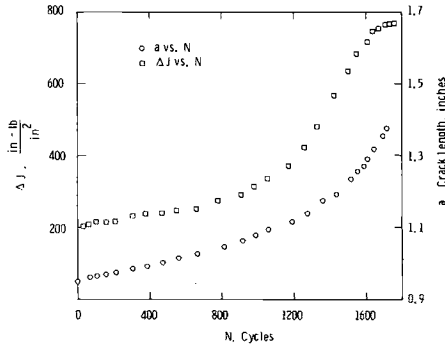


FIG. 7—Variation with cycles of crack length and J for Specimen 15.

sloping line as illustrated in Fig. 9. Again, it was possible to obtain gradually increasing crack growth rates. All sloping line control tests conducted are described in Tables 1 and 2. During these tests, load versus deflection hysteresis loops as in Figs. 6 and 9 were periodically recorded on an X-Y recorder. In addition to the sloping line control tests, two ordinary linear elastic, constant load, fatigue crack growth rate tests were conducted and are described in Table 3.

*Data Reduction*

Cyclic crack growth rates were determined from *a* versus *N* data, as in Figs. 7 and 8, by an incremental polynomial procedure. A second order polynomial was fitted through the first seven *a* versus *N* data points using least squares regression techniques. The first derivative of this polynomial was then evaluated at the central data point to obtain a crack growth rate,  $da/dN$ . The same procedure was then applied to the second through

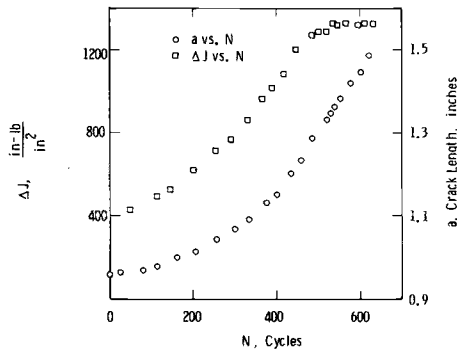


FIG. 8—Variation with cycles of crack length and J for Specimen 16.

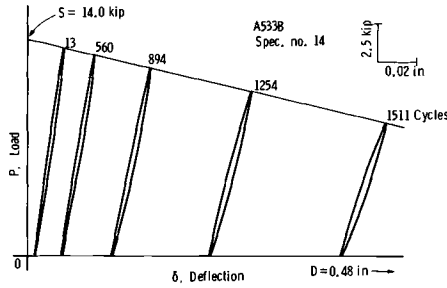


FIG. 9—Load versus deflection hysteresis loops during load control to a sloping line.

eighth, third through ninth, etc., data points so as to obtain crack growth rates at various numbers of cycles during each test.

Values of cyclic  $J$  were determined from areas under load versus deflection lines during rising load as indicated in Fig. 10. Note that the operational definition of  $\Delta J$  employed is related to the Rice et al approximation [15], discussed previously relative to Fig. 2b and Eq 3. As macroscopic crack closure behavior occurred, it was necessary to estimate the point at which the crack opened and to calculate  $\Delta J$  from the area above this point as indicated in Fig. 10. Others have detected crack closure by means of strain gages near the crack tip [31] or by changes in an electric potential applied to the specimen [32]. Unfortunately, neither of these methods could be used in this case due to difficulties associated with large plastic deformations. The best method available was, therefore, to measure displacements across the crack tip using a clip gage attached to the side of the specimen.

Deflection from the side clip gage was plotted versus deflection from the clip gage at the loading pin holes. Changes in slope on such plots were observed and were interpreted as approximately corresponding to opening and closing of the crack. Crack opening deflections estimated from

TABLE 1—Tests under deflection control to a sloping line.

| Specimen No.  | Test Frequency, Hz | Deflection Intercept $D$ , in. | Load Intercept $S$ , kip |
|---------------|--------------------|--------------------------------|--------------------------|
| 2, $a < 1.25$ | 1.0                | 0.0591                         | 10.45                    |
| 2, $a > 1.25$ | 0.5                | 0.0750                         | 9.18                     |
| 5, $a < 1.15$ | 0.5                | 0.1000                         | 13.33                    |
| 5, $a > 1.15$ | 0.05               | 0.1133                         | 13.33                    |
| 15            | 0.2                | 0.0770                         | 14.82                    |
| 16            | 0.1                | 0.0963                         | 18.44                    |
| 18            | 0.04               | 0.1250                         | 21.00                    |
| 19            | 0.02               | 0.1722                         | 18.83                    |

TABLE 2—Tests under load control to a sloping line.

| Specimen No.   | Test Frequency, Hz | Deflection Intercept $D$ , in. | Load Intercept $S$ , kip |
|----------------|--------------------|--------------------------------|--------------------------|
| 14             | 0.1                | 0.480                          | 14.0                     |
| 17, $a < 1.03$ | 0.1                | 0.160                          | 14.0                     |
| 17, $a > 1.03$ | 0.1                | 0.320                          | 14.0                     |

side clip gage measurements and from stiffness changes in load versus deflection hysteresis loops, as in Figs. 6 and 10, were compared. The values obtained never differed by an amount that was significant compared to the maximum deflection, typical data being shown in Fig. 11. Therefore, it was possible to estimate the crack opening point from load versus deflection hysteresis loops, which was found to be more convenient than the direct use of side clip gage data. As illustrated in Fig. 10, the specific procedure used involved the easily identifiable point where the curvature of the  $P$ - $\delta$  line changed prior to the peak compressive load being reached. This convention constitutes only a first order correction for the effect of crack closure, and no significance is attached to its details.

For calculating  $\Delta J$  values, one might consider using the area above zero load, area  $CDEC$  in Fig. 10. However, significant reversed plasticity occurred during compressive loading, and even low-power visual observation indicated that crack closure often did not occur until considerable compressive load had been applied. The total area under the loading curve, area  $ADGA$  in Fig. 10, is also a possibility for estimating  $\Delta J$ . However, it was not thought reasonable to assign any importance to that portion of a cycle during which the crack was closed. Also,  $\Delta J$  values estimated from the total area under the loading line were observed to increase as the crack growth rate decreased during preliminary tests under simple deflection control.

Thus,  $\Delta J$  values were estimated from load versus deflection hysteresis loops in a manner related to the Rice et al approximation [15], and an attempt was made to account for the effect of crack closure. Values of  $\Delta J$  determined in this manner are shown in Figs. 7 and 8 along with the corresponding  $a$  versus  $N$  plots.

For the tests under load control to a sloping line, as in Fig. 9, there were

TABLE 3—Linear elastic fatigue crack growth rate tests.

| Specimen No. | Test Frequency, Hz | Minimum Load, kip | Load Range, kip |
|--------------|--------------------|-------------------|-----------------|
| 9            | 1.0                | 0.40              | 3.60            |
| 13           | 1.0                | 0.60              | 5.40            |

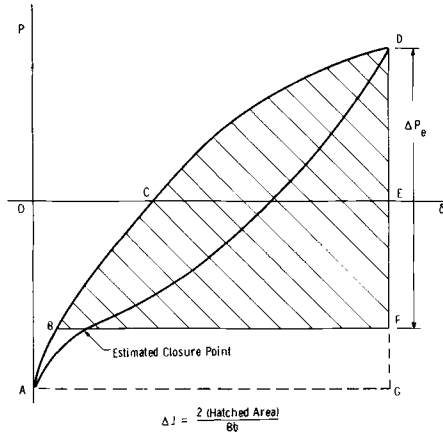


FIG. 10—Operational definition of cyclic  $J$ .

no indications of crack closure from side clip gage measurements. Values of  $\Delta J$  were estimated as previously described except that zero load was taken as the crack opening point. As shown in Fig. 9, the cyclic plasticity during these tests was small. Hence, the  $\Delta J$  values obtained were approximately equal to  $(\Delta K)^2/E$ ,  $\Delta K$  being simply related to load and crack length by the methods of linear elastic fracture mechanics.

**Test Results**

For two of the tests under deflection control to a sloping line, values of  $\Delta J$  at various numbers of cycles are plotted in Figs. 7 and 8. Note that  $\Delta J$  increases with fatigue crack growth rate,  $da/dN$ , for the first part of each test, and then becomes approximately constant. Later, in most tests, both

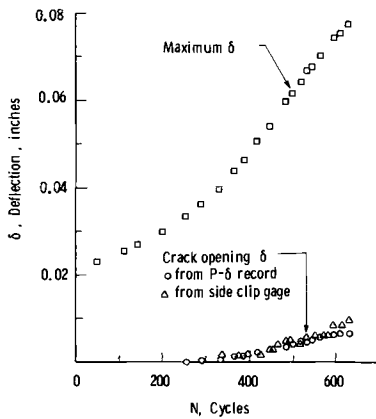


FIG. 11—Estimated crack opening deflections for Specimen 16.

$da/dN$  and  $\Delta J$  began to decrease. The data during decreasing  $da/dN$  were rejected due to the possible influence of delay effects.

A plot of  $da/dN$  versus  $\Delta J$  is shown in Fig. 12 for all of the tests under deflection control to a sloping line. Also shown is a least squares line fit through these data which has the following equation

$$\frac{da}{dN} = 2.13 \times 10^{-8} (\Delta J)^{1.587} \tag{5}$$

Data are shown in Fig. 13 for the two tests under load control to a sloping line, and these data are compared to Eq 5. In Fig. 14, the deflection control  $\Delta J$  data of Fig. 12 are compared to linear elastic fracture mechanics data for the same material. Results for the two linear elastic tests conducted in this investigation are shown, as are extensive test results from Paris et al [18] on a different heat of the same material,

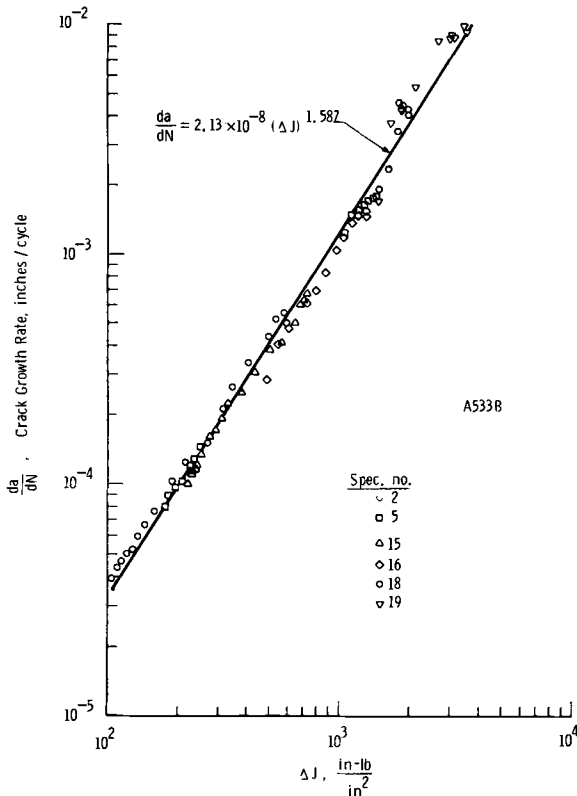


FIG. 12—Fatigue crack growth rate as a function of  $J$  for deflection control to a sloping line.

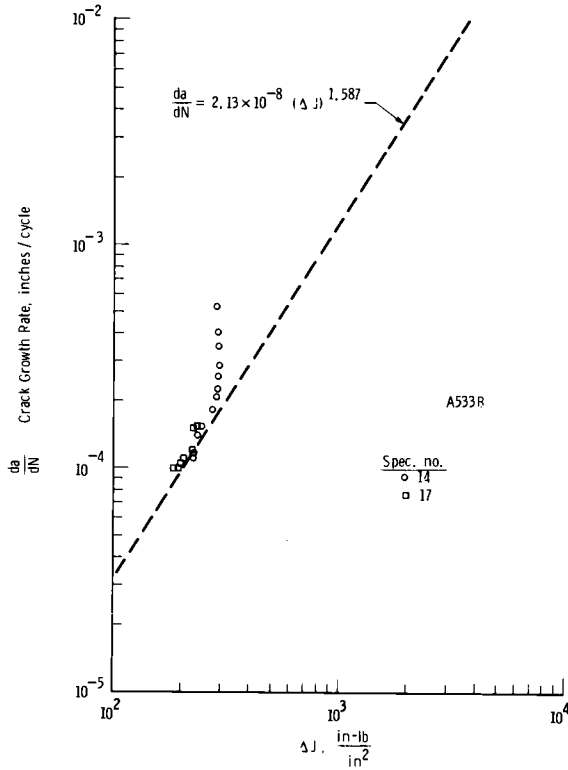


Fig. 13—Fatigue crack growth rate as a function of  $J$  for load control to a sloping line.

A533B with 70 ksi yield. Note that  $\Delta J$  values for the linear elastic data in Fig. 14 are obtained from  $\Delta K$  using Eq 2.

The deformation behavior during deflection control to a sloping line was characterized by large cyclic plastic deformations, hysteresis loops as shown in Fig. 6 being typical. In the latter part of each test, gross stiffness changes due to closing of the crack at high compressive loads were observed.

Where load, rather than deflection, was controlled to a sloping line, the cyclic plastic deformations were small, but large plastic deformations in the tensile direction accumulated during the tests. This incremental plastic deformation behavior is evident in Fig. 9, where the zero load deflection is observed to increase significantly with number of applied cycles. Figure 15 is a photograph taken near the end of the same test illustrated in Fig. 9, the increase in zero load deflection being also evident in this photograph.

Several fracture surfaces resulting from fatigue crack growth during

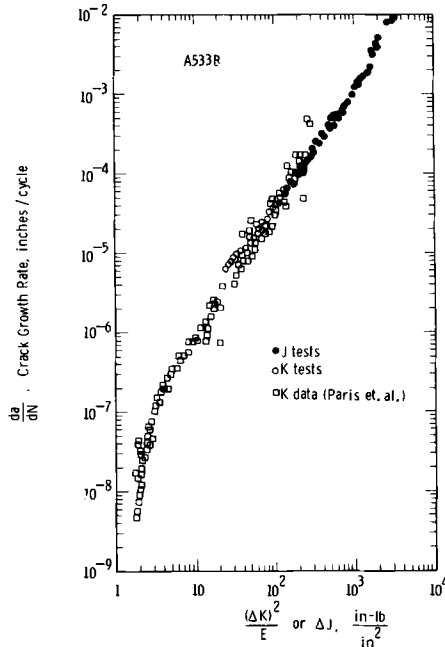


FIG. 14—Comparison of fatigue crack growth rates during gross plasticity with linear elastic data.

gross plasticity are shown in Fig. 16. The specimens farther to the right in Fig. 16 had higher growth rates. Note that fracture surface roughness and shear lip size increase with growth rate. Shear lips occupied only a small fraction of specimen width, and the crack front curvature was small, except for growth rates near  $10^{-2}$  in./cycle. The specimen on the extreme left in Fig. 16 is from one of the linear elastic tests, and all of the others are from tests under deflection control to a sloping line. The reader may refer to Tables 1 to 3 for the test conditions employed and to Fig. 12 for the crack growth rates involved.

### Discussion

In Fig. 12, it can be seen that excellent correlation is obtained between cyclic  $J$  and fatigue crack growth rates for the tests under deflection control to a sloping line. The test data from all six specimens fall near a single straight line in Fig. 12. Wherever data points from more than one test fall together along this line, the combination of  $da/dN$  and  $\Delta J$  obtained occurred at different crack lengths. For any given crack length between 1.0 and 1.4 in., test results were obtained over approximately two orders of magnitude in crack growth rate. Thus, over a range of crack lengths in the single specimen geometry tested, the cyclic  $J$  criterion employed is

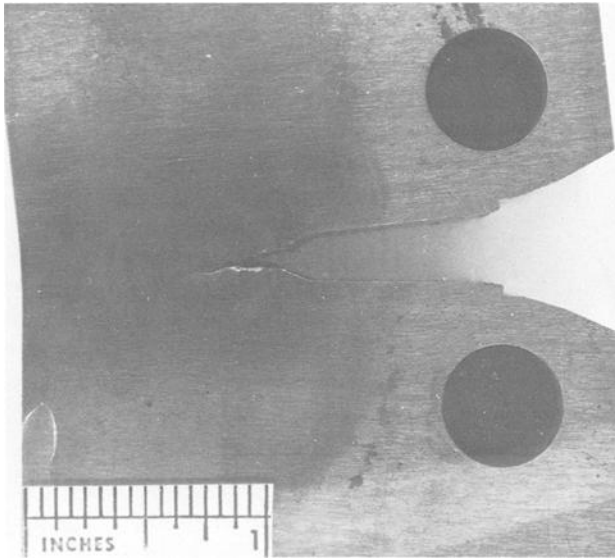


FIG. 15—Specimen 14 after testing.

independent of crack length. Note that the following interrelated quantities are involved in the convention used for computing  $\Delta J$ : load range, elastic-plastic deflection range, crack opening deflection, and crack length. The success of the correlation between  $da/dN$  and  $\Delta J$  implies that all of these factors, at least in an approximate manner, are taken correctly into account.

As indicated in Fig. 14, the linear elastic data from this investigation are in reasonable agreement with the more extensive similar data from Ref 18, which are for a different heat of the same steel. In Fig. 14, the results of the gross plasticity  $J$  tests conducted under deflection control to a sloping line are shown as solid circles. Excellent agreement with the linear elastic test results is obtained in the limited region where both are available. Furthermore, all of the data in Fig. 14 for crack growth rates above  $10^{-7}$  in./cycle fall along a single straight line. Thus, the gross plasticity  $da/dN$  versus  $\Delta J$  data are in agreement with the straight line extrapolation on a log-log plot of the linear elastic fracture mechanics data.

The reader may question the necessity of employing a complex  $\Delta J$  criterion which involves both load and deflection, and may ask if it is not sufficient to specify only the load and crack length as in linear elastic fracture mechanics. To illustrate that gross plastic deformation invali-

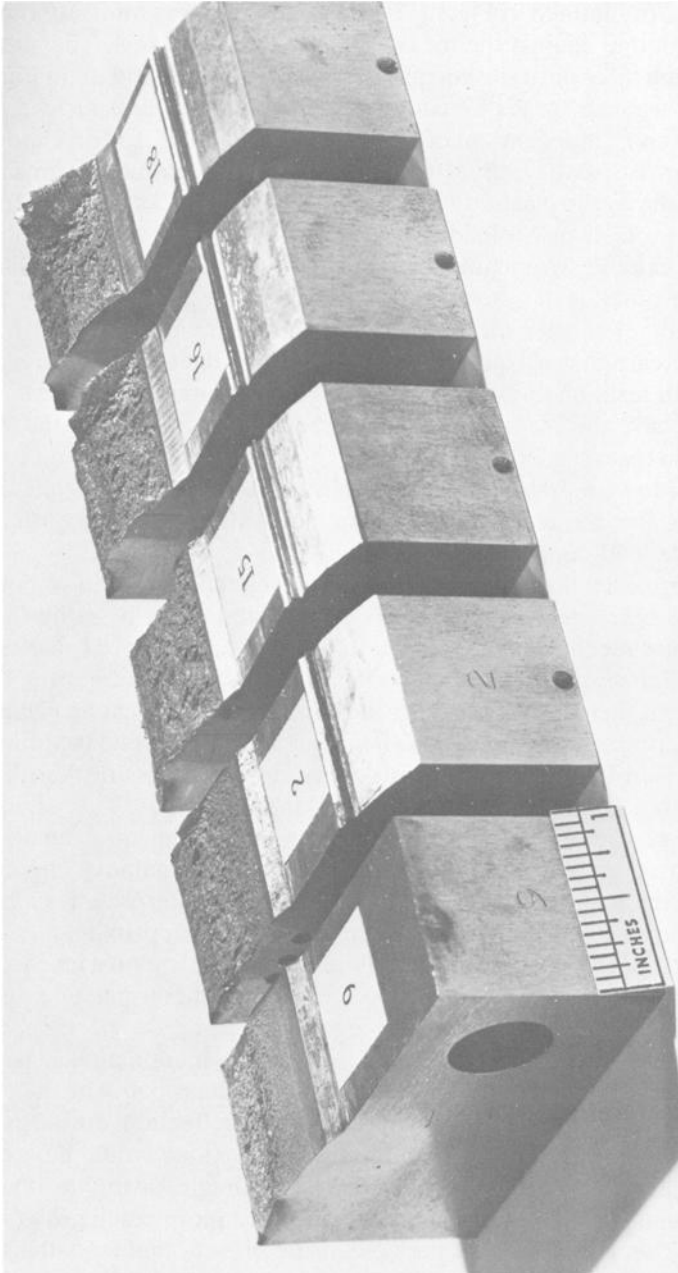


FIG. 16—Fracture surfaces.

dates linear elastic fracture mechanics, stress intensity ranges were determined (ASTM Method E 399-73) from the crack length and effective load range,  $\Delta P_e$ , defined in Fig. 10. These effective stress intensity ranges,  $\Delta K_e$ , were plotted against the measured crack growth rates. The correlation was much inferior to the correlation between  $da/dN$  and  $\Delta J$  in Fig. 12. There were separate trends for each specimen, and the crack growth rates tended to become independent of  $\Delta K_e$ . The failure of  $\Delta K_e$  to correlate with the crack growth data is due to the fact that this parameter does not account for the cyclic plasticity effects which are important in these tests.

The data for tests under load control to a sloping line, which are shown in Fig. 13, exhibit significant deviation from the straight line behavior observed in other tests. Above a certain  $\Delta J$  value, crack growth rates increase without further increase in  $\Delta J$ . This behavior is related to the unstable increase in crack growth rate observed at the end of linear elastic crack growth tests on ductile materials. The only significant difference is that in this case the maximum load is gradually decreased as the mean deflection increases, as illustrated in Fig. 9. This control condition causes the behavior to be more stable in that the increase with cycles of the crack growth rate and mean deflection is gradual, rather than very rapid as under simple load control.

Thus, it appears that incremental plastic deflection has an important effect on the crack growth rate that is not accounted for by either linear elastic fracture mechanics or by the definition of  $\Delta J$  employed. Note that  $\Delta J$  values determined as described earlier differ significantly from  $(\Delta K)^2/E$  only if there is significant cyclic plasticity. As the cyclic plasticity was small during the tests under load control to a sloping line (see Fig. 9), the  $\Delta J$  criterion is not expected to be any more successful than linear elastic fracture mechanics in explaining the behavior. The effect of incremental plasticity should be viewed as an effect of mean  $J$ , analogous to the effect of mean  $K$  in linear elastic fracture mechanics. The crack growth behavior shown in Fig. 13, therefore, is interpreted as being caused by an increasing mean  $J$ , while  $\Delta J$  remains approximately constant. It is not surprising that, just as in linear elastic fracture mechanics, the range and the mean value of the controlling parameter must be known to predict the fatigue crack growth rate.

It may be desirable in the future to investigate incremental plasticity (mean  $J$ ) effects in detail. An important variable will probably be the crack closure level. Because of the increased mean deflection during a test similar to Figs. 9 and 15, considerable compressive load would have to be applied to cause the crack to close. Thus, one might postulate that the crack tip radius at zero load is significant and that more crack growth will occur during each cycle than if the crack were closed, that is, had a small tip radius, at zero load.

It is important to note that geometric independence of cyclic  $J$  has not been demonstrated. The highest priority for future experimental work is,

therefore, to conduct similar tests on another specimen geometry, such as a center cracked panel. Also, it should be shown that  $da/dN$  versus  $\Delta K$  data for large linear elastic specimens correlate with  $da/dN$  versus  $\Delta J$  data from smaller specimen gross plasticity tests. Growth rates for small surface cracks in plastically deformed regions, both in uniform strain fields and near notches, should also be investigated. Hopefully, it will be eventually possible to develop a general criterion so that fatigue crack growth rate data for various geometries, specimen sizes, and conditions of plasticity will all fall along a single line on a plot similar to Fig. 14. Appropriate analytical work will of course also be necessary if significant advances are to be made toward developing a general elastic-plastic criterion for fatigue crack growth.

### Conclusions

The results of this preliminary experimental study indicate that the J-integral concept may be applicable to fatigue problems where cyclic plasticity precludes the use of linear elastic fracture mechanics. If the trends observed for 1-in.-thick compact tension specimens of A533B steel are confirmed for other geometries, specimen sizes, and materials, it will become possible to handle practical elastic-plastic fatigue problems in a manner analogous to the linear elastic fracture mechanics approach to fatigue. Regardless of the future success or failure of the J-integral as a criterion for fatigue crack growth, the need will remain for a general elastic-plastic criterion which characterizes the crack tip strain field for cyclic loading.

Some conclusions related to the specific test results obtained for compact tension specimens of A533B steel subjected to gross cyclic plasticity are as follows:

1. Crack growth rates between  $4 \times 10^{-5}$  and  $10^{-2}$  in./cycle show excellent correlation with values of  $\Delta J$  determined using the Rice et al approximation for bending type fracture specimens.
2. The high crack growth rate  $da/dN$  versus  $\Delta J$  data are in agreement with the straight line extrapolation on a log-log plot of the linear elastic fracture mechanics data.
3. Macroscopic crack closure during gross plasticity is an important effect and significantly influences the fatigue crack growth rate.
4. Growth rates during incremental plastic deflection cannot be predicted by a  $\Delta J$  criterion alone; a more general criterion that includes the effect of the mean  $J$  level is needed.

### Recommendations

The encouraging test results obtained indicate that experimental work on the application of the J-integral concept to fatigue under elastic-plastic

conditions should definitely continue. Test results for other specimen geometries, specimen sizes, and materials are needed. An important goal of further research should be to develop methods for handling the difficult problem of small surface cracks growing in regions of plasticity associated with notches.

The experimental work should be accompanied by, and should interact with, additional analytical work. Convenient methods of estimating  $J$  values for various geometries are needed, as are analytical results relating specifically to cyclic loading. In the event that future analytical or experimental results show that  $J$  is not a valid criterion for elastic-plastic fatigue crack growth, work of this general nature should nevertheless continue, and a more suitable criterion should be sought.

### References

- [1] Irwin, G. R., *Journal of Applied Mechanics*, Sept. 1957, pp. 361-364.
- [2] Paris, P. C. and Sih, G. C. in *Fracture Toughness Testing and Its Applications*, ASTM STP 381, American Society for Testing and Materials, 1965, pp. 30-83.
- [3] Brown, W. F., Jr., and Srawley, J. E., *Plane Strain Crack Toughness Testing of High Strength Metallic Materials*, ASTM STP 410, American Society for Testing and Materials, 1966.
- [4] Paris, P. C. in *Fatigue—An Interdisciplinary Approach*, Syracuse University Press, Syracuse, N.Y., 1964, pp. 107-127.
- [5] Wetzel, R. M., "A Method of Fatigue Damage Analysis," Ph.D. thesis, Department of Civil Engineering, University of Waterloo, Ontario, Canada, 1971. See also Technical Report No. SR 71-107, Scientific Research Staff, Ford Motor Co., Dearborn, Mich. Aug. 1971.
- [6] Stadnick, S. J. and Morrow, J. in *Testing for Prediction of Material Performance in Structures and Components*, ASTM STP 515, American Society for Testing and Materials, 1972, pp. 229-252.
- [7] Mowbray, D. F. and McConneelee, J. E. in *Cyclic Stress-Strain Behavior—Analysis, Experimentation, and Failure Prediction*, ASTM STP 519, American Society for Testing and Materials, 1973, pp. 151-169.
- [8] Landgraf, R. W. and LaPointe, N. R., "Cyclic Stress-Strain Concepts Applied to Component Fatigue Life Prediction," Paper No. 740280, Society of Automotive Engineers, Automotive Engineering Congress, Detroit, Mich., Feb. 1974.
- [9] Begley, J. A., Landes, J. D., and Wilson, W. K. in *Fracture Analysis, Proceedings of the 1973 National Symposium of Fracture Mechanics, Part II*, ASTM STP 560, American Society for Testing and Materials, 1974.
- [10] Rice, J. R. in *Fracture—An Advanced Treatise, Vol. II, Mathematical Fundamentals*, Academic Press, New York, 1968, pp. 191-311.
- [11] Begley, J. A. and Landes, J. D. in *Fracture Toughness, Proceedings of the 1971 National Symposium on Fracture Mechanics, Part II*, ASTM STP 514, American Society for Testing and Materials, 1972, pp. 1-20.
- [12] Landes, J. D. and Begley, J. A. in *Fracture Toughness, Proceedings of the 1971 National Symposium on Fracture Mechanics, Part II*, ASTM STP 514, American Society for Testing and Materials, 1972, pp. 24-39.
- [13] Irwin, G. R. and Kies, J. A., *Welding Journal*, American Welding Society, Vol. 33, No. 4, April 1954, pp. 193s-198s.
- [14] Landes, J. D. and Begley, J. A. in *Fracture Analysis, Proceedings of the 1973 National Symposium on Fracture Mechanics, Part II*, ASTM STP 560, American Society for Testing and Materials, 1974.
- [15] Rice, J. R., Paris, P. C., and Merkle, J. G. in *Progress in Flaw Growth and Fracture Toughness Testing*, ASTM STP 536, American Society for Testing and Materials, 1973, pp. 231-245.

- [16] Barsom, J. M., *Journal of Engineering for Industry*, American Society of Mechanical Engineers, Nov. 1971, pp. 1190-1196.
- [17] Bucci, R. J. et al in *Stress Analysis and Growth of Cracks, Proceedings of the 1971 National Symposium on Fracture Mechanics, Part I, ASTM STP 513*, American Society for Testing and Materials, 1972, pp. 125-140.
- [18] Paris, P. C. et al in *Stress Analysis and Growth of Cracks, Proceedings of the 1971 National Symposium on Fracture Mechanics, Part I, ASTM STP 513*, American Society for Testing and Materials, 1972, pp. 141-176.
- [19] Carmen, C. M. and Katlin, J. M., *Journal of Basic Engineering*, American Society of Mechanical Engineers, 1966, pp. 792-800.
- [20] Imhof, E. J. and Barsom, J. M. in *Progress in Flaw Growth and Fracture Toughness Testing, ASTM STP 536*, American Society for Testing and Materials, 1973, pp. 182-205.
- [21] Irwin, G. R. in *Mechanical and Metallurgical Behavior of Sheet Metals, Proceedings of the 7th Sagamore Ordnance Materials Research Conference, Part 4*, 1960, pp. 63-71.
- [22] McEvily, A. J. in *Proceedings of the Air Force Conference on Fatigue and Fracture of Aircraft Structures and Materials*, Miami, 15-18 Dec. 1969, pp. 451-458.
- [23] Solomon, H. D., *Journal of Materials*, American Society for Testing and Materials, Vol. 7, No. 3, Sept. 1972, pp. 299-306.
- [24] Gowda, C. V. B. and Topper, T. H. in *Cyclic Stress-Strain Behavior—Analysis, Experimentation, and Failure Prediction, ASTM STP 519*, American Society for Testing and Materials, 1973, pp. 170-184.
- [25] Bell, W. J. and Benham, P. P. in *Symposium on Fatigue Tests of Aircraft Structures: Low-Cycle, Full-Scale, and Helicopters, ASTM STP 338*, American Society for Testing and Materials, 1962, pp. 25-46.
- [26] Coffin, L. F., Jr., *Journal of Basic Engineering*, American Society of Mechanical Engineers, Dec. 1964, pp. 673-680.
- [27] Morrow, J. and Sinclair, G. M. in *Symposium on Basic Mechanisms of Fatigue, ASTM STP 237*, American Society for Testing and Materials, 1958, pp. 83-103.
- [28] Hudson, C. M. and Hardrath, H. F., "Effects of Changing Stress Amplitude on the Rate of Fatigue Crack Propagation in Two Aluminum Alloys," NASA TN D-960, National Aeronautics and Space Administration, Washington, D.C., Sept. 1961.
- [29] Dowling, N. E. and Begley, J. A., "Fatigue Crack Growth During Gross Plasticity and the J-Integral," Scientific Paper 74-1E7-CREEP-P1, Westinghouse Research Laboratories, Pittsburgh, Pa., Aug. 1974.
- [30] Richards, F. D. and Wetzel, R. M., "Mechanical Testing of Materials Using an Analog Computer," Technical Report No. SR 70-126, Scientific Research Staff, Ford Motor Co., Dearborn, Mich., Sept. 1970. See also *Materials Research and Standards*, American Society for Testing and Materials, Vol. 11, No. 2, Feb. 1971, p. 19.
- [31] Schmidt, R. A. and Paris, P. C. in *Progress in Flaw Growth and Fracture Toughness Testing, ASTM STP 536*, American Society for Testing and Materials, 1973, pp. 79-94.
- [32] Shih, T. T. and Wei, R. P., "A Study of Crack Closure in Fatigue," Report No. IFSM 72-25, Institute of Fracture and Solid Mechanics, Lehigh University, Bethlehem, Pa., Nov. 1972.

H. L. Oh<sup>1</sup>

## A Simple Method for Measuring Tearing Energy of Nicked Rubber Strips

---

**REFERENCE:** Oh, H. L., "A Simple Method for Measuring Tearing Energy of Nicked Rubber Strips," *Mechanics of Crack Growth, ASTM STP 590*, American Society for Testing and Materials, 1976, pp. 104–114.

**ABSTRACT:** A convenient test configuration for measuring critical tearing energy of rubber is to pull thin nicked strips of the rubber in extension. In the past, methods of measurements employed for this configuration are based on concepts which obtain "tearing energy" through differentiation with respect to the crack length. As a consequence, measurements have to be made on several identical specimens having different crack lengths. This paper describes a simple method based on the J-integral which requires no differentiation and calculates the tearing energy from measurements made on one specimen only. This allows an efficient use of test material and reduces the complexity of critical tearing energy measurement.

Implementation of the J-integral method is illustrated on the uniaxial stretching of a nicked rubber strip. The accuracy of results obtained is found to be comparable to that obtained by existing methods.

**KEY WORDS:** crack propagation, tear strength, fractures (materials), elastomers, mechanical properties, deformation

This paper describes a simple method for measuring the so-called "tearing energy" of nicked rubber strips in extension. As defined by Rivlin and Thomas [*I*],<sup>2</sup> the "tearing energy"  $T$  is the rate of decrease of elastically stored energy in a cracked body per unit virtual increment of the crack surface area. When  $T$  exceeds a critical value characteristic of the rubber, crack growth occurs. This critical tearing energy concept was first proposed by Rivlin and Thomas, and it has since been verified in a number of experiments involving fracture and fatigue of rubber specimens [2,3]. To implement this concept in structural design, one has to measure first the critical tearing energy of the material. A convenient

<sup>1</sup> Associate senior research engineer, Mathematics Department, Research Laboratories, General Motors Technical Center, General Motors Corporation, Warren, Mich. 48090.

<sup>2</sup> The italic numbers in brackets refer to the list of references appended to this paper.

test configuration for such measurement is to pull thin nicked strips of rubber in extension. Presently there are two methods for measuring the tearing energy associated with this test configuration. This paper describes a third method based on the J-integral. It will be seen that the J-integral method is the simplest of the three. Using the proposed method, we measure  $T$  for the specimen shown in Fig. 1 and compare the results with those obtained by the other two methods.

**Existing Methods for Measuring Tearing Energy**

For a rubber strip of unit thickness containing a crack, the tearing energy is defined elsewhere [1] by

$$T = - \left( \frac{\partial V_c}{\partial c} \right)_\ell \tag{1}$$

where

- $c$  = length of the crack measured in the undeformed geometry,
- $V_c$  = elastically stored energy at crack length  $c$ , and
- $\ell$  = vertical advance  $\partial_c$  of the crack which occurs while external boundaries are held fixed.

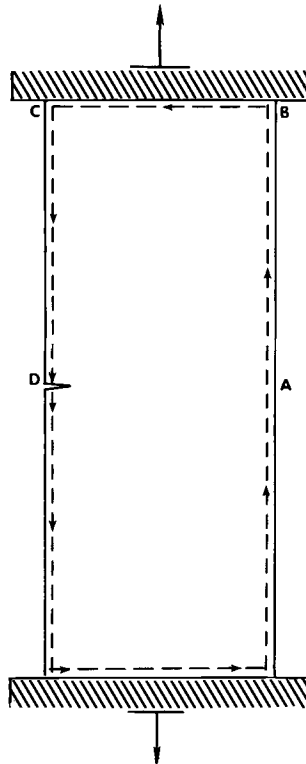


FIG. 1—Simple extension specimen with a cut in one edge. Dotted line shows the integration path chosen to evaluate the J-integral.

One method of measuring  $T$ , known as the total energy drop method, implements directly the definition of the tearing energy, Eq 1. It consists of first obtaining the load-displacement curves for a number of identical specimens having different crack length, Fig. 2a. This is known as compliance calibration. Next, at a given displacement  $\ell$ , areas under the load-displacement curves are obtained which give the stored strain energy  $(V_c)_\ell = \int_0^\ell F dx$ . These values of  $(V_c)_\ell$  are then plotted against corresponding crack length  $c$  and curve fitted to arrive at a  $(V_c)_\ell$  versus  $c$  curve, Fig. 2b. The negative of the slope of tangent to the curve is by Eq 1 the tearing energy at the given displacement  $\ell$  and crack length  $c$ . The tearing energy at other displacements may be similarly obtained. Since it is a direct implementation of the definition, the total energy drop method is applicable in general to any test configuration employed to measure the tearing energy of a cracked body. Its shortcomings are the need to compliance calibrate a large number of specimens and the inherent inaccuracy involved in curve fitting and in performing graphical differentiation of the fitted curve.

For the simple extension of a strip with an edge cut as shown in Fig. 1, compliance calibration may be avoided by postulating through dimensional arguments that the total energy drop in the specimen  $(V_o - V_c)$ , due to the presence of the crack is

$$(V_o - V_c) = k(\lambda)c^2Wh, \quad c/b \leq 0.20 \tag{2}$$

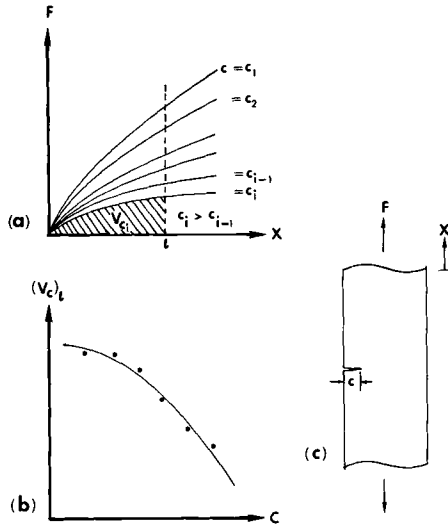


FIG. 2—(a) Load-displacement curves of cracked specimens having various crack lengths, (b) stored strain energy versus crack length for a given displacement  $\ell$ , and (c) notation used in Figs. 2 a and b.

where

- $h$  and  $b$  = undeformed thickness and width of the specimen,
- $W$  = stored strain energy density in the specimen far removed from the crack,
- $V_o$  and  $V_c$  = total energy in the specimen with and without the crack, and
- $k(\lambda)$  = proportionality factor varying mainly with the stretch ratio  $\lambda$  but otherwise independent of the material and the crack length.

Differentiating Eq 2 with respect to the crack length  $c$  gives the tearing energy

$$T = - \left( \frac{\partial V_c}{\partial c} \right)_\ell = 2k(\lambda)c Wh, c/b \leq 0.20 \quad (3)$$

As  $c$ ,  $h$ , and  $W$  are measured easily,  $T$  may be determined from Eq 3 once  $k(\lambda)$  is evaluated. This is accomplished by measuring the total energy drop ( $V_o - V_c$ ) and using Eq 2 to evaluate  $k(\lambda)$ . Following this line of argument suggested by Rivlin and Thomas, Greensmith [4] devised an ingenious experiment to measure the total energy drop. A long strip of rubber is stretched with a force  $F_o$  to a stretch ratio  $\lambda$ . The strain energy density in the specimen in this case is  $W = \int_1^\lambda (F_o/bh)d\lambda$ . The specimen is then clamped at its midsection to make two similar specimens in series. Upon introducing a crack in one of the two specimens, Greensmith measured the additional force ( $F_o - F_c$ ) necessary to return the clamp the distance  $l$  to its original central position and obtained the total energy drop ( $V_o - V_c$ ) =  $\int_0^l (F_o - F_c)dx$ . His results obtained for four natural rubber vulcanizates of widely varying mechanical properties confirm the independence of the total energy drop on  $W$  according to Eq 2 and indicate that  $k(\lambda)$  is indeed independent of crack length and vulcanizate used. Figure 3 shows the variation of the factor  $k(\lambda)$  with the stretch ratio  $\lambda$  as determined by Greensmith. This figure, in conjunction with Eq 3, has since been used to evaluate the tearing energy associated with the simple extension specimen, Fig. 1, which has been employed extensively in studies of crack-growth behavior of rubber. Greensmith's approach is essentially a total energy drop approach except that by assuming the total energy drop to take the form of Eq 2, the need for compliance calibration and graphical differentiation are avoided.

The second method is the crack-surface-displacement method developed by Lake [5] and Lindley [6]. It focuses attention on deformations occurring near the vicinity of the crack tip and evaluates the energy

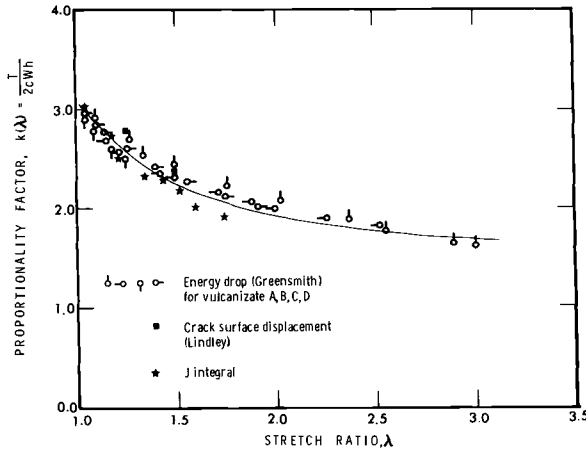


FIG. 3—Values of the proportionality factor  $k(\lambda)$  plotted against stretch ratio  $\lambda$  as determined by various methods.

required to close the crack. By equating this energy with the total energy drop due to the opening of the crack, tearing energy may be estimated. Thus, let  $dx^1$  be the undeformed differential length along the crack plane,  $\sigma(x^1)$  the stress normal to the plane before the crack is made, and  $\delta(x^1)$  the separation of the mating surfaces of the crack after it opens. Assuming a linear relationship between force and deformation, the energy per unit thickness required to close the crack is  $1/2 \int_0^c \delta \sigma dx^1$ . Equating this energy with that lost due to the opening of the crack, we have

$$(V_o - V_c) = 1/2 \int_0^c \delta \sigma dx^1$$

Differentiating the preceding equation with respect to the crack length  $c$  gives the tearing energy

$$T = - \left( \frac{\partial V_c}{\partial c} \right)_\ell = 1/2 \frac{\partial}{\partial c_0} \left( \int_0^c \delta \sigma dx^1 \right) \tag{4}$$

Experimental implementation consists of first measuring along  $x^1$  the strain (to compute stress  $\sigma$ ) before the crack is made and the separation  $\delta$  after the crack opens. The value of the integral  $1/2 \int_0^c \delta \sigma dx^1$  is then obtained by graphical integration. This is taken to be the total energy drop  $(V_o - V_c)$  for a given crack length  $c$ . Other values of  $(V_o - V_c)$  are obtained for identical specimens with different crack length and a  $(V_o - V_c)$  versus  $c$  curve is drawn. Graphical differentiation of the fitted curve then gives, by Eq 4, the tearing energy.

Lindley used this method to measure the tearing energy associated with the simple extension specimen. His results, presented in the form of Eq 3 for comparison purposes, are shown in Fig. 3. They are in agreement with Greensmith's results.

Because the tearing process is highly dependent on the deformations occurring in the vicinity of the crack tip, the crack-surface-displacement method is perhaps more sensitive than the total energy drop approach which measures  $T$  from far field deformations. However, it probably entails a larger experimental error because of the inaccuracy involved in measuring deformations occurring in a small region. The J-integral method to be described in the next section retains the sensitivity to near tip strain field but computes  $T$  based on far field deformations. But more importantly, the J-integral method involves only one specimen. Whereas in the two existing methods measurements have to be made on at least two identical specimens with two crack lengths ( $\Delta c$  apart) so that tearing energy  $T$  can be obtained by graphical differentiation, in the J-integral method the only measurements needed are made with a single specimen.

### J-Integral Method for Measuring Tearing Energy

#### *Theoretical Basis*

Consider, for unit thickness of material, the line integral

$$J = \int_{\Gamma} \left[ W dx^2 - t \frac{\partial u}{\partial x^1} ds \right] \quad (5)$$

where

$\Gamma$  = curve defined in the undeformed geometry which surrounds the crack tip as shown in Fig. 4,

$W$  = strain energy density,

$t$  = nominal traction vector on  $\Gamma$ ,

$u$  = displacement vector, and

$s$  = arc length along  $\Gamma$ .

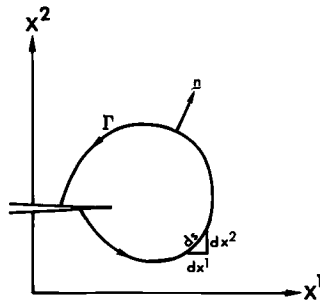


FIG. 4—Notation used in defining the J-integral.

Rice [7] showed that this integral assumes the same value for any choice of curve  $\Gamma$ , that is, it is path independent, and that it may be interpreted as the potential energy drop in the body per unit virtual extension of the crack. Where the crack extends at fixed external boundaries,  $J$  is exactly  $T$  as defined in Eq 1. Consequently,  $J$  may be used to measure  $T$ . Although Rice's proofs were given in the context of infinitesimal deformations with nonlinear stress-strain relation, the same conclusions hold true for finite deformations [8-10].<sup>3</sup> We need only consider an integration path close to the crack tip to realize that  $J$ , hence the method based on  $J$ , is intimately related to deformations there. However, the property of path independence allows us to choose any convenient path far from the crack tip to evaluate  $J$ .

To implement Eq 5, deformations are first measured along the chosen path. One technique is to print a circular grid onto the specimen as shown in Fig. 5. As the specimen is loaded, circles of diameter  $d$  deform into ellipses of diameter  $d_{max}$  and  $d_{min}$ . By measuring these diameters, princi-

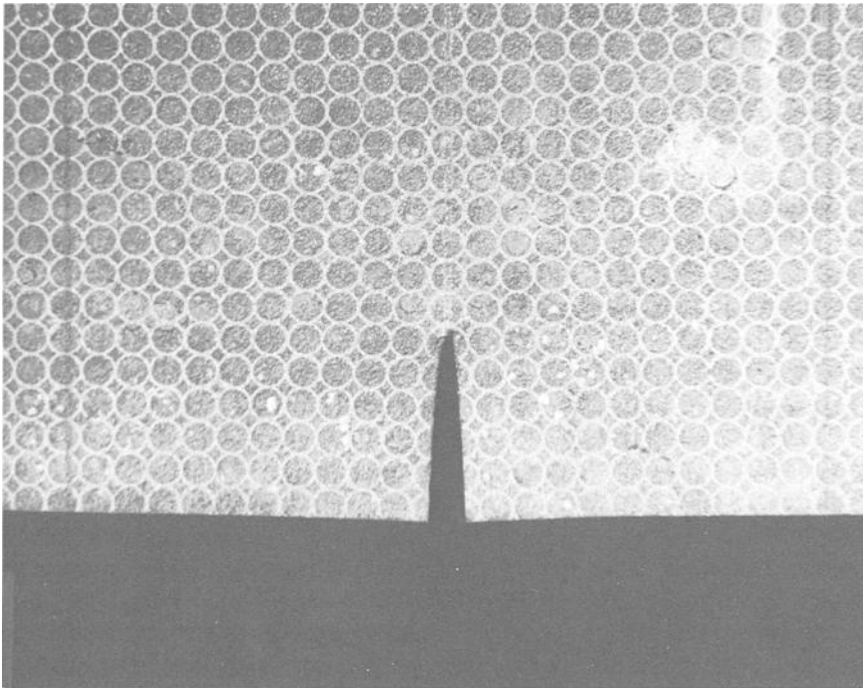


FIG. 5—Circular grid printed on a nickel rubber strip.

<sup>3</sup> References 9 and 10 were brought to author's attention by the reviewers.

pal stretch ratios in the plane of the specimen may be computed:  $\lambda_{11} = (d_{max})/d$  and  $\lambda_{22} = (d_{min})/d$ .

This technique is suitable for rubber since large deformations are involved so that accurate measurements of the diameters can be obtained. Once deformations are known, the strain energy density  $W$  and components of the traction vector  $t$  along the chosen path are calculated from a known dependence of  $W$  on the stretch ratios.  $J$  is then evaluated according to Eq 5. Although in principle any path may be used, it is convenient to choose one which minimizes measurements and calculations. For example, taking a path parallel to the  $x^1$  axis renders the first term in the right hand side of Eq 5 zero, while choosing one along a stress free boundary ( $t = 0$ ) or along a clamped boundary parallel to the  $x^1$  axis ( $\partial u/\partial x^1 = 0$ ) renders the second term zero. These properties are made use of in the example illustrated in the next section.

### Experimental Implementation on the Simple Extension Specimen

Since the tearing energy of the simple extension specimen has been measured already by the other two methods, Fig. 3, we choose to illustrate the experimental implementation of the J-integral method on this same specimen so that comparison between methods can be made.

Two specimens of width = 2.54 cm and length = 15.24 cm are cut from one larger rubber sheet of thickness = 2.03 mm. The material is as received natural rubber catalogue number DR-21-61 vulcanizing recipe and curing of which is available from Detroit Rubber Company, Detroit, Michigan. Circular grids of density 62 circles/cm<sup>2</sup> are then printed onto the specimens. One specimen is used to obtain the stress-stretch ratio measurements in simple tension. From these measurements, the dependence of strain energy density  $W$  on the stretch ratio is calculated. The other specimen serves as the test specimen. A slit of length = 0.50 cm is cut with a wetted razor blade at one edge of the specimen and at its midsection.

Loading of both specimens consists of clamping the two edges of the specimen with grips and pulling these grips in an Instron universal testing machine at a constant rate of separation of 1.0 cm/min. Stretching force is recorded and a photograph taken of the circular grid before pulling the grips apart and at various predetermined grips separations. Photographic negatives of the circular grid are then projected on a large screen and diameters of the ellipses (circles in the undeformed state) measured off the screen. From these measurements, principal stretch ratios are calculated using formulae given earlier. For the simple tension test, stress  $\sigma$  is taken to be the stretching force divided by the undeformed cross-sectional area of the specimen.

Figure 6 shows the stress  $\sigma$  versus stretch ratio  $\lambda$  in simple tension. Here  $\lambda$  is the ratio in which the specimen is stretched in the direction of the

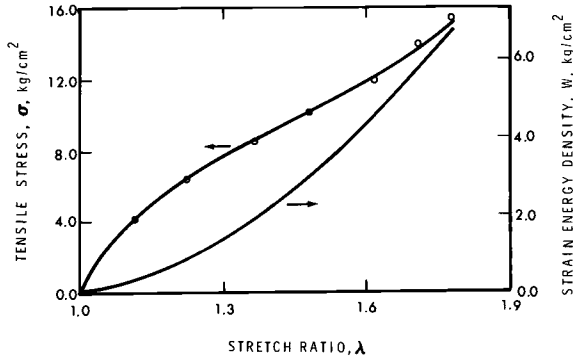


FIG. 6—Variation with stretch ratio  $\lambda$  of tensile stress  $\sigma$  and strain energy density  $W$  in simple tension.

tensile force. Assuming the material to be elastic, the strain energy density is simply  $W(\lambda) = \int_1^\lambda \sigma d\lambda$ . Thus, from the  $\sigma$  versus  $\lambda$  curve,  $W$  as a function of  $\lambda$  may be obtained by evaluating the area under the curve from unity to a given stretch ratio  $\lambda$ . The  $W$  versus  $\lambda$  curve so obtained is shown also in Fig. 6. This curve will be useful in subsequent data reduction.

To evaluate  $J$ , we choose the path shown in Fig. 1 where by symmetry only half the specimen need be considered. The contributions to the  $J$ -integral are those coming from edges  $AB$  and  $CD$

$$J = 2 \left[ \int_{AB} W dx^2 + \int_{CD} W dx^2 \right] = 2 \left[ \int_{AB} W dx^2 - \int_{DC} W dx^2 \right] \quad (6)$$

Note that along the two edges, the rubber is under simple tension so that only edge strain need be calculated. Typical strain distributions measured along the two edges are shown in Fig. 7. It is evident that along edge  $AB$  deformation is one of uniform extension, while along edge  $DC$  strain is zero at the crack plane but within a short distance rises to a level identical to that in edge  $AB$ . Figure 8 shows the strain distributions measured along edge  $DC$  at eight levels of stretching. With the edge strain distribution known, the corresponding strain energy density distribution may be obtained using the  $W$  versus  $\lambda$  curve shown in Fig. 6. For example, Fig. 9 shows the strain energy density distributions corresponding to strain distributions shown in Fig. 7. Implementing Eq 6, the value of the  $J$ -integral, hence the tearing energy, is twice the shaded area shown.

The  $J$ -integral values of the specimen at eight levels of stretching have been obtained. The results presented in the form of Eq 3 are shown in Fig. 3. They are in agreement with results obtained by other methods.

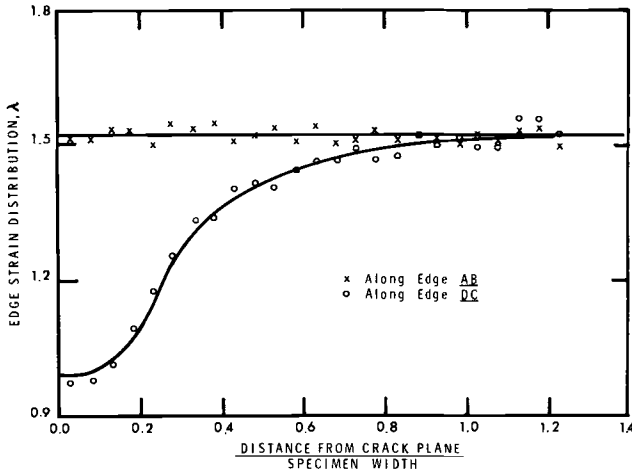


FIG. 7—Strain distribution along the two edges of a nicked rubber strip extended to a stretch ratio of 1.52.

### Concluding Remarks

A method is proposed for measuring tearing energy in nicked rubber strips based on the Rice J-integral. When implemented on the simple extension specimen, results indicate that the method can measure tearing energy in rubber with an accuracy comparable to that obtained by other methods. It is by far the simplest known method and eliminates the

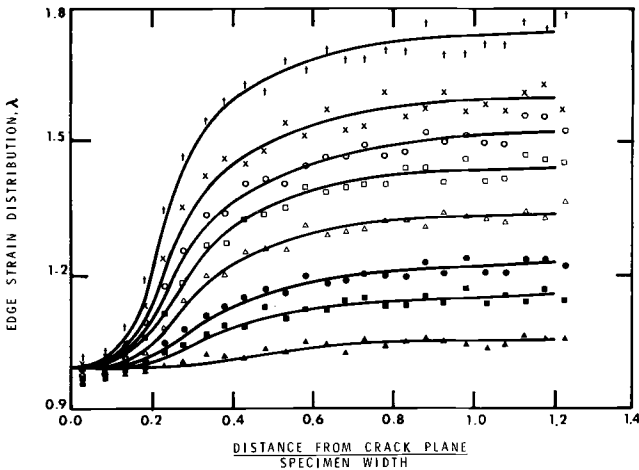


FIG. 8—Strain distribution along the nicked edge of a nicked rubber strip at eight levels of stretching.

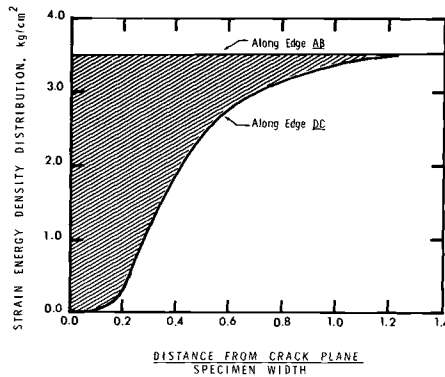


FIG. 9—Strain energy density distribution along the two edges of a nicked rubber strip extended to a stretch ratio of 1.52.

complexity of compliance calibration and graphical differentiation associated with existing methods. Moreover, it requires only one specimen.

In principle, the J-integral method may be used to measure tearing energy of cracked rubber components undergoing two dimensional deformations.

#### Acknowledgments

The author wishes to thank Dr. N. M. Wang for many helpful discussions on the experimental evaluation of the J-integral, Carol Underwood for taking the strain measurements and M. E. Wheatley for the preparation of the specimens.

#### References

- [1] Rivlin, R. S. and Thomas, A. G., *Journal of Polymer Science*, Vol. 10, No. 3, 1953, p. 291.
- [2] Gent, A. N., Lindley, P. B., and Thomas, A. G., *Journal of Applied Polymer Science*, Vol. 8, 1964, p. 455.
- [3] Thomas, A. G., *Physical Basis of Yield and Fracture Conference Proceedings*, Oxford, England, 1966, p. 134.
- [4] Greensmith, H. W., *Journal of Applied Polymer Science*, Vol. 7, 1963, p. 993.
- [5] Lake, G. J., *The Yield, Deformation and Fracture of Polymer Conference Proceedings*, Cambridge, England, 1970.
- [6] Lindley, P. B., *Journal of Strain Analysis*, Vol. 7, No. 2, 1972, p. 132.
- [7] Rice, J. R. in *Fracture*, Vol. 2, H. Liebowitz, Ed., Academic Press, New York, 1968, p. 191.
- [8] Wang, N. M., *International Journal of Solids and Structures*, Vol. 9, 1973, p. 1211.
- [9] Chang, S. J., *Journal of Applied Mathematics and Physics*, Vol. 23, 1972, p. 149.
- [10] Knowles, J. K. and Sternberg, E., *Archive of Rational Mechanics and Analysis*, Vol. 44, No. 3, 1972, p. 187.

*G. E. Tardiff, Jr.,<sup>1</sup> B. A. Kuhn,<sup>1</sup> and L. A. Heldt<sup>2</sup>*

## A Study of Plane Stress Fracture in the Large-Scale Plastic Yielding Regime

---

**REFERENCE:** Tardiff, G. E., Jr., Kuhn, B. A., and Heldt, L. A., "A Study of Plane Stress Fracture in the Large-Scale Plastic Yielding Regime," *Mechanics of Crack Growth, ASTM STP 590*, American Society for Testing and Materials, 1976, pp. 115–127.

**ABSTRACT:** Three independent methods for measuring plane stress fracture resistance in the large-scale plastic yielding regime were tested and were found to give equivalent results. The three methods were the J-integral technique, a method based on the increase in compliance that accompanies the development of a plastic zone, and a method based on the direct measurement of the plastic work that must be done to cause fracture.

**KEY WORDS:** crack propagation, fracture tests, stress analysis, plastic properties, elastic properties, beryllium

### Nomenclature

- $J$  J-integral value or pseudo strain energy release rate,  $J \cdot m^{-2}$
- $J_{crit}$  Value of  $J$  at fracture
- $\mathcal{G}$  Strain energy release rate,  $J \cdot m^{-2}$
- $\mathcal{G}_{crit}$  Value of  $\mathcal{G}$  at fracture
- $\sigma$  Remotely applied gross area stress, MPa
- $F$  Applied force,  $N$
- $\Delta$  Displacement measured remote from crack plane along the line of loading, mm
- $v$  Displacement measured at crack mouth, mm
- $U$  Pseudo potential energy or work done in loading a specimen to a given displacement,  $J$

<sup>1</sup> Project leader, Chemistry and Materials Science Department and technical associate, respectively, Lawrence Livermore Laboratory, University of California, Livermore, Calif. 94550.

<sup>2</sup> Professor of Metallurgical Engineering, Michigan Technological University, Houghton, Mich. 49931.

- $a$  Crack length, mm; or half crack length of center cracked specimen
- $h$  Specimen thickness, mm
- $W$  Specimen width, mm
- $E$  Modulus of elasticity, MPa
- $\sigma_{ys}$  Uniaxial tensile yield strength, MPa
- $\delta$  Displacement of crack surfaces, mm
- $\delta_t$  Displacement of crack surfaces at crack tip
- $\delta_t^*$  Value of  $\delta_t$  at fracture
- $\sigma(\delta)$  Flow strength of the metal within the plastic zone as a function of the separation of imaginary crack surfaces extending through the zone, Mpa
- $Y$  Same as  $\sigma(\delta)$ , but assumed independent of  $\delta$
- $r_u$  Irwin estimate of plastic zone size, mm
- $\rho$  Plastic zone length from Dugdale model, mm

In their original development of the J-integral approach to fracture testing, Begley and Landes [1]<sup>3</sup> experimentally verified the significance of critical  $J$  by showing that it was equal, within limits imposed by variation in materials, to a critical  $\mathcal{G}$  found from large linear elastic specimens of the same material. Such comparisons are not always possible, either because of the absence of linear-elastic data or because extremely large specimens would be required to develop the linear-elastic data. In the case of very tough materials that fail in plane stress, for example, the specimen size required for macroscopic linear-elastic behavior can be immense, and such specimens are all but impossible to acquire or test. It was considered desirable, therefore, to examine other independent approaches to nonlinear analysis of plane stress fracture so that the veracity of critical  $J$  results might be tested experimentally in the absence of linear-elastic data. The two new approaches to nonlinear fracture analysis reported in the present paper are compliance technique and a plastic work method. The results from these are described, and they are compared to the results from critical  $J$  tests.

## Experimental Details

### *Material*

Thin, cross-rolled-ingot sheet beryllium was chosen for the present study because this material can exhibit large nonlinear deflections in the absence of stable crack growth. Thus, the complexities that attend the presence of stable crack growth were avoided. A rather thin sheet (0.80 mm thick) was chosen for the study because it was believed that fracture

<sup>3</sup> The italic numbers in brackets refer to the list of references appended to this paper.

would occur in plane stress in this thin section. The beryllium sheet was annealed at 780°C for 1 h after warm cross rolling. This resulted in a fully recrystallized microstructure and an intercept grain size of 49  $\mu\text{m}$ . The material was found to have a high degree of in-plane isotropy as indicated by the basal plane pole figure given in the Appendix. The chemical composition of the sheet is also recorded in the Appendix.

The uniaxial, engineering tensile properties were determined; the averaged results from two specimens were 151 MPa yield strength, 302 MPa ultimate stress, and 7.8 percent elongation.

### *Fracture Resistance Test Procedures*

*Specimen Types*—Single edge notched (SEN) specimens of two different sizes were used in the present study. The SEN specimens were 31.75 and 95.25 mm wide. Other dimensions were in accord with suggested geometry [2]. Machined edge slots in the specimens were extended, using electrical discharge machining (EDM), by a minimum of 1.3 mm to produce a relatively small slot root diameter ( $\sim 0.12$  mm). Fatigue cracks were extended from the EDM slots using procedures described next. Four small SEN specimens were prepared with edge slots of different lengths (11.43, 12.70, 13.97, and 15.87 mm—measured to the end of the EDM slot) to facilitate J-integral testing. The edge notch length to the end of the EDM slot in the large SEN specimen was 34.29 mm.

Two double-edge notched (DEN) specimens were also tested. These were prepared by using EDM to introduce a slot opposite the edge notch in the small SEN-type specimen just described. The lengths of the two edge slots were adjusted so that a net ligament, 4.57 mm wide, remained centered on the specimen axis. The reasons for this particular specimen design are discussed later in the section on “Results and Discussion.”

*Fatigue Precracking*—All fracture specimens were fatigue precracked using a 200-kN capacity electro-hydraulic machine in tension-tension cycling to develop a sharp crack front. In the case of the SEN specimens cycling was carried out at a calculated stress intensity range of 2 to 15  $\text{MPa}\cdot\text{m}^{1/2}$ . The relation between stress intensity and specimen geometry given by the calibration equation on page 12 in Ref 3 was used for the calculation. The fatigue cycling caused between 0.13 and 0.25 mm of fatigue crack growth in fewer than  $10^5$  cycles. The unusual design of the DEN specimens, however, made it necessary to fatigue precrack above the general yield stress. Reasons for this are discussed further in the “Results and Discussion” section.

*Crack Mouth Displacement*—In all cases except the J-integral tests, the displacement in the fracture test was measured at the crack mouth. The crack mouth displacement gage that was used is described in Ref 3 on pages 35-37. Briefly, the displacement is measured by following the output of a foil resistance strain gage bridge mounted on the arms of the

displacement gage. The output of the gage is calibrated in a fixture incorporating a barrel micrometer. The sensitivity of the method is somewhat better than 0.0025 mm.

*Load Point Displacement*—In the case of the J-integral tests, it was necessary to measure the displacement along the line of loading in order to obtain a well-defined energy input to the specimen. To accomplish this the beam gage method illustrated in Fig. 1 was used. Figure 1 shows the gage sprung between two stops cemented onto the specimen. The gage parameters were designed to maximize linearity and sensitivity over the range of 0.25 mm displacement. The displacement is measured by following the output of foil resistance strain gages bonded to the midsection of the beam gage. The length over which the displacements were measured was chosen equal to twice the specimen width (63.5 mm) because the work by Srawley et al [4] indicated that the rate of change of compliance with crack length is independent of gage length for gage lengths of  $2\times$  width and greater (for fully elastic SEN specimens). Two foil resistance gages were mounted on each side of the gage to form a full bridge. The outputs of two such gages on each side of the specimen were averaged to obtain the load point displacement. The sensitivity of the method is better than 0.002 mm.

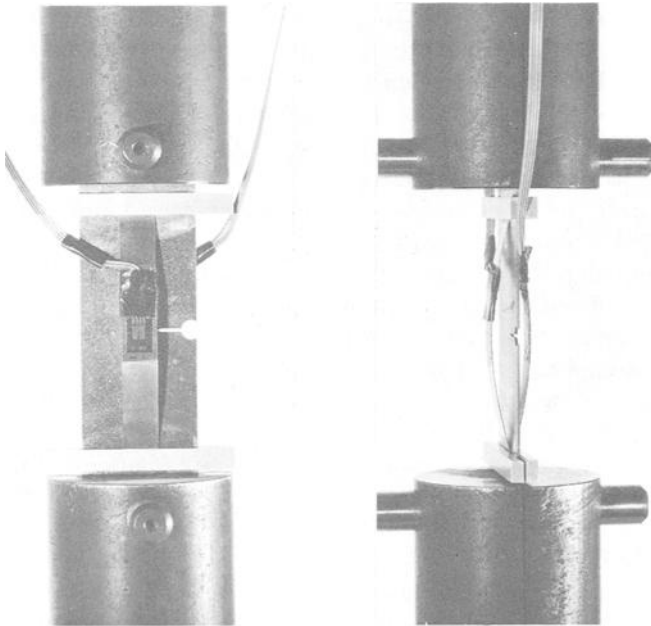


FIG. 1—Photographs of the load point displacement gages in place on the small SEN specimen.

*Fracture Test Procedures*—All of the fracture tests were carried out at a constant cross-head velocity of  $2 \times 10^{-6} \text{ m} \cdot \text{s}^{-1}$ . The J-integral tests were carried out on a screw driven, 600-kN-capacity machine, and the other tests were carried out on a 200-kN electrohydraulic machine. Force and displacement were recorded over the course of the test.

In preliminary studies it was established that no detectable stable growth occurred prior to fast fracture in the present ingot sheet in the 780°C condition of heat treatment. This was concluded following microscopic examination of the crack tip during the course of the test. The absence of stable growth was confirmed by a later test in which the output of a strain gage mounted at the tip of the precrack indicated a gradual increase in strain as force increased with no indication of cracking prior to unstable fracture. It was not necessary, therefore, to develop a sophisticated technique to monitor stable crack extension. Visual observation was used during each test, however, to verify that no observable stable growth had occurred.

**Results and Discussion**

*Nonlinear Methods of Fracture Analysis*

*J-Integral Method*—The approach to the J-integral tests taken in the present study followed that first described by Begley and Landes [1]. The force-displacement behavior for four small SEN specimens, each containing a different crack length, is given in Fig. 2. The J-integral values corresponding to the three shortest crack lengths were determined for a

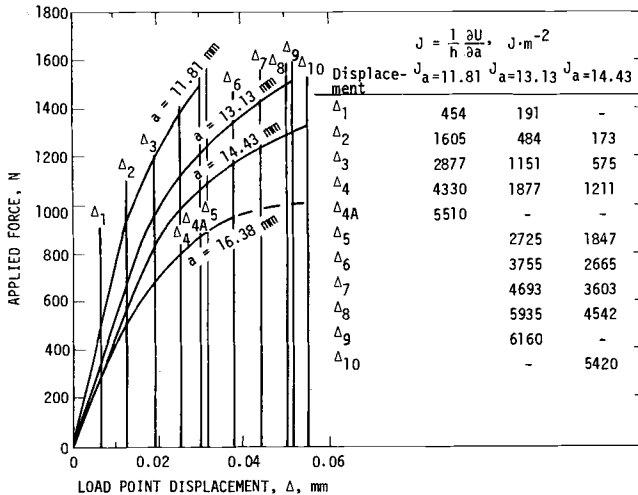


FIG. 2—Force-versus-load point displacement results for the J-integral specimens.

number of different displacements. To do this, the area between adjacent curves was measured with a planimeter to obtain a value for the pseudo energy release,  $dU$ , for various displacements. This energy value was then divided by the difference in crack length,  $da$ , and thickness to obtain a value for  $J$  (a pseudo energy release rate) at each displacement. The resulting  $J$ -versus-displacement relationships for three different crack lengths are given in Fig. 3. The critical  $J$  value is obtained at the point of fracture, and the values corresponding to three crack lengths are indicated in Fig. 3 (6160, 5510, and 5420  $\text{J}\cdot\text{m}^{-2}$ ). These values are considered to be within normally expected material variation.

Begley and Landes found that the value of  $J_{\text{crit}}$  for the steel they investigated was the same within material variation as a linear elastic value of  $\mathcal{G}_{\text{crit}}$  determined for the same steel by a different investigator

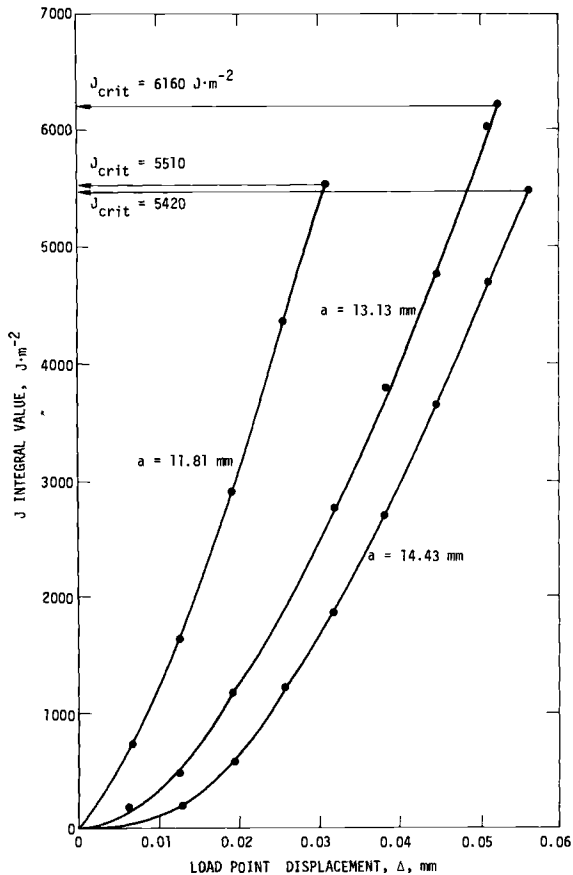


FIG. 3— $J$ -versus-load point displacement for the small SEN specimens.

using larger specimens. Begley and Landes thus concluded that the  $J$  approach to nonlinear analysis yielded a result equivalent to a linear-elastic test. The mathematical basis for the  $J$  test was fully discussed by Begley and Landes and is not repeated here. Suffice it to say that  $J$  describes the elastic-plastic stress field in the same way that  $\mathcal{G}$  describes the elastic field in a linear-elastic situation. The values of  $J_{\text{crit}}$  and  $\mathcal{G}_{\text{crit}}$  are measures of the plastic work done at the crack tip up to the point of fracture.

Begley and Landes pointed up that minimum specimen dimensions (including remaining ligament and crack length) required for a valid  $J$  result are determined by the dimensions over which the  $J$  parameter describes the crack tip stress field. It is necessary, therefore, to verify the validity of the  $J$  result by independent methods until sufficient experience or theoretical understanding or both are acquired to allow minimum specimen size requirements to be defined. In the present instance, two other independent, nonlinear methods were investigated for comparison with the  $J_{\text{crit}}$  results.

*Compliance Method*—Using the expression [5] that gives an approximate dimension of the plane-stress plastic zone,

$$r_y \cong \frac{1}{2\pi} \left( \frac{E \mathcal{G}}{\sigma_{ys}^2} \right) \quad (1)$$

and assuming that  $\mathcal{G}_{\text{crit}} = J_{\text{crit}}$ , a zone of 11 mm is obtained at fracture for the present material. Since this is a very large multiple of the thickness of the present sheet (0.80 mm thick), it is reasonable to conclude that fracture occurs in plane stress. This makes it possible to test a second method of nonlinear analysis based in part on the Dugdale plane-stress model.

Records of force versus crack-mouth displacement for both the large and small SEN specimens are given in Fig. 4. A method of analyzing these records is obtained if it is assumed that all of the deviation from linearity is due to the development of a plastic zone ahead of the crack tip. This is reasonable, since no stable crack growth was observed. If it is assumed that the development of a plastic zone ahead of the crack tip has the same effect on compliance as an amount of crack extension of equal length, then the plastic zone length can be deduced from the apparent compliance at the point of fracture and a prior correlation between compliance and  $a/W$ . As noted in Fig. 4, the apparent compliance is deduced from the reciprocal slope of the line drawn through the fracture point and the origin. A value of compliance compensated for modulus (taken as  $290 \times 10^9 \text{ Nm}^{-2}$  for beryllium) and thickness (0.80 mm) is then computed to give a value for  $Evh/F$ . A value for  $(a + \rho_{\text{app}})W$  (where  $\rho_{\text{app}}$  is the apparent length of the plastic zone) is found from the correlation between

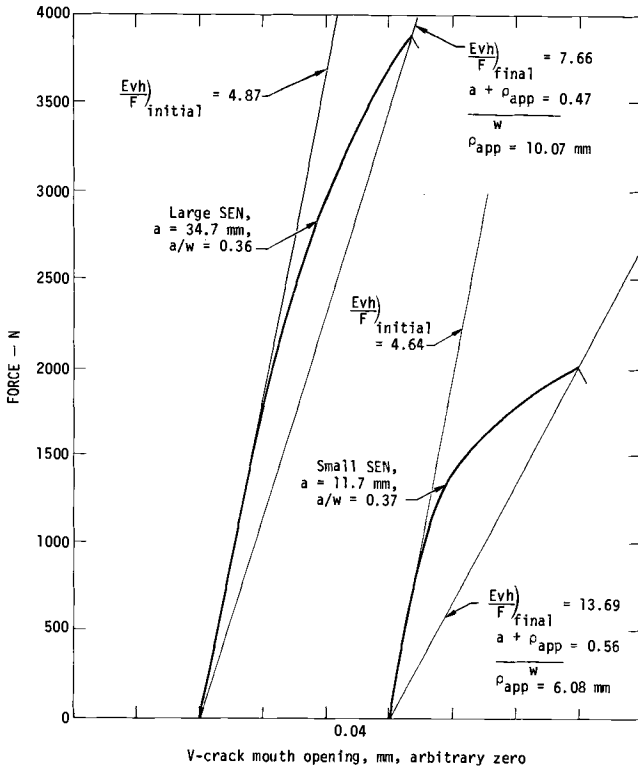


FIG. 4—Force-versus-crack mouth displacement behavior for SEN specimens of two sizes.

$Evh/F$  and  $a/W$  given in Ref 3 on page 37. The apparent plastic zone lengths at fracture found using this method are 10.7 mm for the large SEN and 6.08 mm for the small SEN.

It is now possible to compute the fracture resistance if it is assumed that the plastic zone lengths found above represent the critical zone lengths for fracture independent of specimen configuration. This is done by first computing the remote applied stress required to develop these same plastic zone lengths in infinite center cracked (CC) specimens. The Dugdale [6] elastic-plastic model for plane stress is used for this purpose. This model, originally developed by Dugdale, subsequently extended by Goodier and Field [7], and used by Hahn and Rosenfield [8] to account for the magnitude of plane stress fracture toughness, has proven very useful in the interpretation of the origin of fracture resistance. The basis for and the principle results of this model are described thoroughly in the previous reference and are not repeated here. The appropriate equation for calculation of the remote stress is, from the Dugdale model

$$\sec \frac{\pi \sigma}{2Y} = \frac{\rho}{a} + 1 \quad (2)$$

It is necessary to choose a value for the cohesive stress or the strength of the plastic metal ( $Y$ ) within the zone for this calculation. A value for  $Y$  was taken as an average of the yield and ultimate strengths in uniaxial tension ( $Y = 230$  MPa). The values of the remote stress so computed are 102 MPa ( $\rho = 10.07$  mm,  $a = 34.7$  mm), and 127 MPa ( $\rho = 6.08$  mm,  $a = 11.7$  mm). Values for the fracture resistance can be found from these stresses using the relationship between  $\mathcal{G}$ ,  $\sigma$ , and  $a$  that is appropriate for the infinite CC specimen in plane stress loading [9]

$$\mathcal{G} = \frac{\sigma^2 \pi a}{E} \quad (3)$$

Since  $\rho$  is a large fraction of  $a$  in both cases, a plastically corrected value of  $\mathcal{G}$  is calculated using Eq 3, but with  $a$  replaced by  $a + \rho$ , following a suggestion by McClintock and Irwin [5]. This results in fracture resistance of  $5050 \text{ J} \cdot \text{m}^{-2}$  for the 10.07-mm plastic zone and  $3100 \text{ J} \cdot \text{m}^{-2}$  for the 6.08-mm plastic zone.

The plastic zone found from the test of the small SEN specimen is significantly shorter than that found from the test of the larger SEN specimen. It is this difference in plastic zone length which results in the large difference in the computed values of fracture resistance. The difference results from the assumption that the plastic zone has the same effect on compliance as an equivalent amount of crack extension. Actually, because a cohesive force acts on the elastic-plastic boundary, the specimen will be less compliant than one with the plastic zone replaced by an equivalent amount of crack extension. Thus, the actual plastic zone length will be greater than that found using the method just described. This effect is expected to be greater for smaller specimens in which the zone will occupy a greater fraction of the net ligament width. The fracture resistance computed using the plastic zone length deducted from the compliance test of the large SEN is similar to the magnitude of the  $J_{\text{crit}}$  results given in the previous section. This suggests that the plastic zone length deducted from the compliance data for the large SEN is about right. A more exact deduction of the plastic zone length from the compliance data would be possible by taking into account the effects of the cohesive stress on compliance. It was not within the scope of the present work to investigate this refinement.

*Plastic Work Method*—The third method of fracture analysis is based on Rice's [10] proof that

$$\mathcal{G}_{\text{crit}} = \int_0^{\delta_{\text{cr}}} \sigma(\delta) d\delta \quad (4)$$

This proof applies strictly only to the Dugdale model, in which the plastic zone is a constant height strip that extends directly ahead of the crack tip [10]. Assuming the fracture of the present sheet can be reasonably approximated by such a strip model, it is apparent that the value of  $\mathcal{Q}_{crit}$  can be obtained by measuring the area under the cohesive stress-crack opening displacement directly at the crack mouth if the specimen could be made small enough so that the elastic contribution to crack mouth displacement was small compared to the contribution from crack tip plasticity. To accomplish this it was appropriate to choose a specimen with a net ligament smaller than the plastic zone size at fracture so that the zone would span the entire ligament width. On this basis the net ligament width chosen was 4.57 mm, considerably smaller than the plastic zone length estimated previously (11 mm). A double edge notched specimen was chosen so that  $\delta(\delta)$  could be simply obtained from the applied force and net section area. The principle of the technique is illustrated in Fig. 5. It is evident that the crack tip displacement,  $\delta_t$ , indicated in Fig. 5 will be the same as the displacement of the upper and lower boundaries of the plastic zone and that this displacement, except for a small elastic contribution will be equal to the displacement measured at the crack mouth. This is most easily visualized if the plastic zone is imagined to be a hole in the specimen.

It was necessary to fatigue the two DEN specimens above the general yield stress in order to develop a reasonable amount of fatigue crack growth in a reasonable time. This results because very low stress intensities are developed with this specimen design, even at net section stresses approaching the ultimate tensile stress. The areas under the curves in Fig. 6 were measured with a planimeter to obtain values of  $\mathcal{Q}_{crit}$  for the two specimens. As indicated in Fig. 6, the values obtained were 5260 and 4660 J·m<sup>-2</sup>.

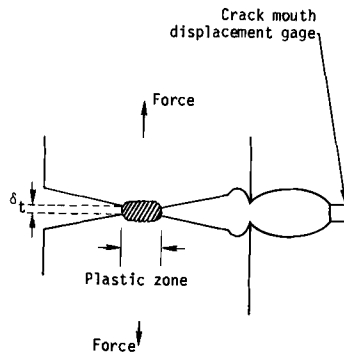


FIG. 5—Principle of plastic work method for measuring fracture resistance.

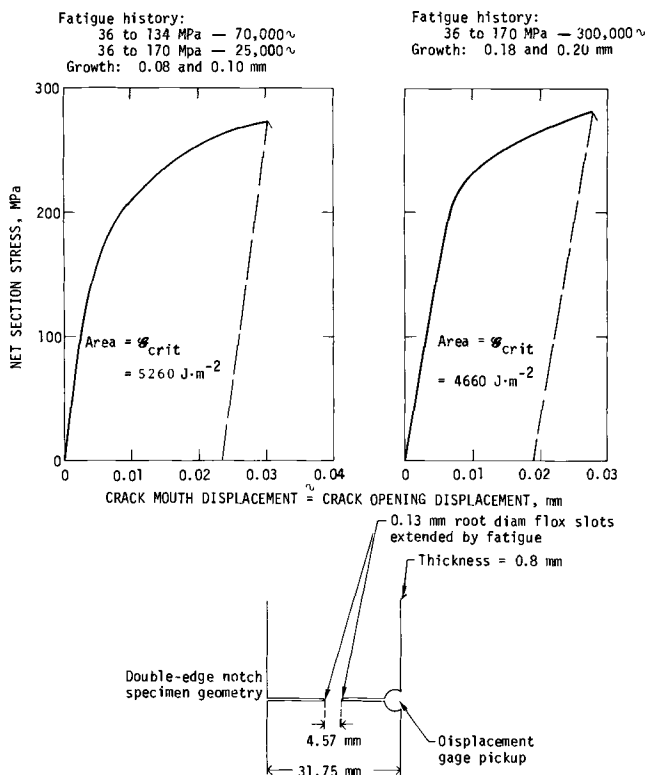


FIG. 6—Net section stress-versus-displacement for double-edge notched specimens used to determine fracture resistance by plastic work method.

## Conclusions

The results from each of the methods of analysis are summarized in Table 1. It is evident that all three methods of nonlinear analysis resulted in values that can, in view of normally expected material variation, be considered the same. This correspondence is taken as evidence that the methods used resulted in correct values for the fracture resistance. It might be expected that similar values would result from linear-elastic tests of very large specimens of the same thickness. The demonstration of this was, however, beyond the scope of the present program.

## Acknowledgments

Work performed under the auspices of the U.S. Atomic Energy Commission. This paper is part of a thesis submitted by G. E. Tardiff, Jr., in partial fulfillment of the requirements of the degree of Doctor of

TABLE 1—Summary of fracture resistance values found using three independent methods of nonlinear fracture analysis.

|                              | $J_{crit}$ or $Q_{crit} J m^{-2}$ |
|------------------------------|-----------------------------------|
| J-integral method            | 6160, 5510, 5420                  |
| Compliance method, large SEN | 5050                              |
| Compliance method, small SEN | 3100 <sup>a</sup>                 |
| Plastic work method          | 5260, 4660                        |

<sup>a</sup> This low result probably results from the assumption that the plastic zone has the same effect on compliance as an equivalent amount of crack extension as discussed in the text.

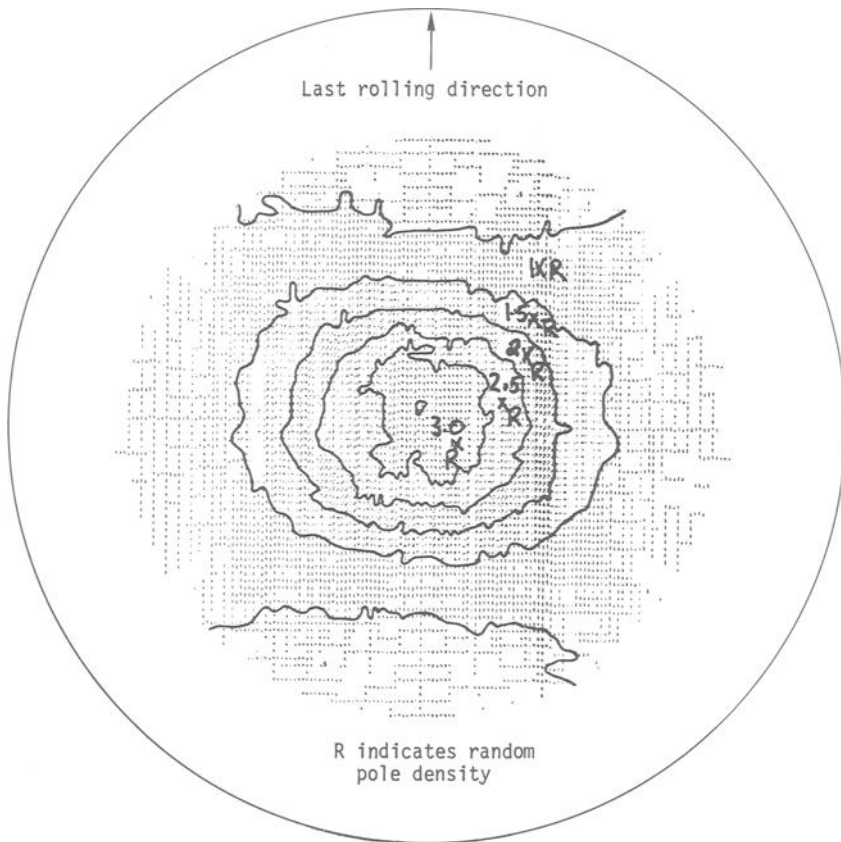


FIG. 7—Basal plane pole figure and chemical composition of beryllium.

Philosophy in Metallurgical Engineering at the Michigan Technological University, Houghton, Michigan.

## APPENDIX

### Basal Plane Pole Figure and the Chemical Composition of the Beryllium Sheet

The extent of in-plane isotropy of the annealed beryllium sheet is shown by the basal plane pole in Fig. 7. The chemical content is:

|    |        |     |        |
|----|--------|-----|--------|
| C  | 0.069  | Co  | <0.001 |
| Fe | 0.138  | Cu  | 0.007  |
| Al | 0.072  | Pb  | <0.001 |
| Mg | <0.001 | Mn  | 0.013  |
| Si | 0.061  | MO  | 0.003  |
| Ca | <0.003 | Ni  | 0.015  |
| CR | 0.012  | BeO | <0.01  |

### References

- [1] Begley, J. A. and Landes, J. D. in *Fracture Toughness, Proceedings of the 1971 National Symposium on Fracture Mechanics, Part II, ASTM STP 514*, American Society for Testing and Materials, 1972, p. 1.
- [2] Srawley, J. E. and Brown, W. F., Jr. in *Fracture Toughness Testing and Its Applications, ASTM STP 381*, American Society for Testing and Materials, 1964, p. 133.
- [3] Brown, W. F. and Srawley, J. E., *Plane Strain Crack Toughness Testing and its Applications, ASTM STP 410*, American Society for Testing and Materials, 1967.
- [4] Srawley, J. E., Jones, M. M., and Gross, B., *Experimental Determination of the Dependence of Crack Extension Force on Crack Length for a Single Edge Notch Tension Specimen*, Report TN D-2396, National Aeronautics and Space Administration, Washington, D.C., 1964.
- [5] McClintock, F. A. and Irwin, G. R. in *Fracture Toughness Testing and Its Applications, ASTM STP 381*, American Society for Testing and Materials, 1964, p. 84.
- [6] Dugdale, D. S., *Journal of Mechanics and Physics of Solids*, Vol. 8, No. 2, Feb. 1960, p. 100.
- [7] Goodier, J. N. and Field, F. A. in *Fracture of Solids*, Interscience, New York, 1963, p. 103.
- [8] Hahn, G. T. and Rosenfield, A. R., *Acta Metallurgica*, Vol. 13, No. 1, March 1965, p. 239.
- [9] Paris, P. C. and Sih, G. C. in *Fracture Toughness Testing and Its Applications, ASTM STP 381*, American Society for Testing and Materials, 1964, p. 30.
- [10] Rice, J. R. in *Fracture*, Vol. II, Academic Press, New York, 1968, p. 191.

*J. D. Landes<sup>1</sup> and J. A. Begley<sup>2</sup>*

## A Fracture Mechanics Approach to Creep Crack Growth

---

**REFERENCE:** Landes, J. D. and Begley, J. A., "A Fracture Mechanics Approach to Creep Crack Growth," *Mechanics of Crack Growth, ASTM STP 590*, American Society for Testing and Materials, 1976, pp. 128–148.

**ABSTRACT:** A fracture mechanics approach was used to study high-temperature creep crack propagation. Crack growth rates were correlated with the  $C^*$ -parameter which is an energy rate line integral. For materials conforming to a nonlinear stress and strain rate relationship in the steady-state creep range, specifically, those which can be properly idealized as purely viscous (negligible elastic and transient creep effects),  $C^*$  characterizes the crack tip stress and strain rate fields.

Crack growth rate tests were conducted in the creep range on a discalloy superalloy at 1200°F (920 K). Two specimen geometries were tested, a center cracked panel and a compact geometry, to establish the geometry independence of this approach. The results showed that crack growth rate correlated with the  $C^*$ -integral, while other parameters ( $K$  and nominal stress) failed to adequately characterize crack growth rate.

**KEY WORDS:** crack propagation, stress analysis, mechanical properties, fracture properties, crack initiation, creep rate

High-temperature creep behavior has been the subject of extensive research. Much of the work has been focused on studying bulk material behavior. Typical tests usually involve uniaxial tension specimens where time to rupture or strain rate is measured as a function of stress under an applied constant load. In some cases, the response of a structure to multiaxially applied loading has been investigated. In this work on bulk material behavior, the effect of macroscopic defects has been largely ignored.

Under a uniform stress field in the creep range, defects often develop as

<sup>1</sup> Senior engineer, Mechanics Department, Westinghouse Research Laboratories, Pittsburgh, Pa. 15235.

<sup>2</sup> Department of Metallurgical Engineering, Ohio State University, Columbus, Ohio 43210.

voids and microcracks are formed in the material. These defects are frequently fairly uniformly dispersed. An analysis which considers an average strain response to an average applied stress is usually adequate to describe this creep behavior. However, there is some creep behavior where failure occurs by the initiation and propagation of a single macroscopic crack. In these cases, the material behavior might better be characterized by an analysis which accounts for this single defect.

A fracture mechanics approach provides a technique where material behavior is analyzed with the assumption of pre-existing cracklike defects. Analysis of material fracture frequently considers the initiation and propagation of cracks and the final failure as three individual steps. Each step can be analyzed separately. In the case of linear elastic behavior, the crack tip stress intensity factor,  $K$ , is a single parameter which can be used to analyze each of these separate steps of fracture behavior.  $K$  is a parameter which uniquely characterizes the crack tip stress and strain field.

A fracture mechanics approach to creep cracking behavior must identify a parameter which successfully characterizes the crack tip behavior. A first approach to this analysis might be one to identify a parameter which can correlate creep crack propagation rates. A study by Siverns and Price on a 2 1/4Cr-1Mo steel has attempted to correlate creep crack growth rate with  $K [I]$ .<sup>3</sup> The results shown in Fig. 1 demonstrate the

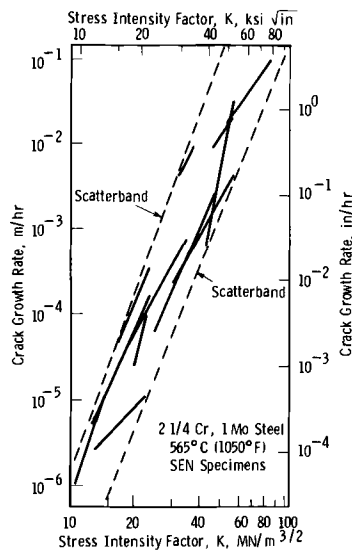


FIG. 1—Crack growth rate versus stress intensity factor [1].

<sup>3</sup> The italic numbers in brackets refer to the list of references appended to this paper.

moderate success of this approach. Crack growth rates have been measured over five orders of magnitude. However, the growth rate at a given value of  $K$  exhibits a scatterband of about a factor of 30. The data were collected on a single specimen geometry, a single edge cracked tension specimen. To demonstrate that  $K$  is a successful correlating parameter, data should be collected on different specimen geometries where the crack tip parameter can be analyzed separately from the other stress field parameters.

It could be postulated that high-temperature creep behavior is not a typical linear elastic phenomena. Therefore, the linear elastic parameter,  $K$ , may not be the appropriate parameter to correlate creep crack growth rate behavior. A different parameter,  $C^*$ , is proposed in this work as a parameter which better describes the crack tip region.  $C^*$  is an energy rate line integral which uniquely characterizes the crack tip stress and strain rate field for materials following a nonlinear steady-state creep law.  $C^*$  appears to be a more appropriate parameter to use for correlating creep crack growth rates.

Crack growth rate studies were performed on a discalloy superalloy at 1200°F (920 K) to test the applicability of the  $C^*$ -parameter to correlate growth rates. Two different specimen geometries were used, a center cracked panel (CCP) and a wedge opening loading specimen, 1T-CT. The success of the  $C^*$ -parameter in correlating creep crack growth rates was compared with attempts to use linear elastic parameters,  $K$ , and nominal stress, to correlate growth rate.

### **$C^*$ -Parameter**

#### *Definition of $C^*$*

The  $C^*$ -parameter is an energy rate line integral. It is defined for the two-dimensional case by

$$C^* = \int_{\Gamma} W^* dy - T_i \left( \frac{\partial \dot{u}_i}{\partial x} \right) ds \quad (1)$$

where

$$W^* = \int_0^{\dot{\epsilon}_{mn}} \sigma_{ij} d\dot{\epsilon}_{ij} \quad (2)$$

As illustrated in Fig. 2,  $\Gamma$  is the line contour taken from the lower crack surface in a counterclockwise direction to the upper crack surface.  $W^*$  is the strain energy rate density associated with the point stress  $\sigma_{ij}$  and strain rate  $\dot{\epsilon}_{ij}$ .  $T_i$  is the traction vector defined by the outward normal  $n_j$

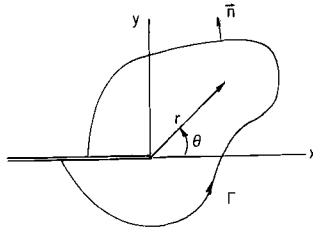


FIG. 2—Crack tip coordinate system and arbitrary line integral contour.

along  $\Gamma$ ,  $T_i = \sigma_{ij}n_j$ ,  $u_i$  is the displacement vector and  $s$  is the arc length along  $\Gamma$ .  $C^*$  was originally suggested by Rice [2] as a path independent energy rate line integral. It is simply a modification of the J-integral where strain and displacement,  $\epsilon_{ij}$  and  $\dot{u}_i$ , are replaced by their rates,  $\dot{\epsilon}_{ij}$  and  $\dot{u}_i$ .

Goldman and Hutchinson [3] discussed how this parameter could be applied to secondary or steady-state creep. A creep law in the form

$$\frac{\dot{\epsilon}}{\epsilon_0} = \alpha \left( \frac{\sigma}{\sigma_0} \right)^n \tag{3}$$

where  $\epsilon_0$ ,  $\alpha$ ,  $\sigma_0$ , and  $n$  are constants, describes a nonlinear viscous behavior in materials. This law can be generalized to multiaxial stress state by

$$\frac{\dot{\epsilon}_{ij}}{\epsilon_0} = \frac{3}{2} \alpha \left[ \frac{\sigma_e}{\sigma_0} \right]^{n-1} \frac{s_{ij}}{\sigma_0} \tag{4}$$

where  $\sigma_e$  is an effective stress

$$\sigma_e^2 = \frac{3}{2} s_{ij}s_{ij} \tag{5}$$

and  $s_{ij}$  is the stress deviator. For a steady-state creep behavior conforming to this law Goldman and Hutchinson [3] described how  $C^*$  is a single parameter characterizing the near-tip stress and strain-rate fields.

$$\sigma_{ij} = \sigma_0 [C^*/\alpha \sigma_0 \epsilon_0 I_n]^{1/(n+1)} r^{-1/(n+1)} \tilde{\sigma}_{ij}(\Theta) \tag{6}$$

$$\dot{\epsilon}_{ij} = \alpha \epsilon_0 [C^*/\alpha \sigma_0 \epsilon_0 I_n]^{n/(n+1)} r^{-n/(n+1)} \tilde{\dot{\epsilon}}_{ij}(\Theta) \tag{7}$$

$I_n$  is a numerical constant determined by  $n$  and mode of crack opening. It is tabulated for a given range of  $n$  elsewhere [4].  $\tilde{\sigma}_{ij}(\Theta)$  and  $\tilde{\epsilon}_{ij}(\Theta)$  are dimensionless functions which characterize the distribution of stress and strain rate.

For linear elastic behavior, the parameter  $K$  uniquely characterizes the near-tip stress and strain field. For crack propagation behavior under linear elastic conditions,  $K$  correlates growth rate behavior. It is reasonable to assume that for materials following a steady-state creep law (Eq. 4),  $C^*$  will correlate the growth rate behavior.

It is important to note that the application of the  $C^*$ -parameter to correlate creep crack growth rates assumes that the material is following a steady-state creep law as expressed by Eq. 4. This assumes that all transient effects as well as elastic and short time plasticity effects can be ignored. Since the  $C^*$ -parameter is expressed as a path independent line integral, this assumption must apply not only to the crack tip area but to each point in the structure being analyzed.

The use of  $C^*$  to characterize creep crack growth is limited to a specific range of cracking behavior. However, this approach is not intended to be universal in its application. Rather it is intended as a first step in an approach to a complex problem.

#### *Power Rate Interpretation*

The relationship between the J-integral and the  $C^*$ -parameter suggests a method for measuring it experimentally.  $J$  is an energy integral, and  $C^*$  is an energy rate or power integral. An energy rate interpretation of  $J$  has been discussed by Rice [5] and Begley and Landes [6].  $J$  can be interpreted as the energy difference between two identically loaded bodies having incrementally differing crack lengths.

$$J = -\frac{dU}{d\ell} \quad (8)$$

where

$U$  = potential energy and  
 $\ell$  = crack length.

$C^*$  can be calculated in a similar manner using a power rate interpretation. Using this approach  $C^*$  is the power difference between two identically loaded bodies having incrementally differing crack lengths.

$$C^* = -\frac{\partial U^*}{\partial \ell} \quad (9)$$

where  $U^*$  is the power or energy rate defined for a load  $P$  and displacement  $\dot{u}$  by

$$U^* = \int_0^{\dot{u}} P d\dot{u} \tag{10}$$

This method for determining  $J$  is a pseudo-compliance measure of  $J[6]$ . It is shown schematically in Fig. 3. The similar method for measuring  $C^*$  is shown in Fig. 4 for multiple specimens tested at differing displacement rates. The data are collected as load and crack length versus time for a constant displacement rate, Step 1. These data are then used to determine load as a function of displacement rate for various crack lengths, Step 2, and crack growth rate versus crack length, Step 5. The power or energy rate input,  $U^*$ , is measured as the area under the curves in Step 2.  $U^*$  is plotted versus crack length in Step 3. The slope of the curves in Step 3 is then  $C^*$  as defined in Eq 9.  $C^*$  can be plotted as a function of displacement rate, Step 4. Combining the curves from Steps 4 and 5 gives the desired result of crack growth rate versus  $C^*$ , Step 6.

This method for analyzing the data is not simple. However,  $C^*$  appears to be an appropriate parameter for correlating crack growth rate data. This data reduction method can be used to demonstrate the feasibility of using the  $C^*$ -parameter. In future work, an easier method for measuring  $C^*$  can be studied.

**Experimental Technique**

The material used in this study was a Fe-Ni-Cr superalloy (Heat No. 4574-7) generically labeled discalloy. The details of the material chemistry and mechanical properties are given in Table 1.

Two specimen types were tested, a center cracked panel, CCP, 0.50 in.

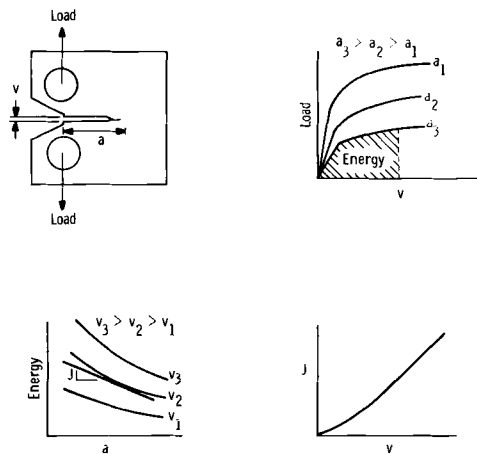


FIG. 3—Energy rate determination of  $J$ .

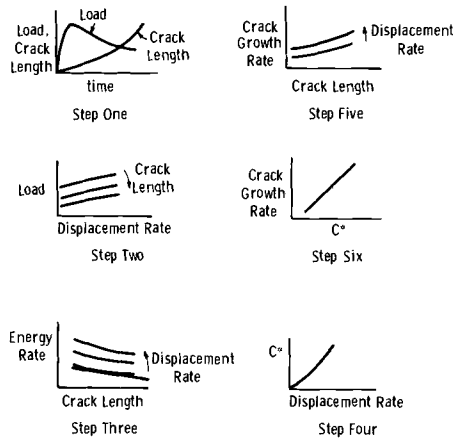


FIG. 4—Schematic showing six steps involved in  $C^*$  data reduction.

(13 mm) thick, Figs. 5a, and a 1T-CT compact specimen 1 in. (25 mm) thick, Fig. 5b.

Attempts were first made to conduct the testing under constant loading conditions to conform with common practice in creep testing. However, under these conditions, the significant portion of the crack growth occurred during a small percent of the total test time. Adequate crack growth data could not be gathered with this test technique. Therefore, tests were conducted using a constant displacement rate. The tests were conducted on a closed loop electrohydraulic test machine where any desired transducer could be used to control loading. For the CCP specimens, the controlling transducer was a linear variable differential transducer (LVDT) placed across a 5 in. gage length on the specimen, Fig. 6. For the 1T-CT specimens, the controlling transducer was an LVDT placed in the load line. Controlling displacement rate meant that one of the important variables in the data reduction scheme could be held constant. The variables monitored during the test were load and crack length. Crack length was monitored using an electrical potential system, Fig. 6. This could monitor crack length to within an accuracy of  $\pm 0.010$  in. (0.25 mm). The input current for this system was 10 A producing a voltage drop in the range of 300 to 600  $\mu\text{V}$ . This signal was then amplified and continuously recorded.

The test temperature was 1200°F (920 K) for all specimens. This is about 100 K above half the absolute melting temperature for the discaloy material putting the tests well into the creep range. The temperature control was good for the CCP specimens  $\pm 2^\circ\text{F}$ . However, for the 1T-CT specimens, temperature control was not as good. Average temperatures for these specimens were estimated to be 10 to 15°F above 1200°F.

TABLE 1—*Properties of discalloy superalloy [11] (Heat 4574-7).*

| A. Chemical Composition |      |      |      |      |       |       |       |      |      |      |      |       |         |
|-------------------------|------|------|------|------|-------|-------|-------|------|------|------|------|-------|---------|
| Ni                      | Cr   | Co   | Mo   | Cu   | C     | P     | S     | Si   | Mn   | Ti   | Al   | B     | Fe      |
| 25.1                    | 13.7 | 0.14 | 3.09 | 0.06 | 0.043 | 0.004 | 0.010 | 0.33 | 0.58 | 1.87 | 0.05 | 0.007 | balance |

| B. Room Temperature Tensile Properties |                                 |                      |               |
|--|---------------------------------|----------------------|---------------|
| Yield Strength, ksi                    | Ultimate Elongation, %          | Reduction of Area, % | Strength, ksi |
| 96<br>(690 MN/m <sup>2</sup> )         | 143<br>(990 MN/m <sup>2</sup> ) | 21                   | 31            |

| C. Stress Rupture Test at 1200°F |         |               |                  |
|----------------------------------|---------|---------------|------------------|
| Stress, ksi                      | Time, h | Elongation, % | Hardness Brinell |
| 63<br>(435 MN/m <sup>2</sup> )   | 329     | 20.7          | 284              |

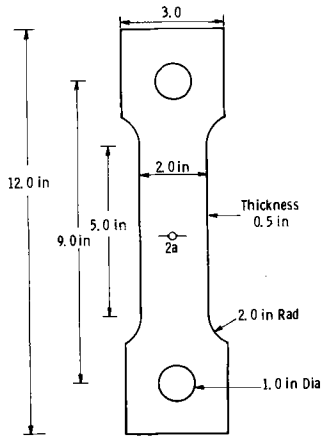


FIG. 5a—CCP specimen.

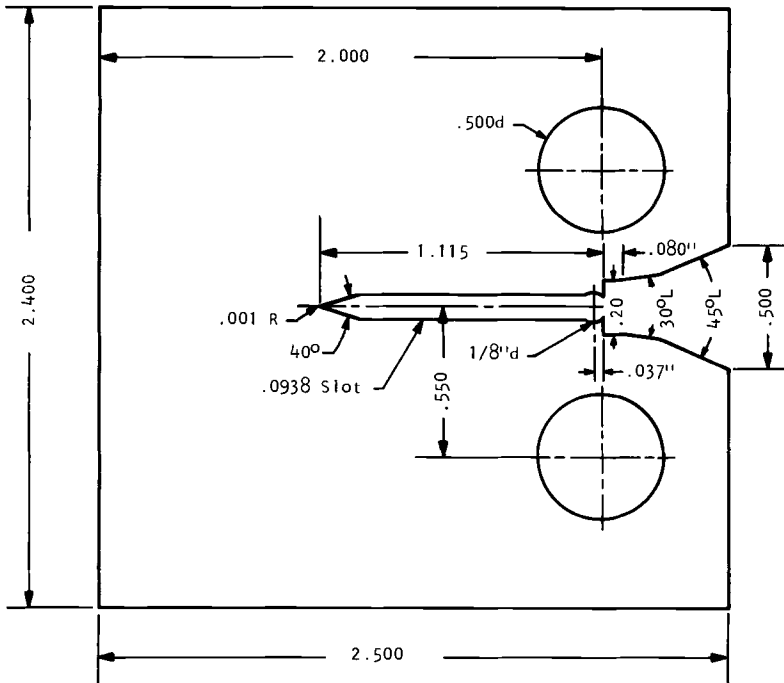


FIG. 5b— $J_{1c}$  type toughness specimen (1 in. thick).

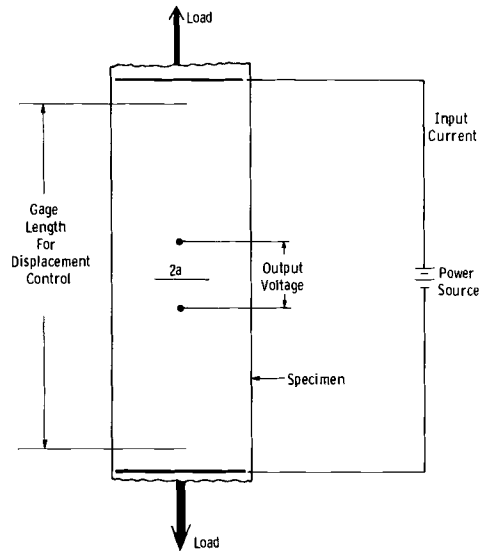


FIG. 6—Schematic showing displacement controlled loading and electrical potential crack monitoring system on a CCP specimen.

The initial tests were all conducted at a single displacement rate on a given specimen for the entire test. Displacement rates ranged from 0.00013 in./h (0.0033 mm/h) to 0.0153 in./h (0.39 mm/h) for the CCP specimens and from 0.0010 in./h (0.025 mm/h) to 0.0080 (0.20 mm/h) in./h for the 1T-CT specimens. Later tests were conducted using a rate cycling technique where three separate displacement rates were used in sequence on a single test. An example of this is shown in Fig. 7, where rates of 0.001, 0.002, and 0.004 in./h (0.025, 0.050, 0.10 mm/h) were used on a single CCP specimen. The rate cycling technique was used to try to get

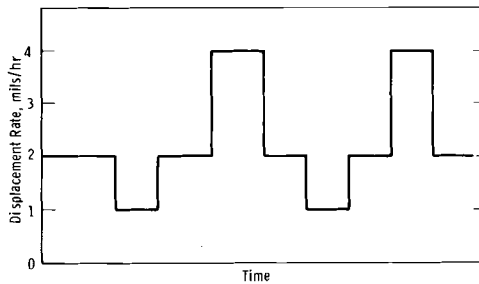


FIG. 7—Schematic of displacement rate cycling sequence.

enough data from a single specimen to complete the entire data reduction scheme.

## Results

### Data Reduction Scheme

Since the data reduction technique used for these tests was somewhat complex, an example of each step will be demonstrated for some of the data gathered on the CCP specimens. The schematic of the data reduction, Fig. 4, shows six different steps. These are illustrated by the actual data.

Step 1 in Fig. 4 shows load and crack length measured as a function of time. Step 1 represents the actual data collected during the test. Since the tests were conducted at a constant displacement rate, time and displacement are interchangeable independent variables. Load and crack length are the dependent variables. Two examples of the data collected are shown in Figs. 8 and 9. These data represent over an order of magnitude difference in displacement rate. Figure 8 shows data collected for a rate of 0.0010 in./h (0.025 mm/h), and Fig. 9 shows data for a rate of 0.0153 in./h (0.39 mm/h). These results show a pattern which was consistent for all CCP tests. The load increased initially with displacement and reached a maximum early in the test. Crack growth occurred just prior to the point of maximum load. Shortly after crack growth began, the curve of crack length versus time shows an almost constant rate of crack growth. This constant rate of crack growth is accompanied with a nearly constant rate of load decrease. Since the results considered in these tests were concerned with a secondary or steady-state creep phenomena, these

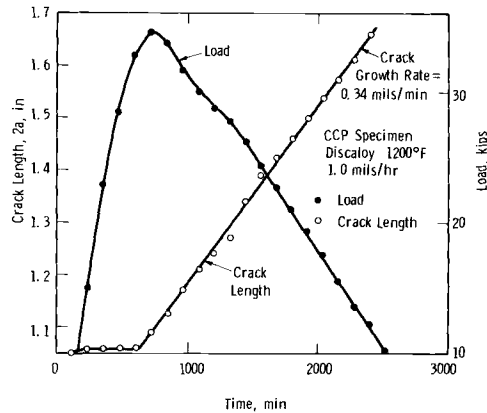


FIG. 8—Load and crack length versus time for discoloy at 1200°F (displacement rate = 1.0 mils/h).

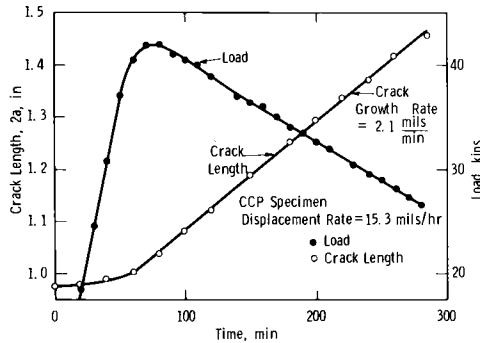


FIG. 9—Load and crack length versus time for discaloy at 1200°F (displacement rate = 15.3 mils/h).

constant rates were taken to imply a steady-state region of creep crack growth. Data were analyzed only after maximum load; all transient effects were ignored.

From the basic Step 1 data as represented in Figs. 8 and 9, two separate directions are taken in the data reduction scheme. They are the evaluation of  $C^*$ , Steps 2 through 4 in Fig. 4, and the calculation of crack growth rate, Step 5 in Fig. 4. As illustrated, the crack growth rate is constant for each CCP test and can be easily calculated and tabulated for each specimen. This, however, was not the case for the 1T-CT tests; crack growth rate had to be evaluated as a function of crack length as shown in Step 5.

The method for evaluating  $C^*$  is not as easy and is demonstrated using the type of data shown in Figs. 8 and 9. An intermediate plot was used in going from Steps 1 to 2. This was a plot of load versus crack length for each displacement rate, that is, each individual test, Fig. 10. This intermediate step was an aid in constructing the Step 2 plot of load versus displacement rate for differing crack lengths (crack length =  $2a$  for the CCP specimens), Fig. 11. The load versus displacement rate plot was used for determining the energy rate or power input,  $U^*$ .  $U^*$  was measured graphically by taking the area under the curve in Step 2, Fig. 11.  $U^*$  was then plotted versus crack length, Fig. 12; this is Step 3 in the data reduction scheme. The slope of the curves in Fig. 12 is then a measure of  $C^*$  per unit thickness. Taking the slopes of these curves and dividing by specimen thickness gives the final evaluation of  $C^*$ . This is shown in Fig. 13, Step 4, where  $C^*$  is plotted as a function of displacement rate. In the general case,  $C^*$  is a function of both displacement rate and crack length. However, for the CCP specimen tests conducted at constant displacement rates,  $C^*$  was independent of crack length as was crack growth rate.

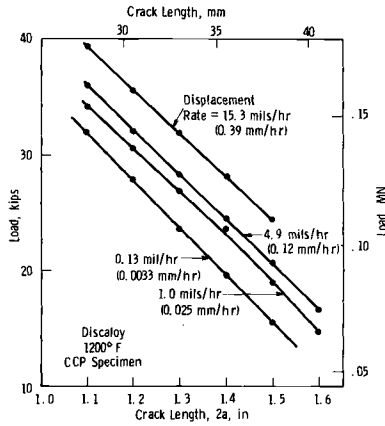


FIG. 10—Load versus crack length for various displacement rates (discaloy at 1200°F).

The final step leading to the desired result is the combination of Steps 4 and 5 to produce a plot of crack growth rate versus  $C^*$  Step 6.

*Crack Growth Rate Correlation*

Crack growth rate versus  $C^*$  is plotted on log-log scales for all of the CCP specimens where each specimen was tested at a single displacement rate, Fig. 14. This plot shows a nearly straight line correlation except for the test run at the slowest rate of 0.00013 in./h (0.0033 mm/h). Although the data reduction is somewhat complex, the final result illustrates a good correlation. In Fig. 14, each point represents a single specimen.

In an attempt to simplify the data collection, single specimens were run

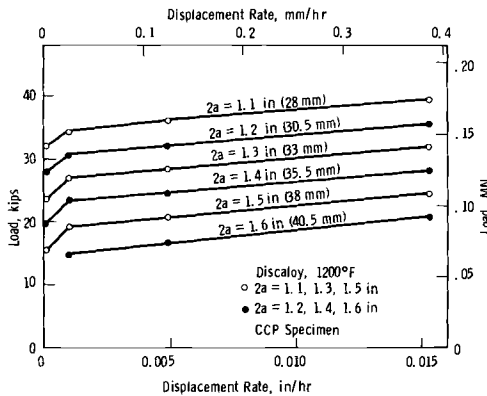


FIG. 11—Load versus displacement rate for various crack lengths.

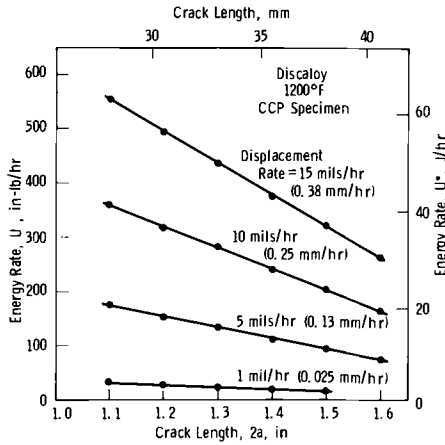


FIG. 12—Energy rate versus crack length for various displacement rates.

at multiple sequenced displacement rates, Fig. 7. A single test then provides enough data to complete the data reduction scheme for  $C^*$ . An example of the plot of load versus crack length (intermediate to Steps 1 and 2) is shown in Fig. 15. In this test, load and crack length were evaluated after steady-state conditions had been achieved following a displacement rate change. Following the data reduction scheme shown in Fig. 4, crack growth rate versus  $C^*$  could be evaluated for a single specimen. The values obtained by these tests are shown superimposed on the values obtained from single displacement rate tests, Fig. 16. These results show good agreement with the tests run at a single displacement rate.

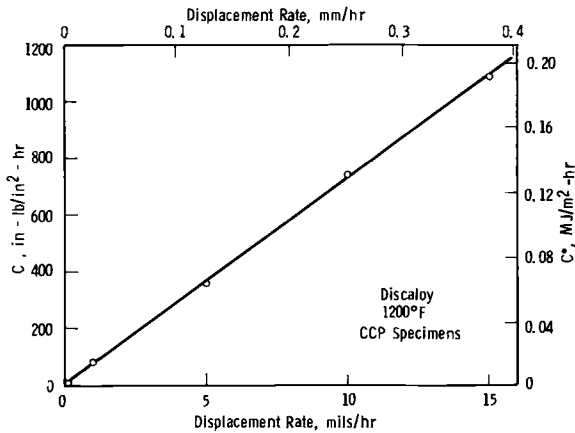


FIG. 13— $C^*$  versus displacement rate for discaloy at 1200°F.

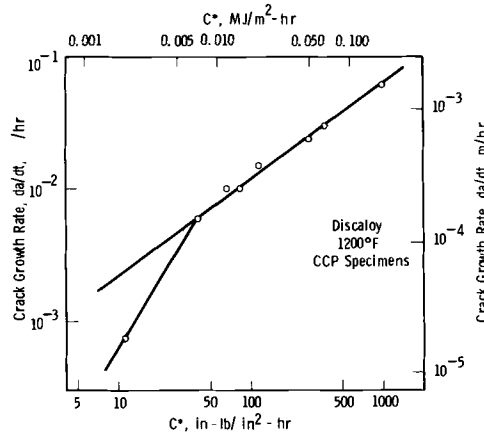


FIG. 14—Crack growth rate versus  $C^*$  for CCP specimens tested at constant displacement rates.

Tests were conducted on the 1T-CT specimen to demonstrate the effect of a radically different specimen geometry. The data reduction scheme was identical to that illustrated for the CCP specimens; however, crack growth rate and  $C^*$  were not constant for a single test conducted at a constant displacement rate. The results from the 1T-CT specimens are shown in Fig. 17. A compilation of all data collected for both specimen types is shown in Fig. 18.

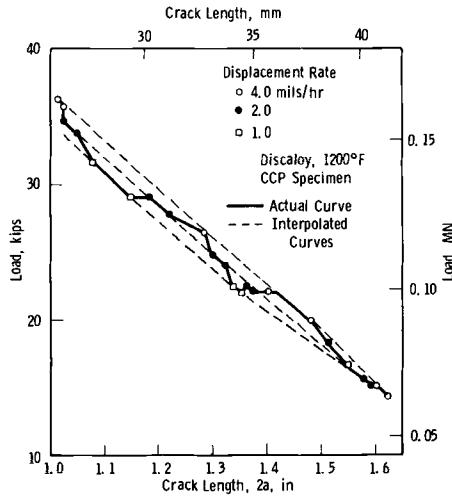


FIG. 15—Load versus crack length for a single CCP specimen tested at multiple displacement rates.

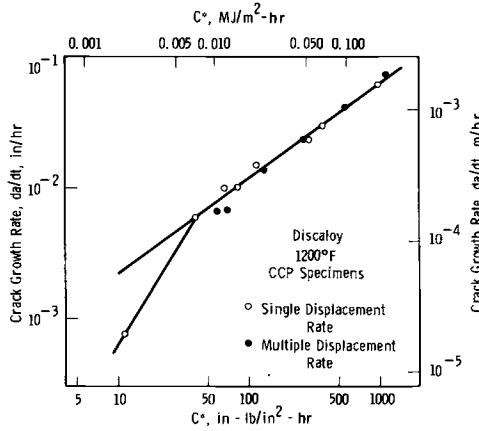


FIG. 16—Crack growth rate versus  $C^*$  for all CCP specimens.

To illustrate the success of  $C^*$  as a parameter in correlating creep crack growth rate other correlating parameters were considered. They are the stress intensity factor,  $K$ , and nominal stress.

Crack growth rate versus  $K$  is plotted in Fig. 19.  $K$  was evaluated from crack length and load using the calibration given elsewhere [7]. Crack growth rate versus nominal stress is plotted in Fig. 20. The nominal stress values,  $\sigma_n$ , used here were the net section stress on the uncracked ligament for the CCP specimen,

$$\sigma_n = \frac{P}{B(W - 2a)} \tag{11}$$

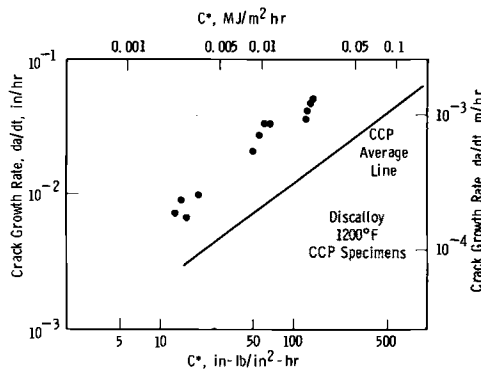


FIG. 17—Crack growth rate versus  $C^*$  for IT-CT specimens at a constant displacement rate.

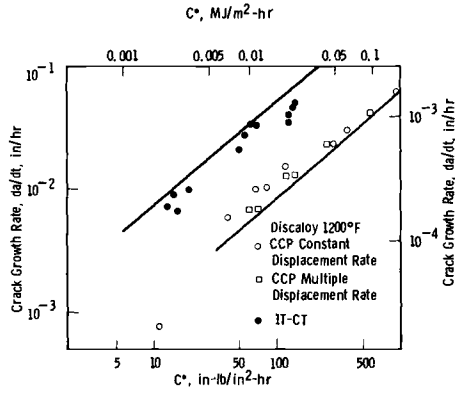


FIG. 18—Crack growth rate versus  $C^*$  for CCP and 1T-CT specimens.

where

- $B$  = specimen thickness,
- $W$  = specimen width, and,
- $2a$  = crack length.

For the 1T-CT specimen the nominal stress is a crack tip stress calculated from the combined tension and bending stresses

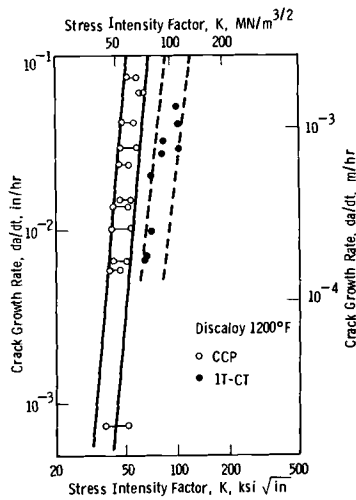


FIG. 19—Crack growth rate versus stress intensity factor.

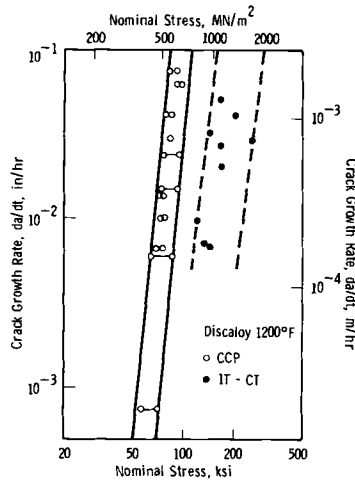


FIG. 20—Crack growth rate versus nominal stress.

$$\sigma_n = \frac{P}{B(W - a)} \left[ 1 + 3 \frac{W + a}{W - a} \right] \tag{12}$$

where  $a$  is the crack length.

**Discussion**

The results demonstrate the success with which the  $C^*$ -parameter can be used to correlate creep crack growth rate. Considering each specimen type separately, the scatter in growth rate for a given  $C^*$  is less than a factor of two. This is illustrated for the CCP specimen in Figs. 14 and 16 and for the 1T-CT specimen in Fig. 17. Combining the results from both specimens, Fig. 18 gives a scatter in growth rate of slightly greater than five for a given  $C^*$ .

Attempts to correlate growth rate using linear elastic parameters such as stress intensity factor,  $K$ , and nominal stress show results very similar to those of Siverns and Price [1]. For a consistent specimen type the scatterband on growth rate correlated with  $K$  is about a factor of 30, Fig. 19. However, comparing two radically different specimen types such as the CCP and 1T-CT geometries shows virtually no correlation of the growth rates. The range of  $K$  which produces a given growth rate on the CCP specimens is completely different from the range of  $K$  needed to produce the same order of magnitude growth rate on the 1T-CT specimen. The results from correlating growth rate with nominal stress show the same trend, Fig. 20. Given a consistent specimen type the correlation is fair; however, changing the specimen types gives virtually no consistent

correlation. Results from individual tests indicated this lack of correlation using  $K$  and nominal stress. For the CCP specimens growth rate was constant for the entire test, while  $K$  decreased with increasing crack length. For the 1T-CT specimens crack growth rate decreased with increasing crack length, while nominal stress increased. In contrast to this the evaluation of  $C^*$  showed a consistent trend. In the CCP specimens both  $C^*$  and growth rate were constant throughout the entire test for tests conducted at a single displacement rate. For the 1T-CT specimens  $C^*$  and growth rate both decreased with increasing crack length.

An important technique in a fracture mechanics approach is illustrated by these results. That is, in separating parameters which characterize the crack tip region from parameters which do not, radically different specimen types must be tested. The CCP specimen is loaded purely in tension, whereas the 1T-CT specimen is primarily a bend type specimen. While the growth rate correlation with  $C^*$  is extremely good for all of the CCP tests and is only fair for  $K$  and nominal stress, these tests alone would not establish  $C^*$  as a crack tip parameter. Using a CCP specimen geometry, growth rate could be correlated reasonably well with any parameter which increases as the loading on the crack increases. Gathering growth rate data on a specimen type which nearly modeled the application geometry might be successful with many parameters. However, if the geometry of the application were to differ slightly from the specimen geometry used, attempts to apply data in terms of the noncrack tip parameter might be seriously in error. Therefore, the establishment of a crack tip parameter such as  $C^*$  can be extremely valuable for application to structural components. Testing can be performed on conveniently designed specimens, and the resulting data can be applied to a multitude of structural geometries.

The data gathered by Siverns and Price [1] cover five orders of magnitude in growth rate and are very impressive from this standpoint. Results reported here cover only slightly more than two orders of magnitude. These tests were conducted so that the correlation could be studied in a reasonable amount of time; the longest test time was in the order of one month. However, for structural application, the slower growth rates would be of most interest. The data shown in Fig. 14 show almost a straight line correlation with the exception of the slowest test which lies significantly below the line through the other test results. This raises an important question of how the  $C^*$  correlation will extrapolate to the slower growth rates. Although the results from one test are not conclusive, it appears that there may be a radical change in the slope of the correlation line for slower rates. This is similar to the results of fatigue crack growth rate correlated with  $\Delta K$  where the radical change in slope for slower growth rates leads to a threshold value of  $\Delta K$  below which cracks do not propagate in fatigue [8]. If a similar trend is followed by creep crack growth, perhaps a similar threshold  $C^*$  could be postulated.

The establishment of such a threshold parameter would be extremely valuable for applications. Future testing will concentrate in this area; however, the establishment of a  $C^*$  threshold may possibly require testing times in the order of several years.

An important criticism of the study of macroscopic creep crack growth is that creep damage does not often occur by the propagation of a single macroscopic crack. Rather creep damage occurs as voids, and micro-cracks develop somewhat homogeneously throughout the specimen. Some materials such as discaloy are known to develop single cracks; however, such materials seem to be in a minority. Most of these observations have resulted from tests on uniform specimens loaded in uniaxial tension. Some other observations have shown that nearly any material can develop a predominant macroscopicly propagating crack under special geometry and stress conditions. [9]. Such conditions are either a region of high stress concentration or a predominantly bend type of loading where the highest stresses are concentrated in a small area. Under these conditions, cracking is localized, and the result is a single predominant macroscopic crack. In structural applications, it is often these regions of high-stress concentration that are of most concern rather than regions of uniform stress. Therefore, the study of creep behavior in terms of single propagating crack is important.

An important part of the study of material behavior is the anticipated subsequent application to structural components. An approach that cannot be applied to structures may be of some value in material evaluation and selection; however, this approach will ultimately be abandoned in favor of an approach which has a direct application. In concept  $C^*$ -parameter is a very good prospect for application to structures. Since it represents a parameter which characterizes the crack tip region, results from a single specimen geometry can be applied to a multitude of structural geometries. The problem of calculating  $C^*$  for a crack in a structure is in practice somewhat complicated. If the material can be characterized in terms of Eq 4, where strain rate is measured as a nonlinear function of stress,  $C^*$  could be calculated using the line integral definition given in Eq 1. This calculation would require a numerical analysis such as the finite element approach. A similar approach has been used to calculate the J-integral for the nonlinear stress-strain behavior encountered in plasticity considerations [10]. If the material properties represented in Eq 4 were known, this same approach could be used to calculate the  $C^*$  for a crack in a structure.

## Conclusions

1. A fracture mechanics approach is used to correlate creep crack growth behavior. The  $C^*$ -parameter which is an energy rate line integral is shown to characterize the crack tip stress and strain rate field.

2. The  $C^*$ -parameter can successfully correlate creep crack growth rates for a discalloy superalloy tested at 1200°F (920 K).

3. The stress intensity factor,  $K$ , and nominal stress do not adequately characterize crack growth rates. This is demonstrated by considering two radically different specimen geometries, the center cracked panel and the compact specimen.  $C^*$  correlates creep crack growth rates for these geometries, while  $K$  and nominal stress show no correlation.

4.  $C^*$  can be used as a parameter to predict crack growth rate for structural applications.

### Acknowledgments

The authors are indebted to their colleagues at the Research Laboratories who contributed to various aspects of this program. Particular appreciation is expressed to F. X. Gradich who conducted most of the testing in this program and to E. F. Vandergrift who helped with the design and evaluation of experiments. W. H. Pryle helped with the material handling and specimen machining. L. J. Ceschini and R. T. Blackham also helped with various phases of this program.

This work was supported by the Gas Turbine Systems Division.

### References

- [1] Siverns, M. J. and Price, A. T., *International Journal of Fracture*, Vol. 9, No. 2, June 1973.
- [2] Rice, J. R., private communication, 1972.
- [3] Goldman, N. L. and Hutchinson, J. W., "Fully Plastic Crack Problems: The Center-Cracked Strip Under Plane Strain," Harvard University, Cambridge, Mass., 1973.
- [4] Hutchinson, J. W., *Journal of the Mechanics and Physics of Solids*, Vol. 16, No. 5, 1968, pp. 337-347.
- [5] Rice, J. R., *Journal of Applied Mechanics, Transactions, American Society of Mechanical Engineers*, Vol. 35, June 1968, pp. 379-386.
- [6] Begley, J. A. and Landes, J. D. in *Fracture Toughness, Proceedings of the 1971 National Symposium on Fracture Mechanics, Part II, ASTM STP 514*, American Society for Testing Materials, 1972, pp. 1-20.
- [7] Brown, W. F., Jr. and Srawley, J. E., *Plane Strain Crack Toughness Testing of High Strength Metallic Materials, ASTM STP 410*, American Society for Testing and Materials, 1966.
- [8] Paris, P. C., "Testing for Very Slow Growth of Fatigue Cracks," *Closed Loop Magazine*, MTS Systems Corporation, Vol. 2, No. 5, 1970.
- [9] Begley, J. A., unpublished results.
- [10] Hayes, D. J., "Some Applications of Elastic-Plastic Analysis of Fracture Mechanics," doctoral dissertation, Department of Mechanical Engineering, Imperial College, University of London, London, Oct. 1970.
- [11] Moon, D. M. and Beck, C. G., unpublished results.

*J. G. Kaufman,<sup>1</sup> K. O. Bogardus,<sup>1</sup> D. A. Mauney,<sup>1</sup> and R. C. Malcolm<sup>1</sup>*

## Creep Cracking in 2219-T851 Plate at Elevated Temperatures

---

**REFERENCE:** Kaufman, J. G., Bogardus, K. O., Mauney, D. A., and Malcolm, R. C., "Creep Cracking in 2219-T851 Plate at Elevated Temperatures," *Mechanics of Crack Growth, ASTM STP 590*, American Society for Testing and Materials, 1976, pp. 149-168.

**ABSTRACT:** The susceptibility of 2219 to time-dependent (creep) crack growth under sustained load has been evaluated, and, while no crack growth was observed at room temperature, it was observed at elevated temperatures at stress intensities ( $K_{Icc}$ ) well below  $K_{Ic}$ . It appears that creep cracking will take place at stress intensities down to a threshold, designated  $K_{Icc,t}$ , about 40 percent of  $K_{Ic}$  at 300°F, and preliminary check tests suggest that similar behavior would be in evidence at 212 and 350°F in both the L-T and T-L orientations, though much work remains to be done in defining the extent of the temperature dependence. The rate of crack growth is controlled primarily by the instantaneous stress intensity factor and can be described by the following relationship:  $\log da/dt = 0.085K - 4.14$ .

**KEY WORDS:** crack propagation, mechanical properties, deformation, creep tests, fracture strength, stress analysis

In 1968, Kaufman and Holt [1]<sup>2</sup> reported on their findings of time-dependent crack growth in 2219-T851 plate at elevated temperatures. In that work, the notch-stress rupture strength decreased significantly below the smooth-specimen stress rupture strength with increase in rupture time at temperatures in the range from 300 to 500°F, as illustrated by the representative data in Fig. 1. Examination of the fractured specimens revealed that the reduction in stress rupture life was associated with a concentration of intergranular crack growth from the root of the notch;

<sup>1</sup>Manager, Engineering Properties and Test Division, senior engineer, group leader, and technician, respectively, Alcoa Laboratories, Aluminum Company of America, Alcoa Center, Pa. 15069.

<sup>2</sup>The italic numbers in brackets refer to the list of references appended to this paper.

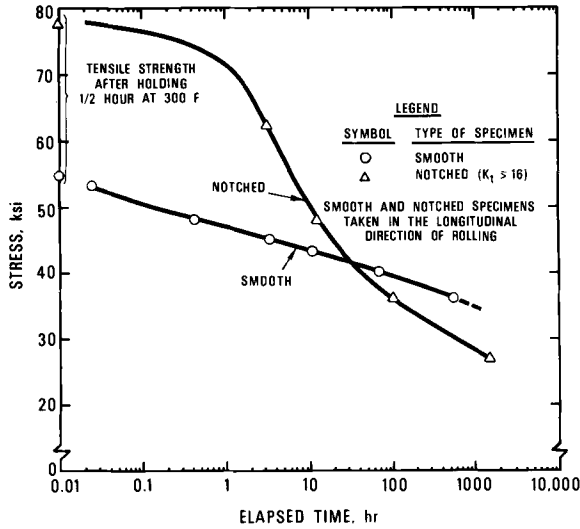


FIG. 1—Effects of notches on stress-rupture strengths of 2219-T851 (1-in.) at 300 °F.

the same cracking was found to be well distributed in smooth specimens. As a result of those findings, a program was begun to investigate the significance of this phenomenon on the service ability of this alloy utilizing fracture-mechanics concepts.

In the intervening years, starting with the work of Lindborg on an austenitic steel [2], time-dependent creep crack growth has been reported by others [2-9]. In 1970, Siverns and Price [5] noted that crack growth rates ( $da/dt$ ) could be expressed simply in terms of stress intensity factor ( $K$ ) in the form

$$da/dt = \text{constant } K^n \tag{1}$$

and data developed by some other investigators have supported this general trend [2,7]. Landes and Wei [6,9] developed a model for creep crack growth rate based on their work on 4340; the steady-state crack growth rate was related to the steady-state creep rate in smooth specimens, both being controlled by the time-dependent deformation process occurring at the crack tip. They also noted the presence of the three stages of creep in both types of behavior. In the first reported work on aluminum, Kenyon et al [7] showed the rate process dependency of creep crack growth in aluminum alloy RR58, equivalent to 2618, and proposed the relationship

$$da/dt = A K^n e^{-Q/RT} \tag{2}$$

In the present work we have evaluated the resistance of 2219-T851 to creep growth to establish the relationship between the notch stress rupture behavior observed previously and the creep crack growth properties of this material, and evaluated this behavior in light of the relationship shown in Eq 1.

### Object

The object of this investigation was to determine the rate at which cracks in 2219-T851 plate grow during exposure to sustained loads at elevated temperatures in the range from 212 to 350°F.

### Material

A single lot of 3-in.-thick 2219-T851 plate was used for this investigation. The chemical composition is shown in Table 1 along with the tensile properties at room temperature and at temperatures as high as 350°F, after 1/2 and 100-h holding periods at these elevated temperatures. These strengths are in good agreement with the typical tensile and yield strengths for 2219-T851 plate which are presented in Fig. 2. It is apparent from the curves of Fig. 2 that, in the temperature range up to 300°F, where most tests were made in this investigation, there is little effect of time at temperature on tensile strength and yield strength.

The plane-strain fracture toughness,  $K_{Ic}$  of this material, determined in accordance with ASTM Test for Plane-Strain Fracture Toughness of Metallic Materials (E 399-72) 2-in.-thick specimens of the type shown in Fig. 3, under the time-temperature exposures contemplated for the sustained-load tests, are plotted as a function of temperature in Fig. 4. It is evident that the plane-strain fracture toughness of this material is also essentially independent of time and temperature over most of the range studied. For longer times at 350°F there is some indication that  $K_{Ic}$  is increasing with exposure time, as would be anticipated because of the increased ductility associated with substantial overaging.

### Procedure

Plane-strain fracture toughness specimens of the type shown in Fig. 3 were exposed to sustained loads in Satec Model D creep machines. The specimens were enclosed in a quartz lamp oven built especially for this purpose; the temperature of each specimen was monitored continuously with a fully embedded thermocouple near the center of the thickness of each specimen just below the region of the crack. A strain-transfer device was attached to the faces of the compact tension specimen above and below the notch slot; differential transformers outside the furnace on the opposite end of the strain-transfer device were used to continuously record crack opening displacement as a function of time. Crack opening displacements (COD) were converted to crack lengths with calibration

TABLE 1—2219-T851 plate, 3-in.-thick.

| Chemical Composition, % |      |      |      |      |      |      |      |      |      |      |      |
|-------------------------|------|------|------|------|------|------|------|------|------|------|------|
|                         | Si   | Fe   | Cu   | Mn   | Mg   | Cr   | Ni   | Zn   | Ti   | V    | Zr   |
| Actual                  | 0.09 | 0.21 | 5.90 | 0.28 | 0.01 | 0.01 | 0.01 | 0.04 | 0.07 | 0.11 | 0.15 |
| Nominal <sup>a</sup>    | ...  | ...  | 6.3  | 0.30 | ...  | ...  | ...  | ...  | 0.06 | 0.10 | 0.18 |
| Limits <sup>a</sup>     | {    | min  | 5.8  | 0.20 | ...  | ...  | ...  | ...  | 0.02 | 0.05 | 0.10 |
|                         |      | max  | 6.8  | 0.40 | ...  | ...  | ...  | 0.10 | 0.10 | 0.15 | 0.25 |

| Tensile Properties<br>(Long Transverse Direction) |                        |                       |                     |                     |  |
|---|------------------------|-----------------------|---------------------|---------------------|--|
| Testing Temperature, °F                           | Time at Temperature, h | Tensile Strength, ksi | Yield Strength, ksi | Elongation in 4D, % |  |
| Room  | ...                    | 65.7                  | 49.6                | 9.8                 |  |
|   | 0.5                    | 59.4                  | 46.9                | 12.5                |  |
| 300   | 100                    | 59.3                  | 46.4                | 12.5                |  |
|   | 0.5                    | 52.7                  | 42.7                | 14.5                |  |
| 350   | 100                    | 56.2                  | 43.3                | 13.5                |  |
|   | 0.5                    | 47.2                  | 39.7                | 16.0                |  |
|   | 100                    | 46.7                  | 38.6                | 15.0                |  |

<sup>a</sup> Aluminum Standards and Data, The Aluminum Association, 1972-1973.

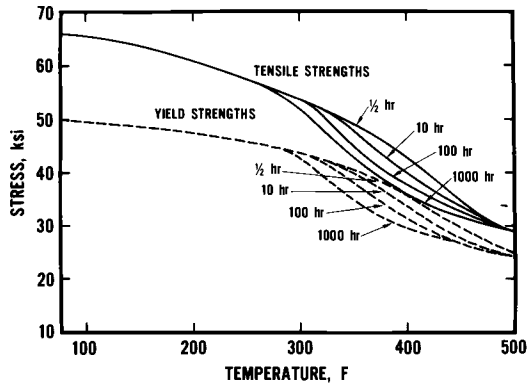


FIG. 2—Effect of time at temperature on tensile strength and yield strength of 2219-T851 plate.

curves, determined at each test temperature for the specimen and the strain-transfer system by gradually applying various loads to a calibration specimen in which various crack lengths had been simulated using a fine saw cut.

Prior to sustained loading of the specimens, each was precracked by fatigue loading as required for plane-strain fracture toughness testing in ASTM Method E 399-72. This was done in Krouse axial-stress fatigue machines, and the final stages of crack growth were carried out at a stress intensity of about  $12 \text{ ksi}\sqrt{\text{in.}}$  (38 percent of  $K_{Ic}$ ).

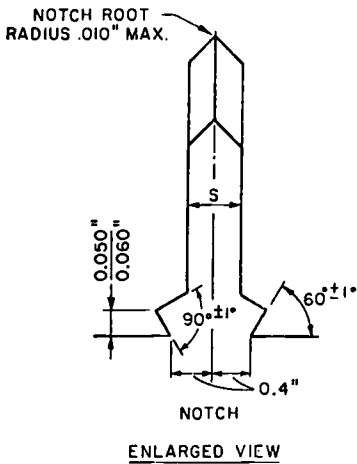
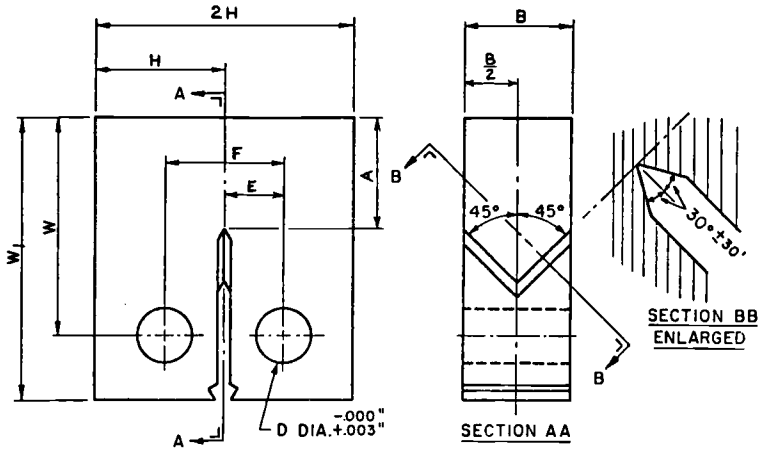
In initiating each test, the specimen was heated to the desired temperature, allowed to stabilize for 1/2 h, and the desired load was applied.

Tests were made at a variety of stress intensity levels at 300°F using T-L (long-transverse) specimens and a single test was made at 300°F with an L-T (longitudinal) specimen to check the influence of specimen orientation. Tests were also made at room temperature, 212 and 350°F to compare the general behavior at these temperatures.

Once the COD data had been obtained and converted to crack length as a function of elapsed time, the data were computer analyzed to calculate and plot (a) rate of crack growth,  $da/dt$ , as a function of elapsed time; (b) change in stress intensity as a function of elapsed time; and (c) rate of crack growth,  $da/dt$ , as a function of the instantaneous stress intensity level. In all calculations the relationship for plane-strain stress intensity factor given in ASTM Method E 399-72 was used.

## Results

Applied  $K_I$  versus time to fracture in all tests is presented in Fig. 5; the corresponding values of  $K_I$  at fracture are plotted in Fig. 6. The COD



| PROPORTIONS            | DIMENSIONS, IN. |
|------------------------|-----------------|
| $B = \text{THICKNESS}$ | 2.00            |
| $A = 1.1B$             | 2.20            |
| $W = 2B; W_1 = 2.5B$   | 4.000-5.000     |
| $S = 0.1B$             | 1/4             |
| $F = 2E = 1.10B$       | 2.20            |
| $H = 1.2B$             | 2.400           |
| $D = 0.5B$             | 1.000           |

FIG. 3—Compact fracture toughness specimen.

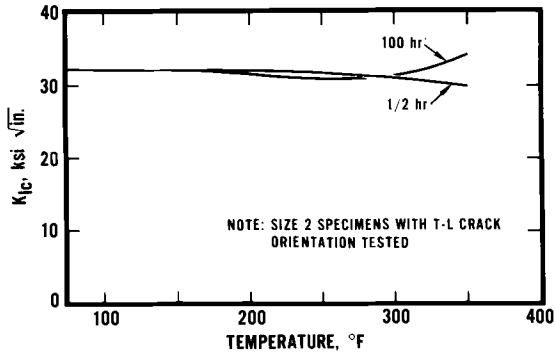


FIG. 4— $K_{Ic}$  versus temperature for 2219-T851 plate (3-in-thick).

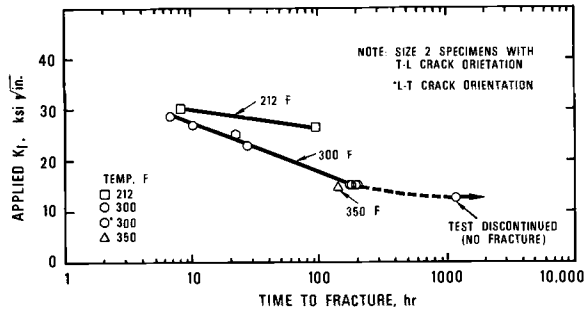


FIG. 5—Applied  $K_I$  versus time to fracture for 2219-T851 plate (3-in-thick) at elevated temperatures.

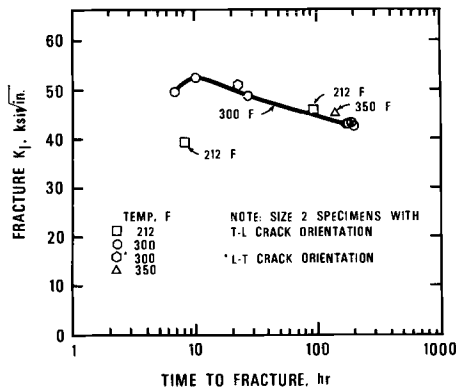


FIG. 6—Fracture  $K_I$  versus time to fracture for 2219-T851 plate (3-in-thick) at elevated temperatures.

data from the tests at 300°F are presented in Fig. 7, and the derived curves showing crack length as a function of elapsed time are presented in Fig. 8. Computer printouts of  $da/dt$  and the instantaneous stress intensity factor as a function of time are shown in Figs. 9 and 10, respectively, and the computer printout of  $da/dt$  as a function of instantaneous stress intensity factor is shown in Fig. 11. Macro- and micrographs of fracture surfaces are shown in Figs. 12 through 19.

### Discussion of Results

The data in Figs. 5 through 11 illustrate that at elevated temperatures a substantial amount of crack growth takes place in 2219-T851 plate at stress intensities considerably below  $K_{Ic}$ . At a stress intensity of 74 percent complete fracture occurs in 27 h. Even at 49 percent  $K_{Ic}$ , only about 190 h are required for complete fracture.

The times to fracture for T-L specimens at 300°F (Fig. 5) are nearly linear on a semilog plot to about 200 h. A single test at about 12  $\text{ksi}\sqrt{\text{in.}}$  or 40 percent  $K_{Ic}$  was carried far enough (about 1200 h) to indicate that the linear trend does not continue and there is an indication of a threshold for crack growth (designated ( $K_{Icct}$ ) in the vicinity of about 12  $\text{ksi}\sqrt{\text{in.}}$ . While the apparent "threshold" corresponds approximately to the stress intensity level at which the specimens were precracked, it is not believed that the two are related, though it is recognized that there is a need for experimental verification of this point.

The relationship between applied stress intensity and time to fracture seems to be essentially independent of specimen orientation (L-T versus T-L) at 300°F, and nearly identical at 300 and 350°F for T-L specimens. At

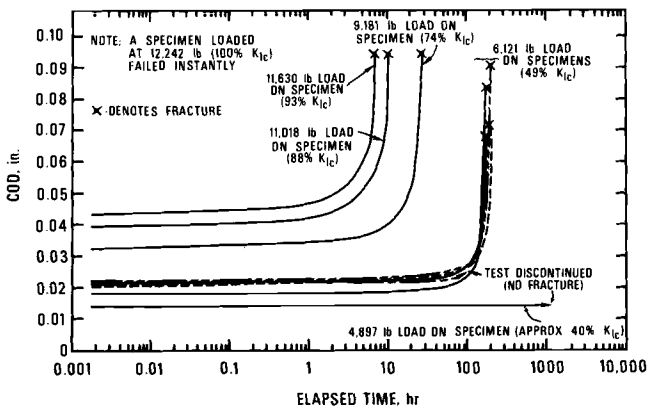


FIG. 7—Displacement data from tests (T-L crack orientation) of 2219-T851 plate (3-in-thick) at 300°F.

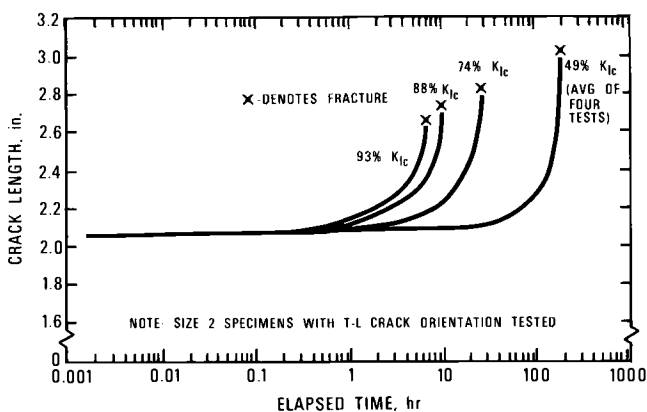


FIG. 8—Crack length versus time for 2219-T851 plate (3-in-thick) at 300°F.

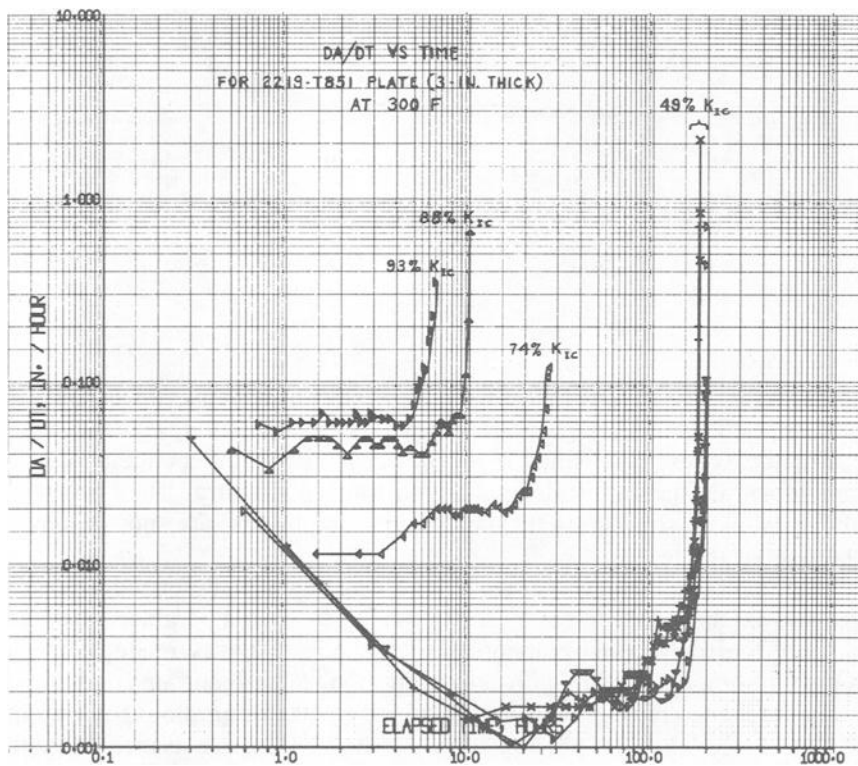


FIG. 9—da/dt versus time for 2219-T851 plate (3-in-thick) at 300°F.

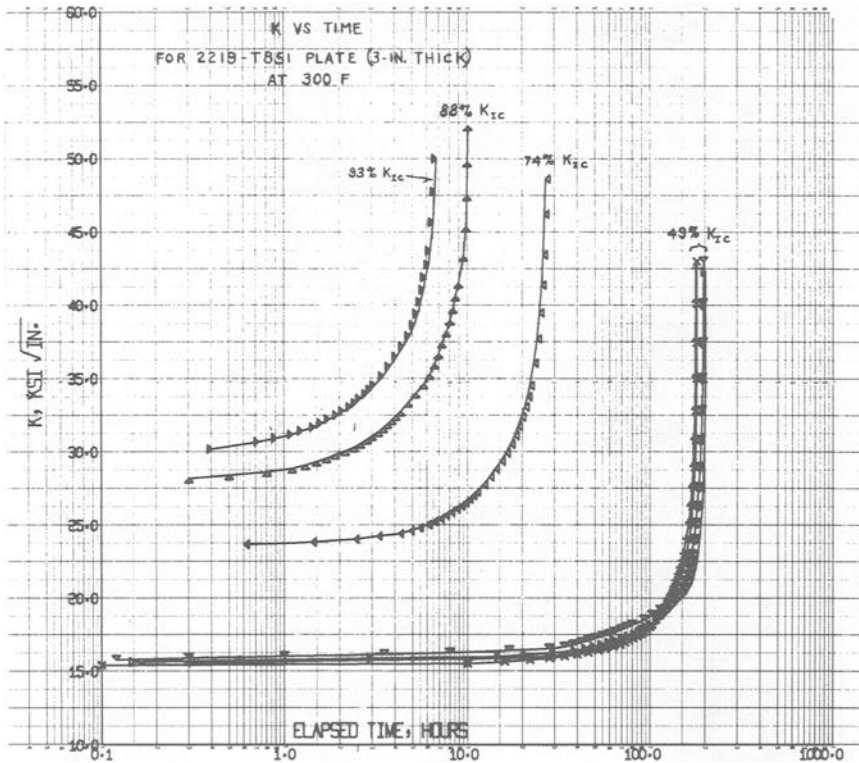


FIG. 10— $K$  versus time for 2219-T851 plate (3-in-thick) at 300°F.

212°F, indicating that the behavior is temperature dependent. A need for further study of this temperature dependence is indicated.

Fracture stress intensities (Fig. 6), seem nearly independent of test conditions and generally decrease with time to fracture. They are well above  $K_{Ic}$ , illustrating that plane-strain conditions are not retained throughout the test.

It should be noted at this stage that no significant time-dependent crack growth has been observed in 2219-T851 at room temperature, even in severely corrosive environments [1]. A check test was made at room temperature as part of this investigation, and, in ambient air conditions, no appreciable crack growth was obtained in 1000 h at about 95 percent  $K_{Ic}$ . It is clear that the phenomena described herein are associated with moderately high temperatures; it is assumed to be related primarily to creep deformations because of the absence of environments that result in

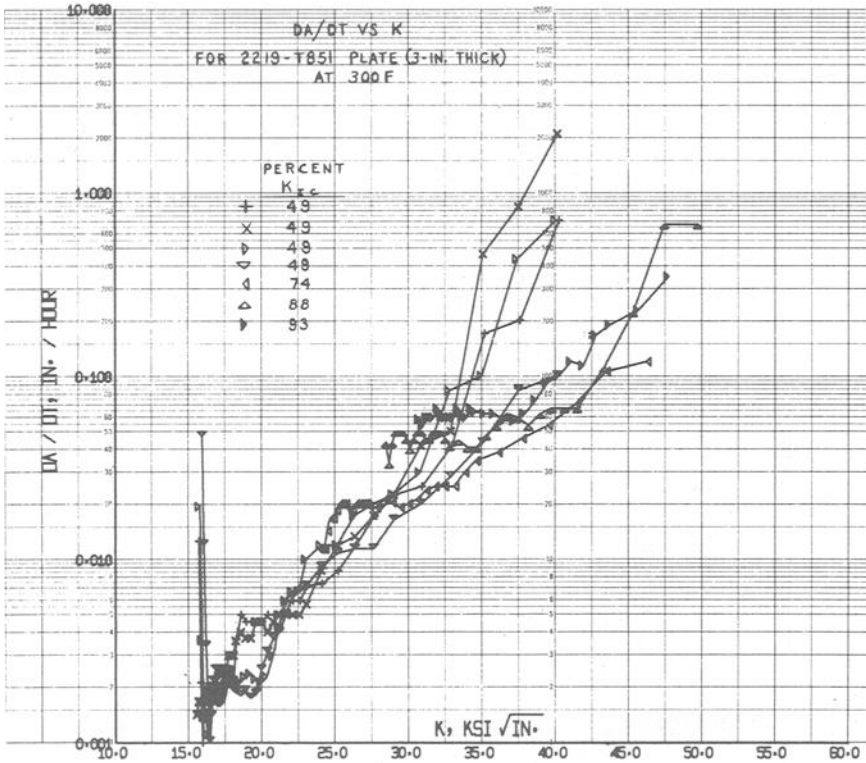


FIG. 11—da/dt versus K for 2219-T851 plate (3-in-thick) at 300°F.

stress corrosion cracks of 2219-T851, but additional verification is also needed on this point.

With the use of the calibration relationships, the crack growth data in Fig. 8 were derived from the COD data in Fig. 7. These crack length versus time curves serve as a basis for development of the curves of Figs. 9, 10, and 11.

From the data in Figs. 8 and 9, it is clear that the general trend is for the rate of crack growth to increase with time during the test. However in most tests, and particularly those at the lower  $K_I$  level, there was an apparent decrease in crack growth rate during the early part of the tests. This initial decrease is believed to be associated with the decreasing creep rate during the primary stage of creep in smooth specimens, that is, the re-initiation of crack growth in the material in the crack-tip plastic zone upon loading. Thus, it is possible that little or no crack extension occurred



FIG. 12—Fracture surface of  $K_{Icc}$  fracture in 2219-T851 plate at 300°F.

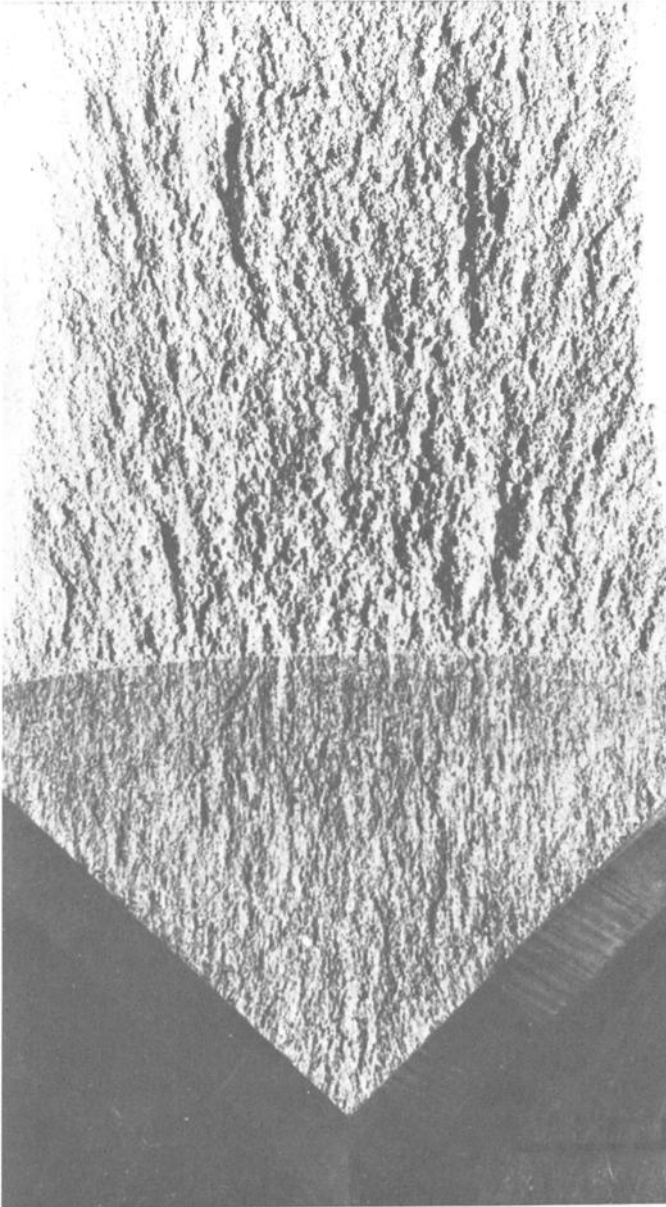


FIG. 13—Fracture surface of  $K_{Ic}$  fracture in 2219-T851 plate at 300°F.

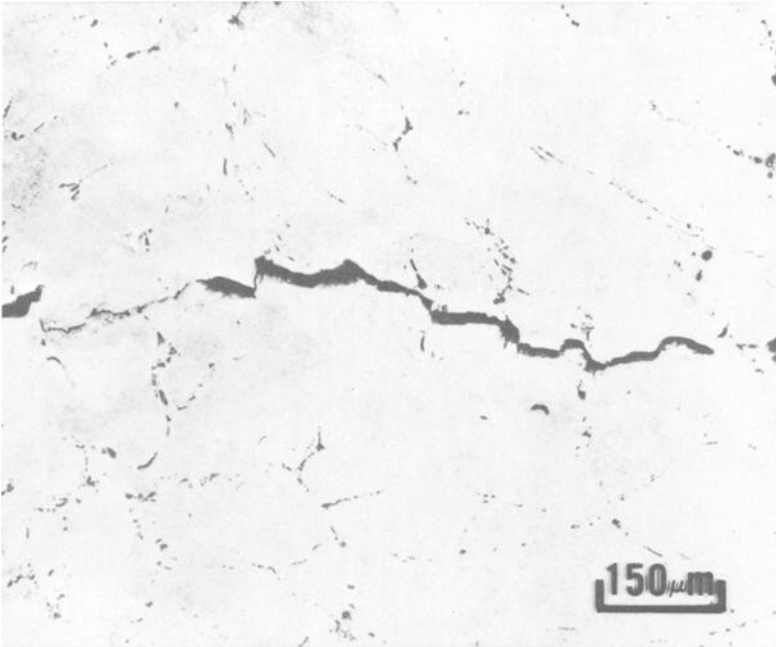


FIG. 14—Crack tip profile of a  $K_{Icc}$  fracture in 2219-T851 plate at 300°F.

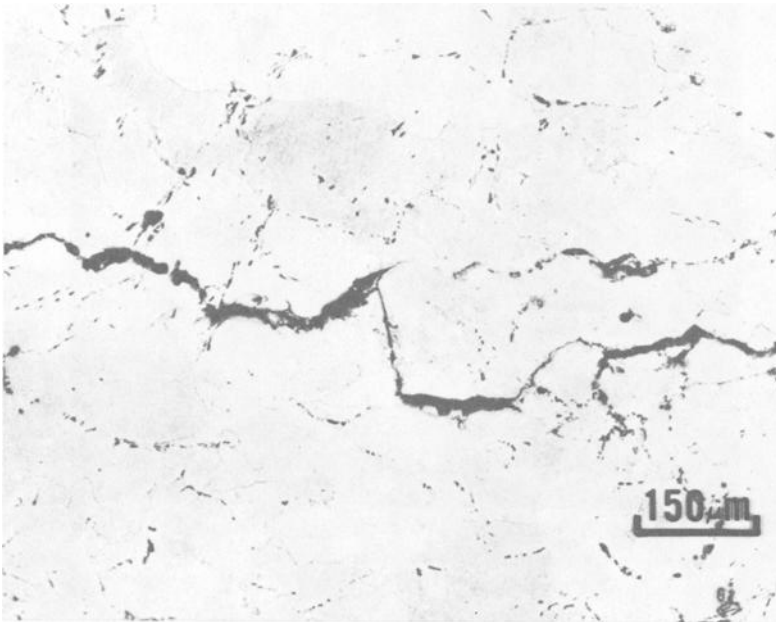


FIG. 15—Crack profile of a  $K_{Icc}$  fracture in 2219-T851 plate at 300°F.

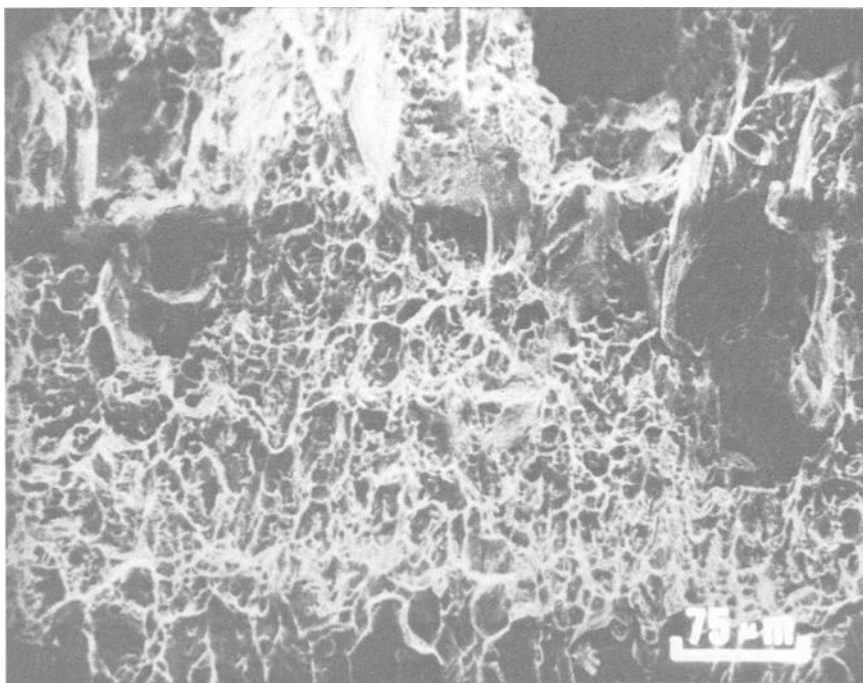


FIG. 16—Initial  $K_{Ic}$  fracture in 2219-T851 plate at 300°F.

during this part of the test; the increase in COD measurements might reflect only local creep strain. As the test progresses, however, the creep cracking phenomenon clearly prevails.

The curves of Fig. 10 indicate that the instantaneous stress intensity factor continues to increase during the test, and fracture takes place at stress intensities well above the plane-strain fracture toughness of the material, as noted earlier. This observation is consistent with the presence of the large shear lips as shown in Fig. 12, and it is clear that final fracture is of a mixed mode, not in plane strain. The rate at which crack growth takes place appears directly related to the instantaneous stress intensity factor (Fig. 11) with two notable deviations: (1) spikes at low stress intensity levels, believed to be associated with the primary-creep-type behavior just described, and (2) divergence of data at the upper (tertiary stage) end of the range, when the stress intensity factor increases above the plane-strain fracture toughness (around  $32 \text{ ksi}\sqrt{\text{in.}}$ ), a range associated with mixed mode crack growth and fracture.

The steady-state crack growth rate  $da/dt$  in Fig. 11 can be expressed in terms of  $K$  rather well by the expression

$$\log da/dt = 0.85K - 4.14$$

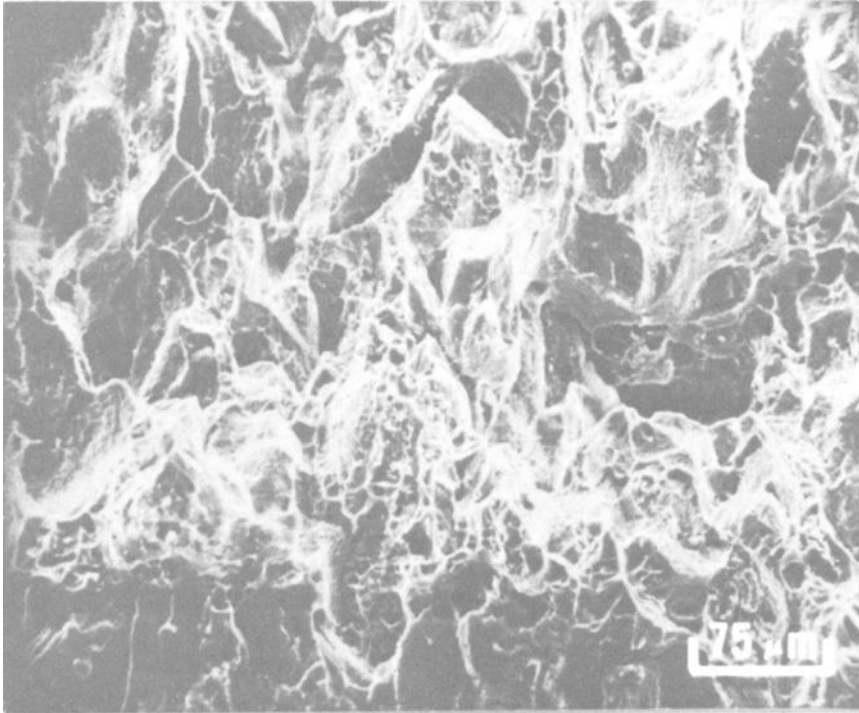


FIG. 17— $K_{Icc}$  fracture in 2219-T851 plate at 300°F.

This differs in form from that presented by Siverns and Price, but the data are better represented thus than as a linear log-log relationship. Additional work with other sizes and types of specimens is required to establish with certainty the generality of the stress intensity dependence, and whether or not it is superior to the suggested dependence on the net section stress, as proposed by Harrison and Sandor [11], or the J-integral, as suggested by Landes and Begley.<sup>3</sup>

The fracture face of Fig. 12 shows the continuous growth of shear lips all the way along the fracture, not unlike that in the  $K_{Ic}$  specimen in Fig. 13. However, it is evident in the  $K_{Icc}$  fracture that there is a time-dependent region of crack growth which shows up somewhat lighter than the rest; this is taken to be the extent of creep crack growth during the life of the specimen. Crack profiles are shown in Figs. 14 and 15 and suggest that the fracture is neither wholly transgranular or intergranular; there is a suggestion, yet to be verified by a significant number

<sup>3</sup>See pp. 128–148.

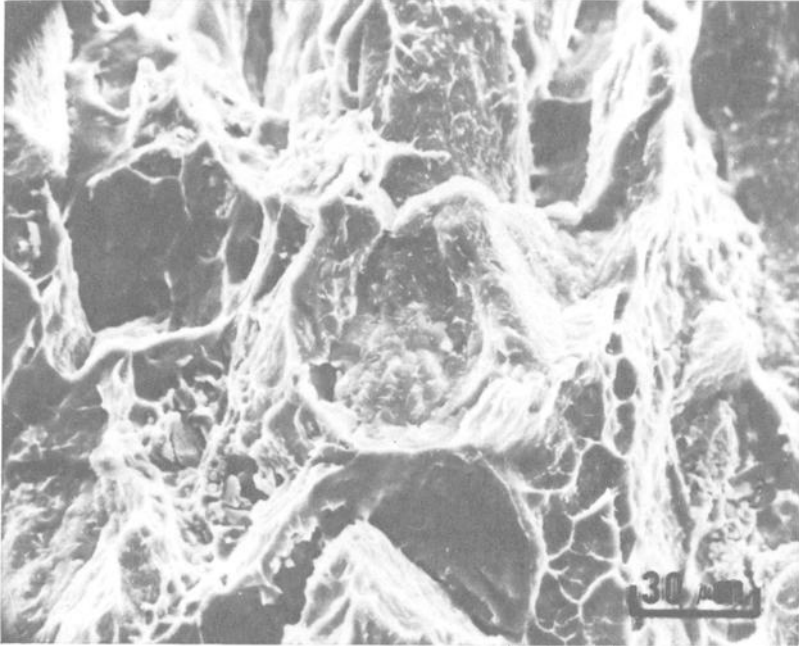


FIG. 18—Low ductility facet of a  $K_{Icc}$  fracture in 2219-T851 plate at 300°F.

of observations, that the cracking is following lined-up constituent. There is no evidence of stress-corrosion cracking, as typified by the branching type of cracking seen in those alloys, orientations, and environments, where stress corrosion cracking is observed in aluminum alloys. Scanning electron microscope photographs in Figs. 16 and 17 demonstrate that the  $K_{Icc}$  type of fracture has fewer small dimples than the  $K_{Ic}$  fracture and a number of flat facets which do not show up in the  $K_{Ic}$  fracture. One of these is shown at progressively higher magnifications in Figs. 18 and 19. Intermetallic particles appear on the surface of these flat facets, again presumably associated with the regions of lined-up constituents. While this would suggest that higher purity alloys would be less susceptible to creep cracking, preliminary work on such alloys does not support this expectation.

### Summary

The susceptibility of 2219 to time-dependent crack growth under sustained load has been evaluated, and, while no crack growth was observed at room temperature, it was observed at elevated temperatures at stress intensities ( $K_{Icc}$ ) well below  $K_{Ic}$ . The crack growth was substantially different in nature from stress-corrosion crack growth observed for

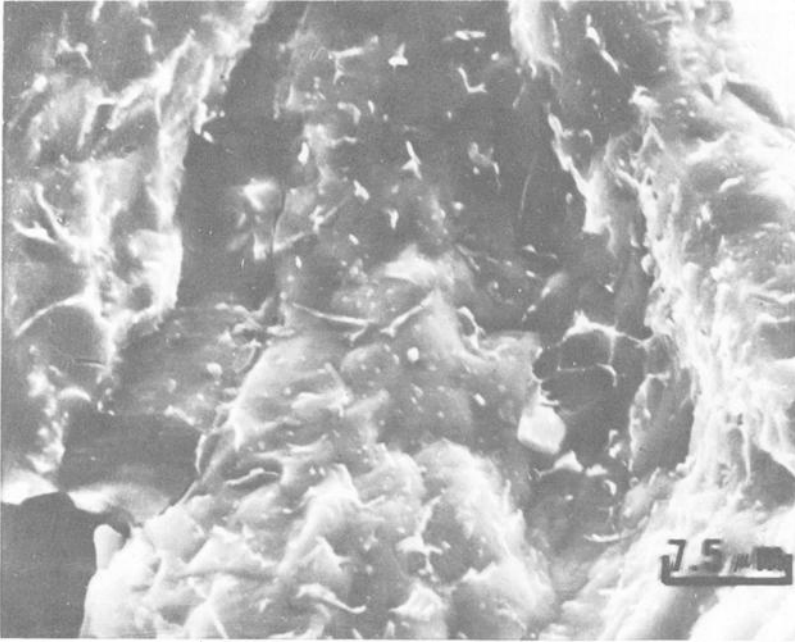


FIG. 19—Detail of low ductility facet of a  $K_{Icc}$  fracture in 2219-T851 plate at 300°F.

some alloys in certain environments (2219-T851 is resistant to stress-corrosion cracking in all known environments) and is believed to be essentially a creep phenomenon; it is recognized that tests in a vacuum or inert gas will be required to prove this beyond any doubt. It appears that crack growth will take place at stress intensities down to a threshold, designated  $K_{Icc}$ , of about 40 percent of  $K_{Ic}$  at 300°F, and preliminary tests suggest that similar behavior would be in evidence at 212 and 350°F in both the L-T and T-L orientations, though much work remains to be done in defining the extent of the temperature dependence. The rate of crack growth is controlled primarily by the instantaneous stress intensity factor and can be described by the following relationship

$$\log da/dt = 0.85K - 4.14 \quad (3)$$

This behavior has significance in service applications at elevated temperatures, as shown in Fig. 20, where the combinations of gross-section stress and crack size which would be expected to cause problems in 2219-T851 at 300°F are shown. The normal level for anticipation of problems with a material which is not susceptible to stress-corrosion

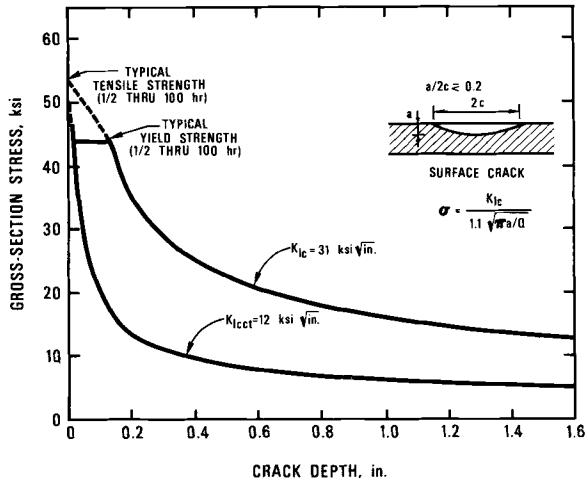


FIG. 20—Critical crack sizes for 2219-T851 plate at 300°F.

cracking and not subject to fatigue loading would be that associated with the  $K_{Ic}$  level. However, the tests described herein show that crack growth will initiate at stress intensities anywhere above about  $12 \text{ ksi}\sqrt{\text{in.}}$ , so that the  $K_{Icct}$  curve, not the  $K_{Ic}$  curve, is the design curve of concern. In any application in which 2219 is exposed to stress intensities above  $12 \text{ ksi}\sqrt{\text{in.}}$  at moderate to high elevated temperatures, one should consider the possibility of subcritical crack growth.

A number of questions remain to be answered about this behavior including (a) degree to which this behavior is independent of stress state, specimen size, and displacement measurement technique, (b) degree to which other alloys are subject to creep cracking, for example, 2124, 2419, and 2618, which show widely different resistance to creep rupture with sharply notched specimens, and (c) whether or not a true threshold for this behavior does exist.

## References

- [1] Kaufman, J. G. and Holt, Marshall in *Materials Technology An Inter-American Approach*, American Society of Mechanical Engineers, 1968, pp. 426-436.
- [2] Lindborg, U., *Acta Metallurgica*, Vol. 17, Feb. 1969, pp. 157-165.
- [3] Williams, J. A., *Philosophical Magazine*, Vol. 20, Sept. 1969, No. 165.
- [4] Popp, H. G. and Coles, A., "Subcritical Crack Growth Criteria for Inconel 718 at Elevated Temperatures," *Proceedings*, Air Force Conference on Fatigue and Fracture of Aircraft Structures and Materials, AFFDL-TR-70-144, Air Force Flight Defense Laboratory, Dec. 1969.
- [5] Siverns, M. J. and Price, A. T., *Nature*, Vol. 228, 21 Nov. 1970, pp. 760-761.
- [6] Landes, J. D. and Wei, R. P., *Transactions, Journal of Engineering Materials and Technology*, Jan. 1973, pp. 2-9.

- [7] Kenyon, J. L. et al in *Proceedings*, International Conference on Creep and Fatigue in Elevated Temperature Applications, Philadelphia, Pa., Sept. 1973, p. 156.
- [8] Siverns, M. J. and Price, T. A., *International Journal of Fracture*, Vol. 9, No. 2, June 1973, pp. 199-207.
- [9] Landes, J. D. and Wei, R. P., *International Journal of Fracture*, Vol. 9, No. 3, Sept. 1973, pp. 277-293.
- [10] Contract No. NAS 8-21487, "Evaluation of Stress-Corrosion Cracking Susceptibility Using Fracture Mechanics Techniques," by D. O. Sprowls, M. B. Shumaker, J. D. Walsh, and J. W. Coursen; prepared for George C. Marshall Space Flight Center, Final Report, Part 1, 31 May 1973.
- [11] Harrison, C. B. and Sandor, G. N., "High-Temperature Crack Growth in Low-Cycle Fatigue," *Engineering Fracture Mechanics*, 1971, Vol. 3, pp. 403-420.

D. Y. Wang<sup>1</sup> and D. E. McCabe<sup>2</sup>

## Investigation of R-Curve Using Comparative Tests with Center-Cracked-Tension and Crack-Line-Wedge-Loaded Specimens

---

**REFERENCE:** Wang, D. Y. and McCabe, D. E., "Investigation of R-Curve Using Comparative Tests with Center-Cracked-Tension and Crack-Line-Wedge-Loaded Specimens," *Mechanics of Crack Growth, ASTM STP 590*, American Society for Testing and Materials, 1976, pp. 169-193.

**ABSTRACT:** This paper provides a comparison of the crack-line-wedge-loaded (CLWL) and center-cracked-tension (CCT) test methods for determining R-curves on a number of high-strength aluminum sheet alloys. In general, R-curves were reasonably close, differing only by amounts which could be explained by differences in testing procedure and in crack driving force curve. Gross stress,  $K_c$ , and crack length at instability were predicted satisfactorily for CCT panels from CLWL R-curves. The test results for CCT specimens show that consistent  $K_c$  values are obtainable from specimens of various widths provided that the net-section stress at failure is below general yielding.

**KEY WORDS:** crack propagation, residual stress, fracture strength, plastic properties, elastic properties, stresses, aluminum alloys

The principles involved in crack growth resistance or R-curve have been known for over a decade, but very little has been done to demonstrate the predictive capability inherent in this technology. The purpose of this work, therefore, was to present experimental evidence demonstrating the application of these principles by using R-curves developed with crack-line-wedge-loaded (CLWL) specimens to predict the results obtained in center-cracked-tension tests (CCT). The property of R-curves upon which such predictive capability is predicated is that

<sup>1</sup>Senior engineer, Douglas Aircraft Co., McDonnell Douglas Corporation, Long Beach, Calif. 90846.

<sup>2</sup>Senior research metallurgist, Armco Steel Corporation, Middletown, Ohio 45042.

they are a function of slow-stable crack extension only, independent of starting crack length in the specimen. Instability  $K_c$  can be predicted for an untested configuration by determining the appropriate stress level for a tangency condition between the crack driving force curve and the R-curve for the material. This instability prediction principle has been discussed in a number of reports [1-3]<sup>3</sup> but has seldom been applied.

In some present analyses, the residual strength of a structure is calculated using a failure criterion based on a known initial crack length, and crack length at instability is not measured. If the slow-stable crack growth is appreciable as has been observed in tests on some very tough materials, the error may be quite appreciable. The R-curve, on the other hand, provides the complete material fracture characterization, and can be used to calculate the residual strength more accurately.

One very important aspect on the nature of R-curves which has been challenged by some investigators and to be tested in this investigation is an assumption that R-curves are independent of the specimen type [4]. Certainly, overall elastic stress distributions and hence crack driving force characteristics vary appreciably from one specimen type to another, and it has been suggested that the R-curve is affected by these differences. On the other hand, if crack growth resistance development is controlled by the crack and Mode I opening conditions, specimen type should be immaterial. The center-cracked-tension panel and the crack-line-loaded specimens of the present investigation provide a suitable contrast by which the foregoing consideration can be tested. The literature contains only a few examples where CLWL and CCT specimen R-curves have been compared [5,6]. These results have indicated that some small differences in R-curves exist, favoring slightly higher  $K_R$  and  $K_c$  values for CCT tests. Generally the differences were so small as to be within expected experimental variability.

### Validity of Plane Stress Fracture Toughness, $K_c$

No standard test procedure has been established for the determination of plane stress fracture toughness  $K_c$ , mainly because of the lack in consistency of  $K_c$  data. The major problem has been the variation of  $K_c$  values obtained from various test specimen widths and crack lengths. For many very tough materials, lower  $K_c$  values are obtained from specimens having insufficient width such that net-section yielding develops prior to fracture. Secondary effects, such as lack of crack buckling restraint and inability to measure critical crack length accurately, have also caused variation in  $K_c$  and are well known.

<sup>3</sup>The italic numbers in brackets refer to the list of references appended to this paper.

On 28 August 1972, D. Y. Wang presented a report at the Sixth National Symposium on Fracture Mechanics, giving the results of a number of wide panel tests made on a variety of aluminum alloys [7] showing a consistent pattern of  $K_c$  values. In addition to the determination of  $K_c$ , R-curves were shown for the slow-stable crack growth portion of the test records. The data tended to confirm some fundamentals of R-curve, namely, the independence of R-curve on specimen size and starting crack length. This, therefore, presented an excellent opportunity to make comparisons to CLWL developed R-curves and to make failure condition predictions from such tests. Specimen blanks were taken from broken halves of 48-in.-wide panel specimens. The materials and CCT specimens used are fully documented in Ref 7. To verify the consistent  $K_c$  value and the full range of the R-curve as an intrinsic material property, additional narrow width CCT specimens were added for the present study. The 18 and 24-in.-wide CCT specimens were made from the broken halves of the 36 and 48-in.-wide panels. In these narrow panels containing various initial crack lengths, a few panels were expected to fail in net-section yielding, but most specimens provided valid elastic  $K_c$  data.

This program also afforded an opportunity to check some of the recently proposed specimen size requirements for R-curve evaluation as stipulated in the new proposed recommended standard [8] which is presently available in Part 10 of the *ASTM Annual Book of Standards* under related material. In the proposed standard, it is optional to plot R-curves either in terms of physical or effective crack extension. Since the CCT panel R-curves had been reported in terms of physical crack extension, the CLWL developed R-curves will be presented here on the same basis using a procedure to be described in a later section.

### **Program and Procedure**

The CCT program consisted of testing panels varying in width from 18 to 120 in. Starting crack length to width ratios (aspect ratios,  $2a/W$ ) varied from 0.10 to 0.32. Crack extension was followed optically using two closed circuit TV cameras focused at each crack tip and also by direct visual recording as in Fig. 1. The composite pictures together with load were recorded on a video tape deck. In the tests of the 18 and 24-in.-wide specimens and some wider panels, an MTS clip gage was also used to measure the center crack opening displacement (COD) for compliance indicated crack lengths. A confirmation was obtained between the measured displacement and that calculated by an elastic-plastic analysis, the discussion of which is beyond the scope of this paper. The critical crack lengths at instability were determined both from the TV video recording and the computed crack length from the critical COD data. The instability usually occurred at an abrupt drop in the load versus displacement curve for the panels which failed at stress levels below net-section yielding.

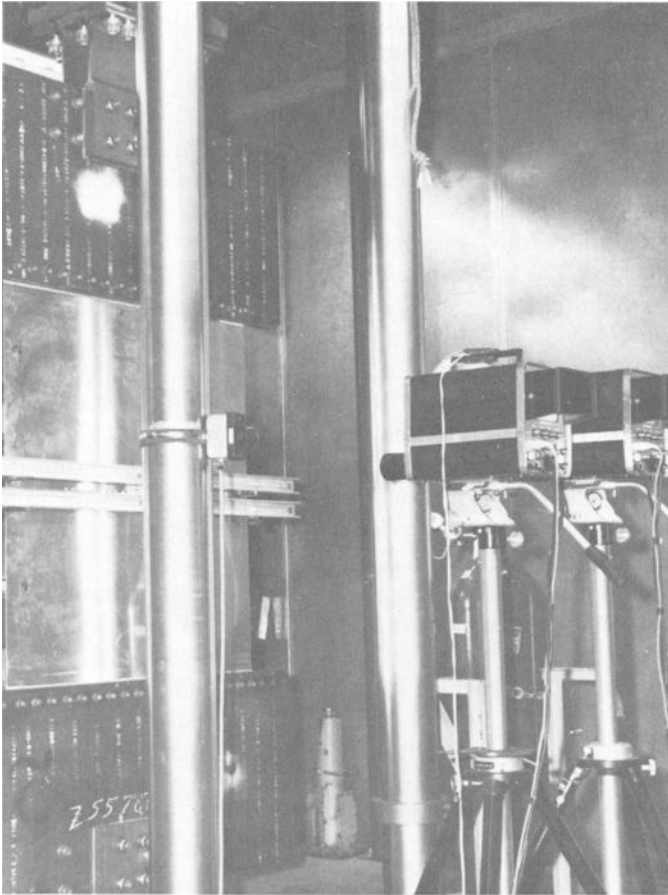


FIG. 1—Overall view of the test setup for a 48-in.-wide panel.

All panels contained a 1-in. initial saw cut crack starter, and fatigue crack growth rate information was obtained during cracking to the desired starting crack length. In all cases, the highest final  $\Delta K$  was less than 45 ksi  $\sqrt{\text{in.}}$ , which was about 80 percent of  $K_R$  at the start of slow-stable crack growth in the R-curves of 2024-T3 and 7475-T761. Despite this, no significant adverse effect was noted on the resulting R-curves.

In the wide panel tests, calculations for  $K_R$  and  $\Delta a$  were made in terms of physical crack dimensions, neglecting plastic zone contribution to crack length. This is usually not allowed in  $K_R$  determinations, but, since overall crack lengths were large with respect to plastic zone contribution, the corresponding error in  $K_R$  calculation was relatively minor. In CLWL tests, the cracks are somewhat shorter, and in some cases plastic zone

correction to the physical crack length could not be ignored without significant error in  $K_R$ .

The CLWL specimens were oriented so the crack propagated in the same direction, T-L, as in the CCT tests. Two sizes of specimens were selected, 4C and 7C shown in Fig. 2. The testing procedure is available as a proposed standard and has been reported elsewhere [9]. All information necessary for determination of an R-curve is obtained from a double compliance test record, an example of which is shown in Fig. 3. Displacement at locations V1 and V2, indicated in Fig. 2, are plotted on an x-y recorder using the output from two special clip gages shown in Fig. 4. The ratio of V1 to V2 at any selected point along the test record can be related to the effective crack length (physical crack plus plastic zone correction) using a double compliance calibration curve. If the specimen is periodically partially unloaded, the return slopes are related to the physical crack lengths at those stopping points. The test record shows several locations of partial unloading.

### Results and Discussion

In order to produce CLWL R-curves in terms of physical crack growth,  $\Delta a_p$ , it was necessary to determine the compliance indicated plastic zone sizes. This is achieved by subtracting the compliance indicated physical crack length from the effective crack length at certain points. Compliance

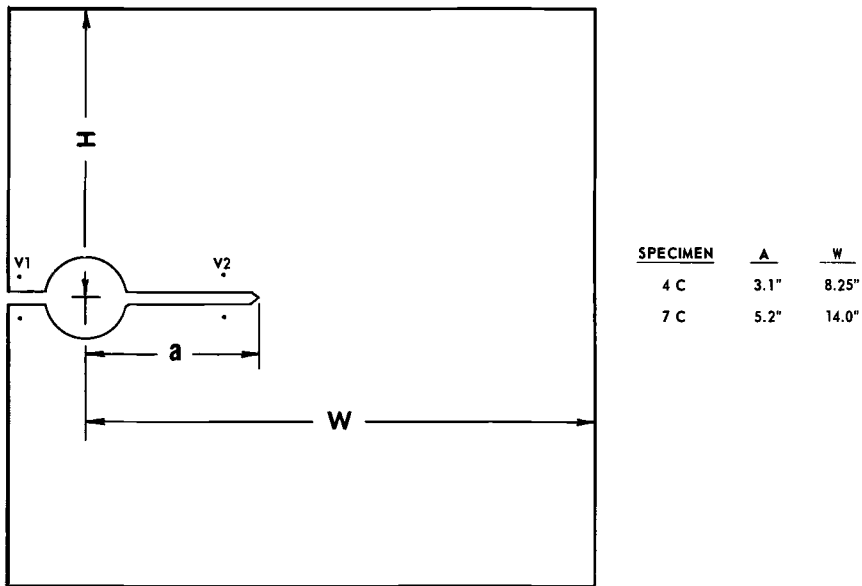


FIG. 2—Compact wedge-loaded specimen  $H/W = 0.6$ .

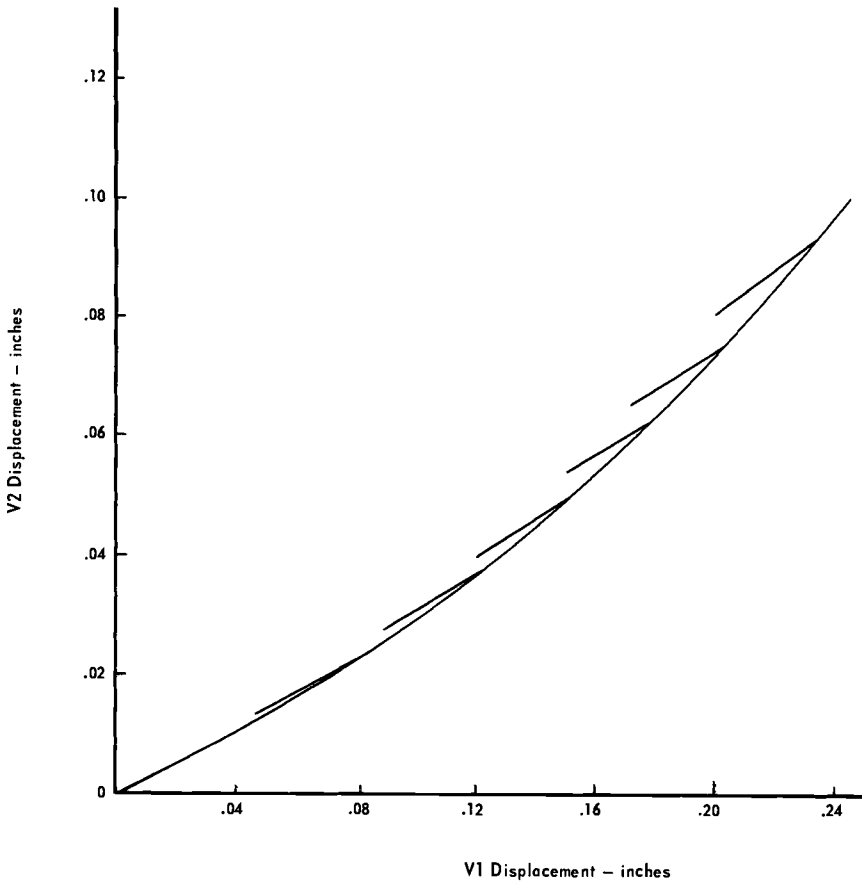


FIG. 3—Test record for 2024-T3 CLWL 7C specimen.

methods inherently reflect experimental variability on individual physical crack and effective crack length determinations, so the errors were diminished through the use of plots of compliance indicated plastic zones like those shown in Figs. 5 and 6. The CLWL R-curve plotting points were then adjusted on the abscissa by subtracting the median  $r_p$  values from  $\Delta a$  effective at selected  $K_R$  values. An interesting feature in Figs. 5 and 6 is the comparison between compliance indicated plastic zone size and that calculated using the well known Irwin expression:  $r_p = 1/2\pi K_R^2 / \sigma_{ys}^2$ . It appears that the Irwin expression works best on materials of high yield strength and low toughness.

Figures 7 through 11 compare CLWL and CCT developed R-curves on the five materials tested. Some small discrepancy in the initial crack growth portion of the CCT panel R-curves was anticipated because crack

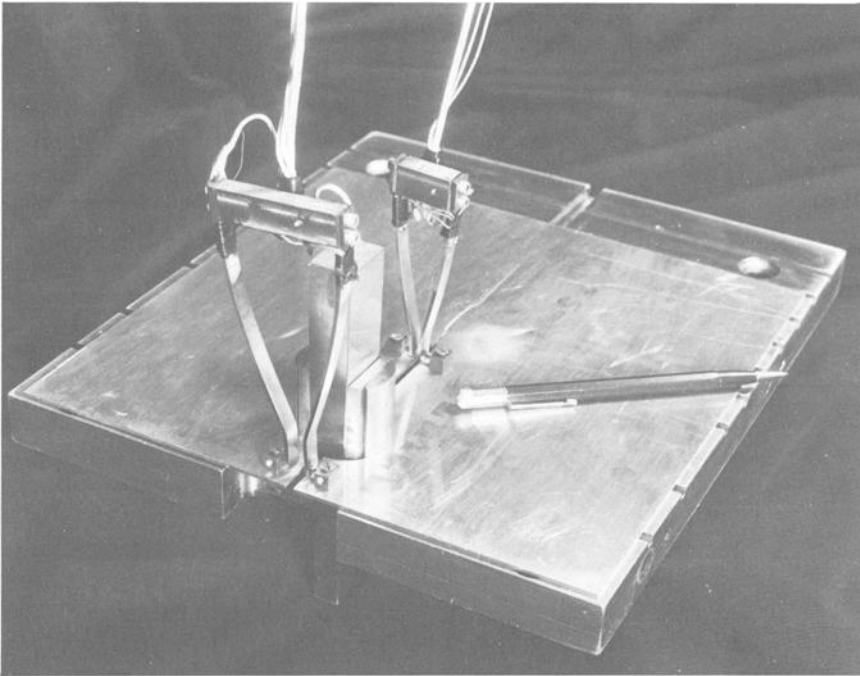


FIG. 4—Photograph showing instrumentation for double compliance measurements.

extension less than 0.05 in. was ignored. Otherwise, it may be concluded that CLWL and CCT developed R-curves compare well, and no consistent pattern of difference was developed.

The obvious difference between the R-curves derived from the tests of CLWL and CCT specimens is the amount of crack extension prior to termination. The crack extension can be greater in CLWL specimens than in CCT specimens due to the dissimilar shape of crack driving force curves, which in turn is related to the relative stiffness of the loading systems. In general, cracks tend to remain stable in crack-line-loaded specimens having rigid loading devices such as the wedge and split pin arrangement used here. The theoretical background on crack stability has been well documented in the work of Clausing [10] and of Gurney [11].

#### **Prediction of CCT Panel Instability**

One principal objective of this investigation was to determine if  $K_c$  and gross stress at fracture could be predicted for the wide panel tests using R-curves developed with CLWL specimens. For this purpose, plots of  $K_R$

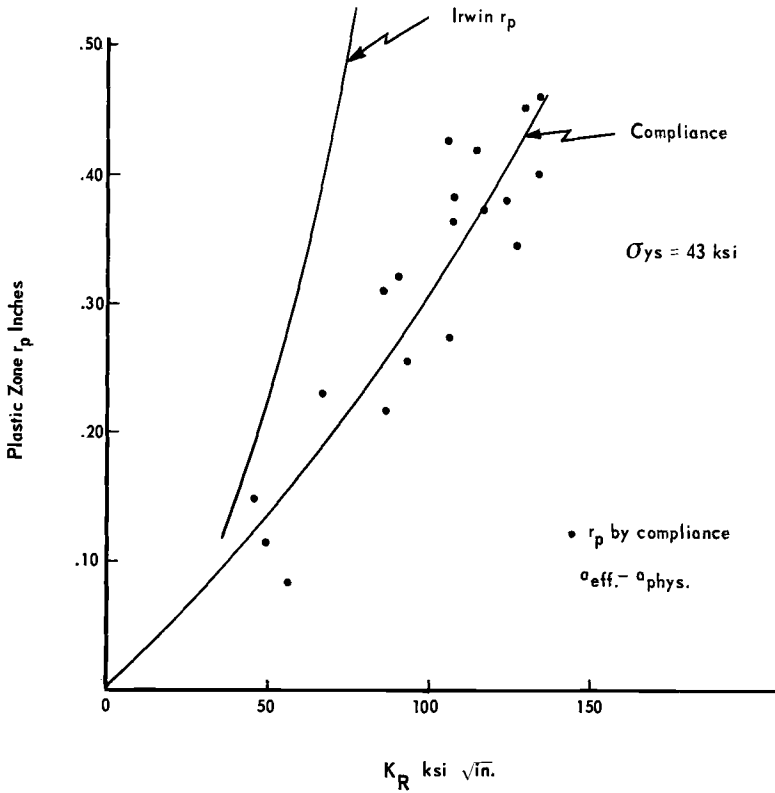


FIG. 5— $r_p$  for 2024-T3, as a function of  $K_R$ .

versus  $\Delta a$  effective were used to match to the CCT crack driving force relationship. The following CCT relationship was used

$$K = \sigma (\pi a \sec \pi a / w)^{1/2} \tag{1}$$

where

- $\sigma$  = gross applied stress,
- $a$  = half crack length ( $a$  effective), and
- $W$  = panel width.

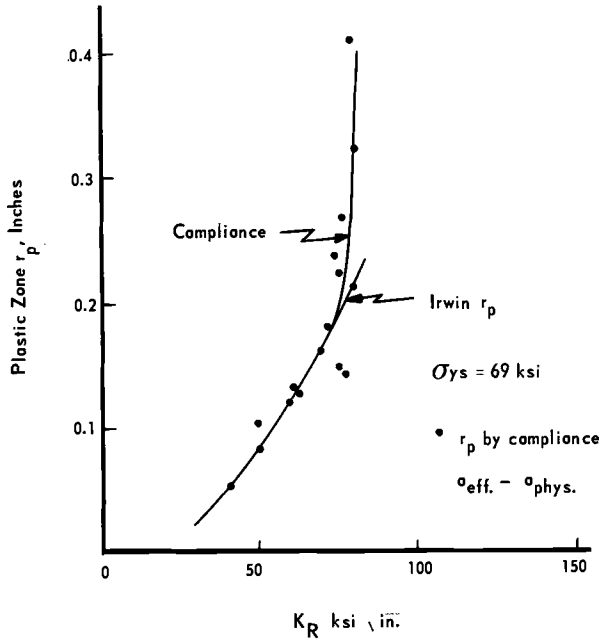


FIG. 6— $r_p$  for 7079-T6, as a function of  $K_R$ .

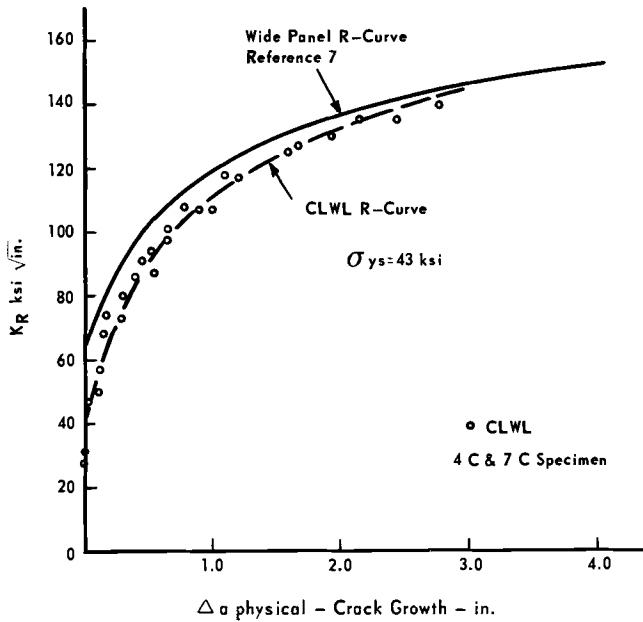


FIG. 7—2024-T3 R-curve.

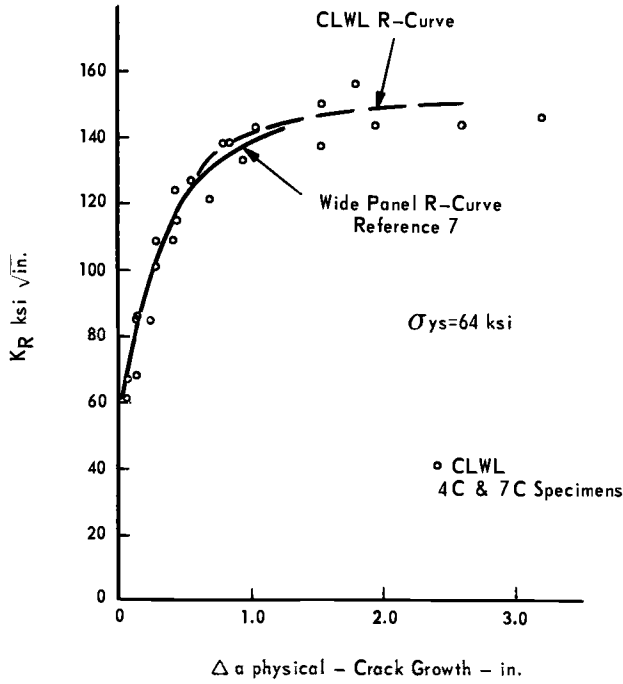


FIG. 8—7475-T761 R-curve.

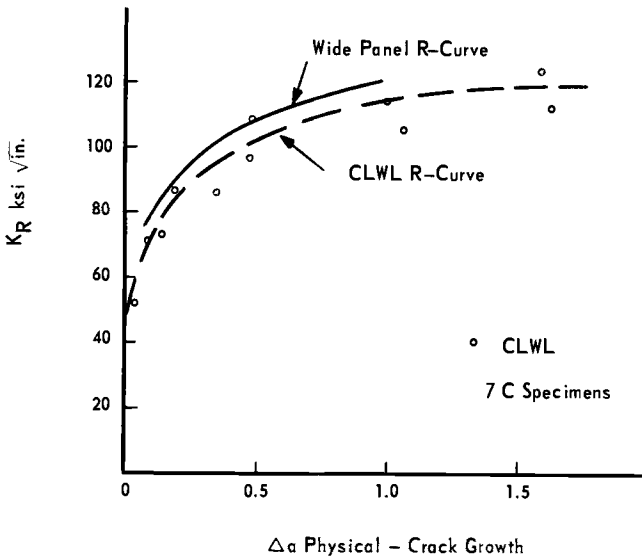


FIG. 9—7475-T61 R-curve.

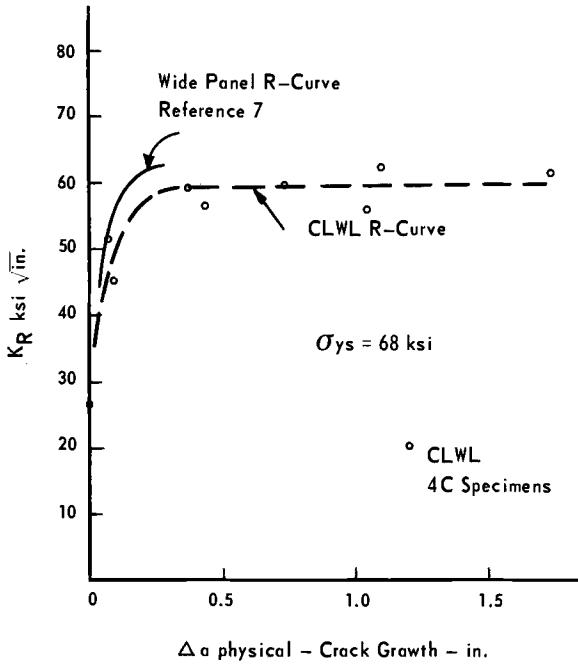


FIG. 10—7075-T6 R-curve.

The CLWL R-curve was described in terms of a least squares fit of a second order polynomial to the portion of the R-curve where tangency with the crack driving force curve was expected.

$$K_R = C_0 + C_1 (\Delta a_e) + C_2 (\Delta a_e)^2 \tag{2}$$

Solve for  $\Delta a_e$  and  $K_c$

Given

$$K_R = K \text{ at tangent} \tag{3}$$

$$\frac{\partial K_R}{\partial (\Delta a_e)} = \frac{\partial K}{\partial (a_e)} \tag{4}$$

where

- $K$  = CCT crack driving force,
- $a_e = a_o + \Delta a_e$ , and
- $a_o$  = initial half crack length.

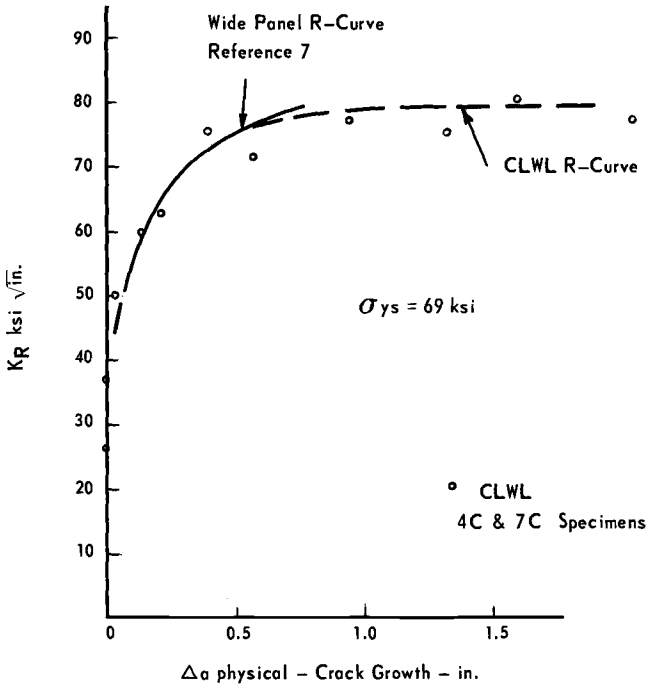


FIG. 11—7079-T6 R-curve.

Solution

$$\frac{\partial K}{\partial a_e} = 1/2 \left( \sigma \pi a_e \sec \frac{\pi a_e}{w} \right)^{-1/2} \times \left( \pi \sec \frac{\pi a_e}{w} + \frac{\pi 2a_e}{w} \sec \frac{\pi a_e}{w} \tan \frac{\pi a_e}{w} \right)$$

from Eq 3

$$K_R = K = \sigma \left( \pi a_e \sec \frac{\pi a_e}{w} \right)^{1/2}$$

therefore

$$\frac{\partial K}{\partial a_e} = K_R \frac{1}{2} \left( \frac{1}{a_e} \frac{\pi}{w} \tan \frac{\pi a_e}{w} \right)$$

from Eq 4

$$\frac{\partial K_R}{\partial(\Delta a_e)} / K_R = \frac{1}{2} \left( \frac{1}{a_e} + \frac{\pi}{w} \tan \frac{\pi a_e}{w} \right)$$

$$\frac{C_1 + 2C_2(\Delta a_e)}{C_0 + C_1(\Delta a_e) + C_2(\Delta a_e)^2} = \frac{1}{2} \left[ \frac{1}{(a_0 + \Delta a_e)} + \frac{\pi}{w} \tan \frac{\pi(a_0 + \Delta a_e)}{w} \right]$$

Solve for  $\Delta a_e$  by iteration

$$\sigma = \frac{C_0 + C_1(\Delta a_e) + C_2(\Delta a_e)^2}{\left[ \pi(a_0 + \Delta a_e) \sec \frac{\pi(a_0 + \Delta a_e)}{w} \right]^{\frac{1}{2}}}$$

In order to compare the preceding predicted  $K_c$  values to those reported in the CCT experiment, it was necessary to convert  $\Delta a$  effective to  $\Delta a$  physical and then recalculate  $K_c$  using  $a$  physical in Eq 1.

Predicted and experimental results in terms of critical crack length, gross fracture stress, and  $K_c$  values are given in Table 1 and graphically compared in Figs. 12 through 14. Perhaps the best correlation is given in Fig. 12; where gross stress at fracture is reasonably predicted over a wide range of material toughnesses and with specimens varying in width from 24 to 120 in. and starting crack lengths,  $2a_0$ , from 3.6 to 30 in. This correlation perhaps best demonstrates the usefulness of R-curve analysis.

Figure 13 shows the comparison of  $K_c$  values. The greatest variation shown is at the highest  $K_c$  values from 120-in.-wide panel tests where instability crack length is most difficult to determine.

Figure 14 compares predicted slow-stable crack growth prior to instability to experimental. This is the most sensitive part of estimation procedures, affected strongly by the way that the R-curve is faired through the data points. Therefore, these predictions gave the poorest comparison.

### General Observations

R-curves are developed generally by selecting specific locations along the crack growth history to determine  $K_R$  and  $\Delta a$ , and individual datum is plotted. A smooth curve is then faired through the plotted points to represent the R-curve. The double compliance method of measurement is a continuum record of  $K_R$  development, and it is oftentimes demonstrated that true crack extension history can be noncontinuous. In Figs. 8 and 9,

TABLE 1—Comparison of CLWL predicted instability conditions to experimentally determined values.

| Material  | Width | $a_0$ , in. | Half Crack Length, $a_c$ |                   | Gross Stress, fracture |              | $K_c$     |              | Net Section Stress, predicted |
|-----------|-------|-------------|--------------------------|-------------------|------------------------|--------------|-----------|--------------|-------------------------------|
|           |       |             | Predicted, in.           | Experimental, in. | Predicted              | Experimental | Predicted | Experimental |                               |
|           |       |             |                          |                   |                        |              |           |              |                               |
| 2024-T3   | 24    | 4.0         | 5.64                     | 4.79              | 24.9                   | 26.7         | 121.9     | 116          | 46.6                          |
|           | 36    | 5.4         | 7.43                     | 7.03              | 24.1                   | 26.1         | 130.5     | 134          | 40.8                          |
|           | 120   | 10.0        | 12.57                    | 13.46             | 21.6                   | 24.22        | 139.5     | 162          | 27.3                          |
|           | 120   | 15.0        | 17.66                    | 19.05             | 17.8                   | 18.7         | 140.1     | 156          | 25.2                          |
| 7475-T761 | 36    | 1.8         | 2.91                     | 2.65              | 43.5                   | 45.2         | 133.8     | 133          | 51.8                          |
|           | 36    | 3.6         | 4.85                     | 4.75              | 34.1                   | 33.1         | 139.4     | 135          | 46.6                          |
|           | 36    | 5.4         | 6.70                     | 6.50              | 28.1                   | 27.2         | 141.1     | 134          | 44.8                          |
|           | 48    | 4.8         | 6.12                     | 5.90              | 31.1                   | 31.2         | 142.2     | 139          | 41.7                          |
| 7075-T6   | 120   | 10.0        | 11.46                    | 11.05             | 23.8                   | 27.2         | 146.1     | 164          | 29.3                          |
|           | 120   | 15.0        | 16.50                    | 16.05             | 19.5                   | 18.1         | 147.3     | 133          | 26.9                          |
|           | 30    | 4.87        | 5.28                     | 5.23              | 13.4                   | 14.35        | 59.2      | 63           | 20.7                          |
|           | 48    | 7.0         | 7.42                     | 7.3               | 11.5                   | 12.5         | 59.0      | 63           | 16.6                          |
| 7079-T6   | 48    | 7.0         | 7.49                     | 8.05              | 14.9                   | 14.95        | 77.0      | 78           | 21.6                          |
| 7475-T61  | 36    | 1.8         | 2.54                     | 2.65              | 35.9                   | 39.8         | 102.6     | 118          | 41.8                          |
|           | 48    | 4.8         | 6.13                     | 5.7               | 25.1                   | 29.25        | 114.8     | 129          | 33.7                          |
|           | 120   | 10.0        | 11.67                    | 19.3              | 19.3                   | 119.7        | 119.7     | 24.0         |                               |

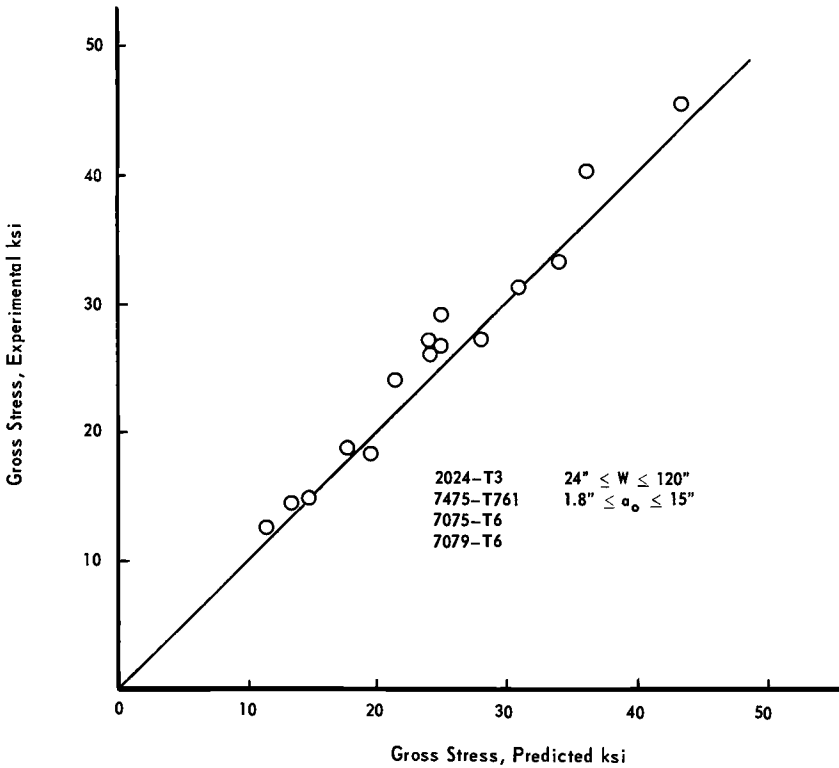


FIG. 12—Failure stress of center cracked panels predicted by CLWL R-curves.

smooth plots of  $K_R$  versus  $\Delta a$  physical are used to represent the R-curves of 7475. A more precise representation is given in Figs. 15 and 16. The sporadic nature of these R-curves is evidence of sudden short bursts of crack extension. This same behavior was detected using visual methods of measuring crack growth in the CCT wide panels.

#### Specimen Size Limitations

It was of interest to test the specimen size requirements according to Section 6 in the Proposed R-Curve Standard using the present results. For the CLWL specimen, the method stipulates that the uncracked ligament,  $(W - a)$ , should be greater than  $4/\pi (K_{\max}/\sigma_{ys})^2$  at the termination of the test, where  $K_{\max}$  is the upper plateau  $K_R$ . Table 2 compares specified  $(W - a)$ , requirements to those developed in the present investigation. The preceding limit was set to ensure fully elastic behavior through plateau  $K_R$ , but when some of the specimens of 2024-T3 and

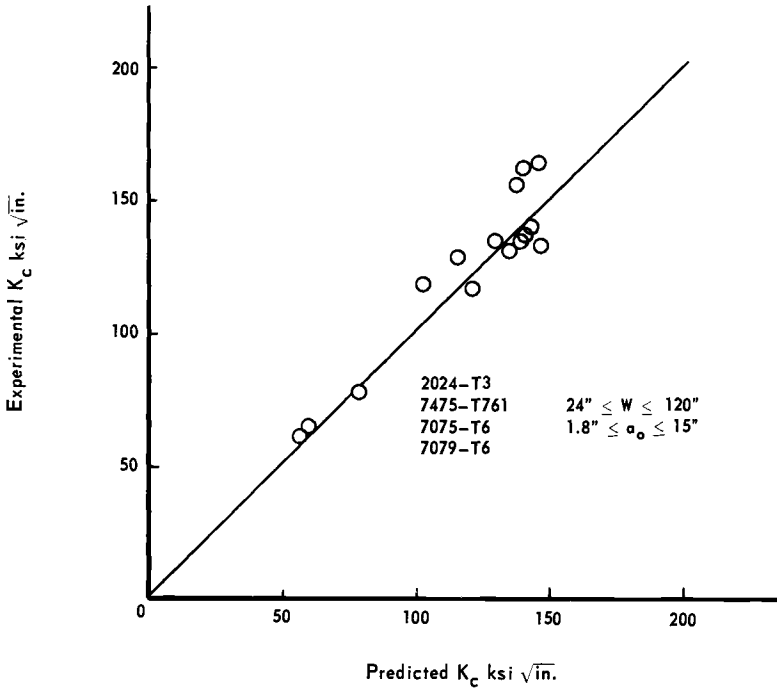


FIG. 13— $K_c$  of center cracked panels predicted by CLWL R-curves.

7475-T761 went plastic as indicated by strain gage on the back edge, the  $K_R$  values reported are at this event. The table shows that the 4C size CLWL specimen is too small to test 7475-T761 and 2024-T3 up to plateau  $K_R$  values. The 7C size was just marginal for the 7475-T761 but too small to test 2020-T3 to upper plateau. Since the plateau of about 160 ksi  $\sqrt{\text{in.}}$  in 2024-T3 was not achieved, the size requirements of the method, therefore, are supported by these results.

For CCT tests, Figs. 17 through 19 compare experimentally determined  $K_c$  values for panels of varied sizes and aspect ratios ( $2a/W$ ) to curves calculated for limiting  $K_c$  based on net-section yielding. In all three materials, the specimens that failed at stress below net-section yielding exhibited quite consistent  $K_c$  values which appear to be independent of panel width and aspect ratio. The maximum valid  $K_c$  data points are represented by horizontal dashed lines. In Fig. 17, the 2024-T3 specimens of widths up to 48 in. were failed through net-section yielding in which the apparent  $K_c$  increases with panel width and aspect ratio. The invalid  $K_c$  data points fell according to the analytical K-curves at net-section

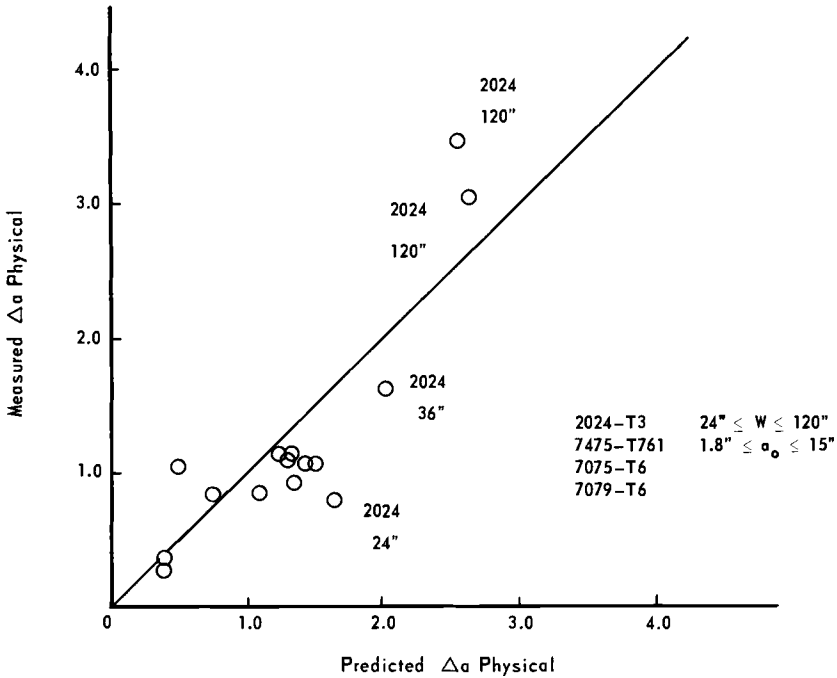


FIG. 14—Crack growth to instability of center cracked panels predicted by CLWL R-curves.

yielding. The slight scatter probably resulted from the variation in yield strength of the specimens from different sheets. For 7475-T61, only specimens with an aspect ratio of 0.10 developed net-section yielding in Fig. 18. Two 7475-T761 specimens developed yielding at an aspect ratio of 0.10, as is shown in Fig. 19.

Table 3 compares the experimentally indicated minimum width requirement at  $2 a/W = 0.3$  to those stipulated in the "Proposed Recommended Standard for R-Curve Determination." Since the minimum specimen width requirements appear to be satisfied, and they are within the boundary of a net-section yielding criterion, the experimental data support a net-section yielding limitation for valid  $K_{R}$ .

**Conclusions**

1. R-curves developed independently using CLWL and CCT specimens compare favorably when tested within the range of validity as stipulated in the "Proposed Recommended Standard for R-Curve Testing."

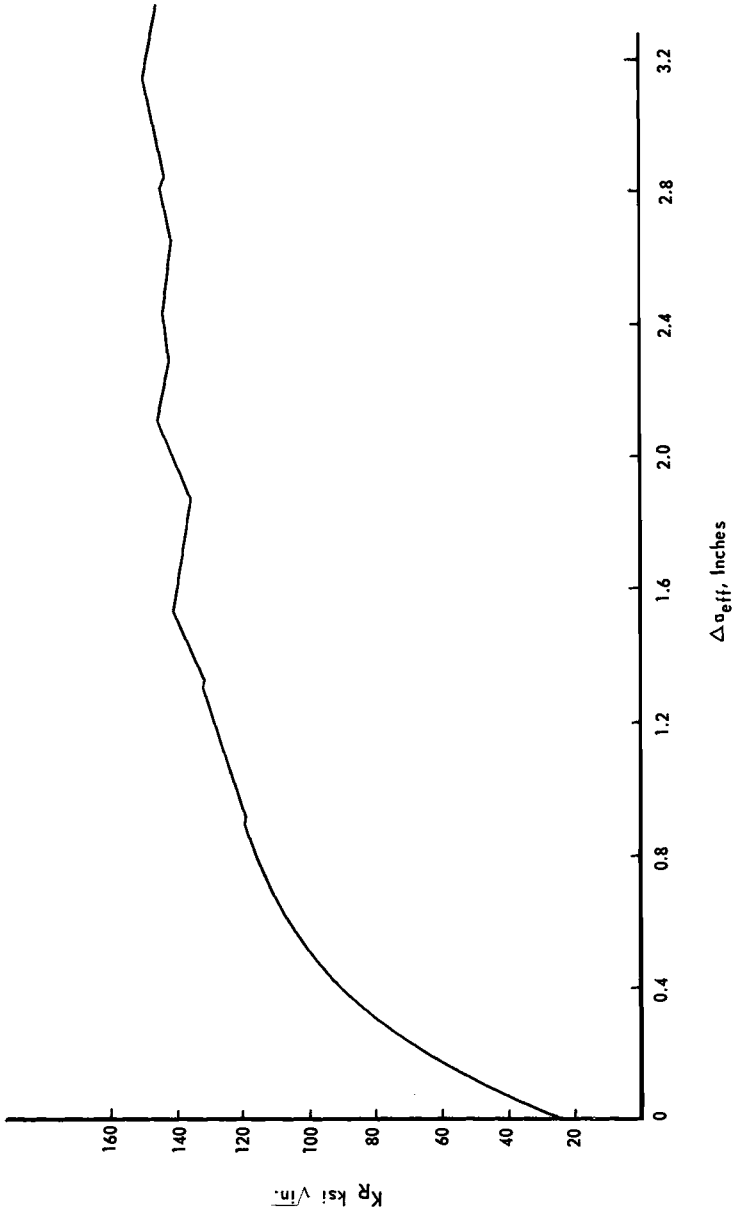


FIG. 15—7475-T761 R-curve  $K_R$  versus  $\Delta\sigma$  effective.

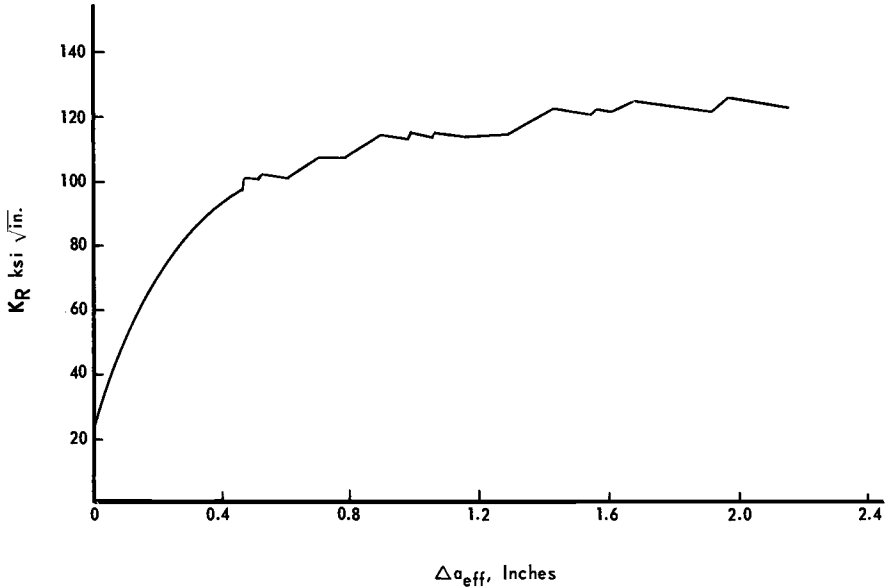


FIG. 16—7475-T61 R-curve versus  $\Delta a$  effective.

2. Consistent,  $K_c$  data and R-curves which were independent of panel width and initial crack length, were established from the test results of the 18, 24, 36, 48, and 120-in.-wide CCT specimens in two alloys. The specimens which failed by net-section yielding produced the invalid  $K_c$  values.

3. Instability stress, crack lengths, and  $K_c$  values were predicted for the CCT panel tests from the CLWL developed R-curves. Although there was some scatter in predicting crack growth prior to instability,  $K_c$  values and gross section stresses at failure were reasonably comparable to experimental results.

4. Plastic zone estimates using the Irwin correction equation compare well with compliance indicated plastic zones only on materials with relatively high yield strength.

5. The minimum specimen size requirements of the "Proposed Recommended Standard for R-Curve Determination" were tested and appear to be satisfactory and conservative according to the results obtained in the present investigation.

TABLE 2—Comparison of specified specimen size requirements to experimental W-a @  $K_{max}$  or K at back edge yielding.

$$\text{CLWL tests } \left[ (w - a) \text{ required } \geq \frac{4}{\pi} \frac{K_{max}^2}{\sigma_{ys}^2} \right]$$

| Material  | Specimen | Width, in. | $K_R$ at Termination | Required $W - a$ for Plateau $K_R$ | Experimental $W - a$ at Termination, in. |
|-----------|----------|------------|----------------------|------------------------------------|--|
| 7475-T761 | 7C       | 14         | 145.3 <sup>a</sup>   | 5.6                                | 5.14 <sup>b</sup>                        |
|           | 7C       | 14         | 155.4                | 5.6                                | 5.53 <sup>b</sup>                        |
|           | 4C       | 8.25       | 138.1                | 5.6                                | 4.40 <sup>b</sup>                        |
|           | 4C       | 8.25       | 109.4                | 5.6                                | 4.10 <sup>b</sup>                        |
| 2024-T3   | 7C       | 14         | 135.6                | 17.6                               | 6.4 <sup>b</sup>                         |
|           | 7C       | 14         | 140.6                | 17.6                               | 6.0 <sup>b</sup>                         |
|           | 4C       | 8.25       | 108.2                | 17.6                               | 4.4 <sup>b</sup>                         |
|           | 4C       | 8.25       | 107.3                | 17.6                               | 4.25 <sup>b</sup>                        |
| 7079-T6   | 7C       | 14         | 79.5 <sup>a</sup>    | 1.7                                | 5.85                                     |
|           | 4C       | 8.25       | 80.6 <sup>a</sup>    | 1.7                                | 3.65                                     |
| 7075-T6   | 7C       | 14         | 60.0 <sup>a</sup>    | 1.1                                | 8.2                                      |
|           | 4C       | 8.25       | 65.0 <sup>a</sup>    | 1.1                                | 4.25                                     |

<sup>a</sup>Upper plateau  $K_R$ , all other tests were stopped at strain gage indications of back edge yielding.

<sup>b</sup>At back edge yield as indicated by strain gage.

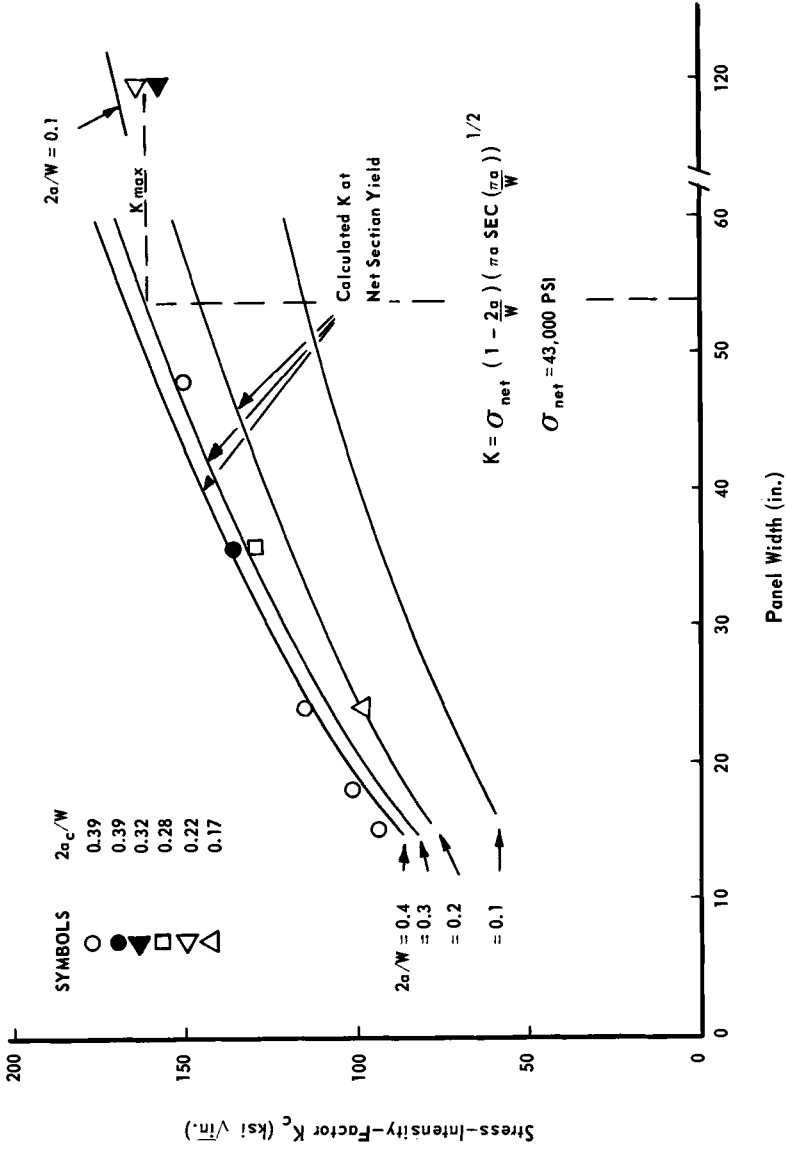


FIG. 17—Comparison of plane stress fracture toughness  $K_c$  data for 2024-T3 (T-L) and  $K$  at net-section yielding.

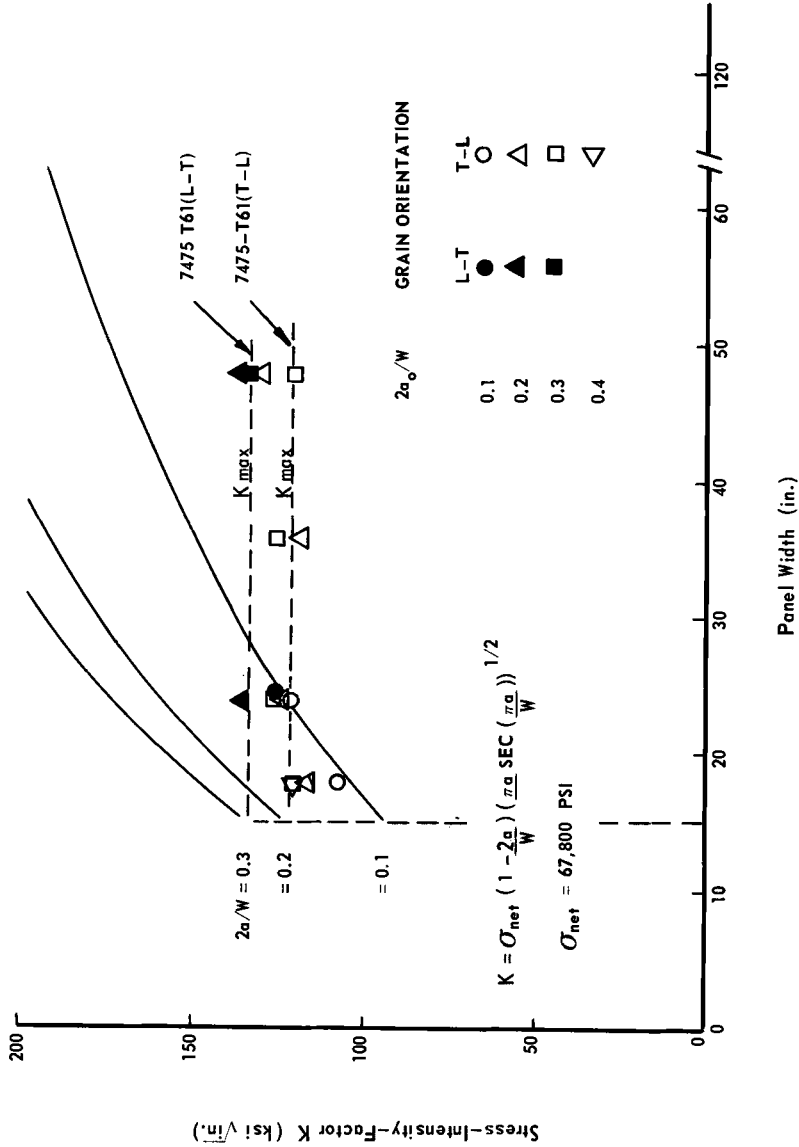


FIG. 18—Comparison of plane stress fracture toughness  $K_c$  data for 7475-T61 and  $K$ -curve at net-section yielding.

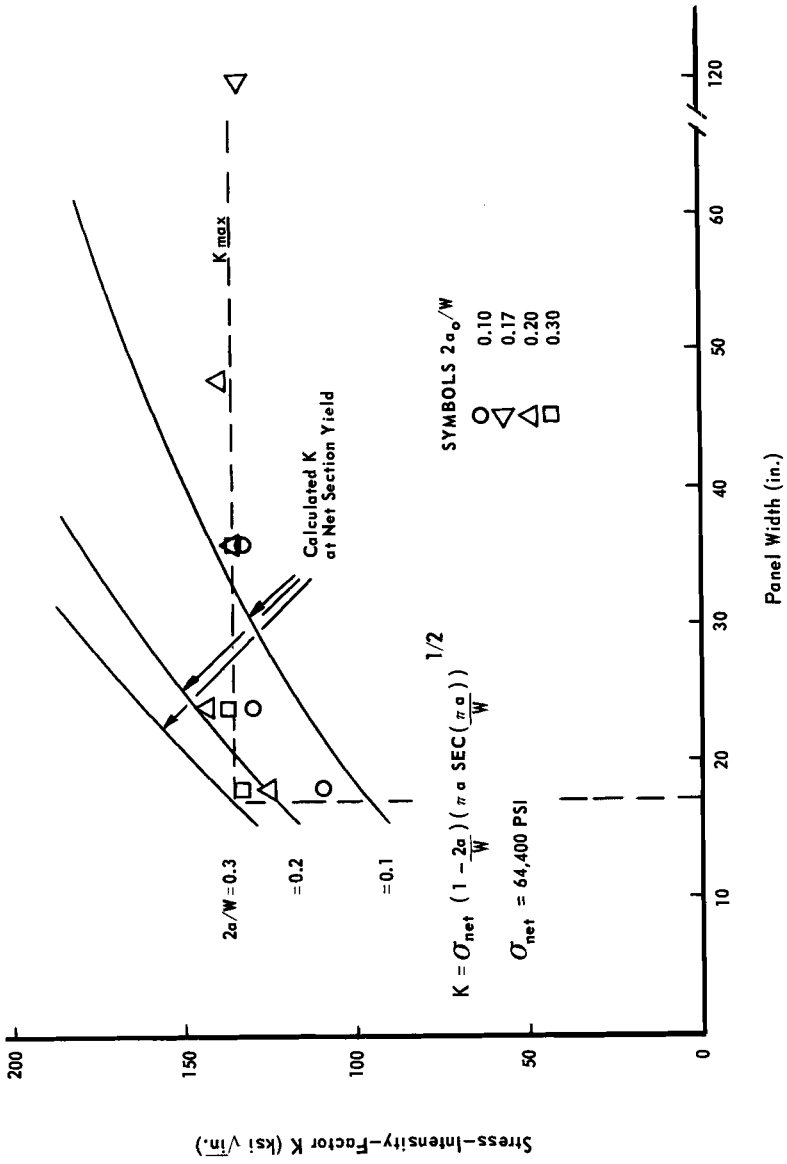


FIG. 19—Comparison of plane stress fracture toughness  $K_{Ic}$  data for 7475-T761 (T-L) and  $K$ -curves at net-section yielding.

TABLE 3—Comparison of specified size requirements to experimental for CCT panels.

| Size Requirements     |                                      | Experimental  |           |               |                    |  |
|-----------------------|--------------------------------------|---------------|-----------|---------------|--------------------|--|
| $K_{max}/\sigma_{ys}$ | At $a/W = 0.3$<br>Minimum Width, in. | Material      | $K_{max}$ | $\sigma_{ys}$ | Size Required, in. | Size Required by Figs. 17-19 at $2a/W = 0.3$ , in. |
| 0.5                   | 3                                    | 2024-T3       | 160       | 43            | >48                | 53   |
| 1.0                   | 6                                    | 7475-T761     | 135       | 64.4          | 20                 | 17.5   |
| 1.5                   | 12                                   | 7475-T61(L-T) | 132       | 67.8          | 20                 | 15   |
| 2.0                   | 20                                   |               |           |               |                    |  |
| 3.0                   | 48                                   |               |           |               |                    |  |

## References

- [1] Kraft, J. M., Sullivan, A. M., and Boyle, R. W., *Proceedings, Crack Propagation Symposium*, Cranfield, England, Sept. 1961.
- [2] ASTM Special Committee on Fracture Testing of High Strength Material, *ASTM Bulletin*, Jan. 1960, pp. 2940.
- [3] Heyer, R. H. and McCabe, D. E., *Engineering Fracture Mechanics*, Vol. 4, 1972, pp. 393-412.
- [4] Walker, E. K., "A Resistance-Slope Concept for Thin Sheet Fracture," Progress Report for Discussion at the Oct. 1970 Meeting of Subcommittee 1, ASTM Committee E-24.
- [5] Sullivan, A. M., Freed, C. N., and Stoop, J. in *Fracture Toughness Evaluation by R-Curve Methods*, ASTM STP 527, American Society for Testing and Materials, 1973, pp. 85-104.
- [6] Heyer, R. H. and McCabe, D. E., *Engineering Fracture Mechanics*, Vol. 4, 1972, pp. 413-104.
- [7] Wang, D. Y., "Plane Stress Fracture Toughness and Fatigue Crack Propagation of Aluminum Alloy Wide Panels," *Sixth National Symposium on Fracture Mechanics*, 28-30 August 1972.
- [8] Proposed Recommended Standard for R-Curve Determination, Committee E-24 American Society for Testing and Materials, E24.01.04, Task Group on R-Curves.
- [9] Heyer, R. H. and McCabe, D. E., *Fracture Toughness Evaluation by R-Curve Methods*, ASTM STP 527, American Society for Testing and Materials, 1973, pp. 17-35.
- [10] Clausing, D. P., *International Journal of Fracture Mechanics*, Vol. 5, Sept. 1969, pp. 211-227.
- [11] Gurney, C. and Mai, Y. W., *Engineering Fracture Mechanics*, 1972, Vol. 4, pp. 853-863.

## Ductility, Fracture Resistance, and R-Curves

---

**REFERENCE:** Weiss, Volker and Sengupta, Mukulesh, "Ductility, Fracture Resistance, and R-Curves," *Mechanics of Crack Growth, ASTM STP 590*, American Society for Testing and Materials, 1976, pp. 194–207.

**ABSTRACT:** A method for analytical predictions of the thickness effect on fracture toughness, and of R-curves is presented. It is based on the recent observation that the fracture resistance  $K_R$  is proportional to the local fracture strain  $\epsilon_{F,\alpha\beta}$ , where  $\alpha = \sigma_2/\sigma_1$ , and  $\beta = \sigma_3/\sigma_1$  characterize the local stress state. As this stress state varies from the surface, where it is plane stress ( $\alpha = 0, \beta = 0.61$ ), to the center, where it approaches plane strain ( $\alpha = 0.81, \beta = 0.61$ ) for sufficiently thick specimens, the local fracture resistance varies correspondingly. The model proposed here assumes that the measured fracture resistance represents the average of the local  $G_R$  values along the crack front. The calculated thickness effect is in excellent agreement with experimental results. From the same model an analytical expression for R-curves is suggested with the additional consideration of the relation between the plastic zone size as a function of crack growth. The preliminary results of the predicted R-curves are in reasonable agreement with the experimental curves.

**KEY WORDS:** crack propagation, ductility, fracture strength, stress analysis, plastic deformation, aluminum, stainless steels

Effective utilization of fracture mechanics for engineering design and failure analysis requires that the fracture resistance of a material be known in the entire size range of its application. For thick sections fracture toughness characterization by  $K_{Ic}$  is now well established as the applicable design criterion. For thin sections the fracture resistance curve concept, R-curve, has been proposed by Irwin [1-2]<sup>2</sup> and is finding increasing interest. For a review of R-curve testing and analysis the reader is referred to the paper by Brown and Srawley [3] or to the recent papers by Heyer and McCabe [4-5].

<sup>1</sup> Professor and research assistant, respectively, Department of Materials Science, Syracuse University, Syracuse, N.Y. 13210.

<sup>2</sup> The italic numbers in brackets refer to the list of references appended to this paper.

Figure 1 is a schematic representation of a typical R-curve where the fracture resistance  $R$  is plotted as a function of the crack length  $a$ . Crack propagation occurs under rising load until the point of tangency  $G_c$  between the R-curve and the crack driving force G-curve is reached. For a Griffith crack (infinite plate) this curve would be a straight line going through the origin, since  $G = \sigma^2 \pi a$ . At  $G_c$  the propagation becomes unstable. R-curves can be determined experimentally. However, it would also be highly desirable to develop an analytical model which can predict R-curves for various thicknesses from a limited number of tests. Such an analytical model is presented in the following. The same model can also be used to predict thickness effect on fracture toughness.

### Foundations of the Model

The model postulates that the fracture resistance of a material, as determined experimentally, is the average of the local resistance values of all the elements along the crack front and that the resistance of each element is related directly to the local stress state through its relation to material ductility. These relationships have been discussed recently [6-7]. Accordingly, the fracture resistance  $K_R$  can be expressed as

$$K_R = E\sqrt{S\rho^*} \bar{\epsilon}_{F,\alpha\beta} \quad (1)$$

where

- $E$  = elastic modulus,
- $S$  = shape factor of the plastic zone ( $\approx 1$ ),
- $\rho^*$  = Neuber's micro support effect constant ( $\rho^* \approx 0.001$  in.), and
- $\bar{\epsilon}_{F,\alpha\beta}$  = local fracture ductility.

The subscripts  $\alpha = \sigma_2/\sigma_1$  and  $\beta = \sigma_3/\sigma_1$  denote the local stress state. Plane strain is characterized by  $\alpha = 0.81$  and  $\beta = 0.61$ . At the surface, plane stress,  $\alpha = 0$  and  $\beta = 0.61$ . As the local ductility decreases with increasing stress biaxiality, so does the fracture resistance  $K_R$ . Thus, a decrease in thickness or an increase in crack length influences the deformation mode such that the "plane stress character" of the crack front is increased. Increased plane stress results in an increased fracture ductility [6], and, since the local fracture resistance  $K_R$  (in units of stress intensity factor) is proportional to the local multiaxial fracture ductility [7] a decrease in thickness or an increase in crack length will increase the average fracture resistance. This is illustrated in Fig. 2.

### Stress Distribution at the Crack Front

To determine the local fracture toughness along the crack front with the help of Eq 1 it is necessary to know the stress state,  $\alpha(z)$  and  $\beta(z)$ , along the crack front as a function of distance from the surface,  $z$ . Unfortu-

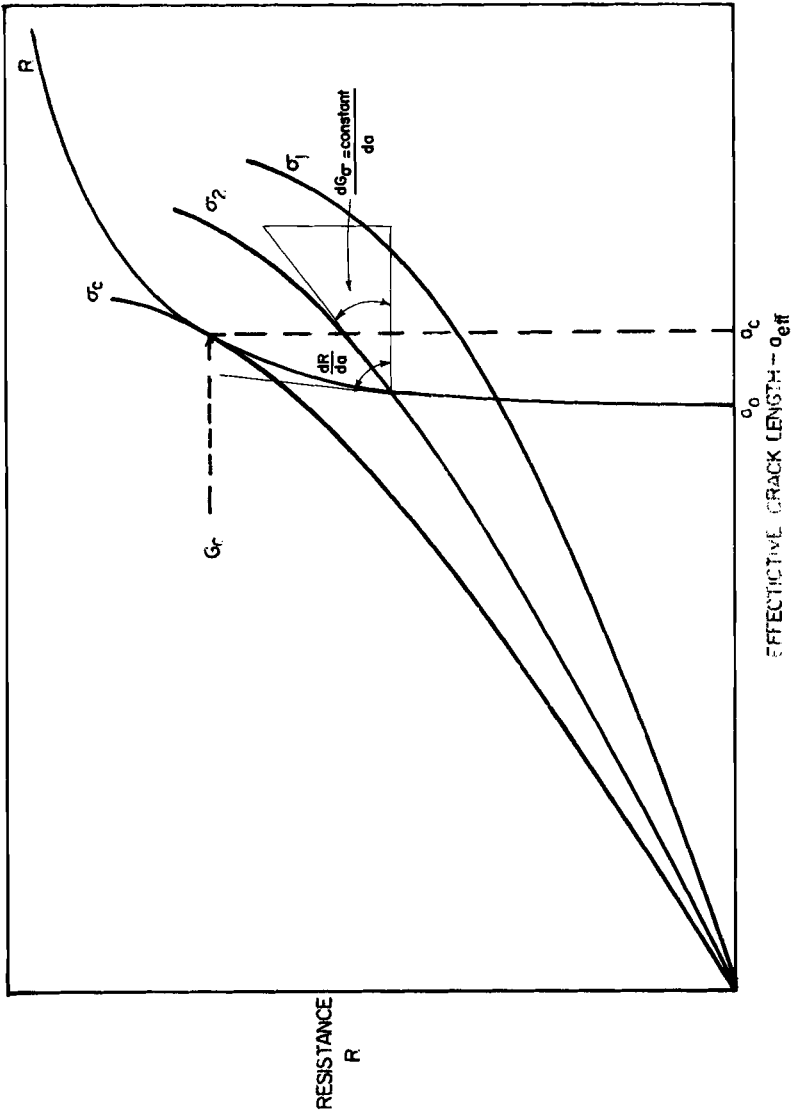


FIG. 1—Schematic representation of a R-curve.  $G_c$  represents the value of  $G$ , crack extension force, at instability.

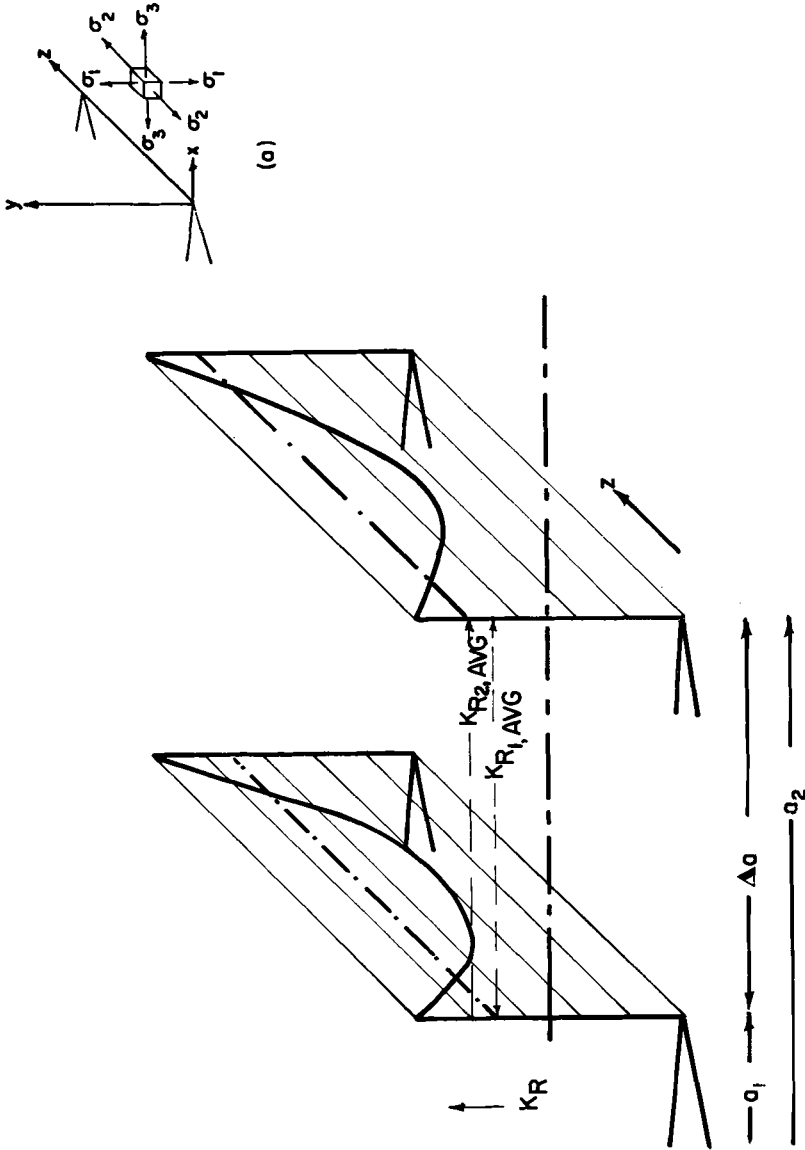


FIG. 2—(a) Coordinate system and (b) schematic illustration of local and average fracture resistance ( $K_R$ ) as a function of distance from the surface and crack length.

nately, experimental data on the values of  $\alpha(z)$  and  $\beta(z)$ , except for the limiting conditions of plane stress and of plane strain, are not available. For the present purposes a closed form solution which is believed to represent a fair approximation was developed, as indicated next.

At the surface, that is, at  $z = 0$  and  $z = t$ , where  $t$  is the plate or sheet thickness,  $\alpha = \sigma_2/\sigma_1 = 0$ . The value of  $\beta$  is not known; however, Allen's [8] study of the stress distribution in the plastic zone suggests a value of  $\beta$  at the surface to be between 0.55 and 0.65 and its variation with thickness to be rather small. At any location at the crack front, where the plane strain condition is reached,  $\alpha = 0.81$  and  $\beta = 0.61$ , as determined from slip-line field theory [9]. It was assumed that  $\alpha$  changes from 0 at the surface to 0.81 under plane strain and that  $\beta$  remains constant at 0.61. For  $\alpha$  the form

$$\alpha = \frac{0.81}{Q} \left[ \frac{z}{\{1 + (z/Q)^u\}^{1/u}} \right] \quad (2)$$

is suggested. For low  $z/Q$  values,  $\alpha$  increases linearly, turns around at  $z \approx Q$  and asymptotically approaches 0.81 for  $z \rightarrow \infty$ . The sharpness of the transition is determined by the choice of the exponent  $u$ .  $Q$  is a measure of the transition zone, the region from the surface to where plane strain is reached, and will be related to the plastic zone size  $r_p$ . Figure 3 shows  $\alpha$  as a function of  $z/Q$  for  $u = 4$ . As illustrated, a plane strain condition is nearly reached at  $z = Q$ .

#### *Relationship Between Stress State and Ductility*

For the effect of stress state on fracture ductility Weiss [6] proposed a volume strain fracture criterion. Accordingly

$$\frac{\bar{\epsilon}_{F,\alpha\beta}}{\bar{\epsilon}_{TF}} = (WM)^{1/n} \quad (3)$$

where  $\bar{\epsilon}_{F,\alpha\beta}$  is the effective fracture strain for the stress state  $(\alpha, \beta)$ ;  $\bar{\epsilon}_{TF}$  is the fracture ductility in tension, that is,  $\alpha = 0, \beta = 0$ ;  $n$  is the strain hardening coefficient in the exponential stress strain relation  $\bar{\sigma} = k\bar{\epsilon}^n$ ,

$$W = \frac{1}{1 + \alpha + \beta},$$

$$M = \{(1 + \alpha + \beta)^2 - 3(\alpha + \beta + \alpha\beta)\}^{1/2}$$

Using the balanced biaxial or bulge ductility  $\bar{\epsilon}_{F,\alpha=1,\beta=0}$  as a reference, the foregoing relationship becomes

$$\bar{\epsilon}_{F,\alpha\beta} = (2WM)^{1/n} \bar{\epsilon}_{F,\alpha=1,\beta=0} \quad (4)$$

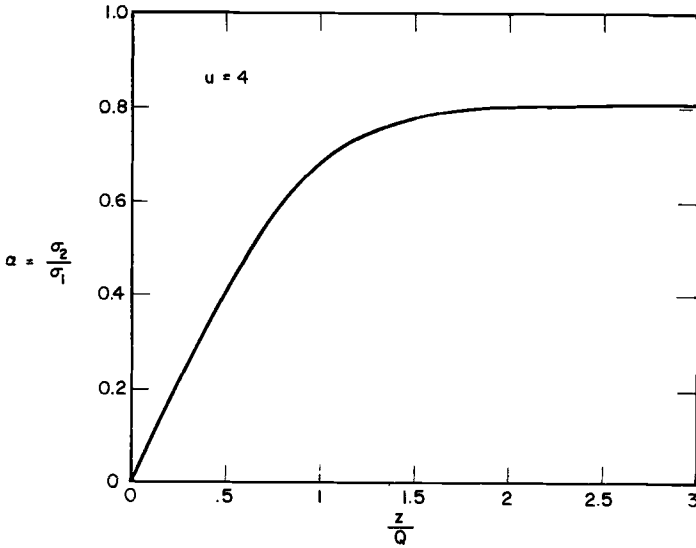


FIG. 3—Distribution of stress ratio  $\alpha$  as a function of the location ( $z/Q$ ) below the specimen surface as predicted by Eq 2.

#### *Variation of Local Fracture Ductility and Fracture Resistance Through the Thickness Along the Leading Edge of the Crack*

Combining Eqs 2 and 4 one obtains the local effective fracture strain distribution along the crack front. The distribution of the ratio ( $\bar{\epsilon}_{F,\alpha\beta}/\bar{\epsilon}_{F,\alpha=1,\beta=0}$ ) as a function of  $z/Q$ , the distance from the surface, has been calculated on the computer and is shown in Fig. 4 for  $n = 1$ .<sup>3</sup> The fracture strain has its maximum at the surface and decreases with distance from the surface until it reaches the plane strain value. The local fracture resistance  $K_R$ , in terms of stress intensity units, can be related to the multiaxial fracture ductility through Eq 1, and its variation with the distance from the surface along the leading edge of the crack will be similar to the ductility distribution shown in Fig. 4. The low fracture resistance in the interior explains the crack tunnelling effect frequently observed during experiments.

<sup>3</sup> It should be noted that the  $n$  value as used here is not the conventional  $n$  value obtained from logarithmic plastic strain versus stress plots. Rather it is that value of  $n$  which best characterizes the effective stress strain curve  $\bar{\sigma} = K\bar{\epsilon}^n$ , where  $\bar{\epsilon}$  is the total strain, from zero load to the onset of fracture. Experimental  $K_{Ic}$  versus  $\epsilon_{F,\alpha=1,\beta=0}$  relationships obtained from Eq 1 correlate well with the assumption of  $n = 1$  [10]. Ductility relationships are in good agreement with  $0.45 \leq n \leq 1$  [11]. For the sake of simplicity the following development assumes  $n = 1$ ; however, a correction for other values of  $n$  can be incorporated.

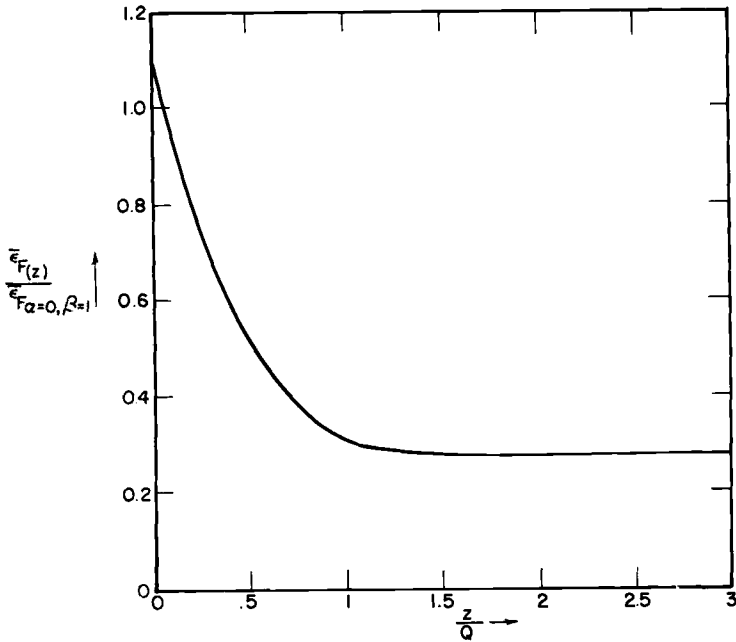


FIG. 4—Variation of local fracture ductility as a function of the distance ( $z/Q$ ), below the specimen surface as predicted by Eq 4, with  $n = 1$ .

*Average Fracture Resistance*

The average fracture resistance value for a specimen of a given thickness is obtained from the local  $G_R(z)$  or  $R(z)^4$  values as

$$R = \frac{1}{t} 2 \int_0^{t/2} R(z) dz \tag{5}$$

From Eq 1, the local fracture resistance,  $R(z)$  is written as

$$R(z) = ES\rho^*(\bar{\epsilon}_F)^2(z) \tag{6}$$

Rewriting Eq 5, one obtains from Eqs 4 and 6

$$\bar{R} = ES\rho^*(\bar{\epsilon}_{F,\alpha=1,\beta=0})^2 \frac{2}{t} \int_0^{t/2} (2WM)^2 dz \tag{7}$$

$$n = 1$$

<sup>4</sup> Note that the average is taken over the local  $G_R$  (energy release rate resistance) and not  $K_R$  (stress intensity) values, following the practice by Bluhm [12] for similar calculations.

When the plate thickness is such that the plane strain condition prevails over a substantial portion of the crack front,  $\bar{\epsilon}_F(z)$  is essentially the same as  $\bar{\epsilon}_F$  (plane strain) and the corresponding  $WM$  value (for  $\alpha = 0.81$  and  $\beta = 0.61$ ) is 0.1395. Since the average fracture resistance under this condition is the plane strain crack extension force  $G_{Ic}$ , one obtains

$$G_{Ic} = ES\rho^*(0.279)^2(\bar{\epsilon}_F)^2, \alpha=1, \beta=0 \quad (8)$$

Eliminating the ductility term from Eq 7 by using Eq 8

$$R = \frac{G_{Ic}}{(0.279)^2} \frac{2}{t} \int_0^{t/2} (2WM)^2 dz \quad (9)$$

Since  $\alpha, \beta$  can be expressed as a function  $z$  (Eq 2),  $W(z)M(z)$  is known, and  $R$  can be obtained as a function of thickness for any given material. Because of the form of Eq 2,  $\bar{R}$  is determined completely by  $R_{max}$  (plane stress fracture resistance) or  $R_{min}$  (plane strain fracture resistance) and the ratio  $(Q/t)$ . Since  $Q$  is assumed to be a multiple of the plastic zone size  $r_p$ ,  $(Q/t)$  is also proportional to  $(r_p/t)$  or to  $(G/t)$ . Figure 5 shows the results of a computer calculation of  $\bar{R}$  versus  $(Q/t)$  for 7075-T6 aluminum.

### Thickness Effect

In order to utilize the above concept to predict the effect of thickness on fracture resistance, the  $\bar{R}$  versus  $(Q/t)$  relationship has to be translated to  $\bar{R}$  versus  $(G/t)$  relationship. According to the model,  $Q$  is proportional to  $r_p$ , that is

$$Q = Dr_p = FG \quad (10)$$

where  $F = DE/2\pi\sigma_y^2$ , is a material constant. For precise conversion of  $Q$  to  $G$ , it is necessary to know the value of  $D$ . Previous studies [13] indicate that  $D = 4$  represents a reasonable estimate. With 7075-T6 aluminum ( $\sigma_y = 66$  ksi and  $E = 10 \times 10^3$  ksi),  $F \approx 1.5$  (ksi)<sup>-1</sup>. From Fig. 5 and from the condition  $R = G$  for crack advance, we obtain the desired  $R$  versus thickness relationship as shown in Fig. 6. Figure 7 shows the predicted fracture resistance in terms of stress intensity units,  $K_{Rc}$ , as a function of thickness for three chosen values of  $G_{Ic}$ . The experimental values of  $K_{Ic}$  for various thickness for 7075-T6 and T651 aluminum along with the range of  $K_{Ic}$  values reported by Kaufman [14] are also identified in the same plot. Comparison of the experimental values with those predicted by the model shows good agreement with  $G_{Ic} = 61.5$  in·lb/in.<sup>2</sup> corresponding to  $K_{Ic} = 26$  ksi $\sqrt{\text{in}}$ .

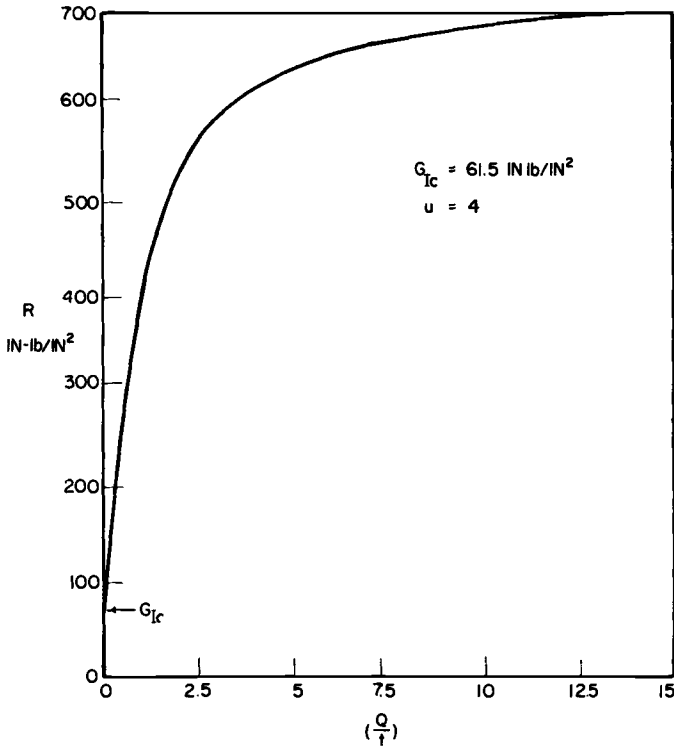


FIG. 5—Average fracture resistance,  $\bar{R}$  versus  $(Q/t)$  or  $(r_p/t)$  curve for aluminum alloy 7075-T6, calculated from Eq 9.

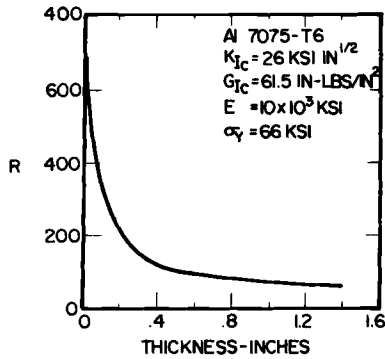


FIG. 6—Average fracture resistance  $\bar{R}$  versus thickness calculated for aluminum alloy 7075-T6.

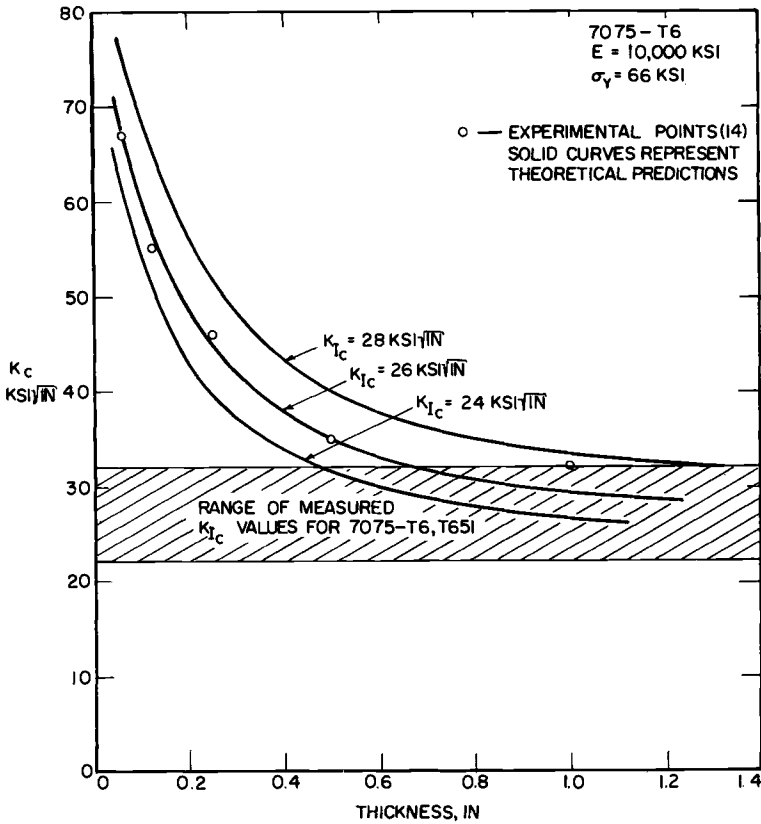


FIG. 7—Experimental and theoretical fracture toughness values for aluminum alloy 7075-T6 and T651 as a function of thickness.

### R-Curves

It should be possible to extend these considerations to obtain an expression for R-curves, that is, to obtain a relationship  $R = f(a_0 + \Delta a)$ . A schematic illustration of the model is given in Fig. 2. From this and from Fig. 5 it is clear that increasing the plastic zone size increases the average crack extension resistance  $R$ . The problem is to obtain an expression between  $Q$  or  $r_p$  and the instantaneous crack length  $a$ . No such relation is readily available. It might, however, be possible to obtain one as follows. The plastic zone size at crack crack advance,  $R = G$  is known to be a linear function of  $R$ , that is

$$r_p = AR = AG = A\sigma^2 g(a/w) \quad (11)$$

where

$A$  = proportionality constant,

$g(a/w)$  = function of the specimen geometry and type of loading according to ASTM Test for Plane-Strain Fracture Toughness of Metallic Materials (E 399-73),

$a$  = crack length, and

$w$  = specimen width.

From Eq 11 we obtain

$$dG_{\sigma = \text{const}} = Gd \ln g(a/w) \quad (12)$$

and since  $G = R$

$$\frac{dR}{dG_{\sigma = \text{const}}} = \left( \frac{G_c}{R} \right)^\alpha = \frac{dR}{R \ln g(a/w)} \quad (13)$$

Equation 13 can be integrated and yields for the R-curve

$$R_a^\alpha = R_{a_0}^\alpha + \alpha \ln \frac{g(a/w)}{g(a_0/w)} \quad (14)$$

Figure 8 shows a family of curves according to Eq 14 with  $R_{a_0} = 0$  and  $\alpha = 1, 2, 3,$  and  $4$ .

The proposed model was tested on R-curves obtained from D. E. McCabe<sup>5</sup> on 7079-T6 aluminum, 7475-T761 aluminum, and PH 14-8Mo stainless steel. The  $K_R$  curves for these materials are shown in Fig. 9. From the points of tangency of R-curve and G-curve, the value of  $G_c$  (or  $K_c$ ) at instability is obtained. Using these values in Eq 14,  $K_R$  is calculated as a function of  $\Delta a$ . The predicted  $K_R$  curves,  $\alpha = 4$ , for 7079-T6 aluminum, 7475-T651 aluminum, and PH 14-8Mo stainless steel are also shown in Fig. 9. The approach presented here needs further experimental verification, especially with respect of the applicability of Eq 13. Furthermore, a more accurate solution would require a numerical treatment based on Eq 9 which can be readily carried out on a computer.

#### Acknowledgment

The work presented here was sponsored by the United States Navy Air Systems Command, Contract No. N-62269-73-C-0261. The authors gratefully acknowledge this support as well as the special interest and encouragement of R. Schmidt, S. Goldberg, and M. Valentine. The au-

<sup>5</sup> Private communications, 18 Jan. 1974; D. E. McCabe, senior research metallurgist, Armco Steel Corporation, Middletown, Ohio 45042.

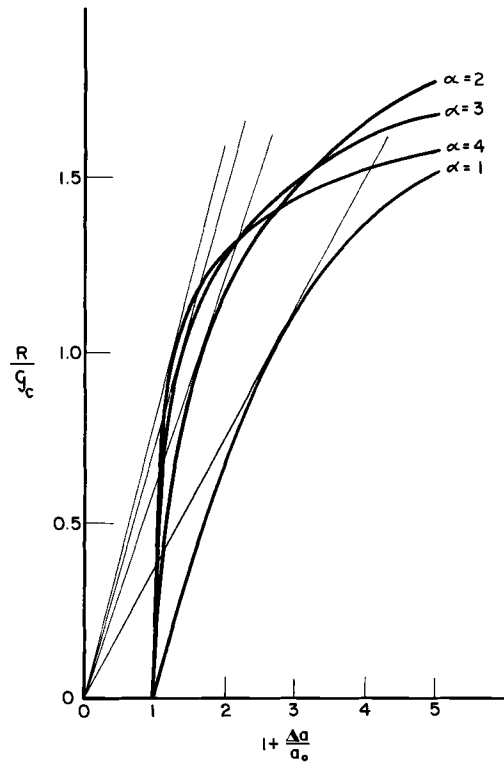


FIG. 8—Normalized *R*-curves according to Eq 14.

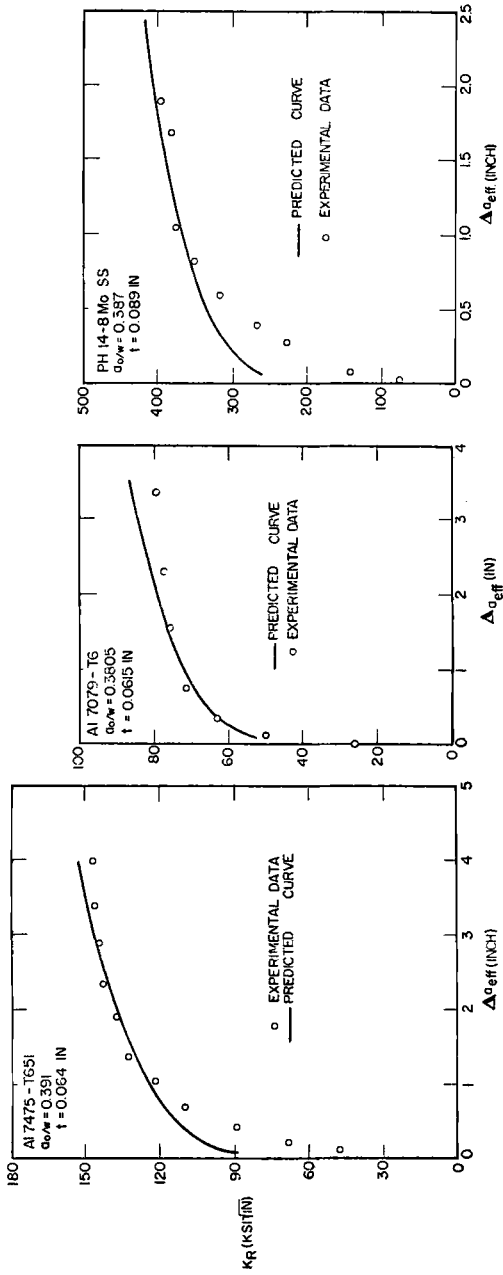


FIG. 9.—Predicted and experimental  $K_R$  curves for three materials, as indicated. The predicted curves are according to Eq 14 with  $R_0 = 0$  and  $\alpha = 4$ .

thors wish to express special thanks to Prof. H. W. Liu for his valuable advice in the revision of the manuscript.

### References

- [1] Irwin, G. R., Report of a Special Committee, "Fracture Testing of High Strength Sheet Materials," *ASTM Bulletin*, Jan. 1960, p. 29.
- [2] Irwin, G. R., "Fracture Testing of High Strength Sheet Materials Under Conditions Appropriate for Stress Analysis," Report No. 5486, Naval Research Laboratory, July 1960.
- [3] Srawley, J. E. and Brown, W. F., Jr., in *Fracture Toughness Testing and Its Applications*, *ASTM STP 381*, American Society for Testing and Materials, 1965, p. 133.
- [4] Heyer, R. H. and McCabe, D. E., *Engineering Fracture Mechanics*, Vol. 4, No. 3, 1972, p. 393.
- [5] Heyer, R. H. and McCabe, D. E., *Engineering Fracture Mechanics*, Vol. 4, No. 3, 1972, p. 413.
- [6] Weiss, V. in *Proceedings of the International Conference on Mechanical Behavior of Materials*, Kyoto, Japan, 1971, Vol. 2, p. 458.
- [7] Weiss, V. and Sengupta, M. in *Proceedings of the Third International Conference on Fracture*, Munich, Germany, April 1973, Chapter III, p. 341.
- [8] Allen, F. C. in *Damage Tolerance in Aircraft Structures*, *ASTM STP 486*, American Society for Testing and Materials, 1971, p. 16.
- [9] Hill, R., *Mathematical Theory of Plasticity*, Clarendon Press, Oxford, England, 1950.
- [10] Weiss, V., Sengupta, M., and Sanford, W., "Significance of Material Ductility to the Reliability and Load-Carrying Capacity of Peak Performance Structures," Final Report to NASC, No. MTS-VW-1708-F674, Syracuse University, Syracuse, N.Y., 1974.
- [11] Sailors, R. H., "Relationship Between Tensile Properties and Microscopically Ductile Plane Strain Fracture Toughness," Ph.D. dissertation University of Illinois, Urbana, Ill., 1973.
- [12] Bluhm, J. I., "A Model for the Effect of Thickness on Fracture Toughness," *Proceedings*, American Society for Testing and Materials, Vol. 61, 1961, p. 1324.
- [13] Weiss, V. in *Treatise on Fracture*, Vol. III, H. Liebowitz, Ed., Academic Press, New York, 1968, p. 227.
- [14] Kaufman, J. G. in *Review of Developments in Plane-Strain Fracture Toughness Testing*, *ASTM STP 463*, American Society for Testing and Materials, 1971, p. 3.

R. L. Lake<sup>1</sup>

## What R-Curves Can Tell Us About Specimen Size Effects in the $K_{Ic}$ Test

---

**REFERENCE:** Lake, R. L., "What R-Curves Can Tell Us About Specimen Size Effects in the  $K_{Ic}$  Test," *Mechanics of Crack Growth, ASTM STP 590*, American Society for Testing and Materials, 1976, pp. 208–218.

**ABSTRACT:** Size effects in the  $K_{Ic}$  test were investigated by testing duplicate compact specimens in ten different combinations of five thicknesses and five widths. Curves of crack resistance as a function of crack extension were calculated in terms of strain energy release rate,  $G$ , rather than stress intensity factor,  $K$ . It was found that the entire set of data could be represented by a single linear equation of the form,  $R = R_o + \rho\Delta a$ . The coefficient,  $\rho$ , was found to be an inverse function of specimen thickness.

When this family of R-curves is compared with the driving force,  $G$ , curves for the various specimen sizes, it can be seen that the ratio of maximum load to the measuring point load ( $P_{max}/P_Q$ ) in the record of a plane strain toughness test, depends primarily on the width/thickness ratio of the specimen. This ratio appears to bear no relation to the contribution of crack tip plasticity to the apparent crack extension at the measuring point. Accordingly, inclusion of a maximum value of this ratio in the validity requirements of ASTM Method E 399 for the purpose of restricting such a contribution is questioned.

**KEY WORDS:** crack propagation, fracture tests, crack initiation, aluminum alloys, toughness, plastic analysis, strains, stresses

To obtain greater assurance of linear elastic behavior in the  $K_{Ic}$  test, material specifications for the B-1 bomber required the use of specimens having in-plane dimensions substantially greater than those required by ASTM Test for Plane-Strain Fracture of Metallic Materials (E 399). This requirement had two effects. First, because the measuring point in ASTM Method E 399 is a function of relative, rather than absolute, crack extension, the larger specimens tend to give slightly higher values of  $K_{Ic}$ .

<sup>1</sup>Staff research engineer, Engineering Properties Section, Kaiser Aluminum and Chemical Corporation, Pleasanton, Calif. 94566.

Second, because the specimen thickness requirement of ASTM Method E 399 was unchanged, the use of specimens with  $W > 2B$ ,<sup>2</sup> called the "alternate specimen" in ASTM Method E 399, was encouraged. The full consequences of the latter effect were not immediately apparent.

The author's company had made measurements to determine  $K_{Ic}$  values on a considerable number of lots of 2000 and 7000 series aluminum alloy plate to establish a data base for statistical characterization of toughness resulting from normal production practices. The standard,  $W = 2B$ , specimen had been used for this work, and the larger specimen would certainly produce an upward shift in the data base. A preliminary investigation of specimen size effects was undertaken in an effort to assess the nature and extent of this shift without retesting all of this material.

### Material

A lot of 2 1/2-in.-thick 2124-T851 alloy plate was chosen, more or less at random, from among those available. The chemical analysis of this plate is shown in Table 1, together with the composition limits published by the Aluminum Association for this alloy. The composition was typical for the alloy as it was then being produced.

All of the toughness tests to be reported here were in the L—T orientation; hence, only the longitudinal tensile properties are of interest. They are: ultimate tensile strength — 71.6 ksi; yield strength (0.2 percent offset) — 67.3 ksi; and elongation in 4 diameters 6.8 percent. The yield strength was somewhat above the typical value published by the Aluminum Association but not unusually so.

Duplicate measurements of toughness by ASTM Method E 399 using compact specimens ( $B = 1$  in.,  $W = 2$  in.) centered at quarter thickness, gave valid  $K_{Ic}$  values of 25.4 and 25.0 ksi $\sqrt{\text{in}}$ . The minimum thickness for a plane strain test was, therefore, a bit less than 3/8 in.

### Procedure

All tests were in strict compliance with ASTM Method E 399 with the exception of some specimen dimensions.

Since a more accurate compliance curve was not immediately available, R-curves were calculated with the help of a curve "eyeballed" through pairs of values of  $a/W$  and  $EBv/P$  obtained from the measured specimen dimensions and initial slopes of the load displacement records, respectively, of some 125  $K_{Ic}$  tests. The  $a/W$  values ranged from 0.423 to 0.650. This curve has since been compared with values of  $EBv/P$  calculated from Table 2, ASTM Proposed Recommended Practice for R-Curve Determi-

<sup>2</sup>Throughout this paper any notation pertaining to specimen dimensions is that of ASTM Method E 399.

TABLE 1—Chemical composition of test material.

|                                | Si   | Fe   | Cu   | Mn   | Mg   | Cr   | Zn   | Ti   | Others               |
|--------------------------------|------|------|------|------|------|------|------|------|----------------------|
| Test material                  | 0.04 | 0.08 | 4.34 | 0.69 | 1.47 | 0.00 | 0.02 | 0.02 | not analyzed         |
| Aluminum Association<br>limits |      |      |      |      |      |      |      |      |                      |
| Min                            | ...  | ...  | 3.8  | 0.3  | 1.2  | ...  | ...  | ...  |                      |
| Max                            | 0.20 | 0.30 | 4.9  | 0.9  | 1.8  | 0.10 | 0.25 | 0.15 | 0.05 each 0.15 total |

TABLE 2—Comparison of empirical compliance calibration with one based on Table 2 of Proposed Recommended Practice for R-curve Determination.

| $a/w$ | $EBv/P$<br>Empirical | $EBv/P$ , Table 2<br>of Recommended Practice | Difference, % |
|-------|----------------------|--|---------------|
| 0.425 | 40.06                | 40.99  | -2.32         |
| 0.450 | 44.48                | 45.21  | -1.64         |
| 0.475 | 49.68                | 50.05  | -0.74         |
| 0.500 | 55.64                | 55.61  | +0.05         |
| 0.525 | 62.22                | 62.08  | +0.22         |
| 0.550 | 69.36                | 69.66  | -0.43         |
| 0.575 | 77.47                | 76.67  | +1.03         |
| 0.600 | 87.66                | 89.50  | -2.10         |

nation.<sup>3</sup> Calculation was made by linear extrapolation from values of  $EBv/P$  at the load line and 0.1576  $W$  outside the load line to the specimen face, 0.25  $W$  from the load line. Results are shown in Table 2.

Initial slope versus  $a/W$  data seem to be characterized by considerable scatter. At least this was found to be the case in setting up the compliance curve and in constructing the R-curves. This scatter was treated as though it resulted from variations in  $E$ . All slopes from a particular test were multiplied by the factor necessary to make the initial slope equal to that which, according to the compliance curve, corresponded to the measured value of  $a_o/W$  for that specimen.

### Results and Discussion

The work was carried out in two phases with somewhat different objectives. During the first, which was frankly exploratory, interest was primarily in obtaining a feel for the test—seeing if there were any experimental difficulties with the relatively thinner specimen and making a rough estimate of the size effect. Duplicate specimens were tested in three sizes:  $B = 1$  in.;  $W = 4$  and 6 in.; and  $B = 2$  in.,  $W = 4$  in.

Results of these tests compared about as expected with the results from the earlier  $B = 1$ -in.,  $W = 2$ -in. specimens. There was a size effect.  $K_{Ic}$  values for the 1-in.-thick specimens increased from 1 to 1 1/2  $\text{ksi}\sqrt{\text{in.}}$  with each 2 in. increase in  $W$ , and the 2-in.-thick specimens gave slightly lower values than 1-in.-thick specimens of the same width. One aspect of the results was very disturbing, however. Both sets of “standard” specimens gave completely valid results. Both sets of “alternate” specimens, in which  $W > 2B$ , failed to meet the  $P_{\max}/P_Q < 1.10$  requirement of ASTM

<sup>3</sup>1974 Annual Book of ASTM Standards, American Society for Testing and Materials, pp. 669-683.

Method E 399. Visual examination showed that the standard specimens simply did not provide enough crack extension to allow the shear lips to reach their equilibrium size. At this point, R-curves were constructed for all eight specimens to see if they could shed further light on the reasons for the invalidity of the alternate specimens. They only added to the confusion since the curves for all six of the 1-in.-thick specimens fell within a narrow band whose limits were set by the two specimens with  $W = 4$  in. The band was no wider than would be expected from the same number of "identical" specimens, and the data from the two larger sizes should have been just as valid as that from the smaller.

The purpose of the  $P_{\max}/P_Q$  requirement is stated in footnote 4 where it says, with respect to a proposal to establish a limit on this ratio,

The rationale behind this suggestion was to provide a restriction on the contribution of crack tip plasticity to the displacement at the measurement point  $P_Q$ . The inherent assumption is that as the plasticity contribution to  $P_Q$  increases, it will be reflected in the increasing amounts of stable crack extension under rising load, and consequently in a progressively higher ratio of  $P_{\max}/P_Q$  . . .

It is difficult to see how this reasoning applies in the present case. Plasticity at the crack tip should result from one or the other of two causes, acting alone or together. If the crack length were too short, linear elasticity could be violated, or, if the specimen were not thick enough, through-the-thickness yielding could occur. The in-plane dimensions could hardly be at fault here, for it was the data from the longer crack lengths which were being rejected. Nor could the thickness be too small to provide plane strain restraint, since standard specimens of the same thickness gave valid results. Indeed, a specimen less than half as thick would have met the plane strain requirements of ASTM Method E 399. Evidently there was something special about the proportions of the standard specimen, and more testing with several different specimen sizes would be necessary to find out what it was.

For the second phase of the investigation, duplicate specimens in six more sizes were machined from the broken halves of those already tested. The new sizes were  $B = 1/4$  in.,  $W = 1$  in., and  $W = 2$  in.;  $B = 1/2$  in.,  $W = 1$  in., and  $W = 2$  in.; and  $B = 3/4$  in.,  $W = 1\ 1/2$  in., and  $W = 2$  in. Some idea of the range of specimen sizes may be gained from Fig. 1. Again, all of the standard specimens gave valid  $K_{Ic}$  values, and all of the alternate specimens, save one of the  $3/4$  by 2 in. size which squeaked by with a ratio of 1.09, failed to meet the  $P_{\max}/P_Q$  requirement.

<sup>4</sup>Brown, W. F., Revision of E 399-70 T, Memorandum to Members of E 399-70 T Revision Task Group, and E-24 Executive Committee, 23 Sept. 1971.

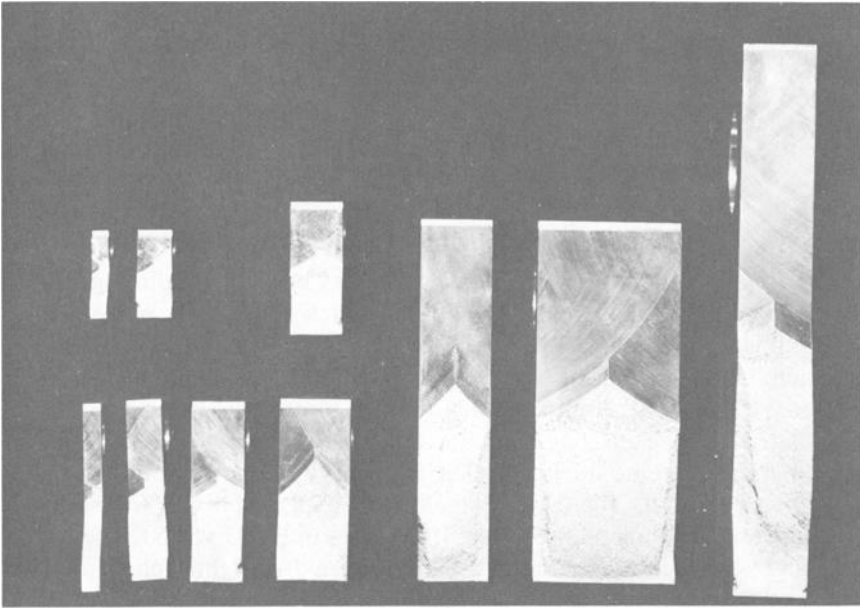


FIG.1—Range of compact specimen sizes. The smallest was 1/4 in. thick; the largest was 2 in. thick.

Following the publication of the R-curve approach contained in the J-integral guidelines,<sup>5</sup> it was decided to plot our resistance curves in terms of  $G$  rather than  $K$ . The picture which resulted from this approach was surprisingly consistent. The curves were essentially straight lines sharing a common intercept on the  $G$  axis and having slopes which decreased regularly with specimen thickness. Using least square methods, we fitted an equation of the form

$$R = R_0 + \rho \Delta a$$

to each of the sets of crack resistance data. The number of points per set ranged from 8 to 18, averaging just over 14. In every case, the data points extended beyond the maximum of the load displacement curve. The values of  $R_0$  and  $\rho$  obtained from the fitting process are listed in Table 2.

The values of the slope parameter,  $\rho$ , appeared to be such a regular function of thickness that a least square fit was attempted here also. The quantity  $\beta_{1c} = (K_{1c}/\sigma_y)^2/B$  was chosen as the thickness variable. A value of  $K_{1c} = 23.7 \text{ ksi}\sqrt{\text{in.}}$ , obtained by the usual relation,  $K = \sqrt{GE}$ , from a

<sup>5</sup> ASTM Task Group E24.01.09 Guidelines for  $J_{1c}$  Tests, distributed with the minutes of the 10 Oct. 1973 meeting of the Task Group.

value of  $G$  which was the average of the 20 values of  $R_0$  listed in Table 3 was used to calculate  $\beta_{1c}$ .  $(K_{1c}/\sigma y)^2$  turned out to be 0.124 in. Again, a linear relationship was found. All of the data, over 280 points on 20 curves, can be represented by the single equation

$$R = 53 + (2787\beta_{1c} - 57)\Delta a$$

where the units of  $R$  are inch-pounds per square inch.

The fit of the equation to the data points may be judged from Figs. 2 and 3 showing the curves for the 1/4 and 2-in.-thick specimens, respectively. In each figure the lines are derived from the foregoing equation. (All lines in each figure represent the same calculated R-curve, displaced as necessary to avoid confusion among the plotted points.) The points associated with each line are the actual data points for a different specimen of the same thickness. The first curve in Fig. 2 should probably have been omitted. The fatigue crack in this specimen was too short on one side and too long on the other. If the lines in Fig. 3 seem too low with respect to the points, remember that they were drawn through an average value of  $G_0$  obtained from 20 curves.

An explanation of the  $P_{\max}/P_Q$  problem is fairly apparent in Fig. 4 where the family of R-curves represented by the single equation given earlier (dashed lines) are superimposed on the family of curves showing

TABLE 3—Equations for R-curves.

| Specimen | $W$ , in. | $B$ , in. | $R$ , in. lb/in. <sup>2</sup> |
|----------|-----------|-----------|-------------------------------|
| 1        | 1         | 1/4       | 42.7 + 1207 $\Delta a$        |
| 2        | 1         | 1/4       | 49.0 + 1421 $\Delta a$        |
| 3        | 2         | 1/4       | 58.8 + 1378 $\Delta a$        |
| 4        | 2         | 1/4       | 49.0 + 1430 $\Delta a$        |
| 5        | 1         | 1/2       | 52.4 + 606 $\Delta a$         |
| 6        | 1         | 1/2       | 56.9 + 741 $\Delta a$         |
| 7        | 2         | 1/2       | 51.3 + 634 $\Delta a$         |
| 8        | 2         | 1/2       | 48.2 + 556 $\Delta a$         |
| 9        | 1 1/2     | 3/4       | 50.5 + 360 $\Delta a$         |
| 10       | 1 1/2     | 3/4       | 53.6 + 419 $\Delta a$         |
| 11       | 2         | 3/4       | 48.5 + 394 $\Delta a$         |
| 12       | 2         | 3/4       | 53.3 + 361 $\Delta a$         |
| 13       | 2         | 1         | 55.8 + 297 $\Delta a$         |
| 14       | 2         | 1         | 50.9 + 335 $\Delta a$         |
| 15       | 4         | 1         | 54.8 + 289 $\Delta a$         |
| 16       | 4         | 1         | 53.3 + 321 $\Delta a$         |
| 17       | 6         | 1         | 55.2 + 289 $\Delta a$         |
| 18       | 6         | 1         | 59.0 + 279 $\Delta a$         |
| 19       | 4         | 2         | 57.6 + 117 $\Delta a$         |
| 20       | 4         | 2         | 59.9 + 114 $\Delta a$         |

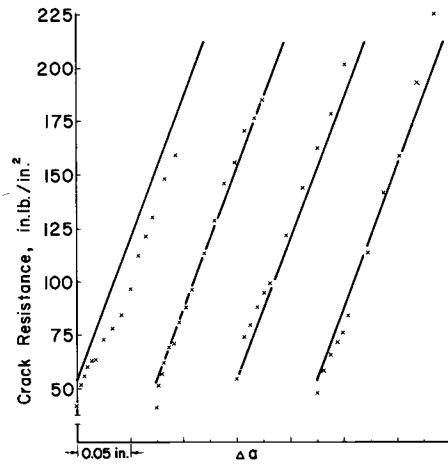


FIG. 2—Comparison of experimental and fitted R-curves. The points associated with each line were calculated from the load-displacement record of a different 1/4-in.-thick compact specimen. Both  $W = 1$ -in. (left two curves) and  $W = 2$  in. specimens are represented.

the change in  $G$  with  $a$  at constant load (solid lines) for each of the specimen sizes tested. The  $G$ -curves are all drawn on the assumption that the initial value of  $a/W$  was 0.45.

The standard specimen does possess special properties, at least for materials with the general level of crack initiation toughness shown here. The initial slope of the  $G$ -curve for a particular specimen size is just

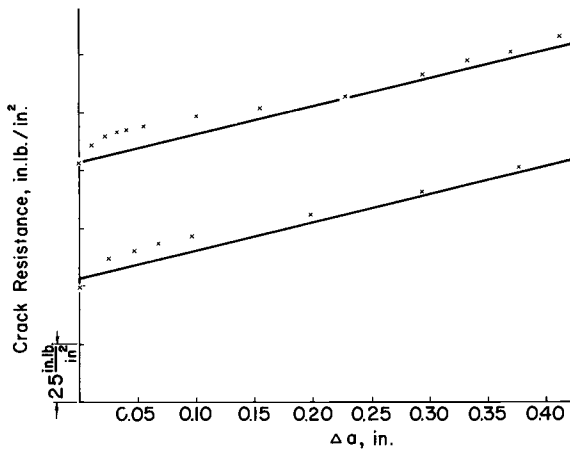


FIG. 3—Further comparison of experimental and fitted R-curves. The points were derived from the test records of the 2-in.-thick specimens.

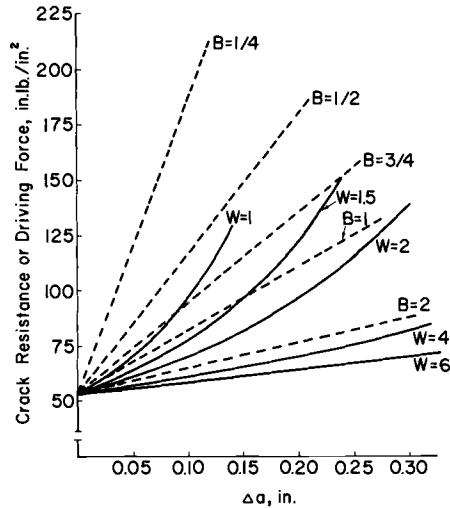


FIG. 4—Comparison of crack resistance curves (dashed lines) with crack driving force curves (solid lines).

slightly less than the slope of the R-curve for the corresponding thickness. Only a modest increase in load is required to bring the two curves into tangency. When a thinner alternate specimen is used, a much greater increase is necessary to elevate and rotate the G-curve by the required amount.

If a material of greater initiation toughness were being considered, the R-curves would be moved up in the diagram. We can only speculate as to how their slopes might change. There is qualitative evidence that initiation and propagation toughness of aluminum alloys do not respond in the same way to changes in microstructure. It is known, however, that the G-curves will rotate to the left as they move up, and it is quite possible that the relatively thinner specimens might meet the  $P_{\max}/P_Q$  requirement under such circumstances.

It is clear that the  $P_{\max}/P_Q$  requirement rejected data from specimens showing excess plasticity but which nevertheless passed all of the validity checks of ASTM Method E 399-70 T. However, we believe the bad data were rejected for the wrong reason. At least some of the objectionable data cited in footnote 4 as having been rejected by the  $P_{\max}/P_Q$  test were obtained from specimens in which  $B < W/4$  — outside the range of sizes permitted by ASTM Method E 399. The reference does not list the proportions of the specimens from which the rest of the rejected data were obtained, but it does indicate that they were less than 0.2 in. thick. It seems reasonable that all of these small specimens would have employed the same  $W$  dimension to minimize the cost of test fixtures. Judging from

the thickness and proportions of the thinnest specimens listed,  $W$  was probably either  $5/8$  or  $3/4$  in. Even if it were as small as half an inch, the specimens could not have been of standard proportions.<sup>6</sup>

Before leaving Fig. 4, another interesting feature of these curves should be noted. The relative positions of the  $W = 1$ ;  $B = 1$ ; and the  $W = 2$ ,  $B = 2$  curves indicate that square specimens of this type should exhibit a classic "brittle" load-deflection curve with no slow crack growth. Is it coincidence that the J-integral guidelines recommend such a specimen with thickness equal to twice the unbroken ligament length to obtain crack initiation at maximum load?

Parenthetically, it should be noted that truly unstable crack propagation probably did not coincide with attainment of maximum load in any of these specimens. Certainly it did not in any of the standard specimens. Observation of the progress of the test and the very considerable crack extension which occurred under slightly decreasing load in such specimens indicate that complete fracture of the specimen could have been easily prevented by stopping cross-head motion after reaching maximum load.

To those familiar with the R-curve method which has been proposed for the determination of  $J_{1c}$ , these results should not be surprising. Both approaches construct a portion of the curve of crack resistance versus crack extension and extrapolate it back to zero crack extension to find the strain energy release rate at crack initiation. (There are minor differences, which can be easily reconciled, in the way in which the contribution of the crack tip plastic zone to effective crack extension has been handled.) Both approaches find the index of crack initiation toughness to be independent of thickness throughout most of the range. Both agree that the index is nearly equivalent to the  $K_{1c}$  value determined by ASTM Method E 399. The two approaches appear to be identical in principle. The main difference seems to be that one specimen is sufficient to provide the entire R-curve when we work in the range of small-scale yielding.

Such a unified picture of fracture under both large- and small-scale yielding seems to indicate a need to rethink and clarify the meaning of the terms "plane strain" and "plane stress fracture" and the material thickness range associated with each term. Certainly, it is no longer meaningful to classify a thickness as belonging to one regime or the other without specifying whether crack initiation or crack propagation is under consideration. In the case of crack initiation, the value,  $K_{1c}$ , which we are accustomed to think of as plain strain seems to apply at any thickness above the maximum at which full slant fracture can occur. If by

<sup>6</sup>It has since been learned, through private communication, that the  $W$  dimension of these specimens was, indeed, half an inch. Thus, they were within the requirements of ASTM Method E 399. They were "alternate" rather than "standard" specimens, and the conclusion is unchanged.

plane strain crack propagation we imply, as I think most of us do, propagation against a near constant crack resistance, then attention must be confined to material many times thicker than that normally associated with this term. A plate 4 to 5 in. thick would be required to obtain a substantially horizontal R-curve in the 2124-T851 used in this work. We wonder if it is useful to continue to apply these terms, implying contrasting behavior to what is becoming increasingly apparent as a continuous spectrum?

### **Conclusions**

We have found a pattern of fracture behavior for one aluminum alloy which distinguishes between crack initiation and crack propagation toughness. The former is independent of thickness, the latter strongly dependent on it. The pattern explains many of the size effects which have been observed in the  $K_{Ic}$  test. Inasmuch as many of these effects have been observed in alloys of different base metals, there is reason to believe that other materials will follow a somewhat similar pattern.

### *Acknowledgment*

The author would like to thank G. C. Wolfer, D. P. Stone, and J. R. Schultz for producing and testing the specimens used in this work and the Kaiser Aluminum and Chemical Corporation for permission to present the paper.

D. Munz,<sup>1</sup> K. H. Galda,<sup>1</sup> and F. Link<sup>1</sup>

## Effect of Specimen Size on Fracture Toughness of a Titanium Alloy

---

**REFERENCE:** Munz, D., Galda, K. H., and Link, F., "Effect of Specimen Size on Fracture Toughness of a Titanium Alloy," *Mechanics of Crack Growth, ASTM STP 590*, American Society for Testing and Materials, 1976, pp. 219–234.

**ABSTRACT:** This paper describes the effect of specimen size on slow crack growth and fracture toughness of the titanium alloy Ti-6Al-4V. The load versus crack opening displacement curve rises steeply after reaching the end of the linear part. Stable crack extension starts within the linear part of the  $P$ - $v$ -curve. The crack growth resistance curve is independent of thickness  $B$  until  $K_Q$  in the range  $2 < B < 20$  mm, leading to the conclusion that slow crack growth can occur in plane strain.

The secant method, leading to  $K_Q$  at 2 percent crack extension, yields a specimen geometry dependent fracture toughness.  $K_Q$  increases with width,  $W$  and is only slightly dependent on thickness,  $B$ .

The consequences of this behavior for fracture toughness determination in connection with the ASTM recommendation are discussed.

**KEY WORDS:** fracture properties, crack propagation, toughness, titanium alloys, tests

After the application of the Griffith concept on metallic materials by Irwin, the effect of the thickness of the material on the characteristic values of fracture toughness received research emphasis. During the first investigations the stress intensity factor at the onset of unstable crack propagation  $K_c$  was measured. It was established that  $K_c$  approaches a threshold with increasing thickness and that  $K_c$  increases with decreasing thickness and after reaching a maximum decreases again  $[1]$ .<sup>2</sup> Later, it was found that the threshold value, the fracture toughness  $K_{Ic}$ , could also be measured with thinner specimens, provided that in the center of the specimen there is small unstable crack propagation. This propagation

<sup>1</sup> DFVLR, Institut für Werkstoff-Forschung, Linder Höhe, Germany.

<sup>2</sup> The italic numbers in brackets refer to the list of references appended to this paper.

mode is characterized by a discontinuity (pop-in) of the load-crack opening displacement curve [2]. After the observation that the crack propagation can also occur continuously and that the crack opening displacement curve changes continuously from the linear to the nonlinear part, the secant method was introduced [3], leading to  $K_Q$ , corresponding to a crack growth of 2 percent (neglecting plasticity effects). Different investigations showed an increase of  $K_Q$  below a critical specimen thickness [3-5]. Therefore, for the determination of  $K_{Ic}$ , it was proposed that specimens be chosen with a thickness larger than a minimum value of  $B_c = 2.5 (K_{Ic}/\sigma_y)^2$ .

In *ASTM STP 463* results concerning the increase of  $K_Q$  with increasing thickness have been reported for the first time. May [6] observed this effect on a titanium alloy, whereas Jones and Brown [7] observed it on a 4340 steel for a small specimen width, whereas a decrease of  $K_Q$  was observed for larger specimen width. Brown and Srawley [7] traced the thickness effect to a thickness dependent crack growth resistance curve. Jones and Brown however, had not measured  $K-\Delta a$  curves, but determined  $\Delta a$  from the  $P-v$  diagram.

Finally Kaufman et al [9,10] have established an increase of  $K_Q$  with increasing specimen thickness for different aluminum alloys. By varying thickness  $B$  and width  $W$  it was found that  $K_Q$  is not a direct function of  $B$ , but of the crack length  $a_0$ . Crack growth resistance curves were not determined by Kaufman et al.

This paper presents results of experiments with the titanium alloy Ti-6Al-4V.  $K_Q$  and the crack growth resistance curve have been measured for different specimen geometries.

### Characteristic Values of Fracture Mechanics

In order to characterize the material behavior, some parameters must be calculated from the experimental results. In the following these parameters are summarized.

#### *Crack Growth Resistance Curves*

The behavior of a material with sharp cracks under increasing load can be described by the crack growth resistance curve ( $R-\Delta a$  or  $R-a$  curve, Fig. 1), indicating the energy growth necessary for crack propagation. Crack growth begins at a critical value  $R_e$ . With increasing crack growth  $R$  increases, reaching a maximum value  $R_u$ . Unstable crack growth occurs in a load controlled test if the  $G-a$  curve touches the  $R-a$  curve. Between  $R_e$  and  $R_c$  stable crack growth occurs.

The  $R-a$  curves are dependent on the stress state at the crack tip. It is possible that very thick specimens, where the plane strain state in the specimen center predominates, show no stable crack growth but unstable crack growth starts at  $R_e$ .

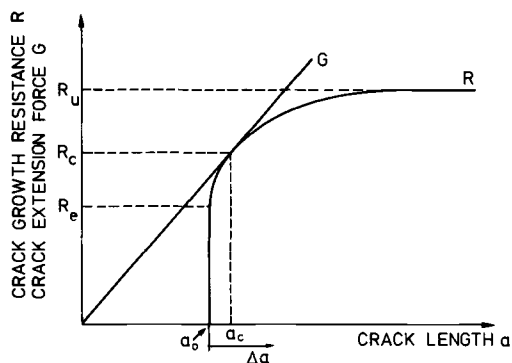


FIG. 1—Crack growth resistance—crack extension-curve.

The stress intensity factors corresponding to the  $R$  values are:

$K_e$ : At the onset of stable crack growth.

$K_c$ : At the onset of unstable crack growth.

$K_{Ic}$ : At the onset of unstable crack growth at plane strain state, for example, in very thick specimens.

For very thick specimens the threshold  $K_{Ie}$  of  $K_e$  should be equal to  $K_{Ic}$ . This point will be considered further.

According to common fracture mechanics concepts, the crack growth starts in the center of a specimen of medium size if  $K = K_{Ic} = K_{Ie}$ . With increasing  $K$  the crack front bows outwards until at  $K_c$  unstable crack growth occurs. Below a critical thickness  $B_c$ , the minimum thickness for  $K_{Ic}$  determination, there is also no plane strain state in the specimen center and therefore  $K_c$  is increasing with decreasing thickness (Fig. 2).  $K_c$  reaches the thickness independent value  $K_{Ic}$  at a thickness  $B_c$  larger than  $B_c$ .

#### *Load Versus Crack Opening Displacement Curves*

The evaluation of a load-crack opening displacement-curve yields the following  $K$  values:

$K_Q$ : From pop-in load or from load, determined according to the secant method.

$K_{Ic5}$ :  $K_Q$ , determined with the secant method, if all requirements of the ASTM recommendation are fulfilled.

$K_{max}$ : From maximum load and  $a = a_0$  (neglecting the stable crack growth).

$K_c$ : From load at the onset of unstable crack extension (in a load controlled experiment the maximum load) and the real crack

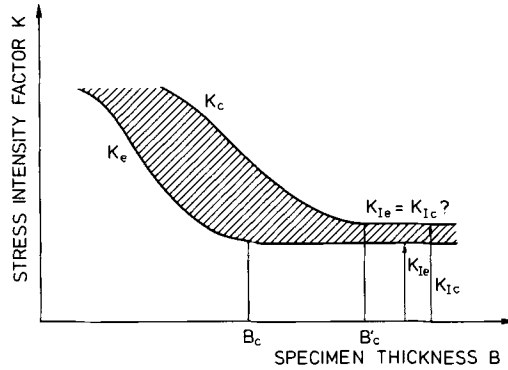


FIG. 2—Effect of specimen thickness on  $K_e$  and  $K_c$

length including the stable crack extension. Due to the curved crack front at the onset of unstable crack extension, the correct value of  $K_c$  is difficult to determine. The calculation is therefore done, assuming a straight through crack front.

$K_A$ : From load at the first deviation from the linear part of the  $P$ - $v$  diagram.

It is necessary to examine for a given material whether  $K_Q$  or  $K_{Ic5}$  is in agreement with  $K_{Ic}$  according to the preceding definition.

**Effect of Thickness on  $K_Q$**

*Different Components of Crack Opening Displacement*

The crack opening displacement, measured in a fracture mechanics test, can be separated into three components:

(a) *Elastic Deformation*—During elastic deformation the relation between the crack opening displacement  $v_{el}$  (measured with a clip gage) and the load is as follows

$$\frac{EBv_{el}}{P} = f\left(\frac{a}{W}\right) \tag{1}$$

(b) *Plastic Deformation at the Crack Tip*—Plastic deformation at the crack tip yields to an additional crack opening displacement  $v_{pl}$ . The relation between  $v_{pl}$  and load  $P$  or stress intensity factor  $K$  can only be approximately calculated. Brown and Srawley [8] have published results of finite element calculations, obtained by Swedlow and Roberts. Somewhat different results were obtained by Markström [11]. According to Markström [11] a relation exists for each material between the nondimen-

sional qualities  $K_I/\sigma_y\sqrt{B}$  and  $v_{pl}/v_{el}$  for specimens with a fixed ratio crack length  $a_0$ : specimen width  $W$ : specimen thickness  $B$ . Given the validity of this relation, it becomes possible to modify the relations of Swedlow and Roberts for other specimen sizes.

(c) *Crack Extension*—During a crack extension  $\Delta a$ , the function  $f(a/W)$  in Eq 1 is altered, corresponding to an increase of the crack opening displacement at a fixed load by  $v_{cr}$ . The relation between  $v_{cr}$  and  $\Delta a$  is given by

$$\frac{v_{cr}}{v_{el}} = \frac{1}{W} \frac{f'\left(\frac{a}{W}\right)}{f\left(\frac{a}{W}\right)} \times \Delta a \tag{2}$$

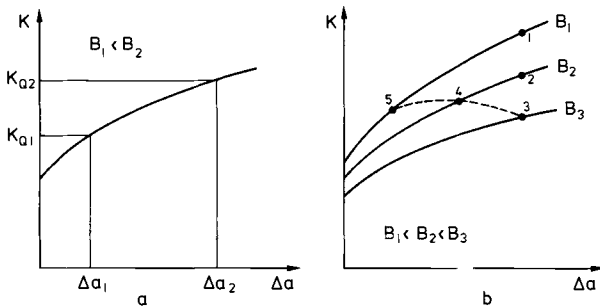
If fracture toughness is to be determined with the secant method, then at  $K_{Ic5}$  the ratio  $(v_{pl} + v_{cr})/v_{el}$  is equal to 0.05.

$$v_{pl} \ll v_{cr}$$

If the plastic component of the crack opening displacement  $v_{pl}$  can be neglected, the crack extension at  $K_Q$  can be calculated from Eq 2 with  $a_0/W = 0.5$ ,  $v_{cr}/v_{el} = 0.05$ ,  $f/f' = 0.2$ .

$$\Delta a = 0.02 \times a_0 = 0.01W \tag{3}$$

It follows that the crack extension at  $K_Q$  increases with increasing specimen width  $W$ . If  $K$ - $\Delta a$  curves are independent of thickness  $B$  (Fig. 3a)  $K_Q$  increases with increasing  $B$ ; this holds for specimens with fixed ratio  $a_0:W:B$ . It can be expected that the  $K$ - $\Delta a$  curves are dependent on thickness below a minimum thickness, in such a way that for thinner specimens the crack growth resistance curve is shifted upwards (Fig. 3b).



(a)  $K$ - $\Delta a$  curves independent of  $B$ .  
 (b)  $K$ - $\Delta a$  curves depend on  $B$ .

FIG. 3—Influence of  $K$ - $\Delta a$  curves on  $K_Q$ .

Subsequently  $K_Q$  decreases with increasing thickness for specimens with  $a_0 = W/2 = \text{constant}$  ( $1 \rightarrow 2 \rightarrow 3$  in Fig. 3b). For specimens with fixed ratio  $a:W:B$  the crack extension  $\Delta a$  at  $K_Q$  decreases with decreasing  $B$ . Dependent on the  $K$ - $\Delta a$  curves for different thickness,  $K_Q$  can decrease or increase with increasing thickness ( $5 \rightarrow 4 \rightarrow 3$  in Fig. 3b).

$$v_{pl} \gg v_{cr}$$

If  $v_{cr}$  can be neglected with respect to  $v_{pl}$  at  $K_Q$ , the plastic behavior at the crack tip will determine the value of  $K_Q$ . The plastic component of the crack opening displacement can be attributed to a crack extension  $\Delta a_{eff}$ . In Fig. 4  $K$ - $\Delta a_{eff}$  curves are plotted, calculated from the nondimensional curves of the paper of Markström [11] for a low-strain hardening material and a yield strength of 910 MN/m<sup>2</sup>. It can be seen that in any case  $K_Q$  decreases with decreasing thickness  $B$ , even if the stress state at the crack tip does not change ( $1 \rightarrow 3$ ). The decrease of  $K_Q$  is greater, if the reduction in thickness is connected with a transition from plane strain to plane stress ( $1 \rightarrow 4$ ).

#### $v_{pl}$ and $v_R$ Comparable

If at  $K_Q$  the components of crack opening displacement  $v_{pl}$  and  $v_{cr}$  are of the same order of magnitude, the curves of Figs. 3 and 4 must be superposed.  $K_Q$  increases with increasing  $W$  and, for specimens with fixed  $B/W$  ratio, also with increasing  $B$ , given that the  $K$ - $\Delta a$  curves are independent of  $B$ . Only if the  $K$ - $\Delta a$  curves are shifted higher up with decreasing thickness, is it possible that  $K_Q$  decreases with increasing thickness.

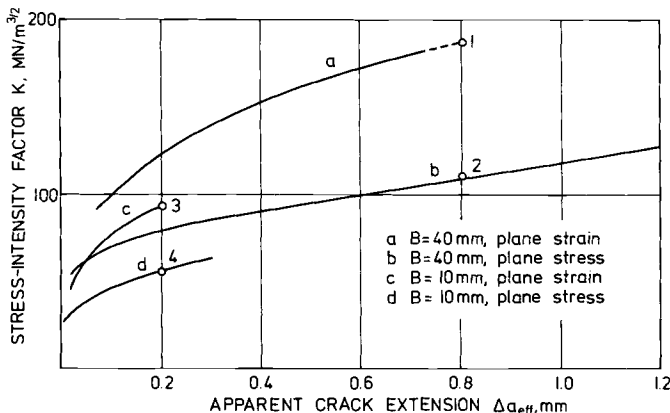


FIG. 4—Stress intensity factor as a function of apparent crack extension (after Markström [11]).

## Procedure

### Material

Two plates of the alloy Ti-6Al-4V were investigated.

- A. A forged and annealed plate of Contimet GmbH with a size of 44 by 880 by 880 mm. The results of tension tests in L-direction were:  $\sigma_y = 910 \text{ MN/m}^2$   $\sigma_u = 1017 \text{ MN/m}^2$ .
- B. A rolled and annealed plate of Friedr. Krupp GmbH<sup>3</sup> with a size of 82 by 285 by 800 mm. The results of tension tests in L-direction were  $\sigma_y = 937 \text{ MN/m}^2$   $\sigma_u = 974 \text{ MN/m}^2$ .

Both plates had a Widmanstätten microstructure, Plate B having unusual large grains of about 1 mm. Due to the large influence of microstructure on fracture toughness [12-15], both plates were investigated metallographically at different positions. It was found that Plate B had a region of deviating microstructure, and the segment was discarded subsequently. Otherwise the homogeneity of the plates were satisfactory. Part of the scatter of the results nevertheless may be due to a varying microstructure.

### Specimens

Single edge notched specimens were made with the fracture plane in LS-orientation. Specimen dimensions are shown in Table 1. Besides ASTM standard specimens with  $W/B = 2$ , square specimens and specimens with  $W/B > 2$  were used. Specimens of one geometry were taken at random from the plates. The smaller specimens were machined from the fractured halves of the larger specimens. Fatigue cracks were produced in two load steps in 3-point bending. Final crack lengths were in the range  $0.4 < a/W < 0.06$ .

### Test Procedure

Nearly all fracture mechanics tests were done in 3-point bending with a Zwick testing machine. Only the thinner specimens (2 by 12, 6 by 6, 6 by 12, 12 by 12 of Plate A and 2 by 10, 2 by 20, 2 by 40 of Plate B) were loaded in 4-point bending. The loading rate was 1 mm/min in 3-point bending and 0.5 mm/min in 4-point bending, leading to  $\dot{K}$  between  $0.8 \text{ MN m}^{-3/2} \text{ s}^{-1}$  and  $2.5 \text{ MN m}^{-3/2} \text{ s}^{-1}$ . In this range of  $K$ , fracture toughness is nearly independent of the loading rate [16].

In order to evaluate the crack growth resistance curve, different specimens of the same geometry were loaded to different  $K$  values, unloaded, and refatigued. By looking on the fracture surface with a light

<sup>3</sup> This plate was placed at our disposal by VFW-Fokker GmbH.

TABLE 1—Results of fracture toughness tests (mean values).

| $B$ , mm | $W$ , mm | $W/B$ | $K_A^a$ ,<br>MN m <sup>-3/2</sup> | $K_Q^a$ ,<br>MN m <sup>-3/2</sup> | $K_{max}^a$ ,<br>MN m <sup>-3/2</sup> | $\frac{K_{max}}{K_Q}$ | $\frac{K_Q}{K_A}$ | $\frac{\Delta v_{0.8P_Q}}{\Delta v_{P_Q}}$ |
|----------|----------|-------|-----------------------------------|-----------------------------------|---------------------------------------|-----------------------|-------------------|--|
| Plate A  |          |       |                                   |                                   |                                       |                       |                   |  |
| 42       | 84       | 2     | 59.8 (6)                          | 92.7 (5)                          | 95.5 (5)                              | 1.03                  | 1.66              | 0.15                                       |
| 38       | 38       | 1     | 55.2 (8)                          | 82.5 (8)                          | 89.3 (8)                              | 1.09                  | 1.50              | 0.20                                       |
| 19       | 38       | 2     | 54.9 (8)                          | 77.2 (8)                          | 88.7 (4)                              | 1.11                  | 1.41              | 0.17                                       |
| 19       | 19       | 1     | 51.5 (9)                          | 72.5 (9)                          | 80.6 (8)                              | 1.12                  | 1.43              | 0.16                                       |
| 10       | 40       | 4     | 50.8 (3)                          | 73.9 (3)                          | 85.9 (2)                              | 1.20                  | 1.43              | 0.24                                       |
| 10       | 20       | 2     | 46.8 (15)                         | 72.2 (15)                         | 83.4 (15)                             | 1.16                  | 1.45              | 0.17                                       |
| 12       | 12       | 1     | 54.6 (7)                          | 70.6 (6)                          | 79.4 (6)                              | 1.12                  | 1.29              | 0.11                                       |
| 6        | 20       | 3.3   | 52.4 (3)                          | 73.8 (3)                          | 90.5 (3)                              | 1.22                  | 1.41              | 0.29                                       |
| 6        | 12       | 2     | 48.9 (15)                         | 67.0 (15)                         | 80.4 (14)                             | 1.20                  | 1.58              | 0.18                                       |
| 6        | 6        | 1     | 49.9 (4)                          | 61.0 (4)                          | 71.6 (4)                              | 1.18                  | 1.19              | 0.0  |
| 2        | 12       | 6     | 48.1 (5)                          | 58.0 (5)                          | 72.5 (5)                              | 1.25                  | 1.21              | 0.10                                       |
| Plate B  |          |       |                                   |                                   |                                       |                       |                   |  |
| 78       | 78       | 1     | 38.8 (2)                          | 79.3 (2)                          | ...                                   | ...                   | 2.04              | 0.34                                       |
| 39       | 78       | 2     | 40.9(3)                           | 83.5 (3)                          | ...                                   | ...                   | 2.15              | 0.29                                       |
| 39       | 39       | 1     | 46.6 (2)                          | 72.1 (2)                          | 78.5 (5)                              | 1.12                  | 1.57              | 0.22                                       |
| 20       | 78       | 3.9   | 38.1 (4)                          | 79.3 (4)                          | ...                                   | ...                   | 2.08              | 0.32                                       |
| 20       | 38.4     | 1.92  | 33.7 (4)                          | 67.6 (4)                          | ...                                   | ...                   | 2.00              | 0.38                                       |
| 20       | 20       | 1     | 33.0 (5)                          | 63.1 (5)                          | 76.1 (3)                              | 1.14                  | 1.93              | 0.30                                       |
| 10       | 78       | 7.8   | 54.5 (3)                          | 78.2(3)                           | ...                                   | ...                   | 1.51              | 0.11                                       |
| 10       | 40       | 4     | 35.9 (4)                          | 68.4 (4)                          | ...                                   | ...                   | 1.94              | 0.32                                       |
| 10       | 20       | 2     | 33.3 (2)                          | 58.2 (8)                          | 78.6 (2)                              | 1.27                  | 1.76              | 0.36                                       |
| 10       | 10       | 1     | 32.9 (3)                          | 48.9 (3)                          | 56.9 (1)                              | 1.18                  | 1.49              | 0.26                                       |
| 5        | 40       | 8     | 39.7 (2)                          | 68.3 (2)                          | ...                                   | ...                   | 1.72              | 0.28                                       |
| 5        | 20       | 4     | 24.8 (2)                          | 45.0 (2)                          | ...                                   | ...                   | 1.81              | 0.42                                       |
| 5        | 10       | 2     | 26.4 (2)                          | 45.0 (2)                          | ...                                   | ...                   | 1.71              | 0.39                                       |
| 2        | 40       | 20    | 32.7 (1)                          | 61.3 (1)                          | ...                                   | ...                   | 1.88              | 0.31                                       |
| 2        | 20       | 10.   | 31.4 (4)                          | 58.2 (4)                          | ...                                   | ...                   | 1.89              | 0.40                                       |
| 2        | 10       | 5     | 25.0 (5)                          | 43.5 (5)                          | ...                                   | ...                   | 1.75              | 0.85                                       |

<sup>a</sup> Number of tests are in brackets.

microscope or a scanning microscope it was possible to measure the crack extension which occurred during the unidirectional loading.

For determination of the onset of crack extension the potential method was used for Plate A in addition to the fracture surface observation. For titanium alloys the potential method is very sensitive [12].

## Results

### *P-v curves*

The *P-v* curves have a continuous transition from the linear to the nonlinear part. Characteristic for all *P-v* diagrams is the heavy rise of the curve after reaching  $P_A$ , the load at the deviation from the linear part. Therefore, the ratio  $K_Q/K_A$  is very high (see Table 1) varying between 1.19 and 1.66 for Plate A, and between 1.49 and 2.15 for Plate B. The

determination of  $K_Q$  is dependent strongly on the accuracy of the determination of the slope of the linear part of the  $P$ - $v$  curve. For both plates and for nearly all specimens, however, the slope-determination presented no problem. Nevertheless small changes in the slope yield considerable changes in  $K_Q$ .

For Plate B the criterion of the ASTM recommendation  $\Delta v_{0.8P_Q}/\Delta v_{P_Q} < 0.25$  is not fulfilled for nearly all specimen geometries (see Table 1). Some specimens of Plate A also showed values greater than 0.25, the mean values for each geometry are, however, mostly smaller.

The criterion  $P_{\max}/P_Q < 1.1$  will be discussed later on.

### *Effect of Specimen Geometry on $K_Q$*

The mean values of  $K_Q$  are included in Table 1. In Fig. 5  $K_Q$  is plotted against specimen thickness  $B$  and in Fig. 6 against width  $W$ . There is a general trend of  $K_Q$  increasing with  $W$ . Apart from a few exceptions (2 by 40, 5 by 20 for Plate B, 2 by 12, 10 by 40 for Plate A) through all values of  $K_Q$  a common curve can be drawn. Figure 5 shows clearly the independence of  $K_Q$  from  $B$  for  $W = 20$  mm (Plate A) and  $W = 78$  mm,  $W = 40$  mm,  $W = 20$  mm with exception  $B = 5$  mm (Plate B). For  $W = 12$  mm,  $W = 40$  mm (Plate A) and  $W = 10$  mm (Plate B)  $K_Q$  increases with increasing  $B$ .

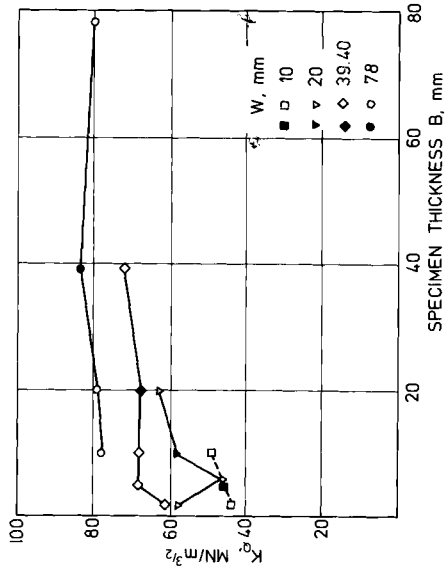
### *K- $\Delta a$ Curves*

Figure 7 shows the scatterband of the  $K$ - $\Delta a$  curves for Plate A. For any geometry the measurements were performed in a range a little beyond  $K_Q$ . Therefore, the larger crack extension could only be measured with specimens with larger  $W$ . The values for different specimen geometries were distributed randomly on the whole scatterband. No thickness dependence of the  $K$ - $\Delta a$  curves could be found. Figure 7 shows clearly the strong increase of  $K$ , especially at small crack extensions. In order to obtain a crack extension from 10  $\mu\text{m}$  to 0.1 mm,  $K$  must be increased from 48  $\text{MN m}^{-3/2}$  to 66  $\text{MN m}^{-3/2}$ .

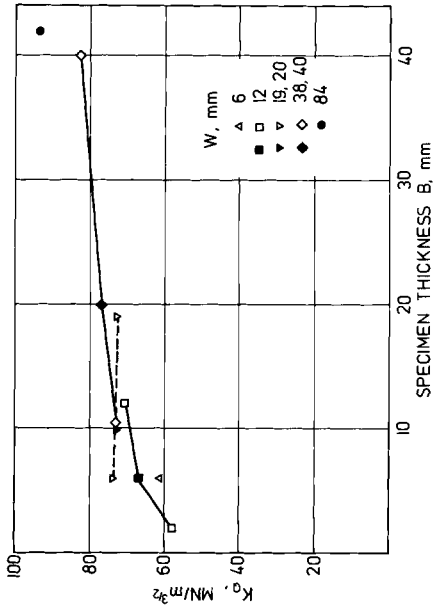
### *Onset of Crack Extension*

It is convenient to define the onset of crack extension at  $K$  for  $\Delta a = 10 \mu\text{m}$ , because the dimple size of the fracture surface is about 10  $\mu\text{m}$ . Extrapolation of the  $K$ - $\Delta a$  curves to 10  $\mu\text{m}$  yields in  $K_{1e} = 48.8 \pm 8 \text{ MN m}^{-3/2}$  for Plate A. With the potential method a mean value of  $K = 42 \text{ MN m}^{-3/2}$  was determined for the onset of crack extension for all specimen geometries.

A comparison of  $K_{1e}$  with  $K_A$  (see Table 1) demonstrates the known result [12] that the onset of crack extension occurs in the "linear" part of the  $P$ - $v$  diagram.

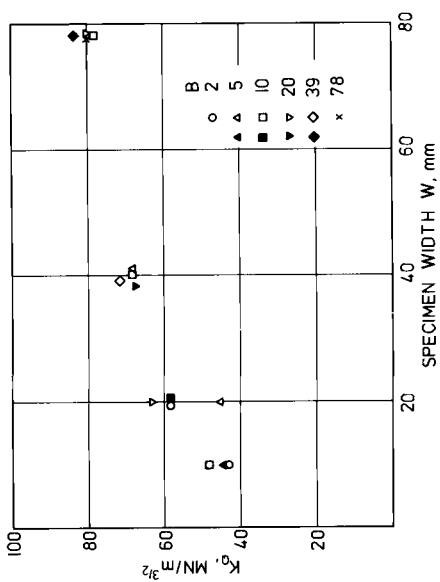


(a) Plate A.

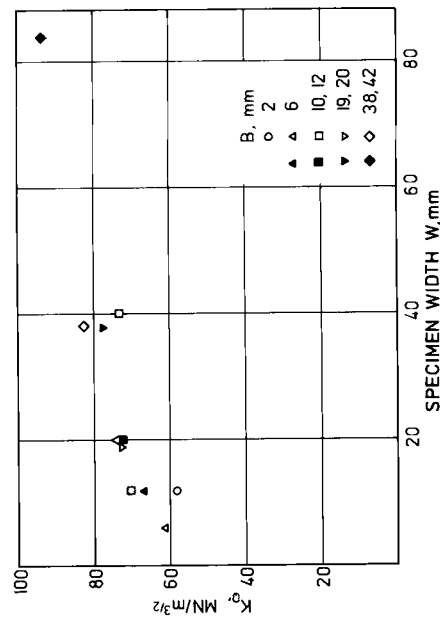


(b) Plate B.

FIG. 5— $K_Q$  as a function of thickness B. (Filled points: ASTM standard specimens).



(a) Plate A.



(b) Plate B.

FIG. 6— $K_I$  as a function of width W (filled points: ASTM standard specimens).

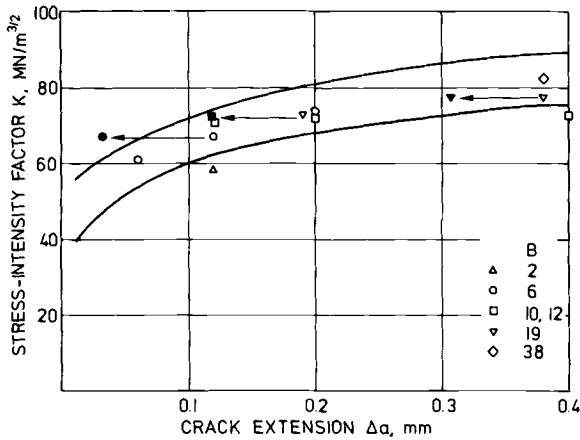


FIG. 7—Scatterband of crack growth resistance curve and  $K_Q$  plotted at  $\Delta a = 0.02 a_0$  and  $\Delta a = 0.02 a_0 - \Delta a_{eff}$  (filled points).

**Discussion**

*Effect of Thickness and Width on  $K_Q$*

From the observation of the independency of  $K_e$  and of the  $K-\Delta a$  curves of the specimen thickness it can be concluded that the crack extension to the point  $K_Q$  is governed by the plane strain state in the specimen center for all investigated specimens. The radius of the plastic zone at  $K_{Ie} = 48 \text{ MN m}^{-3/2}$  for Plate A is given by

$$r_{pl} = \frac{1}{6\pi} \left( \frac{K_{Ie}}{\sigma_y} \right)^2 = 148 \mu\text{m} \tag{3}$$

For specimens with  $W = 84 \text{ mm}$  the radius increases at  $K_Q$  to  $550 \mu\text{m}$ . The ratio  $B/r_{pl}$  at  $K_{Ie}$  is equal to 14 for the thinnest specimens with  $B = 2 \text{ mm}$ . For ASTM standard specimens ( $B:W = 1:2$ )  $B/r_{pl} = 76$  for  $B = 42 \text{ mm}$  and  $B/r_{pl} = 21$  for  $B = 6 \text{ mm}$  at  $K_Q$ . For all these cases the plastic zone sizes are obviously small enough to determine the crack propagation by the plane strain state. According to this viewpoint the ASTM recommendation concerning the minimum specimen size ( $B/r_{pl} > 50$ ) is sufficient. Nevertheless this recommendation cannot avoid thickness dependent  $K_Q$  values.

Because of the independence of the crack growth resistance curves from  $B$ ,  $K_Q$  should increase with  $W$  according to the slope of the  $K-\Delta a$  curve, and should be independent of  $B$  for constant  $W$ , but only if at  $K_Q$  the crack opening displacement  $v_{pl}$  can be neglected in comparison with

$v_{cr}$ . In a first approach  $K_Q$  is independent of  $W$ . The slight increase of  $K_Q$  with increasing  $B$  for constant  $W$ , which occurs in some cases is not in agreement with the considerations mentioned previously. A quantitative comparison between  $K_Q$  and  $K$  at  $\Delta a = 0.02 a_0(K_{2\%})$  is given in Fig. 7. In addition to the scatterband of the  $K$ - $\Delta a$  curves, the different  $K$ - $\Delta a$  values are plotted at  $\Delta a = 0.02a_0 = 0.01W$ . All  $K_Q$  values, with the exception of the specimens with cross section 2 by 12 and 10 by 40, are within the scatterband of the  $K$ - $\Delta a$  values. Specimens with 42 by 48 cross section could not be compared, because the  $K$ - $\Delta a$  curve was only measured up to the point  $\Delta a = 0.4$  mm. The good agreement between  $K_Q$  and  $K$  at  $\Delta a = 0.02a_0$  supports the conclusion that  $v_{pl}$  at  $K_Q$  is negligible. If  $v_{pl}$  is considered a smaller crack extension than 2 percent at  $K_Q$  a shift of  $K_Q$  in Fig. 7 to the left results. The amount of the shifting can only be estimated from the calculations by Markström [11] or Roberts and Swedlow [8]. For this reason, the crack opening displacement  $v_{pl}$ , at  $K_Q$ , of specimens with  $W/B = 2$ , was determined from the diagram of Markström for a low-strain hardening material and converted into an apparent crack extension  $\Delta a_{eff}$  according to Eq 2. In Fig. 7  $K_Q$  is shifted to the left by  $\Delta a_{eff}$  (filled symbols). It can be seen that for the specimens with cross section 6 by 12 the corrected values are outside the scatterband. Obviously the plastic component of the crack opening displacement is smaller than calculated according to Markström.

### *Consequences for Fracture Toughness Determination*

From the experimental results some conclusions can be drawn concerning the determination of fracture toughness  $K_{Ic}$ . From the thickness independence of the  $K$ - $\Delta a$  curves, between  $B = 2$  mm and  $B = 20$  mm, it can be concluded that stable crack growth occurs also in the case of a pure plane strain state. Therefore in a plane strain state the crack propagation behavior cannot be characterized by only  $K_{Ic}$ , but by the whole  $K$ - $\Delta a$  curve. Characteristic values are  $K_{Ie}$  at the onset of crack extension and the maximum value of  $K$  ( $K_u$  corresponding to  $R_u$  in Fig. 1). Each  $K$  value between  $K_{Ie}$  and  $K_u$  is arbitrary.  $K_{Ic5}$ , determined with the secant method, is also arbitrary, because  $K_{Ic5}$  is a specimen width dependent point on the  $K$ - $\Delta a$  curve.  $K_{Ie}$  is a real material constant, which is not only important as the stress intensity factor at the onset of crack extension but also in stress corrosion tests. Reference 17 showed that  $K_{Ie}$  and  $K_{ISCC}$  are nearly identical.  $K$  at the onset of unstable crack extension, which should be indicated as  $K_{Ic}$  according to the definition mentioned previously, is, contrary to  $K_{Ie}$ , dependent on machine stiffness, loading rate, and specimen geometry.

$K_{Ie}$  determinations require much time and many specimens. Therefore, another way should be found to determine a material constant which is independent of specimen geometry. One possibility is to specify a fixed

specimen geometry for each material or for a group of materials for  $K_{Ic}$  determination. It is also possible to use a width dependent slope of the secant in such a way that for all specimen geometries  $K_{Ic}$  is measured at the same point of the  $K$ - $\Delta a$  curve.

The additional recommendation of ASTM that  $K_{max}/K_Q$  should be less than 1.1 leads to specimen sizes for which  $K_Q = K_{Ic5}$  is in the upper range of the  $K$ - $\Delta a$  curves. In Fig. 8  $K_{max}/K_Q$  is plotted against thickness  $B$  for Plate A. This figure shows that  $B$  should be larger than 20 mm. This arbitrary restriction of valid tests leads to  $K_{Ic}$  values close to the maximum value  $K_u$ . Nevertheless, this restriction also cannot avoid geometry dependent fracture toughness.

It was shown that  $\Delta v$  at  $0.8 P_Q$  is in some cases larger than  $0.25\Delta v$  at  $P_Q$ . The motivation behind the restriction of tests with too large  $\Delta v$  at  $0.8 P_Q$  was to eliminate all specimens with too large  $v_{pl}$  at  $K_Q$ . Even if the plastic deformation at the crack tip is so small that  $v_{pl}$  at  $K_Q$  can be neglected, there can be considerable departure from the linear part of the  $P$ - $v$  diagram at  $0.8 P_Q$ . The amount of the departure can be calculated from the  $K$ - $\Delta a$  curve. From the  $K$ - $\Delta a$  curve of Fig. 7 one can calculate that for specimens with  $W = 40$  mm  $\Delta v_{0.8P_Q}/\Delta v_{P_Q} = 0.23$  and for specimens with  $W = 10$  mm  $\Delta v_{0.8P_Q}/\Delta v_{P_Q} = 0.22$ . It is not possible to make a statement about the amount of plastic deformation at the crack tip from the amount of the deviation from the linear part at  $0.8 P_Q$ . Therefore, the question arises, whether the restriction  $\Delta v_{0.8P_Q}/\Delta v_{P_Q} < 0.25$  is significant for titanium alloys.

## Conclusions

The investigation of the effect of thickness on fracture toughness of Ti-6Al-4V yield the following results and conclusions:

1. The load-crack opening displacement-curves rise steeply after reaching  $P_A$ , the load at the end of the linear region. Therefore, fracture toughness  $K_{Ic5}$ , determined according to the secant method, is dependent strongly on the accuracy of the determination of the slope of the linear part of the  $P$ - $v$  diagram.
2. In a first approximation  $K_Q$  increases with specimen width independent of thickness. This general tendency is partly superposed by a slight increase of  $K_Q$  with thickness.
3. The crack growth resistance curve is independent of thickness until  $K_Q$  in the investigated range  $2 < B < 20$  mm.
4. The effect of specimen dimensions on  $K_Q$  can be traced back to the crack length dependent crack extension at  $K_Q$ .
5. The restrictions of the ASTM recommendations for valid tests ( $K_{max}/K_Q < 1.1$ ,  $\Delta v_{0.8P_Q}/\Delta v_{P_Q} < 0.25$ ) cannot exclude the thickness effect.
6. Characterization of crack propagation behavior in the plane strain state can only be done with the  $K$ - $\Delta a$  curve. It should be considered in

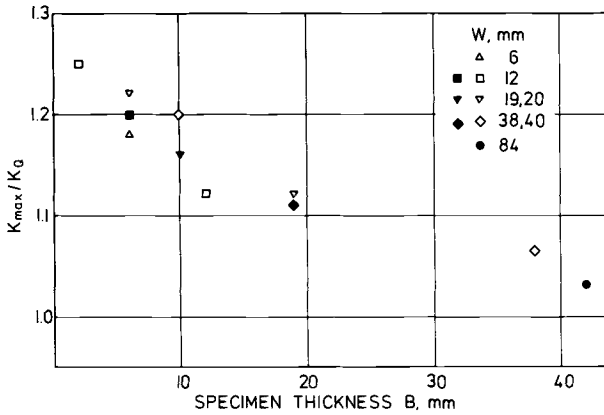


FIG. 8— $K_{max}/K_Q$  as a function of thickness  $B$  (filled points: ASTM standard specimens).

which way a characteristic point on this curve can be simply determined such that the material behavior is characterized by one material constant.

#### Acknowledgments

The authors gratefully acknowledge the assistance of J. Eschweiler and H. Weber in the experimental work. The research was sponsored by the Deutsche Forschungsgemeinschaft.

#### References

- [1] Irwin, G. R., Kies, J. A., and Smith, H. L., *Proceedings, American Society for Testing and Materials*, Vol. 58, 1958, pp. 640-657.
- [2] *Fracture Toughness Testing and Its Applications, ASTM STP 381*, American Society for Testing and Materials, 1965.
- [3] Brown, W. F., Jr., and Srawley, J. E., *Plane Strain Crack Toughness Testing of High Strength Metallic Materials, ASTM STP 410*, American Society for Testing and Materials, 1967, pp. 1-65.
- [4] Srawley, J. E., Jones, M. H., and Brown, W. F., Jr., *Materials Research and Standards*, Vol. 7, 1967, pp. 262-266.
- [5] Kaufmann, J. G., Nelson, F. G., Jr., and Holt, M., *Engineering Fracture Mechanics*, Vol. 1, 1968, pp. 259-274.
- [6] May, M. J. in *Review of Developments in Plane Strain Fracture Toughness Testing, ASTM STP 463*, American Society for Testing and Materials, 1970, pp. 41-62.
- [7] Jones, M. H. and Brown, W. F., Jr., in *Review of Developments in Plane Strain Fracture Toughness Testing, ASTM STP 463*, American Society for Testing and Materials, 1970, pp. 63-101.
- [8] Brown, W. F., Jr., and Srawley, J. E. in *Review of Developments in Plane Strain Fracture Toughness Testing, ASTM STP 463*, American Society for Testing and Materials, 1970, pp. 216-248.
- [9] Nelson, F. G., Schilling, P. E., and Kaufmann, J. G., *Engineering Fracture Mechanics*, Vol. 4, 1972, pp. 33-50.
- [10] Kaufman, J. G. and Nelson, F. G. in *Fracture Toughness and Slow-Stable Cracking, Proceedings of the 1973 National Symposium on Fracture Mechanics, Part 1, ASTM STP 559*, American Society for Testing and Materials, 1974, pp. 74-85.
- [11] Markström, K., *Engineering Fracture Mechanics*, Vol. 4, 1972, pp. 593-603.

- [12] Link, F. and Munz, D., *Materialprüfung*, Vol. 13, 1971, pp. 407-412.
- [13] Galda, K. H., "Untersuchungen über den Einfluß von Temperatur und Probengeometrie auf die bruchmechanischen Kennwerte von TiA16V4," *Deutsche Luft und Raumfahrt*, Forschungsbericht, Munich, 1973, Report 73-107.
- [14] Piper, D. E., Smith, S. H., and Carter, R. V., "Corrosion Fatigue and Stress-Corrosion Cracking in Aqueous Environment," Boeing Document D6-60067, The Boeing Corporation, 1967.
- [15] Curtis, R. E. and Spurr, W. F., *Transactions of the American Society for Metals*, Vol. 61, 1968, pp. 115-127.
- [16] Galda, K. H., Link, F., and Munz, D., "The Effect of Temperature and Loading Rate on the Fracture Toughness of Ti-6Al-4V and 7075," *Third International Conference on Fracture*, Vol. III, 1973, pp. 11-34.
- [17] Link, F. and Munz, D., *Corrosion Science*, Vol. 13, 1973, pp. 809-811.

S. R. Novak<sup>1</sup>

## Resistance to Plane-Stress Fracture (R-Curve Behavior) of A572 Structural Steel\*

---

**REFERENCE:** Novak, S. R., "Resistance to Plane-Stress Fracture (R-Curve Behavior) of A572 Structural Steel," *Mechanics of Crack Growth, ASTM STP 590*, American Society for Testing and Materials, 1976, pp. 235–242.

**ABSTRACT:** The R-curve behavior of A572 Grade 50 steel was established over the temperature range  $-40$  to  $+72^{\circ}\text{F}$  by using state-of-the-art procedures. Both linear-elastic-fracture-mechanics (LEFM) and crack-opening-stretch (COS) analytical techniques were used in assessing experimental results obtained under load-control and displacement-control testing conditions. This study represents a pioneer effort in that it is the first known attempt to evaluate the R-curve behavior of a low-strength structural steel in some depth.

Results showed a steep  $K_c$  transition behavior for 1.5-in.-thick (38 mm) plate, with minimum  $K_c$  values of 57, 155, and 318 ksi  $\sqrt{\text{in.}}$  (63, 171, and 350  $\text{MNm}^{-3/2}$ ) obtained at  $-40$ ,  $+40$ , and  $+72^{\circ}\text{F}$  ( $-40$ ,  $+4.5$ , and  $+22^{\circ}\text{C}$ ), respectively. A similar behavior was observed for 0.5-in.-thick (12.7 mm) plate, with minimum  $K_c$  values of 150, 273, and  $>380$  ksi  $\sqrt{\text{in.}}$  (165, 300, and  $>418$   $\text{MNm}^{-3/2}$ ) obtained at the corresponding test temperatures. The results are discussed in relation to the influence of material and testing method, as well as in relation to earlier  $K_{Ic}$  results obtained at cryogenic temperatures.

The minimum  $K_c$  values measured demonstrate extensive crack tolerance for A572 Grade 50 steel under all combinations of the test conditions studied. With one exception, these minimum behaviors can be translated into total critical flaw lengths that are at least seven times the plate thickness ( $2a_{cr} \geq 7B$ ) for cracks embedded in large planar structures and subjected to tensile-stress levels equal to three fourths the yield strength. The applicability of  $a_{cr}$  calculations obtained from R-curve measurements generally, and on the A572 Grade 50 steel specifically, is discussed in relation to typical structural members such as H-beams.

**KEY WORDS:** crack propagation, fracture (materials), mechanical properties, stresses, strains

\* This paper is a summary of the complete paper published as *ASTM STP 591*.

<sup>1</sup> Senior research engineer, Heavy Products Division, Research Laboratory, United States Steel Corporation, Monroeville, Pa. 15146.

### Summary

Results of an extensive study concerning the R-curve behavior of ASTM A572 Grade 50 steel are presented. The study was conducted using fatigue precracked specimens to characterize the basic fracture behavior of this steel under conditions normally encountered in most structural applications. Under these conditions  $K_{Ic}$  measurements cannot be made; therefore, R-curve techniques were used to determine the (plane-stress) fracture behavior. Specifically, the study was conducted over the temperature ( $T$ ) range from  $-40$  to  $+72^\circ\text{F}$ , under so-called "static" loading rates ( $\dot{\epsilon} = 10^{-5} \text{ s}^{-1}$ ) and on plate thicknesses ( $B$ ) of  $1/2$  and  $1\ 1/2$  in. Under such conditions the state-of-stress at fracture corresponds to plane stress ( $K_c$ ) rather than plane strain ( $K_{Ic}$ ), and the most efficient method of fracture characterization is that of an R-curve (plot of crack driving force,  $K_R$ , versus crack extension,  $\Delta a$ ).

State-of-the-art experimental and analytical procedures were used throughout the study. This included the use of both linear-elastic-fracture-mechanics (LEFM) and crack-opening-stretch (COS) analytical techniques. Experimental techniques included the use of both load-control and displacement-control testing conditions. Results were obtained on various size compact-tension (CT) specimens using the double-compliance (two clip gage) procedures for monitoring crack extension ( $\Delta a$ ) developed earlier by McCabe and Heyer.

Specific R-curve results were obtained on two different heats of ASTM A572 Grade 50 steel using a total of 24 CT specimens. Of this total, 14 specimens had in-plane dimensions corresponding to 2T and 4T specimens and were tested under load-control conditions; the remaining 10 specimens had in-plane dimensions corresponding to 4C and 7C specimens and were tested under displacement-control conditions. Twenty-two of the specimens tested were of a 50-ksi ( $345 \text{ MN/m}^2$ ) yield-strength A572 Grade 50 steel, and the two remaining specimens were of a 62-ksi ( $427 \text{ MN/m}^2$ ) yield-strength A572 Grade 50 steel. Both 1.5 and 0.5-in.-thick (38 and 12.7 mm) specimens were evaluated from the 50-ksi steel; the two specimens of the 62-ksi steel were both 1.5 in. thick.

The current study represents the first known attempt to evaluate the R-curve behavior of a medium-strength structural steel in detail—including the influence of temperature ( $T$ ), plate thickness ( $B$ ), yield strength ( $\sigma_{ys}$ ), and testing procedure (load-control versus displacement control). In addition, the present R-curve and  $K_c$  results from  $-40$  to  $+72^\circ\text{F}$  are compared with  $K_{Ic}$  results obtained earlier on the same two steels at lower (cryogenic) temperatures. Because of the unique character of this work and also because some of the results are contrary to prior expectations, the results of the investigation are reported in detail under a separate publication, *ASTM STP 591*, in order to preserve the documenta-

tion of the study. Such results are expected to be of value in the future for assessing studies of a similar nature conducted on constructional steels.

The results, in general, demonstrate extensive crack tolerance at fracture for A572 Grade 50 steel under the conditions studied—with most fractures occurring under elastic-plastic conditions and requiring analysis by COS. The results show further that care must also be exercised in the application of plane-stress fracture data ( $R$ -curve and  $K_c$ ) to structural components in order to ensure proper predictions of behavior in service. The specific results obtained from this study can be summarized as follows:

1. A steep transition was observed in the plane-stress fracture behavior for the  $B = 1.5$ -in. specimens of the 50-ksi steel, with *minimum*  $K_c$  values of 57, 155, and 318 ksi  $\sqrt{\text{in.}}$  (63, 171, and 350  $\text{MNm}^{-3/2}$ ) occurring at temperatures of  $-40$ ,  $+40$ , and  $+72^\circ\text{F}$  ( $-40$ ,  $+4.5$ , and  $+22^\circ\text{C}$ ), respectively.

2. No significant differences were observed in the  $K_c$  behavior of the 50 and 62-ksi A572 Grade 50 steels.

3. Greater overall resistance to fracture was observed for the  $B = 0.5$ -in. specimens than for the  $B = 1.5$ -in. specimens of the 50-ksi steel, with *minimum*  $K_c$  values of 150, 273, and  $>380$  ksi  $\sqrt{\text{in.}}$  (165, 300, and  $>418$   $\text{MNm}^{-3/2}$ ) occurring at temperatures of  $-40$ ,  $+40$ , and  $+72^\circ\text{F}$ , respectively. However, this difference in the minimum resistance to fracture for the 0.5 and 1.5-in.-thick specimens is partially the result of differences due to testing method (see conclusions 6 and 7).

4. With the exception of three specimens, the fracture instability for all specimens was catastrophic in nature. The excepted specimens, all tested at  $+72^\circ\text{F}$ , included a 7C specimen with  $B = 1.5$  in. that exceeded testing-machine capacity at  $K_R = 477$  ksi  $\sqrt{\text{in.}}$  (525  $\text{MNm}^{-3/2}$ ) and  $\Delta a = 0.86$  in. (22 mm), and duplicate 4T specimens that exhibited slow, stable crack extension corresponding to  $\Delta a_c \geq 3.50$  in. ( $\geq 90$  mm) at  $K_c$  values of  $>380$  and  $>503$  ksi  $\sqrt{\text{in.}}$  (418 and 550  $\text{MNm}^{-3/2}$ ).

5. The repeatability of results for three of four sets of duplicate specimens was within  $\pm 15$  percent of the average  $K_c$  value measured. The repeatability of results for the fourth set of specimens was within  $\pm 30$  percent of the average  $K_c$  value measured.

6. The choice of testing procedure (load-control versus displacement-control) was found to influence the results. The  $K_c$  values for the 4T specimens tested under load-control conditions were 40 to 80 percent higher than the values for the corresponding 4C specimens tested under displacement-control conditions in direct comparison tests at three different temperatures. This influence of testing procedure was consistent and appears real, but could not be fully verified using statistical analysis procedures.

7. The effects of specimen thickness ( $B = 1.5$  in. versus  $B = 0.5$  in.) on  $K_c$  behavior evaluated in direct-comparison tests using only the load-control testing procedure were inconclusive. Results from 2T specimens tested at three different temperatures indicated a consistent influence, while results from 4T specimens tested at similar temperatures were consistent in indicating no influence. Local variations in fracture toughness were apparently large enough to mask the true effects of specimen thickness on  $K_c$  behavior.

8. In relation to effects of specimen size, normal plane-stress fracture behavior (increasing  $K_c$  values corresponding to increasing values of  $a_0$ ) was generally obtained with both the load-control and the displacement-control testing methods at all temperatures. However, an inversion in this behavior occurred with each test method at  $-40^\circ\text{F}$ . These departures from expected behavior may be related to inherent variations in the local fracture toughness.

9. The  $K_c$  results of the present study were shown to be consistent with earlier  $K_{Ic}$  results obtained from tests on the same steel at cryogenic temperatures. The central concept in resolving obvious differences in the corresponding  $K_c$  and  $K_{Ic}$  transition temperatures was the apparent existence of an intermediate  $K_{Ic}$  shelf, a behavior supported by the results of each of three different and entirely independent methods of analysis (J-integral,  $K_T$ -suppression effect, and CVN specimen results).

10. For normal stress levels used in design ( $\sigma_D = 3/4 \sigma_{ys}$ ), critical flaw sizes ( $a_{cr}$ ) for the  $B = 1.5$ -in. plate of the 50-ksi A572 Grade 50 steel were shown to be  $a_{cr} = 1.80, 5.2,$  and  $23.0$  in. (46, 132, and 585 mm) for *minimum* representative behavior at  $-40, +40,$  and  $+72^\circ\text{F}$ , respectively.

11. For normal stress levels used in design, the critical flaw sizes for the  $B = 0.5$ -in. plate of the 50-ksi A572 Grade 50 steel were shown to be  $a_{cr} = 4.0, 16.0,$  and  $>32.0$  in. (100, 400, and  $>800$  mm) for *minimum* representative behavior at  $-40, +40,$  and  $+72^\circ\text{F}$ , respectively.

12. With two exceptions, the total critical flaw size ( $2a_{cr}$ ) for cracks centrally located in a large plate subjected to uniform tension stress were shown to be in excess of seven times the plate thickness, ( $2a_{cr} \cong 7B$ ) for all the eight different combinations of plate thickness and temperature investigated for the A572 Grade 50 steels.

13. Values of  $a_{cr}$  calculated from measurements of plane-stress fracture resistance (R-curve and  $K_c$  measurements) can be applied validly only when the state of stress in the structural application is plane stress, and then only under the assigned material and test conditions ( $T, \dot{\epsilon},$  and  $B$ ). Accordingly, such values would be directly applicable to structures with larger planar dimensions (direction of crack propagation), including the web location for large H-beams. Such  $a_{cr}$  values would not be directly applicable in confined structural regions, such as in the tension-flange region of H-beams (complete inapplicability) and the web region of

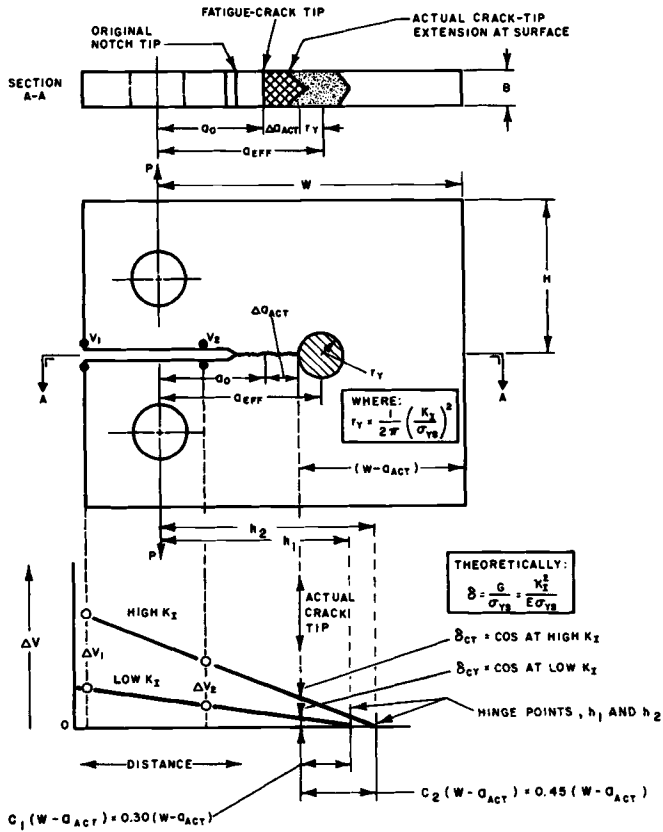


FIG. 1—Schematic of procedure for measuring  $\delta_{ct}$  or  $COS$  at the actual crack tip ( $a_{act}$ ) relative to applied load level ( $K_I$ ) under plane-stress conditions.

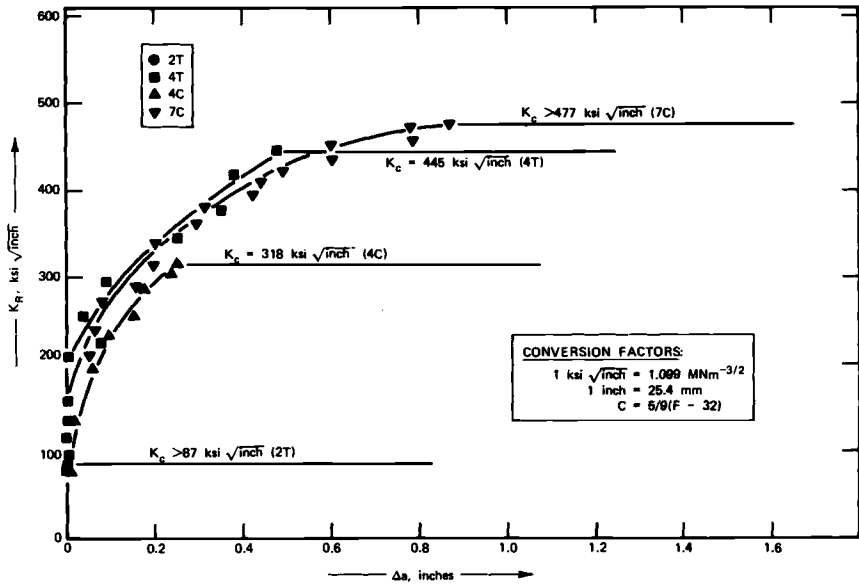


FIG. 2—*R*-curve and  $K_{Ic}$  results for full-thickness ( $B = 1.5$  in.) specimens of A572 grade 50 steel tested at +72°F.

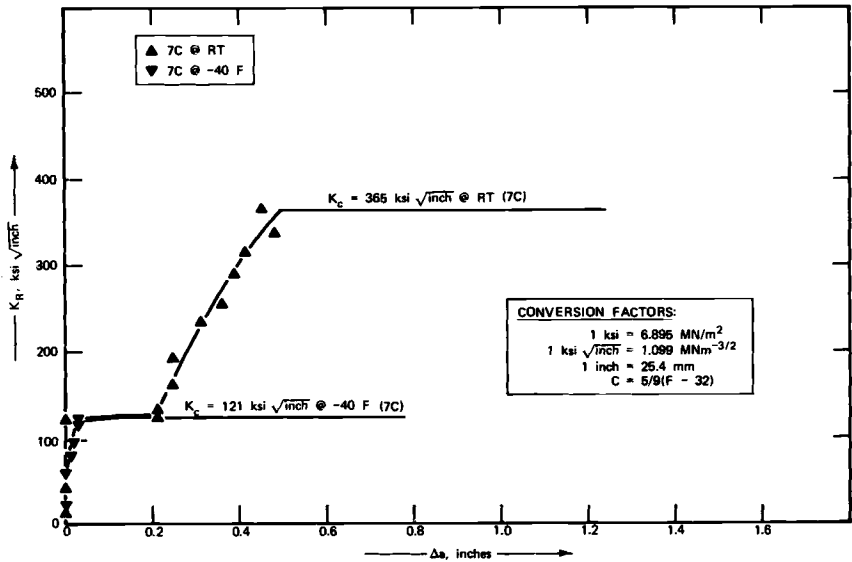


FIG. 3—*R*-curve and  $K_{Ic}$  results for full-thickness ( $B = 1.5$  in.) specimens of A572 steel processed to 62-ksi strength level at two different temperatures.

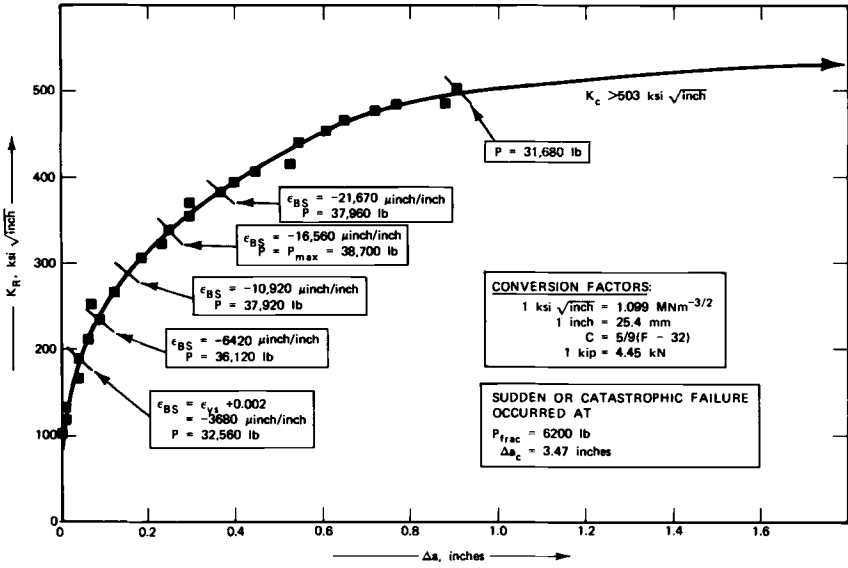


FIG. 4—Superposition of  $\epsilon_{bs}$  and  $P$  in the development of the  $R$ -curve for the 4T subthickness ( $B = 0.5 \text{ in.}$ ) specimen of A572 grade 50 steel tested at  $-72^\circ\text{F}$ .

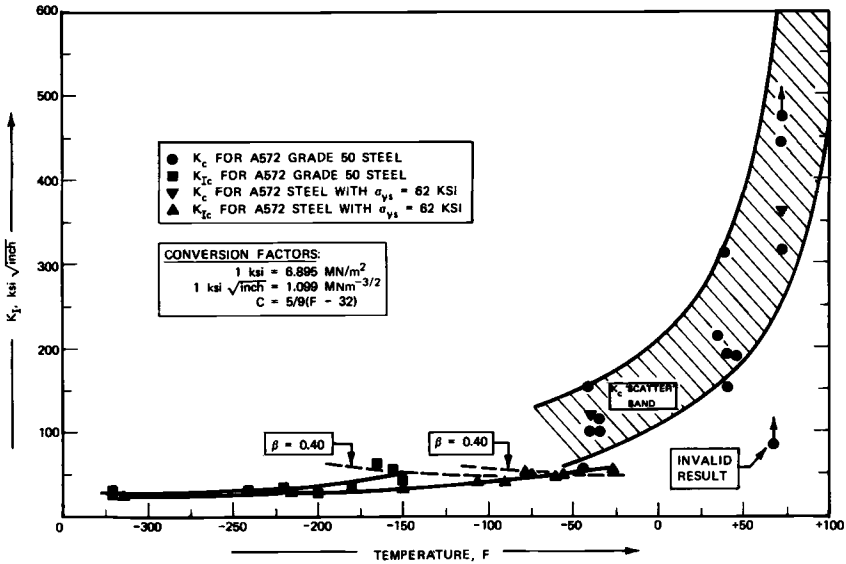


FIG. 5—Summary comparisons of  $K_c$  and  $K_{Ic}$  behavior obtained from 1.5-in.-thick plates of A572 steel.

H-beams with small web dimensions (indirect applicability of  $a_{cr}$  values for assessing the confidence level of structural integrity).

Many of the results above were obtained by using the COS analysis method under state-of-the-art conditions. Because this method of analysis is still undergoing development, the limitations of this technique are not defined precisely. Furthermore, many questions still remain concerning plane-stress fracture generally, even for results obtained under LEFM conditions. Nevertheless, the present studies have been an encouraging first step in the understanding of the plane-stress fracture behavior of A572 Grade 50 steel, and similar medium-strength constructional steels, and of the general applicability of plane-stress-fracture data (R-curve and  $K_c$  measurements) to structural components.

In summary, a complete manuscript describing the results of the entire study in detail has been published by the photo offset method and is available under identical title as *ASTM STP 591*. Figures 1 through 5, taken from the complete manuscript, illustrate the nature of the experimental technique employed, typical R-curve results obtained under three of the test conditions investigated, and a summary comparison of part of the resulting  $K_c$  and earlier  $K_{Ic}$  behaviors measured as a function of temperature.

L. B. Freund,<sup>1</sup> D. M. Parks,<sup>2</sup> and J. R. Rice<sup>1</sup>

## Running Ductile Fracture in a Pressurized Line Pipe

---

**REFERENCE:** Freund, L. B., Parks, D. M., and Rice, J. R., "Running Ductile Fracture in a Pressurized Line Pipe," *Mechanics of Crack Growth, ASTM STP 590*, American Society for Testing and Materials, 1976, pp. 243–262.

**ABSTRACT:** A model is developed for steady state propagation of a ductile crack in an initially pressurized line pipe. The analysis is directed toward the high toughness range of material behavior, for which extensive yielding occurs in the pipeline walls, and the material is represented as rigid-ideal plastic. Further, to obtain a tractable model, kinematical assumptions are made so that the deformation of the shell is expressed in terms of a single unknown function of position along the shell axis, which is determined in accordance with a variational statement of the equations of motion. Separation of material is represented by a Dugdale zone of localized yielding, in which a critical opening displacement is attained for fracture. With these approximations, the required decay length of the pressure distribution necessary to drive the crack, for a given exit plane pressure and decay shape, and the profile of the opened fracture, are estimated. Inertial effects due to the shell walls and backfill and crack arrest by branching are discussed, although it is pointed up that a complete analysis must await further progress on the fluid dynamics of gas escape through the fracture opening.

**KEY WORDS:** crack propagation, pipe lines, fracture properties, stresses, strains, plastic deformation

Service experience has shown that ductile shear fractures can propagate long distances at very high rates in a large diameter pressurized line pipe, such as that used in gas transmission pipelines. With a view toward developing an understanding of this phenomenon, the American Iron and Steel Institute has sponsored a series of full-scale tests of large diameter pipes to determine the propagation and arrest characteristics of running ductile fractures. In each of these tests the pipe was instrumented with

<sup>1</sup> Professor, Division of Engineering, Brown University, Providence, R.I. 02912.

<sup>2</sup> Assistant professor, Department of Engineering and Applied Science, Yale University, New Haven, Conn. 06520.

crack detectors, strain gages, and pressure transducers, and the electronically recorded data which were obtained are summarized elsewhere [1].<sup>3</sup> The present analytical investigation was undertaken in an effort to resolve various discrepancies which arose between observations and the basic assumptions of previous analytical models of the process.

The mathematical model which has been proposed to represent the ductile fracture of line pipe by Hahn et al [2,3] and Duffy et al [4] has two main features. First, the crack is considered to be small in length compared to the pipe diameter, and, in the case of a long running fracture, a small "effective" crack length is employed. The driving force for this crack is taken to be a modified or reduced hoop stress derived from a measure of internal pressure at the crack tip. The second main feature is a fracture criterion which is a modified form of a critical crack tip opening displacement condition. In the analysis summarized by Maxey et al [5], the hoop stress acting at the crack tip was first reduced from the hoop stress corresponding to the nominal line pressure by taking into account the escape of gas through the crack opening. The crack driving force was then taken to be this reduced hoop stress, amplified by a factor which accounted for outward bulging associated with an axial crack in a cylindrical pressure vessel. The amplification factor was determined from Folias' analysis [6], wherein it is assumed that the crack length is small compared to the cylindrical shell radius and that the material remains elastic everywhere. This driving force was then substituted into the fracture criterion. By equating the fracture toughness to the product of critical crack opening displacement (COD) and apparent yield stress, the fracture condition was reduced to a relationship between the modified hoop stress and the fracture toughness, the latter being considered determinable from Charpy tests.

The continued development of this work by Hahn et al [3] has included other features to make the model more realistic, such as decompression of the gas due to radial expansion of the pipe walls, strain rate sensitivity of the flow stress of the material, and further consideration of the ductile cracking process. Poynton and Fearnough [7] recently summarized this work, and they concluded that two main factors contribute to maintenance of a running crack, these being related to the radial velocity of the pipe walls and the COD.

The results from the instrumented full-scale tests, as reported by Ives et al [1], indicate that the appropriate model of a running ductile fracture in a line pipe is not one in which the crack driving force is derived from the nominal hoop stress acting just ahead of the fracture. It appears instead that the crack is driven by the residual pressure acting on the flaps formed by the separated pipe walls behind the crack tip. The main results from

<sup>3</sup> The italic numbers in brackets refer to the list of references appended to this paper.

the measurements, which support this conclusion, are that at about two pipe diameters ahead of the crack the circumferential strain distribution indicates ovalization of the pipe, the crack line being at one end of the minor axis of the oval. The longitudinal strains are much larger than the circumferential strains at this point, and they indicate deformation well into the plastic region. As the crack tip approaches the measuring station, the circumferential strain changes from a bending to a stretching mode. The inward motion and accompanying bending ahead of the crack is attributed [1] to the radial outward flaring of the shell walls under the action of the residual pressure. As the crack opens, the pipe walls experience significant circumferential displacement near the crack line, and this is associated with the large extensional strains in both the axial and circumferential directions near the crack tip.

### **Deformation Field**

The work reported upon here was motivated by the desire to provide an analytical description of a running ductile fracture in a pressurized pipe which included the salient results of the full-scale tests as reported elsewhere [1]. In particular, relationships among the main parameters of the system were sought which had to be satisfied in order to sustain the running fracture. The complexity of the problem is well known, and, in order to obtain results in a reasonably short time, several major assumptions were made. First of all, the ratio of pipe wall thickness to mean pipe radius is generally small compared to unity, and the theory of thin shells [8,9] is thus assumed to apply. While the subsequent method of analysis does not preclude the use of strain-displacement gradient relations appropriate to large deflections, this complicating aspect is neglected for the time being, and the small deflection formulation for thin shells is adopted.

In the actual tests, crack extension is clearly a transient process. The data indicate, however, that after the crack tip has moved from the initiator a distance of about four pipe diameters, a deformation field is achieved around the crack tip which is maintained essentially as the crack continues to grow. This implies that the fracture process is insensitive to the length of the crack, and, for the purposes of analysis, the crack is taken to be semi-infinite in length. In those tests in which the crack did indeed propagate from the initiator without arrest, it frequently did so at a constant rate in each uniform test section. Therefore, it is assumed that the tip of the semi-infinite crack moves at a constant speed along a generator of the cylindrical pipe, and that the deformation field as viewed by an observer moving with the crack tip is time independent.

On the basis of these assumptions, the problem is still not in a form which can be analyzed without resorting to extensive numerical calculations. Therefore, it is assumed that the entire deformation field of the shell

is determined by a single function of the axial coordinate, that is, all displacement and strain components are known once this single function of distance along the axis of the cylindrical shell is known. An important observation in making assumptions concerning the deformation is that generally thin shells tend to deform predominantly by bending, with minimal stretching of the middle surface. For a cylindrical shell, the only deformations satisfying strict inextensibility are those for which all generators of the cylinder remain straight during deformation. In the case of an axial fracture in a cylindrical shell, the generator ahead of the crack tip which forms the prospective fracture path is split by the crack into the two fracture surfaces. Behind the crack tip the shell walls flare outward, and the crack surfaces separate. This deformation is clearly incompatible with each generator remaining straight. Some middle surface stretching must accompany the flaring out of the shell walls at the tip of the advancing crack. Study of the shell strain-displacement relations suggests that the observed flaring of the walls is accompanied by stretching of the middle surface in the axial direction, which was reported in Ref 1. Thus, it is assumed in proposing a deformation field that the in-plane strain of the middle surface of the shell consists only of extension in the axial direction. The in-plane shear strain and the extension in the circumferential direction are taken to be zero, except for the latter within a line Dugdale zone of plastic separation.

Spatial coordinates on the shell surface are defined in Fig. 1. The mean radius of the undeformed shell is  $a$ , the shell thickness is  $h$ , the circumferential coordinate is  $\theta$ , and the axial coordinate is  $\xi$ , the origin  $\xi = 0$  being fixed at the moving crack tip. If  $x$  is a spatially fixed axial coordinate and  $V$  is the speed of the crack tip, then  $\xi = Vt + x$ . Because of the assumption of a quasi-stationary condition, all field variables depend on  $x$  and  $t$  only through  $\xi$ . The crack faces coincide with the lines  $0 < \xi < \infty$ ,  $\theta = \pm \pi$  on the shell. Following the fairly standard notation [8,9], the axial, circumferential and radial components of the displacement vector of a point initially at  $(\xi, \theta)$  are denoted by  $u, v, w$ . The assumed displacement field is expressed in terms of a single unknown

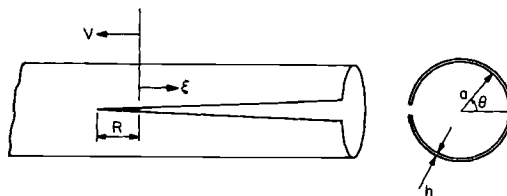


FIG. 1—Geometry of steady-state crack propagation in a pressurized pipeline.

function of  $\xi$ , namely,  $\psi(\xi)$ , by

$$w = \psi(\xi) \tag{1}$$

$$v = -\theta\psi(\xi) \tag{2}$$

$$u = \frac{1}{2} a\psi'(\xi)\theta^2 + g(\xi) \tag{3}$$

This displacement field was constructed by assuming that each circular cross section deforms into a concentric circle, and then by requiring that the circumferential and shear strains of the middle surface vanish. The function  $g(\xi)$  is arbitrary at this point. The corresponding strains are given by

$$\epsilon_\xi = \frac{\partial u}{\partial \xi} = \frac{1}{2} a\psi''(\xi)\theta^2 + g'(\xi) \tag{4}$$

$$\kappa_\xi = -\frac{\partial^2 w}{\partial \xi^2} = -\psi''(\xi) \tag{5}$$

$$\kappa_\theta = -\frac{1}{a^2} \frac{\partial^2 w}{\partial \theta^2} + \frac{1}{a^2} \frac{\partial v}{\partial \theta} = -\frac{1}{a^2} \psi(\xi) \tag{6}$$

$$\kappa_{\xi\theta} = -\frac{1}{a} \frac{\partial^2 w}{\partial \xi \partial \theta} + \frac{1}{a} \frac{\partial v}{\partial \xi} = -\frac{1}{a} \theta\psi'(\xi) \tag{7}$$

where

$\epsilon_\xi$  = axial strain,

$\kappa_\xi$  and  $\kappa_\theta$  = changes in axial and circumferential curvature of the middle surface, and

$\kappa_{\xi\theta}$  = change in torsion of the middle surface.

According to the usual theory of thin shells, the force variables conjugate to these strains are  $N_\xi$ , the axial force per unit length along the middle surface in the circumferential direction,  $M_\xi$  and  $M_\theta$ , the bending moments per unit length in the circumferential and axial directions, and  $M_{\xi\theta}$ ,  $M_{\theta\xi}$ , the twisting moments per unit length in the coordinate directions. The assumed constitutive relations for the force and deformation variables are stated in a later section.

The deformation field (Eqs 1 to 3) results in zero circumferential strain, while the measurements indicate the occurrence of significant circumferential strains near the crack line ahead of the crack tip. This is accounted

for in the model by including a one-dimensional plastic zone of the Dugdale type [10] ahead of the advancing crack tip. In effect, this concentrates all of the circumferential strain in this one-dimensional plastic zone. The plastic zone occupies the interval  $0 > \xi > -R$ , as shown in Fig. 1, implying that  $\psi \equiv 0$  for  $\xi < -R$ . Of course,  $R$  is ultimately to be determined as part of the analysis. Within the plastic zone, relative motion of the crack faces is resisted by a cohesive stress which is defined in terms of  $T(\xi)$ , the cohesive force per unit length of middle surface. No bending moment is transmitted across the cohesive zone. The amount of crack opening  $\delta(\xi)$  is given by

$$\delta(\xi) = -2v(\xi, \pi) = 2\pi\psi(\xi) \quad (8)$$

and the crack tip opening displacement is defined as  $\delta_t \equiv 2\pi\psi(0)$ . The definition of  $T(\xi)$  is extended so that  $T(\xi) = 0$  for  $\xi > 0$ .

#### Distribution of Applied Pressure

The applied loading in this problem is the internal pressure, and, because  $\psi = 0$  for  $\xi < -R$ , this must be specified in the range  $-R < \xi < \infty$ . The experimental data suggest that the angular variation in pressure acting on the pipe wall is small, for any fixed value of  $\xi$ . Consequently, it is assumed that the pressure distribution acting on the pipe wall is a function of axial coordinate, say  $p(\xi)$ , and is independent of the angular coordinate  $\theta$ . The data also indicate that the pressure is reasonably uniform a diameter or so ahead of the crack, and hence in the cohesive zone interval  $-R < \xi < 0$ , and the magnitude there is equal to the velocity dependent pressure at the crack tip employed in the analysis elsewhere [3] and [5]. Denoting this magnitude by  $p_0(V)$ , it can be shown that

$$\frac{p_0(V)}{p_L} = \left[ \frac{2}{\gamma + 1} + \frac{(\gamma - 1)V}{(\gamma + 1)c_L} \right]^{\frac{2\gamma}{\gamma - 1}} \quad (9)$$

where  $p_L$  and  $c_L$  are line pressure and sonic speed of the gas at  $\xi \rightarrow -\infty$ , and  $\gamma$  is the ratio of specific heat at constant pressure to specific heat at constant volume for the gas. For air  $\gamma \approx 7/5$ . The relation (Eq 9) is determined by analyzing a certain transient, one-dimensional flow in a semi-infinite pipe. Initially, the pressure and density of the gas within the pipe are spatially uniform and constant in time. At a certain instant the gas is allowed to escape through the end of the pipe, and, simultaneously, the pipe begins to "shorten" at a rate identified with the speed of crack propagation in the fracture model. If the boundary condition imposed at

the open end of the pipe is that the local particle velocity of the gas, relative to the moving end of the pipe, is the local sound speed, then it can be shown by the method of characteristics that the pressure at the exit is given by Eq 9. While the profile of the expansion wave propagating down the pipe from the open end is time dependent, the exit plane pressure itself does not depend on time explicitly. Behind the moving crack tip the pressure is assumed to decay continuously from  $p_0$  at the tip to zero at some distance, say  $\lambda$ , behind the crack tip. Thus, to complete the definition

$$p(\xi) = \begin{cases} p_0 & -R < \xi \leq 0 \\ p(\xi) & 0 < \xi \leq \lambda \\ 0 & \lambda < \xi < \infty \end{cases} \quad (10)$$

**Equation of Motion for the Pipe Wall**

The fundamental physical principle governing the deformaion of the shell is taken to be the principle of virtual work. For any deformable body the principle can be stated in terms of any equilibrium distribution of internal stresses or generalized stresses which balance the applied loads (including, by D'Alembert's principle, inertial forces) and any unrelated distribution of compatible strains and associated displacements. For the problem at hand, the internal generalized stresses are  $N_\xi, M_\xi, M_\theta, M_{\xi\theta}, M_{\theta\xi}$  and the conjugate strains are (written in the more conventional form as variations in strain)  $\delta\epsilon_\xi, \delta\kappa_\xi, \delta\kappa_\theta, \delta\kappa_{\xi\theta}$  so that the internal virtual work is

$$\delta W_{int} = \int_s \left[ N_\xi \delta\epsilon_\xi + M_\xi \delta\kappa_\xi + M_\theta \delta\kappa_\theta + \frac{1}{2} (M_{\xi\theta} + M_{\theta\xi}) \delta\kappa_{\xi\theta} \right] ds \quad (11)$$

where  $S$  represents the entire middle surface of the shell. For application of the principle of virtual work to dynamical problems, the inertial resistance to motion is viewed as an external body force. Thus, the external virtual work has three contributions, namely, the virtual work due to the internal pressure  $p(\xi)$ , the cohesive stress in the plastic zone  $T(\xi)$ , and the inertial force per unit surface area which has components  $-\rho \partial^2 u / \partial t^2, -\rho \partial^2 v / \partial t^2, -\rho \partial^2 w / \partial t^2$  where  $\rho$  is the mass density per unit area of the middle surface. Because the problem is quasi-stationary, the operation of time differentiation can be replaced by  $V \partial / \partial \xi$ . The virtual displacements through which the external forces work are  $\delta w(\xi, \theta), \delta v(\xi, \pm \pi)$  and the vector with components  $\delta u(\xi, \theta), \delta v(\xi, \theta), \delta w(\xi, \theta)$ , respectively.

The external virtual work is then

$$\delta W_{\text{ext}} = \int_s \left[ p \delta w - \rho V^2 \left( \frac{\partial^2 u}{\partial \xi^2} \delta u + \frac{\partial^2 v}{\partial \xi^2} \delta v + \frac{\partial^2 w}{\partial \xi^2} \delta w \right) \right] ds \quad (12)$$

$$+ \int_{-R}^{\infty} 2T \delta v d\xi$$

The principle of virtual work then requires that  $\delta W_{\text{int}} = \delta W_{\text{ext}}$ , and this is fully equivalent to the Cauchy equations of stress equilibrium or of motion, if satisfied for every possible virtual deformation field. The approximation made here consists of requiring validity of the principle only for all virtual deformations generated by our kinematic assumptions, Eq 1 through 7. It remains to specify the behavior of the material of the shell walls. Because of the very extensive plastic deformation of the pipe which was observed in the tests, it is assumed as a first approximation that the walls of the shell behave in a rigid-perfect plastic manner. Even for this relatively simple type of material behavior, an analysis which takes into account all of the terms appearing in the virtual work equation would be prohibitively complicated. A preliminary analysis in which the shell walls were taken to be elastic showed that the effects of terms in the final differential equation arising from axial bending and torsion of the middle surface were negligible compared to those arising from circumferential bending and axial extension, the latter being by far the dominant effect. With this as guidance, it is assumed that the shell offers negligible resistance to axial bending or torsion, that is,  $M_\xi = 0$  and  $M_{\xi\theta} = M_{\theta\xi} = 0$ . Furthermore, inertial effects in the radial and circumferential directions appeared to be much greater than in the axial direction; therefore, the latter is neglected. Incorporating these assumptions and the deformation described in Eqs 1 to 3, the principle of virtual work implies that

$$\int_{-\infty}^{\infty} \left\{ \int_{-\pi}^{\pi} \left[ \left[ \frac{1}{2} a \theta^2 \delta \psi''(\xi) + \delta g'(\xi) \right] N(\xi, \theta) - \frac{1}{a^2} \delta \psi(\xi) M(\xi, \theta) \right. \right. \\ \left. \left. - p(\xi) \delta \psi(\xi) + \rho V^2 (1 + \theta^2) \psi''(\xi) \delta \psi(\xi) \right] a d\theta \quad (13) \right. \\ \left. + 2T(\xi) \pi \delta \psi(\xi) \right\} d\xi = 0$$

where  $N_\xi \equiv N$  and  $M_\theta \equiv M$ . Finally, consistent with the idealized rigid-plastic description of material behavior to be described shortly and

with the kinematic assumptions,  $M(\xi, \theta)$  can be viewed as being independent of  $\theta$  and the magnitude of  $N$  is constant on any cross section, its sign being the same as that of  $\epsilon_\xi$ . As can be seen from Eq 4, the resultant axial force on any cross section of the shell will be zero if  $g(\xi) = -1/2a\psi'(\xi)\pi^2/4$ , and this choice is made. The integration with respect to  $\theta$  can then be carried out in Eq 13. An integration by parts in the remaining integral yields

$$\int_{-\infty}^{\infty} \left[ \frac{1}{8} a^2 \pi^2 N''(\xi) - \frac{1}{a} M(\xi) - ap(\xi) + T(\xi) + \rho V^2 a \left( 1 + \frac{\pi^2}{3} \right) \psi''(\xi) \right] \delta\psi(\xi) d\xi = 0 \tag{14}$$

where it has been assumed that  $N'$  and  $\psi'$  vanish as  $|\xi| \rightarrow \infty$ , and that  $\psi''$  and  $N''$  are piecewise continuous. The principle of virtual work applies for any arbitrary variation  $\delta\psi$ . The coefficient of  $\delta\psi$  in Eq 14 must vanish identically, which yields the field equation governing the deformation, that is

$$\frac{1}{8} a^2 \pi^2 N''(\xi) - \frac{1}{a} M(\xi) = ap(\xi) - T(\xi) - \rho V^2 a \left( 1 + \frac{\pi^2}{3} \right) \psi''(\xi) \tag{15}$$

**Rigid-Perfect Plastic Model**

The yield surface for the shell, phrased in terms of the retained shell generalized stresses  $N$  and  $M$  of Eq 15, was formulated assuming a Tresca condition. Because the axial normal traction  $N$  and circumferential bending moment  $M$  act on orthogonal planes of an element of the shell, it is perhaps obvious that the yield surface for these generalized stresses is precisely the same as that obtained when the generalized stresses used are the circumferential normal traction and the axial bending moment, respectively, since these act on corresponding faces. The derivation of this yield surface is given in Ref 11, and one quadrant of the yield surface obtained is shown in Fig. 2.

The solid curve is the exact yield surface. The problem is further simplified by employing the approximate rectangular yield surface shown by dashed lines, and crossing the axial force axis at the 0.75 point. The axes are normalized with respect to  $N_0$  and  $M_0$ , the yield resultants in pure extension and pure bending, respectively, which are given by

$$N_0 = \sigma_0 h, M_0 = \sigma_0 h^2/4 \tag{16}$$

where  $\sigma_0$  is the uniaxial tensile yield stress and  $h$  is the shell thickness.

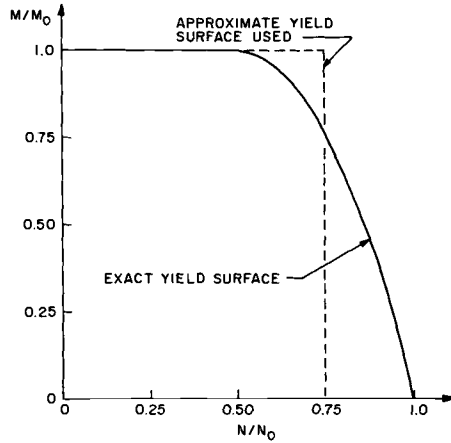


FIG. 2—One quadrant of exact and approximate yield surfaces for the generalized stresses  $N$  and  $M$ .

Before proceeding with the solution, it is worthwhile to note that the deformation field  $\psi$  is intimately coupled with the stress fields  $N$  and  $M$  for this rigid-plastic model. From Eq 4 and the choice made for  $g(\xi)$ , the axial stretching rate  $\dot{\epsilon}_z$  is proportional to  $\psi''(\xi)$ , and from Eq 6 the circumferential bending curvature rate  $\dot{\kappa}_\theta$  is proportional to  $-\psi'(\xi)$ . But these work-conjugate generalized strain rates, which are the components of the normal to the yield surface, apply only when the stress state is at yield. From Eq 8, the crack face opening  $\delta(\xi)$  is proportional to  $\psi$ . Thus, for example, the bending moment  $M$  must be equal to  $-M_0$  at all points where the crack face opening profile has nonzero slope, including the Dugdale plastic zone. Because the crack faces are postulated to be separating in the deforming region, the moment stress may be taken as  $M(\xi) = -M_0$  in Eq 15.

In order to simplify Eq 15 further, the inertial terms, which were assumed to be small, were dropped, in essence by letting the mass density tend to zero. A perturbation technique, to be discussed later, demonstrates the validity of the assumption.

This effectively removes the deformation field from the governing field equation to give

$$\frac{a^2\pi^2}{8} N''(\xi) = ap(\xi) - T(\xi) - M_0/a \quad (17)$$

However, an associated deformation field consistent with the plastic potential relations in terms of the (to be determined) stress field is also obtained.

Since deformation begins at the tip of the Dugdale zone, and  $\psi(-R) = 0$ , we must have a discontinuity in the crack face curvature across  $\xi = -R$  of some unknown magnitude  $\psi''_0$ . We assume the curvature change to be positive; hence,  $N(-R) = 0.75N_0$ . Because there are no concentrated forces at the tip of the Dugdale zone,  $N'(-R) = 0$ .

Although no particular magnitude or distribution of the cohesive force in the Dugdale zone has been assumed, it will be at least of size  $\sigma_0 h$ , since the material is yielding. In any event, its magnitude will exceed that of  $ap_0$ , for otherwise the entire uncracked portion of the shell would be at yield. For the analysis performed here, the usual Dugdale assumption is made, and  $T(\xi)$  is taken to be a constant,  $T_0$ , in the plastic zone. Thus the sign of  $N''(\xi)$  is negative in  $-R < \xi < 0$ , and so  $N(\xi)$  decreases from its yield value at  $\xi = -R$ . Hence, the curvature of the crack face opening remains constant in this region, so that the crack tip opening displacement  $\delta_t$  is given by

$$\delta_t = \pi R^2 \psi''_0 \tag{18}$$

At the crack tip, the right hand side of Eq 17 increases discontinuously by an amount  $T_0$  to the positive value  $ap_0 - M_0/a$ . The axial force resultant  $N$  continues to decrease in the region  $0 < \xi < \lambda_1 < \lambda$  with positive second derivative. The distance  $\lambda_1$  is specified by the requirements that the axial force reach reversed yielding with zero slope, so as not to violate the yield condition, that is

$$N(\lambda_1) = -0.75N_0, \quad N'(\lambda_1) = 0 \tag{19}$$

At this point, the curvature of the crack face opening, which has remained at the constant value  $\psi''_0$ , changes sign to the negative value  $\psi''_1$ , which is admissible since the axial force is at yield in compression. The right hand side of Eq 17 is still positive at  $\xi = \lambda_1$ , so that  $N$  starts to increase away from yield. Hence, the crack face curvature remains at the constant value  $\psi''_1$ .

At some point a small distance to the left of  $\xi = \lambda$ , the right hand side of Eq 17 changes sign continuously to a negative value, and, for  $\lambda \leq \xi < \lambda_2$ , is given by the constant value  $-M_0/a$ . That this is a small distance to the left of the point  $\xi = \lambda$  is seen by noting that  $ap_0$  is typically of order  $T_0$ , while  $M_0/a$  is of order  $T_0(h/a)$ . The distance  $\lambda_2$  is given, in a similar manner to  $\lambda_1$ , by the conditions that the axial force reach tensile yield with zero slope

$$N(\lambda_2) = 0.75N_0, \quad N'(\lambda_2) = 0 \tag{20}$$

Here, the curvature of the crack face which has been the constant  $\psi''_1$  in  $\lambda_1 < \xi < \lambda_2$  increases discontinuously to zero. It is also assumed that the slope of the crack profile is zero at  $\xi = \lambda_2$ , and that no further deformation takes place for  $\xi > \lambda_2$ . Thus, the entire crack profile consists of two parabolas, which have matching values and slopes at  $\lambda_1$ , and which have zero slopes at  $-R$  and  $\lambda_2$ , respectively. The shape of the crack face is shown schematically in Fig. 3. Because this is essentially a quasi-static plastic limit analysis, there is no characteristic displacement amplitude associated with the field  $\psi$ . Hence, this amplitude is determined by the critical crack tip opening  $\delta_c$ , which is meant to characterize the fracture toughness of the material.

Another displacement parameter, to be discussed later, is the terminal crack face separation  $\delta_{term}$  for  $\xi > \lambda_2$ , also shown in Fig. 3, which is given by

$$\delta_{term} = \delta_c(1 + \lambda_1/R)(1 + \lambda_2/R) \tag{21}$$

A simple graphical technique can be used to determine if an arbitrary pressure distribution  $p(\xi)$ , characterized by a magnitude  $p_0$ , a decay length  $\lambda$  and a particular shape, is sufficient to drive the crack. If pressure shape and decay length are given, then the pressure amplitude must be at least a specified value. Alternatively, if the pressure magnitude and shape are given, a necessary decay length is determined. This is the approach used here.

Because the decay length  $\lambda$  must be determined in terms of the material, structural, and other loading parameters, the axial coordinate  $\xi$  is nondimensionalized by dividing by  $\lambda$ . Hence defining

$$r = R/\lambda, \quad l_1 = \lambda_1/\lambda, \quad l_2 = \lambda_2/\lambda \tag{22}$$

the right-hand side of Eq 17 can be drawn as a function of the dimension-

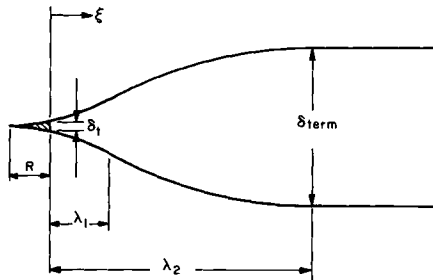


FIG. 3—Schematic representation of the crack face opening profile.

less coordinate  $\eta = \xi/\lambda$ , as shown in Fig. 4. Since there is no change in the first derivative of  $N$  between  $-r$  and  $l_2$ , there must be no net area under the curve of Fig. 4 between  $-r$  and  $l_2$ . Further, there is no change in the value of  $N$  evaluated at  $-r$  and  $l_2$ . Hence, because there is no net area under the curve, an elementary application of the moment area theorem furnishes a second requirement on the load distribution, namely, the total moment of the curve between  $-r$  and  $l_2$  about any point be zero.

Let  $q = T_0 + M_0/a - ap_0$  and  $m = M_0/a$ . Further, let the total area of the pressure part of the loading in  $0 \leq \eta \leq 1$  be  $\alpha(ap_0)$ , with  $0 < \alpha \leq 1$  (for nonincreasing  $p(\xi)$ ), and the moment of this portion of the pressure about the point  $\eta = 0$  be given by  $\beta(\alpha ap_0)$ , with  $0 < \beta \leq 1/2$ . Thus, the two conditions become

$$rq + ml_2 = \alpha ap_0 \tag{23}$$

$$\frac{1}{2} qr^2 - \frac{1}{2} ml_2^2 = \beta \alpha ap_0 \tag{24}$$

which readily furnish the dimensionless plastic zone size and the point of terminal deformation behind the crack in terms of the load magnitude,  $p_0$ , as

$$r = \frac{\alpha ap_0}{(q - m)} \left\{ 1 - \left( \frac{m}{q} + 2 \frac{\beta m}{\alpha ap_0} \left[ 1 - \frac{m}{q} \right] \right)^{1/2} \right\} \tag{25}$$

$$l_2 = \frac{\alpha ap_0}{(q - m)} \left\{ \frac{a}{m} \left( \frac{m}{q} + 2 \frac{\beta m}{\alpha ap_0} \left[ 1 - \frac{m}{q} \right] \right)^{1/2} - 1 \right\} \tag{26}$$

The nondimensional distance from the crack tip to the change of crack face curvature,  $l_1$ , is obtained implicitly from the fact that there is no

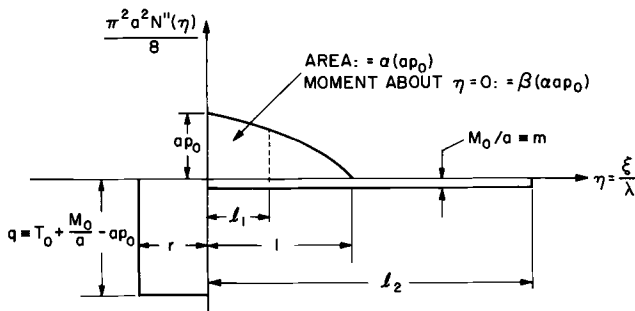


FIG. 4—Graphical solution of field equation for prescribed pressure amplitude.

change in the first derivative of  $N$ , evaluated at  $-r$  and  $l_1$ , that is

$$rq = \int_0^{l_1} [ap(\eta) - m] d\eta \quad (27)$$

Finally, the absolute size of the loading decay distance  $\lambda$  can be obtained by noting that the absolute value of the change in  $N$  from  $-r$  to  $l_1$  is  $1.5N_0$ . Applying the moment-area theorem again

$$\frac{1}{2}qr^2 + \int_0^{l_1} \eta [ap(\eta) - m] d\eta = \frac{a^2\pi^2}{8\lambda^2} (1.5N_0) \quad (28)$$

It may be observed that a pressure level and the loading distances which are then obtained from Eqs 23 to 28 are sufficient to continue crack propagation regardless of material toughness as measured by  $\delta_t$ , a consequence simply of the rigid-perfect plastic constitutive model. This is represented by the vertical line of Fig. 5. In reality, the true elastic-plastic value of  $\delta_t$ , as would be calculated to correspond to fracturing under a given pressure magnitude at fixed shape and loading distance, is an increasing function of that magnitude and would have the form shown by the curved line of Fig. 5. This curve consists of the typical quadratic increase with load magnitude associated with small-scale yielding, fol-

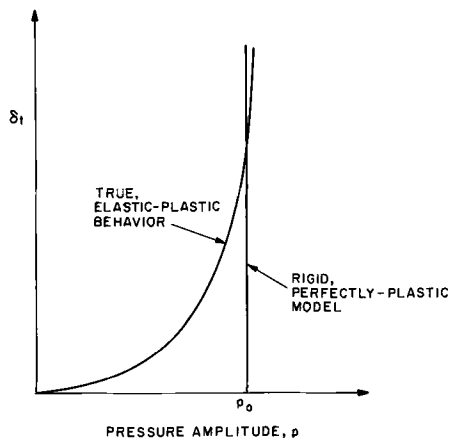


FIG. 5—Crack opening displacement as function of pressure amplitude for fixed shape and loading distance.

lowed by a steep rise in the vicinity of the particular “limit pressure” chosen, perhaps existing even for pressure magnitudes in excess of this limit pressure, due to strain hardening. Thus the significance of the limit pressure and associated load decay lengths of the rigid-perfect plastic idealization becomes clear: it is a measure of the driving force necessary to sustain crack propagation for high toughness (high  $\delta_t$ ) materials and will vary only slightly from the true magnitude of driving force required, regardless of toughness, provided only that the toughness is sufficiently high.

**Linear Pressure Decay**

The analysis of the preceding sections was applied to the case of a linear pressure decay, from  $p_0$  to 0, over the decay length  $\lambda$ . That is,

$$p(\xi) = \begin{cases} p_0 & , -R \leq \xi \leq 0 \\ p_0(1 - \xi/\lambda) & , 0 \leq \xi \leq \lambda \\ 0 & , \lambda < \xi \end{cases} \quad (29)$$

Thus, for this particular distribution,  $\alpha = 1/2$  and  $\beta = 1/3$ . The constant  $T_0$  was chosen to be equal to  $\sigma_0 h$ . The shell parameter  $a/h$  was set equal to 56.

The various loading distances were computed and are shown in Fig. 6, after making each dimensionless by dividing by the mean shell radius  $a$ , as a function of exit pressure magnitude  $p_0$ . For typical line pressurizations and observed ductile crack velocities, most running fractures appear to have exit pressures in the range  $0.3 < (ap_0/T_0) < 0.6$ , if  $T_0$  is based on the static yield strength. Thus, as we read from the figure, the required decay length  $\lambda$  for propagation of the fracture under pressures in this range is predicted to lie between approximately 3.5 and 6.5 radii, the higher figure corresponding to the lower pressure and vice versa. The observed pressure decays [1] do not, of course, strictly comply with a linear variation; however, decay lengths in the range of 2 to 4 radii appear typical. The somewhat greater  $\lambda$  predicted may be a result of the many approximations that have been made but may also reflect the fact illustrated in Fig. 5 that our calculations apply to the high toughness limit. The Dugdale plastic zone size  $R$  is predicted to lie between one and two radii.

The first transition point  $\lambda_1$ , at which the curvature of the outward flaring of the wall reverses, is seen to lie at approximately 70 percent of  $\lambda$ , whereas the second transition point  $\lambda_2$  beyond which motion has come to a stop occurs much further downstream at a distance of approximately 32 radii over the entire pressure range of interest. The terminal opening can be computed from Eq 21 for a given crack tip opening displacement by using the results of Fig. 6 as shown in Fig. 7 in the form  $\delta_{term}/a$ , where again

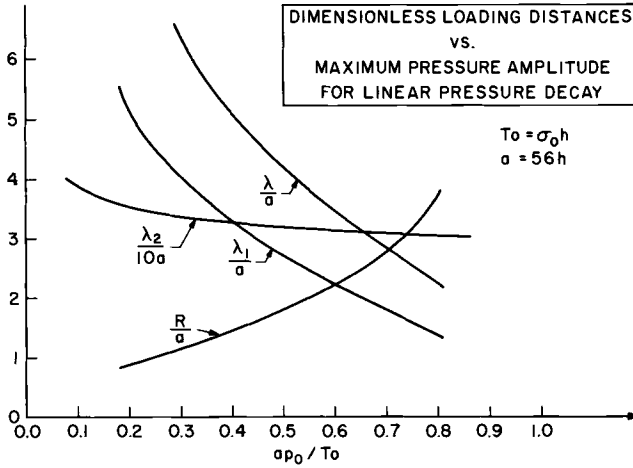


FIG. 6—Loading distances as a function of pressure magnitude for linear pressure decay.

we have chosen  $a/h = 56$  and where the crack tip opening displacement for fracture has been set equal to the wall thickness. Hence, terminal openings between a half and two radii are predicted, with the greatest opening at the lower driving pressure but longer decay length. These estimates seem to be of the correct general size, although terminal openings in this range can be accurately predicted only within an analysis which adopts the strain-displacement gradient relations appropriate to large gradients.

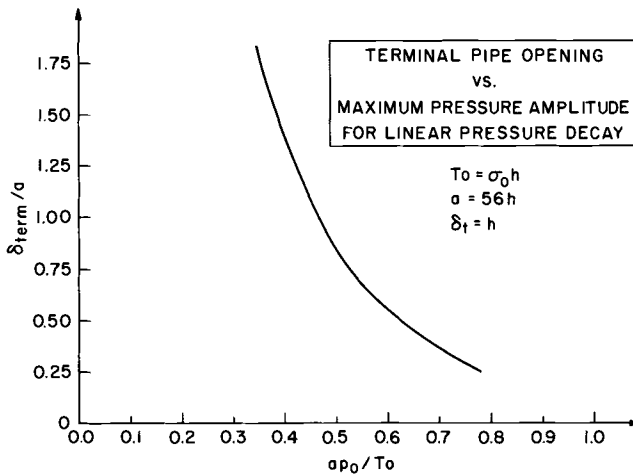


FIG. 7—Terminal crack separation  $\delta_{term}$  as a function of pressure magnitude for fixed toughness and linear pressure decay.

**Effects of Wall Inertia**

The last two sections have neglected inertia of the pipe wall by setting  $\rho = 0$  in Eq 15. Actual effects of wall inertia are assessed here in two ways. Somewhat surprisingly, both lead to the conclusion that wall inertia is a small effect over the crack speed range of interest, although there may be significant inertial effects due to backfill. A first estimate may be made by adopting the deformation function  $\psi$  as computed quasi-statically in the last section, and computing the pressure magnitude  $p_i$  that would be the equivalent of the inertia term in Eq 15, namely

$$p_i = -\rho V^2 \left( 1 + \frac{\pi^2}{3} \right) \psi''(\xi) \tag{30}$$

For steel the density  $\rho$  per unit wall surface area is 15.5 lb s<sup>2</sup>/ft<sup>4</sup> times  $h$ . Also, from Fig. 3, Eq 8, and the discussion following Eq 19

$$\psi''(\xi) = \frac{1}{2\pi} \delta''(\xi) = \begin{cases} \delta_t/\pi R^2, & -R < \xi < \lambda_1 \\ -(\delta_t/\pi R^2)(R + \lambda_1)/(\lambda_2 - \lambda_1), & \lambda_1 < \xi < \lambda_2 \end{cases} \tag{31}$$

Thus, for the two ranges, the pressure in psi is

$$p_i = \frac{15.5}{144\pi} \left( 1 + \frac{\pi^2}{3} \right) \left( V \frac{s}{ft} \right)^2 \left( \frac{h}{a} \right)^2 \left( \frac{\delta_t}{h} \right) \left( \frac{a}{R} \right)^2 \left\{ 1, -\frac{\frac{R}{a} + \frac{\lambda_1}{a}}{\frac{\lambda_2}{a} - \frac{\lambda_1}{a}} \right\} \tag{32}$$

Taking  $a/h = 56$ ,  $\delta_t = h$ , the ratios of  $R$ ,  $\lambda_1$ , and  $\lambda_2$  to  $a$  as in Fig. 6 for  $a\rho_0/T_0 = 0.45$ , and  $V = 600$  ft/s leads to equivalent pressures

$$p_i = - 6.6 \text{ psi}, 1.0 \text{ psi} \tag{33}$$

These are so small by comparison to pressure levels of order 1000 psi at the crack tip that wall inertia seems to be a minor factor.

Wall inertia was further examined through solving Eq 15 for the rigid-plastic pipeline by a linear perturbation in mass density from the quasi-static solution with  $\rho = 0$ . Thus  $p_0$  and the shape of the pressure decay, as well as  $\delta_t$ , are assumed to be given,  $\rho$  is perturbed from 0 to  $\Delta\rho$  (where  $\Delta\rho$  is the actual areal mass density of the shell), and the required change  $\Delta\lambda$  in the pressure decay length, as well as the associated quantities  $\Delta R$ ,  $\Delta\lambda_1$ ,  $\Delta\lambda_2$ ,  $\Delta\psi''_0$ , and  $\Delta\psi''_1$  are calculated through equations that are linearized in the  $\Delta$  quantities. These equations are solved in a similar manner to the graphical solution of a previous section. The

resulting formulae are cumbersome and are omitted here for brevity. However, we find that except at very high crack speeds, the changes  $\Delta$  in all computed quantities due to inertia are typically two orders of magnitude less than their initial values. The most striking result of the perturbation scheme, however, is that to first order in  $\Delta\rho$ , the change  $\Delta\lambda$  in the required pressure decay distance is precisely zero.

While we have not attempted detailed calculations, it would seem by comparison of the masses involved that the inertia of any soil backfill would be of far greater importance than the inertia of the pipe wall. Since soil has typically one fourth the density of steel, a 1 1/2 in. thickness of soil around the pipeline is the inertial equivalent of a 3/8-in. steel wall. Many such thicknesses could be fit into a representative backcover depth, and the resulting inertia together with the small shear strength of the soil might make for effective negative pressure in Eq 17 of a magnitude sufficient to substantially affect the fracture propagation.

### Concluding Discussion

The present analysis is incomplete in that we have considered only the structural portion of the problem. Specifically, for a given exit plane pressure  $p_0$ , shape of pressure decay, and crack tip opening  $\delta_t$  for fracturing, we compute the required pressure decay length  $\lambda$  (Fig. 6, for example) and the distribution  $\delta(\xi)$  of crack opening (Figs. 3, 6, and 7). In fact, apart from all the approximations involved, we compute these only in the high toughness regime, as illustrated in Fig. 5.

However, for a given  $p_0$ ,  $\delta(\xi)$ , and velocity of propagation, the actual shape and length of the pressure decay is determined by the fluid dynamics of the gas escape. The solution of the latter problem is necessary to fully close the analysis and establish conditions involving material properties, geometric dimensions, and initial pressure levels for which the postulated long-running fracture can occur. This will require further work. However, the analysis done in conjunction with Fig. 4 shows how the opening gap  $\delta(\xi)$  can be found through moderately straightforward calculations for an arbitrary pressure decay shape, and, if the fluid dynamics problem can be solved approximately in equally simple and general terms, it may be possible to couple the structural and fluid solutions effectively for a full analysis. We examined a simple formulation of the fluids problem as quasi-one dimensional flow along the pipeline axis, with mass loss by sonic exit through the crack opening. The local outflow rate at a point along the pipeline was taken as that appropriate to a slit opening of uniform gap size, equal to  $\delta(\xi)$  at that point, in a large tank at an average pressure equal to the local pressure in the one-dimensional flow model at that point. However, opening gaps  $\delta$  of the general size observed in the pressure decay lengths that it predicted were much in excess of the two to four radii observed.

The tacit assumption in the foregoing remarks is that arrest will occur whenever conditions for a long running fracture cannot be met. This is sufficient but may not be necessary for arrest. In particular, the possibility arises [1] that crack arrest may occur as a bifurcation in which strains in the axial direction, induced by the flaring out of the shell walls, cause the easiest directions for fracture to lie at angles to the crack line rather than straight ahead. Thus even if conditions for a long-running straight fracture, of the kind modelled here, can be met in principle, it is possible that the crack will branch to a helical path and rapidly arrest.

To study this possibility, we may estimate the nominal axial strain  $\epsilon_\xi$  near the crack tip by setting  $\theta = \pm\pi$  in Eq 4, taking  $g'$  as indicated after Eq 13, and setting  $\psi'' = \delta_t/\pi R^2$  from, Eq 32. Hence

$$\epsilon_\xi = \frac{3\pi}{8} \frac{a\delta_t}{R^2} \quad (34)$$

While this ignores local strain amplification by the crack tip itself, it does indicate that the tendency for crack branching, as measured by  $\epsilon_\xi$ , will increase inversely with  $R$  for a given  $\delta_t$ . From Fig. 6 the tendency for branching will thus be greatest during steady-state propagation under conditions of low exit plane pressures but correspondingly long decay lengths. For a given initial line pressure, these lower exit plane pressures, which favor branching, result at the lower propagation velocities. Further, as we move through what seems to be the representative exit plane pressure range,  $0.3 < ap_0/T_0 < 0.6$ , the amount of nominal axial strain at the crack tip changes by a factor of four. The nominal strain magnitude itself, for  $\delta_t = h$  and  $a/h = 56$ , varies from approximately 2 to 0.5 percent at the limits of this range. Axial strains of approximately 1 percent were observed just ahead of the crack in the full-scale tests [1].

Finally, we have taken no account of rate sensitive material behavior, it being understood instead that parameters such as  $T_0$ ,  $N_0$ , and  $M_0$  are to be chosen in accord with the strain rates involved. For example, the time taken for the end zone to traverse a material point within it is  $R/V$ . Further, if the deformation consists of localized necking throughout the entire zone, the plastic strains are of the order  $\delta/h$ , and hence an approximate strain rate in accord with which  $T_0$  should be chosen, is  $\delta_t V/hR$ . For  $\delta_t = h = 3/8$  in.,  $a = 20$  in., and  $R/a$  as in Fig. 6 for  $ap_0/T_0 = 0.45$ , this strain rate is approximately  $2 \times 10^2/s$  when  $V = 600$  ft/s, although the rate would be appreciably greater if localized necking does not set in at a material point until it is very near the crack tip.

#### *Acknowledgment*

This work was performed while the authors were serving as technical consultants to a committee of American Iron and Steel Institute members

which was overseeing a full-scale line pipe burst test program. We are grateful to the program director, Dr. A. K. Shoemaker of the United States Steel Research Laboratories, for several helpful discussions of the work.

### References

- [1] Ives, K. D., Shoemaker, A. K., and McCartney, R. F., *Journal of Engineering Materials and Technology*, Vol. 96, 1974, pp. 309-317.
- [2] Hahn, G. T., Sarrate, M., and Rosenfield, A. R., *International Journal of Fracture Mechanics*, Vol. 5, 1969, pp. 187-210.
- [3] Hahn, G. T., Sarrate, M., Kanninen, M. F., and Rosenfield, A. R., *International Journal of Fracture*, Vol. 9, 1973, pp. 209-221.
- [4] Duffy, A. R., "Studies of Hydrostatic Test Levels and Defect Behavior," Symposium on Line Pipe Research, American Gas Association, New York, 1965.
- [5] Maxey, W. A., Kiefner, J. F., Eiber, R. J., and Duffy, A. R. in *Fracture Toughness, Proceedings of the 1971 National Symposium on Fracture Mechanics, Part II, ASTM STP 514*, American Society for Testing and Materials, 1972.
- [6] Folias, E. S., *International Journal of Fracture Mechanics*, Vol. 1, 1965, pp. 104-113.
- [7] Poynton, W. A. and Fearnough, G. D., "An Analysis of Ductile Fracture Propagation in Gas Pipelines," presented at International Conference on Dynamic Crack Propagation, Lehigh University, Bethlehem, Pa., July 1972.
- [8] Timoshenko, S. and Woinowsky-Krieger, S., *Theory of Plates and Shells*, McGraw-Hill, New York, 1959.
- [9] Novozhilov, V. V., *Thin Shell Theory*, translation by P. G. Lowe, Noordhoff, Groningen, 1964.
- [10] Rice, J. R., *Fracture*, Vol. II, H. Liebowitz, Ed., Academic Press, New York, 1968.
- [11] Hodge, P. G., Jr., *Plastic Analysis of Structures*, McGraw-Hill, New York, 1959.

S. T. Chiu<sup>1</sup> and A. F. Liu<sup>2</sup>

## Mixed-Mode Fracture of Shear Panels— A Finite Element Analysis

---

**REFERENCE:** Chiu, S. T. and Liu, A. F., “Mixed-Mode Fracture of Shear Panels — A Finite Element Analysis,” *Mechanics of Crack Growth, ASTM STP 590*, American Society for Testing and Materials, 1976, pp. 263–280.

**ABSTRACT:** The mixed-mode fracture behavior of shear panels is analyzed in this study to provide suitable fracture criteria for the prediction of the residual strength of crack panels under a combined tension and shear loading condition. Finite element models which incorporate a special crack tip element are utilized in the analysis to compute the values of  $K_I$  and  $K_{II}$  and the detailed stress distribution in the crack tip regions. For comparison purposes, analyses are made using the initial crack configurations of the shear panels and a number of selected configurations after a small increment of slow stable crack growth. Failure analysis is made using these results together with test results obtained in a previous experimental study by Liu. It is found that a simple failure criterion of  $K_I / (K_I)_{cr} + K_{II} / (K_{II})_{cr} = 1$  is applicable to materials that are not extremely ductile. However, the maximum tensile stress theory should be used to complement this criterion for the purpose of predicting the crack growth direction. The mixed-mode criteria of the strain energy density function and the “angular” stress intensity factor are also examined. In addition, it is shown that a predominantly Mode I condition is produced by oblique crack growth even after a relatively small crack growth increment. Hence, a pure Mode I fracture criterion can be used to predict the slow stable crack growth and subsequent failure of damage structures subjected to combined loads if a practical method can be found to estimate  $K_I$  during the crack growth period. It should be noted that the present study is restricted to a monotonically increasing loading condition.

**KEY WORDS:** crack propagation, fracture properties, stresses, strains, damage, models, residual stress, shear panels

For a damaged two-dimensional structural member under combined inplane loads, both the Mode I and Mode II singularities exist. Hence the failure behavior of such a damaged structure is, consequently, of a mixed

<sup>1</sup> Research specialist, Lockheed-California Company, Burbank, Calif. 91503.

<sup>2</sup> Formerly with Lockheed-California Company, Burbank, Calif. 91503. Presently, member of technical staff, Structures Analysis, Space Shuttle Program, Space Division, Rockwell International Corp., Downey, Calif. 90241.

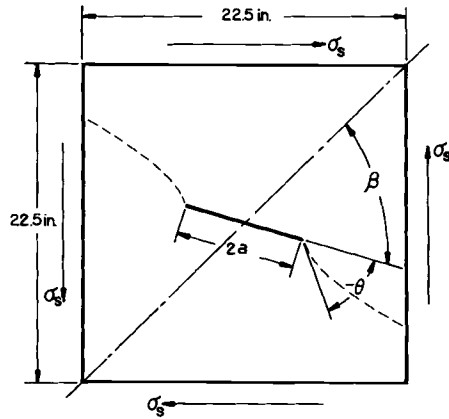


FIG. 1—Cracked shear panel configuration.

mode nature. The problem of mixed-mode<sup>3</sup> fracture was first discussed in detail in 1963 by Erdogan and Sih [1].<sup>4</sup> However, it is only recently that this problem came under close scrutiny [2-5].

To simulate mixed-mode fracture behavior, center-cracked tension specimens with a slanted crack were used [2-4]. This type of specimen is inherently deficient in providing a complete range of mixed-mode fracture conditions. Furthermore, the width of these center-cracked specimens were inadequate in some instances, and gross plastic yielding of the net section occurred at the fracture load. Fracture specimens used in Ref 5, however, were of the shear panel type (see Fig. 1). With this type of specimen the complete range of mixed-mode conditions can be obtained by varying the crack orientation. The dimensions of these specimens were also large enough to eliminate the possibility of gross plastic yielding.

In the past, various mixed-mode fracture criteria have been proposed either based on theoretical considerations or test results. Erdogan and Sih [1] proposed the maximum tensile stress theory and the critical strain energy density function criterion based on the Griffith-Irwin fracture theory [6]. The functional form of the strain energy density function,  $S$ , was derived recently [7]. Another proposed mixed-mode fracture criterion utilizes the concept of the "angular" stress intensity factor [8] which takes into account the directionality of the impending crack growth. The criterion of the additive strain energy release rate is then used to define the critical state. Lastly, it was shown [4-5] that the normalized quantities  $K_I / (K_I)_{cr}$  and  $K_{II} / (K_{II})_{cr}$  obtained empirically can be approximated by a

<sup>3</sup> The term "mixed-mode fracture" is used herein to refer to the mixed Mode I and Mode II fracture.

<sup>4</sup> The italic numbers in brackets refer to the list of references appended to this paper.

straight line on the normalized  $K_I - K_{II}$  plane. This experimental observation provided yet another possible mixed-mode fracture criterion. In view of the numerous failure criteria proposed, a review of these criteria clearly is needed.

To conduct such a review on mixed-mode fracture criteria, an accurate stress analysis method is needed. Of the various analysis methods used in fracture analysis, the finite element method has proved to be applicable. However, the extremely detailed finite element modelling required in the crack tip region results in high computer and analysis costs. Furthermore, in spite of the extremely detailed finite element modelling, the accuracy of the resultant stress intensity factor usually is limited.

In 1970 a special singular finite element [9] was introduced which was designed specially for the analysis of crack problems. Since then several researchers [10-13] have presented various special finite elements suitable for fracture analysis applications. All the special elements developed were found to be more accurate and efficient as compared to the conventional finite elements.

The three requirements of adequate test data, a suitable stress analysis technique, and applicable fracture criteria are indispensable for a thorough examination of the phenomenon of mixed-mode fracture. These requirements are all available independently as discussed in the preceding paragraphs. It is the intention of this study to utilize the approach of the special cracked finite element to analyze test data generated from the shear panel tests. The emphasis is placed on a critical review of the three mixed-mode fracture criteria: (1) the empirical mixed-mode criterion,  $K_I / (K_I)_{cr} + K_{II} / (K_{II})_{cr} = 1$ , (2) the strain energy density function criterion, and (3) the angular stress intensity factor concept. The maximum tensile stress theory is considered only in its applicability to the prediction of the crack growth direction. The additive strain energy release rate criterion is considered only in conjunction with the angular stress intensity factor concept.

### Shear Panel Finite Element Model

The shear panel finite element models are constructed using a combination of the singular cracked finite element and other conventional finite elements. The singular cracked finite element used in this study was developed based on the assumed stress function approach and consequently has the correct stress singularity of the crack problem. The initial development work of this singular element was done by Dr. Matthew Creager<sup>5</sup> in 1970. With subsequent improvements, the accuracy

<sup>5</sup> Dr. Creager is presently with the Del-West Associates, Inc., Woodland Hills, California. The development work on the cracked finite element was conducted under a company sponsored independent research program at the Lockheed-California Company, Burbank, California.

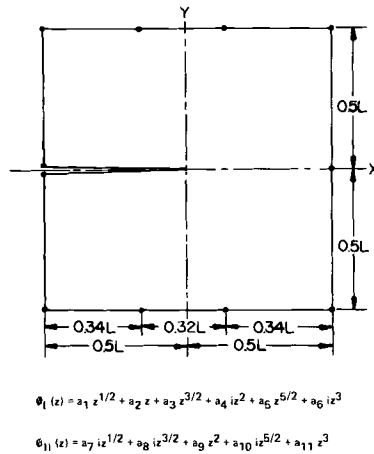


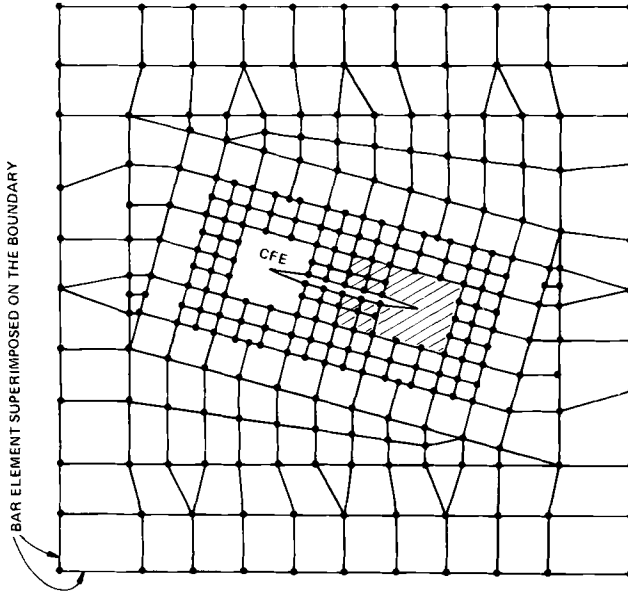
FIG. 2—The singular cracked finite element.

of this particular cracked finite element has been demonstrated by correlation with existing solutions. Both the theoretical background and the numerical procedure involved are discussed in detail, with example problems, in Chapter 11 of Ref 14. The cracked finite element developed is square in shape and has a total of eleven nodal points as shown in Fig. 2. There are a total of eleven independent stress variables in the two complex stress functions of the element. The model solution is obtained using the NASA structural analysis (NASTRAN) system. The numerous built-in features of the NASTRAN system provide flexibility in the model setup and the solution procedure. The average central processing unit (CPU) time for a model with 450 nodes is approximately 200 s.

The finite element model for a typical shear panel in its initial configuration is shown in Fig. 3a. The dimensions of the shear panels are the same as those tested in the experimental study [5]. The crack orientations of the shear panel models are  $\beta = 45, 60, 75,$  and  $90$  deg. Two cracked finite elements are used in each model, one for each end of the crack. Conventional triangular elements and quadrilateral elements, each consisting of four constant strain triangular elements, are used for the rest of the model. Bar elements are also used along the panel boundaries to simulate the actual pin-jointed loading frame.

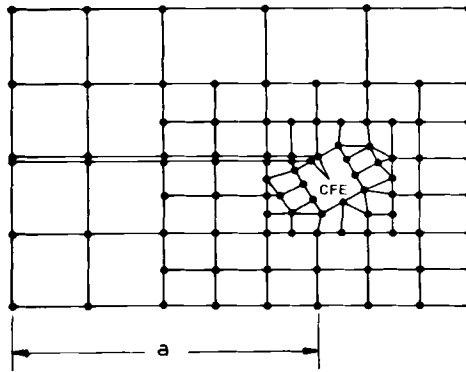
In addition to the four shear panel models analyzed, models of two shear panels after a small increment of crack growth are also studied. These two shear panels have the original crack orientations of  $\beta = 60$  and  $75$  deg. The additional small crack increment has a length of 0.25 in. and is oriented in the new crack growth direction. At each crack tip, one singular cracked finite element is used to cover the entire crack increment, as

294 NODES  
 229 QUADRILATERAL AND TRIANGULAR FINITE ELEMENTS  
 2 CRACKED FINITE ELEMENTS (CFE)  
 40 BAR FINITE ELEMENTS



(a) Initial configuration,  $\beta = 60$  deg.

SHADED AREA IN FIGURE 3-(a)



(b) After 0.25 in. crack growth,  $\beta = 60$  deg.

FIG. 3—Detailed finite element models.

shown in Fig. 3*b*. A detailed discussion on the crack growth direction is presented later in the results and discussion section. It should be noted that the crack growth direction for the  $\beta = 60$  deg panel is  $\theta = -60$  deg. This angle is an average value based on various theoretical predictions and the test result. For the  $\beta = 75$  deg case, however, two crack growth directions,  $\theta = -40$  and  $-30$  deg, are chosen. The first angle value is based on the test result.

Besides the element stress distributions for the conventional elements and the nodal displacements, the finite element model analysis also provides the values of the independent stress variables for the singular cracked finite elements. From these values, one can obtain the values of  $K_I$ ,  $K_{II}$ , and the local stress distribution within the singular elements. The  $K_I$  and  $K_{II}$  values, in turn, can be used to calculate the values of strain energy release rate,  $\mathcal{G}$ , and the strain energy density function,  $S$ .

### Mixed-Mode Fracture Criteria

In summarizing the various mixed-mode fracture criteria, one must begin with the additive strain energy release rate which was developed with the assumption that the crack will grow in its initial direction [1]. However, it was also pointed out in Ref 1 that the strain energy release rate for crack extension under general two-dimensional loading conditions may have a homogeneous quadratic form in terms of the Mode I and the Mode II stress intensity factors and can be written as

$$\frac{\Delta U}{\delta} \text{ or } \mathcal{G} = a_{11}K_I^2 + 2 a_{12}K_I K_{II} + a_{22}K_{II}^2 \quad (1)$$

The crack growth direction is the one that gives a maximum strain energy release rate calculated using Eq 1. This hypothesis, however, was not developed completely until recently [7] when the strain energy density function,  $S$ , was introduced as the critical parameter

$$S = a_{11}K_I^2 + 2 a_{12}K_I K_{II} + a_{22}K_{II}^2 + a_{33}K_{III}^2 \quad (2)$$

The coefficients  $a_{11}$ ,  $a_{12}$ ,  $a_{22}$ , and  $a_{33}$  are functions of the material elastic constants and the angle  $\theta$ , where  $\theta$  is an angle measured counterclockwise from the crack line. One of the advantages of the strain energy density function over the concept of the additive strain energy release rate is its ability to estimate the crack growth direction. To provide this capability for the additive strain energy release rate criterion, the concept of the angular stress intensity factor was introduced recently [8] based on a limiting process as the propagating branched crack approaches zero

length. The additive strain energy release rate theory can then be redefined as

$$\mathcal{G}(\theta) = [ \tilde{K}_I^2(\theta) + \tilde{K}_{II}^2(\theta) ] / E \quad \text{for plane stress} \quad (3)$$

where  $\tilde{K}_I(\theta)$  and  $\tilde{K}_{II}(\theta)$  are the newly defined angular stress intensity factor for Mode I and Mode II, respectively. Crack growth will occur in the direction of maximum  $\mathcal{G}(\theta)$  when this maximum reaches a critical value.

Besides the three mixed-mode fracture criteria just discussed, it was observed experimentally [4-5] that the critical state for mixed-mode fracture of certain materials can be approximated by a straight line on the  $K_I/(K_I)_{cr} - K_{II}/(K_{II})_{cr}$  plane. However, this fracture criterion cannot predict the direction of crack growth; therefore, an additional criterion is needed to provide this information.

The maximum tensile stress theory [1] originally stated that crack growth will occur when the local maximum tensile stress in the crack tip region reaches a critical value and the crack growth direction is determined by the orientation of the maximum tensile stress. However, it is difficult to justify the validity of a critical maximum tensile stress value within the framework of elasticity theory. Nonetheless, the loci of the maximum tangential stress in a region adjacent to the crack tip can be used to estimate the direction of impending crack growth.

## Results and Discussion

The values of the Mode I and Mode II stress intensity factors and the distributions of the tangential stress are the primary analysis results used in this study. These results are presented here together with relevant discussions. The presentation is divided roughly into two groups, with one group consisting of results obtained using the initial crack configurations and the other group consisting of results obtained using configurations after a small increment of crack growth. Furthermore, the discussions of the critical state and the crack growth direction for the various criteria are presented as two separate subjects.

The stress distributions of two finite element models ( $\beta = 45$  and  $90$ , deg), representing the initial crack configurations, are first examined to determine whether a pure shear condition exists in locations adjacent to the simulated loading frame. As shown in Fig. 4, the stress fields along the edges of the finite element models for the two cases of  $\beta = 45$  and  $95$  deg. are fairly close to a pure shear condition. This is particularly evident in the  $\beta = 90$  deg case where the crack tips are furthest away from the model boundary among all cases studied.

The values of the Mode I and Mode II stress intensity factors are shown

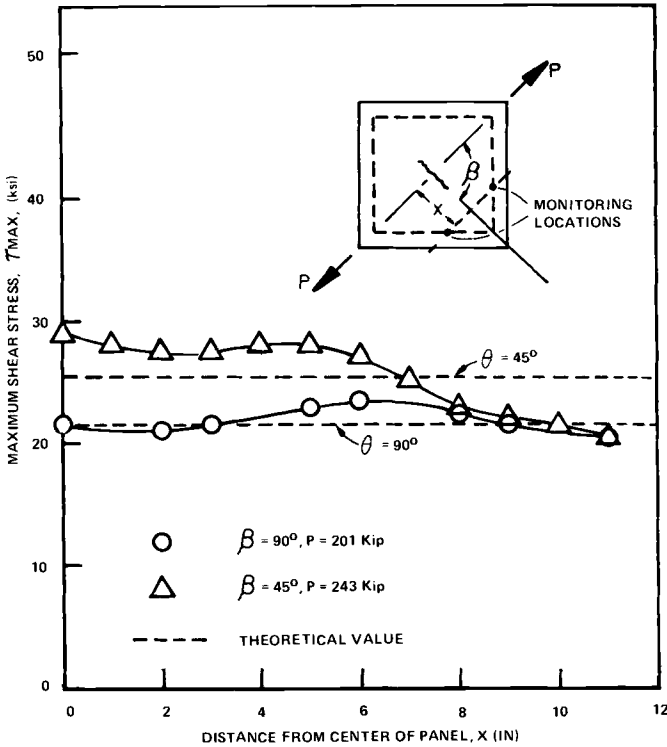


FIG. 4—Shear stress distributions at two crack orientations.

in Fig. 5 and tabulated in Table 1. It is interesting to note that the values obtained based on the initial crack configurations are quite close to the estimates [5]. The correlation of  $K_{II}$  values is particularly good, while differences in  $K_I$  are more appreciable. Note that the deviation in  $K_I$  increases when the condition of pure Mode II is approached. The existence of  $K_I$  in the pure shear case of  $\beta = 45$  deg implies that the expected pure Mode II condition was not attained. However, the ratio of  $K_I/K_{II}$  is small, and it is evident that a predominantly Mode II condition was reached.

To avoid undue complexities, it is prudent and practical to seek a mixed-mode fracture criterion which is defined in terms of the initial crack configuration. In Fig. 5 it is seen that the values of the critical  $K_I$  and  $K_{II}$  derived using the initial crack configurations and fracture loads do not form a straight line on a  $K_I$ - $K_{II}$  plot as predicted by the empirical criterion. However, after the slow stable crack growth for the  $\beta = 90$  deg case is taken into consideration, an excellent correlation to a straight line can be established. From Table 1, it can be seen that the amount of slow stable crack growth in the  $\beta = 90$  deg case is substantially larger

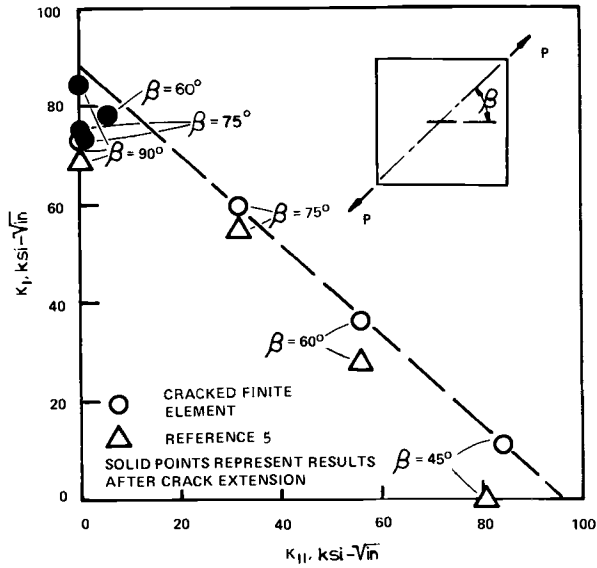


FIG. 5—Values of Mode I and Mode II stress intensity factors at various crack orientations.

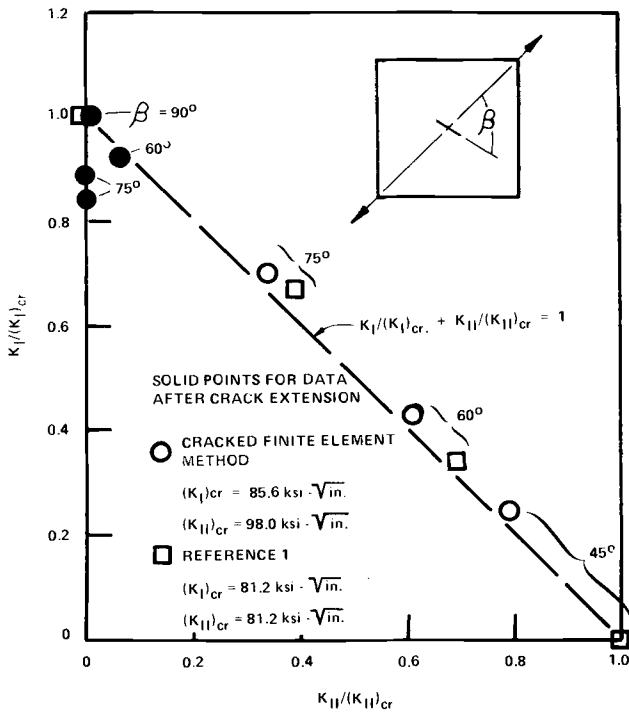


FIG. 6—Values of normalized stress intensity factors.

TABLE 1—Stress intensity factors for shear panels.

| Panel No. | Orientation<br>$\beta$ , deg | $2a_0$ ,<br>in.  | $F_{cr}$ ,<br>kip | $K_I^a$ ,<br>ksi $\sqrt{\text{in.}}$               | $K_{II}^a$ ,<br>ksi $\sqrt{\text{in.}}$             | $K_{I,II}^b$ ,<br>ksi $\sqrt{\text{in.}}$ | $K_{I,II}^b$ ,<br>ksi $\sqrt{\text{in.}}$ |
|-----------|------------------------------|--|-------------------|--|---|---|---|
| SP-3      | 45                           | 6 in.; no crack growth                                     | 242.75            | 11.37  | 84.55   | 0   | 81.2                                      |
| SP-4      | 60                           | 6 in.; possible 0.25 in. crack growth on each side         | 189.25            | 36.26<br>(77.8) <sup>c</sup>                       | 55.95<br>(-5.8) <sup>c</sup>                        | 27.6                                      | 56.0                                      |
| SP-5      | 75                           | 6 in.; 3/16 in. crack growth one side, 13/16 on other side | 189               | 59.6<br>(72.1) <sup>d</sup><br>(74.8) <sup>e</sup> | 32.2<br>(-1.1) <sup>d</sup><br>(-0.08) <sup>e</sup> | 54.6                                      | 31.8                                      |
| SP-6      | 90                           | 6.25 in.; 0.5 in. to 1 in. crack growth on each side       | 201               | 73.54<br>(84.5) <sup>f</sup>                       | ...   | 68.7                                      | 0   |

MATERIAL—7075-T7651 high strength clad aluminum.

NOTE—Unless otherwise noted stress intensity factor values were computed using the original crack length.

<sup>a</sup> Results of finite element analysis.

<sup>b</sup> Estimated values [5].

<sup>c</sup>  $\Delta a = 0.25$  in. The crack growth directions is -60 deg,

<sup>d</sup>  $\Delta a = 0.25$  in. The crack growth direction is -40 deg,

<sup>e</sup>  $\Delta a = 0.25$  in. The crack growth direction is -30 deg,

<sup>f</sup>  $\Delta a = 1$  in. The crack growth direction is along the crack line.

than in any of the other three cases and, consequently, cannot be neglected. With this justification, it can be concluded that straight line can be used to represent the critical state of mixed-mode fracture. However, since the slow stable crack growth is neglected except in the  $\beta = 90$  deg case, this criterion can only be applied to materials that do not exhibit a substantial amount of slow stable crack growth under combined loads.

A linear least square fit, as shown in Fig. 5, provides the two critical values of  $(K_I)_{cr} = 85.6 \text{ ksi } \sqrt{\text{in.}}$ , and  $(K_{II})_{cr} = 98 \text{ ksi } \sqrt{\text{in.}}$ . The normalized  $K_I$  and  $K_{II}$  values obtained based on these critical values are presented in Fig. 6. The mixed-mode fracture criterion of  $K_I/(K_I)_{cr} + K_{II}/(K_{II})_{cr} = 1$  is then established readily. In view of the approximate nature of this criterion, estimates of the stress intensity factors obtained by Liu in Ref 5 can be utilized to further simplify the prediction procedure. However, it should be noted that an assumption of  $(K_{II})_{cr} = (K_I)_{cr}$  was used.

To evaluate the strain energy density function criterion, values of  $S$  were calculated using the  $K_I$  and  $K_{II}$  values in Table 1. The results are shown in Fig. 7. It can be seen that an excellent agreement is obtained between the two cases of  $\beta = 45$  and  $90$  deg is the slow stable

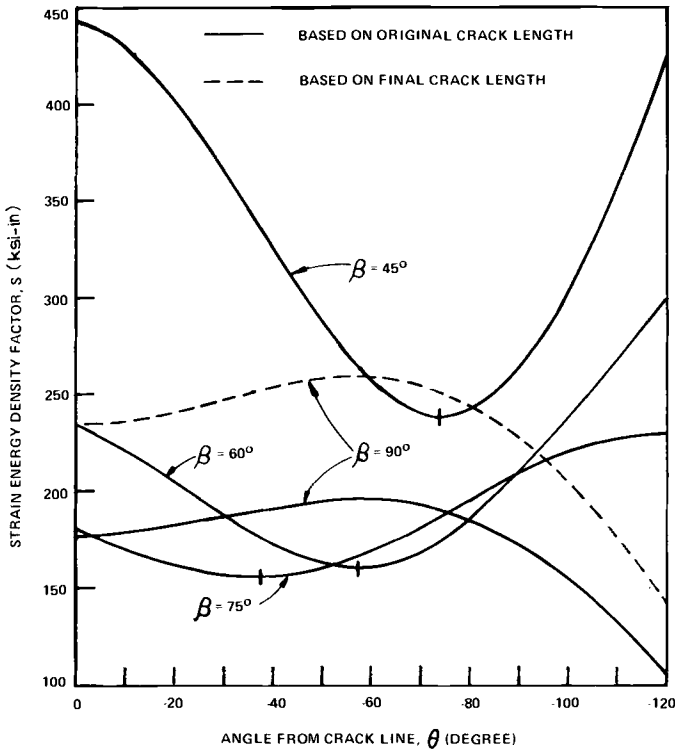


FIG. 7—Values of strain energy density function,  $S$ .

crack growth for the latter case is taken into account. The same excellent agreement is obtained between the two cases of  $\beta = 60$  and  $75$  deg. However, no correlation can be obtained between these two groups. It is unfortunate that the number of presently available shear panel test results is not sufficient to render a definite conclusion or explanation to this discrepancy.

To evaluate the concept of the angular stress intensity factor, the critical energy release rates are obtained using Eqs 95 through 97 in Ref 8.

$$G(\theta) = \frac{1}{E} [K_I^2(\theta) + K_{II}^2(\theta)] \quad (4)$$

where  $\tilde{K}_I$  and  $\tilde{K}_{II}$  are the angular stress intensity factors, and they can in turn be expressed in terms of the conventional stress intensity factors.

$$\tilde{K}_I(\theta) = \left( \frac{4}{3 + \cos^2\theta} \right) \left( \frac{1 - \theta/\pi}{1 + \theta/\pi} \right)^{\theta/2\pi} \left( \tilde{K}_I \cos\theta + \frac{3}{2} \tilde{K}_{II} \sin\theta \right) \quad (5)$$

$$\tilde{K}_{II}(\theta) = \left( \frac{4}{3 + \cos^2\theta} \right) \left( \frac{1 - \theta/\pi}{1 + \theta/\pi} \right)^{\theta/2\pi} \left( K_{II} \cos\theta - \frac{1}{2} K_I \sin\theta \right) \quad (6)$$

The estimated  $K_I$  and  $K_{II}$  values are used as well as those obtained from finite element analysis. Both the initial crack configurations and the configurations after crack growth are used in the calculation. The computed values of the maximum energy release rate, however, do not support the hypothesis of a constant critical value. It is clear then that the critical state cannot be determined based on the initial crack configuration and the angular stress intensity factor concept.

Although the maximum tensile stress theory was discounted in the preceding section as a possible mixed-mode fracture criterion, an interesting observation can be made if the distributions of the tangential stress are examined. The distributions are shown in Fig. 8 in the normalized quantity of  $\sigma_\theta/\sigma_s$ , where  $\sigma_s$  is the applied shear stress. It can be seen that the influence of the higher order stress terms have a negligible effect on the location and the values of  $(\sigma_\theta/\sigma_s)_{\max}$  in the two cases of  $\beta = 45$  and  $90$  deg. However, their effects are more prominent for the two other cases of  $\beta = 60$  and  $75$  deg. Furthermore, it can be shown that, if the slow stable crack growth is taken into account, a fairly good correlation of the  $(\sigma_\theta/\sigma_s)_{\max}$  values can be obtained among all cases studied (values of  $\sigma_\theta$  are computed at a constant radial distance of  $r = 0.02$  in. from the crack tip.)

Based on the initial configurations of the shear panels, the predicted crack growth directions using various criteria are summarized in Table 2. The direction of crack growth based on the maximum tensile stress theory and the strain energy density function theory are determined from the distributions of the tangential stress shown in Fig. 8 and the distributions of the strain energy density function shown in Fig. 7, respectively. The predicted directions based on the angular stress intensity factor concept is obtained from the distributions of the strain energy release rate. As shown in Table 2, the maximum tensile stress theory and the strain energy density function criterion offer a comparable accuracy in predicting the crack growth direction.

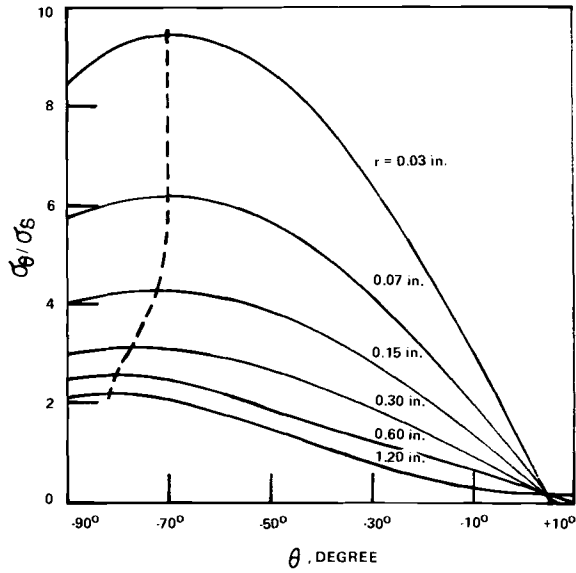
The angular stress intensity factor concept, however, cannot offer a similar accuracy. This is particularly evident if the predicted values are based on values of  $K_I$  and  $K_{II}$  obtained in this study. It should be pointed out that the predicted crack growth directions using the maximum tensile theory provide a slightly better correlation with the test results than those obtained using the strain energy density function theory, particularly in the  $\beta = 75$  deg case. In view of this advantage on the part of the maximum tensile stress theory, it is suggested that this theory be used in the prediction of the crack growth direction. It should be of particular interest that the best prediction is obtained when the higher order stress terms are included as shown in Fig. 8.

Discussion up to this point has been confined mostly to analysis based on the initial crack configurations. Finite element results were also

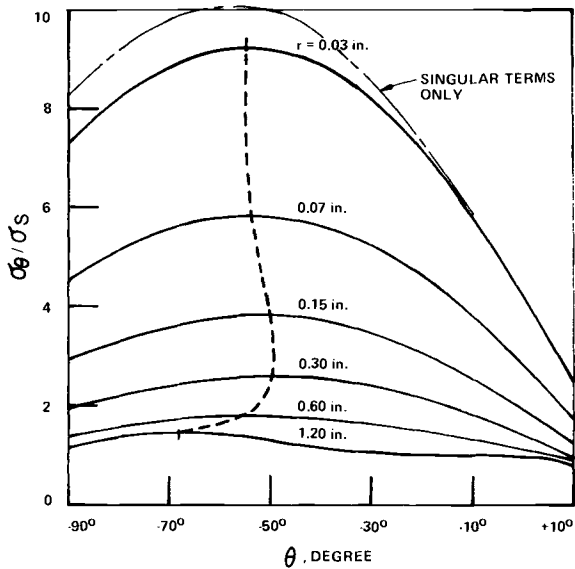
TABLE 2—Crack growth direction for shear panels with various initial crack orientations.

| Test Results  | $\beta = 45$ deg          | $\beta = 60$ deg          | $\beta = 75$ deg          | $\beta = 90$ deg      |
|---|---------------------------|---------------------------|---------------------------|-----------------------|
|   | -72/-75                   | -60/-60                   | -27/-32                   | 0                     |
| Strain energy density function using estimated $K_I$ and $K_{II}$ values            | -80                       | -60                       | -40                       | 0                     |
| Strain energy density function using finite element results                         | -73.5                     | -57.5                     | -37.5                     | 0                     |
| Maximum tensile stress theory using estimated $K_I$ and $K_{II}$ values             | -70.5                     | -60                       | -43.2                     | 0                     |
| Maximum tensile stress theory using finite element results                          | -69<br>(-69) <sup>a</sup> | -55<br>(-59) <sup>a</sup> | -32<br>(-39) <sup>a</sup> | 0<br>(0) <sup>a</sup> |
| “Angular” stress intensity factor concept using estimated $K_I$ and $K_{II}$ values | -75.2                     | -64.7                     | -46.5                     | 0                     |

<sup>a</sup> Singular terms only.



(a)  $\beta = 45$  deg.



(b)  $\beta = 60$  deg.

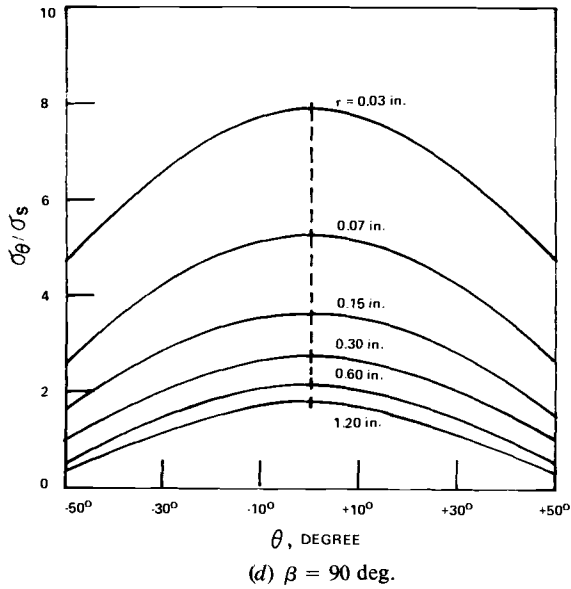
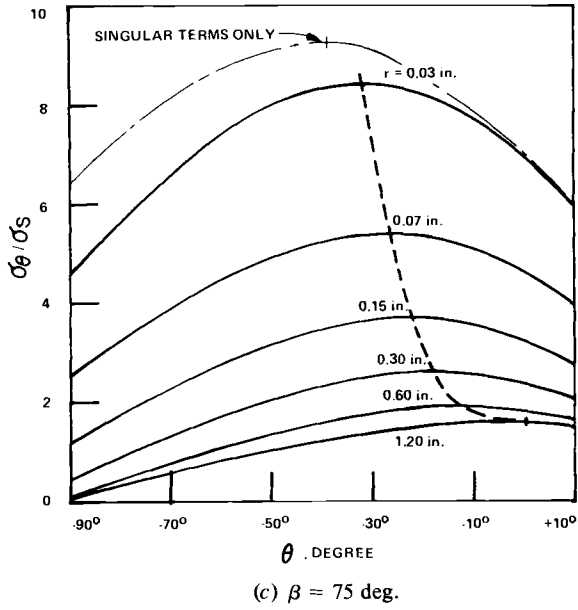


FIG. 8—Distributions of the tangential stress at various angles.

obtained for two cases ( $\beta = 60$  and  $75$  deg) based on the configurations after a small increment of oblique crack growth was implemented as shown in Fig. 3b. The  $\beta = 45$  deg case was not included due to its insignificantly small amount of crack growth prior to instability. From Table 2, it can be seen that the experimental crack growth direction for the  $\beta = 60$  deg case was approximately  $-60$  deg which agrees well with all the theoretical predictions. Hence the angle of  $-60$  deg was chosen as the crack growth direction. For the  $\beta = 75$  deg case, however, the situation was more complex. The predicted crack growth angle based on various criteria, with one exception, was approximately  $-40$  deg. The one exception was the predicted angle based on the maximum tensile stress theory using the values of  $K_I$  and  $K_{II}$  obtained in this study with the higher order terms included. The predicted angle in this case was  $-32$  deg /  $-27$  deg shown in Table 2. Hence two crack growth angles of  $-40$  and  $-30$  deg were used for the  $\beta = 75$  deg case.

Values of the Mode I and Mode II stress intensity factors after the small increment of crack growth indicate that a predominantly Mode I condition exists after crack growth, as shown previously for a slanted crack [15]. The respective values of  $K_I$  and  $K_{II}$  are included in Table 1 and Figs. 5 and 6. These values show an almost complete elimination of the Mode II condition. It is of interest to note that the two shear panels analyzed have relatively high initial  $K_{II}$  values. The almost complete transition from a mixed-mode condition to a pure Mode I condition indicates that, for materials capable of significant crack extension before fracture under monotonically increasing load, only the  $K_I$  value needs to be considered. An analysis based on the R-curve concept would be more appropriate for these materials. However, there remains to be resolved the difficulties involved in finding a  $K_I$  value for a crack configuration which includes a curved crack growth increment.

As intended a comparison of the two models with different crack growth directions for the  $\beta = 75$  deg case can be made based on the resulting values of  $K_I$  and  $K_{II}$ . From Table 1, it can be seen that a higher  $K_I$  value is obtained for a crack growth angle of  $-30$  deg as compared to  $K_I$  for a crack growth angle of  $-40$  deg. The  $K_{II}$  values are negligible in both cases. This higher  $K_I$  value further substantiates the selection of the maximum tensile stress theory for use in the prediction of the crack growth direction.

The strain energy density function theory and the angular stress intensity factor concept can again be examined using values of  $K_I$  and  $K_{II}$  after the crack growth increment. However, as in the previous case, no correlation can be found for the calculated critical values using either criterion.

As for the prediction of subsequent crack growth direction after this increment of crack growth, all criteria predict essentially the same

direction of approximately 0 deg. The zero angle of crack growth is expected because a pure Mode I condition exists after the crack increment. The formation of the curved crack growth path as observed in Ref 5 is possibly the result of directional instability.

### Conclusions

1. The singular cracked finite element is useful for the application of the finite element method to fracture analysis.

2. The simple mixed-mode criterion of  $K_I/(K_I)_{cr} + K_{II}/(K_{II})_{cr} = 1$  can be used to predict failure for materials which are not extremely ductile. The maximum tensile stress theory can be used to predict the crack growth direction.

3. The higher order stress terms should be included in the analysis of branched crack subjected to combined loads.

4. A transition from a mixed-mode condition to an essentially Mode I condition occurs after a small increment of crack growth. Hence, a Mode I fracture criterion such as the R-curve concept should be used to predict mixed-mode failure for materials capable of exhibiting significant slow stable crack growth before fracture under monotonically increasing load provided that a practical means can be found to calculate the  $K_I$  value during this period.

### Acknowledgment

This research work was sponsored by the Lockheed-California Company under its independent research program. The authors wish to thank their colleagues J. C. Ekvall, E. K. Walker, and L. Young for reviewing the manuscript. Special thanks should go to Dr. T. R. Brussat for his help in preparing the final draft.

### References

- [1] Erdogan, R. and Sih, G. C., *Journal of Basic Engineering, Transaction, American Society of Mechanical Engineers*, Dec. 1963, pp. 519-527.
- [2] Wilson, W. K., Clark, W. E., and Wessel, E. T., "Fracture Mechanics Technology for Combined Loading. Low to Intermediate Strength Metals," Technical Report No. 10276, AD 082754, Westinghouse Research Laboratories, 1968.
- [3] Pook, L. P., *Engineering Fracture Mechanics*, Vol. 3, 1971, pp. 205-216.
- [4] Shah, R. C. in *Fracture Analyses, Proceedings of the 1973 National Symposium on Fracture Mechanics, Part II, ASTM STP 560*, American Society for Testing and Materials, 1973, pp. 29-52.
- [5] Liu, A. F., "Crack Growth and Failure of Aluminum Plate Under In-Plane Shear," Paper 73-253, Eleventh Aerospace Sciences Meeting, American Institute of Aeronautics and Astronautics, Jan. 1973.
- [6] Irwin, G. R., *Handbook of Physics*, Vol. 6, Springer Verlag, Berlin, 1958, p. 551.
- [7] Sih, G. C., Ed., "Methods of Analysis and Solutions of Crack Problems," *Mechanics of Fracture*, Nordhoff International Publishing, Leyden, The Netherlands, 1973.

- [8] Hussain, M. A., Pu, S. L., and Underwood, J. in *Fracture Analyses, Proceedings of the 1973 National Symposium on Fracture Mechanics, Part II*, American Society for Testing and Materials, 1973, pp. 2-28.
- [9] Byskow, E., *International Journal of Fracture Mechanics*, Vol. 6, No. 2, June 1970, pp. 159-157.
- [10] Pian, T. H. H., Tong, P., and Luk, C. H., "Elastic Crack Analysis by a Finite Element Hybrid Method," 3rd Conference on Matrix Methods in Structural Mechanics, Wright-Patterson Air Force Base, Ohio, Oct. 1971.
- [11] Mendelson, A., Gross, B., and Srawley, J. E., "Evaluation of the Use of a Singularity Element in Finite-Element Analysis of Center-Cracked Plates," NASA TN D-6703, National Aeronautics and Space Administration, Washington, D.C., March 1972.
- [12] Wilson, W. K., "Some Crack Tip Finite Elements for Plane Elasticity," Scientific Paper 71-1E7-FMPWR-Pr, Westinghouse Research Laboratories, Aug. 1971.
- [13] Aberson, J. A., "Crack Finite Element Development at Lockheed-Georgia Company," Report No. LG73ER0007, Lockheed-Georgia Company, Marietta, Ga., Sept. 1973.
- [14] Robinson, J., *Integrated Theory of Finite Element Methods*, Wiley, New York, 1973, p. 368.
- [15] Kobayashi, A. S., Maiden, D. E., Simon, B. J., and Iida, S., "Application of Finite Element Analysis Method to Two-Dimensional Problems in Fracture Mechanics," ASME Paper No. 69-WA/PVP-12, presented at the Winter Annual Meeting, American Society of Mechanical Engineers, 16-20 Nov. 1969.

*J. C. Newman, Jr.*<sup>1</sup>

## A Finite-Element Analysis of Fatigue Crack Closure

---

**REFERENCE:** Newman, J. C., Jr., "A Finite-Element Analysis of Fatigue Crack Closure," *Mechanics of Crack Growth, ASTM STP 590*, American Society for Testing and Materials, 1976, pp. 281-301.

**ABSTRACT:** Experiments have shown that fatigue cracks close at positive loads during constant-amplitude load cycling. The crack-closure phenomenon is caused by residual plastic deformations remaining in the wake of an advancing crack tip. The present paper is concerned with the application of a two-dimensional, non-linear, finite-element analysis using an incremental theory of plasticity to predict crack-closure and crack-opening stresses during the crack-growth process under cyclic loading.

A two-dimensional finite-element computer program, which accounts for both elastic-plastic material behavior and changing boundary conditions associated with crack extension and intermittent contact of the crack surfaces under cyclic loading, has been developed. An efficient technique to account for changing boundary conditions under cyclic loading was also incorporated into the nonlinear analysis program. This program was used subsequently to study crack extension and crack closure behavior in a center-cracked panel under constant-amplitude and two-level block loading. The calculated crack-opening stresses were found to be quantitatively consistent with experimental measurements.

**KEY WORDS:** crack propagation, plastic deformation, cyclic loads, stresses, residual stress, fatigue (materials), mechanical properties, plasticity tests

### Nomenclature

- $\{Q\}$  "Effective" plastic load vector, N
- $R$  Stress ratio (ratio of minimum to maximum applied stress)
- $S$  Applied gross stress, N/m<sup>2</sup>
- $S_{\max}$  Maximum gross stress, N/m<sup>2</sup>
- $S_{\min}$  Minimum gross stress, N/m<sup>2</sup>
- $S_o$  Crack-opening stress, N/m<sup>2</sup>
- $\{U\}$  Generalized nodal displacement vector, m

<sup>1</sup> Research engineer, NASA Langley Research Center, Hampton, Va. 23665.

|                         |   |
|-------------------------|---|
| $u, v$                  | Displacements in $x$ - and $y$ -direction, respectively, $m$  |
| $W$                     | Total plate width, $m$  |
| $x, y$                  | Cartesian coordinates   |
| $\Delta a$              | Incremental crack growth, $m$   |
| $\Delta K_{\text{eff}}$ | Effective stress-intensity factor range, $N/m^{3/2}$  |
| $\Delta N$              | Incremental number of cycles  |
| $\sigma_{yy}$           | Normal stress acting in $y$ -direction, $N/m^2$   |
| $\sigma_0$              | Tensile yield stress, $N/m^2$   |
| $a$                     | Half length of crack, $m$   |
| $[B]$                   | Matrix relating total strains to nodal displacements, $m^{-1}$  |
| $C, n$                  | Material crack-growth constants   |
| $\{dP\}$                | Incremental applied load vector, $N$  |
| $\{dQ\}$                | Incremental plastic load vector, $N$  |
| $dV_m$                  | Differential volume of triangular element, $m^3$  |
| $\{d\epsilon\}$         | Incremental total strain vector   |
| $\{d\sigma_e\}$         | Incremental elastic stress vector, $N/m^2$  |
| $\{d\sigma^0\}$         | Incremental "initial" stress vector, $N/m^2$  |
| $[D_e]$                 | Elasticity matrix relating stress to total strain, $N/m^2$  |
| $g$                     | Relaxation parameter  |
| $k_{sx}, k_{sy}$        | Spring stiffness in $x$ - and $y$ -direction, respectively, $N/m$   |
| $[K_e]$                 | Elastic stiffness matrix, $N/m$   |
| $[K_s]$                 | Diagonal matrix containing spring stiffnesses, $N/m$  |
| $K_T$                   | Elastic-stress concentration (ratio of $\sigma_{yy}$ in the highest stressed element to the applied stress, $S$ ) |
| $\{P\}$                 | Applied load vector, $N$  |

Until recently, fatigue cracked propagation was assumed to be related directly to the linear elastic stress-intensity factor  $[I]^2$  during cyclic loading. Implicit in this concept were the assumptions that only the tensile portion of the load cycle was effective in growing the crack, and that cracks close precisely at zero load. Elber [2-4] has shown experimentally that fatigue cracks close at positive loads during zero-tension constant-amplitude load cycling. He has indicated that fatigue-crack closure may be a significant factor in causing the stress-interaction effects on crack growth (retardation or acceleration) under general cyclic loading. He has also postulated that the crack-closure phenomenon was caused by residual plastic deformations remaining in the wake of the advancing crack tip.

Kobayashi et al [5], and Anderson [6] using the finite-element method analyzed the steadily growing crack under a single monotonically increasing load. Since these investigations did not consider cyclic loading, crack-closure effects were not accounted for in the analysis.

Newman and Armen [7], also using the finite-element method, have

<sup>2</sup> The italic numbers in brackets refer to the list of references appended to this paper.

analyzed an extending crack under cyclic loading which included the effects of crack closure. Their study was an initial attempt to analytically determine crack-closure effects and employed an element-mesh size which had elastic-stress concentration of about seven. In their analysis, the ratio of the smallest element size to the crack half length was about 0.025. Their analysis demonstrated that the phenomenon of fatigue-crack closure could be modeled qualitatively by use of the finite-element method.

In the present paper, a more efficient two-dimensional, nonlinear, finite-element analysis [8] was used to investigate crack extension and crack closure in a center-crack panel under cyclic loading. (The more efficient computer program required about one half of the central processing unit (CPU) time and about one half of the storage requirements as the program used in Ref 7 for the same element mesh.) The present paper also demonstrates how the element-mesh size in the crack-tip region influences the calculated crack-closure and crack-opening stresses. Element-mesh sizes nearly an order of magnitude smaller than that used in Ref 7 were investigated. The finer mesh size also allows for simulated crack-growth increments per cycle (as small as 0.08 mm) to be consistent with experimental observations for some of the applied stress levels studied.

The panel material was assumed to be elastic-perfect plastic. The cyclic loads applied to the finite-element models of the panel were either constant-amplitude or two-level block loading. The crack-closure stresses, crack-opening stresses, crack-surface displacements, and residual stresses in the crack-tip region were determined as functions as applied stress.

### **Finite-Element Analysis**

The elastic-plastic analysis of the center-cracked panel (Fig. 1) employed the finite-element method and the initial-stress concept [9]. The finite-element model, Fig. 2, was composed of two-dimensional constant-strain triangular elements (unit thickness). Three different mesh sizes were used to model the crack-tip region, Fig. 3. In the initial-stress approach, the load-displacement relations for a discretized structure are written to include the effects of initial stresses, which are required in order to satisfy the yield criterion (von Mises) for an elastic-plastic material. These initial stresses produce effective plastic-load vectors which are applied to all elements which have become plastic and which maintain the permanent plastic deformation on those elements while the external loads are applied. The governing matrix equations for a discretized structure are reviewed only briefly here to demonstrate how the material nonlinearity is accounted for and what is required to treat crack extension and intermittent contact or separation of the crack surfaces.

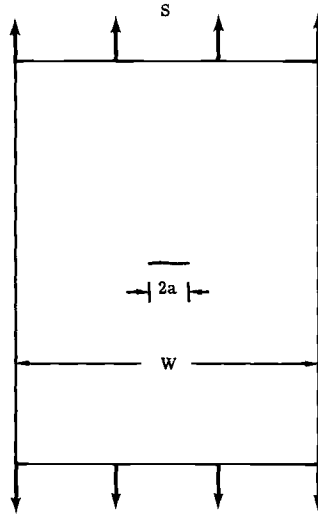


FIG. 1—Center-crack panel subjected to uniform stress.

#### *Solution Procedure for Elastic-Plastic Structures*

The application of the finite-element method to problems involving linearly elastic materials is straightforward because the material properties are constant and only one solution is required to obtain displacements for the elastic structure. However, for elastic-plastic structures the coefficients in the stiffness matrix are functions of loading. Thus, the displacements usually are obtained by applying small load increments to the structure and either updating the coefficients of the stiffness matrix or applying an "effective" plastic-load vector after each load increment. The latter technique was used here.

In general, the matrix equation which governs the response of a discretized structure under loads which cause plastic deformation is

$$[K_e] \{U\}^i = \{P\}^i + \{Q\}^i \quad (1)$$

where

- $[K_e]$  = elastic stiffness matrix,
- $\{U\}$  = generalized nodal displacement vector,
- $\{P\}$  = applied load vector, and
- $\{Q\}$  = effective plastic-load vector which accounts for elements in a plastic state.

In the initial-stress method, the solution to an elastic-plastic problem is obtained by applying a series of small load increments to the structure until the desired load is reached,  $\{P\}^i = \{P\}^{i-1} \pm \{dP\}$ .  $\{dP\}$  was chosen

to be 5 percent of the load required to yield the first element.) The superscript  $i$  in Eq 1 denotes the current load increment, and  $i - 1$  denotes the preceding increment. After each load increment an iterative process is required to stabilize the plastic-load vector. The subscript  $I$  in Eq 1 denotes the current iteration, and  $I - 1$  denotes the preceding iteration. During the  $i^{\text{th}}$  increment a purely elastic problem is solved, and the increments in total strain  $\{d\epsilon\}$  and corresponding elastic stress  $\{d\sigma_e\}$  are computed from the displacements for every element. Because of the

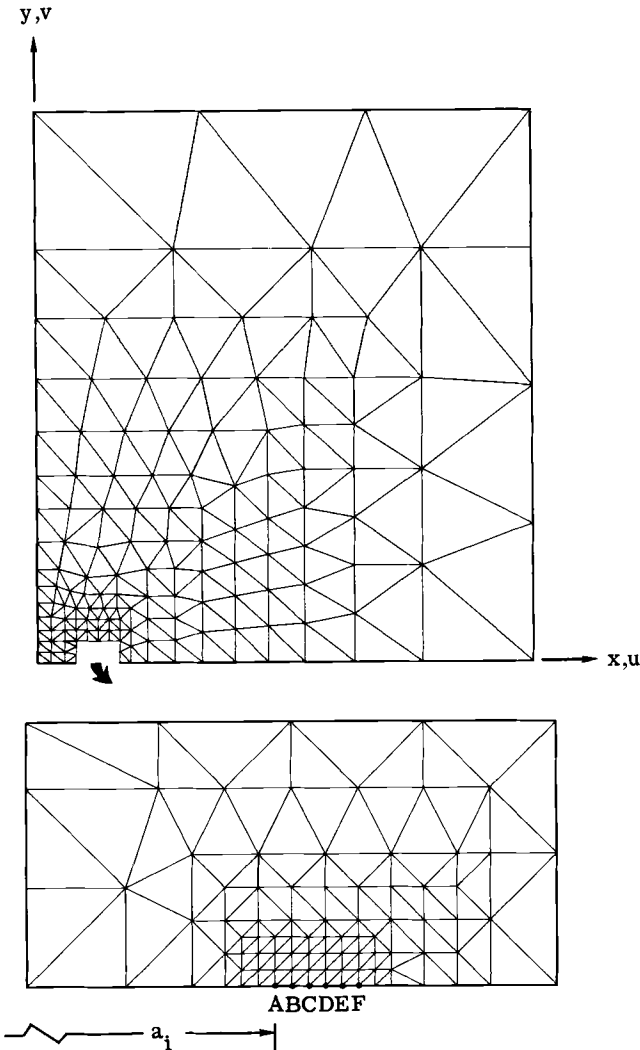


FIG. 2—Finite-element idealization of the center-crack panel.

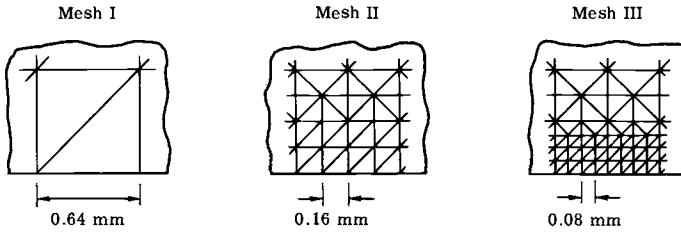


FIG. 3—Typical crack-tip region element sizes for Meshes I, II, and III.

material nonlinearity the stress increments are not, in general, correct. If the correct stress increment for the corresponding strain increment is  $\{d\sigma\}$ , then a set of body forces or plastic-load vectors  $\{dQ\}$  caused by the "initial" stress  $\{d\sigma^0\}$  ( $= \{d\sigma_e\} - \{d\sigma\}$ ) is required to maintain the stress components on the yield surface. The correct stress increment  $\{d\sigma\}$  is computed from the equations given in Ref 9. The plastic-load increments are computed from

$$\{dQ\} = \sum_{m=1}^M \int [B]^T \{d\sigma\} dV_m \quad (2)$$

where

$M$  = total number of elements,

$[B]$  = strain-displacement relationship, and

$T$  = matrix transpose.

The integration is taken over the volume of each element, and the summation is over all elements in the structure. For elements which are in an elastic state or unloading from a plastic state,  $\{dQ\} = 0$ . The total plastic-load vector is then computed as

$$\{Q\}_i^i = \{Q\}_{i-1}^i + \{dQ\} \quad (3)$$

At the second state of computation the new force system  $\{Q\}_i^i$  is added to the applied load vector, and a new set of displacements is obtained. Again, some of the stresses are likely to exceed the yield criterion, and a new set of plastic-load increments is computed. The iteration process is repeated until the change in the plastic-load vector (Eq 2) is sufficiently small (0.1 percent of the final values was chosen here). Usually, 5 to 15 iterations are required to stabilize the plastic-load vector. However, for configurations which have large strain gradients, more iterations are required. For the cracked plate considered here and the particular element mesh used, 10 to 30 iterations were required. In order to reduce

the number of iterations, a relaxation technique was incorporated into the nonlinear analysis program by using the equation

$$\{Q\}_I^i = \{Q\}_I^{i-1} + g \{dQ\} \quad (4)$$

Where  $g$  is the relaxation parameter. Because the displacements from the preceding increment or iteration are used to compute the plastic-load increment, the plastic-load vector is underestimated. Thus, the relaxation parameter is used to increase the plastic-load vector and, consequently, increase the rate of convergence. For the finite-element mesh used here, the displacements were found to converge roughly twice as fast using  $g = 2$  than using  $g = 1$  (usual value for the initial-stress method).

#### *Solution Procedure for Changing Boundary Conditions*

As previously mentioned, the finite-element analysis of an extending crack under cyclic loading must be able to account for changing boundary conditions during a specified load history. Usually, boundary conditions (free or fixed) in the finite-element method are satisfied by adding equations to, or deleting equations from, the overall system of equations. But the approach selected here was to connect two springs to each boundary node, as shown in Fig. 4. One spring was used to satisfy boundary conditions in the  $x$ -direction, and the other to satisfy conditions in the  $y$ -direction. Therefore, all nodes in the system had two degrees of freedom. For free nodes, the spring stiffness,  $k_{sx}$  or  $k_{sy}$ , was set equal to zero. For fixed nodes, the spring stiffness was assigned an extremely large value ( $10^7$  times the modulus of elasticity of the plate material). The spring stiffness was added to the diagonal coefficient in the conventional elastic stiffness matrix. The use of springs to satisfy boundary conditions was

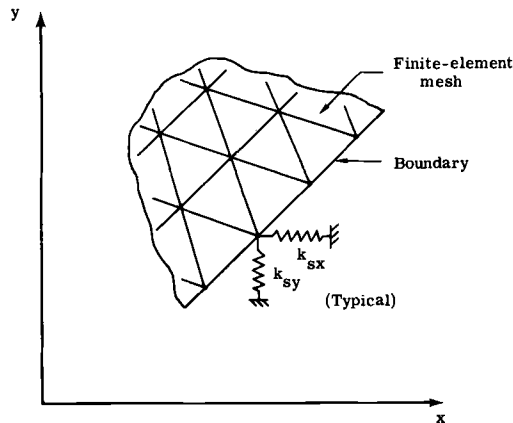


FIG. 4—Springs connected to boundary nodes of a finite-element mesh.

selected because an efficient technique to modify coefficients of the elastic stiffness matrix was incorporated into the nonlinear analysis program. This technique involved modifying the coefficients of the Cholesky decomposition [10] of the elastic stiffness matrix. The number of computer operations required to compute the modified Cholesky factors was of the order of  $n^2$  ( $n$  was the total number of degrees of freedom). In contrast, the number of operations required to obtain the original Cholesky factors was of the order of  $n^3$ . A detailed discussion of the coefficient-modification technique may be found in Refs 8 or 10.

The coefficients of the elastic stiffness matrix are obtained from

$$[K_e] = \sum_{m=1}^M \int [B]^T [D_e] [B] dV_m + [K_s] \quad (5)$$

where  $[D_e]$  is the elasticity matrix and the diagonal matrix  $[K_s]$  contains the elastic stiffness of the springs connected to the boundary nodes.

The procedure for treating the nonlinear material behavior in the presence of changing boundary conditions remains unchanged from that previously presented for an elastic-plastic structure, except that all nodal displacements along the crack line were monitored to determine whether the nodes are to be released (crack extends), to open (crack opening), or to close (crack closure).

To extend the crack, the crack-tip node was chosen arbitrarily to be released at maximum load (the stiffness of the boundary spring was set equal to zero and the stiffness matrix was updated) and the crack tip advanced to the next node. During crack extension, the nodal force carried by the crack-tip node was released automatically due to the change in the spring stiffness. To ensure that the stresses and total strain increments in the adjacent elements satisfied the yield condition and the Prandtl-Reuss flow rule, the iterative procedure, previously discussed, was used to redistribute the force previously carried by the broken node, and to stabilize the plastic-load vector.

During each load increment (loading or unloading), the nodal displacements along the crack line were monitored to determine whether the crack surfaces had opened or closed. If the crack surfaces had opened (positive displacement of the spring), the stiffness of the boundary spring was set equal to zero, and the stiffness matrix was updated. If the crack surfaces had closed (negative displacement of the spring), the spring stiffness was set to the extremely large value, and the stiffness matrix was updated.

#### **Application of the Finite-Element Analysis to Cyclic Crack Extension**

Elber [4], on the basis of fatigue crack-closure experiments with constant-amplitude loading, proposed the following equation for fatigue-crack-propagation rates

$$\frac{\Delta a}{\Delta N} = C (\Delta K_{\text{eff}})^n \quad (6)$$

where  $C$  and  $n$  are material constants and  $\Delta K_{\text{eff}}$  is the effective stress-intensity factor range. He proposed that the effective stress-intensity factor range be calculated by

$$\Delta K_{\text{eff}} = \Delta S_{\text{eff}} \sqrt{\pi a} \alpha \quad (7)$$

where

$a$  = half length of the crack,

$\alpha$  = boundary-correction factor, and

$\Delta S_{\text{eff}}$  = effective stress range,

given by

$$\Delta S_{\text{eff}} = S_{\text{max}} - S_o \text{ for } S_o \geq S_{\text{min}} \quad (8)$$

where

$S_{\text{max}}$  = maximum stress,

$S_{\text{min}}$  = minimum stress, and

$S_o$  = crack-opening stress.

Thus, the crack is assumed to propagate only during that portion of the load cycle in which the crack tip is open. Equations 6 to 8 suggest, then, that the crack-opening stress can significantly influence crack growth under both constant- and variable-amplitude loading.

The following sections give the results of applying the finite-element analysis to an extending crack under cyclic loading. The center-cracked panel, Fig. 1, was subjected to either constant-amplitude or two-level block loading.

The panel material was assumed to be elastic-perfect plastic with a tensile (and compressive) yield stress,  $\sigma_0$ , of 350 MN/m<sup>2</sup> and a modulus of elasticity of 70000 MN/m<sup>2</sup>. These properties are representative of an aluminum alloy material. The cyclic stress-strain curve assumed for this material is shown in Fig. 5. The cyclic stress-strain curve was also taken to be the stabilized curve, that is, the stress-strain behavior was assumed to be unaffected by further cycling. (Crews [11] has shown that in some materials the local stress-strain behavior at a notch root stabilizes in approximately 10 cycles.) The solid line in Fig. 5 shows the behavior under tensile loading. The dashed line indicates the typical behavior during unloading. The dash-dot line shows the behavior during reloading from a compressive plastic state.

In this study, no attempt was made to establish a failure criterion for

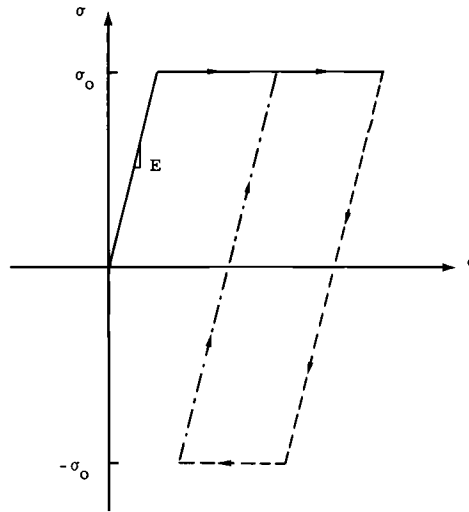


FIG. 5—Cyclic stress-strain curve for an elastic-perfectly plastic material.

crack growth. For any cyclic loading, the crack-tip node (for example, Nodes A, B, . . . , or F in Fig. 2) was chosen arbitrarily to be released at the maximum applied stress regardless of the magnitude of the applied stress and of any prior stress history. Thus, the model provides no direct information on the amount of crack growth per cycle; this information must be obtained from Eq 6. Instead, the analysis provides only the crack-opening stress,  $S_o$ , to be used in Eq 8. Of course, the accuracy of the calculated crack-opening stresses would be affected by the mesh size chosen to model the crack-tip region. A finer element-mesh size would give more accurate results. Therefore, three different element-mesh sizes with progressively smaller elements, Fig. 3, were used to model the crack-tip region. Table 1 shows the elastic-stress concentration, the smallest element size, and the total number of elements and nodes used for the three different meshes.

TABLE 1—Comparison of stress concentration, smallest element size, and the number of elements and nodes for Meshes I, II, and III.

| Mesh | $K_T$ | $\Delta a,^a$<br>mm | Elements | Nodes |
|------|-------|---------------------|----------|-------|
| I    | 7.2   | 0.64                | 398      | 226   |
| II   | 14.4  | 0.16                | 533      | 300   |
| III  | 20.9  | 0.08                | 639      | 358   |

<sup>a</sup>  $W = 460$  mm and  $a \approx 28$  mm.

*Crack Extension Under Constant-Amplitude Loading Using Mesh I*

The following sections give the results of applying a constant-amplitude loading ( $R = 0$ ) to Mesh I. These results are shown to demonstrate how the crack was allowed to propagate under cyclic loading and how the residual plastic deformations remaining in the wake of the advancing crack cause the crack surfaces to close during unloading. Crack-surface displacements and residual stress distributions during the crack-growth process are also presented.

The finite-element idealization and the coordinate system used for the center-crack panel are shown in Fig. 2 for Mesh I. The initial crack tip was located at Node A (see Fig. 2), so that the initial crack half length,  $a_i$ , was 27.3 mm. The total panel width was 460 mm.

The constant-amplitude loading applied to the center-crack panel is shown in Fig. 6. The maximum gross stress was  $0.4 \sigma_0$ . As the cyclic stresses were applied, the crack initially opened at a infinitesimal stress due to the assumption of no prior plastic deformation. The symbol  $x$  indicates the point at which the most highly stressed crack-tip element initially yielded. The plastic-zone size along the  $x$ -axis at maximum stress was about 4.6 mm. At the maximum applied stress, Node A was allowed to displace (crack extension), and the crack tip advanced to Node B. (Note that the crack extension increment, Node A to Node B, is solely a consequence of the element-mesh size used and does not imply a crack-growth law.) The crack-growth increment (0.64 mm) was about 14 percent of the plastic-zone size. During unloading, Node A was found to

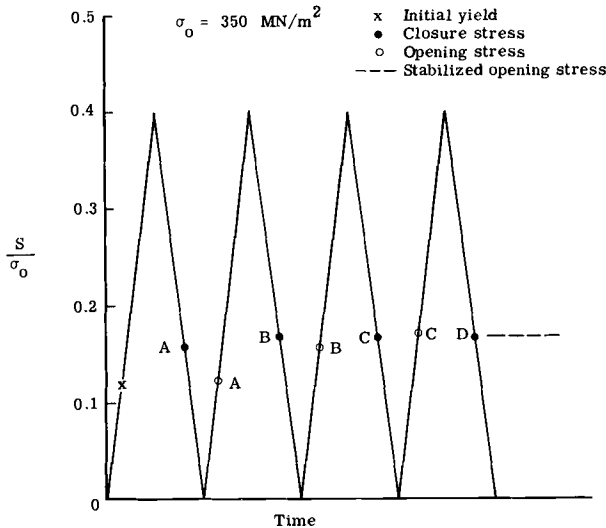


FIG. 6—Constant-amplitude crack extension with  $S_{max} = 0.4 \sigma_0$  and  $R = 0$  using Mesh I.

close at a positive stress (solid symbol) and was constrained against further motion. At zero applied stress, the contact (closure) stresses near Node A were large enough to cause the material along the crack surfaces to yield in compression. When the panel was reloaded, Node A opened (open symbol) at a considerably lower stress than at which it had previously closed. Again, upon reaching the maximum stress, the next node (B) was also allowed to displace and the crack tip extended to Node C. During unloading, Node B closed at a slightly higher stress than that at which Node A had closed on the previous cycle. Further cycling and sequential release of the nodes indicated that the closure stress rapidly stabilized to approximately 43 percent of the maximum applied stress. The opening stress increased after each cycle until it converged to the previously established closure stress.

Because the crack-closure and crack-opening stresses are a function of the crack-surface displacements, the variation of surface displacements with crack extension was investigated. The crack surface displacements for constant-amplitude crack extension with  $S_{max} = 0.4 \sigma_0$  are shown in Fig. 7. The displacement,  $v$ , in the  $y$ -direction was plotted as a function of the coordinate location,  $x$ . The lowest curve shows the displacements at maximum stress with the crack tip located at Node A (before crack extension). The other curves represent the crack-opening displacements at the maximum applied stress after each increment of crack extension. The sharp knee (slightly to the left of Node A) in the displacement curves is an indication of the extent of plastic deformation.

To gain a qualitative understanding of the relationship between the

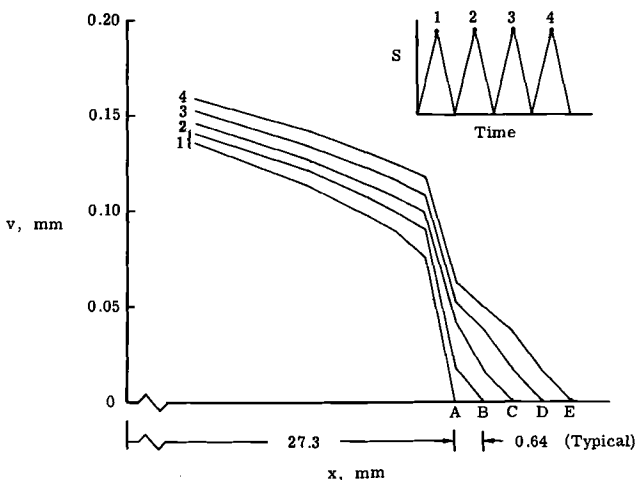


FIG. 7—Crack-surface displacements under constant-amplitude crack extension with  $S_{max} = 0.4 \sigma_0$  and  $R = 0$  using Mesh I.

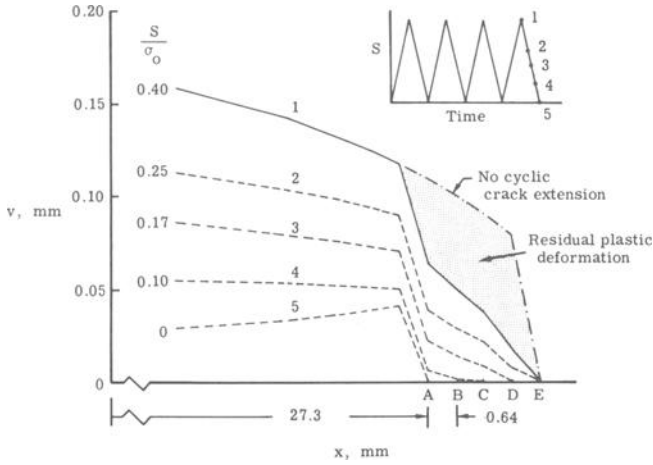


FIG. 8—Crack-surface displacements during unloading after constant-amplitude crack extension ( $S_{max} = 0.4 \sigma_0$ ) with crack tip at Node E.

residual plastic deformations near the crack tip and the crack-closure stresses, crack-surface displacements were computed for two similar configurations. The first configuration was a crack, with the tip initially at Node E, being opened for the first time by the maximum applied stress ( $S_{max} = 0.4 \sigma_0$ ). The second configuration was a crack which was grown incrementally from Node A to Node E by cyclic loading (also with  $S_{max} = 0.4 \sigma_0$ ). The results are shown in Fig. 8. The dash-dot curve is the surface displacements for the first configuration under the maximum stress. The solid curve is for the second configuration under the same maximum stress. The fully dashed curves show the displacements for the second configuration under a sequence of lower stresses for which the crack has closed successively from Node E to Node A.

The difference between the maximum surface displacements for the two configurations, as identified by the shaded region in Fig. 8, is a measure of the residual plastic deformations which are left in the wake of the advancing crack tip, and which Elber has postulated as the major cause of crack closure during unloading.

The displacement curves for lower stress levels further illustrate the crack-closure phenomenon. For example, a drop to  $0.17 \sigma_0$  in applied stress caused the crack to close back to Node D. Upon complete removal of the applied stress, the crack closed back to Node A but remained open to the left of Node A.

The stress distributions near the crack tip associated with these stages of unloading are shown in Fig. 9. At the maximum applied stress, the near-tip stress  $\sigma_{yy}$  (solid curve), reaches at plateau in front of the crack tip (characteristic of an elastic-perfect plastic material). Because the local

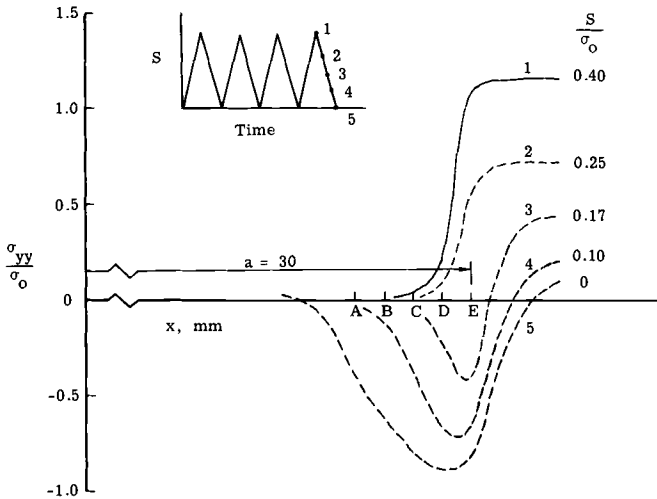


FIG. 9—Local crack-tip stress distributions during unloading after constant-amplitude crack extension ( $S_{max} = 0.4 \sigma_0$ ) with crack tip at Node E.

stresses are computed at the centroid of the elements ( $\approx 0.3$  mm from the crack surface), the stresses do not drop to zero immediately behind the crack tip. During unloading, the crack surfaces contact initially at Node D and the crack surfaces between Nodes A and E begin to support compressive stresses, as illustrated by Curves 3 to 5 of Fig. 9.

#### *Crack Extension Under Constant-Amplitude Loading Using Mesh II or III*

The following sections give the results of applying various constant-amplitude loading to Meshes II or III. These results are also compared with previous results obtained from Ref 8 using Mesh I. A comparison between the element sizes in the crack-tip region for Meshes I, II, and III are shown in Fig. 3. The smallest element size for Mesh III was nearly an order of magnitude smaller than that for Mesh I. The elastic-stress concentration for Meshes II and III was about 14 and 21, respectively.

**Stress Level**—The constant-amplitude loading ( $R = 0$ ) applied to Mesh III is shown in Fig. 10. The maximum gross stress was  $0.4 \sigma_0$ , identical to that applied to Mesh I, Fig. 6. The crack half length,  $a_i$ , was 25.4 mm and was located initially in a mesh size identical to Mesh I. After eight cycles and eight growth increments, the crack tip was located in the finest mesh. The open symbols indicate the stresses at which the crack tip opens during loading, and the solid symbols indicate the stresses at which the crack tip closes during unloading. After the eighth cycle, the closure stress stabilized at about 75 percent of the maximum stress. The step in the closure stress between the seventh and eighth cycle was caused by the

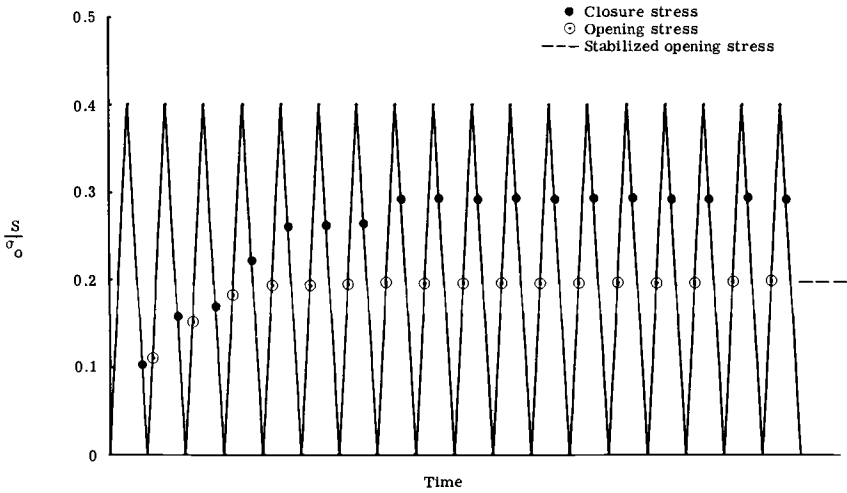


FIG. 10—Constant-amplitude crack extension with  $S_{max} = 0.4 \sigma_o$  and  $R = 0$  using Mesh III.

change in mesh size. The closure stress seems to be governed by the maximum strain reached on the crack-tip element prior to crack extension. However, the crack-opening stress was found to stabilize, after five cycles, at about 50 percent of the maximum applied stress. This value of crack-opening stress is in good agreement with the experimental value (also 50 percent of  $S_{max}$ ) obtained by Elber [4].

The plastic-zone size at maximum stress ( $0.4 \sigma_o$ ) and a crack half length of 28 mm was again about 4.6 mm. Thus, the crack-growth increments per cycle (0.08 mm) were about 2 percent of the plastic-zone size. At this stress level and crack length, the actual crack-growth increment per cycle for a 2024-T3 aluminum alloy material was about 0.1 mm [12]. Therefore, the simulated crack-growth rates and the actual crack-growth rates were in good agreement. In fact, the same stress history applied to Mesh II gave the same crack-opening stress as Mesh III, even though the growth increment per cycle was twice as large as that for Mesh III.

Figure 11 shows the stabilized crack-opening stress normalized to the maximum applied stress as a function of mesh size for various applied stress levels. The stress ratio ( $R$ ) for all cases was zero. For stress levels greater than  $0.2 \sigma_o$  and less than  $0.5 \sigma_o$ , Meshes II and III gave crack-opening stresses within 10 percent of  $0.5 S_{max}$ . For stress levels less than  $0.2 \sigma_o$ , a finer mesh size than Mesh III should be used. At an applied stress level of  $0.5 \sigma_o$ , Meshes I, II, and III gave almost the same crack-opening stress. Stress levels greater than  $0.5 \sigma_o$  were attempted, but the crack-opening stresses did not stabilize before the crack grew out of the fine mesh region. For stress levels greater than  $0.5 \sigma_o$ , the

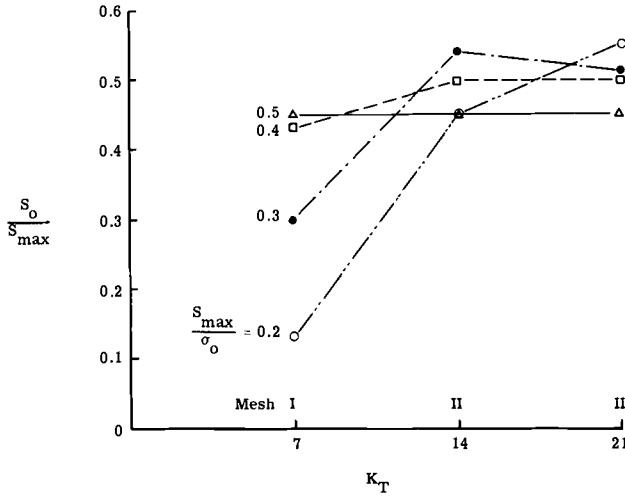


FIG. 11—Stabilized crack-opening stresses as a function of mesh size under constant-amplitude loading ( $R = 0$ ).

crack-opening stresses are expected to be considerably lower than  $0.5 S_{max}$  because yielding would occur over a substantial portion of the net section.

**Stress Ratio**—To study the effects of stress ratio on crack closure, calculations were made for  $R$  values between 0.5 and  $-1$  using Mesh III. Figure 12 shows a cyclic stress history with  $R = 0.5$  and  $S_{max} = 0.4 \sigma_o$ .

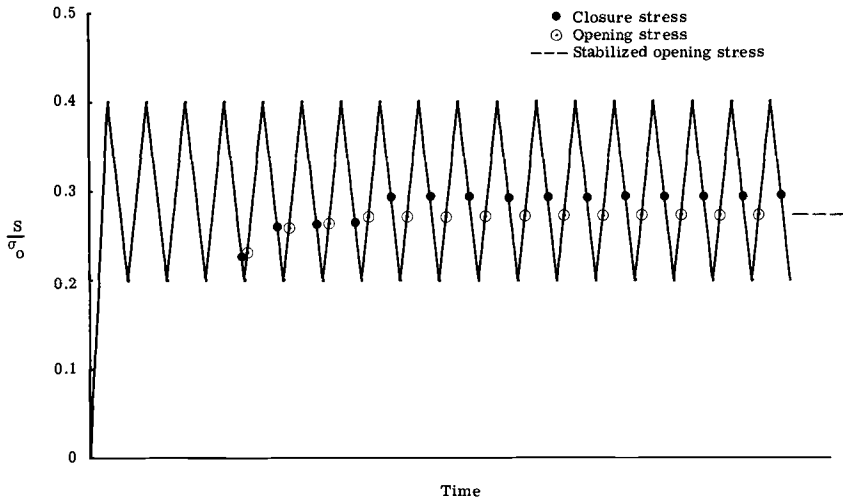


FIG. 12—Constant-amplitude crack extension with  $S_{max} = 0.4 \sigma_o$  and  $R = 0.5$  using Mesh III.

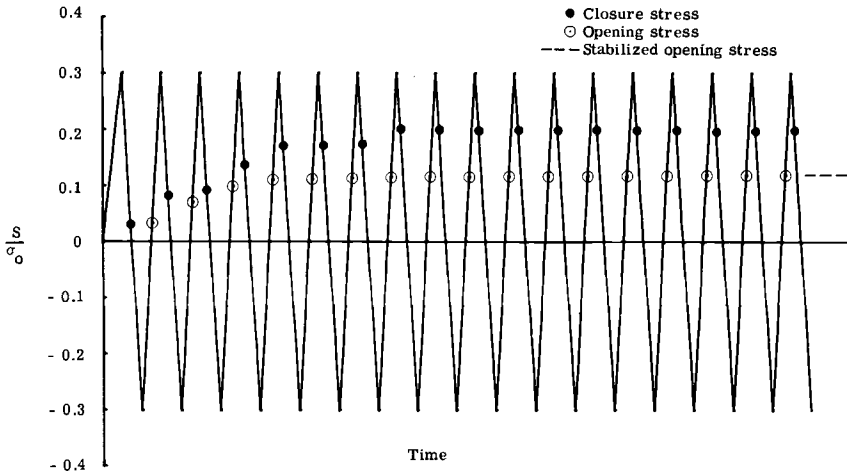


FIG. 13—Constant-amplitude crack extension with  $S_{max} = 0.3 \sigma_0$  and  $R = -1$  using Mesh III.

Again, the crack-tip nodes were released at succeeding occurrences of maximum stress. But in this case, the crack surfaces did not close until the fourth cycle. The opening stress stabilized at about 68 percent of the maximum stress. This value of opening stress was about 5 percent higher than that measured by Elber [4] on an aluminum alloy.

Figure 13 shows the crack-closure and crack-opening stresses for  $R = -1$  and  $S_{max} = 0.3 \sigma_0$ . During the compressive loading, all nodes along the crack surfaces closed. The crack-opening stress for all cycles was lower than the corresponding opening stress obtained for the  $R = 0$  case ( $S_{max} = 0.3 \sigma_0$ ). This implies that the applied compressive stress caused the material along the contacting crack surfaces to yield further in compression than the  $R = 0$  case. The crack-opening stress stabilized at 50 percent of the maximum stress. Therefore, according to Eq 6 the fatigue-crack-growth rates for  $R = -1$  should be approximately two times faster than the rates for  $R = 0$  ( $n = 4$  in Eq 6). This inference is consistent with the results obtained by Hudson [12], who found about the same difference between the crack-growth rates for a 2024-T3 aluminum alloy sheet material at  $R = 0$  and  $R = -1$ .

To summarize the effects of stress ratio on crack-opening stresses, Fig. 14 shows the stabilized crack-opening stresses normalized to the maximum applied stress as a function of stress ratio using Mesh III. The solid symbols denote the results at  $S_{max} = 0.3 \sigma_0$  and the open symbols at  $S_{max} = 0.4 \sigma_0$ . The dashed curve shows the experimental results obtained by Elber [4] for  $R$  values between  $-0.1$  and  $0.7$ . The agreement between the calculated and experimental results at  $R = 0$  and  $0.5$  are considered good. The results at negative  $R$  values show that the crack

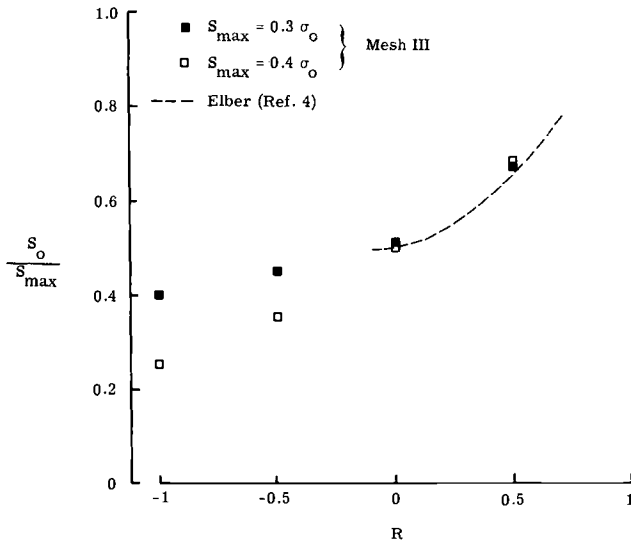


FIG. 14—Comparison of calculated (stabilized) and experimental crack-opening stress as a function of stress ratio ( $R$ ).

opening stresses were influenced strongly by the magnitude of the compressive stress. The applied compressive stresses cause the crack surfaces near the crack tip to yield in compression, thereby lowering the subsequent crack-opening stress. Further studies on measuring crack-opening stresses during fatigue-crack-growth rate tests at negative  $R$  values should be made to investigate this stress level effect.

#### Crack Extension Under Two-Level Block Loading Using Mesh III

*High-to-Low Loading*—The high-to-low block loading applied to Mesh III is shown in Fig. 15. The maximum stress  $S_{max1}$  (first level) was  $0.4 \sigma_o$  and  $S_{max2}$  (second level) was  $0.3 \sigma_o$ . The crack closure and opening stresses for the eight cycles of  $S_{max1}$  were identical to those previously shown in Fig. 10. On the first cycle of  $S_{max2}$ , the crack-tip node was allowed to displace (crack extends). During unloading, the crack tip closed at a stress which was considerably lower than the previous closure stress for  $S_{max1}$ . When the panel was reloaded, the crack tip opened at a slightly higher stress than the stabilized opening stress for  $S_{max1}$  (dashed line). During further cycling, the crack-opening stress increased after each cycle and reached a peak at the ninth cycle of  $S_{max2}$ . If more than eleven cycles of  $S_{max2}$  were to be applied, the closure and opening stresses would be expected to converge to the dash-dot line (the stabilized opening stress for  $S_{max2}$ ) as the crack grows out of the material yielded by  $S_{max1}$ . The last two cycles of  $S_{max2}$  show crack-opening stresses less than the peak value.

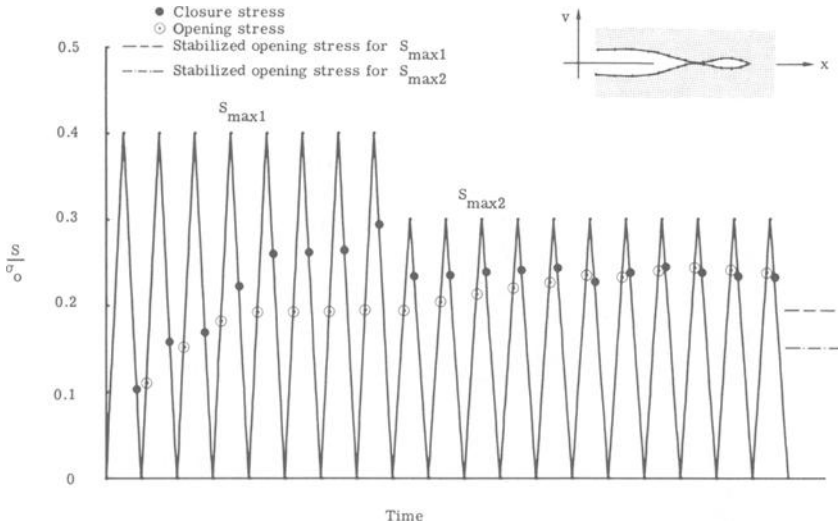


FIG. 15—High-to-low block loading crack extension with  $S_{max1} = 0.4 \sigma_o$  and  $S_{max2} = 0.3 \sigma_o$  using Mesh III.

The closure and opening stresses are governed usually by the node adjacent to the crack tip along the crack surface, but, under the high-to-low loading during the sixth to 11th cycle of  $S_{max2}$ , the closure and opening stresses were governed by nodes not adjacent to the crack-tip node. This behavior is illustrated in the sketch on Fig. 15. The sketch shows the crack-surface displacements along the crack line. Crack closure during unloading or crack opening during loading occurs at a node several element sizes to the left of the crack tip. This behavior shows the existence of a “hump” in the crack surfaces which was caused by the high loading.

Because the crack-opening stresses for  $S_{max2}$  are considerably higher than the stabilized opening stress for  $S_{max2}$  the crack-growth rates (computed from Eq 6 are expected to be considerably lower than if the eight cycles of  $S_{max1}$  had not been applied. This behavior has been observed and is referred to as crack-growth retardation or delay (see, for example, [13]).

*Low-to-High-Loading*—Figure 16 shows the low-to-high block loading applied to Mesh III, for which  $S_{max1} = 0.3 \sigma_o$  and  $S_{max2} = 0.4 \sigma_o$ . The crack closure and opening stresses for  $S_{max1}$  has stabilized at the eighth cycle. On the first cycle of  $S_{max2}$ , the crack-tip node was released again. During unloading, the crack tip closed at approximately 75 percent of the maximum applied stress. At zero applied stress, the material along the crack surface near the crack tip yielded in compression, and the subsequent opening stress was considerably lower than the stabilized opening

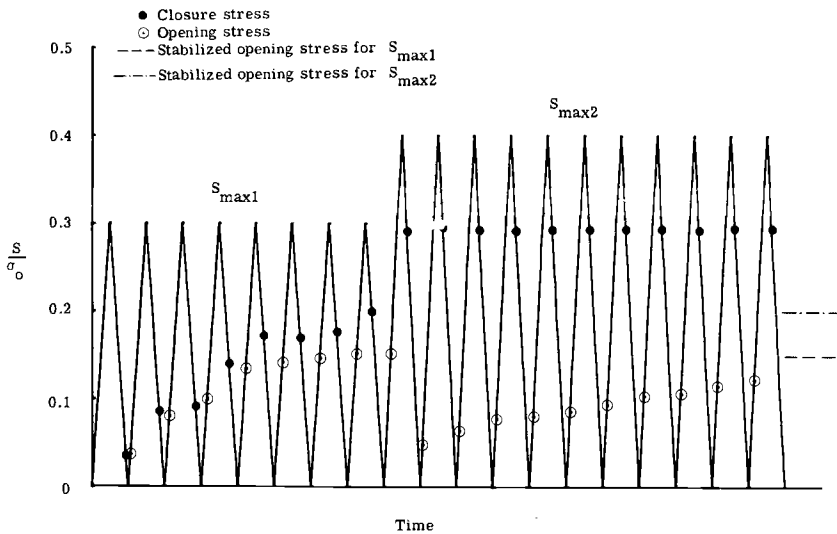


FIG. 16—Low-to-high block loading crack extension with  $S_{\max 1} = 0.3 \sigma_0$  and  $S_{\max 2} = 0.4 \sigma_0$  using Mesh III.

stress for  $S_{\max 1}$ . During further cycling, the closure stress remained constant, while the opening stress increased after each cycle. The opening stress had not converged to the stabilized opening stress for  $S_{\max 2}$  (dash-dot line) after eleven cycles. If more cycles had been applied the opening stress should be expected to converge to the dash-dot line. Because the opening stresses for  $S_{\max 2}$  are considerably lower than the stabilized opening stress, the crack-growth rates (computed from Eq 6) are expected to be higher than the crack-growth rates computed using the stabilized opening stress for  $S_{\max 2}$ . This behavior in crack-growth rates has also been observed experimentally and is referred to as crack-growth acceleration [14].

### Concluding Remarks

A two-dimensional (plane stress) finite-element analysis which accounts for both nonlinear material behavior and changing boundary conditions under cyclic loading has been presented and used to study crack extension and crack closure in a center-cracked panel. The finite-element models of the panel were assumed to be composed of an elastic-perfect plastic material and was subjected to either constant-amplitude or two-level block loading.

Although the failure criterion used in growing the crack was arbitrary, the calculated crack-opening stresses under constant-amplitude loading were quantitatively consistent with experimental measurements. The calculated crack-opening stresses under two-level block loading, when

used with Elber's crack-growth equation, gave crack-growth-rate trends (retardation or acceleration) consistent with experimental observations. Therefore, the finite-element analysis performed here gives further insight into the mechanism of fatigue-crack growth during cyclic loading.

## References

- [1] Paris, P. C., Gomez, M. P., and Anderson, W. E., *The Trend in Engineering*, University of Washington, Seattle, Wash., Vol. 13, No. 1, 1961.
- [2] Elber, W., "Fatigue Crack Propagation," Ph. D. thesis, University of New South Wales, Australia, 1968.
- [3] Elber, W., *Engineering Fracture Mechanics*, Vol. 2, No. 1, 1970.
- [4] Elber, W. in *Damage Tolerance in Aircraft Structure*, American Society for Testing and Materials, 1970, pp. 230-242.
- [5] Kobayashi, A. S., Chiu, S. T., and Beeuwkes, R., *Engineering Fracture Mechanics*, Vol. 5, No. 2, 1973.
- [6] Anderson, Hans, *International Journal of Fracture*, Vol. 9, 1973.
- [7] Newman, J. C., Jr., and Armen, Harry, Jr., "Elastic-Plastic Analysis of a Propagating Crack Under Cyclic Loading," AIAA Paper No. 74-366, presented at the AIAA/ASME/SAE 15th Structures, Structural Dynamics, and Materials Conference, Las Vegas, Nev., 17-19 April 1974.
- [8] Newman, J. C., Jr., "Finite-Element Analysis of Fatigue Crack Propagation—Including the Effects of Crack Closure," Ph. D. thesis, Virginia Polytechnic Institute and State University, Blacksburg, Va., May 1974.
- [9] Zienkiewicz, O. C., Valliappan, S., and King, I. P., *International Journal for Numerical Methods in Engineering*, Vol. 1, 1969, pp. 75-100.
- [10] Gill, P. E., Golub, G. H., Murray, W., and Saunders, M. A., "Methods for Modifying Matrix Factorizations," STAN-CS-72-322, Computer Science Department, Stanford University, Los Angeles, 1972, pp. 18-24.
- [11] Crews, J. H., Jr., "Elastoplastic Stress-Strain Behavior at Notch Roots in Sheet Specimens Under Constant-Amplitude Loading," NASA TN D-5253, National Aeronautics and Space Administration, Washington, D.C., 1969.
- [12] Hudson, C. M., "Effect of Stress Ratio on Fatigue-Crack Growth in 7075-T6 and 2024-T3 Aluminum-Alloy Specimens," NASA TN D-5390, National Aeronautics and Space Administration, Washington, D.C., 1969.
- [13] Trebules, V. W., Roberts, R., and Hertzberg, R. W. in *Progress in Flaw Growth and Fracture Toughness Testing*, ASTM STP 536, American Society for Testing and Materials, 1972, pp. 115-146.
- [14] Matthews, W. T., Baratta, F. I., and Driscoll, G. W., *International Journal of Fracture Mechanics*, Vol. 7, 1971.

W. N. Sharpe, Jr.,<sup>1</sup> and A. F. Grandt, Jr.<sup>2</sup>

## A Preliminary Study of Fatigue Crack Retardation Using Laser Interferometry to Measure Crack Surface Displacements

---

**REFERENCE:** Sharpe, W. N., Jr., and Grandt, A. F., Jr., "A Preliminary Study of Fatigue Crack Retardation Using Laser Interferometry to Measure Crack Surface Displacements," *Mechanics of Crack Growth, ASTM STP 590*, American Society for Testing and Materials, 1976, pp. 302-320.

**ABSTRACT:** A laser interferometry technique is described which is capable of resolving crack surface displacements to about 0.2  $\mu\text{m}$ . The method provides continuous measurements of the free surface crack profile in metal specimens without being limited by rigid body displacements. Using the laser interferometry procedure to determine fatigue crack profiles in 2024-T851 aluminum specimens, it was possible to measure the load at which the crack faces completely separate. These opening loads were correlated with peak tensile overloads and subsequent crack retardation. These results are discussed in terms of the Elber concept of fatigue crack closure.

**KEY WORDS:** crack propagation, lasers, interferometry, fatigue (materials), measurement, cyclic loads, retarding, stresses, deformation

### Nomenclature

- $a$  Crack length
- $\alpha, \alpha_0$  Angles between incident laser beam and fringe pattern
- $d$  Distance between reference grooves
- $\delta d$  Relative displacement of grooves
- $da/dN$  Fatigue crack growth rate
- $K$  Stress intensity factor
- $K_{Ic}$  Fracture toughness
- $\Delta K$  Cyclic range in stress intensity factor =  $K_{\max}$  to  $K_{\min}$

<sup>1</sup> Professor, Department of Metallurgy, Mechanics, and Materials Science, Michigan State University, East Lansing, Mich. 48823.

<sup>2</sup> Air Force Materials Laboratory, Wright-Patterson Air Force Base, Dayton, Ohio 45433.

|                   |   |
|-------------------|---|
| $K_{\max}$        | Maximum stress intensity in baseline load cycle |
| $K_{\min}$        | Minimum stress intensity in baseline load cycle |
| $K_{\text{open}}$ | Stress intensity factor to separate crack faces |
| $K_{\text{peak}}$ | Peak value of stress intensity during overload  |
| $\lambda$         | Wavelength of light                             |
| $m, \delta m$     | Fringe order and change in fringe order         |
| $N$               | Number of cycles                                |
| $Q$               | Load ratio = $K/K_{\max}$                       |
| $Q_{\text{open}}$ | Load ratio = $K_{\text{open}}/K_{\max}$         |
| $Q_{\text{peak}}$ | Overload ratio = $K_{\text{peak}}/K_{\max}$     |
| $R$               | Stress ratio = $K_{\min}/K_{\max}$              |

Accurate determination of crack surface displacements is often required for fundamental investigations of crack behavior. As suggested by the following examples, displacement measurements may serve a variety of research purposes. Interferometric measurements of crack displacement in glass specimens, for example, were used by Sommer [1]<sup>3</sup> and by Crosley et al [2] for stress intensity factor calibrations. The crack opening displacement (COD) occurring at fracture has been suggested as a possible failure criteria for ductile materials [3]. Attempts to quantify the sensitivity of nondestructive methods of flaw inspection [4] have shown crack surface displacement to be an important variable (for example, flaws held shut by compressive stresses are more difficult to detect than those loaded in tension). Finally, determining the separation of fatigue crack surfaces as a function of applied load has received considerable interest during recent studies of crack closure as a possible mechanism for fatigue crack retardation [5-10].

A new method for measuring crack surface displacements applicable to these types of problems has been recently developed [11]. The technique, which employs laser interferometry, is quite sensitive (about 0.1  $\mu\text{m}$  resolution), is readily adaptable to laboratory measurements and has the capability of obtaining the entire crack displacement profile. The purpose of this paper is to use this new technique for some fundamental observations of fatigue crack surface displacements under tensile peak overload conditions.

Elber [5,6] explained fatigue crack retardation by the residual strains in the plastically deformed wake of the propagating crack. Since the residual compression must be overcome before the crack surfaces separate to allow propagation, the effective cyclic range in stress intensity factor is reduced. Elber suggests that peak loads change the local plastic deformation, alter the closure stresses, and thus perturb subsequent crack growth.

Elber originally observed closure with a clip gage which bridged the fatigue crack. Changes in linearity of load-displacement records indicated

<sup>3</sup> The italic numbers in brackets refer to the list of references appended to this paper.

a significant tensile load was required to overcome the residual compression. Similar measurements were made by Roberts et al [7] with foil strain gages instead of clip gages, and by Adams [8] who employed microscopic observations of reference points to obtain the load-displacement curve. It is important to note in all of these experiments that the opening load was determined from changes in the slope of the load-displacement record of two fixed points astride the crack.

Buck et al [9] used ultrasonics to measure average crack depth in surface flawed specimens. Changes in apparent crack length determined the opening load. Although this ultrasonic technique was useful for part-through crack geometries, the closure load was inferred from a change in average crack size rather than by direct observation of the crack profile. Pitoniak et al [10] used interferometric techniques to study fatigue crack closure in polymethylmethacrylate specimens. Examination of the interference fringes provide a quantitative mapping of the entire three-dimensional crack profile as a function of load, but measurements were restricted to transparent materials.

The technique described here has the significant advantage of providing continuous displacement measurements along the entire crack length in metal specimens with a sensitivity capable of determining when the crack physically separates at the specimen surface. This simple displacement measurement technique is described in the next section, followed by some observations of crack displacement profiles and a preliminary study of fatigue crack closure and retardation.

### Experimental Procedure

The opening of a crack at a free surface can be obtained by laser interferometric measurement of the displacement of two grooves ruled on either side of the crack. This is illustrated schematically in Fig. 1. The grooves are V-shaped, causing the light rays to be reflected (diffracted) at angles  $\pm\alpha$  from the laser beam incident perpendicular to the specimen surface. Since the laser radiation is monochromatic and coherent, optical interference patterns are formed in space. This phenomenon is similar to Bragg X-ray diffraction. The equation locating the bright interference fringes is

$$d \sin \alpha = m\lambda \quad m = \pm 1, 2, 3, \dots \quad (1)$$

where  $\lambda$  is the wavelength of light and  $d$  is the spacing between grooves. In order to measure the displacement,  $\delta d$ , it is convenient to fix the observation angle at  $\alpha_0$  and observe the change in fringe order  $\delta m$ . The governing equation is then

$$\delta d = \frac{\lambda}{\sin \alpha_0} \delta m \quad (2)$$

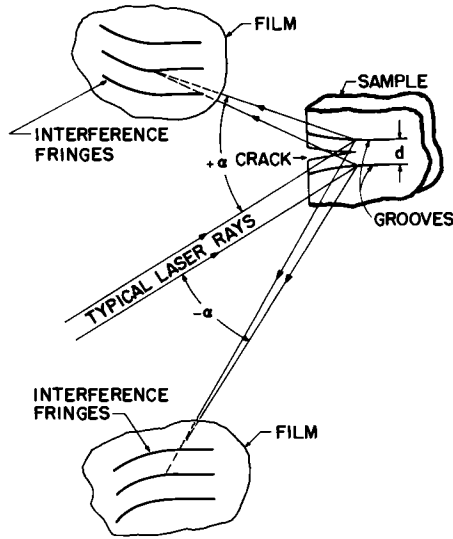


FIG. 1—Schematic of the laser interferometric displacement technique.  $d$  is typically 0.51 mm (0.020 in.), and  $\alpha$  is typically 65 deg.

The fringe shift,  $\delta m$ , is obtained by comparing fringe pattern photographs before and after the crack has opened (or partially opened). The distance on the film that a fringe has moved is converted to a fringe shift value,  $\delta m$ , by dividing it by the original spacing between fringes. One can thus measure the displacement along the crack by measuring the shift of any one of the fringes at various positions along its length. In effect, the fringe motion is a magnified picture of the crack displacement at the specimen surface. Comparison of the fringe photographs requires an indexing procedure; a suitable reference is the pattern of fringes emanating from the undeformed region in front of the crack. This concept of having the reference marks attached to the specimen removes the problem of relative motion between the optical system and testing machine and also permits before-and-after-test displacement measurements.

The quantity  $\lambda/\sin \alpha_0$  in Eq 2 is the calibration factor for this technique and is approximately  $0.7 \mu\text{m}$  using  $\lambda = 0.6328 \mu\text{m}$  and  $\alpha_0 = 67 \text{ deg}$ . Note that establishment of  $\alpha_0$  is all that is needed to calibrate the system. The resolution of the measurement is easily  $0.1 \mu\text{m}$  which turns out to be quite adequate for our purposes. It has been demonstrated [12] that this laser interferometric technique can be used to measure strains as small as 2 microstrain ( $5 \times 10^{-4} \mu\text{m}$  displacement).

Although specimen preparation is not difficult, a fairly smooth and flat surface is required. Current practice is to lap one side of the specimen and

then polish it using standard metallographic techniques. The lapping is not required; it is just more expedient. The grooves are applied by pressing a wedge-shaped diamond (110 deg wedge, 2.5 mm (0.1 in.) long) into the surface. This diamond is mounted in a holder adjacent to a toolmaker's microscope. A set of grooves is produced by pressing a row of indentations below and parallel to the crack, and then shifting the diamond across the crack and repeating the process. The procedure is to polish the surface, initiate a fatigue crack, apply the grooves, and then test. Figure 2 is a photomicrograph of a set of grooves with a spacing of 0.25 mm (0.010 in.) straddling a fatigue crack. Grooves with a spacing of 0.51 mm (0.020 in.) were used in the series of experiments discussed in this paper.

The equipment needed for measurement is a small laser and two single-lens-reflex cameras without lenses. A 5 mW helium-neon laser was used, but a 1 mW laser would be adequate. The laser and cameras are mounted, as schematically illustrated in Fig. 1, on a stand adjacent to the testing machine. Panatomic X film is used and typically requires 1/30 s exposure.

Figure 3 is a montage of fringe photos. The straight fringes on the left are in front of the crack tip and hence undistorted. The fringes emanating from grooves straddling the crack are distorted somewhat because of the distortion of the reflecting surfaces as the crack grows between them. However, one still makes valid displacement measurements as the crack opens; the zero fringe is simply no longer straight. Larger displacements than those in Fig. 3c are difficult because the fringes become too dense to resolve. The distortion of the fringes is affected by how straight the fatigue crack is and whether it wanders over toward one groove. In our experiments we had no problems with the crack wandering out of the 0.51 mm (0.020 in.) groove spacing.

Reduction of the data is effected by projecting the 35-mm film onto a ground glass screen and tracing a series of fringes obtained for various loads on the same piece of paper. A small computer with a digitizer is used to measure the fringe displacement from the zero load fringe and plot the curves. Data from both the upper and lower camera are plotted and then averaged. This averaging helps eliminate any local groove rotation and in effect smooths the displacement curves. Figure 4 is a typical plot; note that the crack is not fully open until  $Q = K/K_{\max} = 0.25$ .

The foregoing description is brief; however, the procedure is straight forward. More information on the optical aspects may be found in Refs 11 and 13.

### Crack Displacement Profiles and Opening Load Determination

Fatigue crack surface displacements were studied in ASTM standard compact specimens machined from a single sheet of 2024-T851 aluminum (thickness = 2.54 cm = 1.0 in.). All specimens were oriented so that the crack grew perpendicular to the rolling direction of the plate. Tensile



FIG. 2—Photomicrograph of a set of grooves applied parallel to a fatigue crack. The grooves are  $5\ \mu\text{m}$  wide and  $0.25\ \text{mm}$  ( $0.010\ \text{in.}$ ) apart.

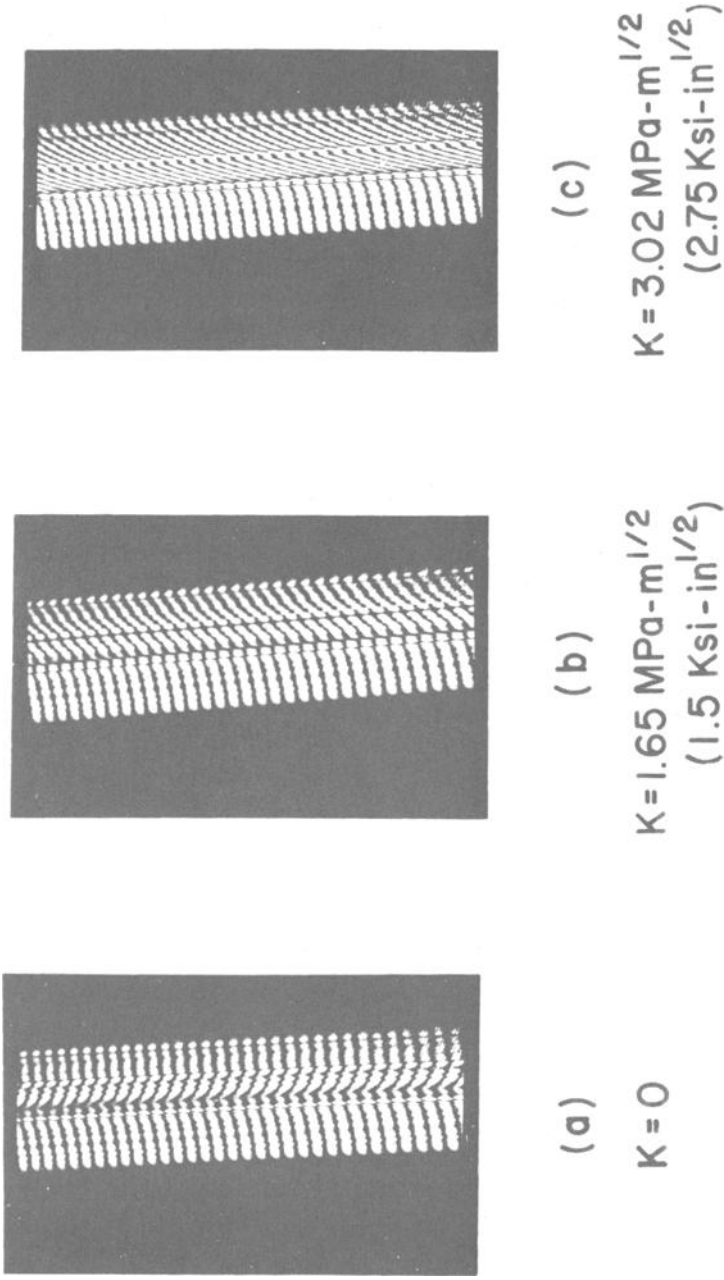


FIG. 3—Fringe photographs for the unloaded and two loaded conditions.

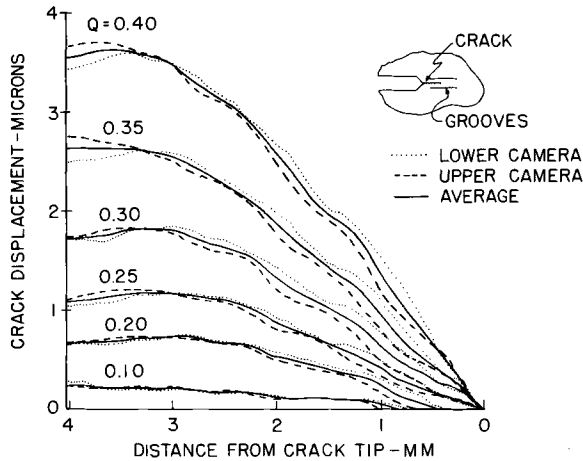


FIG. 4—Typical crack surface displacements for various load conditions,  $Q = K/K_{max}$ . The 2024-T851 compact specimen was cycled between  $K_{max} = 5.5 \text{ MPa} \cdot \text{m}^{1/2}$  ( $5 \text{ ksi} \cdot \text{in.}^{1/2}$ ) and  $K_{min} = 0.55 \text{ MPa} \cdot \text{m}^{1/2}$  ( $0.5 \text{ ksi} \cdot \text{in.}^{1/2}$ ).

properties of the test material are a 0.2 percent yield strength of 448 MPa (65 ksi) and an ultimate stress of 483 MPa (70 ksi). Two instrumented specimens tested to ASTM Test for Plane-Strain Fracture Toughness of Metallic Materials (E 399) gave  $K_{Ic}$  values of 23.0 and 23.3  $\text{MPa} \cdot \text{m}^{1/2}$  (20.9 and 21.2  $\text{ksi} \cdot \text{in.}^{1/2}$ ). Baseline fatigue crack growth rate data obtained at constant cyclic load ( $R = K_{min}/K_{max} = 0.1$ ) are shown in Fig. 5. All fatigue tests were conducted at 40 Hz on a closed loop electrohydraulic fatigue machine at laboratory temperature and environment.

Figure 6 shows the displacement curves for a crack grown at  $K_{max} = 5.5 \text{ MPa} \cdot \text{m}^{1/2}$  ( $5.0 \text{ ksi} \cdot \text{in.}^{1/2}$ ) with  $R = 0.1$  as it opens (solid line) and as it closes (dashed line). As load is applied to the specimen, the crack as observed on the surface is completely open by  $Q = 0.25$ . As the load is decreased to complete the cycle, the crack remains open at  $Q = 0.20$  and is closed at the tip for  $Q = 0.10$ . The small amount of hysteresis in the load-displacement cycle indicated by the crack tip closing at a smaller load than it opens has been reported previously [14].

Figure 7a is a plot of the displacement profiles resulting from various loads applied to a cracked compact specimen. The crack length was 8.4 mm (0.33 in.) from the 1.27 cm (0.5 in.) notch as measured on both sides of the specimen. A load of 4.27 kN (960 lb) corresponds to  $K_{max} = 5.5 \text{ MPa} \cdot \text{m}^{1/2}$  ( $5.0 \text{ ksi} \cdot \text{in.}^{1/2}$ ). As load is applied to the specimen, the displacements become large enough to measure. However, measurable displacement to the crack tip is not observed here until a load of 1.33 kN (300 lb) is applied. Then, very small displacements are measured across the tip until a load of 2.45 kN (550 lb) is applied. Higher loads lead

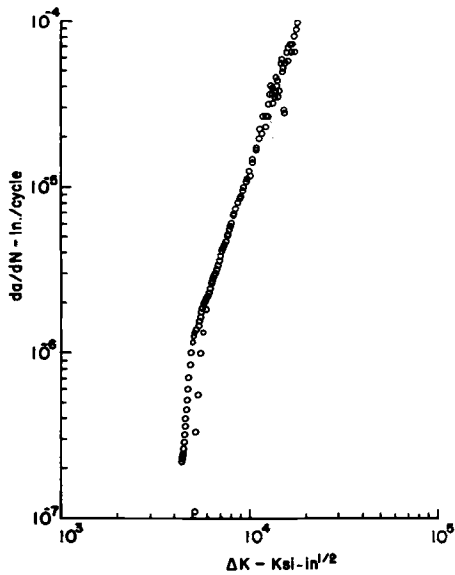


FIG. 5—Baseline  $da/dN$  versus  $\Delta K$  data for 2024-T851 aluminum.

to larger displacements across the tip, and the resolvable displacement profile moves ahead of the tip. Note that these profiles represent the displacement between grooves located 0.25 mm (0.010 in.) above and below the crack.

At higher loads, the response of the specimen should be given by the

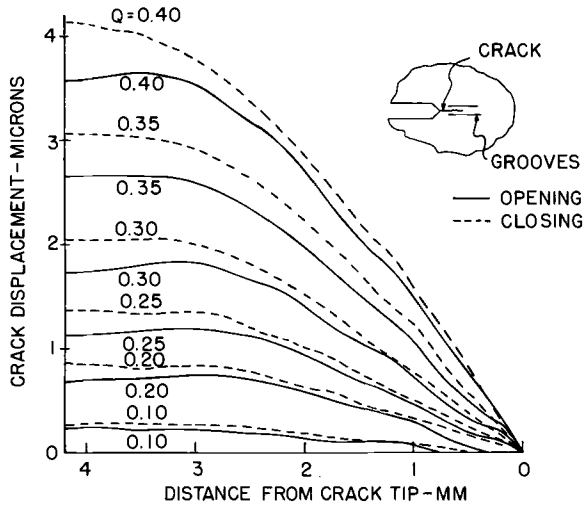


FIG. 6—Crack displacement profiles as the crack opens and closes.

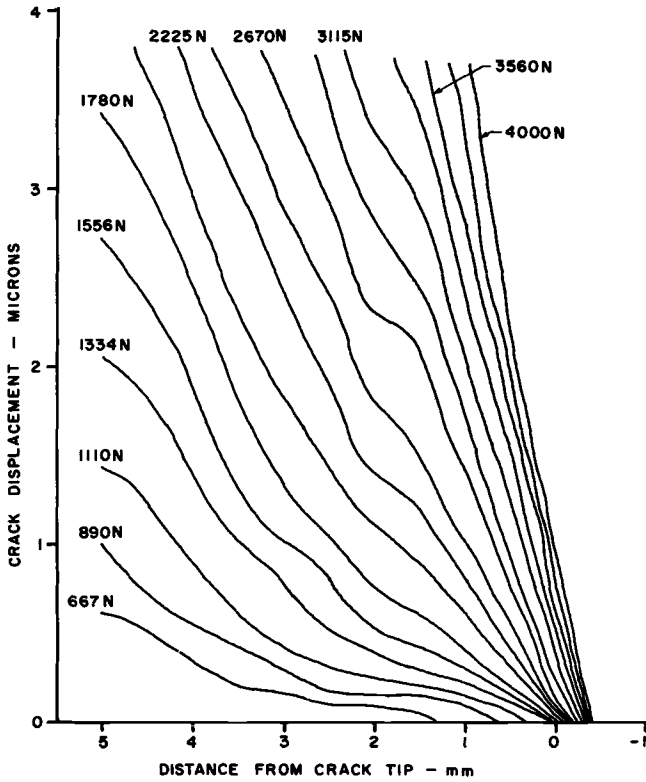


FIG. 7a—Displacement profiles used to determine the opening load.

elastic crack tip displacement equations (see, for example, Ref 15). Figure 7b is a plot of the displacement profile measured as the load is incremented from 2.67 kN (600 lb) to 3.78 kN (850 lb) and compared with the theoretical elastic displacement for a 1.12 kN (250 lb) increment. After the crack is fully open, the agreement is excellent near the tip.

One way to determine when a crack is open all the way to its tip is to observe the crack on the surface with a microscope. This is, of course, rather difficult and insensitive. The laser measurement used here in effect magnifies the crack surface displacement to permit better resolution. The crack tip location is known *a priori* because it is measured relative to the groove placement. The opening load is defined as the load required to measurably displace the grooves along the entire crack length (for example, the 1.33 kN (300 lb) profile in Fig. 7a). At a position 0.1 mm behind the tip, the theoretical elastic displacement on the crack face is only 8 percent less than that of a line 0.25 mm (0.010 in.) above it. Since this difference becomes smaller as one moves away from the tip, the

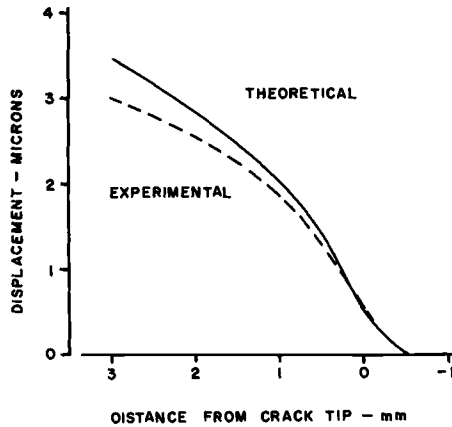


FIG. 7b—Elastic displacement for lines 0.51 mm (0.020 in.) apart straddling the crack. For load increment from 2.67 kN (600 lb) to 3.78 kN (850 lb).

groove displacements closely approximate the crack surface displacement profile. Although this procedure for determining the opening load differs from the load-displacement [5-8] or ultrasonic [9] methods, it provides a conservative measure of the opening load by determining the earliest opening of the crack on the specimen surface. This criterion, thus, represents an alternative to the other procedures used to measure the opening load.

An experiment was performed to compare the opening load obtained by this method with that established by the resistance strain gage procedure discussed in Ref 7. A 0.125 in. (3.18 mm) long by 0.086 in. (2.18 mm) foil strain gage was placed across the crack. The foil gage was placed with its centerline 3 mm (0.118 in.) from the crack tip on the opposite side of the specimen from the grooves. A 2.39 mm (0.094 in.) wide band of Teflon spray was applied over the crack area prior to gage application to prevent adhesion of the central portion of the gage.

Figure 7c is a plot of the load-displacement curves from that experiment. The interferometrically determined curves were obtained at positions 1, 3, and 5 mm from the tip by measuring the fringe displacements from photos taken at discrete loads. The foil gage displacement curve was recorded continuously on an X-Y recorder. Note that the foil gage, which averages the displacement over the region between 2 and 4 mm from the crack tip agrees reasonably well with the displacement measured interferometrically at 3 mm. The foil gage experiences some resistance change due to strain under the portion of the grid attached to the specimen, so its indicated displacement should be slightly less. In addition, note the near agreement in the slopes of the linear portions of the foil gage and the 3 mm interferometry curves with the theoretical elastic load-displacement curve

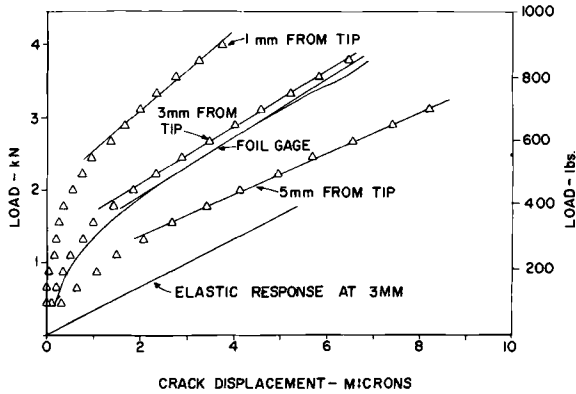


FIG. 7c—Load-displacement curves obtained interferometrically and with a resistance strain gage.

for two points separated by 51 mm (0.020 in.) at a location 3 mm behind the crack tip.

The opening load determined by locating the point of tangency between the upper part of the load-displacement curve and a straight line is 2.45 kN (550 lb)  $\pm$  10 percent for the 1 mm curve, 2.24 kN (500 lb)  $\pm$  10 percent for the curve 3 mm from the tip, 2.00 kN (450 lb)  $\pm$  10 percent for the foil gage curve, and 1.56 kN (350 lb)  $\pm$  10 percent for the curve 5 mm from the tip. Note that since the opening load determined from the load displacement curves depends on the distance from the crack tip, location of the strain gage would be important for this method. In viewing the interferometrically determined profiles in Fig. 7a, it is clear that the crack is open fully by the time the load has reached 1.33 kN (300 lb). Thus, the opening load established by this latter criterion is between 1.11 and 1.33 kN (250 and 300 lb), significantly smaller than the opening load determined by the other method.

### Overload Experiments

A set of overload/retardation experiments was conducted using the laser interferometry method to study the fatigue crack closure phenomenon. Fatigue cracks were grown under conditions of constant range in stress intensity factor ( $\pm$  5 percent) by shedding load in predetermined amounts as the crack extended. Crack lengths were measured to the nearest 0.002 in. by means of a scale calibrated in 0.005-in. increments placed next to the crack. The baseline  $K_{\max}$  was maintained at 5.5 MPa $\cdot$ m<sup>1/2</sup> (5 ksi $\cdot$ in.<sup>1/2</sup>), while  $R$  was kept at 0.1. Single peak loads with  $Q_{\text{peak}}$  values ( $Q_{\text{peak}} = K_{\text{peak}}/K_{\max}$ ) of 2.0, 2.25, 2.5, and 3.0 were applied to determine their effect on subsequent crack growth and on the opening

level of stress intensity ( $K_{open}$ ). In all cases, the initial crack growth was allowed to stabilize prior to application of the overloads.

In order to minimize stress relaxation effects on the opening load measurements, efforts were made to standardize the time base associated with the overload cycle. After the initial crack growth at 40 Hz, the test was stopped and the crack length measured. Next, the overload was applied in predetermined increments to photograph the series of fringe patterns. After completing the overload cycle, the crack length was measured again and the 40 Hz baseline cycling continued. By following this procedure it was possible to complete the overload cycle in approximately 3 to 5 min.

The influence of these tensile overloads on crack extension is shown in Fig. 8. Note that the  $Q_{peak} = 2.0$  overload had little effect on subsequent crack growth, while  $Q_{peak} = 2.25$  delayed extension for a significant number of cycles. When the baseline cycling was resumed after

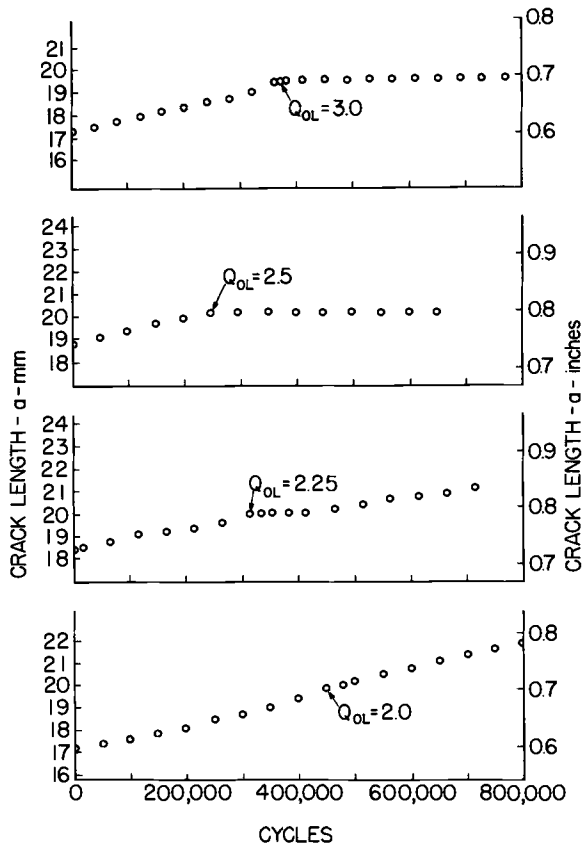


FIG. 8—Influence of overload on crack growth.

$Q_{\text{peak}} = 2.5$  and  $3.0$ , the cracks did not grow in 400 000 cycles, at which time the tests were terminated.

The influence of the peak loads on the force required to separate the crack faces and on corresponding crack growth is shown in Figs. 9a-d. Note here that cycles following the overload are plotted on a semilogarithmic scale to show both immediate and long-term effects of peak loading. The shaded bands in Figs. 9a-d represent the steady-state value of  $K_{\text{open}}$  prior to the overload, while the vertical bars show the observed  $K_{\text{open}}$  following the peak load. The uncertainty represented for  $K_{\text{open}}$  stems from the fact that fringe patterns were photographed at discrete load increments. This uncertainty could be, of course, reduced by recording more fringe patterns as the crack opens. The actual crack tip profiles at various points in the load spectrum are shown in Fig. 10 for the  $Q_{\text{peak}} = 2.25$  overload condition. Note that the profiles determined by the laser interferometry method provide a distinctive measure of the load required to separate completely the crack faces.

Examining Fig. 9a, one notices that a significant tensile load (20 to 25 percent  $K_{\text{max}}$ ) is required to completely open the crack faces for steady-state cycling to  $K_{\text{max}} = 5.5 \text{ MPa} \cdot \text{m}^{1/2}$  ( $5 \text{ ksi} \cdot \text{in.}^{1/2}$ ). Since the crack is closed partially at the minimum load ( $K_{\text{min}} = 0.1 K_{\text{max}}$ ), the effective range in stress intensity is reduced from 90 percent to approximately 75 percent of  $K_{\text{max}}$ . When the  $Q_{\text{peak}} = 2.0$  overload was applied,  $K_{\text{open}}$  was raised to 30 to 35 percent of  $K_{\text{max}}$  but decayed to the original steady-state value. Since the reduction in effective  $\Delta K$  caused by raising  $K_{\text{open}}$  lasted less than 100 cycles, there was no observable perturbation in subsequent crack growth.

For the higher overload, however, crack growth was retarded significantly. As shown in Fig. 9b, The  $Q_{\text{peak}} = 2.25$  overload raised  $K_{\text{open}}$  to 35 to 40 percent of  $K_{\text{max}}$ , and although  $K_{\text{open}}$  again dropped after ten cycles, the steady-state value was not reached for 100 000 cycles. At this time measurable crack extension occurred, gradually returning to the baseline rate. The  $Q_{\text{peak}} = 2.5$  and  $3.0$  overloads again caused an increase in  $K_{\text{open}}$  followed by a slight drop after 10 cycles. In both cases, however, the opening load failed to return to the original value and subsequent crack growth was arrested for at least 400 000 cycles. In both instances, the effective  $\Delta K$  was reduced by the change in  $K_{\text{open}}$ . Since  $K_{\text{max}} = 5.5 \text{ MPa} \cdot \text{m}^{1/2}$  ( $5.0 \text{ ksi} \cdot \text{in.}^{1/2}$ ) is close to the threshold range in stress intensity factor for fatigue crack growth (see Fig. 5), this reduction in effective  $\Delta K$  has particular significance.

The results of these tests indicate that the peak loads caused an increase in  $K_{\text{open}}$  which was related to fatigue crack retardation as suggested by Elber. In all cases,  $K_{\text{open}}$  was raised on the first cycle following the overload but dropped after ten cycles had elapsed. As the overload ratio was increased,  $K_{\text{open}}$  was also raised.

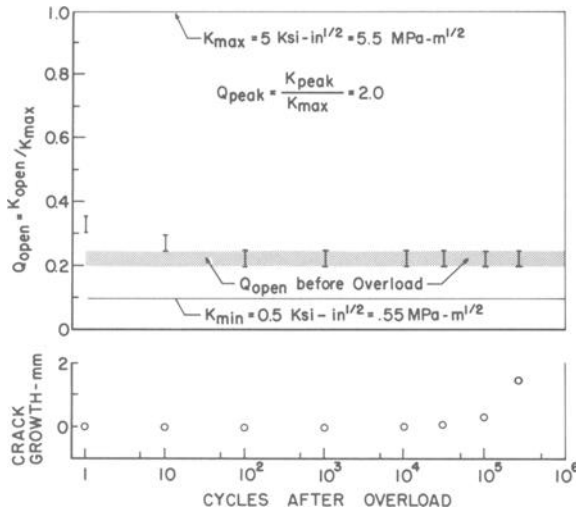


FIG. 9a— $Q_{open}$  and crack growth versus cycles after overload for  $Q_{peak} = 2.0$ .

**Concluding Remarks**

A laser interferometry technique has been described which is capable of resolving crack surface displacements to about  $0.1 \mu\text{m}$ . The technique possesses a significant advantage over other commonly employed crack displacement methods in that measurements are not restricted to the motion of two fixed points but enable one to obtain the entire free surface

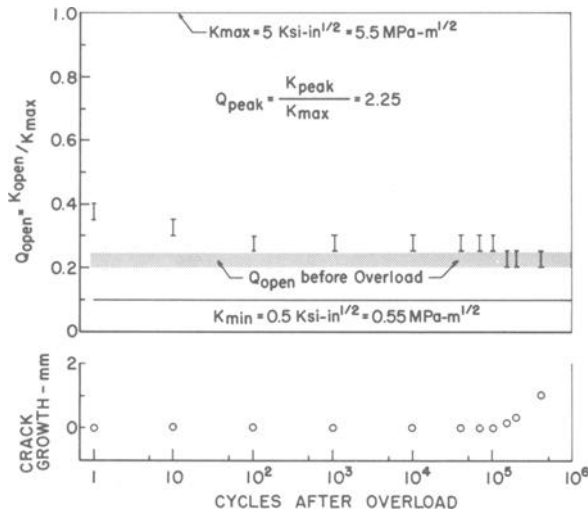


FIG. 9b— $Q_{open}$  and crack growth versus cycles after overload for  $Q_{peak} = 2.25$ .

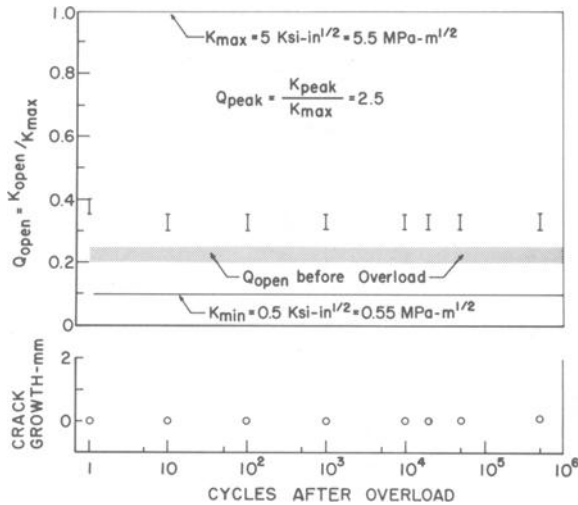


FIG. 9c— $Q_{open}$  and crack growth versus cycles after overload for  $Q_{peak} = 2.5$ .

displacement profile. Since the method is not hampered by the rigid body motions which limit holographic techniques, the procedure is readily adaptable for laboratory measurements on standard testing machines.

The laser interferometry procedure can be used to determine the opening loads required for studies of the closure mechanism for fatigue crack retardation. In this paper, the opening load was defined as the

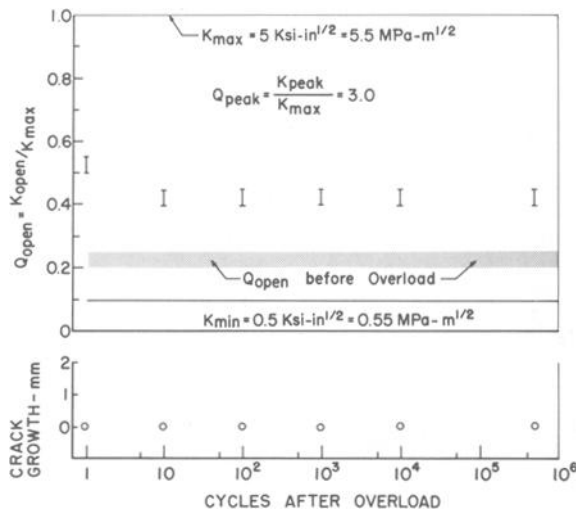


FIG. 9d— $Q_{open}$  and crack growth versus cycles after overload for  $Q_{peak} = 3.0$ .

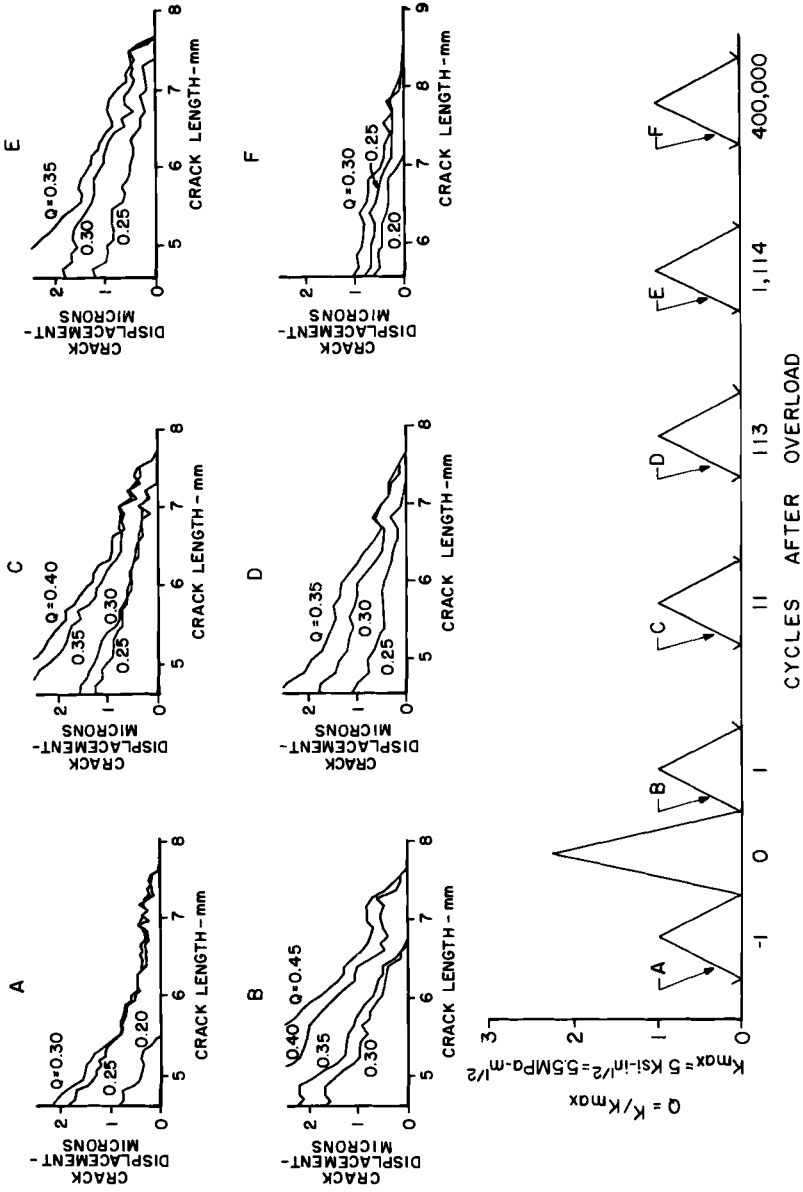


FIG. 10—Displacement profiles at various cycles for  $Q_{peak} = 2.25$ .

remote load required to produce measurable displacement along the entire crack length. Opening loads determined in this manner for a fatigue crack grown under conditions of constant range in stress intensity factor were found to be significantly less than those obtained by the strain gage method. This discrepancy is most likely due to the fact that the laser technique determines when the crack faces measurably separate on the specimen surface, whereas the strain gage method determines when the specimen behaves as if a fully open crack were present.

Single peak tensile loads were found to perturb subsequent crack growth under constant  $\Delta K$  baseline conditions. The opening load was observed to increase on the first cycle after the overload and then to decrease under additional cycling. This immediate increase in  $K_{open}$  differs from the gradual rise observed by Elber [6], who used clip gages to obtain load-displacement curves.

Changes in closure loads were correlated successfully with peak overloads and subsequent fatigue crack retardation as suggested by the closure model. The authors feel a precautionary note is needed, however, since all closure loads were based on observations of the crack displacement profile at the free surface under conditions of plane stress. This same limitation is, of course, also inherent in the clip gage and strain gage methods. Recent work in transparent polymers using optical interference procedures [10] and in aluminum with ultrasonic techniques [16] indicate that the closure effect may not be as significant in the plane strain interior of the specimen.

Finally, it should be noted that the laser interferometry method for measuring crack surfaces is not restricted to closure studies. Indeed, the technique may be used whenever accurate measurements of the free surface crack profile are desired.

### *Acknowledgments*

The authors appreciate the assistance of B. Strobe with the tests and J. Wagner with the data reduction. W. N. Sharpe, Jr., very gratefully acknowledges the support of the National Research Council and the Air Force Materials Laboratory while on sabbatical at the Air Force Materials Laboratory from Michigan State University.

### **References**

- [1] Sommer, E., *Engineering Fracture Mechanics*, Vol. 1, No. 4, 1970, pp. 705-718.
- [2] Crosley, P. B., Mostovoy, S., and Ripling, E. J., *Engineering Fracture Mechanics*, Vol. 3, No. 4, 1971, pp. 421-433.
- [3] Boyd, G. M., *Engineering Fracture Mechanics*, Vol. 4, No. 3, 1972, pp. 459-482.
- [4] Yee, B. G. W., "Currently Used NDT Characterization Techniques," Proceedings of the Interdisciplinary Workshop on Nondestructive Testing-Materials Characterization, Technical Report AFML-TR-73-69, Wright-Patterson Air Force Base, Ohio, April 1973.
- [5] Elber, W., *Engineering Fracture Mechanics*, Vol. 2, No. 1, 1970, pp. 37-45.
- [6] Elber, W. in *Damage Tolerance in Aircraft Structures*, ASTM STP 486, American Society for Testing and Materials, 1971, pp. 230-242.

- [7] Roberts, R. and Schmidt, R. A., *International Journal of Fracture Mechanics*, Vol. 8, 1972, pp. 469-471.
- [8] Adams, N. J., *Engineering Fracture Mechanics*, Vol. 4, No. 3, 1973, pp. 543-554.
- [9] Buck, O., Ho, C. L., and Marcus, H. L., *Engineering Fracture Mechanics*, Vol. 5, No. 1, 1973, pp. 23-34.
- [10] Pitoniak, F. J., Grandt, A. F., Montulli, L. T., and Packman, P. F., *Engineering Fracture Mechanics*, Vol. 6, No. 4, 1974, pp. 663-670.
- [11] Sharpe, W. N., Jr., and Grandt, A. F., Jr., "A Laser Interferometric Technique for Crack Surface Displacement Measurements," Proceedings of the 20th International Instrumentation Symposium of the Instrument Society of America, Albuquerque, N. Mex., May 1974.
- [12] Sharpe, W. N., Jr., *Experimental Mechanics*, Vol. 14, No. 9, 1974, pp. 373-378.
- [13] Sharpe, W. N., Jr., *International Journal of Nondestructive Testing*, Vol. 3, 1971, pp. 56-76.
- [14] Katcher, M. and Kaplan, M. in *Fracture Toughness and Slow-Stable Cracking*, ASTM STP 559, American Society for Testing and Materials, 1974, pp. 264-282.
- [15] Paris, P. C. and Sih, G. C., *Fracture Toughness Testing and Its Applications*, ASTM STP 381, American Society for Testing and Materials, 1965, pp. 30-81.
- [16] Sharpe, W. N., Jr., Corbly, D. M., and Grandt, A. F., Jr., "The Effects of Rest-Time on Fatigue Crack Retardation and Observations of Crack Closure," presented at ASTM Symposium on Fatigue Crack Growth under Spectrum Loads, Montreal, Canada, June 1975.

*M. K. Himmelein<sup>1</sup> and B. M. Hillberry<sup>2</sup>*

## Effect of Stress Ratio and Overload Ratio on Fatigue Crack Delay and Arrest Behavior Due to Single Peak Overloads

---

**REFERENCE:** Himmelein, M. K. and Hillberry, B. M., "Effect of Stress Ratio and Overload Ratio on Fatigue Crack Delay and Arrest Behavior Due to Single Peak Overloads," *Mechanics of Crack Growth, ASTM STP 590*, American Society for Testing and Materials, 1976, pp. 321–330.

**ABSTRACT:** In this investigation stress interaction effects on fatigue crack propagation following single peak overloads in 2024-T3 aluminum alloy were studied. The two parameters investigated were the overload stress ratio,  $R_{OL} = K_{min}/K_{OL}$ , and the overload ratio,  $K_{OL}/K_{max}$ . Tests were run with quasi-constant stress intensity fatigue loading following the overload. The effect of overload on the crack growth rate through the overload plastic zone was observed. Additional tests were run to determine only whether or not crack arrest would occur. The delay effect due to single peak overloads was found to increase with overload stress ratio,  $R_{OL}$ , and overload ratio,  $K_{OL}/K_{max}$ . The higher values of both  $R_{OL}$  and  $K_{OL}/K_{max}$  produced nonpropagating fatigue cracks, and the delay/arrest boundary was defined.

**KEY WORDS:** crack propagation, fatigue tests, aluminum alloys, stresses, residual stress, stress ratio, loads (forces)

### Nomenclature

|           |                                |
|-----------|--------------------------------|
| $a$       | Crack length                   |
| $K_{max}$ | Maximum stress intensity       |
| $K_{min}$ | Minimum stress intensity       |
| $K_{OL}$  | Overload stress intensity      |
| $K_{OP}$  | Crack opening stress intensity |

<sup>1</sup> Mechanical design engineer, Aluminum Company of America, Pittsburgh, Pa.

<sup>2</sup> Professor, School of Mechanical Engineering, Purdue University, West Lafayette, Ind. 47907.

|            |   |
|------------|---|
| $\Delta K$ | Stress intensity range  |
| $n$        | Empirically determined constant   |
| $N$        | Number of stress cycles   |
| $N_D$      | Number of delay cycles  |
| $R_f$      | Ratio of minimum stress intensity to maximum stress intensity,<br>$K_{\min}/K_{\max}$ |
| $R_{OL}$   | Ratio of minimum stress intensity to overload stress intensity,<br>$K_{\min}/K_{OL}$  |
| $Z_{OL}$   | Measured delay affected zone size   |

One of the major problem areas associated with fatigue design, especially when using fracture mechanics, is the ability to predict fatigue crack growth behavior. It has been recognized for some time that a change in the load level significantly influences the subsequent crack growth rate. However, the common crack growth or life prediction methods do not account for these load interaction effects. As a result the crack growth behavior under spectrum loading conditions remains difficult to predict.

Schijve [1]<sup>3</sup> and more recently Hudson and Raju [2], Jonas and Wei [3], Von Euw, Hertzberg, and Roberts [4], Trebules, Roberts, and Hertzberg [5], Probst and Hillberry [6], Corbly and Packman [7], Wei, Shih, and Fitzgerald [8], and Porter [9], examined the crack growth delay behavior resulting from single or multiple peak tensile overloads. The tensile overload frequently creates an initial accelerated crack growth followed by a slowing down of the growth to some value below the original growth rate and then an acceleration back to the original rate. The reduced growth rate is of primary interest since the overall effect of the overload is to cause a net delay in the crack growth. The region over which the crack growth is affected is believed to be related to the plastic zone created by the overload, although there is some question on this and also the correlation has been less than gratifying. The number of delay cycles, defined as the number of cycles following the overload until the crack growth rate returns to the steady-state value, is influenced significantly by many factors including the loading conditions, the environmental conditions, and the material parameters. The load sequence conditions including the magnitude of the overload, the stress ratio and underload levels can significantly influence the delay behavior. However, the exact dependence is not fully understood. Probst and Hillberry [6] observed complete crack arrest when the overload stress intensity,  $K_{OL}$ , was greater than or equal to  $2.3 \times K_{\max}$  ( $K_{\max}$  is the maximum level of the subsequent fatigue cycling) for a fatigue stress ratio,  $R_f$ , of 0.3.

Hsu and Lassiter [10] studied the effect of compressive overloads and found that a tensile overload followed by a compressive underload resulted in less delay than when there was no compressive underload.

<sup>3</sup> The italic numbers in brackets refer to the list of references appended to this paper.

Gallagher [11] and others showed that when high overloads are present in spectrum type loadings a significant delay can result. Prediction methods which account for the delay effects are necessary.

There are several hypotheses for explaining the delay phenomena. It has been suggested that under high loading the crack tip is blunt while under low loading it is much sharper [12]. Immediately following the overload the blunted crack causes a lower stress concentration effect on the crack tip which accounts for the delay. Another theory is that the overload creates a residual stress field at the crack tip due to the plastic strain that occurs within the plastic zone. The resulting compressive residual stress then decreases the local tensile stresses at the crack tip thereby delaying the crack growth. Gallagher [11] showed that the Willenborg [14] and Wheeler [15] models could be expressed in terms of a residual stress concept.

Elber's crack closure model [13] has also been used to describe the delay effect [5]. Elber showed that the crack remained closed until a certain stress intensity level was reached and then it opened. Since crack growth can only occur when the crack is open, the overload raises the applied stress intensity level necessary to open the crack. This results in a lower net applied stress intensity range for propagating the crack.

There have been several models proposed to account for the delay effects due to tensile overloads. These models, in general, are based on some reduced effective stress level resulting from the overload. The Wheeler model [14] modifies the constant amplitude growth rate equation by multiplying by a parameter which is a function of the overload and fatigue plastic zone sizes and an empirically determined exponent. The Willenborg, Engle, and Wood model [15] utilizes a reduced effective stress in the constant amplitude growth rate equation where this effective stress is related to the overload and fatigue plastic zone sizes. Gallagher and Stalnaker [11] modified the Willenborg model, while Gray [16] gives a modification of the Wheeler model.

This study [18] was undertaken to determine the effect of the stress ratio on the delay behavior due to single overloads using 2024-T3 aluminum alloy. Also, the growth rate through the plastic zone was determined by carefully measuring the crack growth following the overload and numerically differentiating these data. From this, the minimum growth rate following the overload was determined.

## **Experimental Procedure**

### *Test Program*

A test program was designed to ascertain the effects of overload stress ratio ( $R_{OL} = K_{min}/K_{OL}$ ) and overload ratio ( $K_{OL}/K_{max}$ ) on crack propagation rates following single peak tensile overloads. Five values of overload ratio

were selected ranging from 1.3 to 2.5; however, based on Probst's [6] results, crack arrest was expected for some of the tests. Six values of the stress ratios ( $R_{OL} = K_{min}/K_{OL}$ ) were selected between 0.01 (nearly zero) and 0.6. Since a range of crack propagation rates was desired, five values of crack propagation rate between  $10^{-7}$  and  $10^{-5}$  in./cycle were chosen and assigned randomly throughout the test matrix. Using these growth rates, particular values of  $\Delta K$  were selected from the constant amplitude growth rate test results. The value of  $\Delta K$ , corresponding to the expected growth rate, was then used as the constant amplitude fatigue loading for the test.

Following the completion of the tests in the original test matrix, the tests in which complete crack arrest occurred indicated that additional tests were required to define the delay arrest boundary. These tests were run only to determine whether or not arrest would occur, and no  $a$  versus  $n$  data were recorded. Arrest in this investigation is defined as no observable crack growth (less than 0.01 mm) in  $1.5 \times 10^6$  cycles.

#### *Test Specimen*

The material used throughout the investigation was 2024-T3 aluminum alloy. Center crack specimens (22 by 6 by 0.100 in. thick) identical to those used by Probst and Hillberry [6], were used for the fatigue testing. Fatigue loading was applied parallel to the direction of rolling of the material. Since the material was obtained with a mill finish, the surface in the area near the stress raiser was polished to a near mirror finish in order to facilitate optical observation of the fatigue crack. Tada's modification of Feddersen's formula was used to calculate the stress intensity factor for this geometry [17].

#### *Test Equipment*

A closed-loop electrohydraulic, fatigue test system was used to load the specimens. The crack growth was measured optically with a X100 microscope mounted on a horizontal measurement traverse. The resolution of the traverse was 0.01 mm. A strobe light was used to illuminate the specimen which allowed viewing the crack in the open-most position without stopping the system. A digital printer, pushbutton actuated, provided a means for rapid data acquisition. Data were taken by incrementing the microscope on crack length, usually 0.01 to 0.05 mm and recording the corresponding number of cycles,  $N$ , when the crack reached that length.

#### **Test Procedure**

All tests were run in an environment of air desiccated with silica gel and at temperatures between 18 and 21°C (65 and 70°F). Loading frequencies were between 15 and 20 Hz. The stress intensity was controlled within 3 percent by load shedding, which provided quasi-constant  $K$  test condi-

tions. Pre-overload data provided a growth rate comparison with separate constant amplitude data and published data.

Overloads were applied at a frequency of 0.02 Hz and recorded on an oscillograph. In all cases the preoverload loading was the same as the postoverload loading. Following an overload, the specimen was cycled continuously, until steady-state growth rate was again reached.

For further details on the experimental methods, see Ref 18.

**Results**

The constant amplitude growth rate test results along with the preoverload growth rate data were used to compare with published data. The results were found to agree with the following equation [20]

$$da/dN = 6.8 \times 10^{-10} [(1 + 0.698 R_f) \Delta K]^{3.58}$$

Tension tests of three specimens gave the following average values.

- yield strength = 56.9 ksi
- ultimate strength = 69.0 ksi
- elongation = 14.2 percent

As mentioned in the experimental procedure section, all crack propagation data were taken in the form of crack length, *a*, versus the corresponding number of cycles, *N*. Based on a second order least squares fit over overlapping intervals of seven data points, the function *a* versus *N* and the derivative *da/dN* versus *a* were found. Figures 1 and 2 show typical results. Figure 1 also shows the method of defining the extent of the

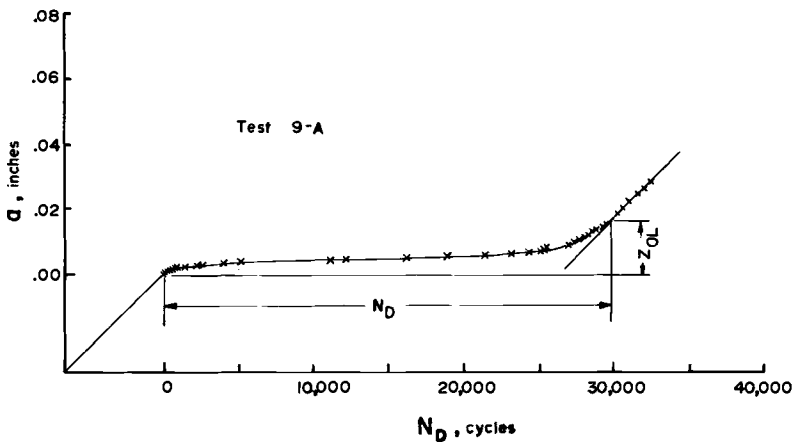


FIG. 1—Typical *a* versus *N* data (Test 9-A).

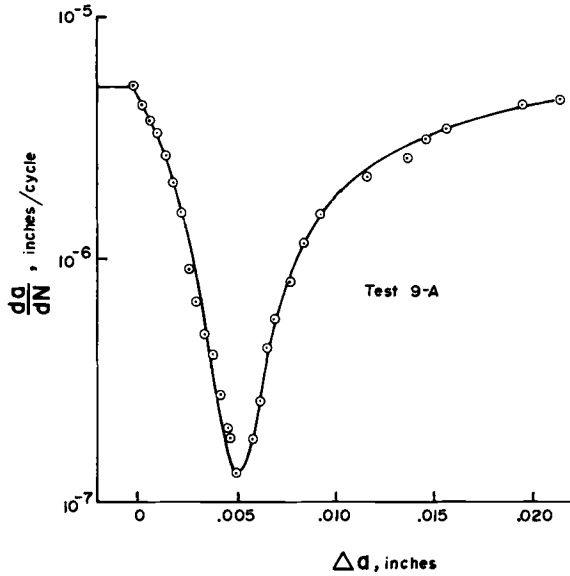


FIG. 2—Typical  $da/dN$  versus  $a$  results (Test 9-A).

overload affected plastic zone,  $Z_{OL}$ , and the number of delay cycles,  $N_D$ . Table 1 gives the results of the tests.

Since different crack propagation rates resulted from various tests and the overload affected zone size differed with each overload, normalized variables were chosen to compare the results. An average crack propagation rate,  $da/dN = Z_{OL}/N_D$ , over the delay interval, was calculated and then normalized on the preoverload propagation rate to compare the relative reductions in the crack propagation rate. Figures 3 and 4 show these results plotted against the test parameters,  $R_{OL}$  and  $K_{OL}/K_{max}$ , respectively. Large ranges of growth rates were observed, and definite trends in the growth rate with respect to the test variables are evident.

Probst found that for  $R_f = 0.3$ , large overloads ( $K_{OL}/K_{max} \geq 2.3$ ) would produce complete crack arrest. Continuing this further, this investigation showed that an arrest/delay boundary exists as a function of the overload stress ratio,  $R_{OL}$ . This boundary is shown in Fig. 5. Notice that as  $R_{OL}$  increases, the overload ratio,  $K_{OL}/K_{max}$  necessary to produce complete crack arrest decreases.

Applying the crack closure concept [13] to the overload cycle gives

$$U = \frac{K_{OL} - K_{OP}}{K_{OL} - K_{min}} = 0.5 + 0.4 R_{OL}$$

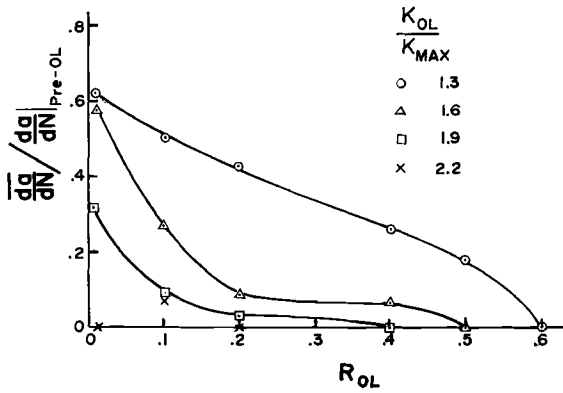


FIG. 3—Normalized average crack propagation rate versus  $R_{OL}$ .

Assuming crack arrest occurs when  $K_{OP} \geq K_{max}$  this equation can be solved for the arrest boundary. This is compared with the test results in Fig. 5.

Table 1 gives the complete test results for each of the tests of the original test matrix. Included in the table are the values for  $N_D$ , overload

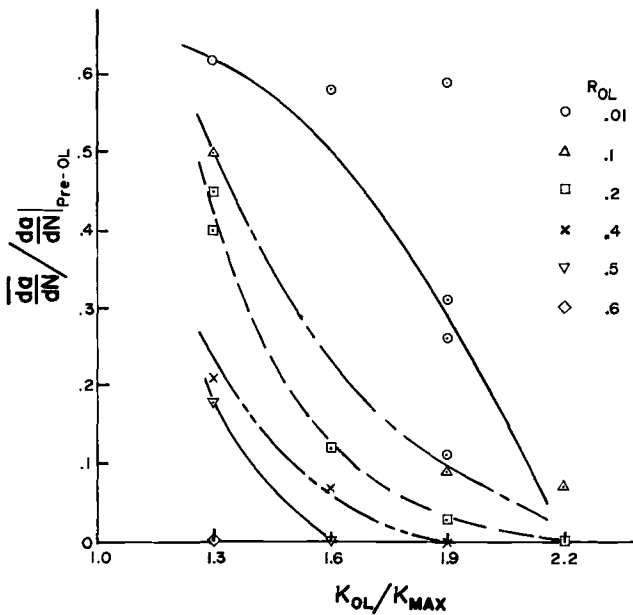


FIG. 4—Normalized average crack propagation rate versus  $K_{OL}/K_{MAX}$ .

TABLE 1—Overload test results.

| Test Number     | $K_{ou}/K_{max}$ | $R_{ou}$ | $R_f$ | $K_{max}$ ,<br>ksi $\sqrt{in.}$ | $K_{min}$ ,<br>ksi $\sqrt{in.}$ | $K_{ol}$ ,<br>ksi $\sqrt{in.}$ | $Z_{ol}$ , in. | $N_{Dp}$ ,<br>cycles | $\frac{da}{dN}$ pre ol.,<br>in./cycle | $Z_{ou}/N_{Dp}$ ,<br>in./cycle | $\frac{da}{dN}$ min,<br>in./cycle |
|-----------------|------------------|----------|-------|---------------------------------|---------------------------------|--------------------------------|----------------|----------------------|---------------------------------------|--------------------------------|-----------------------------------|
| 1-A             | 1.3              | 0.01     | 0.013 | 9.12                            | 0.12                            | 11.9                           | 0.0138         | $4.8 \times 10^3$    | $3.35 \times 10^{-6}$                 | $2.88 \times 10^{-6}$          | $1.23 \times 10^{-6}$             |
| 1-B             | 1.3              | 0.01     | 0.013 | 9.12                            | 0.12                            | 11.9                           | 0.0051         | 3.4                  | 3.25                                  | 1.50                           | 0.963                             |
| 1-C             | 1.3              | 0.01     | 0.013 | 9.12                            | 0.12                            | 11.9                           | 0.0067         | 4.7                  | 3.25                                  | 1.43                           | 1.29                              |
| 2               | 1.3              | 0.1      | 0.13  | 10.35                           | 1.35                            | 13.4                           | 0.0063         | 4.6                  | 3.15                                  | 1.37                           | 0.796                             |
| 3-A             | 1.3              | 0.2      | 0.26  | 10.13                           | 2.63                            | 13.2                           | 0.0039         | 3.0                  | 1.88                                  | 1.30                           | 0.886                             |
| 3-B             | 1.3              | 0.2      | 0.26  | 10.13                           | 2.63                            | 13.2                           | 0.0055         | 4.2                  | 2.62                                  | 1.31                           | 1.17                              |
| 4               | 1.3              | 0.4      | 0.52  | 18.75                           | 9.75                            | 24.4                           | 0.0118         | 4.4                  | 7.18                                  | 2.68                           | 1.07                              |
| 5               | 1.3              | 0.5      | 0.65  | 40.00                           | 26.0                            | 52.0                           | 0.0787         | 9.7                  | 15.2                                  | 8.11                           | 1.07                              |
| 6 <sup>a</sup>  | 1.3              | 0.6      | 0.78  | 24.09                           | 18.79                           | 31.3                           | ...            | $\infty$             | 0.78                                  | 0                              | ...                               |
| 7               | 1.6              | 0.01     | 0.016 | 4.57                            | 0.07                            | 7.3                            | 0.0024         | 9.0                  | 1.08                                  | 0.267                          | 0.0941                            |
| 8               | 1.6              | 0.1      | 0.16  | 8.93                            | 1.43                            | 14.3                           | 0.0083         | 16.0                 | 2.77                                  | 0.518                          | 0.229                             |
| 9-A             | 1.6              | 0.2      | 0.32  | 13.23                           | 4.23                            | 21.2                           | 0.0157         | 29.5                 | 5.03                                  | 0.532                          | 0.128                             |
| 9-B             | 1.6              | 0.2      | 0.32  | 13.23                           | 4.23                            | 21.2                           | 0.0157         | 36.0                 | 1.97                                  | 0.436                          | 0.101                             |
| 10              | 1.6              | 0.4      | 0.64  | 10.35                           | 5.85                            | 20.0                           | 0.0067         | 206.0                | 3.75                                  | 0.0325                         | 0.0096                            |
| 11 <sup>a</sup> | 1.6              | 0.5      | 0.80  | 19.27                           | 13.97                           | 42.4                           | ...            | $\infty$             | 1.80                                  | 0                              | ...                               |
| 13-A            | 1.9              | 0.01     | 0.019 | 7.65                            | 0.15                            | 14.5                           | 0.0035         | 10.0                 | 1.18                                  | 0.350                          | 0.460                             |
| 13-B            | 1.9              | 0.01     | 0.019 | 7.65                            | 0.15                            | 14.5                           | 0.0098         | 21.0                 | 1.48                                  | 0.467                          | 0.215                             |
| 13-C            | 1.9              | 0.01     | 0.019 | 7.65                            | 0.15                            | 14.5                           | 0.0102         | 49.0                 | 1.28                                  | 0.208                          | 0.091                             |
| 14              | 1.9              | 0.1      | 0.19  | 17.28                           | 3.28                            | 32.8                           | 0.0551         | 125.0                | 29.9                                  | 0.441                          | 0.107                             |
| 15              | 1.9              | 0.2      | 0.38  | 12.10                           | 4.60                            | 23.0                           | 0.0102         | 86.0                 | 3.70                                  | 0.119                          | 0.0433                            |
| 16 <sup>a</sup> | 1.9              | 0.4      | 0.76  | 22.08                           | 16.78                           | 42.0                           | ...            | $\infty$             | 1.80                                  | 0                              | ...                               |
| 19 <sup>a</sup> | 2.2              | 0.01     | 0.022 | 5.42                            | 0.12                            | 11.9                           | ...            | $\infty$             | 0.20                                  | 0                              | ...                               |
| 20              | 2.2              | 0.1      | 0.22  | 5.77                            | 1.27                            | 12.7                           | 0.0043         | 166.5                | 1.88                                  | 0.0258                         | 0.0167                            |
| 21 <sup>a</sup> | 2.2              | 0.2      | 0.44  | 25.00                           | 11.00                           | 55.0                           | ...            | $\infty$             | 1.90                                  | 0                              | ...                               |

<sup>a</sup> Crack arrested.

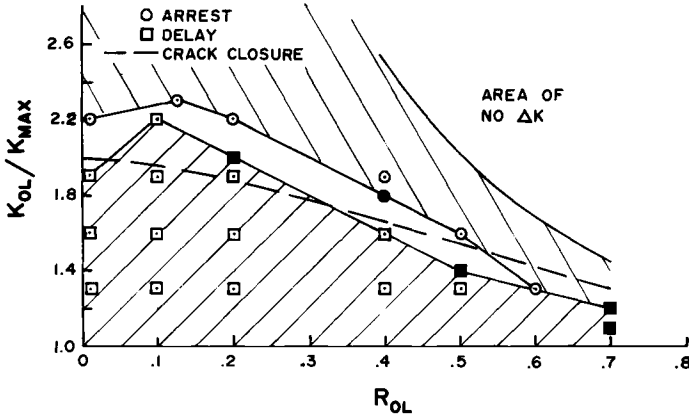


FIG. 5—Arrest/delay boundary (shaded symbols indicate supplemental tests).

affected zone,  $Z_{OL}$ , as well as the preoverload growth rate,  $\left. \frac{da}{dN} \right|_{pre-OL}$ , average growth rate,  $Z_{OL}/N_D$ , and the minimum growth rate,  $\left. \frac{da}{dN} \right|_{min}$ .

**Conclusion**

These test results show that as the overload stress ratio,  $R_{OL} = K_{min}/K_{OL}$ , increased, the value of  $K_{OL}/K_{max}$  along the delay/arrest boundary decreases. Furthermore, it was shown that the crack closure model as applied to the overload cycle agrees reasonably well with the experimental arrest/delay boundary.

*Acknowledgments*

Partial support for this study was provided by the Air Force Flight Dynamics Laboratory, Wright-Patterson Air Force Base under contract No. F33615-74-C-3056. The specimens were provided by the Aluminum Company of America.

This study was completed in partial fulfillment for the degree of Master of Science in Mechanical Engineering, Purdue University.

**References**

- [1] Schijve, J., "Fatigue Crack Propagation in Light Alloy Sheet Material and Structures," Report NLR MP 195, National Aerospace Laboratory, 1962.
- [2] Hudson, G. M. and Raju, K. N., "Investigation of Fatigue Crack Growth Under Single Variable-Amplitude Loading," NASA TN D-5702, National Aeronautics and Space Administration, Washington, D.C., March 1970.
- [3] Jonas, O. and Wei, R. P., *Report of Current Research, International Journal of Fracture Mechanics*, Vol. 7, No. 1, March 1971, pp. 116-118.
- [4] von Euw, E. F. J., Hertzberg, R. W., and Roberts, R. in *Stress Analysis and Growth of Cracks, Proceedings of the 1971 National Symposium on Fracture Mechanics, Part I, ASTM STP 513*, American Society for Testing and Materials, 1973, pp. 230-259.

- [5] Trebules, V. W., Jr., Roberts, R., and Hertzberg, R. W. in *Progress in Flaw Growth and Fracture Toughness Testing*, ASTM STP 536, American Society for Testing and Materials, 1973, pp. 115-146.
- [6] Probst, E. P. and Hillberry, B. M., *Journal, American Institute of Aeronautics and Astronautics*, Vol. 12, No. 3, March 1974, p. 330.
- [7] Corbly, D. M. and Packman, P. F., *Engineering Fracture Mechanics*, Vol. 5, 1973, pp. 479-497.
- [8] Wei, R. P., Shih, T. T., and Fitzgerald, J. H., "Load Interaction Effects on Fatigue Crack Growth in Ti-6Al-4V Alloy," NASA CR-2239, National Aeronautics and Space Administration, Washington, D.C., April 1973.
- [9] Porter, T. R., *Engineering Fracture Mechanics*, Vol. 4, 1972, pp. 717-736.
- [10] Hsu, T. M. and Lassiter, L. W., "Effects of Compressive Overloads on Fatigue Crack Growth," presented at AIAA/ASME/SAE 15th Structures, Structural Dynamics and Materials Conference, Las Vegas, Nev., April 1974.
- [11] Gallagher, J. P. and Stalnaker, H. D., "Methods for Analyzing Fatigue Crack Growth Rate Behavior Associated with Flight-by-Flight Loading," AIAA Paper No. 74-367, presented at AIAA/ASME/ASE 15th Structures, Structural Dynamics and Materials Conference, Las Vegas, Nev., April 1974.
- [12] McMillan, J. C. and Pelloux, R. M. N. in *Fatigue Crack Propagation*, ASTM STP 415, American Society for Testing and Materials, 1967, pp. 505-535.
- [13] Elber, W. in *Damage Tolerance in Aircraft Structures*, ASTM STP 486, American Society for Testing and Materials, 1971, pp. 230-242.
- [14] Wheeler, O. E., *Journal of Basic Engineering, Transactions*, American Society of Mechanical Engineers, Series D, Vol. 94, No. 1, March 1972, pp. 181-186.
- [15] Willenborg, J. D., Jr., Engle, R. M., and Wood, H. A., "A Crack Growth Retardation Model Using an Effective Stress Concept," AFFDL-TM-71-1-FBR, Air Force Flight Dynamics Laboratory, Jan. 1971.
- [16] Gray, T. D., "Fatigue Crack Retardation Following a Single Overload," AFFDL-TM-73-137-FBR, Air Force Flight Dynamics Laboratory, Oct. 1973.
- [17] Tada, H., Paris, P. C., and Irwin, G. R., *Stress Analysis of Cracks Handbook*, Del Research Corporation, Hellertown, Pa., 1973.
- [18] Himmelein, M. K., "The Effect of Stress Ratio and Overload Ratio on Fatigue Crack Delay and Arrest Behavior Due to Single Peak Overloads," M.S. thesis, Purdue University, West Lafayette, Ind., May 1974.
- [19] Gallagher, J. P., "A Generalized Development of Yield Zone Models," AFFDL-TM-FBR-74-28, Air Force Dynamics Laboratory, Jan. 1974.
- [20] Gallagher, J. P., personal communication, Jan. 1974.

T. D. Gray<sup>1</sup> and J. P. Gallagher<sup>1</sup>

## Predicting Fatigue Crack Retardation Following a Single Overload Using a Modified Wheeler Model

---

**REFERENCE:** Gray, T. D. and Gallagher, J. P., "Predicting Fatigue Crack Retardation Following a Single Overload Using a Modified Wheeler Model," *Mechanics of Crack Growth, ASTM STP 590*, American Society for Testing and Materials, 1976, pp. 331-344.

**ABSTRACT:** A modification to the Wheeler fatigue crack retardation model is proposed. The modification allows the model to be used without reliance on data fitting and, therefore, without the subsequent limiting to a specific material or to a specific set of loading parameters. The new model is used to predict existing data for the number of delay cycles following a single overload in 2024-T3 aluminum, 4340 steel, and Ti-6Al-4V titanium alloy. All predictions were within essentially a factor of two of the experimental data.

**KEY WORDS:** crack propagation, retardation models, cyclic loads, stresses, residual stress, mechanical properties, fatigue (materials)

### Nomenclature

|                                     |   |
|-------------------------------------|---|
| $a$                                 | Crack length                                  |
| $a_{OL}$                            | Crack length immediately after overload       |
| $\Delta a$                          | Current crack growth increment since overload |
| $C, n, q, t$                        | Crack growth rate constants                   |
| $C_p$                               | Wheeler crack growth reduction factor         |
| $\left. \frac{da}{dN} \right _{sp}$ | Crack growth rate under spectrum loading      |
| $\left. \frac{da}{dN} \right _{ss}$ | Crack growth rate under steady state loading  |
| $K$                                 | Stress Intensity                              |
| $K_{max}$                           | Maximum stress intensity                      |
| $K_{min}$                           | Minimum stress intensity                      |

<sup>1</sup> Structures Division, Air Force Flight Dynamics Laboratory, Wright-Patterson Air Force Base, Dayton, Ohio, 45433.

|                         |  |
|-------------------------|--|
| $K_{\max}^{\text{OL}}$  | Overload stress intensity                              |
| $K_{\max}^*$            | Stress intensity required for no-load-interaction      |
| $\Delta K$              | Stress intensity range ( $K_{\max} - K_{\min}$ )       |
| $\Delta K_{\text{eff}}$ | Effective stress intensity range                       |
| $\Delta K_{\text{th}}$  | Threshold stress intensity range                       |
| $m$                     | Wheeler shaping exponent                               |
| $N^*$                   | Observed delay cycles                                  |
| $P$                     | Load   |
| $R$                     | Stress intensity ratio ( $K_{\min}/K_{\max}$ )         |
| $r_y$                   | Plane stress plastic zone radius                       |
| $r_y^*$                 | Plane strain plastic zone radius                       |
| $S$                     | Overload shut-off ratio                                |
| $Z$                     | Load interaction zone                                  |
| $Z_c$                   | Current load interaction zone                          |
| $Z_{\text{OL}}$         | Overload created load interaction zone                 |
| $Z^*$                   | Load interaction zone required for no-load-interaction |
| $\alpha$                | Load interaction zone constant                         |
| $\sigma_{\text{ys}}$    | Yield stress   |

The qualitative effect of an overload on a fatigue crack propagating at some lower, cyclic load is well known. A tensile overload will delay or retard subsequent fatigue crack growth below that expected for the steady state case (no overload). Any crack growth analysis that does not account for this high-to-low load interaction will predict an overly conservative crack growth life.

Wheeler [1]<sup>2</sup> proposed that the linear cumulative damage fatigue crack growth predictive technique could be improved by introducing a factor to suppress the crack growth calculation following an overload. Although it is a substantial improvement over the linear cumulative damage rule, the original Wheeler retardation model is more of a data fitting technique than it is a predictive technique. In reducing the growth rate following an overload, the model utilizes an empirical shaping exponent,  $m$ , which is a constant for any particular case but varies according to type of material, specific load spectrum, and possibly other factors. Forcing the shaping exponent to be a constant may provide a good correlation between the model and a particular set of experimental data, but an important loss of generality is incurred in doing so. This paper proposes a modification to the Wheeler retardation model which (1) relates the exponent,  $m$ , to the primary factors that affect it and (2) allows the model to be used without reliance on data fitting.

<sup>2</sup> The italic numbers in brackets refer to the list of references appended to this paper.

**Model Development**

*Load Interaction Zone Concept*

Any crack growth retardation model must provide for a proper characterization of the crack tip residual stress state created by prior spectrum loads. In general, the maximum extent of any load-generated residual stress state, can be defined using a parameter  $Z$ , called the load interaction zone (LIZ).

A schematic showing the relationship between load and its corresponding LIZ is shown in Fig. 1. Load  $P_1$  applied at crack length  $a_1$  develops a zone  $Z_1$  which extends to some future crack length position  $a_3$ . Load  $P_2$  applied at crack length  $a_2$  develops an LIZ which spans the distance between  $a_2$  and some future crack length position  $a_4$ . An assumption basic to the Wheeler model is that if the load  $P_2$  develops an LIZ which extends out to or past the furthest extent of a previously developed LIZ, that is,  $a_2 + Z_2 \geq a_1 + Z_1$ , the growth increment associated with the  $P_2$  loading is calculated using a steady-state (no retardation) growth rate equation. Conversely, a crack growth rate reduction is assumed if the load  $P_2$  applied at crack length position  $a_2$  develops a load interaction zone which is smaller than that required to reach the furthest extent of any previously developed LIZ boundary, that is,  $a_1 + Z_2 < a_1 + Z_1$ .

Wheeler [1] assumed that the load interaction zone  $Z$ , was equal to the plastic zone (radius) size created under plane strain loading

$$Z = \frac{1}{4\pi\sqrt{2}} \left[ \frac{K}{\sigma_{ys}} \right]^2 = r^*_{\nu} \tag{1}$$

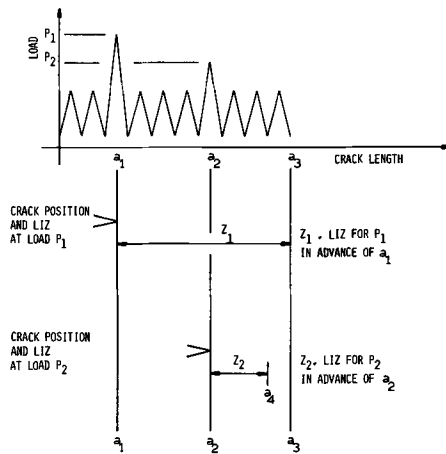


FIG. 1—Schematic illustrating the load interaction zone (LIZ) concept.

while others [2] suggest that the plane stress plastic zone (radius) size might be a more appropriate approximation of  $Z$ , that is

$$Z = \frac{1}{2\pi} \left[ \frac{K}{\sigma_{ys}} \right]^2 = r_y \quad (2)$$

To generalize Eqs 1 and 2, one could assume that

$$Z = \alpha \left[ \frac{K}{\sigma_{ys}} \right]^2 \quad (3)$$

where  $\alpha$  would be a function of material and thickness.

#### *Stress Intensity Format*

The Wheeler model was not derived originally in a stress intensity format, but such a format could be easily developed. Wheeler proposed that the crack growth rate under spectrum loading was equal to a reducing factor times the steady-state growth rate, or

$$\left. \frac{da}{dN} \right|_{sp} = C_p \times \left. \frac{da}{dN} \right|_{ss} \quad (4)$$

where

$$C_p = \begin{cases} \left[ \frac{Z_c}{Z^*} \right]^m, & Z_c < Z^* \\ 1, & Z_c \geq Z^* \end{cases} \quad (5)$$

In Eqs 4 and 5, the quantity  $Z_c$  is the extent of the current LIZ or the LIZ caused by the current maximum applied cyclic stress intensity,  $K_{max}$ . The quantity  $Z^*$  is the difference between the LIZ due to a previous overload and the current crack growth increment since that overload, that is

$$Z^* = Z_{OL} - \Delta a \quad (7)$$

Figure 2 shows that  $Z^*$  is also the LIZ that would be necessary in order to have no retardation, that is, after the crack has grown some increment,

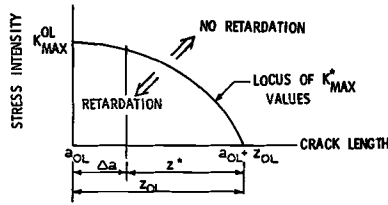


FIG. 2—Stress intensity ( $K^*_{max}$ ) required for coincident load interaction zone boundaries.

$\Delta a$ , away from the crack position immediately after the overload,  $a_{OL}$ , the quantity  $Z^*$  is the LIZ required to be coincident with the LIZ due to the overload. As the crack grows away from the overload position,  $a_{OL}$ , that is, as  $\Delta a$  increases,  $Z^*$  decreases. For the case of coincident LIZ boundaries (no retardation), there must be some stress intensity,  $K^*_{max}$ , which would be necessary to cause an LIZ of size  $Z^*$  and which continuously decays as the crack grows away from the overload position. Assuming that the extent of an LIZ is related to stress intensity by Eq 3 and substituting this relation into Eq 7 yields

$$\alpha \left[ \frac{K^*_{max}}{\sigma_{ys}} \right]^2 = \alpha \left[ \frac{K_{max}^{OL}}{\sigma_{ys}} \right]^2 \times \left[ 1 - \frac{\Delta a}{Z_{OL}} \right] \tag{8}$$

which can be rearranged in terms of  $K^*_{max}$ ,  $K_{max}^{OL}$ ,  $\Delta a$ , and  $Z_{OL}$  to give

$$K^*_{max} = K_{max}^{OL} \times \left[ 1 - \frac{\Delta a}{Z_{OL}} \right]^{1/2} \tag{9}$$

The locus of  $K^*_{max}$  values, defined by Eq 9, is illustrated graphically in Fig. 2.

The Wheeler reducing factor,  $C_p$ , may now be expressed in a stress intensity factor format by substituting the LIZ size relation (Eq 3) into Eqs 5 and 6, resulting in

$$C_p = \begin{cases} \left[ \frac{K_{max}}{K^*_{max}} \right]^{2m}, & K_{max} < K^*_{max} \\ 1, & K_{max} \geq K^*_{max} \end{cases} \tag{10}$$

$$\tag{11}$$

As seen in Eq 10 the Wheeler model considers the ratio of  $K_{max}$  to  $K^*_{max}$  as the driving force for the amount of retardation applied to the low

amplitude load induced crack growth rates. Stating the Wheeler retardation concept in a stress intensity factor format implies that if  $K_{\max} < K^*_{\max}$ , crack growth rates below steady-state levels can be expected for those cycles associated with  $K_{\max}$ . If  $K_{\max} \geq K^*_{\max}$ , no suppression in crack growth rates below steady-state levels is predicted.

The steady-state crack growth rate in Eq 4 can be, in general, expressed as

$$\left. \frac{da}{dN} \right|_{ss} = C \times [f(\Delta K, R)]^n \tag{12}$$

where

$C$  = constant which varies according to the type of material and the specific steady-state equation being used.

$n$  = constant which depends only on the material, and

$f(\Delta K, R)$  = controlling stress intensity function which drives the fatigue cracking process.

Three familiar forms for the function  $f(\Delta K, R)$  are given next.

Paris [3] equation:  $f(\Delta K, R) = \Delta K$  (13)

Walker [4] equation:  $f(\Delta K, R) = \Delta K(1 - R)^{t-1}$  (14)

Elber [5] equation:  $f(\Delta K, R) = \Delta K(1 + qR)$  (15)

Equations 10 through 12 can be substituted into Eq 4 to obtain

$$\left. \frac{da}{dN} \right|_{sp} = \begin{cases} C \times \left[ \left[ \frac{K_{\max}}{K^*_{\max}} \right]^{\frac{2m}{n}} \times (f(\Delta K, R)) \right]^n, & K_{\max} < K^*_{\max} \tag{16} \\ C \times (f(\Delta K, R))^n, & K_{\max} \geq K^*_{\max} \tag{17} \end{cases}$$

which is the stress intensity format for the Wheeler model in conjunction with a general expression for steady-state crack growth.

Equation 16 shows that Wheeler crack growth reduction factor may be applied directly to the stress intensity range function. With this fact in mind, Eqs 16 and 17 can be rearranged in terms of an effective stress

intensity range,  $\Delta K_{\text{eff}}$ , to yield

$$\left. \frac{da}{dN} \right|_{\text{sp}} = C \times [\Delta K_{\text{eff}}]^n \tag{18}$$

where

$$\Delta K_{\text{eff}} = \begin{cases} \left[ \frac{K_{\text{max}}}{K_{\text{max}}^*} \right]^{\frac{2m}{n}} \times f(\Delta K, R), & K_{\text{max}} < K_{\text{max}}^* \\ f(\Delta K, R) & , K_{\text{max}} \geq K_{\text{max}}^* \end{cases} \tag{19}$$

*Crack Arrest Condition*

Experiments involving single overloads in 2024-T3 aluminum [6] and Ti-6Al-4V [7] indicate that there is a particular value,  $S$ , of  $K_{\text{max}}^{\text{OL}}/K_{\text{max}}$  such that when  $K_{\text{max}}^{\text{OL}}/K_{\text{max}} \geq S$ , crack arrest occurs. In particular, Probst and Hillberry [6] showed that the condition for crack arrest was independent of  $K_{\text{max}}$ . In the absence of any additional definitive experimental work, it will be assumed that the overload shut-off ratio,  $S$ , is constant. For 2024-T3 aluminum, Probst and Hillberry [6] determined that  $S$  is approximately 2.3. Wei et al [7] provided data which indicate that  $S$  for Ti-6Al-4V is about 2.8.

The limiting condition for crack arrest is  $K_{\text{max}}^{\text{OL}}/K_{\text{max}} = S$ . Immediately after an overload,  $\Delta a = 0$ . Substituting these relations into Eqs 9 and 19 yields

$$\Delta K_{\text{eff}} (\text{at arrest}) = \left[ \frac{1}{S} \right]^{\frac{2m}{n}} \times f(\Delta K, R) \tag{21}$$

For the limiting case of crack arrest, the residual stresses induced by the overload adjust the stress state such that the effective stress intensity range just equals the threshold stress intensity range ( $\Delta K_{\text{th}}$ ), the point below which no measurable fatigue crack growth occurs. Thus

$$\Delta K_{\text{eff}} (\text{at arrest}) = \Delta K_{\text{th}} \tag{22}$$

In research associated with  $\Delta K_{\text{th}}$ , Grandt and Gallagher [8] showed that the threshold stress intensity range can be, in general, expressed as a

function of  $\Delta K_{th}$  at an  $R$  ratio equal to zero and the actual  $R$  ratio, as illustrated in the following equation

$$\Delta K_{th} = g \left( \Delta K_{th} \Big|_{R=0}, R \right) \quad (23)$$

Using the concept of Eq 22 in conjunction with Eq 23 and the modified Wheeler formulation for  $K_{eff}$  (at arrest) (Eq 21) and solving for the exponent,  $m$

$$m = \frac{n}{2} \times \left( \frac{\log \left[ \frac{f(\Delta K, R)}{g(\Delta K_{th} \Big|_{R=0}, R)} \right]}{\log S} \right) \quad (24)$$

Thus, it is evident that the Wheeler exponent,  $m$ , is not a constant but depends on the specific material being used and the loading subsequent to the overload.

### Data Correlation

To illustrate the accuracy of the modified Wheeler model, predictions made using the model were compared to existing experimental data [6,7,9,10,11,12] for the number of delay cycles ( $N^*$ , see Fig. 3) following a single overload. The data include three materials, 2024-T3 [6,9,10], 4340 steel [11], and Ti-6Al-4V [7,12], and a number of different values of loading parameters (see Table 1). A delay cycle is defined as any postoverload cycle of loading in which the growth rate is less than that expected for the case of no overload. In the 2024-T3 and 4340 experiments, load shedding techniques were employed to obtain constant  $\Delta K$  loading before and after an overload. Because of slightly different experimental techniques, the observed delay cycles in the Ti-6Al-4V experiments correspond only approximately to  $N^*$  as defined in Fig. 3.

To simplify the delay cycle calculations, it was assumed that  $\Delta K_{th}$  is a constant with no dependence on stress intensity ratio,  $R$ , and that the Paris equation (Eq 13) can describe adequately steady-state crack growth

for any particular  $R$  ratio. With these assumptions, Eq 24 becomes

$$m = \frac{n}{2} \times \left[ \frac{\log \left( \frac{\Delta K}{\Delta K_{th}} \right)}{\log S} \right] \tag{25}$$

Equations 18, 19, and 25 were programmed in a computer routine to analyze the postoverload crack growth on a cycle by cycle basis. This routine applies one load cycle at a time and counts it while computing the growth increment  $\left. \frac{da}{dN} \right|_{sp}$ , updating the current growth increment since

overload ( $\Delta a$ ), and checking the condition  $K_{max} < K_{max}^{OL} \times \left[ 1 - \frac{\Delta a}{Z_{OL}} \right]^{1/2}$

As soon as this condition is violated, the total number of cycles up to that point, that is, the delay cycles, is printed out.

The overload shut-off ratios,  $S$ , for 2024-T3, 4340, and Ti-6Al-4V were taken to be 2.3, 2.3, and 2.8, respectively. Table 2 summarizes the Paris growth rate equation constants,  $C$  and  $n$ , that were used for the various materials and  $R$  ratios. These constants were determined by a least squares fit to  $da/dN$  versus  $\Delta K$  data presented in Refs 6,7,9,10,11, and 12, or, where applicable, the constants were taken directly from these references. Threshold stress intensity ranges for 2024-T3, 4340, and Ti-6Al-4V were assumed to be 2, 6, and 6 ksi  $\sqrt{\text{in}}$ . (2.2, 6.6, and 6.6 MN/m<sup>3/2</sup>, respectively.

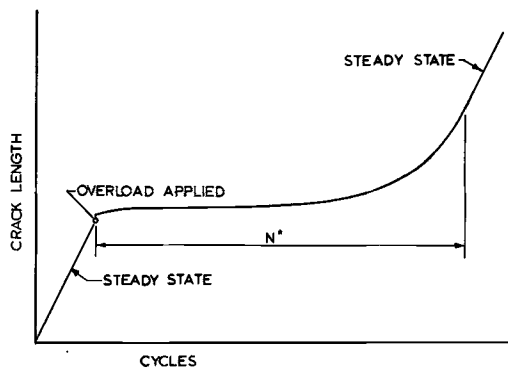


FIG. 3—Crack growth curve (for constant  $\Delta K$  loading) depicting the number of delay cycles,  $N^*$ , following a single overload.

TABLE 1—Single overload delay data.

| Material | Reference | R   | $K_{max}$        |                        | $K_{max}^{OL}$   |                        | $K_{max}^{OL}/K_{max}$ | $N^*$ (cycles) |        |                     |                     |
|----------|-----------|-----|------------------|------------------------|------------------|------------------------|------------------------|----------------|--------|---------------------|---------------------|
|          |           |     | ksi $\sqrt{in.}$ | (MN/m <sup>3/2</sup> ) | ksi $\sqrt{in.}$ | (MN/m <sup>3/2</sup> ) |                        |                |        |                     |                     |
| 2024-T3  | 6         | 0.3 | 6.8              | (7.5)                  | 13.7             | (15.1)                 | 2.01                   | 120 000        |        |                     |                     |
|          |           |     | 9.9              | (10.9)                 | 17.1             | (18.8)                 | 1.73                   | 35 000         |        |                     |                     |
|          |           |     |                  |                        | 20.4             | (22.4)                 | 2.06                   | 87 500         |        |                     |                     |
|          |           |     |                  |                        | 21.5             | (23.6)                 | 2.17                   | 104 000        |        |                     |                     |
|          |           |     |                  |                        | 12.2             | (13.4)                 | 19.5                   | (21.4)         | 1.60   | 36 000              |                     |
|          |           |     |                  |                        |                  |                        | 23.7                   | (26.1)         | 1.94   | 107 000             |                     |
|          |           |     |                  |                        |                  |                        | 26.5                   | (29.2)         | 2.17   | 246 000             |                     |
|          |           |     |                  |                        | 14.4             | (15.8)                 | 22.3                   | (24.5)         | 1.55   | 9 500               |                     |
|          |           |     |                  |                        |                  |                        | 30.6                   | (33.7)         | 2.13   | 398 800             |                     |
|          |           |     |                  |                        |                  |                        | 32.4                   | (35.6)         | 2.25   | 278 500             |                     |
|          |           |     |                  |                        |                  |                        | 27.8                   | (30.6)         | 1.66   | 21 000              |                     |
|          |           |     |                  |                        |                  |                        | 35.9                   | (39.5)         | 2.15   | 244 000             |                     |
|          |           |     | 9                |                        | 0.29             | 12.6                   | (13.9)                 | 26.1           | (28.7) | 2.07                | 332 000             |
|          |           |     |                  |                        |                  | 21.0                   | (23.1)                 | 28.5           | (31.4) | 1.36                | 5 000 <sup>a</sup>  |
|          |           |     |                  |                        |                  |                        |                        | 36.0           | (39.6) | 1.71                | 52 200 <sup>a</sup> |
|          |           | 8.2 |                  |                        |                  | (9.0)                  | 12.5                   | (13.8)         | 1.52   | 10 000 <sup>a</sup> |                     |
|          |           |     |                  |                        |                  |                        | 14.9                   | (16.4)         | 1.82   | 32 000              |                     |
|          |           |     |                  |                        |                  |                        | 17.1                   | (18.8)         | 2.09   | 50 000 <sup>a</sup> |                     |
| 9        |           | 0   | 13.7             | (15.1)                 | 21.2             | (23.3)                 | 1.55                   | 9 000          |        |                     |                     |
|          |           |     |                  |                        | 28.5             | (31.4)                 | 2.08                   | 72 000         |        |                     |                     |
|          |           |     | 15.0             | (16.5)                 | 30.0             | (33.0)                 | 2.00                   | 98 000         |        |                     |                     |



TABLE 2—Crack growth rate constants.

$$\frac{da}{dN} = C \times \Delta K^n$$

| Material          | Reference | R    | C                                       |                                     |      |
|-------------------|-----------|------|---|-------------------------------------|------|
|                   |           |      | in.                                     | m                                   |      |
|                   |           |      | (ksi $\sqrt{\text{in.}}$ ) <sup>n</sup> | (MN/m <sup>3/2</sup> ) <sup>n</sup> |      |
| 2024-T3           | 6, 9, 10  | 0.3  | 1.48 × 10 <sup>-9</sup>                 | [2.67 × 10 <sup>-11</sup> ]         | 3.59 |
| 2024-T3           | 9, 10     | 0    | 8.66 × 10 <sup>-9</sup>                 | [1.70 × 10 <sup>-10</sup> ]         | 2.68 |
| 2024-T3           | 10        | 0.67 | 3.21 × 10 <sup>-9</sup>                 | [5.97 × 10 <sup>-11</sup> ]         | 3.27 |
| 4340 <sup>a</sup> | 11        | 0.1  | 1.38 × 10 <sup>-10</sup>                | [2.58 × 10 <sup>-12</sup> ]         | 3.20 |
| 4340 <sup>b</sup> | 11        | 0.1  | 3.46 × 10 <sup>-10</sup>                | [6.48 × 10 <sup>-12</sup> ]         | 3.20 |
| Ti-6Al-4V         | 7         | 0    | 5.18 × 10 <sup>-9</sup>                 | [1.03 × 10 <sup>-10</sup> ]         | 2.60 |
| Ti-6Al-4V         | 12        | 0.1  | 8.85 × 10 <sup>-9</sup>                 | [1.77 × 10 <sup>-10</sup> ]         | 2.48 |

<sup>a</sup>  $\sigma_{ys}$  = 120 ksi (827 MN/m<sup>2</sup>).

<sup>b</sup>  $\sigma_{ys}$  = 220 ksi (1517 MN/m<sup>2</sup>).

For both 2024-T3 and 4340, the load interaction zone was assumed to be equal to the radius of the plane stress plastic zone as given by Eq 2. Wei et al [7] presented data indicating that the LIZ in Ti-6Al-4V is several times the value calculated using Eq 2. Accordingly, the predictions for Ti-6Al-4V were made assuming the LIZ, that is, the extent of the residual stress state's influence, to be approximately four times the plane stress plastic zone radius ( $\alpha = 2/\pi$ , see Eqs 2 and 3).

Figure 4 shows the correlation between the predictions and the experimental data. Note that all predictions are within essentially a factor of two of the actual data, an excellent correlation considering the various types of materials and values of loading parameters included in the data. For all cases considered, the exponent,  $m$ , varied from 1.07 to 4.34 according to Eq 25. The exponent need be computed only once per overload case since, in these calculations, it is assumed that constant  $\Delta K$  loading follows the overload.

Before applying the modified Wheeler model to variable amplitude load spectra, it must be noted that changes in load level can induce changes in the Wheeler exponent  $m$  (see Eq 25). The recalculation to determine  $m$  is conducted for load changes for which retardation modeling is applicable. The reader is cautioned that the model at present does not account for load interaction effects which may change the magnitude of the shut-off ratio  $S$ , that is, multiple overloads and underloads applied subsequent to overloads may influence  $S$ . However, variable amplitude crack growth analyses that include the modeling of first-order, load-interaction effects such as demonstrated herein provide substantial improvements in life prediction capability.

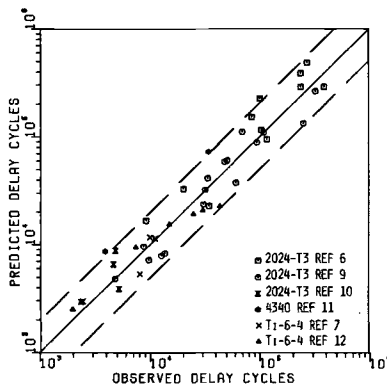


FIG. 4—Predicted delay cycles versus observed delay cycles.

### Summary

The Wheeler fatigue crack retardation model has been modified by formulating the model in a stress intensity factor format and applying a crack arrest condition. The modification relates the exponent,  $m$ , to the primary factors that affect it and allows the model to be used without reliance on data fitting and without the subsequent limiting to a specific material and a specific set of loading parameters.

As evident in Fig. 4, the modified Wheeler model can predict delay cycles following a single overload in 2024-T3, 4340, and Ti-6Al-4V within essentially a factor of two of the actual experimental data. The true measure of any crack growth analysis is its accuracy in predicting growth under a general load spectrum. Nonetheless, this model at present appears to have the basic elements necessary for a generalized analysis, and its success in predicting delay cycles following a single overload is encouraging.

### References

- [1] Wheeler, O. E., *Transactions*, American Society of Mechanical Engineers, *Journal of Basic Engineering*, Vol. 94, Series D, No. 1, March 1972, p. 181.
- [2] Willenborg, James, Engle, R. M., and Wood, H. A., "A Crack Growth Retardation Model Using an Effective Stress Concept," AFFDL-TM-71-1-FBR, Air Force Flight Dynamics Laboratory, Jan. 1971.
- [3] Paris, P. C. in *Fatigue—An Interdisciplinary Approach*, Proceedings of the Tenth Sagamore Army Materials Research Conference, 1964, p. 197.
- [4] Walker, K. in *Effects of Environment and Complex Load History on Fatigue Life*, ASTM STP 462, American Society for Testing and Materials, 1970, pp. 1-14.
- [5] Elber, Wolf in *Damage Tolerance in Aircraft Structures*, ASTM STP 486, American Society for Testing and Materials, 1971, pp. 230-242.
- [6] Probst, E. P. and Hillberry, B. M., *Journal*, American Institute of Aeronautics and Astronautics, No. 12, March 1974, pp. 330-335.
- [7] Wei, R. P., Shih, T. T., and Fitzgerald, J. H., "Load Interaction Effects on Fatigue Crack Growth in Ti-6Al-4V Alloy," NASA CR-2239, National Aeronautics and Space Administration, Washington, D.C., April 1974.
- [8] Grandt, A. F. and Gallagher, J. P. in *Fracture Toughness and Slow-Stable Cracking*, ASTM STP 559, American Society for Testing and Materials, 1974, pp. 283-297.
- [9] Von Euw, E. F. J., Hertzberg, R. W., and Roberts, Richard in *Stress Analysis and Growth of Cracks*, *Proceedings of the 1971 National Symposium on Fracture Mechanics, Part I*, ASTM STP 513, American Society for Testing and Materials, 1972, pp. 230-259.
- [10] Trebules, V. W., Jr., Roberts, Richard, and Hertzberg, R. W. in *Progress in Flaw Growth and Fracture Toughness Testing*, ASTM STP 536, American Society for Testing and Materials, 1972, pp. 230-259.
- [11] Gallagher, J. P. and Hughes, T. F., "The Influence of Yield Strength on Crack Growth Rate Delay in 4340 Steel," AFFDL-TR-73-27, Air Force Flight Dynamics Laboratory, March 1974.
- [12] Jones, R. E., "Fatigue Crack Growth Retardation After Single-Cycle Peak Overload in Ti-6Al-4V Titanium Alloy," AFML-TR-72-163, Air Force Materials Laboratory, Wright-Patterson Air Force Base, Ohio, April 1972.

R. M. Gamble<sup>1</sup> and P. C. Paris<sup>2</sup>

## Cyclic Crack Growth Analysis for Notched Structures at Elevated Temperatures

---

**REFERENCE:** Gamble, R. M. and Paris, P. C., "Cyclic Crack Growth Analysis for Notched Structures at Elevated Temperatures," *Mechanics of Crack Growth*, ASTM STP 590, American Society for Testing and Materials, 1976, pp. 345-367.

**ABSTRACT:** Linear elastic fracture mechanics analysis in conjunction with the appropriate experimental crack growth data were used to predict allowable thermal fatigue crack growth rates in gas turbine disks. The crack growth predictions made for the turbine disks compared favorably with subsequent service data.

Further studies were undertaken to determine the effect of geometric stress concentration on crack initiation and crack propagation. A general method of analysis was developed to provide simple approximations of the crack growth rates for cracks initiating at notches. The crack growth rates predicted by this method are in good agreement with both experimental laboratory specimen data and field service turbine disk data.

**KEY WORDS:** thermal stresses, fatigue (materials), gas turbine disk, crack initiation, crack propagation, elevated temperature, stress concentration

### Nomenclature

- $a_c$  Crack length
- $N$  Fatigue cycles
- $da/dN$  Cyclic crack growth rate
- $K_1$  Tensile range in stress intensity factor
- $n, C_o$  Numerical constants
- $f$  Frequency
- $R$  Load ratio =  $K_{\min}/K_{\max} = \sigma_{\min}/\sigma_{\max}$
- $T$  Temperature
- $K_1$  Crack tip stress intensity factor
- $\sigma_o$  Nominal net section stress

<sup>1</sup> Analytical engineer, Steam Turbine Division, Turbodyne Corporation, Wellsville, N. Y. 14895.

<sup>2</sup> President, Del Research Corporation, Hellertown, Pa. 18055, also professor, Division of Engineering, Brown University, Providence, R. I. 02915.

- $\sigma_G$  Nominal gross section stress
- $a_o$  Depth of geometric notch
- $a_T$  Effective total crack length =  $a_c + a_o$
- $b$  Specimen half width
- $K_\infty$  Stress intensity factor for unnotched infinite plate
- $F(a/b)$  Stress intensity modification function
- $K_t$  Elastic stress concentration factor
- $a_{co}$  Crack length corresponding to crack initiation

Recently, there has been broad application of fracture mechanics to generator and steam turbine rotors [1-3],<sup>3</sup> pressure vessels [4-7], and aircraft structures [8-10]. One area which has apparently received less attention in the literature concerns the application of fracture mechanics to gas turbine design. As the effort to avoid peak power blackouts continues and the need increases for more efficient power generation, it is expected that gas turbines will find increased usage in peaking and combined cycle plants. Since past experience has indicated that gas turbine components often crack during service [11-13], fracture mechanics should become even more important in gas turbine design to help eliminate prolonged and disruptive power outages.

This paper presents an example where fracture mechanics was used to predict allowable limits of thermal fatigue crack growth in gas turbine disks. The results of this study allowed safe, scheduled removal of cracked field units eliminating the possibility of premature return for many of these turbines.

Since the application discussed herein represents an important, general class of problems dealing with crack initiation and subsequent crack growth from notches, a further study was conducted to develop a general method to approximate the crack growth rates for cracks initiating at notches. The cyclic crack growth rates predicted by this generalized method are discussed in relation to their application to laboratory specimen and field service data.

### Nature of the Problem

Figure 1 shows the free turbine rotor assembly containing four gas turbine disks. The rotor is a double flow design powered by the radial flow from two jet engines. Turbines of this type came into prominence after the Northeastern Blackout in 1965 and are primarily used by electric utilities as peaking units where rapid start-stop operation is required. This mode of operation imposes severe cyclic compressive and tensile thermal

<sup>3</sup> The italic numbers in brackets refer to the list of references appended to this paper.

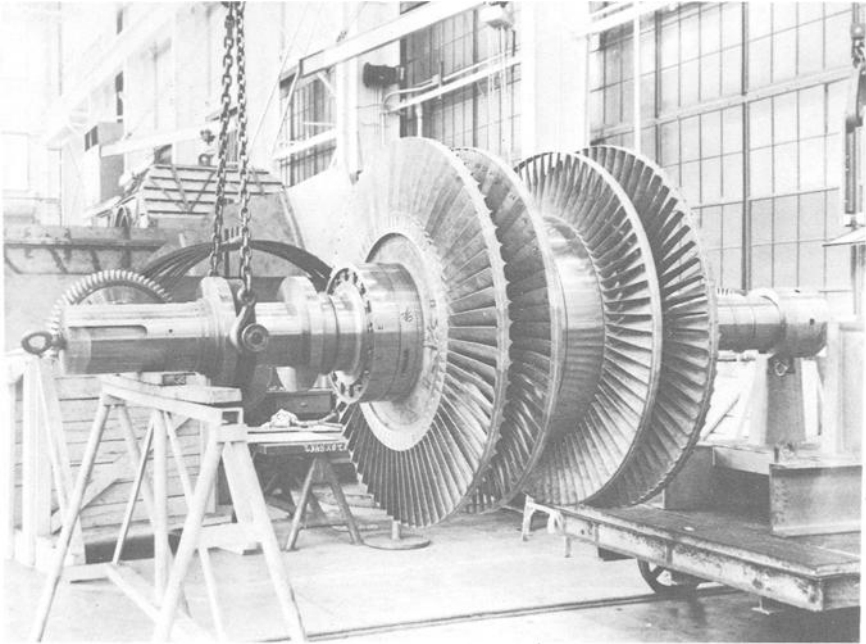


FIG. 1—Free turbine rotor assembly.

stresses on the unit and has resulted in fatigue cracking in each of the four turbine disks.

Figure 2 shows typical thermal fatigue cracks found in a first stage gas turbine disk. The cracks are located at the bottom of each blade slot in an area having a relatively severe geometric stress concentration and high nominal cyclic thermal stress. The cracking is multinucleated with crack initiation first occurring on the gas inlet face of the disk at the corner of the blade slot where the local transient thermal conditions are most severe. Various crack propagation stages are illustrated by the two fracture surfaces in Fig. 3. Figure 3a shows the fracture surface for a first stage turbine disk with 750 service cycles. The crack front is propagating in the radial direction but does not yet extend across the entire axial length of the blade slot. Figure 3b is the fracture surface for a different first stage turbine disk having 1535 cycles. Here one continuous crack front has been formed and is propagating in the radial direction.

The fracture surfaces in Fig. 3 represent the two gas turbine units in which cracks were first found in turbine disks. The immediate problem was to predict the cyclic crack growth rates thought to be representative of all gas turbine disks operating under similar conditions and establish the number of operating cycles that could be safely tolerated by the

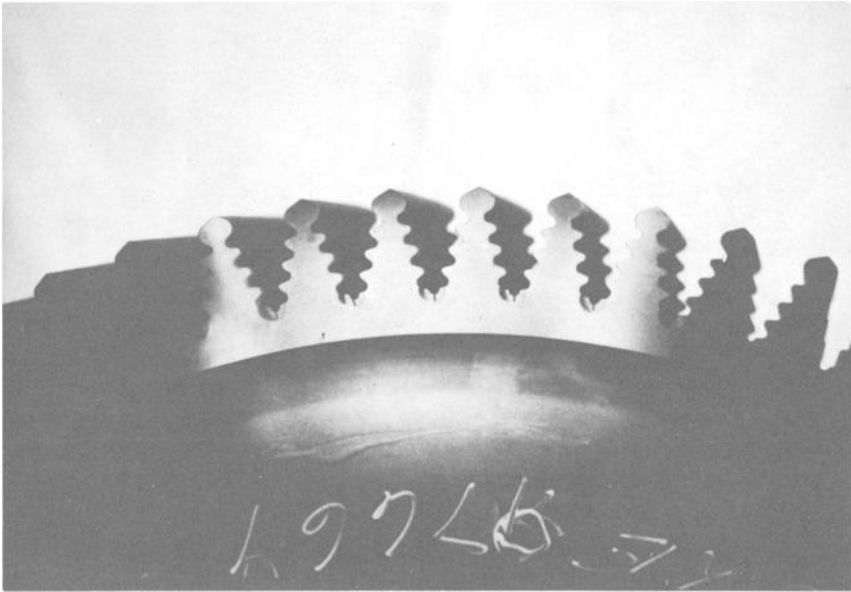
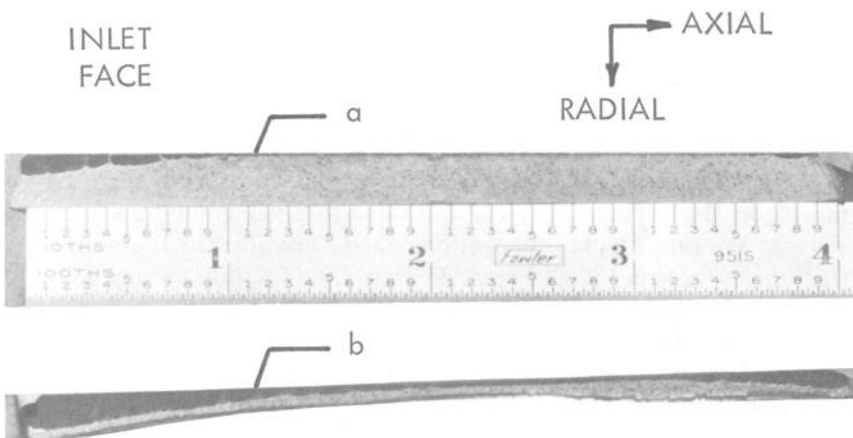


FIG. 2—Thermal fatigue cracks in blade slots of first stage gas turbine disk.



- (a)  $N = 750$  cycles,  $a_c = 0.12$  in.
- (b)  $N = 1535$  cycles,  $a_c = 0.185$  in.

FIG. 3—Fracture surfaces for two gas turbine disks.

TABLE 1—*Chemical composition of A286 forgings (weight percent).*

| C    | Mn   | Si   | P     | S     | Cr    | Ni    | Mo   | Ti   | B     | V    | Al   |
|------|------|------|-------|-------|-------|-------|------|------|-------|------|------|
| 0.06 | 1.21 | 0.66 | 0.006 | 0.009 | 15.31 | 26.17 | 1.29 | 2.25 | 0.006 | 0.18 | 0.28 |

remaining field units. A study was later undertaken to establish a repair procedure to refurbish the cracked turbine disks and extend their useful service life.

### Initial Cyclic Crack Growth Predictions for Turbine Disks

As a first approximation, the turbine disk crack propagation rates were obtained by using the two data points indicated in Fig. 3 in conjunction with cyclic crack growth data generated from small laboratory specimens.

### Experimentation

*Material and Specimens*—The gas turbine disk material is an iron base, precipitation hardening, super alloy forging commonly designated as A286. Initially, it was planned to obtain the test material from the rim area of the cracked turbine disks; however, additional testing, to be discussed later, required very large specimens and precluded obtaining all test material from actual disk forgings. The test samples were finally obtained from a large rectangular bar specifically forged to provide material for all planned tests. Microstructural examination, short-time tension tests, and elevated temperature, strain controlled, low-cycle fatigue tests later indicated that the disk and test forgings were essentially the same. The chemical composition and the average short-time room and elevated temperature tensile properties representative of the disk and test forgings are presented in Tables 1 and 2, respectively.

Experimental crack growth rate tests were conducted using both compact tension (CT) and single edge notch (SEN) specimens. The CT specimens were 0.25 in. thick with a 3-in. square planar dimension, while the SEN specimens were 0.38 in. thick by 2.0 in. wide by 6.0 in. long. Generally, the remaining details for specimen preparation were in accord-

TABLE 2—*Average mechanical properties of A286 forgings, solution treated 1650°F/2 h/oil quenched, aged 1325°F/16 h/air cooled.*

| Temperature,<br>°F | 0.2% Yield<br>Strength,<br>ksi | Ultimate<br>Strength,<br>ksi | Elastic<br>Modulus,<br>ksi | Reduction<br>in Area,<br>% |
|--------------------|--------------------------------|------------------------------|----------------------------|----------------------------|
| 70                 | 111.0                          | 158.0                        | 28700                      | 40.9                       |
| 900                | 98.5                           | 132.0                        | 23100                      | 38.5                       |

ance with ASTM Test for Plane-Strain Fracture Toughness of Metallic Materials (E 399-72).

*Procedure*—All tests were conducted under load control in a closed loop, hydraulically activated, mechanical test machine. Cyclic crack growth was determined by visually monitoring the movement of the crack as it passed reference grid lines photographically printed on the specimen surface. Data were obtained at load ratios of  $R = 0$  and  $R = -1$  using the SEN specimen, and at  $R = 0$  using CT specimens. Crack growth rate tests were conducted for both load ratios at room temperature and 900°F.

#### *Experimental Results and Discussion*

The results for the crack growth rate tests are shown in Fig. 4, where the indicated cyclic stress intensity, at a given load ratio, was determined using only the tensile load component. At cyclic tensile stress intensities up to 90 ksi  $\sqrt{\text{in.}}$ , the data for both load ratios and test temperatures can be expressed in the general form [14]

$$da/dN = C_o(K_I)^n \quad (1)$$

where

$da/dN$  = cyclic crack growth rate,

$K_I$  = tensile stress intensity range, and

$n, C_o$  = material constants determined from experimental results.

Within the range of cyclic tensile stress intensity from 20 to 90 ksi  $\sqrt{\text{in.}}$ , the data in Fig. 4 indicate that  $n$  is independent of the indicated test conditions, while  $C_o$  is a function of both temperature and load ratio.

The room temperature data indicate the load ratio has no effect on the crack growth rate. However, at 900°F, the growth rate for the  $R = -1$  data is approximately three times greater than that of the  $R = 0$  data at a given cyclic tensile stress intensity. There appears to be no effect of specimen geometry on crack growth rate.

#### *Crack Growth Rate Analysis*

The crack growth rates in the gas turbine disks were determined using the service data in Fig. 3, the stress intensity formula for an edge crack in a semi-infinite plate [15]

$$K = 1.13 \sigma_o \sqrt{\pi a_c} \quad (2)$$

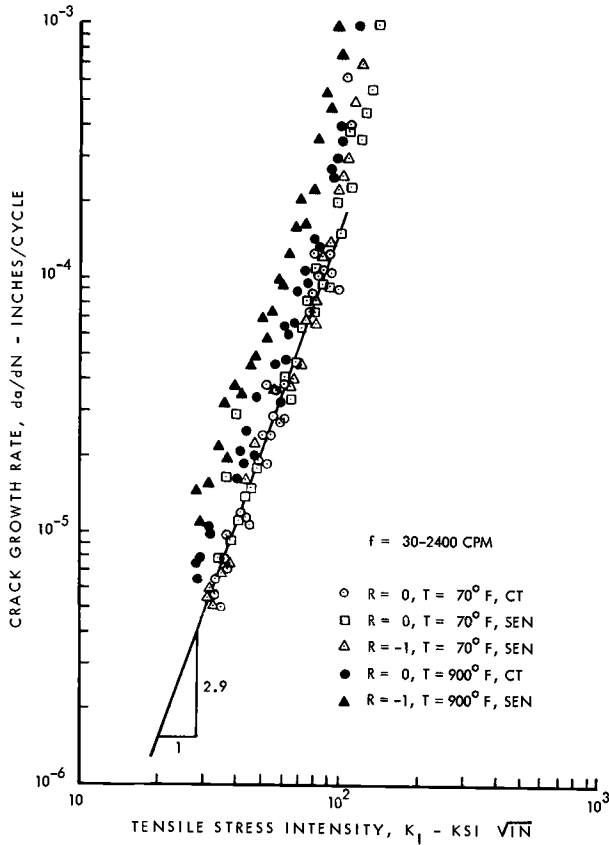


FIG. 4—Laboratory crack growth rate data for A286 forgings.

and the average crack growth rate versus tensile stress intensity relationship

$$da/dN = 8.6 \times 10^{-10} (K_1)^{2.9} \tag{3}$$

determined from Fig. 4. The relationship in Eq 3 was estimated from the data at 900°F for a load ratio  $R = -1.2$  and is representative of the conditions in the turbine disk as determined by transient heat transfer and stress analyses.

Equations 2 and 3 can be combined to express the crack propagation rate in the form

$$a_{c1}^{-0.45} - a_{c2}^{-0.45} = (29) (\sigma_0)^{2.9} (N_2 - N_1) 10^{-10} \tag{4}$$

where

- $a_{c1}$  = initial crack length,
- $a_{c2}$  = subsequent crack length,
- $N_1$  = number of fatigue cycles corresponding to  $a_{c1}$ ,
- $N_2$  = number of fatigue cycles corresponding to  $a_{c2}$ , and
- $\sigma_o$  = effective nominal stress.

The effective nominal service stress propagating the crack in the turbine disk was estimated by substituting the crack lengths and associated fatigue cycles from the initial two service points in Fig. 3 into Eq 4. The resultant effective stress,  $\sigma_o = 68$  ksi, was placed back into Eq 4, and the crack growth rate curve for the first stage gas turbine disks was constructed.

#### *Service Life Prediction and Discussion*

The predicted cyclic crack growth rate service curve for the first stage gas turbine disks is shown in Fig. 5. The extrapolated service curve indicates very high rates of crack growth at approximately 3500 cycles. Based on this estimate, it was decided to employ a factor of two on the maximum service life and recall the gas turbine disks from service at 1750 cycles.

The data designated by the open circles in Fig. 5 indicate first stage turbine disks subsequently returned from service. Represented are approximately 15 percent of all field units operated at a number of various utilities. The data near 1750 cycles are indicative of units returned in accordance with the allowable life predictions. Those units at lower numbers of cycles were returned for reasons unrelated to the disk cracking, but do provide additional information for crack propagation rates in turbine disks. The data indicate that all turbine disks follow the same trend, with crack initiation occurring within 250 cycles, and the subsequent crack propagation rates in good agreement with the curve initially predicted from Eq 4 and the two service points in Fig. 3. It should be pointed up that the crack growth rates for small cracks in the vicinity of the notch cannot be predicted by Eq 4. The portions of the curve extending from crack initiation to a crack length of 0.12 in. were arbitrarily drawn to encompass the remaining service data.

#### **Turbine Disk Repair Procedure and Analysis**

Although the gas turbine disk life had been successfully predicted, the resultant 1750 cycles was an unacceptably short service life. In an effort to extend the service life beyond the original design, a repair procedure was established to refurbish the cracked turbine disks. The repair procedure, illustrated in Fig. 6, involved removing the cracked turbine

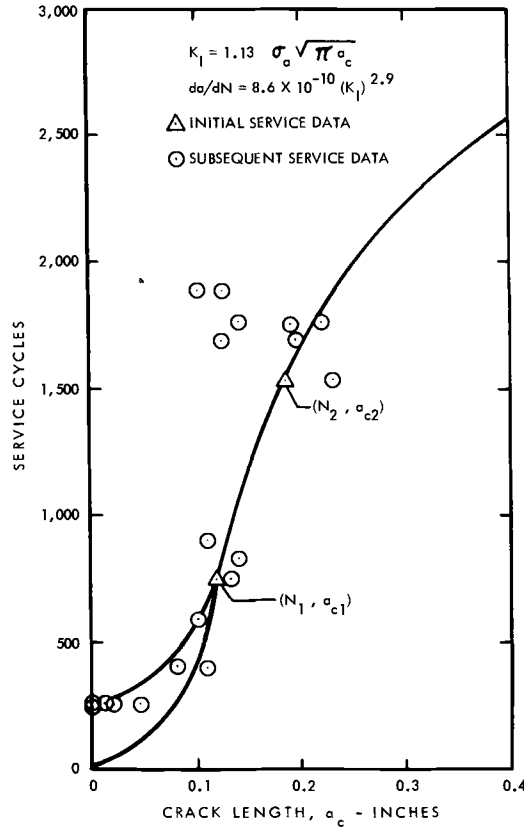


FIG. 5—Laboratory crack growth rate data applied to turbine disk service points.

disks from service after 1750 cycles, machining the existing fatigue cracks from the blade slot and replacing the original notch configuration with one having larger radii. As a supplement to the crack removal and the implementation of the new notch design, it was planned to place heat shields over the blade slots in order to reduce the transient thermal stresses.

An analytical and experimental study was then undertaken to predict and verify the safe and useful service life for repaired turbine disks prior to reinstallation.

*Stress Analysis (results)*

A transient thermal stress analysis was conducted to define the repair disk service life, explore various means to reduce the operating thermal stress, and obtain the required service life without fatigue cracking.

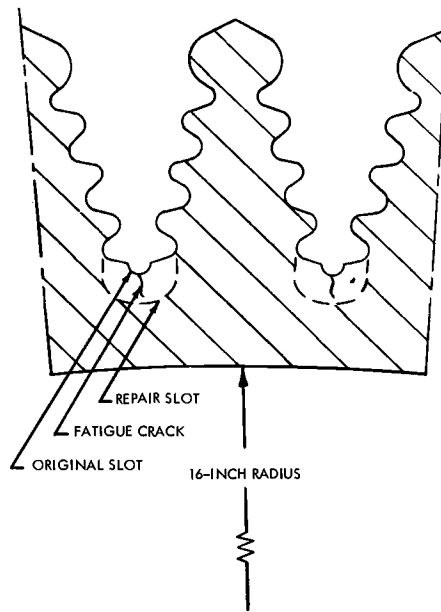


FIG. 6—Repair scheme to remove fatigue cracks from turbine disk blade slots.

It was determined that adding heat shields to the turbine disk rim reduced the transient thermal stress range by 10 to 15 percent. Unfortunately, further significant thermal stress reduction could only be obtained by drastic alteration of the operating cycle. Since these alterations would preclude successful operation of the turbine as a peaking unit, they were not implemented, and the repair was restricted to the addition of heat shields and change in notch geometry.

#### Experimentation

*Material and Specimens*—The material for this portion of the investigation was obtained from the same forging used for the initial crack growth rate tests.

Crack initiation and propagation studies were conducted using the large notched specimens shown in Fig. 7. The specimens were designed to first obtain initiation and propagation data for the original notch, followed by fatigue crack removal to allow testing of the repair notch. Not shown in Fig. 7 are notches positioned on either side of the indicated test notch to simulate the general stress distribution adjacent to the bottom of the blade slot in the turbine disk. The notch radii shown for the test specimen are the same as those in the turbine disk. The remaining specimen dimensions were chosen to simulate both the geometric stress concentration, as

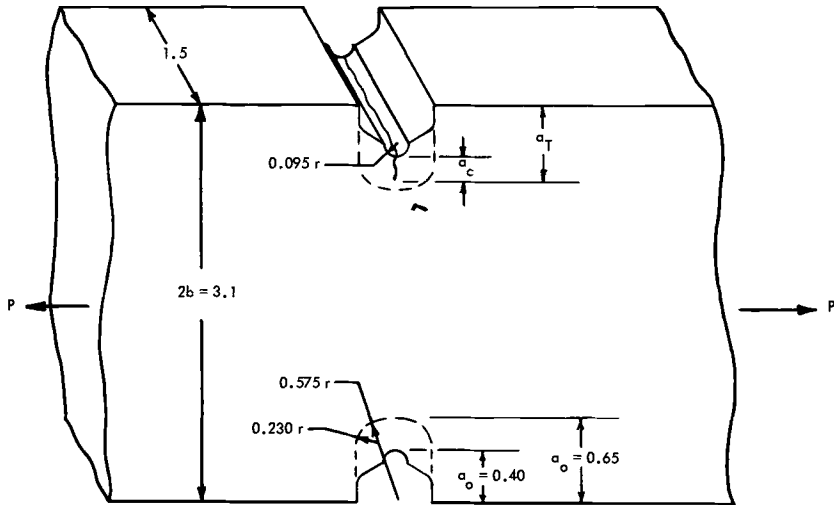


FIG. 7—Notched laboratory fatigue specimen.

determined by laboratory strain gage measurements on the turbine disk, and the range of cyclic stress intensity indicated by the predicted service curve in Fig. 5. A specimen thickness of 1.5 in. was chosen to satisfy plane-strain requirements over the range of cyclic stress intensities studied in accordance with ASTM Test for Plane-Strain Fracture Toughness of Metallic Materials (E 399-72).

To ensure that the fatigue data were not affected by the different notch depths, two further restrictions were placed on the specimen design. First, the two-notch depths shown in Fig. 7 were chosen so that the elastic stress concentration factor [16] at a given notch radius and nominal net stress remained constant. Similarly, the stress intensity associated with a given nominal net stress and crack length extending from the notch was approximately the same for both notch depths as determined by the stress intensity formula for a double edge notched specimen [15].

$$K_I = \sigma_G \sqrt{\pi a_T} \left[ \frac{2b}{\pi a_T} \left( \tan \frac{\pi a_T}{2b} + 0.1 \sin \frac{\pi a_T}{b} \right) \right]^{1/2} \quad (5)$$

where

- $a_T$  = sum of notch depth and fatigue crack length,
- $b$  = specimen half width, and
- $\sigma_G$  = gross stress.

*Procedure*—The fatigue tests were conducted in a load controlled, hydraulically activated test machine shown in Fig. 8. The load schedule used during the tests maintained a stress ratio  $R = -1.2$  and produced a ramp loading having a 10 to 15-s dwell period at the maximum tensile and compressive loads. All test loads were established based on the required nominal net stress range.

To establish correlation with the turbine disks, specimens having the original notch configuration were tested at the nominal net stress level necessary to produce cracking within 200 to 300 cycles. Specimens having the repair notch were then tested at the same nominal net stress to determine the effect of notch geometry on crack initiation and subsequent crack propagation. Since analysis had indicated that heat shields would reduce the thermal stress, additional repair notch specimens were tested at reduced loads to evaluate the change in cycles to initiation and crack propagation rate.

All tests were conducted at a constant 900°F using a split resistance furnace controlled by a chromel-alumel thermocouple spot welded in an unstressed area near the central test notch.

At a predetermined number of cycles the tests were stopped, the specimen was allowed to cool and inspection was made for crack initiation. Crack initiation was defined as the first definite fluorescent penetrant indication observed in the test slot. Maximum crack initiation

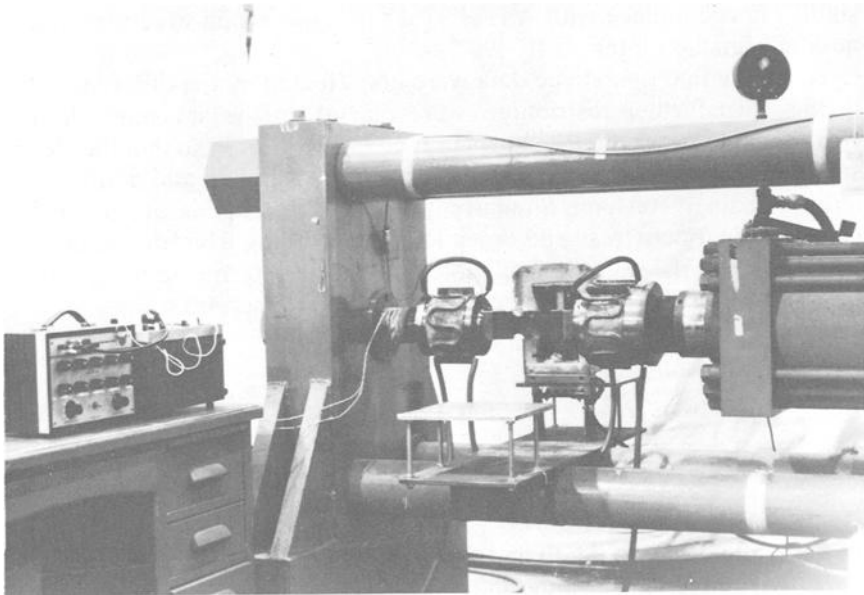


FIG. 8—Setup for elevated temperature, notched fatigue tests.

sensitivity was obtained by applying the penetrant under full tension test load so that the open crack would absorb as much penetrant as possible. The load was then released so that maximum amount of penetrant was observed as it was forced from the crack. For fully developed cracks, the crack lengths were measured at full tension test load using a  $\times 20$  power telescope mounted on a micrometer slide having a least reading of 0.0001 in.

*Results and Discussion*

*Crack Initiation*—The crack initiation data for the large notched fatigue specimens are shown in Fig. 9. Since crack initiation in notches is related generally to the cyclic strain range when local plastic flow occurs [17], the cycles to initiation in Fig. 9 have been plotted as a function of the net nominal strain range. At the nominal net strain range simulating the original transient thermal conditions in the turbine disk, the change from the original notch to the repair notch increases the number of cycles to crack initiation by a factor of four. Within the range of load levels tested, a 25 percent reduction in nominal net strain-range increased the cycles to initiation in the repair notch by a factor of approximately ten.

*Propagation*—Crack propagation data designated by the open circles are shown in Fig. 10 for three typical fatigue specimens. The bottom data set represents a specimen having the original notch geometry and tested at a net cyclic stress range which produced crack initiation between 200 to 300

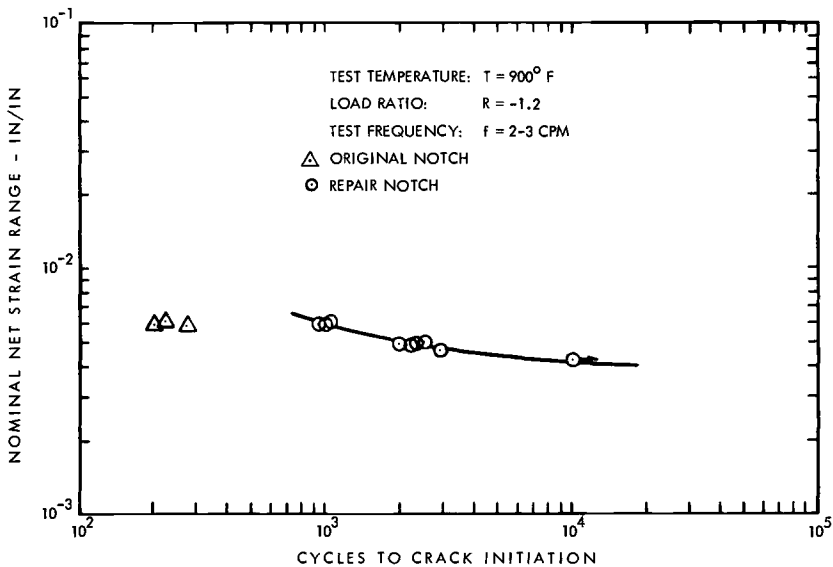


FIG. 9—Crack initiation data for notched laboratory fatigue specimens.

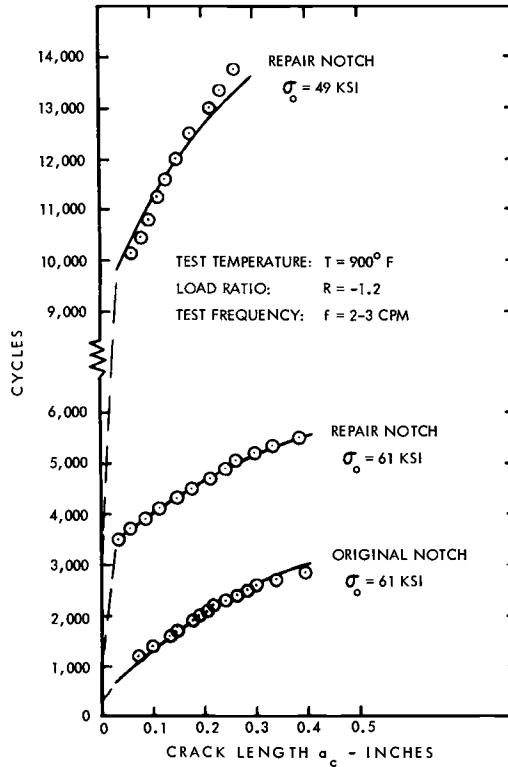


FIG. 10—Typical crack propagation data for notched laboratory fatigue specimens.

cycles. The middle data set represents a specimen run at the same net cyclic stress range but having the repair notch geometry. Comparison of the two data groups indicate the crack propagation rate in the immediate vicinity of the notch is significantly less for the repair notch in comparison to the original notch design. For deeper cracks, the crack propagation rates for the original and repair notch specimens are the same. The upper data set represents a repair notch specimen tested at a stress level 20 percent less than the other two specimens. As expected, the results show decreased crack propagation rates both in the vicinity of the notch and for deeper cracks.

The solid lines drawn through the data in Fig. 10 were obtained by choosing one experimental data point at a crack length greater than 0.1 in. and predicting the crack growth rates for the large specimen using the stress intensity formula in Eq 5 and the crack growth data from Eq 3. Since the resulting curves coincided with the remaining experimental data from the large notched specimen tests, it appeared that the  $da/dN$  versus

$K_i$  data in Fig. 4 were applicable for larger components of different geometry tested at different load levels and significantly reduced cyclic frequencies.

*Turbine Disk Repair Life Predictions*

It was apparent from the various laboratory results that crack initiation could be predicted for the repaired turbine disks and that subsequent crack propagation rates could adequately be described by Eq 3.

Figure 11 shows the final predicted service life for gas turbine disks with both the original and repair notch geometry. The curve at the lower left represents the original design to be returned at 1750 service cycles for repair. At that time the predicted crack length is approximately 0.20 in. with 0.25 in. being removed during the repair machining operation. This

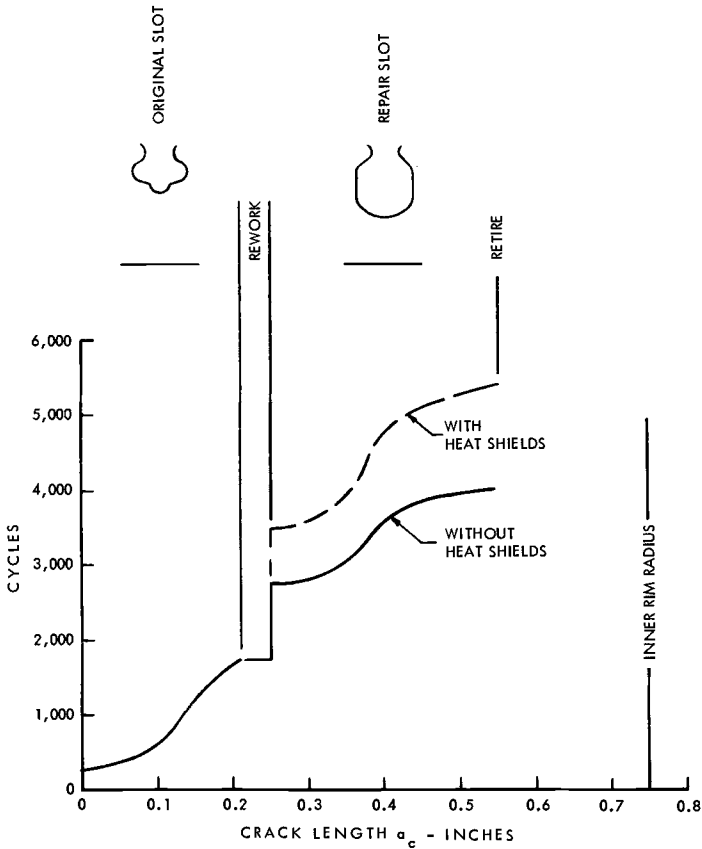


FIG. 11—Prediction of crack initiation and propagation for first stage turbine disks with original and repaired blade slots.

margin is used to eliminate the possibility of residual fatigue cracks remaining in the repaired turbine disks. The curve at the lower right represents a repair disk subjected to the same transient thermal stresses as the original design. The upper curve represents repaired disks having reduced transient thermal stresses due to the addition of heat shields. The reduced stress is reflected in the greater life to crack initiation and reduced crack propagation rates. These results indicate that the repair procedure increases the total gas turbine disk service life by a factor of three.

Due to the absence of service data for repaired turbine disks, two conservative assumptions were used in constructing the crack propagation portion of the service life curves for the repaired disks in Fig. 11. First, at a given stress level, the crack growth rate in the vicinity of the repair notch was taken to be the same as the original notch. Second, the crack growth rates for deep cracks were based on an effective crack length composed of the sum of actual fatigue crack length and the 0.25 in. of material removed to eliminate the original crack. The experimental data shown in Fig. 10 verify the conservatism of these assumptions.

#### Cyclic Crack Growth from Notches—A General Method

Since there is wide application for fatigue loaded notched structures, an attempt was made to develop a simple but general method to approximate cyclic crack growth following fatigue crack initiation at a notch. A technique was first devised to provide a general analytical expression for stress intensity that would account for the notch presence without complicated calculation techniques. Starting at an initial crack length and number of cycles corresponding to crack initiation, the stress intensity relationship, together with the appropriate data from Eq 1, were then used with an incremental crack growth scheme to predict the subsequent fatigue cycles necessary to produce a given crack length.

The proposed cyclic crack growth analysis was verified by generating a number of analytical predictions for both the notched fatigue specimens and turbine disk and by comparing the results with the appropriate experimental and service data.

#### *Stress Intensity*

The stress intensity factor for a crack extending from a notch is often given in the form [18,19]

$$K_1 = K_\infty F(a/b) \quad (6)$$

where  $K_\infty$  is the stress intensity formula for a given unnotched geometry with the crack size small compared to other dimensions and  $F(a/b)$  is a function accounting for the notch presence and any necessary finite width

correction. In this analysis, the stress and crack length associated with the stress intensity in Eq 6 are the nominal net stress,  $\sigma_0$ , and the actual fatigue crack length,  $a_c$ . To be consistent with usual fracture mechanics assumptions, the nominal net stress is restricted to the elastic region. No restriction, however, is placed on local plastic flow in the notch.

### F Functions

*General Development*—To determine the  $F$  function for a given geometry, the following three distinct regions, related to the distance the crack tip extends from the notch, are considered: very small cracks corresponding to initiation, deeper cracks still within the region of stress concentration, and deep cracks unaffected by the notch presence.

At crack lengths approaching zero, the value of  $F$  was obtained from the stress intensity solution for a crack emanating from a hole in an infinite plate [18,19] by generalizing the observation that

$$F = 1.12K_t \quad \text{at } a_c = 0 \quad (7)$$

where

$K_t$  = elastic stress concentration factor.

Equation 7 is assumed to apply for any notch configuration and the associated elastic stress concentration based on nominal net stress.

At crack lengths greater than approximately 0.1 in., the results of this investigation and those of Ref 20 indicate that the crack growth rates are independent of notch tip radius. For deep cracks then,  $F(a/b)$  is simply equal to either 1.0, or, depending on the relative structural dimensions, the appropriate finite width correction.

Finally, for cracks within the notch influence ( $0 \leq a_c \leq 0.1$ ),  $F(a/b)$  is constructed so that a smooth curve, matching the previously determined values at  $a_c = 0$  and 0.1 in. produces increasing values of  $K_t$  with increasing values of  $a_c$  in Eq 6.

*Notched Fatigue Specimens*—Plots of  $F(a/b)$  as a function of  $a_c$  are shown in Fig. 12 for the fatigue specimens having both the original and repair notches. The values of  $F$  at  $a_c = 0$  were calculated from Eq 7 using the experimentally determined values of elastic stress concentration  $K_t = 4.0$  and  $K_t = 2.1$  for the original and repair notches, respectively. For deep cracks,  $F(a/b)$  is independent of notch geometry and was derived in terms of  $a_c$  from the finite width correction indicated for a double edge notch specimen by Eq 5.

*Turbine Disk*—Although the  $F(a/b)$  function for the turbine disk is not shown, it is essentially identical to that derived for the original notch fatigue specimen; however, no finite width correction for deep cracks was

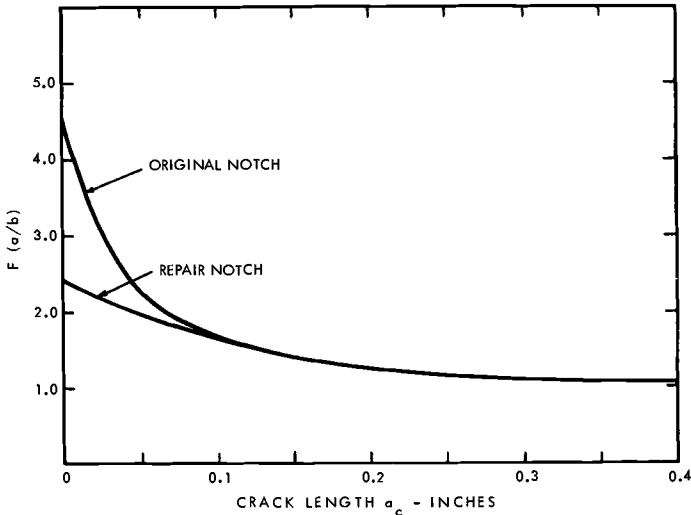


FIG. 12— $F(a/b)$  functions for original and repair notch fatigue specimens.

necessary since the crack lengths are small compared to the disk diameter.

#### Application

In addition to deriving the  $F$  function, successful application of the analysis for predicting crack growth from notches depends on defining  $K_\infty$  obtaining the appropriate crack growth rate relationship similar to Eq 1, and defining the initial crack length and corresponding number of fatigue cycles at crack initiation.

For the turbine disk and notched fatigue specimens,  $K_\infty$  is given by Eq 2, while the experimental cyclic crack growth rate relationship at the appropriate temperature and load ratio is given by Eq 3. Thus, from Eq 6, the stress intensity for the disk and specimen geometries becomes

$$K_I = 1.13 \sigma_0 \sqrt{\pi a_c} F(a/b) \quad (8)$$

with

$$da/dN = 8.6 \times 10^{-10} (K_I)^{2.9}$$

The number of fatigue cycles and the associated nominal net stress,  $\sigma_0$ , producing crack initiation in the notched fatigue specimens were obtained from Fig. 9. Since the exact number of cycles to crack initiation in the turbine disk cannot be defined, two different values, consistent with the

service data in Fig. 5, were considered. Using the previously determined effective nominal service stress,  $\sigma_o = 68$  ksi, the number of cycles to crack initiation in the turbine disk was estimated from Fig. 9 as 200 cycles. Since the service data in Fig. 5 imply that crack initiation may also occur earlier than 200 cycles, a second crack initiation point was chosen at 100 cycles. The nominal service stress corresponding to this initiation point was also estimated from Fig. 9 and is  $\sigma_o = 85$  ksi.

All incremental crack growth predictions calculated from Eq 8 were begun at a crack length corresponding to crack initiation of  $a_{co} = 0.002$  in. This initial value is consistent with the inspection sensitivity used to define crack initiation in Fig. 9 and is a good approximation for the onset of Stage II cracking where a relationship represented by Eq 1 could first be employed.

### *Results and Discussion*

*Notched Fatigue Specimens*—Figure 13 shows the fatigue cycles versus crack length curves predicted for the original and repair notches at various stress levels. Comparison with the experimental data indicate good agreement. The greatest difference is seen for the middle curve where the predicted life at a given crack length is 25 percent greater than that obtained experimentally. Figure 13 is plotted on a log-log scale to emphasize the predicted crack growth rates for small cracks in the notch vicinity where experimental data could not be obtained. The predicted curves indicate that the crack growth rates in the notch vicinity are significantly less for the repair notch in comparison to the original notch. In addition, for a given notch geometry, the predicted curves indicated that small cracks in the notch vicinity have lower growth rates in comparison to deep cracks which extend beyond the region of notch influence. These predictions are consistent with those implied by the plots for the experimental data in Fig. 10.

*Turbine Disk*—The two curves predicted at the stress levels necessary to produce crack initiation in the turbine disk at 100 and 200 cycles are shown in Fig. 14 along with the individual service data points from Fig. 5. The results indicate that the top curve closely describes the service data for deep cracks while the propagation rates for small cracks are better described by the lower curve.

A closer look at the stress condition in turbine disk will help to clarify this difference. First, it should be emphasized that the crack is assumed to grow from the notch due to an applied, uniform nominal stress. For fully developed deep cracks in the turbine disk, this condition is fairly well satisfied, and the upper curve adequately describes the propagation rate. However, a heat transfer analysis indicated that the local heat transfer coefficients at the corner of the blade slot on the inlet face are two to three times greater than those in adjacent areas. This implies that the local

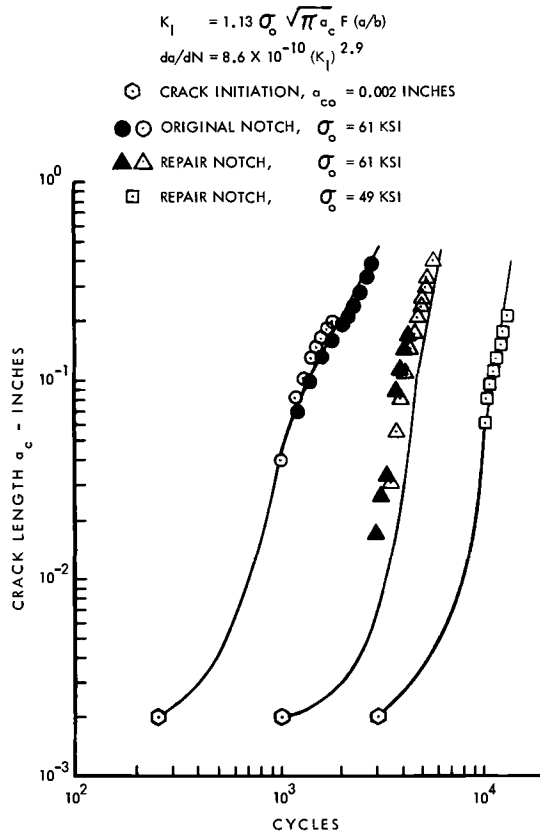


FIG. 13—Comparison of predicted crack propagation rates with experimental data for notched laboratory fatigue specimens.

thermal stress at the notch corner is significantly greater than the nominal value and is consistent with Fig. 3 where crack initiation and significant growth are first seen to occur at this location. Thus, for small cracks, the propagation rates are described properly by the lower curve indicative of the higher stress. From these considerations, a good approximation for crack growth can be obtained by combining the applicable regions for the two predicted curves as shown by the dashed line in Fig. 14.

**Further Discussion**

The available service data shown in Fig. 5 lie in a relatively narrow scatterband and are in good agreement with the service curve first predicted from the two original service points and the cyclic crack growth rate data generated from the CT and SEN specimens. However, due to

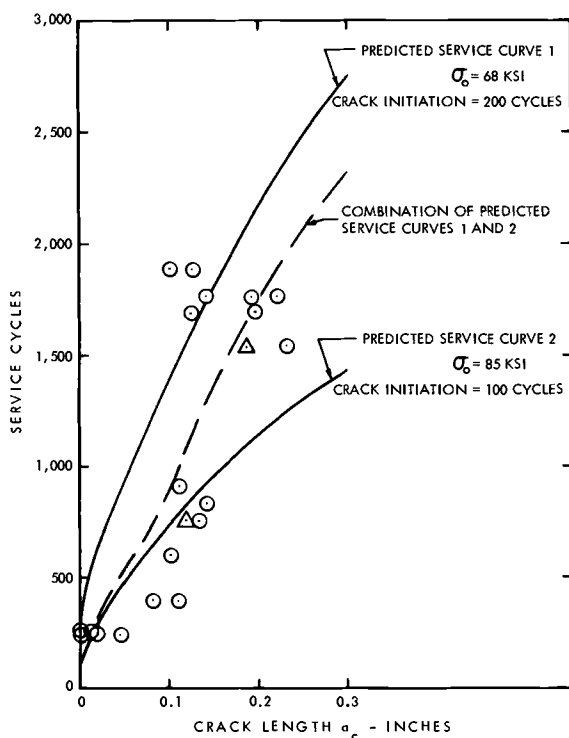


FIG. 14—Comparison of predicted crack propagation rates with service data for first stage turbine disks.

the large variation in fatigue life generally associated with service data, there was some concern that the allowable service life for the remaining 85 percent of the gas turbine units might not be represented by the curve in Fig. 5. Subsequent thermal and stress analyses indicated that extreme variations in operating schedules were necessary to alter the transient thermal stresses by more than  $\pm 5$  percent. Since the remaining turbine units would not experience these extreme operating conditions, the curve in Fig. 5 is considered a good representation for the crack growth rates in all similar service units.

The major difficulty encountered in studying the crack growth rates in the immediate notch vicinity was the inability to observe accurately the propagation of small cracks following initiation. Normally, the cracks initiate at various locations along the notch surface and can be monitored as they grow and coalesce across the specimen width; however, neither the depth nor the shape of the crack front can be observed. As an approximation for predicting the crack depth as a function of fatigue

cycles, the preceding analysis tacitly assumes that beginning at crack initiation the cyclic crack growth rate along the notch is sufficient to maintain a constant flaw shape factor associated with a depth to width ratio approximately equal to zero. The results from this investigation and those from Ref 20 imply that this is a reasonable assumption for edge notches with constrained plastic flow, although it does not appear to be true for all notch types [21]. The use of a constant depth to width ratio approximately equal to zero, however, does provide a convenient device to make qualitative, and, in general, conservative cyclic crack growth rate predictions for small cracks in the notch vicinity when the crack shape cannot be defined.

### Conclusions

1. Experimental and analytical fracture mechanics methods can be used to predict the allowable number of service cycles for gas turbine disks subjected to cyclic thermal stresses.
2. Fracture mechanics techniques can be used to describe the cyclic crack growth rates in the immediate vicinity of notches beginning with very small crack lengths corresponding to initiation.
3. The elastic stress concentration factor provides an effective means to describe qualitatively the effect of notch severity on the cyclic crack growth rates and, as evidenced in this investigation, may provide accurate quantitative predictions as well.

### References

- [1] Winnie, D. H. and Wundt, B. M., *Transactions, American Society of Mechanical Engineers*, Vol. 80, 1958, pp. 1643-1658.
- [2] Greenberg, H. D., Wessel, E. T., and Pryle, W. H., *Engineering Fracture Mechanics*, Vol. 1, No. 4, April 1970, pp. 653-675.
- [3] Thornton, D. V., *Engineering Fracture Mechanics*, Vol. 2, No. 2, Nov. 1970, pp. 125-143.
- [4] Singer, V., *Engineering Fracture Mechanics*, Vol. 1, No. 3, April 1969, pp. 507-517.
- [5] Parry, G. W. and Lazzeri, L., *Engineering Fracture Mechanics*, Vol. 1, No. 3, April 1969, pp. 519-537.
- [6] Tiffany, C. F. and Masters, J. N. in *Fracture Toughness and Its Applications, ASTM STP 381*, American Society for Testing and Materials, 1965, pp. 249-278.
- [7] Duffy, A. R., Eiber, R. J., McClure, G. M., and Maxey, W. A. in *Fracture*, Vol. 5, H. Liebowitz, Ed., Academic Press, New York, 1969, pp. 159-232.
- [8] Kuhn, P. in *Fracture*, H. Liebowitz, Ed., Vol. 5, Academic Press, New York, 1969, pp. 471-500.
- [9] Christensen, R. H. and Harman, M. B. in *Fatigue Crack Propagation, ASTM STP 415*, American Society for Testing and Materials, 1967, pp. 5-24.
- [10] Critchlow, W. J. and Wells, R. H. in *Fatigue Crack Propagation, ASTM STP 415*, American Society for Testing and Materials, pp. 25-70.
- [11] Manson, S. S., "Behavior of Materials Under Conditions of Thermal Stress," Report 1170, National Advisory Committee for Aeronautics, 1954.
- [12] Cook, J. E., "Development Experience with Prototype Gas Turbines," Paper No. 60-GTP-13, American Society of Mechanical Engineers, 1960.
- [13] McLean, H. D., Tangerini, C. C., and Van Colt, W. H., "Report on 9000-Hr. Operation of Marine Propulsion Gas Turbine in the John Sergeant," Paper No. 60-GTP-5, American Society of Mechanical Engineers, 1960.

- [14] Paris, P. C., "The Fracture Mechanics Approach to Fatigue," *Proceedings of the Tenth Sagamore Army Materials Research Conference*, Aug. 1963, Syracuse University Press, Syracuse, N.Y., 1964.
- [15] Paris, P. C. and Sih, G. C. in *Fracture Toughness and Its Applications*, ASTM STP 381, American Society for Testing and Materials, 1965, pp. 40-44.
- [16] Peterson, R. E., *Stress Concentration Design Factors*, Wiley, New York, 1953, pp. 26-27.
- [17] Wundt, B. M. in *Effect of Notches on Low-Cycle Fatigue*, ASTM STP 490, American Society for Testing and Materials, 1972.
- [18] Bowie, O. L., *Journal of Mathematics and Physics*, Vol. 35, 1956, p. 60.
- [19] Newman, J. C., Jr., "An Improved Method of Collocation for the Stress Analysis of Cracked Plates With Various Shaped Boundaries," *NASA Technical Note, NASA TND-6376*, National Aeronautics and Space Administration, Washington, D.C., Aug. 1971.
- [20] Clark, W. G., Jr., in *Fracture Toughness and Slow-Stable Cracking*, ASTM STP 559, *Proceedings of the 1973 National Symposium on Fracture Mechanics, Part I*, American Society for Testing and Materials, 1974, pp. 205-224.
- [21] Schijve, J. in *Fatigue Crack Propagation*, ASTM STP 415, American Society for Testing and Materials, 1967, p. 424.

R. Labbens,<sup>1</sup> A. Pellissier-Tanon,<sup>1</sup> and J. Heliot<sup>1</sup>

## Practical Method for Calculating Stress-Intensity Factors Through Weight Functions

---

**REFERENCE:** Labbens, R., Pellissier-Tanon, A., and Heliot, J., "Practical Method for Calculating Stress-Intensity Factors Through Weight Functions," *Mechanics of Crack Growth, ASTM STP 590*, American Society for Testing and Materials, 1976, pp. 368–384.

**ABSTRACT:** The existence for a plane or axisymmetric cracked body of an influence or Green's function, depending on the geometry of the body, allows calculation by means of a simple integral of the stress intensity factor. In this way the respective influence of geometry and load in  $K$  calculation are separated. The relationship between this function and the compliance for a concentrated force applied on the crack is shown.

Starting from complex mathematical considerations, Bueckner defined weight functions equivalent to the influence functions and of particular advantage for analytic as well as numerical purposes. Moreover he showed that weight functions behave like  $d^{-1/2}$  at the distance  $d$  from the crack tip. In the sequel we shall refer to weight functions, since they are studied more deeply from a mathematical point of view and are known more widely than influence functions.

A practical calculation method of weight functions by finite elements is shown. This method can be used for any bidimensional cracked body, plane or axisymmetric. Curves of nondimensional weight functions are given for cylindrical geometries currently used in engineering.

It is pointed up that this method is more flexible than the use of handbooks which, in spite of their great interest, cannot foresee all the geometries and loads which are met in engineering problems.

**KEY WORDS:** crack propagation, fracture properties, stress intensity, stresses, elastic theory, weight function, plane problems, axisymmetric problems

### Existence of an Influence Function

Let us consider a plane or axisymmetric symmetrical body (Fig. 1a and b), with a straight crack of length  $l$  on the axis  $Ox$ . Let a force  $F$  be applied

<sup>1</sup> Société Creusot-Loire, Branche Mécanique et Entreprise, Paris, France.

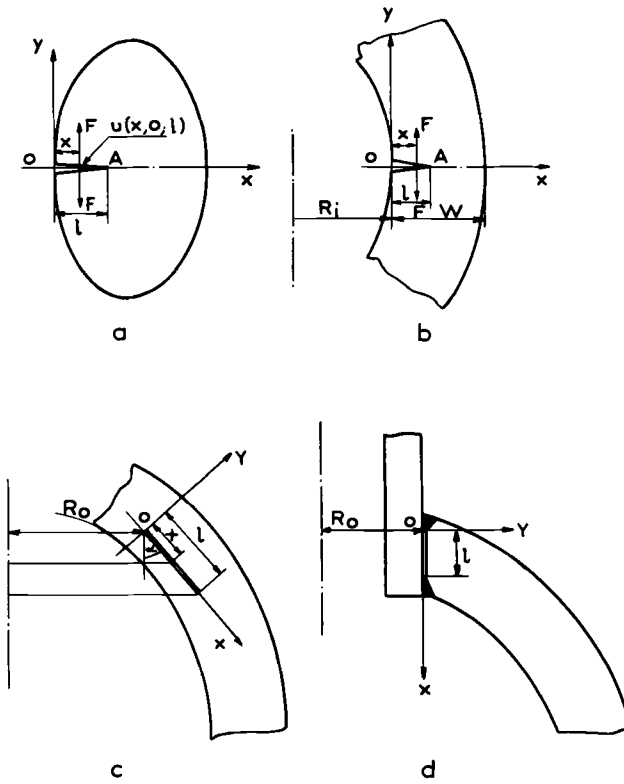


FIG. 1—(a) Plane, (b, c, d) axisymmetric.

on both sides of the crack at abscissa  $x$  ( $0 \leq x \leq l$ ) on a line of action of length  $s(x) = t$ , thickness of the plane body, or  $s(x) = 2\pi(R_i + x)$  on the axisymmetric body. This force results in a stress intensity factor  $K_{IF}(x, l)$ . An influence function can be defined as

$$G_I(x, l) = \frac{s(x)}{F} K_{IF}(x, l) \tag{1}$$

and is equal to the  $K_I$  resulting from the unit force per unit length of the line action  $s(x)$  applied at abscissa  $x$ .

$G_I(x, l)$  depends on all the geometric parameters of the cracked body and on this geometry only.

In fact, a finite force  $F$ , concentrated on a line  $s(x)$  is a theoretical concept. A pressure  $p(x)$  applied on a surface  $s(x)dx$  and equal to the

stress which would exist on the crack line if there was no crack  $[l]^2$  must be considered. This results in an infinitesimal stress intensity factor

$$dK_1(x,l) = G_1(x,l)p(x)dx$$

The  $K_1$  for the whole crack is

$$K_1(l) = \int_0^l G_1(x,l)p(x)dx \quad (2)$$

$G_1(x,l)$  is in a restricted sense, the Green's function for this problem. Emery et al [2] published curves giving functions  $G_1(x,l)$  for strips of finite length calculating stress intensity factors resulting from thermal stresses, but such functions were not published for other plane or axisymmetric geometries which are common in engineering.

Symmetry, with respect to the crack line, has been assumed. The same definition would be possible for Modes II and III for plane bodies and Mode II for axisymmetric bodies. We shall consider only Mode I, omitting the subscript I. Our reasoning can be extended to Modes II and III.

#### Relationship Between the Influence Function and the Compliance

A pressure  $p(x)$  applied at abscissa  $x$  on the surface  $s(x)dx$  results in an opening or double displacement, at the same abscissa  $x$

$$dv(x,l) = 2du(x,l) = 2C(x,l)p(x)s(x)dx$$

The associated energy of deformation is of the second order

$$d^2P(x,l) = -\frac{1}{2} p(x)s(x)dx dv(x,l) = -[p(x)s(x)dx]^2 C(x,l)$$

The length of the crack tip line being  $s(l)$ , the energy release rate in a virtual extension  $dl$  of the crack is

$$d^2g = -\frac{1}{s(l)} \frac{\partial}{\partial l} (d^2P) = \frac{[p(x)s(x)dx]^2}{s(l)} \frac{\partial C(x,l)}{\partial l}$$

<sup>2</sup> The italic numbers in brackets refer to the list of references appended to this paper.

and in plane strain

$$dK = \left[ \frac{Ed^2g}{1 - \nu^2} \right]^{\frac{1}{2}} = p(x)s(x)dx \left[ \frac{E}{1 - \nu^2} \frac{1}{s(l)} \frac{\partial C(x,l)}{\partial l} \right]^{\frac{1}{2}}$$

$$dK = \frac{s(x)}{s(l)} \left[ \frac{E}{1 - \nu^2} s(l) \frac{\partial C(x,l)}{\partial l} \right]^{\frac{1}{2}} p(x)dx$$

By comparison with Eq 2 we find the relationship

$$G(x,l) = \frac{s(x)}{s(l)} \left[ \frac{E}{1 - \nu^2} s(l) \frac{\partial C(x,l)}{\partial l} \right]^{\frac{1}{2}} \tag{3}$$

For a plane problem  $s(x) = s(l) = t$

$$G(x,l) = \left[ \frac{E}{1 - \nu^2} t \frac{\partial C(x,l)}{\partial l} \right]^{\frac{1}{2}} \tag{4}$$

For an axisymmetric problem

$$s(x) = 2\pi(R_i + x) \quad s(l) = 2\pi(R_i + l) \tag{5}$$

$$G(x,l) = \frac{R_i + x}{R_i + l} \left[ \frac{E}{1 - \nu^2} 2\pi(R_i + l) \frac{\partial C(x,l)}{\partial l} \right]^{\frac{1}{2}} \tag{6}$$

**Weight Function**

Bueckner [3,4] has introduced so called fundamental fields. Any such field has a singularity at the crack tip where the displacements are infinite; they are in the order of  $d^{-\frac{1}{2}}$  at the distance  $d$ . The field is regular everywhere else; it has no boundary tractions. Its boundary displacements yield weight functions. In particular a normal displacement  $M(x,l)$  along the crack leads to

$$K(l) = \sqrt{\frac{2}{\pi}} \int_0^l M(x,l)p(x)dx \tag{7}$$

for plane problems and to

$$K(l) = \sqrt{\frac{2}{\pi}} \int_0^l \frac{R_i + x}{R_i + l} M(x,l)p(x)dx \tag{8}$$

for axisymmetric ones.

Comparison with Eq 3, for plane and axisymmetric problems yields

$$M(x,l) = \sqrt{\frac{\pi}{2}} \frac{s(l)}{s(x)} G(x,l) = \left[ \frac{\pi E}{4(1-\nu^2)} s(l) \frac{\partial C(x,l)}{\partial l} \right]^{\frac{1}{2}} \quad (9)$$

By considering the singular displacement field, Bueckner has shown that  $M(x,l)$  is singular at the crack tip and that

$$M(x,l) = (l-x)^{-\frac{1}{2}} + M^*(x,l)$$

with a bounded  $M^*$ .

Consequently, the influence function  $G(x,l)$  has a similar behavior.

For numerical calculation,  $G(x,l)$  and  $M(x,l)$  are equivalent. Since we shall make use of basic properties of weight functions and related information in the open literature, we shall drop the reference to influence functions from here on.

It is advantageous to use the nondimensional and nonsingular function

$$m(x,l) = M(x,l)[l-x]^{\frac{1}{2}} \quad (10)$$

with  $m(l,l) = 1$ .

This dimensionless weight function is the same for homothetical bodies. It depends on the geometrical dimensionless parameters  $\alpha_i$  defining the uncracked body, and  $\beta_j$  defining the crack.  $M(x,l)$  depends also upon the characteristic length of the body.

To compute  $p(x)$  the  $\alpha_i$  must be known. Further, the  $\beta_j$  must be specified if  $p(x)$  depends on the position of the crack. Dimensionless coordinates  $x/l$  or  $x/W$  (Fig. 1) can be used.

Bueckner has given the weight functions for an infinite strip ( $l/W \leq 0.5$ ) [4]

$$m\left(\frac{x}{l}, \frac{l}{W}\right) = 1 + m_1\left(\frac{l}{W}\right) \left(1 - \frac{x}{l}\right) + m_2\left(\frac{l}{W}\right) \left(1 - \frac{x}{l}\right)^2 \quad (11)$$

where  $m_1(l/W)$  and  $m_2(l/W)$  are polynomials in  $l/W$ .

Symmetry may be necessary insofar as the simple relationship previously mentioned between  $dK$  and  $d^2g$  is concerned. Weight functions are not so restricted but apply in a more general manner [3,4]. Some fundamental fields can be obtained by differentiation, with respect to a parameter, of an ordinary field. In this context Rice [5] has demonstrated that if a load  $L_1$  is applied on a plane or axisymmetric body resulting in a

stress intensity factor  $K^{(1)}(l)$  and displacements  $u^{(1)}(x,y,l)$  on a line  $\Gamma$ , the function

$$h(x,y,l) = \frac{E}{2(1-\nu^2)} \frac{1}{K^{(1)}(l)} \frac{\partial u^{(1)}(x,y,l)}{\partial l} \tag{12}$$

is a weight function for the calculation of  $K^{(2)}(l)$  under any other load  $L_2$  applied along  $\Gamma$ .

For loads  $L_2 = p(x)$  applied on the crack sides one finds

$$h(x,o,l) = \frac{1}{\sqrt{2\pi}} M(x,l) = \frac{1}{2} \frac{s(l)}{s(x)} G(x,l) \tag{13}$$

The simple integral from zero to  $l$  is then replaced by a contour integral along both sides of the crack.

**Calculation of the Crack Opening Displacement in a Dugdale Model**

With this model in a plane problem, the plastic zone extends to a length  $l'$  such that

$$\sqrt{\frac{\pi}{2}} K(l') = \int_0^{l'} M(x,l)p(x)dx - \sigma_{ys} \int_l^{l'} M(x,l')dx = 0$$

This equation can be numerically solved for  $l'$ . According to Rice [5] and Eqs 12 and 13, along a crack of length  $l$

$$\frac{\partial u(x,o,l)}{\partial l} = \sqrt{\frac{2}{\pi}} \frac{1}{E_1} M(x,l)K(l)$$

The crack opening displacement (COD) is the opening at  $x = l$  for the crack length  $l'$

$$\delta = 2u(l,o,l') = \sqrt{\frac{2}{\pi}} \frac{2}{E_1} \int_l^{l'} M(l,\lambda)K(\lambda)dx$$

**Calculation of Weight Functions by Finite Element**

The finite element Code TITUS [9] was found convenient to calculate the nondimensional weight function  $m(x,l)$  through the compliances, as explained previously. Calculations could be done at low cost for bidimensional, plane, and axisymmetric geometries, Fig. 2.

Figure 3 gives a schematic representation of the finite element mesh along the crack, which extends the length  $l_p$  from zero to node  $p$ . For the

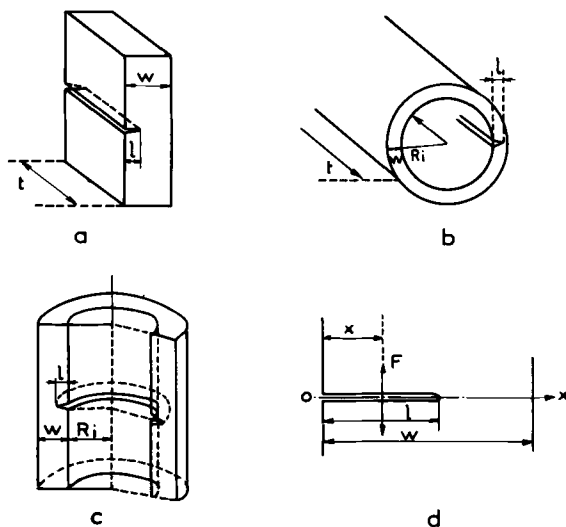


FIG. 2—Plane and cylindrical cracked bodies.

longest crack,  $l_n$ , the force  $F_j$  is applied at node  $j$  along the length  $s(x,y)$ . The equilibrium condition can be expressed through the compliance matrix  $C_{ij}$  which links the opening of the crack  $v_i^{(n)}$  at node  $i$  to the force  $F_j$

$$v_i^{(n)} = 2u_i^{(n)} = 2C_{ij}^{(n)}F_j \tag{14}$$

For crack length  $l_p < l_n$ , the equilibrium conditions can be obtained from the preceding one by closing the crack between  $l_n$  and  $l_p$ . In the finite element analysis, this is obtained by imposing the  $n - p$  conditions

$$u_p = u_{p+1} = \dots = u_{n-1} = 0$$

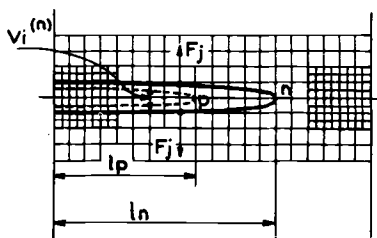


FIG. 3—Finite element mesh near a crack.

The compliance matrix  $C_{ij}^{(p)}$  for the crack length  $l_p$  is obtained by using these conditions to transform the system of  $n - 1$  linear equations (Eq 14) with  $n - 1$  unknowns,  $F_j$  into a system of  $p - 1$  linear equations with  $p - 1$  unknowns, eliminating the  $n - p$  unknowns,  $F_p, \dots, F_{n-1}$

$$u_i^{(p)} = C_{ij}^{(p)} F_j \quad (15)$$

Thus for any crack of length  $l_p$ , this method allows us to calculate the nondimensional weight function  $m(x_i, l_p)$  as defined by Eqs 9 and 10.

For a plane body

$$m(x_i, l_p) = \left[ \frac{\pi E}{2(1 - \nu^2)} t(l_p - x_i) \frac{C_{ii}^{(p+1)} - C_{ii}^{(p)}}{l_{p+1} - l_p} \right]^{\frac{1}{2}} \quad (16)$$

For an axisymmetric body

$$m(x_i, l_p) = \left[ \frac{\pi E}{2(1 - \nu^2)} 2\pi(R_i + l_p)(l_p - x_i) \frac{C_{ii}^{(p+1)} - C_{ii}^{(p)}}{l_{p+1} - l_p} \right]^{\frac{1}{2}} \quad (17)$$

After the compliance matrix  $C_{ij}^{(n)}$  has been calculated, the matrixes  $C_{ij}^{(n-1)}, \dots, C_{ij}^{(p+1)}, C_{ij}^{(p)}, \dots$  can be easily obtained in successive steps, and the weight functions determined by Eqs 16 and 17. Thus, the calculations of the nondimensional weight functions for the values of  $l$  allowed by the mesh requires the solving of only one elastic problem.

### Checking the Method

An accuracy of 5 percent was considered sufficient for current engineering problems. The elements and refinement of the mesh were determined arriving at an agreement within 5 percent with the known solutions for  $K$  given by Gross and Bowie [6] of the problem of an infinite strip under a uniform tension. This was obtained by using isoparametric elements with 12 degrees of freedom and 38 nodes in the section.

The results for  $K$  were also checked for other known problems: (a) a round bar with an external round crack (Bueckner [8]) (Fig. 4) and (b) a hollow cylinder with a long axial crack under pressure (Bowie and Freese [7]) (Fig. 5). For both problems an agreement better than 5 percent was found.

Some difficulties were met for very shallow cracks. It was not necessary for the range of interest in this work to modify the mesh rather deeply since the values of  $K$  for such cracks are known. But a finer mesh might be necessary for shallow cracks in thick cylinders (Fig. 5).

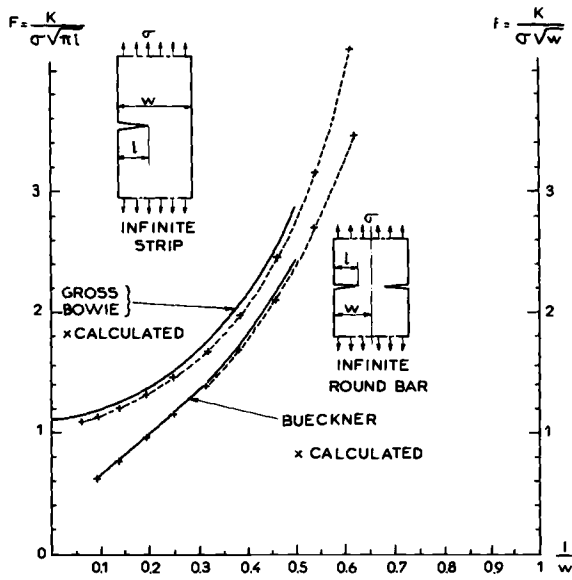


FIG. 4—Infinite strip and infinite round bar.

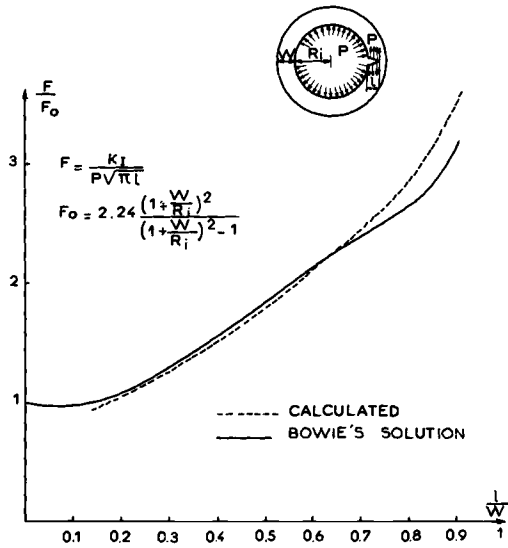


FIG. 5—Axially cracked long cylinder under internal pressure  $R_i/W = 2$ .

The check for the weight functions was done by comparing the results given by Bueckner [4] for an infinite strip. It was then found that a finer mesh was necessary near the faces of the wall (Fig. 3). After this modification an excellent agreement with Bueckner's results was found (Fig. 6). Because of the behavior of the weight function near the crack tip,  $m(l,l) = 1$ , difficult and inaccurate calculations in this region were avoided (Fig. 7).

**Weight Functions for Plane and Cylindrical Problems**

The values of the functions  $m(x/W, l/W)$  obtained for a few geometries, commonly used in engineering, are given by curves for (a) an infinite strip (Fig. 6); (b) a long cylinder  $R_i/W = 5$  with a long axial crack (Fig. 8) and a circumferential crack (Fig. 9); and (c) a long cylinder  $R_i/W = 10$  with a long axial crack (Fig. 10) and a circumferential crack (Fig. 11).

Since the result is rather sensitive to the length of the cylinder kept for the calculations, the length  $5/\beta = 5[(R_i + W/2)W]^{1/2}/[3(1 - \nu^2)]^{1/4}$  was necessary.

On Fig. 12 the influence of the geometry on the weight functions appears clearly. The five curves give  $m(x/W)$  with  $l/W = 0.46$  for an infinite strip, internal axial, and circular cracks, in a cylinder with  $R_i/W = 5$  and  $R_i/W = 10$ . They show that, for a given applied stress field, decreasing values of the weight function and consequently of  $K$  are found for a plate, a cylinder with a long axial crack, and a circumferentially cracked cylinder, with decreasing  $R_i/W$ . Approximating a cracked

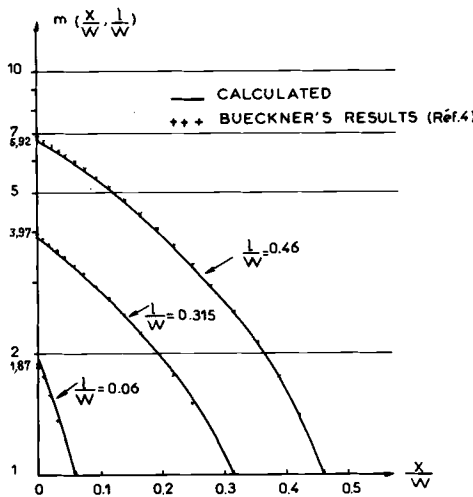


FIG. 6—Function  $m(x/W, l/W)$  for an infinite strip.

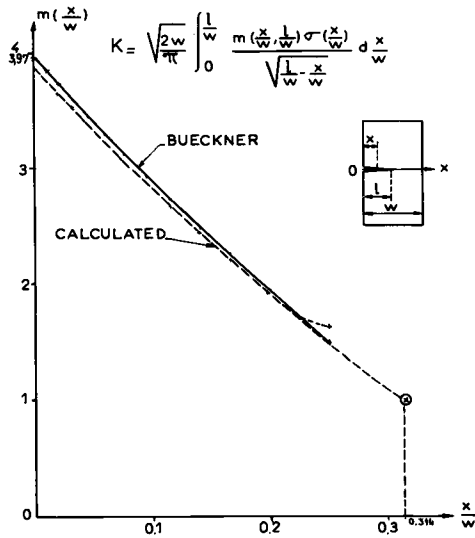


FIG. 7—Infinite strip  $l/W = 0.314$ .

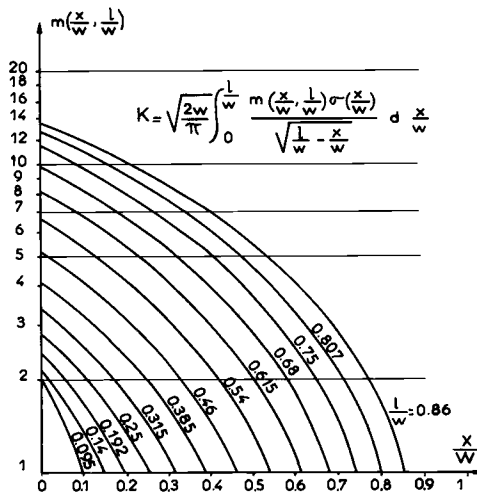


FIG. 8—Axially cracked long cylinder  $R_1/W = 5$ .

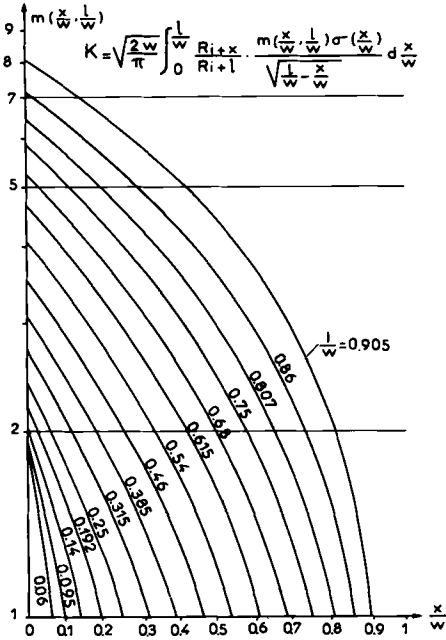


FIG. 9—Circumferentially cracked long cylinder  $R_1/W = 5$ .

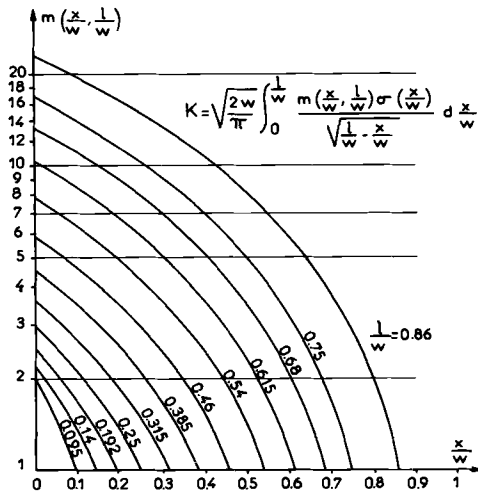


FIG. 10—Axially cracked long cylinder  $R_1/W = 10$ .

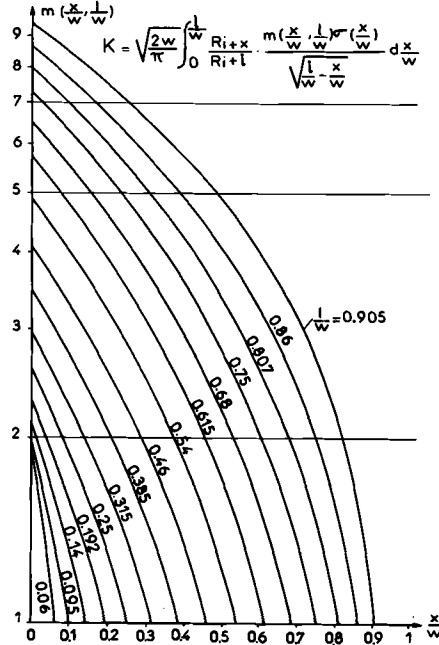


FIG. 11—Circumferentially cracked long cylinder  $R_i/W = 10$ .

cylinder by a cracked strip may be very pessimistic when  $R_i/W$  is not very large.

Weight functions were calculated for internal cracks only, and the eventuality of a nonmonotonic variation for large  $R_i/W$ , as evidenced by Emery [11] for the stress intensity factor of externally cracked pressurized cylinders, was not investigated.

The singularity of the weight functions shows that the stresses near the crack tip have a much more important weight than the stresses far from it. When the crack enters the compressive zone of a thermal stress field, negative elements of the integral appear which may result in a decrease of  $K$  and the crack arrest.

It would be easy to calculate weight functions for other plane or axisymmetric geometries.

**Comparison with Another Method**

Results for the calculation of the stress intensity factors for axial and circumferential cracks in infinite cylinders are presented by Buchalet and Bamford [10] at this meeting. Instead of the weight functions, polynomial influence factors  $F_1, F_2, F_3, F_4$  are used, such that for the load

$$\sigma(x) = A_0 + A_1x + A_2x^2 + A_3x^3 \quad (0 \leq x \leq l)$$

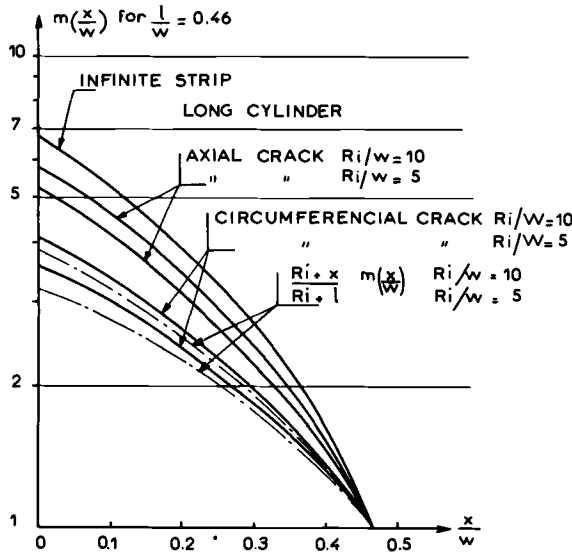


FIG. 12—Function  $m(x/w)$  for  $L/W = 0.46$ .

the stress intensity factor is

$$K = \sqrt{\pi l} \left[ A_0 F_1 + \frac{2l}{\pi} A_1 F_2 + \frac{l^2}{2} A_2 F_3 + \frac{4l^3}{3\pi} A_3 F_4 \right]$$

or

$$K = \sqrt{\pi l} \left[ A_0 f_0 + l A_1 f_1 + l^2 A_2 f_2 + l^3 A_3 f_3 \right]$$

To allow a comparison between both methods, the weight functions of Figs. 10 and 11 were used to calculate the factors  $f$  or  $F$ .

$$f_n = \frac{\sqrt{2}}{\pi} \int_0^1 \frac{m\left(\frac{x}{l}, 1; \frac{R_i}{W}\right)}{\sqrt{1 - \frac{x}{l}}} \left(\frac{x}{l}\right)^3 d\left(\frac{x}{l}\right)$$

resulting from the application on the crack sides of the nondimensional pressures

$$1, \frac{x}{l}, \left(\frac{x}{l}\right)^2, \left(\frac{x}{l}\right)^3$$

for axial and circumferential cracks in a cylinder with  $R_i/W = 10$  (Figs. 13 and 14). The coincidence was found very good. The differences

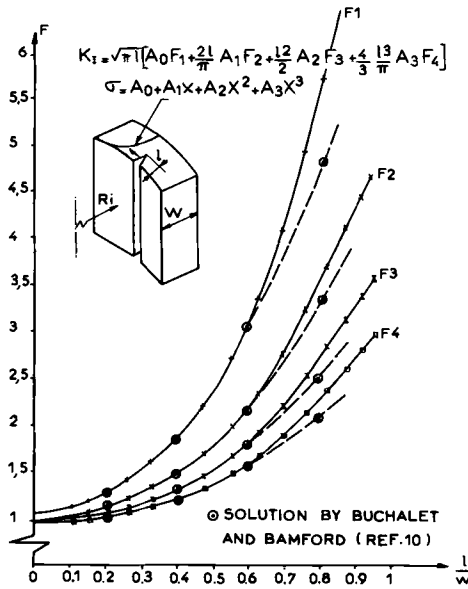


Fig. 13 - POLYNOMIAL INFLUENCE FUNCTIONS AXIAL CRACK  $\frac{R_i}{W} = 10$

FIG. 13—Polynomial influence functions axial crack  $R_i/W = 10$ .

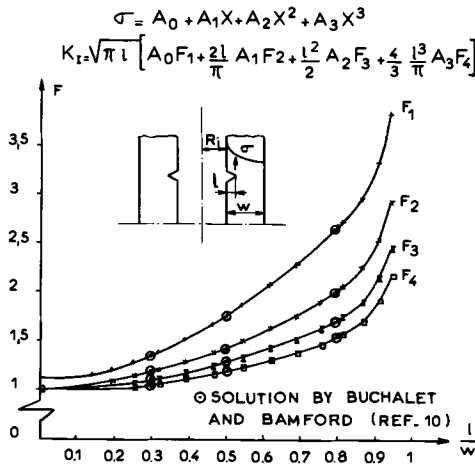


FIG. 14—Polynomial influence functions circumferential crack  $R_i/W = 10$ .

for deep axial cracks can be attributed to errors in the stiffness or the cracked ring which it is difficult to avoid. So deep cracks have no practical importance.

### Conclusion

The use of the weight function is very efficient for calculating the stress intensity factor resulting from any load applied to any cracked body in a two dimensional problem, plane or axisymmetric. When the weight function is known, the calculation of  $K$  is reduced to a very simple integral and requires only the calculation of the stress along the crack line in the uncracked body, which is a nonsingular elasticity problem. In this way it is possible to avoid the rather difficult use of handbooks, which, in spite of their great interest, cannot foresee the variety of geometries and loads which are met in engineering problems.

A rather simple method by finite elements for the numerical calculation of the weight functions has been presented. This method was applied to normal stresses on the crack surface. It can be extended to problems with shear stresses but not to mixed mode problems.

Using weight functions makes it possible to avoid such approximations as replacing a cylinder by a plane, assuming that  $K$  is determined only by the stress at the location at the crack tip, which are allowable in certain cases but may be wrong in others, particularly when rapidly varying stresses are involved.

The importance of the applied stress field near the crack tip is emphasized by the singularity of the weight function, and this explains how cracks may arrest in the compressive region of a thermal stress field.

### Acknowledgments

The authors acknowledge with pleasure helpful discussions with Professors J. R. Rice, Brown University, and D. Radenkovic, Ecole Polytechnique, Paris. This study was supported by the Délégation Générale à la Recherche Scientifique et Technique, under contract 71-7-2885.

### References

- [1] Bueckner, H. F., *Transactions*, American Society of Mechanical Engineers, Aug. 1958, pp. 1226-1230.
- [2] Emery, A. F., Walker, G. E., and Williams, J. A., *Journal of Basic Engineering*, Dec. 1969, pp. 618, 624.
- [3] Bueckner, H. F., *Zeitschrift für Angewandte Mathematik und Mechanik*, 1970, p. 529.
- [4] Bueckner, H. F., *Methods of Analysis and Solutions of Crack Problems*, Chapter V, G. C. Sih, Ed., Noordhoff International Publishing, Leyden, The Netherlands, 1973.
- [5] Rice, J. R., *International Journal of Solids and Structures*, 1972, p. 751.

- [6] Paris, P. C. and Sih, G. C. in *Fracture Toughness Testing and Its Applications*, ASTM STP 381, American Society for Testing and Materials, 1964, p. 30.
- [7] Bowie, O. and Freese, C. E., *Engineering Fracture Mechanics*, June 1972.
- [8] Bueckner, H. F., *Zeitschrift für Angewandte Mathematik und Mechanik*, Vol. 51, 1971, pp. 97-109.
- [9] Hasselin, G., Heliot, J., and Vouillon, C., Paper M 2/3, 2nd International Conference SMIRT, Berlin, 1973.
- [10] Buchalet, C. B. and Bamford, W. H., this publication, pp. 385-402.
- [11] Emery, A. F. and Segedin, C. M., *Journal of Basic Engineering*, 1972, pp. 387-393.

C. B. Buchalet<sup>1</sup> and W. H. Bamford<sup>1</sup>

## Stress Intensity Factor Solutions for Continuous Surface Flaws in Reactor Pressure Vessels

---

**REFERENCE:** Buchalet, C. B. and Bamford, W. H., "Stress Intensity Factor Solutions for Continuous Surface Flaws in Reactor Pressure Vessels," *Mechanics of Crack Growth, ASTM STP 590*, American Society for Testing and Materials, 1976, pp. 385-402.

**ABSTRACT:** A two-dimensional finite element method is used to develop stress intensity factor solutions for continuous surface flaws in structures subjected to an arbitrary loading. The arbitrary loading produces a stress profile  $\sigma$  acting perpendicularly to a given section  $S$  of the structure. The stress profile is represented by a third degree polynomial

$$\sigma = A_0 + A_1x + A_2x^2 + A_3x^3$$

Stress intensity factor solutions are developed for continuous surface flaws introduced in particular sections  $S$  in the structure considered. Solutions are developed for a surface flaw in a flat plate, for both circumferential and longitudinal flaws inside a cylindrical vessel, and for circumferential flaws at several locations inside a reactor vessel nozzle.

The superposition principle is used, and the crack surface is subjected successively to uniform ( $\sigma = A_0$ ), linear ( $\sigma = A_1x$ ), quadratic ( $\sigma = A_2x^2$ ), and cubic ( $\sigma = A_3x^3$ ) stress profiles. The corresponding stress intensity factors ( $K_I^{(0)}$ ,  $K_I^{(1)}$ ,  $K_I^{(2)}$ ,  $K_I^{(3)}$ ) are then derived for various crack depths using the calculated stress profile in the region of the crack tip. The total stress intensity factor corresponding to the cracked structure subjected to the arbitrary stress profile is expressed as the sum of the partial stress intensity factors for each type of loading.

$$K_I = K_I^{(0)} + K_I^{(1)} + K_I^{(2)} + K_I^{(3)} =$$

$$\sqrt{\pi a} \left[ A_0 F_1 + \frac{2a}{\pi} A_1 F_2 + \frac{a^2}{2} A_2 F_3 + \frac{4a^3}{3\pi} A_3 F_4 \right]$$

<sup>1</sup> Senior engineers, respectively, Westinghouse Nuclear Energy Systems, Pittsburgh, Pa. 15320.

where,  $a$  is the crack depth and  $F_1$ ,  $F_2$ ,  $F_3$ , and  $F_4$  are the magnification factors relative to the geometry considered. The results are presented in terms of magnification factors versus fractional distance through the wall ( $a/t$ ) and reveal the strong influence of the geometry of the structure and of the crack orientation.

The stress intensity factor solutions obtained using this method are compared to solutions obtained using other methods, when available. In the case of the plate geometry, the solution obtained for the linear loading ( $\sigma = A_0 + A_1x$ ) is shown to agree well with the boundary collocation solution reported by Brown and Srawley. The stress intensity factor solutions for the circumferential and longitudinal cracks in the cylindrical vessel compare well with solutions obtained by Labbens et al using the weight functions method proposed by Bueckner, and are also in good agreement with the solution for uniform loading ( $\sigma = A_0$ ) obtained using the line spring method proposed by Rice.

**KEY WORDS:** crack propagation, nuclear reactors, pressure vessels, fracture properties, mechanical properties, stresses, deformation

Reactor pressure vessels operate at high temperature ( $\sim 550^\circ\text{F}$ ), and, in general, brittle fracture is not a potential mode of failure of the reactor vessel. However, during postulated accidents such as the loss of coolant accident (LOCA), the temperature of the reactor coolant and, therefore, the temperature of the vessel may approach the transition temperature of the metal. A fracture mechanics evaluation of the component is thus necessary to demonstrate that its integrity would not be impaired under these postulated conditions.

The two most critical locations in the reactor vessel are the cylindrical portion of the vessel directly adjacent to the nuclear core (beltline), because it is subjected to neutron bombardment which degrades the material toughness, and the nozzle region, which is a geometrical discontinuity resulting in stress concentrations. Fracture mechanics analyses of these two critical regions require the determination of stress intensity factor solutions relative to the particular geometry of these regions. Furthermore, the steep stress gradients developed in the vessel wall during the postulated transients require that the actual stress profile be used in the stress intensity factor expressions. The stress intensity factor solutions usually found in the literature are for simple geometries, such as plates or infinite bodies, or for uniform tension and bending or both [1-3].<sup>2</sup>

Finite element models were used in the present work to derive stress intensity factor solutions for continuous surface cracks<sup>3</sup> in a plate, for continuous inside surface cracks in the cylindrical region of the reactor vessel, and in the nozzle region of the reactor vessel, for arbitrary loadings. The finite element solutions compare well with solutions ob-

<sup>2</sup> The italic numbers in brackets refer to the list of references appended to this paper.

<sup>3</sup> A continuous flaw is defined as an infinite or axisymmetric flaw.

tained using other methods and show the strong influence of the geometry on the magnification factors of the stress intensity factor expressions.

**Method**

The method used to determine the stress intensity factor solution consists of applying the superposition principle in the loading of the finite element model and in expressing the stress intensity factor in terms of the coefficients of a third degree polynomial representing the stress profile perpendicular to the section of the structure considered.

*Superposition Method*

Figure 1 illustrates the superposition principle. The stress intensity factor  $K_I$  for the crack in a section  $S$  of the structure, subjected to a remote loading ( $F, M$ ) represented by a force  $F$  and a moment  $M$ , is equal to the stress intensity factor  $K_I$  for the same crack in section  $S$  of the structure, where the crack surface is subjected to a stress profile  $\sigma(x)$  identical to the stress profile developed perpendicularly to the uncracked section  $S$  by the remote loading ( $F, M$ ).

*Stress Intensity Factor*

The stress profile  $\sigma(x)$  developed perpendicularly to section  $S$  of the reactor vessel wall during a transient, in the absence of flaw, can be fitted by a third degree polynomial

$$\sigma = A_0 + A_1x + A_2x^2 + A_3x^3 \tag{1}$$

A higher order polynomial could be used if necessary.

If a continuous surface crack is now assumed to be present in section  $S$  during the transient considered, the stress intensity factor may be

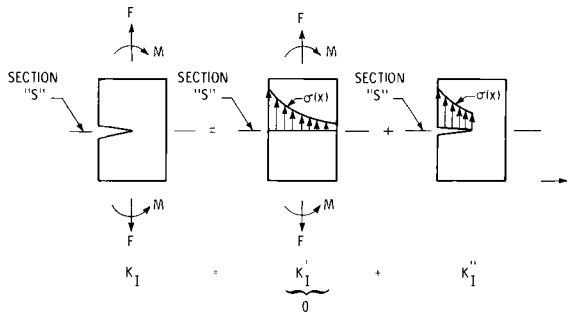


FIG. 1—Superposition principle.

conveniently expressed as follows

$$K_I = \sqrt{\pi a} \left[ A_0 F_1 + \frac{2a}{\pi} A_1 F_2 + \frac{a^2}{2} A_2 F_3 + \frac{4}{3\pi} a^3 A_3 F_4 \right] \quad (2)$$

$A_0, A_1, A_2,$  and  $A_3 =$  coefficients of the polynomial expression Eq 1 representing the stress profile  $\sigma(x)$  in the uncracked section  $S$

$a =$  crack depth, and

$F_1, F_2, F_3,$  and  $F_4 =$  magnification factors corresponding to the geometry analysed.

It is shown in the appendix that if  $F_1, F_2, F_3,$  and  $F_4$  in Eq 2 are taken equal to the front surface magnification factor 1.12 [4] Eq 3 represents the stress intensity factor for a continuous surface flaw in a semi-infinite body

$$K_I = 1.12 \sqrt{\pi a} \left[ A_0 + \frac{2a}{\pi} A_1 + \frac{a^2}{2} A_2 + \frac{4}{3\pi} a^3 A_3 \right] \quad (3)$$

In Eq 2, the magnification factors  $F_1, F_2, F_3,$  and  $F_4$  are functions of the cracked geometry and are independent from the type of loading. Thus, the magnification factors can be determined using any arbitrary stress profile applied to the crack surface. The magnification factors  $F_1, F_2, F_3,$  and  $F_4$  relative to a given crack depth  $a$  are determined by successively loading the crack surface with a uniform ( $\sigma = A_0$ ), linear ( $\sigma = A_1 x$ ), quadratic ( $\sigma = A_2 x^2$ ), and cubic ( $\sigma = A_3 x^3$ ) stress distribution. The procedure is then applied to other crack depths to determine the variation of the magnification factors  $F_1, F_2, F_3,$  and  $F_4$  with the crack depth to thickness ratio ( $a/t$ ). Figure 2 shows the various stress distributions applied to the surface of the crack and the equations used to determine in each case the corresponding magnification factor. Figure 3 shows how the stress intensity factor  $K_I^{(0)}$  is determined from the finite element solution for uniform loading. The same method is used to determine the stress intensity factors  $K_I^{(1)}, K_I^{(2)},$  and  $K_I^{(3)}$  corresponding to the other stress distributions.

For a value of  $r$  small enough compared to the crack depth  $a$ , it is known that the elastic stress distributions  $\sigma_x$  and  $\sigma_y$  in front of the crack can be expressed as follows [5]

$$\sigma_x = \frac{K_I}{\sqrt{2\pi r}} + \sigma_{x0} + O(r^{1/2}) \quad (4)$$

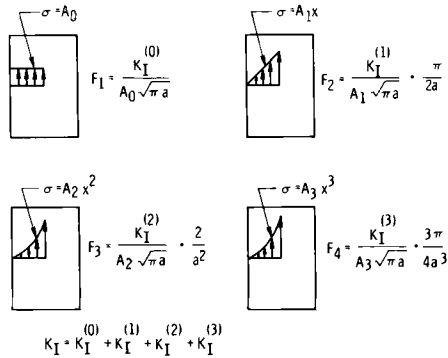


FIG. 2—Magnification factor determination.

$$\sigma_y = \frac{K_I}{\sqrt{2\pi r}} + 0(r^{1/2}) \tag{5}$$

From Eqs 4 and 5

$$\frac{\sigma_x + \sigma_y}{2} = \frac{K_I}{\sqrt{2\pi r}} + \frac{\sigma_{x0}}{2} + 0(r^{1/2}) \tag{6}$$

or

$$\frac{(\sigma_x + \sigma_y)}{2} \sqrt{2\pi r} \approx K_I + \frac{\sigma_{x0}}{2} \sqrt{2\pi r} \tag{7}$$

Equation 7 indicates that  $(\sigma_x + \sigma_y)/2\sqrt{2\pi r}$  is a linear function of  $\sqrt{2\pi r}$  when  $r$  is small compared to crack depth  $a$ . Thus, as shown in Fig. 3,  $K_I^{(0)}$  is obtained at the intercept of this linear function with the axis corresponding to  $r = 0$ . This method requires evaluation of the stresses in the immediate vicinity of the crack tip and, thus, a very refined grid in this region. The several elements immediately adjacent to the crack tip are never small enough to reflect the singularity accurately, but the method circumvents this problem in the linear extrapolation process. The stresses in the first several elements are discarded, but, for the model used, there are enough elements left within the singular region to allow accurate determination of  $K_I$ . This method was found to yield more accurate results than the method based on displacements, because it only requires linear

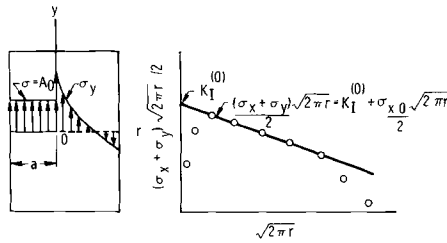


FIG. 3—Stress intensity factor determination.

extrapolations. Some of the results obtained were compared to those obtained using the J-integral technique and agreed within about 1 percent.

To calculate the stress intensity factor for a continuous surface crack in a particular section of the reactor vessel during a transient, the following steps must be followed:

1. For the transient analyzed, calculate the stress profile developed perpendicularly to the section considered, without the crack.
2. Fit the stress profile obtained by a third degree polynomial and obtain the coefficients  $A_0$ ,  $A_1$ ,  $A_2$ , and  $A_3$ .
3. Select the  $K_I$  expression applicable to the section of the vessel and to the crack orientation considered (Eq 2) and replace the coefficients  $A_0$ ,  $A_1$ ,  $A_2$ , and  $A_3$  by their values.
4. Calculate  $K_I$  for various crack depths  $a$ .

#### Crack Tip Model

Conventional constant strain elements were used in the model, and the finite element mesh is shown in Fig. 4, including the refined grid used in the crack tip region. In order to change easily the crack depth  $a$ , the square elements adjacent to the crack tip containing the extremely refined mesh can be removed from one location and placed at another location in the model. The renumbering of the nodes is not necessary due to the fact that the program used<sup>4</sup> utilizes the wave front method of solution. Figure 4 shows how the crack depth  $a$  can be changed by moving the elements adjacent to the crack tip.

#### Stress Intensity Factor Solutions

##### Plate

The finite element model of the plate is shown in Fig. 5. The plate thickness is  $t = 8.625$  in., and the height of the plate is two times the thickness  $t$  (it was verified that changing the height of the model did not change the results). The boundary conditions are indicated in Fig. 5.

<sup>4</sup> A general finite element program.

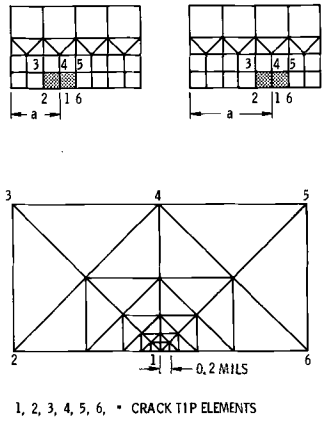


FIG. 4—Crack tip element.

For every crack depth  $a$  considered, the cracked surface is subjected to the loading sequence illustrated in Fig. 2 and described in the previous section. The stress intensity factor solution is shown in Fig. 6. The points in the figure represent the finite element solutions obtained for the seven crack depth value selected, 0.25, 0.5, 1, 2, 4, 6, and 7 in. The solid lines in the figure represent a best fit of the calculated points. The stress profile

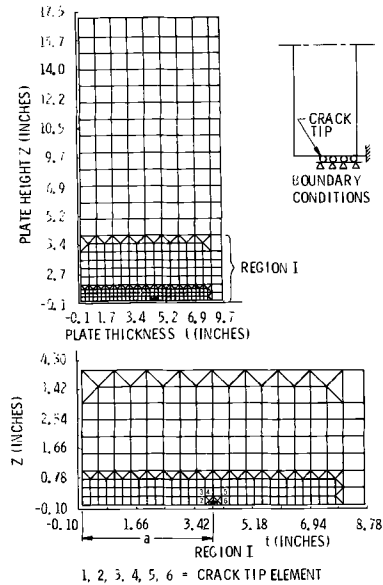


FIG. 5—Plate model.

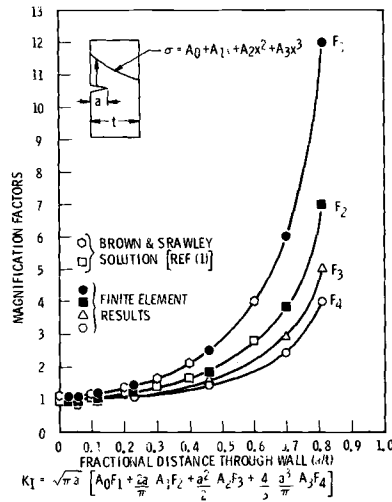


FIG. 6—Single edge cracked plate under arbitrary loading.

shown in the figure acting perpendicularly to the crack surface is the stress profile existing in the section when the crack is not present.

The results indicate that the principal factor  $F_1$  in the  $K_1$  expression corresponds to the uniform portion of the stress profile and that the higher the order of the terms in the polynomial stress distribution (Eq 1), the less influence these terms have on the  $K_1$  values.

The solution reported by Brown and Srawley [1] for the single edge cracked plate, under linear loading using a boundary collocation method, is also shown in Fig. 6 and agrees well with the finite element solution.

*Cylindrical Vessel – Circumferential Flaw*

The axisymmetric model is shown in Fig. 7. The thickness of the cylinder is  $t = 8.625$  in., and the inside radius is  $R = 86.5$  in. The height of the model ( $h$ ) is ten times the thickness  $t$ . This extension in model height is necessary to represent correctly the infinite cylinder. Figure 8 shows the relative deformations of the plate and of two models ( $h = 2t$  and  $h = 10t$ ) of the cylinder when the cracked surface is subjected to a uniform loading of 100 ksi. It is seen that the cylindrical model with  $h = 2t$  does not represent correctly the stiffness of an infinitely long cylinder, which represents<sup>5</sup> the geometry of the beltline of a reactor vessel. The actual

<sup>5</sup> The representation of the reactor vessel by an infinitely long cylinder is in fact, conservative when a continuous crack is assumed, because the motion of the extremities of the actual vessel is prevented by the bottom and top heads of the reactor vessel, thereby reducing the magnitude of the magnification factors in the stress intensity factor expression.

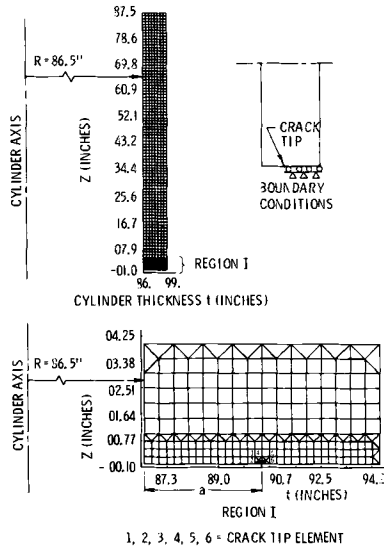


FIG. 7—Cylinder model - circumferential crack.

boundary conditions used are indicated in Fig. 7. Here again, the cracked surface is subjected to the loading sequence illustrated in Fig. 2.

The stress intensity factor solution for the circumferential crack under arbitrary loading is shown in Fig. 9. The solution corresponds to  $t/R$  equal to approximately 0.1 and was found independent of the absolute dimen-

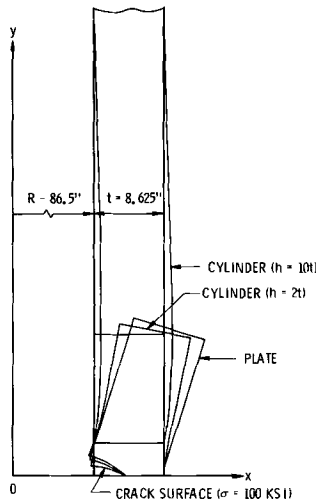


FIG. 8—Relative deformations for plate and cylinders.

sions of the cylinder. The points in the figure represent the finite element solution obtained for the various crack depths considered. The solid lines represent best fits of the calculated points, excluding those for small values of the crack depth, for which the finite element model does not reproduce accurately enough the actual stiffness of the geometry. Thus, the solid line corresponding to  $F_1$  is extrapolated to a value of 1.12 [4] for zero crack depth and the solid lines corresponding to  $F_2$ ,  $F_3$ , and  $F_4$  are extrapolated to a value of 1.0 for zero crack depth. The value of 1.0 is conservative since  $F_2$  is smaller than unity [1] for  $a/t$  equal zero and  $F_3$  and  $F_4$  are always smaller than  $F_2$ .

Qualitatively, the results are similar to the results obtained for the single edge cracked plate (Fig. 6), but the magnitude of the magnification factors for deep cracks is much less in the case of the circumferential crack in the cylinder, thereby showing the strong effect of the stiffness of the cracked geometry on the stress intensity factor.

The solution obtained by Labbens et al [6] for the same geometry, using Bueckner's weight functions [7] is shown in Fig. 10 and is in very good agreement with the finite element solution. The solution obtained using Rice's line spring method [8] is also shown in Fig. 9 for the case of uniform loading. This solution is in good agreement with the finite element solution.

#### *Cylindrical Vessel—Longitudinal Flaw*

The finite element model is shown in Figs. 11-13. The dimensions of the cylinder are the same as for the circumferential flaw. The same loading sequence is again applied to the crack surface. The stress intensity factor solution is shown in Fig. 14. The same extrapolation is made to extend the best fit solid lines to zero crack depth. The maximum value obtained for  $F_1$  ( $\sim 5$ ) indicates that this geometry is stiffer than the plate geometry and less stiff than the geometry obtained with a circumferential flaw in the cylinder.

The solution obtained using Rice's line spring model is shown in Fig. 14 (for uniform loading) and agrees with the finite element solution. Again, the solution obtained by Labbens et al using Bueckner's weight functions agrees with the finite element solution, as shown in Fig. 15.

#### *Nozzle Geometry*

The main reactor coolant pipes are connected to the cylindrical shell by the reactor vessel nozzles. In the analysis, the three dimensional nozzle geometry is axisymmetric around the nozzle axis; the cylindrical vessel is approximated by a sphere having a radius equal to twice the radius of the cylinder. The stress intensity factor solution is obtained for cracks located at three different regions in the nozzle. Region I is close to the pipe juncture where high thermal stresses may develop due to the difference in

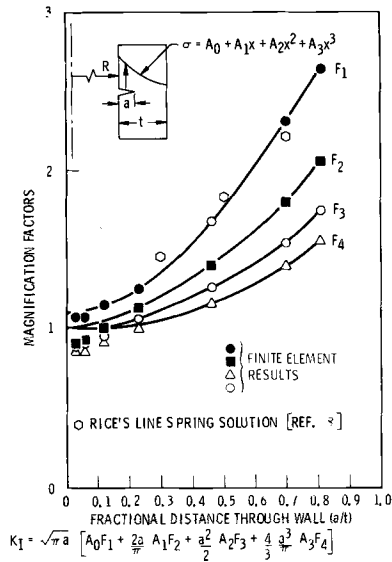


FIG. 9—Circumferential crack in cylinder ( $t/R = 0.1$ ).

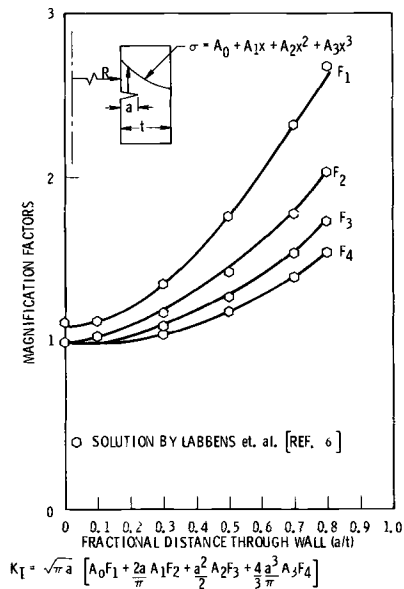


FIG. 10—Circumferential crack in cylinder ( $t/R = 0.1$ ) comparison with solution by Labbens et al [6].

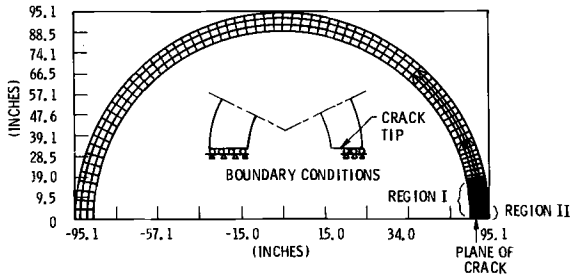


FIG. 11—Finite element model of reactor vessel bellline containing a longitudinal crack.

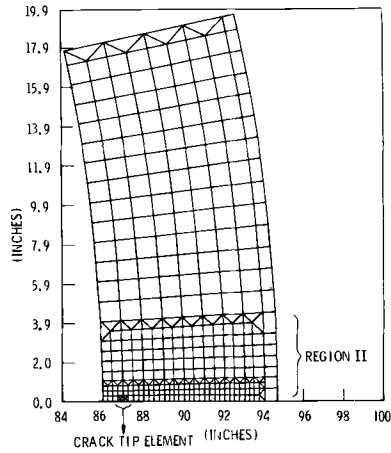


FIG. 12—Refinement of the grid in Region I of the model.

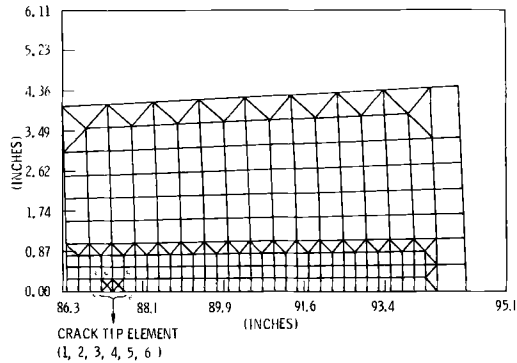


FIG. 13—Refinement of the grid in Region II of the model.

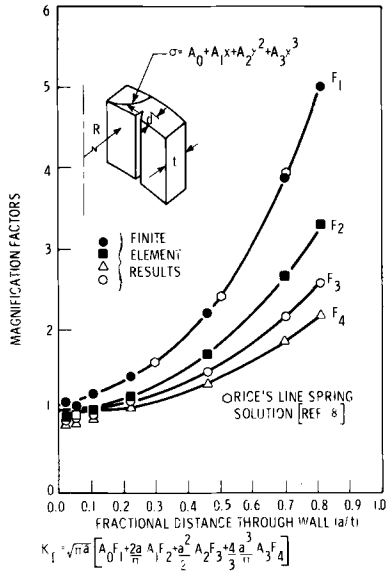


FIG. 14—Longitudinal crack in cylinder ( $t/R = 0.1$ ).

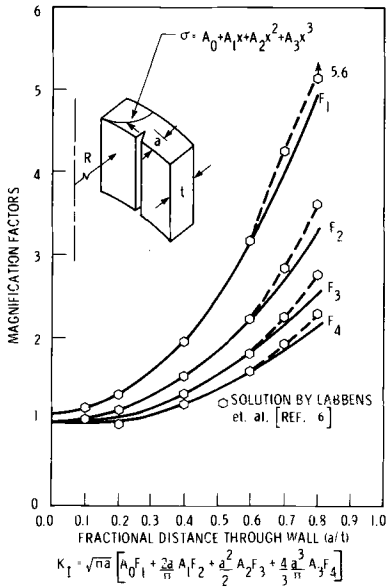


FIG. 15—Longitudinal crack in cylinder ( $t/R = 0.1$ ) comparison with solution by Labbens et al [6].

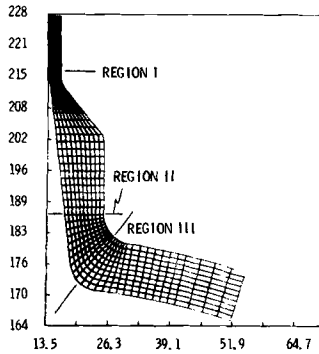


FIG. 16—Reactor vessel nozzle model.

the thermal expansion coefficients between stainless and carbon steels. Region II is at the nozzle reinforcement where the highest stresses develop during the thermal shock produced in the case of a reactor coolant pipe break (LOCA) [9]. Region III is at the nozzle corner where a stress concentration exists when the vessel is under pressure. Figure 16 shows the finite element model of the nozzle, including the three regions of interest. Figures 17-19 show the stress intensity factor solutions for the three regions in the nozzle.

Here again, for every crack depth considered, the same loading

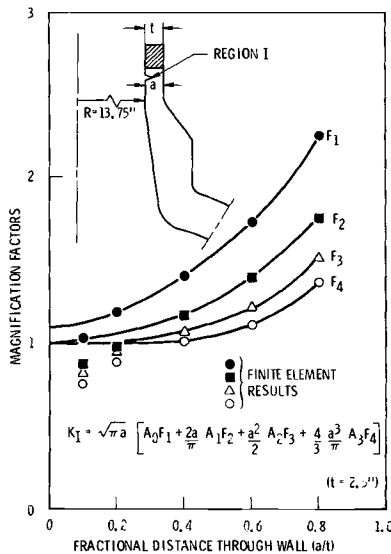


FIG. 17—Stress intensity factor for a circumferential crack in Region I of inlet nozzle ( $t/R = 0.18$ ).

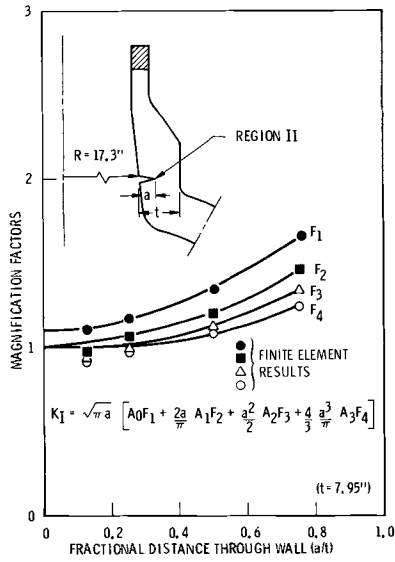


FIG. 18—Stress intensity factor for a circumferential crack in Region II of inlet nozzle ( $t/R = 0.46$ ).

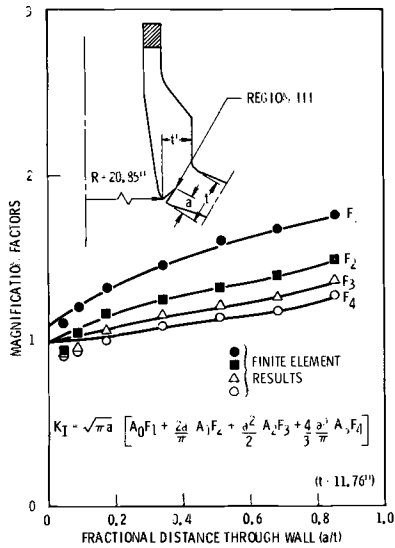


FIG. 19—Stress intensity factor for a circumferential crack in Region III of inlet nozzle ( $t/R = 0.34$ ).

sequence is applied to the cracked surface and results in the points shown in the figures. The  $K_1$  expressions determined can be applied to a given loading situation by using the stress profile developed perpendicularly to the uncracked section of the nozzle selected, as described previously. The maximum values of the  $F_1$  factors show that Region I is less stiff than Regions II and III. Region III presents the particularity that the curvature of the  $F$  functions is reversed for values of crack depth up to about 5.5 in. This result implies that for a given stress profile, the  $K_1$  values for shallow cracks are larger in Region III of the nozzle than in any other sections analyzed.

### Conclusion

Stress intensity factor solutions were obtained using two-dimensional finite element models for continuous surface cracks in a plate, cylinder, and nozzle under arbitrary loading. The following conclusions can be drawn.

1. For the plate and the cylindrical vessel, the finite element solutions agree with other solutions, thereby giving confidence in the solutions obtained for the nozzle geometry.

2. The amplitude of the magnification factors is a function of the stiffness of the cracked structure. The amplitude of the magnification factors decreases when the stiffness of the geometry increases. This is true when going from the plate to the cylinder and from the longitudinal to circumferential crack orientation. For a cylinder, moreover, the stiffness increases when the ratio of the thickness to radius ( $t/R$ ) increases. Thus, the magnification coefficients of the stress intensity factor solutions for Regions II and III. Region III presents the particularity that the curvature coefficients for the solution relative to the circumferential crack in the reactor vessel. This effect becomes increasingly important for cracks depths larger than 20 percent of the wall thickness.

## APPENDIX

### Stress Intensity Factor for a Continuous Surface Crack in a Semi-Infinite Body

Consider a through crack in an infinite body under a stress profile symmetric with respect to the middle of the crack, as shown in Fig. 20a. The stress intensity factor at Point A is as follows [10].

$$K_1 = \frac{1}{\sqrt{\pi a}} \left[ \int_{-a}^0 \sigma(-x) \left( \frac{a+x}{a-x} \right)^{1/2} dx + \int_0^a \sigma(x) \left( \frac{a+x}{a-x} \right)^{1/2} dx \right] \quad (8)$$

where

$$\int_{-a}^0 \sigma(-x) \left( \frac{a+x}{a-x} \right)^{1/2} dx = \int_0^a \sigma(x) \left( \frac{a-x}{a+x} \right)^{1/2} dx \tag{9}$$

thus

$$K_I = \frac{1}{\sqrt{\pi a}} \int_0^a \sigma(x) \left[ \left( \frac{a+x}{a-x} \right)^{1/2} + \left( \frac{a-x}{a+x} \right)^{1/2} \right] dx = \frac{2a}{\sqrt{\pi a}} \int_0^a \frac{\sigma(x)}{\sqrt{a^2-x^2}} dx \tag{10}$$

The stress profile  $\sigma(x)$  is expressed as a third degree polynomial as in Eq 1

$$\sigma(x) = A_0 + A_1x + A_2x^2 + A_3x^3$$

And Eq 10 becomes

$$K_I = \frac{2a}{\sqrt{\pi a}} \int_0^a \frac{A_0 + A_1x + A_2x^2 + A_3x^3}{\sqrt{a^2-x^2}} dx = \frac{2a}{\sqrt{\pi a}} \left[ A_0 \int_0^a \frac{dx}{\sqrt{a^2-x^2}} + \right. \tag{11}$$

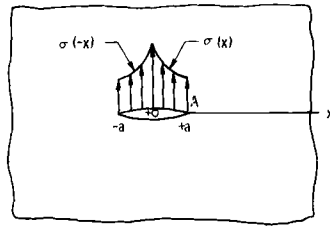
$$\left. A_1 \int_0^a \frac{x dx}{\sqrt{a^2-x^2}} + A_2 \int_0^a \frac{x^2 dx}{\sqrt{a^2-x^2}} + A_3 \int_0^a \frac{x^3 dx}{\sqrt{a^2-x^2}} \right]$$

Replacing the integrals in Eq 11 by their value, one obtains

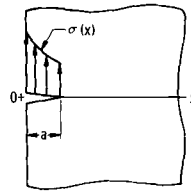
$$K_I = \sqrt{\pi a} \left[ A_0 + \frac{2a}{\pi} A_1 + \frac{a^2}{2} A_2 + \frac{4}{3\pi} a^3 A_3 \right] \tag{12}$$

The continuous surface crack in a semi-infinite body under an arbitrary stress profile  $\sigma(x)$  is shown in Fig. 20b. The stress intensity factor solution is obtained from Eq 12 corrected for free surface effect [4]

$$K_I = 1.12 \sqrt{\pi a} \left[ A_0 + \frac{2a}{\pi} A_1 + \frac{a^2}{2} A_2 + \frac{4a^3}{3\pi} A_3 \right] \tag{13}$$



a. THROUGH CRACK IN INFINITE BODY



b. CONTINUOUS SURFACE CRACK IN SEMI-INFINITE BODY

FIG. 20—Continuous cracks under arbitrary loading.

Note—In reality, the free surface correction factor strictly applies to the uniform component  $A_0$  of the stress profile. In Eq 13, the free surface correction factor is applied conservatively to all the components of the stress profile.

## References

- [1] Brown, W. F., Jr., and Srawley, J. E., *Plane Strain Crack Toughness Testing of High Strength Metallic Materials*, ASTM STP 410, American Society for Testing and Materials, 1966.
- [2] Shah, R. C. and Kobayashi, A. S., *Engineering and Fracture Mechanics*, Vol. 3, 1971, pp. 71-96.
- [3] Kobayashi, A. S., "On the Magnification Factors for Deep Surface Flaws," Structural Development Research Memorandum No. 16, The Boeing Company, Seattle, Wash., Dec. 1965.
- [4] Irwin, G. R., Krafft, J. M., Paris, P. C., and Wells, A. A., "Basic Aspects of Crack Growth and Fracture," Section 7 in Technology of Steel Pressure Vessels for Water-Cooled Nuclear Reactors, ORNL-NSIC-21, Oakridge National Laboratory, Dec. 1967.
- [5] Irwin, G. R., "Analysis of Stresses and Strains Near the End of a Crack Traversing a Plate," *Transactions*, American Society of Mechanical Engineers, *Journal of Applied Mechanics*, Vol. 79, 1957, pp. 361-364.
- [6] R. C. Labbens, A. Pellissier-Tanon, and J. Heliot, this symposium, pp. 368-384.
- [7] Bueckner, H. F. in *Methods of Analysis and Solutions of Crack Problems*, G. C. Sih, Ed., 1973, Chapter V, p. 239.
- [8] Levy, N. and Rice, J. R., "Surface Cracks in Elastic Plates and Shells," to be published by Brown University.
- [9] Buchalet, C. B. in *Fracture Analysis, Proceedings of the 1973 National Symposium on Fracture Mechanics, Part II*, ASTM STP 560, American Society for Testing and Materials, 1974, pp. 240-255.
- [10] Sih, G., Paris, P., and Erdogan, F., "Crack Tip Stress Intensity Factor for Plane Extension and Plate Bending Problems," *Transactions*, American Society of Mechanical Engineers, Vol. 84, Series E, 1962, pp. 306-312.

P. M. Besuner<sup>1</sup>

## Residual Life Estimates for Structures with Partial Thickness Cracks

---

**REFERENCE:** Besuner, P. M., "Residual Life Estimates for Structures with Partial Thickness Cracks," *Mechanics of Crack Growth, ASTM STP 590*, American Society for Testing and Materials, 1976, pp. 403–419.

**ABSTRACT:** This paper presents a practical approach for estimating residual fatigue life of structures with partial thickness cracks under arbitrary Mode I cyclic elastic stress fields. Residual life is defined herein as the number of cycles required to grow the crack from specified initial dimensions to some final configuration that results in static failure. A powerful influence function theory is modified for application to three-dimensional stress analysis of planar crack problems with arbitrary crack front shapes. The resulting procedure allows stress intensity factor solutions and residual fatigue life estimates for any Mode I stress field applied to the crack geometry.

Exact stress intensity factor solutions are presented for the buried ellipse under arbitrary Mode I stress fields. A procedure is outlined to build useful, accurate stress intensity factor algorithms for complex surface crack geometries from a few three-dimensional numerical stress analyses.

**KEY WORDS:** fatigue life, crack propagation, mechanical properties, stress gradients, structural analysis

A problem frequently encountered in thick safe-life structures is the presence of fatigue-initiated buried or surface cracks emanating from notch or material defect stress concentrations as in Figs. 1 and 2. If the cracks are small and do not completely penetrate the thickness, that is, are partial thickness (PT) cracks, they usually pose no immediate danger of brittle static failure in moderate or high toughness materials. The fundamental problem the cracks create is to decrease a structure's fatigue performance to that number of cycles  $N$  required to grow the crack to

<sup>1</sup> Analytical engineer, Failure Analysis Associates, Palo Alto, Calif. 94304. Formerly, senior analytical engineer, Pratt & Whitney Aircraft Division, United Aircraft Division, East Hartford, Conn. 06108.

critical dimension. Reasonable accuracy in estimating the residual life  $N$  is often of paramount importance to those responsible for structural integrity. Residual life estimates may be the sole rational basis for choosing design stresses in fatigue-critical hardware or for solving field problems through properly spaced inspections or new life limits.

Linear elastic fracture mechanics analysis forms the basis of predicting the residual fatigue life of a cracked structural element. The material is characterized in terms of its crack growth rate,  $da/dN$ , versus the cyclic change in the crack tip stress intensity factor,  $\Delta K$ ;  $K$  is a parameter which embodies the effects of the stress field, the crack size and shape, and the local structural geometry. The primary difficulty in analyzing the growth of PT cracks is that no one value of  $K$  may be assigned to characterize the entire crack front; furthermore, the stress state near the crack is three-dimensional due to crack shape and the local structural geometry.

In this paper, a new elastic fracture mechanics approach is given for predicting fatigue growth behavior of PT cracks under Mode I stress cycling. Mode I denotes symmetry of both loads and geometry with respect to the planar crack. Two extreme approaches theoretically may be

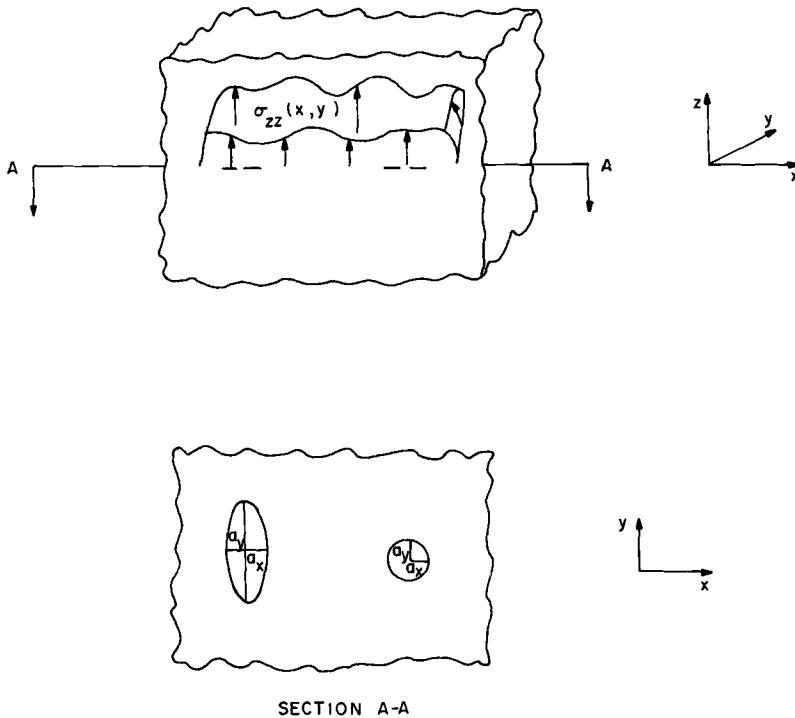


FIG. 1—Buried flaws (usually material defects).

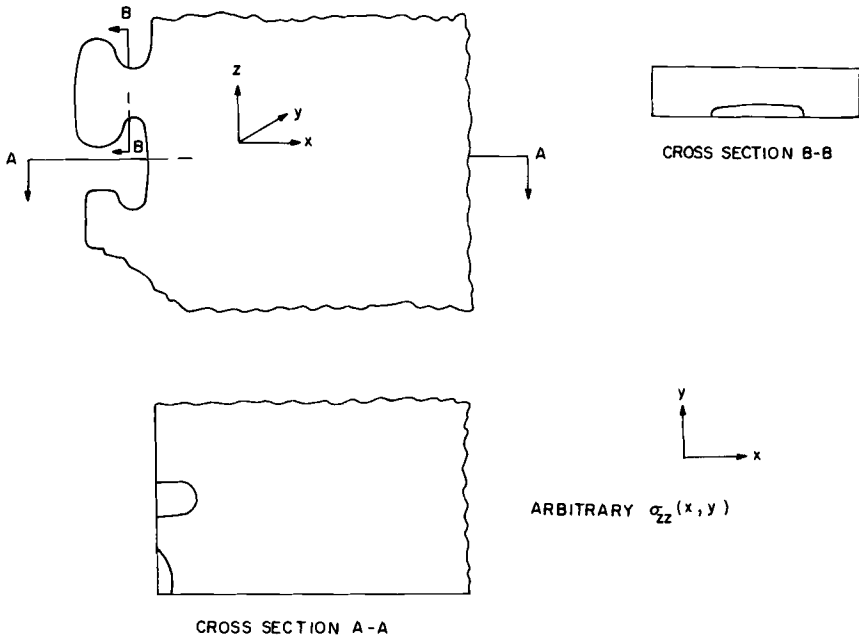


FIG. 2—Partial thickness surface cracks at stress concentrations.

employed to model this three-dimensional cracking problem. An engineering approach might consist of replacing the surface crack by an “equivalent” two-dimensional, or line crack, created mathematically by combining suitable analytical models with correction functions. Unfortunately, the correction functions contain unknown errors for a given problem and often can be selected only when the answer (life) is already known. The other extreme is to develop a special three-dimensional stress analysis model to reanalyze the crack geometry sequentially as it grows; this second approach requires a three-dimensional solution for the crack at each increment in its growth history and for each local stress distribution.

The residual life analysis procedure reported in this paper seeks to achieve the accuracy of three-dimensional stress analysis together with the efficiency of using equivalent two-dimensional crack models. The necessary stress intensity factor computation algorithm for a class of PT cracks is formulated from a small number of three-dimensional stress analyses. The stress analyses may be exact, as used in this paper, to formulate exact  $K$  solutions for the buried elliptical crack under arbitrary Mode I loading. The stress analyses may also be numerical, as is the boundary-integral equation method employed elsewhere [1],<sup>2</sup> to obtain  $K$

<sup>2</sup> The italic numbers in brackets refer to the list of references appended to this paper.

solutions for the quarter-ellipse “corner” crack under arbitrary Mode I loading. Stress intensity factors are computed and crack growth is simulated through the use of a weight function or influence function technique which uses the stresses in the uncracked structural detail. Thus, the details of both PT crack geometry and structural loading and shape are accounted for directly in the residual life prediction.

The next section of this paper presents a simplified crack growth modeling and residual life prediction procedure designed to cope with the complications of three-dimensional cracking accurately and efficiently. Two alternative definitions for approximating the PT crack front  $K$  variation are discussed. Following this section is a section on an influence function theory used to compute the stress intensity factors required for the employed residual life prediction procedure. The theory is applied in a section following this one to obtain exact expressions for the stress intensity factors of the buried elliptical crack under arbitrary Mode I loading. This section also exercises the residual life prediction procedure to calculate lives for buried elliptical cracks under a uniform and a parabolic stress field. A summary of the paper and a discussion of the current research to extend the life prediction procedure presented herein to more general crack models (for example, surface cracks) with the aid of numerical stress analysis is then given.

## **Residual Life Prediction Procedure**

### *Introduction*

Residual lifetime is defined herein as the number of constant load amplitude, nominally elastic stress cycles required to grow the crack from some defined initial configuration to a final size which will produce sudden failure, for example, catastrophic brittle fracture. Paris et al [2] and many later references document a currently accepted method for residual life prediction of two-dimensional cracking, that is, cracks with constant  $K(s)$  along the crack front periphery(s), using linear elastic fracture mechanics. Three-dimensional cracking has complications that are not explicitly treated by Paris et al. The complications are the crack front variation of  $K(s)$  and a tendency of crack shape, as well as size, to change during propagation.

Two concepts are introduced in this section to treat the three-dimensional cracking complications. The first concept is a method to approximate the growing crack's geometry with a finite number of characteristic dimensions and to approximate  $K(s)$  with the same number of discrete stress intensity factors, each associated with one characteristic dimension. The second concept, which is illustrated for a buried elliptical crack model, is a particularly useful definition of the discrete stress intensity factors that facilitates the application of an influence function

theory presented in the next section. This theory is used to build an algorithm for stress intensity factor computation for general loading from crack opening displacements due to a single loading. The algorithm eliminates the need for a full three-dimensional stress analysis for each new loading or each new increment of crack growth.

These two concepts are combined to form a procedure for residual lifetime prediction. The procedure is presented in general terms and is exercised for a specific model.

*Partial Thickness Crack Propagation Modeling*

The basis of reported life analyses is the notion of a finite number,  $n$ , of characteristic dimensions ( $(a_i, i = 1, . . . , n)$ ) to describe crack geometry. Crack propagation is then described by keeping track of the  $a_i$  which are named degrees of freedom (DOF). The continuous stress intensity factor function  $K(s)$  is approximated similarly with a set of discrete stress intensity factors ( $K_i, i = 1, . . . , n$ ), each associated with an  $a_i$ . The applied general empirical model of three-dimensional propagation is then expressed by a set of  $n$  equations

$$\frac{da_i}{dN} = F[K_i, \text{material, environment, history}] \tag{1}$$

where

- $N$  = residual lifetime,
- $K_i$  = stress intensity factor associated with  $a_i$ , and
- $F$  = empirically determined function.

Each equation in Eq 1 states that the local cyclic growth rate  $da_i/dN$  of freedom  $a_i$  is given by the empirically determined function  $F$ . Further, Eq 1 implies that all load and geometry information relevant to each  $da_i/dN$  is contained in one and only one stress intensity factor  $K_i$ . The function  $F$  is itself independent of load and geometry and may be obtained in the traditional way [2] from simple planar laboratory specimens modeled with two-dimensional stress analysis. The stress intensity factors  $K_i$  each contain an alternating component  $\Delta K_i$  and mean value  $K_{\text{mean } i}$  associated with the alternating and mean components of the stress cycle.

Residual life prediction is accomplished by formulation and solution of Eq 1. A four-step method is employed herein for life prediction. The steps are:

1. Obtain  $F$  from simple specimens,  $F$  is often expressed in the form of piecewise power functions of  $K$  (for example,  $da/dN = C\Delta K^B$ ) for given  $K_{\text{mean}}$ , material, environment and history combinations.
2. Determine the uncracked structural detail's geometry, loads, and to the extent required by Step 3, stress.
3. Model the propagating crack. This task includes selection of a model

with an adequate number of DOF; specification of the initial and final crack configuration  $a_{i1}$  and  $a_{fi}$ ; and definition of  $K_i$ . Further, an algorithm must be derived to compute all of the  $K_i$  as functions of stress and geometry, especially the changing crack geometry  $a_i$ .

4. Substitute  $K_i$  in Eq 1 and solve for the life  $N$ .

Steps 1 and 2 are not influenced strongly by three-dimensional cracking complications. Step 4 involves routine numerical analysis. Therefore, only Step 3 is emphasized in the remainder of this paper.

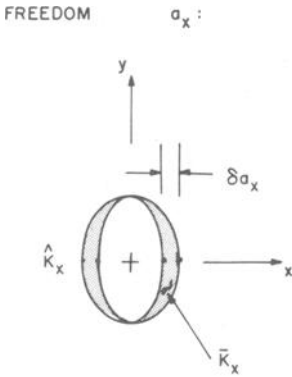
#### *Buried Elliptical Crack in an Infinitely Large Solid: Model and Stress Intensity Factor Definitions*

A simple model is desired to expand the procedure just outlined and to aid the discussion of stress intensity factor definitions. Figure 3 illustrates the chosen example model of a growing buried crack located in the  $x$ - $y$  plane, centered at the origin, and subjected to crack opening pressure  $p = \sigma_{zz}(x,y)$ . The crack front is an ellipse with semi-axes (along the coordinate axes)  $a_x$  and  $a_y$  being the two selected DOF. Having only two DOF, the model sacrifices a portion of the details of crack front geometry and  $K(s)$  variation inherent in more complex models with  $n > 2$ . However, the two DOF model is considered a worthwhile approximation of three dimensional cracking since it does permit some change of crack shape during propagation and promises relative ease of application. The choice of an elliptical model is an especially expedient example since published solutions serve as a starting point for derivation of stress intensity factor formulas discussed later.

Having chosen a model, the stress intensity factors  $K_i$  ( $K_x$  and  $K_y$ ) are to be defined and computed. The question of proper  $K$  definition for residual life computation may be debated, and two alternatives have been considered. The alternatives are illustrated in Fig. 3 as local (or end-point values)  $\hat{K}_x$  and  $\hat{K}_y$ , and "local average" values along specified portions of the crack front,  $\bar{K}_x$  and  $\bar{K}_y$ .

The two end-point values  $\hat{K}_x$  and  $\hat{K}_y$  are likely choices to characterize  $K(s)$  but are not necessarily the most accurate or expedient choices. The end-point values  $\hat{K}_x$  and  $\hat{K}_y$  may best describe the initial propagation rate of the semi-axes  $a_x$  and  $a_y$ . However, the elliptical modeling constraint raises questions as to whether  $\hat{K}_x$  and  $\hat{K}_y$  are the two quantities that best describe propagation of the entire crack front. Clearly, there is justification to consider other possible two DOF characterizations of  $K(s)$  than the two end-point values if some advantage can be gained therefrom.

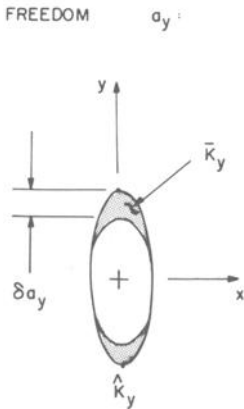
This paper investigates the two local averages  $\bar{K}_x$  and  $\bar{K}_y$  of  $K(s)$  depicted in Fig. 3 to define  $K_i$  for residual life computation. The  $\bar{K}_i$  have two equivalent physical interpretations. Each  $\bar{K}_i$  is related to the strain energy release rate obtained by creation of the corresponding surface area  $\delta A_i$  (shaded in Fig. 3). The area is formed by the perturbation



$$\bar{K}_x^2 = \frac{1}{\delta A_x} \iint_{\delta A_x} K^2(s) dA$$

$$\hat{K}_x = K(\pm a_x, 0)$$

$$\delta A_x = \pi a_y \delta a_x$$



$$\bar{K}_y^2 = \frac{1}{\delta A_y} \iint_{\delta A_y} K^2(s) dA$$

$$\hat{K}_y = K(0, \pm a_y)$$

$$\delta A_y = \pi a_x \delta a_y$$

FIG. 3—A two DOF buried elliptical crack.

of the associated  $a_i$  while holding all other DOF constant. Equivalently, the  $\bar{K}_i$  also represent the area root-mean-square (rms) value of  $K(s)$  in  $\delta A_i$ . Clearly, the rms interpretation indicates that the  $\bar{K}_i$  and  $\hat{K}_i$  definitions coincide for two special cases. The cases are constant  $K(s)$  and asymptotically large  $n$ .

The advantages sought with  $\bar{K}_i$ , rather than  $\hat{K}_i$ , definition are increases in the ease, generality, and accuracy of stress intensity factor computations for partial thickness cracks. The basis for these advantages is that the  $\bar{K}_i$  definition lends itself extremely well to an influence function theory of stress intensity factor computation. The next section presents the influence function theory and provides mathematical definition of the  $\bar{K}_i$  for a general planar partial thickness crack under Mode I loading.

**An Influence Function Theory for the Computation of  $\bar{K}_i$**

The analysis described in this section is an application of theoretical results due to Rice [3] and Key [4]. Reference 3 is the foundation and motivation for the weight or influence function theory presented herein, while Ref 4 proposes a quantity similar to the  $K$  definition for a static failure criterion.

To develop the required formulation consider Fig. 4, a homogeneous elastic body with loads and geometry symmetric about the  $x$ - $y$  crack plane which contains a crack of Area  $A$ . Assume the crack front,  $s$ , undergoes the  $i^{th}$  prescribed smooth virtual perturbation  $\delta l_i(s)$  (in a direction locally normal to  $s$ ) while under constant load. Then each point  $P_j$  will deflect elastically some amount  $\delta q_j/2$  in the direction of load  $Q_j$ . The work done on the solid due to  $\delta l_i(s)$  is

$$\delta W = Q_j \delta q_j - \mathcal{G}_i \delta A_i \text{ (bars indicate no summation over } i) \tag{2}$$

where the repeated index  $j$  implies summation and

$$\delta A_i = \int_s \delta l_i(s) ds = \frac{\partial A}{\partial a_i} \delta a_i \tag{3}$$

is the (upper) surface area exposed by perturbation  $\delta l_i$  which has the form

$$\delta l_i(s) = \frac{f_i(s)}{\int_s f_i(s) ds} \delta A_i = f_i(s) \delta a_i \tag{4}$$

where  $\delta a_i$  is the variation of the associated scalar degree of freedom  $a_i$  while holding any and all other degrees of freedom constant. Also,  $f_i(s)$  is a prescribed dimensionless function that defines perturbation shape such that the perturbed crack front configuration is characterizable in terms of the same discrete scalar degrees of freedom as the original crack configuration. Thus, only those crack front perturbations proportional to and arising from variation of each specified degree of freedom are considered in this paper. It would be incorrect to apply the results derived next to other possible classes of perturbations such as the more general class discussed in the Appendix of Ref 3. Finally

$$\mathcal{G}_i = \frac{\partial W}{\partial A_i} \tag{5}$$

is the strain energy release rate caused by  $\delta a_i$ .

For Mode I loading,  $\underline{G}_i$  may be written

$$\underline{G}_i \delta A_i = \int_s \left[ \frac{K^2(s)}{H} \delta l_i(s) \right] ds \tag{6}$$

where  $H$  is an appropriate elastic modulus. For an isotropic material in plane strain  $H = E/(1 - \nu^2)$ .

Since  $K(s)$  is generally not constant, one further definition is required; let

$$\bar{K}_i \equiv \sqrt{H \underline{G}_i} = h_{ij} Q_j \tag{7}$$

where the  $h_{ij}$  are elastic influence coefficients, associated with  $\bar{K}_i$  and point  $P_j$ , to be derived.

Equations 4, 6, and 7 are combined to obtain

$$\bar{K}_i^2 = \frac{\int_s K^2(s) f_i(s) ds}{\int_s f_i(s) ds} \tag{8}$$

Clearly,  $\bar{K}_i$  is an arc-length rms value of  $K(s)$  weighted by  $f_i$ . In other words,  $\bar{K}_i$  is the rms value of  $K$  in  $\delta A_i$  as shown in Fig. 3. Equation 2 may now be rewritten as

$$\delta W = Q_j \delta q_j - \frac{\bar{K}_i^2}{H} \delta A_i \tag{9}$$

where Eq 9 is a total differential for the class of perturbations just described since  $\delta A_i$  is due to and proportional to  $\delta a_i$ .

Equation 9 is identical in form to expressions given by Rice which include the stress intensity factor  $K$  for a two-dimensional crack rather than  $\bar{K}_i$  for the three-dimensional problem in Fig. 4. It can be shown that the influence function derivation in Ref 3, pp. 752-753, applied to Eqs 7 and 9 leads to

$$h_{ij} = \frac{\partial \bar{K}_i}{\partial Q_j} = \frac{H}{2 \bar{K}_i^*} \frac{\partial q_j^*}{\partial A_i} \tag{10}$$

where the superscripts\* denote any single reference loading state. The  $h_{ij}$  in Eq 10 may be regarded as influence coefficients since they measure the effects on  $\bar{K}$  of the loads  $Q_j$ . The  $h_{ij}$  are functions of position and the crack and structural geometry. However, as proven formally by Ref 3, the  $h_{ij}$  are independent of loading. Therefore, any advantageous loading can be

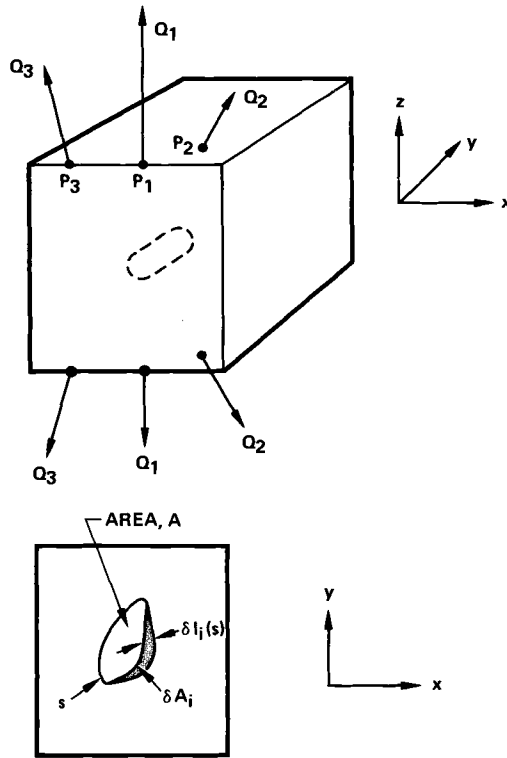


FIG. 4—Schematic of prescribed normal perturbation  $\delta l_i(s)$  of crack front  $s$ .

chosen to be the reference state in Eq 10 and used to compute  $h$  at all points in the analyzed geometry.

A more useful form of Eq 10 may be derived by substitution of Eqs 2 and 7 in Eq 10 to obtain

$$h_{ij} = \left( \frac{2\partial(Q_m^* q_m^*)}{H\partial A_{\underline{i}}} \right)^{-\frac{1}{2}} \frac{\partial q_j^*}{\partial A_{\underline{i}}} \tag{11}$$

where the repeated index  $m$  again denotes summation in Eq 11 which directly relates the  $h_{ij}$  to reference crack opening displacements.

Consider the special case where all loads in the problem to be solved are on the crack face in terms of a bivariate normal pressure  $\sigma_{zz}(x,y)$ . If normal loads are interpreted as

$$dQ(x,y) = \sigma_{zz}(x,y)dA \tag{12}$$

we can combine Eqs 7, 11, and 12 to obtain the final result for stress intensity factor computation.

$$\bar{K}_i = \left( \frac{2\theta \left[ \iint_A \sigma_{zz}^* q^* dA \right]}{H\theta A_i} \right)^{-\frac{1}{2}} \iint_A \sigma_{zz} \frac{\partial q^*}{\partial A_i} dA \quad (13)$$

Consider the principle of superposition illustrated in Fig. 5, as reproduced from Ref 2. This principle allows use in Eq 13 of the "uncracked" stress  $\sigma_{zz}(x,y)$  (that is, stress for the uncracked solid at the crack's locus) to yield correct  $K$  factors for arbitrary geometry and loading.

Initial application of Eqs 1 and 13 for computation of the  $\bar{K}_i$  and

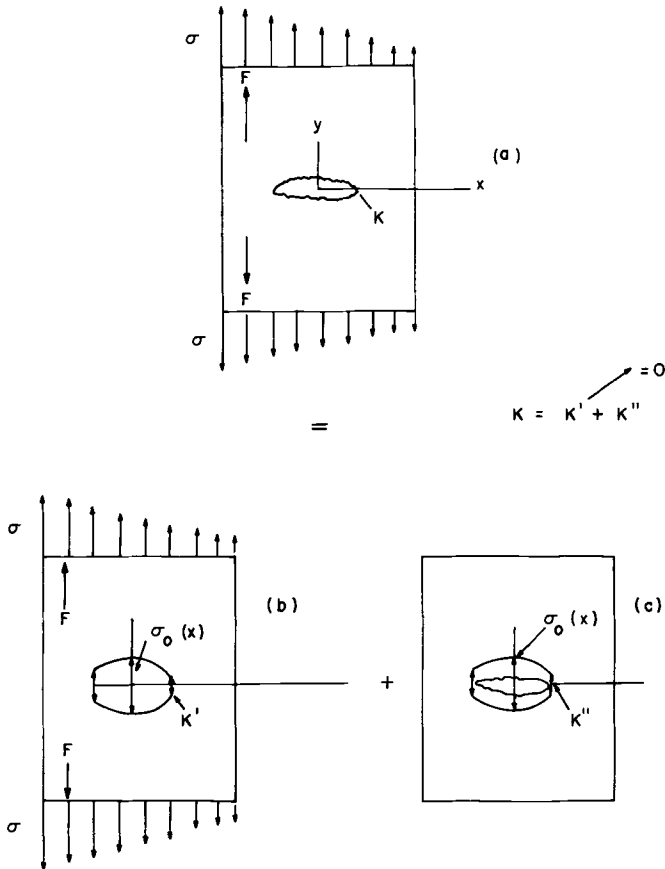


FIG. 5—The reduction of a problem, (a), into two simpler problems, (b) and (c) for computations of stress intensity factor (from Ref 2).

residual life  $N$  has revealed several major advantages of the influence function theory. Influence theory application requires only the characterization of crack opening displacements  $q^*(x,y)$  as a function of the  $a_i$  and significant structural dimensions for a single reference loading. The  $q^*$  function, whether based on a known solution as in the next section or on numerical data as in Ref 1, is substituted into Eq 13. Since known  $q^*$  solutions for three-dimensional crack problems are scarce, the solution of the  $\bar{K}_i$  for most partial thickness crack problems requires accurate numerical crack opening displacements. Numerical solution for the necessary  $q^*$  data is not difficult. For example, Ref 1 documents the numerical solution of a two DOF quarter-ellipse corner crack problem. Solution of the  $\bar{K}_i$  for all corner crack sizes and shapes and all loading states required only twelve three-dimensional stress analysis computer runs for various  $a_i$  values.

The uncracked stress  $\sigma_{zz}(x,y)$  in Eq 13, of course, may be computed or measured with standard methods which ignore the presence of the crack. Numerical integration of Eq 13 then computes  $\bar{K}_i$  for each crack growth increment without recourse to repeated three-dimensional stress analyses. Thus, influence function theory application is extremely inexpensive and efficient as compared to repeated stress analysis procedures.

In addition to generality and ease of application, the influence function method offers advantages in stress intensity factor computational accuracy. The analyst is free to choose any convenient single loading that can be accurately solved by the applied numerical crack stress analysis program. This eliminates numerical errors caused by inclusion of actual, complex loading into computer stress analysis of cracks.

The disadvantage of influence function theory from a user's standpoint is that it is possible to prescribe too few crack DOF to model complex geometry and loading effects. This particular modeling error would probably not occur when using repeated stress analyses for each small crack growth increment.

To eliminate this disadvantage and ensure modeling accuracy, future research should ascertain the minimum number of DOF required for life prediction of various classes of problems. The calculated lives in the next section and the agreements noted between computed and observed residual lives in initial applications, such as reported in Ref 1, indicate that two DOF can model adequately a reasonable number of problems.

### **Stress Intensity Factor and Residual Lifetime Computations for the Two DOF Buried Ellipse**

This section presents stress intensity factor formulas and residual lifetime computations for the two DOF buried elliptical crack in Fig. 3 to illustrate application of the general life prediction procedure. Life computations are also given using the end-point values  $\hat{K}_i$ . This is done to

investigate the dependence of calculated life on stress intensity factor definition for two stress states for which both  $\bar{K}$  and  $\hat{K}$  could be easily computed.

### *Stress Intensity Factor Derivation*

Crack opening displacements for the buried elliptical crack under uniform pressure are given by Green and Sneddon [5]. Substitution of the displacement function into Eq 13 gives stress intensity factors for arbitrary uncracked stress as

$$\bar{K}_x = \frac{\iint_A \left( \frac{1}{a_x} - \frac{\partial E(k)}{E(k)\partial a_x} + \frac{x^2}{a_x^3 \alpha} \right) \alpha^{1/2} \sigma_{zz}(x,y) dA}{\pi a_y \left[ \frac{E(k)}{3} \left( \frac{2}{a_x} - \frac{\partial E(k)}{E(k)\partial a_x} \right) \right]^{\frac{1}{2}}} \quad (14)$$

$$\bar{K}_y = \frac{\iint_A \left( -\frac{\partial E(k)}{E(k)\partial a_y} + \frac{y^2}{a_y^3 \alpha} \right) \alpha^{1/2} \sigma_{zz}(x,y) dA}{\pi \left[ \frac{a_x a_y E(k)}{3} \left( \frac{1}{a_y} - \frac{\partial E(k)}{E(k)\partial a_y} \right) \right]^{\frac{1}{2}}} \quad (15)$$

where  $\alpha = 1 - (x/a_x)^2 - (y/a_y)^2$  and  $E(k)$  if the complete elliptic integral of the second kind with modulus  $k^2 = 1 - (a_x/a_y)^2 \geq 0$ .

Equations 14 and 15 are theoretically valid for substitution into Eq 1 to compute life for any tensile stress field  $\sigma_{zz}(x,y)$ . However, it is suggested that Eqs 14 and 15 be used only with the requirement that  $\sigma_{zz}$  be symmetric about the crack axes. This requirement is physically consistent with the chosen two growth freedoms. A four or five DOF model which allows unsymmetric growth of the buried ellipse, easily derivable from the Ref 5 displacement solutions and Eq 13, is recommended for use with unsymmetric  $\sigma_{zz}(x,y)$  functions.

### *Residual Lifetime Computations*

Given the stress intensity factor solution, Eqs 14 and 15, life computation consists of the numerical solution of the system of Eq 1 for  $N$ . The initial values of the  $a_i$  (that is, the initial crack or crack-like defect) must be specified as with the two dimensional cracking problem [3]. Also, a final crack length criterion must be adopted. A fracture toughness criterion is adopted herein to represent a brittle static failure mode in an infinite solid.

Tables 1 and 2 list calculated lives for several initial cracks under uniform and parabolic stress respectively. The lives  $N_{\bar{K}}$  are obtained by

solution of

$$\frac{da_i}{dN_{\bar{K}}} = 10^{-9} \Delta \bar{K}_i^{2.8}, \quad i = x, y \quad (16)$$

where the  $\bar{K}_i$  are computed from Eqs 14 and 15, and failure is defined to occur at maximum ( $\bar{K}_i$ ) =  $K_{Ic}$ . The lives  $N_{\hat{K}}$  are computed by solving

$$\frac{da_i}{dN_{\hat{K}}} = 10^{-9} \Delta \hat{K}_i^{2.8}, \quad i = x, y \quad (17)$$

TABLE 1—Cyclic life prediction for embedded elliptical cracks in a uniform normal stress field.

| Width<br>2a,<br>mils | Length<br>2b,<br>mils | Life ( $N_{\bar{K}}$ )<br>Using $\bar{K}_i$ ,<br>cycles $\times 10^{-3}$ | Life ( $N_{\hat{K}}$ )<br>Using $\hat{K}_i$ ,<br>cycles $\times 10^{-3}$ |
|----------------------|-----------------------|--|--|
| 2                    | 2                     | 65   | 65   |
| 2                    | 4                     | 56   | 56   |
| 2                    | 10                    | 45   | 45   |
| 2                    | 20                    | 39   | 38   |
| 2                    | 80                    | 31   | 28   |
| 2                    | $\infty$              | 22   | 18   |
| 5                    | 5                     | 44   | 44   |
| 5                    | 10                    | 36   | 37   |
| 5                    | 25                    | 29   | 29   |
| 5                    | 35                    | 27   | 27   |
| 5                    | 50                    | 25   | 24   |
| 5                    | 100                   | 22   | 21   |
| 5                    | 200                   | 19   | 17   |
| 10                   | 10                    | 32   | 32   |
| 10                   | 20                    | 26   | 27   |
| 10                   | 50                    | 21   | 21   |
| 10                   | 70                    | 19   | 19   |
| 10                   | 100                   | 18   | 17   |
| 10                   | 200                   | 15   | 14   |
| 10                   | 400                   | 14   | 13   |
| 10                   | 1000                  | 12   | 11   |
| 10                   | $\infty$              | 10   | 8.2  |
| 20                   | 20                    | 23   | 23   |
| 20                   | 40                    | 19   | 19   |
| 20                   | 100                   | 15   | 14   |
| 20                   | 200                   | 12   | 12   |

- Assumptions:
1. Infinite solid; initial crack sizes above.
  2.  $K_{\text{mean}} = 0.5 \Delta K$ .
  3.  $K_{Ic} = 85 \text{ ksi } \sqrt{\text{in.}}$
  4.  $\sigma_{zz}(x, y) = 100 \text{ ksi}$ .
  5. Text contains modeling and material crack growth rate data assumptions.

TABLE 2—Cyclic life prediction for embedded elliptical cracks in a parabolic normal stress field.

| Width<br>2a,<br>mils | Length<br>2b,<br>mils | Life ( $N_{\bar{K}}$ )<br>Using $\bar{K}_i$ ,<br>cycles $\times 10^{-3}$ | Life ( $N_{\hat{K}}$ )<br>Using $\hat{K}_i$ ,<br>cycles $\times 10^{-3}$ |
|----------------------|-----------------------|--|--|
| 2                    | 2                     | 64   | 65   |
| 2                    | 4                     | 55   | 55   |
| 2                    | 10                    | 45   | 44   |
| 2                    | 20                    | 39   | 38   |
| 2                    | 80                    | 30   | 27   |
| 2                    | $\infty$              | 22   | 20   |
| 5                    | 5                     | 43   | 43   |
| 5                    | 10                    | 37   | 36   |
| 5                    | 25                    | 30   | 29   |
| 5                    | 35                    | 27   | 26   |
| 5                    | 50                    | 25   | 23   |
| 5                    | 100                   | 22   | 20   |
| 5                    | 200                   | 20   | 17   |
| 5                    | $\infty$              | 14   | 13   |
| 10                   | 10                    | 31   | 31   |
| 10                   | 20                    | 27   | 26   |
| 10                   | 50                    | 21   | 20   |
| 10                   | 70                    | 19   | 18   |
| 10                   | 100                   | 18   | 16   |
| 10                   | 200                   | 15   | 14   |
| 10                   | 400                   | 13   | 12   |
| 10                   | 1000                  | 10   | 9.3  |
| 10                   | $\infty$              | 9.9  | 8.4  |
| 20                   | 20                    | 22   | 22   |
| 20                   | 40                    | 19   | 18   |
| 20                   | 100                   | 15   | 14   |
| 20                   | 200                   | 12   | 11   |

- Assumptions: 1. Infinite solid, initial crack sizes given above.  
 2.  $K_{\text{mean}} = 0.5 \Delta K$ .  
 3.  $K_{Ic} = 60 \text{ ksi } \sqrt{\text{in.}}$ .  
 4.  $\sigma_{zz}(x,y) = 100 (1 - 4x^2) \text{ ksi}$  for  $x \leq 0.5$ .  
 5. Text contains modeling and material crack growth rate data assumptions.

where the  $\hat{K}_i$  are obtained from Shah and Kobayashi [6], and failure is defined to occur at maximum ( $\hat{K}_i$ ) =  $K_{Ic}$ . The force, length, and time units in Eqs 16 and 17 are kilopounds, inches, and fatigue cycles, respectively. The constants fit data for AMS 6304, a moderate strength steel, at operational temperatures for a wide range of  $\Delta K$  values. The other assumptions used for life computations are listed in the tables.

Note that the life estimates are nearly independent of the  $K_i$  definition, that is,  $N_{\bar{K}} \approx N_{\hat{K}}$ , for the cases cited. Similar studies for exponents in Eqs 16 and 17 ranging from 2 to 5 also obtain  $N_{\bar{K}} \approx N_{\hat{K}}$ . This independence is

not surprising because the rms property of the  $\bar{K}_i$  guarantees that the two definitions will result in similar stress intensity factor and life computations, given enough DOF. Apparently, two DOF are sufficient for the cases investigated herein. It is certain that additional DOF will be required for some problems with greater complexity. In any case, comparison with empirical results can only serve to reinforce or to discredit the above usage of both definitions of  $K$ , rather than favoring either.

Once the reference displacements and actual uncracked stresses are obtained, the computation of the  $K_i$  in Eq 13 is a simple, inexpensive exercise in numerical integration. For example, a program has been written to evaluate accurately the  $K_i$  in Eqs 14 and 15 in less than 0.03 s central processing unit (CPU) time on the IBM 370-168 computer. Life prediction, through solution of the two simultaneous equations of Eq 16, takes less than 2 s with a typical numerical error of 1.5 percent.

### Summary and Conclusions

An efficient, general procedure for predicting the residual lifetime of structures with partial thickness cracks has been reported. The procedure treats the three dimensional cracking complications of complex crack shape, crack shape change during growth, and stress intensity factor variation along the crack front. The actual crack is modeled with any prescribed mathematical shape with a finite number of key variable parameters or DOF. The cyclic growth rate of each DOF is assumed to be controlled by its associated stress intensity factor. Each factor is defined in terms of the strain energy release rate caused by perturbation of the single DOF, holding the other DOF constant. This definition, demonstrated to be reasonable in its own right, is especially compatible with an advantageous influence function theory derived to compute stress intensity factors. The crack size and shape may then be computed as a function of load cycles by use of the usual linear elastic fracture mechanics modeling of crack growth.

The influence function theory requires only the characterization of the crack opening displacements for various values of the DOF and structural dimensions, for a simple reference loading. These closed form or numerical results are then applied to derive analytically all required values of stress intensity factors for an arbitrary stress state such as due to the presence of a local notch. The influence function theory uses only the stresses in the uncracked structural detail and thereby eliminates the need for full three dimensional stress analysis for each new increment of crack growth as well as for each considered stress state.

The life prediction and stress intensity factor computation procedure is illustrated for a simple two DOF model of the buried elliptical crack. It is shown for several examples that calculated life is independent of the

choice of two considered stress intensity factor definitions. Further, it is indicated that the choice of a stress intensity factor definition becomes immaterial as the number of DOF is increased. Consequently, any empirical results would tend to reinforce or to disprove both equivalent elastic criteria rather than favoring either.

As described, the extension of the life prediction procedure to more complex models is direct, requiring only specification of a model with appropriate number of DOF together with a minimum number of full three-dimensional analyses. For example, Ref 1 uses only twelve stress analysis computer runs to obtain a general, accurate stress intensity factor solution algorithm for a two DOF quarter-ellipse corner crack model. Additional current research is being devoted to the solution and experimental verification of various other partial thickness crack models such as a three DOF half-ellipse surface crack and the extension of the buried ellipse model to four DOF. Thus, it is concluded that the majority of partial thickness crack problems are brought within the scope of an efficient residual fatigue life prediction procedure.

#### *Acknowledgments*

The author gratefully acknowledges the encouragement and significant contributions he received from Drs. E. S. Todd and T. A. Cruse of Pratt & Whitney Aircraft Division.

#### **References**

- [1] Cruse, T. A. and Besuner, P. M. "Residual Life Prediction for Surface Cracks in Complex Structural Details," *Journal of Aircraft* (to appear).
- [2] Paris, P. C., Gomez, M. P., and Anderson, W. E., "A Rational Analytic Theory of Fatigue," *The Trend in Engineering*, Vol. 13, No. 1, University of Washington, Seattle, Wash., Jan. 1961.
- [3] Rice, J. R., *International Journal of Solids Structures*, Vol. 8, 1972, pp. 751-758.
- [4] Key, P. L., *International Journal of Fracture Mechanics*, Vol. 5, No. 4, Dec. 1969, pp. 287-296.
- [5] Green, A. E. and Sneddon, I. N., *Proceedings of the Cambridge Philosophical Society*, Vol. 46, 1950, pp. 159-163.
- [6] Shah, R. C. and Kobayashi, A. S., "Stress Intensity Factor for an Elliptical Crack Under Arbitrary Normal Loading," *Engineering Fracture Mechanics*, Vol. 3, Pergamon Press, London, 1971.

J. I. Bluhm<sup>1</sup>

## Application of Fracture Mechanics to the Calculation of Deflections in Stepped Structural Elements

---

**REFERENCE:** Bluhm, J. I., "Application of Fracture Mechanics to the Calculation of Deflections in Stepped Structural Elements," *Mechanics of Crack Growth*, ASTM STP 590, American Society for Testing and Materials, 1976, pp. 420-428.

**ABSTRACT:** Deflections of structural elements are determined frequently by using simple engineering strength of materials approaches. However, when geometric discontinuities are present, such approaches may lead to excessive errors in the predicted deflection. The present paper suggests a simple technique for refining these deflection predictions using available fracture mechanics data. Use of such techniques leads to predictions which do not differ significantly from "exact" solutions.

**KEY WORDS:** crack propagation, mechanical properties, fracture properties, structural analysis, deflection, discontinuity (mathematics)

The structural analyst is required frequently to predict and limit the elastic deflection or compliance of structures. Exact solutions, frequently entailing sophisticated elasticity analysis, are often not within the scope of the structural analyst's capabilities. Computer codes using finite element techniques are not always accessible to the engineer. As a convenient alternative the engineer uses traditional "strength of materials" approximations such as, for example, the usual beam theory. For many applications, such engineering strength of materials (ESM) approaches are adequate particularly if the structure has no geometric discontinuities; under such conditions more extensive analyses may not be justified.

However consider now the stepped, simply supported beam illustrated in Fig. 1. Suppose it is required to determine the deflection under the central load  $P$ . A usual ESM approach for this type of problem is to treat

<sup>1</sup> Chief, Mechanics Research Laboratory, Army Materials and Mechanics Research Center, Watertown, Mass. 02172.

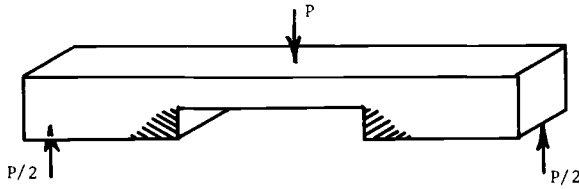


FIG. 1—Actual beam.

each region of the beam as one with constant cross section and then to apply ordinary beam theory to each region. Of course compatibility of deformations must be enforced at section changes. Alternatively the total strain energy in the beam  $U_T$  can be determined using traditional approaches and, then by Castigliano's theorem one can calculate the total deflection  $\delta_T$ , that is

$$\delta_T = \frac{\partial U_T}{\partial P} \tag{1a}$$

It should be clear, however, that the value of the deflection thus computed,  $\delta_T$ , implies the full effectiveness of the entire cross sections in resisting the applied bending. It should also be intuitively evident that such calculations may seriously underestimate the deflection. The material near the discontinuity (that is, the shaded region of Fig. 1) does not contribute its due share of the moment resisting stresses. The effective contour of the beam might be, more realistically, visualized as that suggested in Fig. 2. If, in fact, this effective contour were known, then many of the traditional ESM approaches could be used, with results adequate for all but the most sophisticated or demanding needs. Unfortunately these effective contours are not determined easily, although one simple refinement suggested by a reviewer is to consider the effective contour in the notched region as a straight line at 45 deg. Applications of such a contour obviously reduces the errors associated with the subsequent ESM approach, particularly as the notch width becomes relatively large compared to the notch depth. However for relatively small

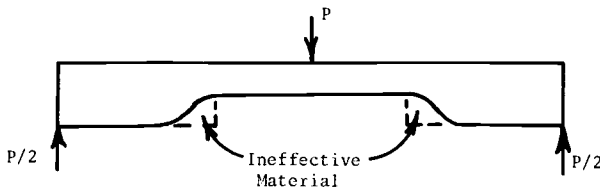


FIG. 2—Effective beam profile.

notch widths, the arbitrary contour suggested still leads to sizeable errors; obviously, as just implied, the unlikely but fortuitous guess as to the proper contour would lead to an exact deflection prediction; fortunately, as we shall see, an alternative approach is possible which does not depend on the subjective wisdom or experience of the engineer.

For the particular beam configuration sketched in Fig. 1, neglect of the local effects at the discontinuity can lead to discrepancies in excess of 50 percent between "exact" solutions and ESM approaches.

It is the purpose of the present paper to describe a concept which combines such approximate ESM approach with catalogued precise crack solutions borrowed from the fracture mechanics discipline. By marrying these approaches it will be shown that substantially exact deflections of such discontinuous structures, as in Fig. 1, can be derived.

Paris [1]<sup>2</sup> and subsequently Tada et al [2] suggested a technique for computing certain displacements in crack related problems. The method, illustrated in Ref 2 for crack opening displacements, entailed use of the established relationship (for constant load)

$$G = \frac{\partial U_T}{\partial A} \quad (1b)$$

where  $G$ ,  $U_T$ , and  $A$  are the elastic strain energy release rate, total strain energy, and crack area, respectively. Integration yields  $U_T$  and then by Eq 1a the desired deflection  $\delta_T$  is obtained readily. Of course  $\delta_T$  is determined at the point of application of the load  $P$  and in its direction.

The form of  $G$  (or its equivalent  $K$  the stress intensity factor) has been catalogued in a number of sources for various crack and structural configurations [2]. Selected specimen configurations are detailed by Brown and Srawley [3].

### Concept

Consider the stepped beam of Fig. 3. As just implied it is necessary to identify that stepped beam with a fracture mechanics crack problem. In the present case the pertinent crack problem is sketched in Fig. 4. It is evident that, as the length  $l_2$  in Fig. 3 approaches zero, the geometry of Fig. 4 is approximated.<sup>3</sup> This latter beam is identified as the degenerate beam.

It is noted that the solution for the stress intensity factor  $K$  for this degenerate beam (Fig. 4) derives from various elasticity approaches which treat the stress singularity at the crack tip. It is evident also that the resulting local perturbations of the stresses are, at least qualitatively, the same as those which dominate the shaded areas of Fig. 1. We make the

<sup>2</sup> The italic numbers in brackets refer to the list of references appended to this paper.

<sup>3</sup> Except for the detailed nature of the singularity.

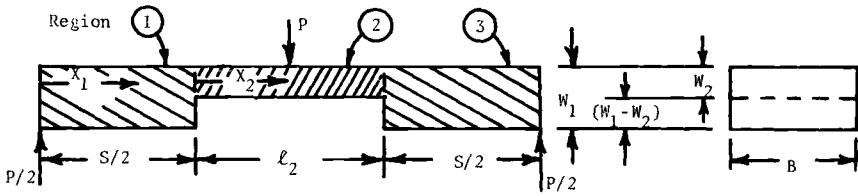


FIG. 3—Actual beam geometry.

more demanding assumption, that for all practical purposes the stress distribution in Region 1 of Fig. 4 is precisely the same as that of Region 1 of Fig. 3 and consequently that the strain energies are the same, that is

$$U_1 = U_3 = U_{1D} = U_{3D} \tag{2}$$

where the subscript  $D$  refers to degenerate beam characteristics.

The strain energy  $U_{1D}$  relating to half the degenerate beam can be determined directly from its definition Eq 1a and in lieu of Eq 2

$$G = \frac{\partial U_T}{B\partial a} = \frac{\partial [U_{1D} + U_{3D}]}{B\partial a} \tag{3}$$

where  $B$  is the beam thickness and  $a$  the crack depth. Integrating, this becomes

$$[U_{1D} + U_{3D}] = 2U_{1D} = B \int_0^a G da + U_0(a = 0) \tag{4}$$

where  $U_0(a = 0)$  represents the strain energy of the degenerate beam with  $a = 0$ . It is further assumed that the strain energy of Region 2 (Fig. 3)  $U_2$  is defined adequately by the usual ESM approaches so that the total strain

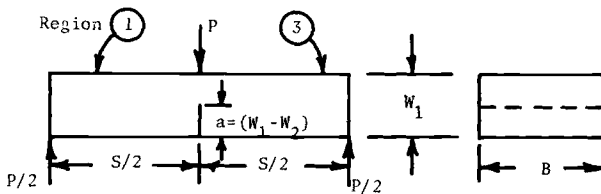


FIG. 4—Degenerate beam geometry.

energy  $U_T$  in that beam configuration can be written

$$\left. \begin{aligned} U_T &= 2U_1 + U_2 \\ U_T &= 2U_{1D} + U_2 \end{aligned} \right\} \text{or in lieu of Eq 2} \tag{5}^4$$

Substituting Eq 4 into the latter of these and using Eq 1a, one obtains for the desired deflection  $\delta_T$

$$\delta_T = \frac{\partial}{\partial P} B \int_0^a G da + U_0(a = 0) + U_2 \tag{6}$$

But note that  $U_0(a = 0)$  is the strain energy associated with the uncracked beam and therefore is computed easily by the usual engineering strength of materials beam approaches. Since also  $U_2$  is the corresponding strain energy of Region 2, this can also be treated by the ESM approaches. We see then that the last terms of Eq 6 relate to strain energies without regard to the discontinuity effects. We define, as  $\delta_0$ , the corresponding deflection

$$\delta_0 = \frac{\partial}{\partial P} [U_0(a = 0) + U_2] \tag{7}$$

In view of Eq 7, Eq 6 can be written in consolidated form as follows

$$\delta_T = \delta_0 + \Delta\delta$$

where

$$\Delta\delta = \frac{\partial}{\partial P} \left[ B \int_0^a G da \right] \tag{8}$$

Here we emphasize that  $\Delta\delta$  represents the increment in deflection at the load application point (Fig. 3) due to the stress perturbation associated with the section discontinuities. Thus the total deflection of a structure such as in Fig. 3 can be considered as that computed from ESM

<sup>4</sup> It is suggested that these two equations are equivalent to within an error  $\epsilon \rightarrow 0$  for  $l_2 \rightarrow 0$  and  $\epsilon \rightarrow 0$  as  $l_2$  gets large. Intuitively then one might expect the proposed equivalence to be reasonably good throughout the range of  $l_2$ 's.

approaches  $\delta_0$  plus a corrective deflection  $\Delta\delta$  derived from fracture mechanics concepts and which accounts for the local discontinuity effects.

**Illustration**

Consider the beam of Fig. 3. The pertinent degenerate beam is that shown in Fig. 4. For this latter beam we have Ref 1

$$G = \frac{1 - \nu^2}{E} K^2 = \frac{36(1 - \nu^2)M_{\max}^2}{EB^2W^4} aY^2 \tag{9}$$

where  $Y$  is a given polynomial in  $(a/W)$ . Inserting this into Eq 4 and nondimensionalizing we obtain

$$2U_{1D} = \frac{9(1 - \nu^2)}{4EB} (S/W)^2 P^2 \int_0^{a/W} Y^2(\xi/W) \times (\xi/W) \times d(\xi/W) + U_0(a = 0) \tag{10}$$

Defining the integral as  $f(a/W)$  and inserting this into Eq 5 we obtain

$$U_T = 2U_{1D} + U_2 = \frac{9(1 - \nu^2)}{4EB} (S/W)^2 P^2 f(a/W) + U_0(a = 0) + U_2 \tag{11}$$

Note however that

$$\left. \begin{aligned} U_0 &= 2 \frac{1}{2EI_1} \int_0^{s/2} M_1^2 dx_1 \\ M_1 &= \frac{P}{2} x_1 \\ U_2 &= 2 \left[ \frac{1}{2EI_2} \int_0^{(l_2)/2} M_2^2 dx_2 \right] \\ M_2 &= \frac{P}{2} \left( \frac{S}{2} + x_2 \right) \end{aligned} \right\} \tag{12}$$

But these are precisely the strain energies of the component spans of the beam neglecting the local discontinuity effects, that is, using ESM analysis. The corresponding deflection  $\delta_0$  is then calculated from Eqs 7 and 12. The correction  $\Delta\delta$ , accounting for these discontinuity effects, is

found from Eqs 8 and 9 to be

$$\left. \begin{aligned} \Delta\delta &= \frac{9}{2EB} (1 - \nu^2) (S/W)^2 f(a/W) P \\ \text{where } f(a/W) &= \int_0^{a/W} Y^2(\xi/W) \times (\xi/W) \times d(\xi/W) \\ \text{and } Y(\xi/W) &= \sum_{n=0}^4 A_n(\xi/W)^n \end{aligned} \right\} \quad (13)$$

Here the coefficients  $A_n$  are given in Ref 3.

It is noted that the approach just described is applicable to such diversified configurations as suggested in Fig. 5.

In particular we have examined the simple geometry sketched in Fig. 6 and computed the deflection between Points A and B using both the ESM approach  $\delta_0$  and the fracture mechanics correction  $\Delta\delta$ . These were then compared with a finite element solution estimated to be correct to  $\pm 2$  percent. The results in percentage error are shown in the Table 1.

Total deflections of this specimen  $\delta_T$  were determined analytically using the following relation

$$\delta_T = \frac{\sigma_0 W}{E} \left[ 2m + \frac{n}{1 - 2a/W} \right] + \frac{\sigma_0 W}{E} f(2a/W) \quad (14)$$

where the first term on the right represents the ESM contribution and the second term the fracture mechanics (or discontinuity) contribution. Note that though in this particular case the maximum error is 20 percent, errors in excess of 50 percent may arise in different geometries. Obviously, a

TABLE 1—Comparative errors in deflection of tension specimen per Fig. 6,  $2(a/W) = 0.5$

|         |           | ESM   | % Error <sup>a</sup><br>ESM (45 deg) <sup>b</sup> | Fracture Mechanics |
|---------|-----------|-------|---|--------------------|
| $m = 1$ | $n = 0.0$ | -20.0 | -12.1   | 0                  |
| $m = 1$ | $n = 0.1$ | -17.4 | -9.9  | +1.5               |
| $m = 1$ | $n = 0.2$ | -15.4 | -8.4  | +2.3               |
| $m = 1$ | $n = 1.0$ | -9.2  | -4.7  | +2.2               |
| $m = 1$ | $n = 2.0$ | -6.3  | -3.1  | +1.6               |

<sup>a</sup> Based upon a finite element solution which was taken as an exact solution.

<sup>b</sup> Basically the same as the ESM analysis except that the sides of the notches were inclined at 45 deg to approximate the effect of the ineffective material.

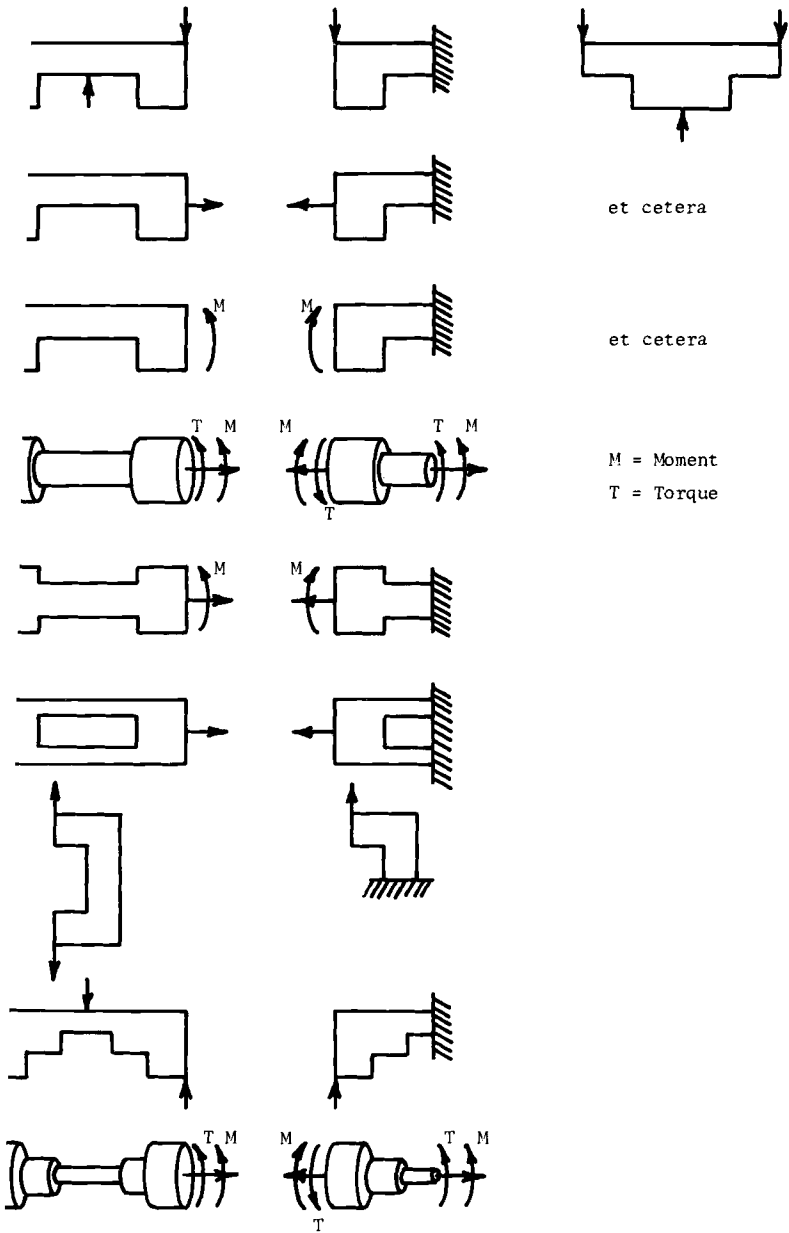


FIG. 5—Alternative configurations tractable to analysis by present concept.

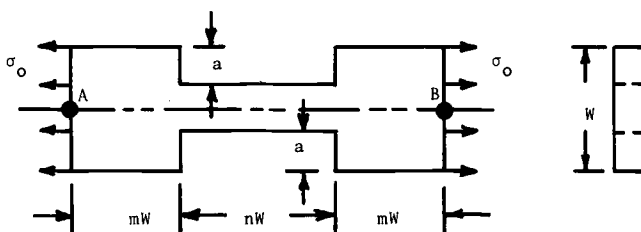


FIG. 6—Reference tension specimen for comparison of solutions.

judicious guess as to an effective shape for the ineffective material should improve markedly such an ESM analysis. To judge one simple such guess an ESM analysis was carried out for essentially the same configuration except that the ineffective material was assumed to be bounded by 45 deg inclined notch sides. Table 1 shows that though significant improvement is obtained the use of the fracture mechanics correction essentially eliminates the error.

### Conclusion

An approach has been suggested which permits precise deflection calculations in specific structural configurations involving discontinuities. The method utilizes conventional engineering strength of materials approaches and combines these with simple results of more sophisticated fracture mechanics analysis to account for the local discontinuity effects. Carried out for a specific case it is illustrated that the deflection can be thus calculated to within an accuracy of approximately 2 percent.

### Acknowledgment

The author wishes to acknowledge Colin Freese of the Mechanics Research Laboratory at the Army Materials and Mechanics Research Center for the finite element solutions used in the illustration problem as a basis for error considerations.

### References

- [1] Paris, P. C., "The Mechanics of Fracture Propagation and Solution to Fracture Arrestor Problems," Document D-2-2195, The Boeing Company, 1957.
- [2] Tada, H., Paris, P. C., and Irwin, G., *The Stress Analysis of Cracks Handbook*, Del Research Corporation, Hellertown, Pa., 1973, p. B-1.
- [3] Brown, W. F., Jr., and Srawley, J. E., *Plane Strain Crack Toughness Testing of High Strength Metallic Materials*, ASTM STP 410, American Society for Testing and Materials, 1966, p. 13.

R. C. Shah<sup>1</sup>

## Stress Intensity Factors for Through and Part-Through Cracks Originating at Fastener Holes

---

**REFERENCE:** Shah, R. C., "Stress Intensity Factors for Through and Part-Through Cracks Originating at Fastener Holes," *Mechanics of Crack Growth, ASTM STP 590*, American Society for Testing and Materials, 1976, pp. 429–459.

**ABSTRACT:** A procedure is formulated to derive approximate stress intensity factors for both part-through and through-the-thickness cracks originating at open holes and holes containing either loaded or unloaded close tolerance fasteners. The procedure is checked with known solutions for stress intensity factors of one or two through-the-thickness cracks emanating from an open hole in a plate subjected to uniaxial or biaxial loading. Stress intensity factors computed from this procedure for the above mentioned cases agree within seven percent of known results for the crack length to hole radius ratios,  $L/r$ , of  $0.05 \leq L/r < \infty$ . The procedure is then used to derive stress intensity factors for through cracks at loaded close tolerance fasteners in a plate, and for semi-elliptical cracks at open holes and at loaded and unloaded close tolerance fastener filled holes in a thick plate. Stress intensity factors for these part-through cracks are presented in graphical forms as a function of position around the crack periphery, for various crack aspect ratios and crack length to hole radius ratios. Finally, these stress intensity solutions for semi-elliptical cracks at a fastener hole in a thick plate are used to estimate stress intensity factors for quarter-elliptical cracks originating at a fastener hole in a finite thickness plate.

**KEY WORDS:** crack propagation, fracture (materials), stress analysis, fastener holes

A recent comprehensive study of failure origins in aircraft structures showed that the most prevalent failure origins are in order; flaws originating from fastener holes, flaws originating from corners, and surface flaws [1].<sup>2</sup> Stress intensity factors (SIF's) for these flaw geometries are required to evaluate the critical flaw sizes that would result in

<sup>1</sup> Senior specialist engineer, Boeing Aerospace Company, Seattle, Wash. 98124.

<sup>2</sup> The italic numbers in brackets refer to the list of references appended to this paper.

component failures and to compute the service life of the component during which the initial flaw could grow to a critical size. As evidenced by Ref 2, considerable work has been done in obtaining SIF's for the surface flaws. Due to the complexity of the problem, very little work has been done to obtain SIF's for cracks originating at fastener holes. Most of the work is limited to derivations of approximate solutions to two-dimensional crack problems of through-the-thickness cracks originating at holes [3-6]. For two-dimensional crack problems, estimates of SIF's for through-cracks originating at loaded filled holes are available only for particular loading conditions and hole diameter [6]. Empirical expressions for SIF's based on experimental data have been developed for quarter-elliptical or quarter-circular part-through flaws (flaws which have penetrated part of a plate) subjected to uniform uniaxial tension in Refs 7 and 8, respectively. However, these empirical solutions compute an effective SIF at an unknown location on the crack periphery and do not take into account the variation of the SIF along the crack periphery. Estimates of SIF's for semi-elliptical cracks at open holes in an infinite solid have been obtained for very short cracks with respect to hole radius, that is, for  $a/R \leq 0.3$  where  $a$  and  $2c$  are crack dimensions and  $R$  is hole radius [9].<sup>3</sup>

Stress analysis of a loaded close tolerance fit fastener in a plate subjected to applied remote loading, even in the absence of a flaw, is a complex nonlinear problem involving variable contact between the fastener and the plate [10,11]. When a flaw originates from the fastener hole, analysis is complicated further, since the crack reduces the rigidity of the structure surrounding the hole and may change the contact condition. Flaws originating at fastener holes are often part-through flaws and are thus three-dimensional problems. At the present time, it is not possible to obtain exact or numerical solutions of the SIF's for these three-dimensional crack problems. SIF's for such three-dimensional crack problems have to be obtained using simplifying assumptions, approximations, and judicious estimates.

The objective of this paper is to derive approximate SIF's for cracks originating at fastener holes. A procedure is formulated to derive SIF's from the stress distribution at the location of the crack in the uncracked plate or solid. The procedure is verified with known solutions for SIF's for two-dimensional (through-the-thickness) cracks originating at a hole. The procedure is then used to derive SIF's for the flaw types and loading cases shown in Fig. 1. These are: (1) through cracks at holes containing loaded close tolerance fasteners, (2) semi-elliptical cracks at open holes, and (3) semi-elliptical cracks at both loaded and unloaded close tolerance fastener filled holes in a thick plate subjected to uniform tension. Finally,

<sup>3</sup> Work in Ref 9 was accomplished concurrently with the work described in this paper.

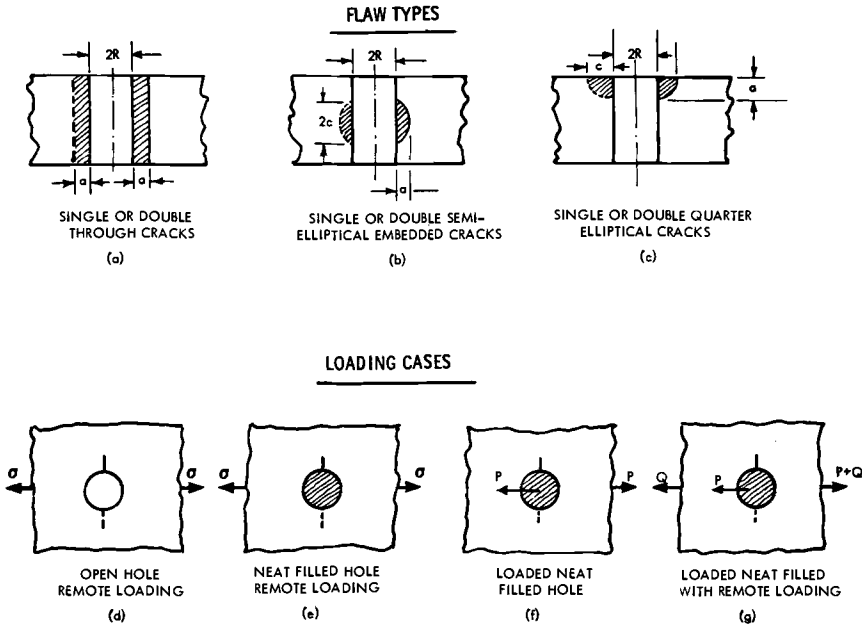


FIG. 1—Flaw types and loading cases considered.

stress intensity factors for quarter-elliptical cracks originating at fastener holes in a thick plate are estimated.

**Formulation of Procedure**

Consider a problem of two symmetric through (or semi-elliptical part-through) cracks, each of length  $L$ , emanating from a fastener hole of radius  $R$  in a plate (or a solid) subjected to a symmetric loading, as shown in Fig. 2a. This problem is considered to be approximately equivalent to the linear superposition of two problems as shown in Fig. 2b and c. The stress distribution  $\sigma_{zz}(x,0)$  in an uncracked plate with the fastener hole is determined at the location of the cracks for the applied loading in question. The crack of length  $2L$ , as shown in Fig. 2c, is pressurized with a symmetric pressure distribution of stress  $-\sigma_{zz}(X,0)$ .<sup>4</sup> The SIF  $K_I$  for both through and part-through cracks pressurized by this stress distribution of  $-\sigma_{zz}(X,0)$  is then derived by using the proper Green's function solution for the crack, such as Eq 1 for two symmetric through cracks [12].

<sup>4</sup> Origins of coordinate systems  $(x,y,z)$  and  $(X,Y,Z)$  are located at the center of the hole and at the periphery of the hole along  $x$ -axis, respectively, such that  $X = x - R$  for  $x \geq R$  and  $X = x + R$  for  $x \leq -R$ ,  $Y = y$ , and  $Z = z$ .

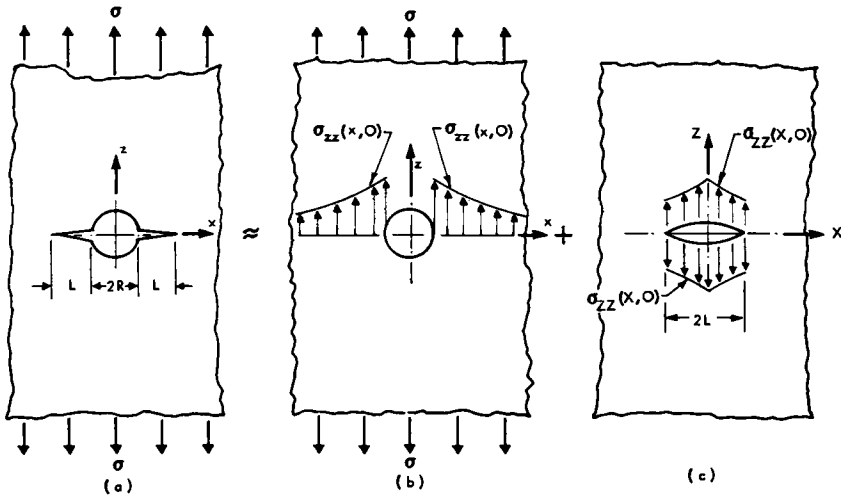


FIG. 2—Approximate procedure for determining stress intensity factors for two symmetric cracks emanating from a fastener hole.

$$K_I = \frac{1}{\sqrt{\pi L}} \int_{-L}^L \sigma_{zz}(X,0) \sqrt{\frac{L+X}{L-X}} dX \tag{1}$$

The SIF, thus derived, is applicable to two symmetric cracks originating at a fastener hole as shown in Fig. 2a.

The reasoning behind the foregoing superposition was as follows: It is known that for infinitely wide plates subjected to uniform tension, the SIF for a single edge crack of length  $L$  is 12 percent higher than that for a center crack of length  $2L$ , due to the introduction of the infinitely long stress free surface in the edge-cracked plate. In the problem of two symmetrical through cracks at an open hole in a plate subjected to uniform tension, the hole periphery is a stress free surface; however, its effect should be offset by the curvature of the hole periphery. Also, the stress free surface for this problem is of finite length; hence, its effect will be very small for long cracks with respect to the hole radius. Symmetrical cracks originating at a hole should be equivalent to a central crack rather than an edge crack. This statement is further supported by Bowie's solution for two very long cracks at an open hole ( $L/R \gg 1$ ) where the SIF for cracks at a hole approaches that of a central crack of length  $2L$  in an infinite plate [3].

Approximate SIF's for one crack of length  $L$  originating at a hole in a plate are obtained by multiplying SIF's for two symmetrical cracks of length  $L$  at a hole by the factor shown in Eq 2.

$$K \Big|_{\text{one crack}} = \sqrt{\frac{2R + L}{2R + 2L}} K \Big|_{\text{two cracks}} \tag{2}$$

This approach resulted from the knowledge that, when the crack length is very large with respect to the hole diameter, the effect of the hole on the SIF is negligible, and SIF's can be calculated using equations for central through cracks of length  $2R + 2L$  (two cracks) and  $2R + L$  (one crack). Since SIF's,  $K$ , vary with the square root of crack length, the relationship between  $K$  for two symmetrical long cracks at a hole and one unsymmetrical long crack at a hole is given by Eq 2. Also, when crack length is very small with respect to the hole radius, SIF's for one and two cracks are approximately the same [3]. This is also shown by Eq 2. Equation 2 is used for all  $L/R$  values to compute SIF's for one crack originating at a fastener hole. This procedure is verified in the next section with the known solutions of one crack originating at a hole.

**Verification of Procedure**

Consider the case of a plate containing two through-the-thickness symmetrical cracks, each of length  $L$ , originating at an open circular hole of radius  $R$ , as shown in Fig. 3. The plate is subjected to uniform tension  $\sigma$  perpendicular to the plane of the crack and a uniform tension (or compression)  $\lambda\sigma$  parallel to the plane of the crack. The stress distribution  $\sigma_{zz}(x,0)$  in the uncracked plate at the location of the cracks for the above loading is given by the following well-known equation [13].

$$\sigma_{zz}(x,0) = \frac{\sigma}{2} \left[ 2 + (1 + \lambda) \frac{R^2}{x^2} + 3(1 - \lambda) \frac{R^4}{x^4} \right] \tag{3}$$

SIF's for two through cracks of length  $L$  are then obtained by pressurizing the central crack of length  $2L$  in Fig. 2c by  $-\sigma_{zz}(X,0)$  given by the following equation.

$$\sigma_{zz}(X,0) = \frac{\sigma}{2} \left[ 2 + (1 + \lambda) \left( \frac{R}{R + |X|} \right)^2 + 3(1 - \lambda) \left( \frac{R}{R + |X|} \right)^4 \right] \tag{4}$$

$0 \leq |X| \leq L$

where  $|X| = |x| - R$ , and  $Z = z$ . SIF's  $K_1$  are obtained by integrating Eq 1 with Eq 4 and are given by Eq 5 [14,15].

$$K_1 = \sigma\sqrt{\pi L} \left\{ 1 + \frac{1}{\pi} [(1 + \lambda)R^2I_2 + 3(1 - \lambda)R^4I_4] \right\} \tag{5}$$

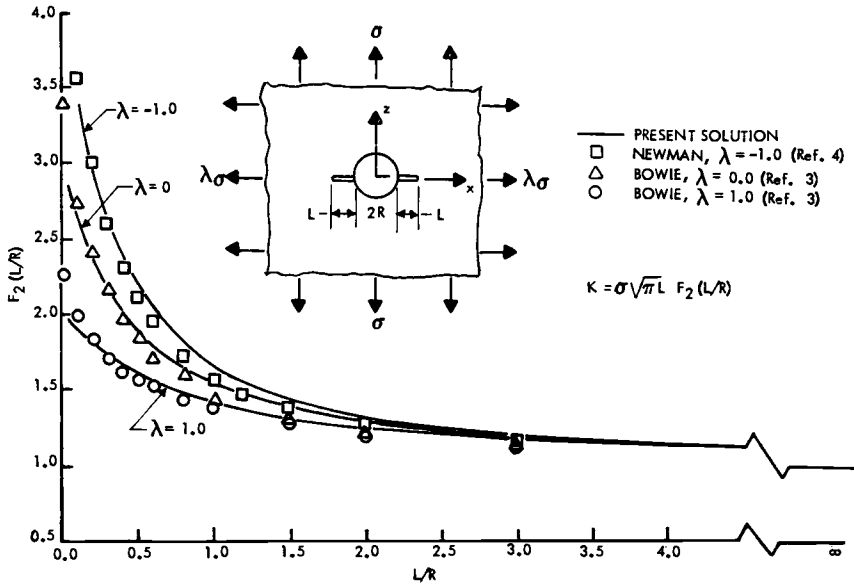


FIG. 3—Stress intensity factors for two through-the-thickness cracks emanating from a hole in a plate subjected to biaxial stress.

where  $R^2I_2$  and  $R^4I_4$  are given by Eqs 6a and b.

$$R^2I_2 = \frac{1}{1 - \xi^2} [-\xi + RI_1] \tag{6a}$$

$$R^4I_4 = \frac{1}{3(1 - \xi^2)} \left[ -\xi + \frac{\xi(\xi^2 - 16)}{2(1 - \xi^2)^2} + \frac{(6 + 9\xi^2)}{2(1 - \xi^2)^2} RI_1 \right] \tag{6b}$$

for  $\xi \neq 1$

$\xi$  and  $RI_1$  are given by the following equations.

$$\xi = L/R \tag{7a}$$

$$RI_1 = \frac{2}{\sqrt{1 - \xi^2}} \tan^{-1} \sqrt{\frac{1 - \xi}{1 + \xi}} \text{ for } \xi < 1 \tag{7b}$$

$$RI_1 = \frac{1}{\sqrt{\xi^2 - 1}} \log \left[ \frac{\sqrt{\xi + 1} + \sqrt{\xi - 1}}{\sqrt{\xi + 1} - \sqrt{\xi - 1}} \right] \text{ for } \xi > 1 \tag{7c}$$

$$RI_1 = 1/\xi = 1 \text{ for } \xi = 1 \tag{7d}$$

In the following, SIF's  $K_I$  are calculated for various values of  $\lambda$  for one or two cracks originating at an open hole and are compared with the known solutions given by Bowie using the approximate mapping technique [3], Newman using the boundary collocation technique [4] and Tweed [5] using Mellin transform and integral equation techniques to assess the accuracy and the validity of the proposed technique.

### 1. Uniaxial Loading ( $\lambda = 0$ )—Two Cracks

SIF's for two symmetrical through cracks of length  $L$  originating at an open hole of radius  $R$  in a plate subjected to uniform uniaxial tension  $\sigma$  ( $\lambda = 0$  in Fig. 3) are calculated with Eqs 5, 6, and 7 for various values of  $L$ . SIF's  $K_I$  are represented in the nondimensional form,  $F_2(L/R)$ , as follows.

$$F_2(L/R) = K_I/(\sigma\sqrt{\pi L}) \quad (8)$$

Results of the foregoing approximate solution are compared to results of Bowie's numerical solution in Fig. 3. Newman's collocation solution for this problem agrees with Bowie's solution within 2 percent; hence, it is not shown in Fig. 3. The maximum discrepancy between the present solution and the Bowie's solution is less than 7 percent for  $0.05 \leq L/R < \infty$ .

### 2. Uniaxial Loading ( $\lambda = 0$ )—One Crack

SIF's for one through crack of length  $L$  emanating from an open hole of radius  $R$  in a plate subjected to uniaxial tension  $\sigma$  ( $\lambda = 0$  in Fig. 4) are calculated with Eqs 2, 5, 6, and 7 for various values of  $L$ . SIF's  $K_I$  are represented in the nondimensional form,  $F_1(L/R)$ , by Eq 9.

$$F_1(L/R) = K_I/(\sigma\sqrt{\pi L}) \quad (9)$$

The results,  $F_1(L/R)$ , of the preceding solution are compared to those from Bowie's solution for the same problem, and the two solutions agree within less than 2 percent for  $0.05 \leq L/R < \infty$ .

### 3. Biaxial Tension ( $\lambda = 1$ )—Two Cracks

Nondimensional SIF's,  $F_2(L/R)$ , computed from Eqs 5 through 8 for two symmetrical through cracks originating at an open hole in a plate subjected to uniform biaxial tension ( $\lambda = 1$  in Fig. 3) agree within 5 percent with those from Bowie's solution for  $0.05 \leq L/R < \infty$ .

### 4. Biaxial Tension ( $\lambda = 1$ )—One Crack

Nondimensional SIF's,  $F_1(L/R)$ , computed from Eqs 2, 5, 6, 7, and 9 for one through crack emanating from a hole in a plate subjected to

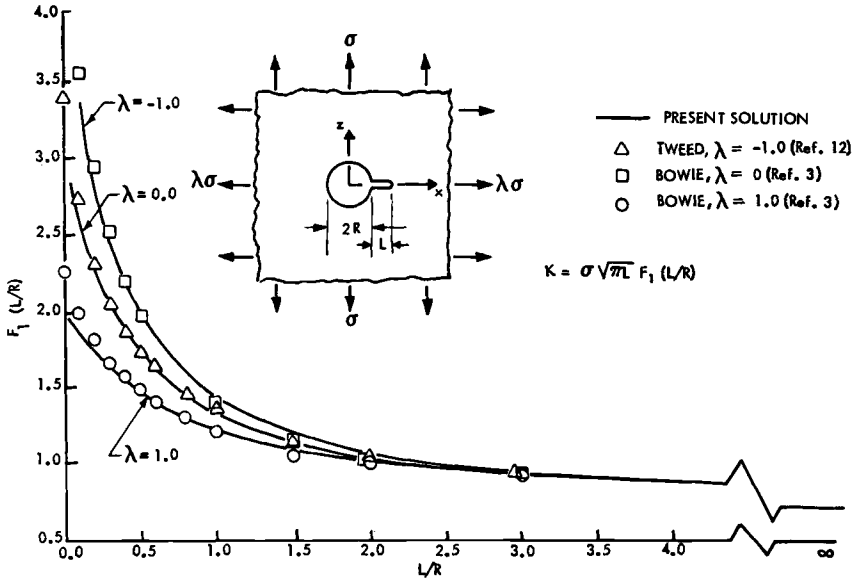


FIG. 4—Stress intensity factors for one through-the-thickness crack emanating from a hole in a plate subjected to biaxial stress.

uniform biaxial tension  $\sigma$  ( $\lambda = 1$  in Fig. 4) compare within 5 percent with those from Bowie's solution for  $L/R$  values of  $0.05 \leq L/R < \infty$ .

5. Biaxial Stresses ( $\lambda = 1$ )—Two Cracks

Nondimensional SIF's,  $F_2(L/R)$ , computed from Eqs 6 through 8 for two through cracks at a hole in a plate subjected to uniform tension,  $\sigma$ , perpendicular to the crack plane and uniform compression,  $-\sigma$ , parallel to the crack plane ( $\lambda = -1$  in Fig. 3) compare within 6 percent with those from Newman's solution [4] for  $L/R$  values of  $0.1 \leq L/R < \infty$ .

6. Biaxial Stresses ( $\lambda = 1$ )—One Crack

Nondimensional SIF's,  $F_1(L/R)$ , for one crack at a hole in a plate subjected to uniform tension,  $\sigma$ , perpendicular to the crack plane and uniform compression,  $-\sigma$ , parallel to the crack plane are computed from Eqs 2, 5, 6, 7, and 9. Maximum discrepancy between  $F_1(L/R)$  given by the present solution and Tweed's solution is 7 percent at  $L/R = 0.1$ . For  $L/R$  ratios of  $0.2 \leq L/R < \infty$ , the maximum discrepancy between the two solutions is less than 5 percent.

For all of the six cases, SIF's computed by the present solutions at  $L/R = 0$  are underestimated by approximately 12 percent as the effect of the stress free surface of the hole is neglected in the present solutions. As observed from Figs. 3 and 4, effect of the stress free surface is felt only by

very small cracks, such as  $L/R \leq 0.3$ . At  $L/R = 0.3$ , values of  $F(L/R)$  given by the present solutions are in the complete agreement with the known solutions for all of these cases except for the cases of one crack at a hole for the loadings of  $\lambda = \pm 1$ , where the present solutions underestimate SIF's by 3 percent. Error due to the effect of the free surface on SIF's for small cracks can be compensated by multiplying  $F_2(L/R)$  in Eq 8 and  $F_1(L/R)$  in Eq 9 by the quantity  $M_{HS}$  given by Eq 10.

$$M_{HS} = 1.0 + 0.12 \left( \frac{0.3 - L/R}{0.3} \right)^2 \quad (10a)$$

SIF's calculated with Eqs 8, 9, and 10 agree with the known solutions within 3 percent for  $L/R$  values of  $0.0 \leq L/R \leq 0.3$ . Thus, the present solution can be used for  $L/R$  values of  $0.0 \leq L/R < \infty$ .

In view of the very good agreement between the SIF's derived from the present procedure and the known solutions for three different loading and two different crack configurations, it is concluded that the foregoing approximate technique can be used to obtain SIF's for cracks originating at fastener holes. No SIF solutions are available for three-dimensional (such as part-through or semi-elliptical) crack problems to compare with the results obtained from this procedure. However, wherever possible and as shown subsequently, the approximate solutions of three-dimensional crack problems are reduced to those for two-dimensional crack problems and then compared with known two-dimensional crack solutions. Agreement between the two solutions is found to be very good. Hence, this approximate technique is used to derive SIF's for three-dimensional crack problems.

### Application of Procedure

Using the procedure outlined in the previous section, approximate SIF's are derived for through cracks and embedded semi-elliptical cracks originating at fastener holes for several different loading and fastener conditions described next and shown in Fig. 1.

#### *Cracks from an Open Hole*

*SIF's for Through Cracks*—SIF's for two or one through cracks originating at an open hole in a plate subjected to different loadings, such as  $\lambda = 0, \pm 1$ , are given in Figs. 3 and 4. Examination of Eq 5, as well as analytical results of Tweed [5], show that SIF's for a given  $L/R$  ratio for any value of  $\lambda$  can be obtained by linearly interpolating or extrapolating the results of SIF's for  $\lambda = \pm 1$  and  $\lambda = 0$  for that value of  $L/R$  ratio. For convenience, Fig. 5 gives SIF's for one or two cracks at a hole in a plate subjected to a biaxial tension stress corresponding to  $\lambda = 0.5$ . This case

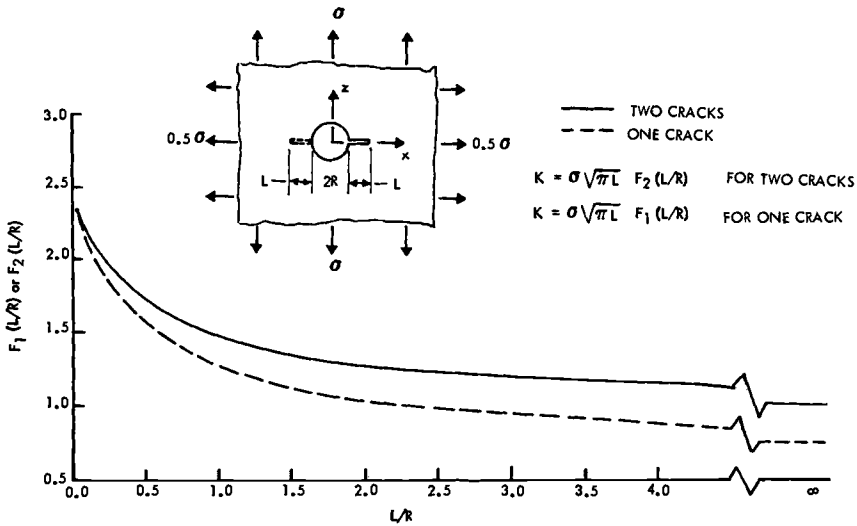


FIG. 5—Stress intensity factors for one or two through-the-thickness cracks emanating from a hole in a plate subjected to biaxial tension.

has some practical significance such as an axial crack in a pressurized cylindrical vessel at a hole where the radius of the vessel is very large such that it can be considered as a plate.

*SIF's for Semi-Elliptical Cracks at a Hole in a Solid*—Consider a problem of two semi-elliptical cracks emanating from a circular hole in a solid, as shown in Fig. 6. The solid is subjected to a uniaxial uniform tensile stress of  $\sigma$  which is perpendicular to the plane of the crack. In Fig. 6,  $2a$  is the crack dimension along the hole length in the  $Y$ -direction and  $c$  is the crack dimension perpendicular to the hole length in the  $X$ -direction. Angle  $\beta$  is the parametric angle of ellipse defined by the following equation and is defined in Fig. 6.

$$X = c \sin\beta \text{ and } Y = a \cos\beta \tag{10b}$$

In order to derive SIF's for two semi-elliptical cracks at a hole, the previously described technique requires a solution for the SIF for an embedded elliptical crack in an infinite solid subjected to a pressure distribution prescribed by Eq 3 where  $\lambda = 0$ . This, in turn, requires a Green's function for the SIF for an embedded elliptical crack in an infinite solid, which is not available. The most general solution available for the SIF of a pressurized elliptical crack is limited to the pressure distribution in the form of a polynomial of  $X$  and  $Y$  defined as follows [16].

$$p(X,Y,0) = \sum_{i=0}^3 \sum_{j=0}^3 A_{ij} X^i Y^j \quad i + j \leq 3 \quad (11)$$

A Green's function is available for circular (penny-shaped) cracks and is used in the following to derive SIF's for two semi-circular cracks at a hole in an infinite solid. As described in the appendix, the Ref 16 solution is used to extend nondimensionalized SIF's for two semi-circular cracks at a hole in a thick plate to those for two semi-elliptical cracks at a hole in a thick plate.

A Green's function for the SIF for a circular crack embedded in an infinite solid is given by Smith et al [17]. However, the Green's function in Ref 17 contains an infinite series, and it is not suitable for use when the pressure distribution prescribed on the crack surfaces is complex since integration cannot be carried out in the closed form and numerical integration is required. Hence, the Green's function for the SIF is modified into a form given by Eq 12 which can be used for general loading and is suitable for numerical integration. For the sake of brevity, details of

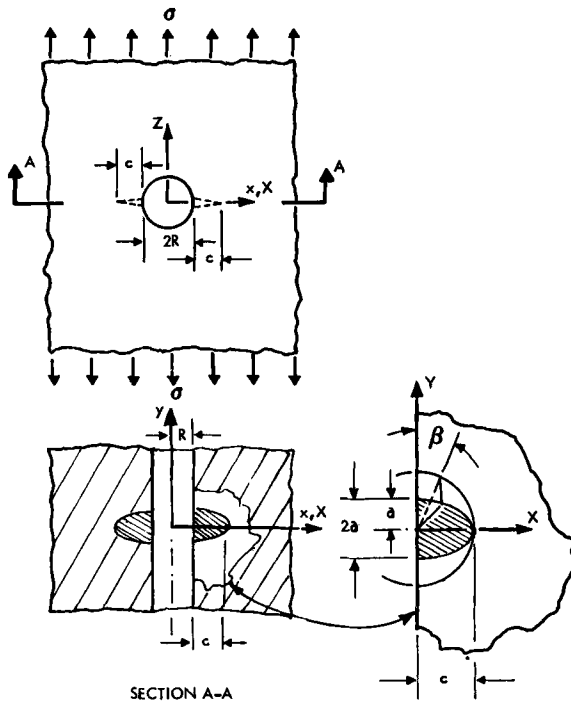


FIG. 6—Two semi-elliptical cracks originating at a hole in a thick plate.

the Green's function, that is, derivation and verification with the known solutions are not given here but are described in Ref 18.<sup>5</sup>

$$K_I(\psi) = \frac{1}{\pi(\pi a)^{1/2}} \int_0^a \int_0^{2\pi} \frac{rp(r,\phi,0)(a^2 - r^2)^{1/2}}{a^2 - 2ar \cos(\psi - \phi) + r^2} d\phi dr \quad (12)$$

In the preceding equation,  $a$  is the radius of the crack,  $p(r,\phi,0)$  is the prescribed arbitrary normal surface tractions applied to both the upper and the lower crack surfaces,  $r$  is the distance from the center of the crack in the crack plane,  $\phi$  is the angle measured with respect to the  $X$ -axis, and the origin of the coordinate axes ( $X, Y, Z$ ) is located at the center of the crack. The SIF  $K_I$  at any point on the crack periphery at the angle  $\psi$  from the  $X$ -axis is then given by Eq 12.

According to the previously described technique, SIF's for two semi-circular cracks of radius  $a$  originating at a hole of radius  $R$  in a solid subjected to uniform uniaxial tension  $\sigma$  is then given by Eq 12 where  $p(r,\phi,0)$  at  $Z = 0$  can be rewritten from Eq 4 as follows.

$$p(r,\phi,0) = \sigma_{zz}(X,Y,0) = \frac{\sigma}{2} \left[ 2 + \left( \frac{R}{R + r |\cos\phi|} \right)^2 + 3 \left( \frac{R}{R + r |\cos\phi|} \right)^4 \right] \quad (13)$$

It is not possible to integrate Eq 12 in the closed form for  $p(r,\phi,0)$  described by Eq 13. Straight forward numerical integration of Eq 12 using a variable step-size Simpson's rule procedure also poses a problem as the integrand defined by Eq 12 is singular at  $r = a$  and  $\phi = \psi$ . As shown in Ref 18, commonly used methods for the numerical evaluation of an improper integral such as ignoring the singularity or proceeding to the limit [19] do not work for Eq 12. A special method was used to evaluate numerically this improper integral which is described here briefly. Equation 12 can be rewritten as follows.

$$K_I(\psi) = \int_0^a \int_0^{\psi-\delta} F(r,\phi,0) d\phi dr + \int_0^{a-\epsilon} \int_0^{\psi+\delta} F(r,\phi,0) d\phi dr + \int_0^a \int_{\psi+\delta}^{2\pi} F(r,\phi,0) d\phi dr + \int_{a-\epsilon}^a \int_{\psi-\delta}^{\psi+\delta} F(r,\phi,0) d\phi dr \quad (14a)$$

<sup>5</sup> Reference 18 is available on request from the author or the Boeing Library.

$$F(r, \phi, 0) = \frac{1}{\pi(\pi a)^{1/2}} \frac{rp(r, \phi, 0)(a^2 - r^2)^{1/2}}{a^2 - 2ar \cos(\psi - \phi) + r^2} \quad (14b)$$

In Eq 13,  $\epsilon$  and  $\delta$  are very small quantities with respect to  $a$  and  $2\pi$ . First, second, and third integrals do not contain any singularity and were integrated numerically with a high degree of accuracy. (In actual computations,  $\epsilon$  and  $\delta$  were taken as  $0.01a$  and  $0.08727$  radian, respectively.) Fourth integral which is improper was evaluated analytically assuming the function  $p(r, \phi, 0)$  to be constant over the region  $\psi - \delta$  to  $\psi + \delta$  and  $a - \epsilon$  to  $a$ . Due to space limitations, details of this integration are given somewhere else [18]. This method was used to evaluate numerically the integral in Eq 12 where  $p(r, \phi, 0)$  was taken as  $r^2 \cos 2\phi$  and  $r^3 \cos 3\phi$  for which exact solutions for SIF's are available. SIF's computed by the numerical quadrature compared within 0.6 percent with those from the exact solutions.

Utilizing the quadrature technique just outlined, SIF's  $K_{Ih}$  for two semi-circular cracks of radius  $a$  (or  $c$ ) originating at a hole of radius  $R$  in a solid subjected to the applied tension  $\sigma$ , as shown in Fig. 6, are computed from Eqs 12 and 13 for various values of angles  $\psi$  from 0 to  $\pi/2$  and for various ratios of  $a/R$  (or  $c/R$ ). The resultant SIF  $K_{Ih}$  at any point on the crack periphery, defined by angle  $\beta$  measured from the  $Y$ -axis as shown in Fig. 6,<sup>6</sup> is normalized with respect to the SIF  $K_{Ie}$  for a penny-shaped crack of radius  $a$  (or  $c$ ) in an infinite solid subjected to the applied uniaxial tension,  $\sigma$ . The nondimensionalized SIF  $F_{0e}(c/R, \beta)$  is defined as follows.

$$F_{0e}(c/R, \beta) = K_{Ih}/K_{Ie} \quad (15a)$$

where

$$K_{Ie} = \sigma(\pi a/Q)^{1/2} (\cos^2\beta + \frac{a^2}{c^2} \sin^2\beta)^{1/4} \quad \text{if } a/c \leq 1.0 \quad (15b)$$

$$K_{Ie} = \sigma(\pi c/Q)^{1/2} (\sin^2\beta + \frac{c^2}{a^2} \cos^2\beta)^{1/4} \quad \text{if } a/c > 1.0 \quad (15c)$$

For convenience in discussion of semi-elliptical cracks at a hole (Fig. 6) later,  $K_{Ie}$  in Eqs 15b and c is represented for a general case of an elliptical crack of diameters of lengths  $2a$  and  $2c$  instead of a penny-shaped crack.

<sup>6</sup> Angle  $\beta$  and angle  $\psi$  defined before are complimentary angles for a semi-circular crack, that is  $\beta + \psi = \pi/2$  radians.

For the case in discussion here,  $a = c$ . The shape parameter  $Q$  is defined by Eq 16 [20].

$$Q = [E(k)]^2/[1.0 - 0.212(\sigma/\sigma_{ys})^2] \quad (16a)$$

where  $\sigma_{ys}$  is the uniaxial tensile yield strength of the material and  $E(k)$  is the complete elliptical integral of the second kind corresponding to the modulus  $k$  where  $k$  is given by either Eq 16b or Eq 16c.

$$k = [1 - a^2/c^2]^{1/2} \quad \text{if } a/c \leq 1.0 \quad (16b)$$

$$k = [1 - c^2/a^2]^{1/2} \quad \text{if } a/c > 1.0 \quad (16c)$$

Angle  $\beta$ , as mentioned before, is defined in Fig. 6 as well as by Eq 10b.

The nondimensionalized factors  $F_{oe}(c/R, \beta)$  are shown in Fig. 7 for two semi-circular cracks at a hole in a thick plate for various values of  $c/R$  from 0.0 to 10.0 and for various values of angle  $\beta$  from 0 to 90 deg. For  $a/c = 1.0$ ,  $K_{Ie}$  is not dependent on angle  $\beta$  and is constant. Figure 7 shows that the SIF  $K_{Ih}$  is maximum at  $\beta = 0$  deg (point on the crack periphery nearest the hole) and decreases monotonically to a minimum at  $\beta = 90$  deg (point on the crack periphery farthest away from the hole).

As outlined in the Appendix, SIF's  $K_{Ih}$  for two semi-elliptical cracks at a hole in a thick plate (Fig. 6) are estimated using the solution in Ref 16 and the previously outlined technique for  $a/c$  values ranging from 0.1 to 1.0,  $c/R$  values ranging from 0.0 to 10.0, and  $\beta$  values ranging from 0 to 90 deg. The analysis for estimating SIF's is outlined in detail in the Appendix. The resulting SIF's  $K_{Ih}$  are nondimensionalized with respect to the SIF  $K_{Ie}$  for an elliptical crack in an infinite solid having the same values of  $a$  and  $c$  as those for the semi-elliptical cracks at a hole. The nondimensionalized factor  $F_{oe}(c/R, \beta)$  and  $K_{Ie}$  are defined by Eqs 15a and b (or c), respectively. Results (Fig. 16 of the Appendix) show that the nondimensionalized SIF's  $F_{oe}$  are quite insensitive to the value of  $a/c$  for any given value of  $c/R$  and  $\beta$ . Accordingly, it is concluded that  $F_{oe}$  could be assumed to be independent of  $a/c$ . Thus, SIF's for two semi-elliptical cracks originating at an open hole in a thick plate subjected to the uniform uniaxial tension (Fig. 6) can be approximated from Eqs 15 and 16 and Fig. 7.

There is no stress intensity factor solution available with which to compare the results of the foregoing approximate solution. However, the approximate solution can be reduced to a two-dimensional crack problem by letting  $a/c \rightarrow \infty$ . The problem then reduces to the two-dimensional problem of two symmetrical through-the-thickness cracks, each of length

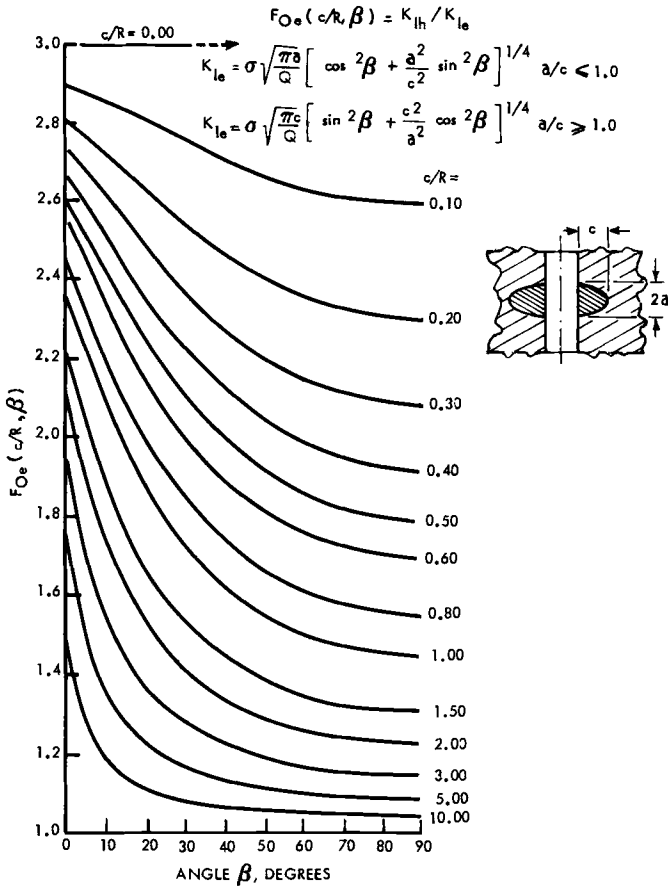


FIG. 7—Nondimensionalized stress intensity factors for two semi-elliptical cracks at a hole in a thick plate.

$c$ , originating at a hole in a thick plate. The stress intensity factor  $K_{Ie}$  from Eq 15c is given by  $\sigma\sqrt{\pi c}$  at  $\beta = 90$  deg. Stress intensity factor  $K_{Ih}$  is then given by the equation  $F_{Oe}(c/R, 90)\sigma\sqrt{\pi c}$ . Values of  $F_{Oe}(c/R, 90)$  agree within four percent with  $F_2(L/R)$  values (Fig. 3) from the corresponding Bowie's solution for the range of  $0.1 \leq c/R \leq 10.0$ . Since the foregoing agreement was not a built-in condition to the approximate solution, such agreement gives confidence in the accuracy of the solution.

An interesting observation can be made from the results of Fig. 7. The SIF  $K_{Ih}$  is always maximum at  $\beta = 0$  deg (point on the crack periphery nearest to the hole) for  $a/c \leq 1.0$ . However,  $K_{Ih}$  at  $\beta = 0$  deg can be smaller than  $K_{Ih}$  at  $\beta = 90$  deg (point on the crack periphery farthest from the hole) for  $a/c \geq 1$  since  $K_{Ie}$  at  $\beta = 0$  deg is significantly smaller than  $K_{Ie}$  at  $\beta = 90$  deg.

*Cracks from an Unloaded Neat Filled Hole*

Many investigators [23-28] have obtained approximate or exact solutions for a neat (close tolerance fastener) filled hole, with a smooth elastic or rigid fastener, in a plate subjected to uniform uniaxial tension. Figure 8 shows the distribution of the normal stress ( $\sigma_{zz}/\sigma$ ) across the minimum section of the plate ( $z = 0$ ) for this problem for various values of  $E_p/E_f$  where  $E$  is modulus of elasticity and the subscripts  $p$  and  $f$  pertain to the plate and the fastener, respectively. Figure 8 also shows the distribution of the normal stress at the same location for a plate with an open hole ( $E_p/E_f = \infty$ ) subjected to uniform tension  $\sigma$ . As seen from Fig. 8, the effect of contact and fastener materials on the stress  $\sigma_{zz}$  along the  $x$ -axis is less than 3 percent for  $x/R$  greater than 1.3 for two extreme cases: (1) a plate containing a rigid fastener and (2) a plate containing highly flexible

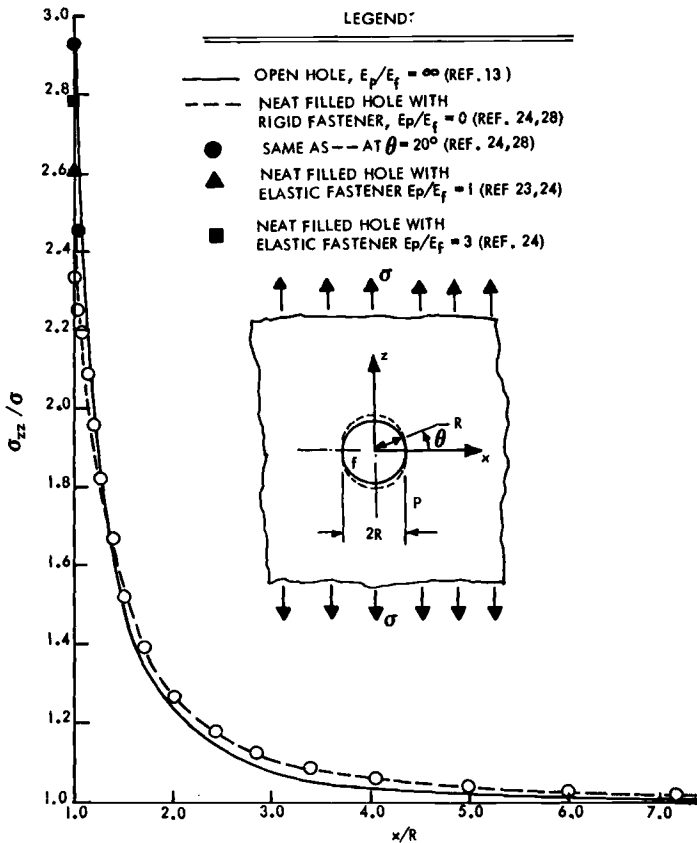


FIG. 8—Variation of normal stress  $\sigma_{zz}/\sigma$  along  $x$ -axis for a plate containing a neat filled hole.

fastener (open hole). For  $1.1 \leq x/R \leq 1.3$ , the difference in the stress  $\sigma_{zz}$  along  $z = 0$  between the previously considered two extreme cases ranges from 3 to 10 percent. For  $x/R = 1.0$ , the difference in the stress  $\sigma_{zz}$  at  $\theta = 0$  deg ( $z = 0$ ) between the two cases is 22 percent. For real structures, the effect of plate-fastener materials on  $\sigma_{zz}$  along  $z = 0$  for a neat filled hole in a plate is equal to or smaller than the preceding noted effects.

It is of interest to note that the maximum tensile stress on the hole-fastener periphery generally occurs at the point of contact separation, that is,  $\theta \approx 20$  deg. Figure 9 shows the distribution of circumferential stress  $\sigma_{\theta\theta}$  around the hole periphery for four different combinations of plate/fastener materials. The difference between maximum stresses for the hole filled with a rigid fastener and the open hole is less than 8 percent, as shown in Fig. 9. In the case of fatigue of a filled hole with no cracks, crack initiation does not have to occur at  $\theta = 0$  deg. In the absence of the influence of other factors, the crack would initiate at the point of maximum stress ( $\theta \approx 20$  deg) and grow toward  $\theta = 0$  deg.

SIF's for through or semi-elliptical cracks originating from a neat filled hole in a plate or a solid subjected to uniaxial uniform tension can be derived with the technique described before and the stress distribution just described. SIF's thus obtained will depend on material properties of both the fastener and the plate. However, as shown before, the difference between the stress distributions along  $z = 0$  for the two extreme cases, namely, the open hole and the neat filled hole with rigid fastener, is very small for  $x/R \geq 1.3$  ( $x/R - 1$ ) is equivalent to  $L/R$  for through cracks and  $c/R$  for semi-elliptical cracks). Hence, the solution derived for SIF's at cracks originating from an open hole can be used for the corresponding case of a neat filled hole when  $L/R$  or  $c/R > 0.3$ . SIF's for extremely small cracks ( $L/R \ll 0.1$  or  $c/R \ll 0.1$ ) at neat filled holes containing very stiff fasteners ( $E_p/E_f \ll 1$ ) could be conceivably overestimated by as much as 20 percent: for  $0.1 \leq L/R \leq 0.3$ , the overestimate would be less than 10 percent; for  $L/R > 0.3$  the overestimate would be negligibly small. In actual structures, the overestimate in SIF's for cracks from neat filled holes due to using the solution for SIF's for cracks from open holes would be smaller than those values just quoted due to fastener flexibility. Hence, it is concluded that the solution derived for SIF's for cracks originating from an open hole in a plate can also be used for the corresponding case of a neat filled hole for all crack size to hole radius ratios except for  $L/R \ll 0.1$  or  $c/R \ll 0.1$ .

#### *Cracks from a Loaded Neat Filled Hole*

The problem of a loaded neat filled hole in a plate (Fig. 1f without crack) has been studied by many investigators [27-33]. Only Refs 27 and 28 consider the effect of contact, and only Ref 28 explicitly gives the stress distribution near the hole obtained from a finite element analysis as-

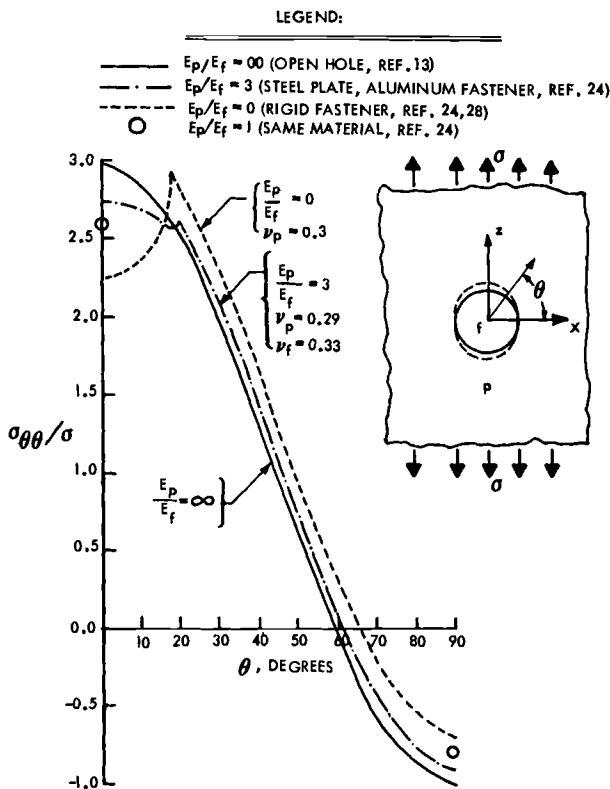


FIG. 9—Variation of circumferential stress  $\sigma_{\theta\theta}/\sigma$  around the hole periphery for a plate containing a neat filled hole.

suming the fastener (insert) as rigid. As shown in Ref 18, contact condition has a significant effect on the stress distribution around the hole and on the stress distribution  $\sigma_{zz}$  across the minimum section of the plate ( $z = 0$  in Fig. 10). Hence, the stress distribution  $\sigma_{zz}$  along  $z = 0$  given by Ref 28 is used to derive SIF's for cracks at loaded neat filled holes. The normal stress  $\sigma_{zz}$  is normalized with the bearing stress  $\sigma_b$  and is expressed within 3 percent for  $x \leq 10R$  by the following equations.

$$\frac{\sigma_{zz}}{\sigma_b} = A_0 + A_2 \frac{R^2}{x^2} + A_4 \frac{R^4}{x^4} + A_6 \frac{R^6}{x^6} \tag{17a}$$

$$\sigma_b = \frac{P}{2Rt} \tag{17b}$$

$$A_0 = 0.04374, A_2 = 0.71304, A_4 = -0.66404, \text{ and } A_6 = 0.91998 \tag{17c}$$

where  $P$ ,  $R$ , and  $t$  are the applied concentrated force, radius of the hole, and thickness of the plate, respectively.

Experimental studies have been conducted to determine the stress concentration and distribution near a loaded neat filled hole [34,35]. The experimental stress concentration factor agrees within 2 percent with that from theoretical analysis [28]. Experimental results on aluminum plates show that a very small increase (less than 4 percent) in the maximum stress occurs when the neat fitting aluminum pin is replaced by a steel pin having the same fit [35]. A steel pin in an aluminum plate can be approximated as a rigid pin. Thus, the stress distribution for a loaded neat filled hole containing a rigid insert can be used to describe the stress distribution for a loaded neat filled hole containing an elastic fastener with little error.

Shear stress  $\tau_{xz}$  across  $z = 0$  ( $x$ -axis) is very small when compared to

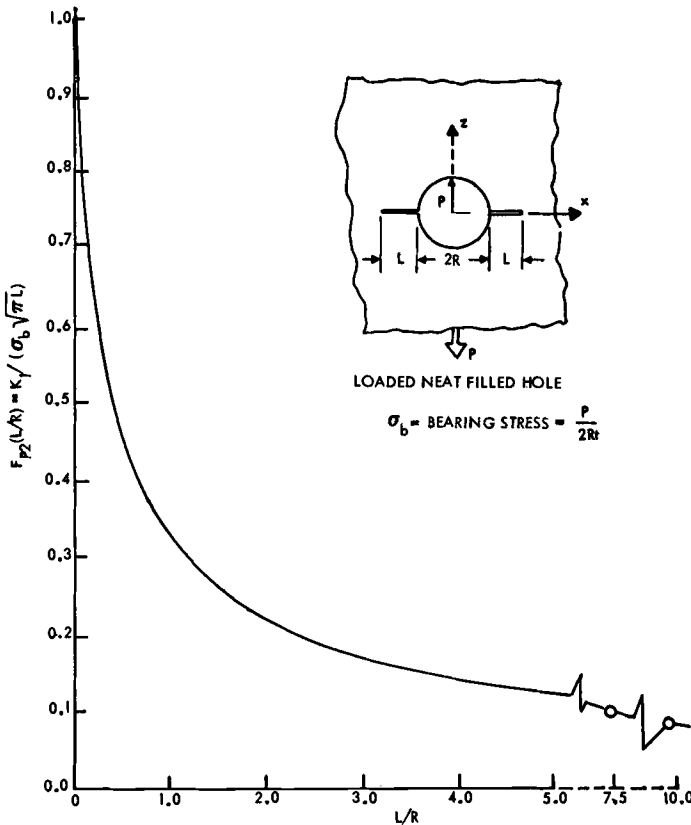


FIG. 10—Nondimensionalized stress intensity factors for two cracks originating from a loaded neat filled hole.

$\sigma_{zz}$  [28]. Hence, shear stresses are ignored and sliding mode SIF's  $K_{II}$  are not derived for cracks originating at loaded neat filled holes.

*SIF's for Through Cracks*—SIF's for two through cracks, each of length  $L$ , originating at a loaded neat filled hole in a plate can now be derived from Eqs 1 and 17 (Eq 17a represented in terms of  $X$  instead of  $x$ ). Integration in Eq 1 can be carried out in the closed form or numerically using a procedure similar to that described before or in Ref 18 for the double integration. A closed form expression for SIF  $K_I$  is given by the following equation.

$$K_I = \sigma_b \sqrt{\pi L} \left[ A_0 + \frac{2}{\pi} (A_2 R^2 I_2 + A_4 R^4 I_4 + A_6 R^6 I_6) \right] \quad (18)$$

where  $A_0, A_2, A_4,$  and  $A_6$  are given by Eq 17c,  $R^2 I_2$  and  $R^4 I_4$  are given by Eqs 6 and 7, and  $R^6 I_6$  is given by Eq 19.

$$\left. \begin{aligned} R^6 I_6 &= \frac{1}{5(1 - \xi^2)} \left[ -\xi + 9R^5 I_5 - 4R^4 I_4 \right] & (19a) \\ R^5 I_5 &= \frac{1}{4(1 - \xi^2)} \left[ -\xi + 7R^4 I_4 - 3R^3 I_3 \right] & (19b) \\ R^3 I_3 &= \frac{1}{2(1 - \xi^2)} \left[ \frac{-\xi(4 - \xi^2)}{1 - \xi^2} + \frac{2 + \xi^2}{1 - \xi^2} R I_1 \right] & (19c) \end{aligned} \right\} \xi \neq 1$$

where, as mentioned before,  $\xi = L/R$  and  $R I_1$  is given by Eq 7.

The SIF,  $K_I$ , for two through cracks, each of length  $L$ , originating at a neat filled hole loaded by a force  $P$ , is represented by the following equation.

$$K_I = \sigma_b \sqrt{\pi L} F_{P2}(L/R) \quad (20)$$

where  $\sigma_b$ , the bearing stress, is defined by Eq 17b, and  $F_{P2}(L/R)$  is the nondimensional factor which is given as a function of the ratio of crack length to hole radius,  $L/R$ , in Fig. 10.

The SIF,  $K_I$ , for one through crack of length  $L$  originating at a neat filled hole loaded by a force  $P$  is given by the following equation.

$$K_I = \sigma_b \sqrt{\pi L} F_{P1}(L/R) \quad (21)$$

where  $\sigma_b$  is the bearing stress and  $F_{P1}(L/R)$  is a nondimensional factor

which is given as a function of the ratio of crack length to hole radius,  $L/R$ , in Fig. 11.  $F_{P1}(L/R)$  is obtained from  $F_{P2}(L/R)$  and Eq 2.

*SIF's for Semi-Elliptical Cracks*—The SIF,  $K_{In}$ , for two semi-circular cracks of radius  $a$  or  $c$ , originating at a neat filled hole of radius  $R$  and loaded by a force  $P$  in a thick plate (Fig. 6) is derived from Eq 12 where

$$p(r, \phi, 0) = \sigma_{zz}(X, Y, 0) = A_0 + A_2 \left( \frac{R}{R + |r \cos \phi|} \right)^2 + A_4 \left( \frac{R}{R + |r \cos \phi|} \right)^4 + A_6 \left( \frac{R}{R + |r \cos \phi|} \right)^6 \quad (22)$$

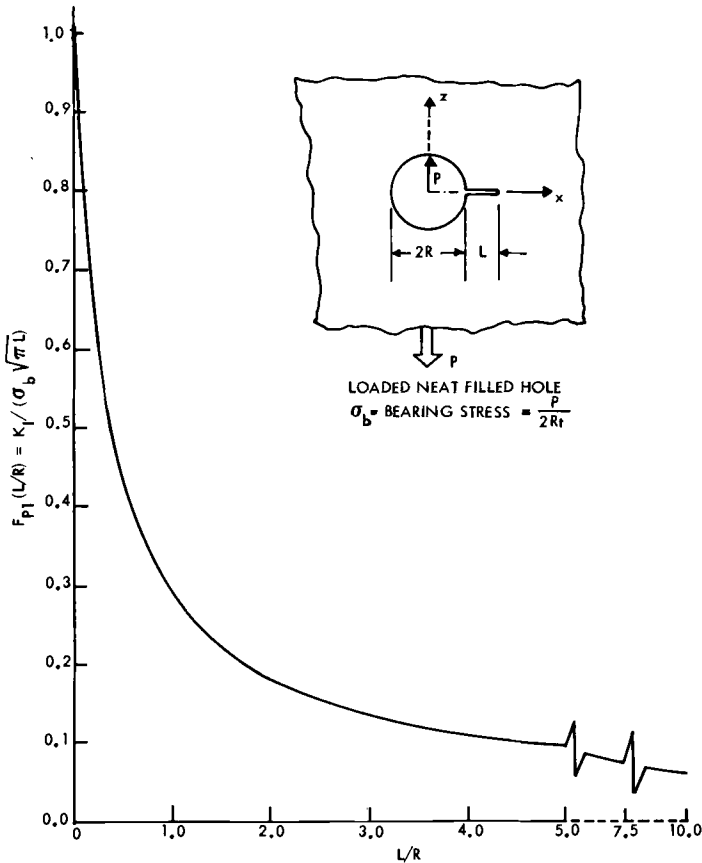


FIG. 11—Nondimensional stress intensity factors for one through crack originating from a loaded neat filled hole.

Equation 22 is the same as Eq 17a represented in a form suitable for the Green's function for the SIF of a penny-shaped crack. Constants  $A_0$ ,  $A_2$ ,  $A_4$ , and  $A_6$  are given by Eq 17c.  $R$ ,  $r$ , and  $\phi$  are defined previously. Utilizing the quadrature technique outlined previously, SIF's  $K_{1h}$  are evaluated from Eqs 12 and 22 for various values of angles  $\psi$  from 0 to  $\pi/2$  radians and for various ratios of  $a/R$  (or  $c/R$ ). The resultant SIF,  $K_{1h}$ , at any point on the crack periphery, defined by angle  $\beta$  measured from the  $Y$ -axis as shown in Fig. 6, is normalized with respect to the SIF  $K_{1eb}$  for a penny-shaped crack of radius  $a$  (or  $c$ ) in an infinite solid subjected to uniform uniaxial tension  $\sigma_b$ .  $\sigma_b$  is the bearing stress defined by Eq 17b. The nondimensionalized SIF,  $F_{pe}(c/R, \beta)$ , is defined as follows.

$$F_{pe}(c/R, \beta) = K_{1h}/K_{1eb} \quad (23a)$$

where

$$K_{1eb} = \sigma_b(\pi a/Q)^{1/2} \left( \cos^2\beta + \frac{a^2}{c^2} \sin^2\beta \right)^{1/4} \quad \text{if } a/c \leq 1.0 \quad (23b)$$

$$K_{1eb} = \sigma_b(\pi c/Q)^{1/2} \left( \sin^2\beta + \frac{c^2}{a^2} \cos^2\beta \right)^{1/4} \quad \text{if } a/c > 1 \quad (23c)$$

$K_{1eb}$  is given for a general case of an elliptical crack of diameters of lengths  $2a$  and  $2c$  instead of a penny-shaped crack. For the penny shaped crack,  $a = c$  in Eq 23. The parametric angle  $\beta$  and the shape parameter  $Q$  are defined before by Eqs 10 and 16, respectively.  $F_{pe}(c/R, \beta)$  is plotted against angle  $\beta$  for various values of  $c/R$  varying from 0 to 10.0 in Fig. 12.

Nondimensionalized SIF's,  $F_{pe}$ , for two semi-elliptical cracks at a loaded filled hole, obtained using the method outlined in the Appendix, do not vary at  $\beta = 0$  deg more than 3 percent for any given value of  $c/R$  and for  $a/c$  ratios from 0.1 to 1.0. However, as  $\beta$  increases,  $F_{pe}$  estimated for  $a/c = 0.1$  differs significantly from  $F_{pe}$  estimated for  $a/c = 1.0$ . At  $\beta = 45$  deg,  $F_{pe}$  estimated for  $a/c = 0.1$  is as much as 10 percent lower than  $F_{pe}$  estimated for  $a/c = 1.0$  for the same value of  $c/R$ . At  $\beta = 90$  deg,  $F_{pe}$  estimated for  $a/c = 0.1$  is as much as 30 percent lower than  $F_{pe}$  at  $a/c = 1.0$ . For any given value of  $\beta$  and  $c/R$ , the estimated  $F_{pe}$  for  $a/c \geq 0.4$  does not differ more than 10 percent from the estimated  $F_{pe}$  at  $a/c = 1.0$ . Thus,  $F_{pe}$  in Eq 23 may be assumed constant for all values of  $a/c$  ratios for  $\beta \leq 45$  deg, and for  $a/c \geq 0.4$  for  $\beta \geq 45$  deg. If  $F_{pe}$  is truly independent of  $a/c$ , then when the problem is reduced to a two-dimensional through crack problem, by letting  $a/c \rightarrow \infty$ ,  $F_{pe}$  at  $\beta = 90$  deg given in Fig. 12 should agree with  $F_{p2}$  given by Fig. 10 for all  $c/R$

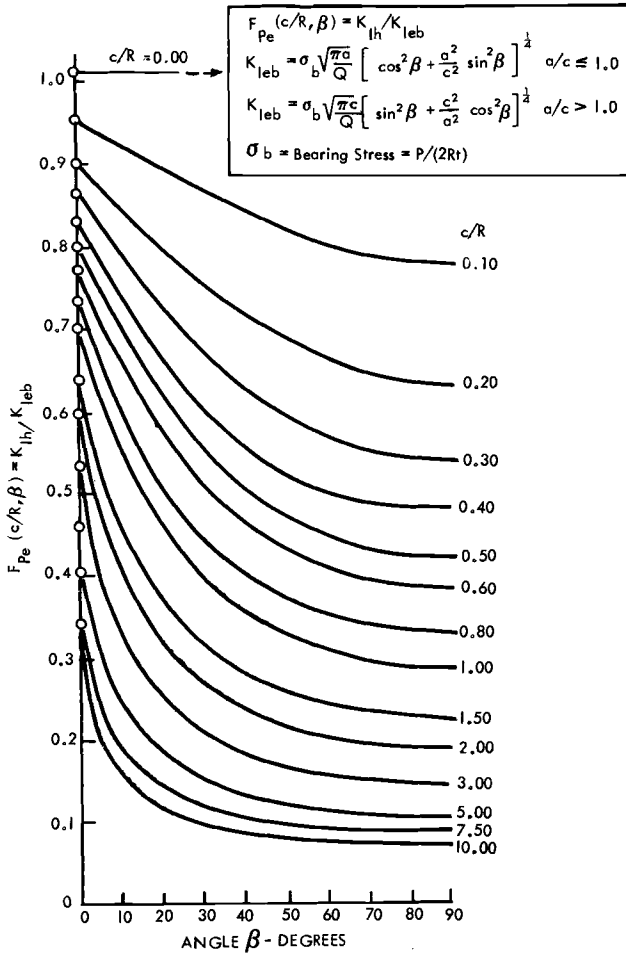


FIG. 12—Nondimensionalized stress intensity factors for two semi-elliptical cracks originating from a loaded neat filled hole in a thick plate.

(same as  $L/R$  in Fig. 10) values.  $F_{Pe}$  for  $a/c = \infty$  at  $c/R = 0$  completely agrees with  $F_{p2}$  at  $L/R = 0$ , and  $F_{Pe}$  at  $c/R = 10$  is 14 percent lower than  $F_{p2}$  at  $L/R = 10$ . For values of  $c/R$  less than 10,  $F_{Pe}$  is less than 14 percent lower than  $F_{p2}$  for the same values of  $L/R$ . Thus, it is possible that for very high values of  $a/c$  ( $a/c \gg 1$ ), SIF's for two semi-elliptical cracks at a loaded neat filled hold may be underestimated as much as 14 percent for large values of  $c/R$  with the use of Eqs 23. Error estimates for  $a/c < 1$  were just discussed.

*Cracks from a Loaded Neat Filled Hole in a Plate Subjected to Tensile Loading*

The term—a loaded neat filled hole in a plate subjected to remote tensile loading—is described schematically in Fig. 13a. Consider the case of a plate containing a neat filled hole and subjected to a remote tensile load  $Q$  (Fig. 13b) and the case of a plate containing a loaded neat filled hole (Fig. 13c). Since the contact area changes between the load cases of Figs. 13a, b, and c, the exact stress distribution for the case of Fig. 13a cannot be obtained just by linearly superposing the stress distributions for load cases of Figs. 13b and c. To the author's knowledge, no general solution for the stress distribution is available for the loading case of Fig. 13a. Using finite element analysis, the problem of a loaded neat filled hole in a plate subjected to remote tensile loading for a particular loading relationship of  $Q = 3P$  in Fig. 13a is solved in Ref 28. The insert is assumed to be rigid and the plate width and the length are taken as ten times the hole diameter. Knowing that the contact problem is nonlinear and still applying the linear superposition principle to the problem of Fig. 13a, the stress distribution for the load case of Fig. 13a is given by the superposition of the stress distributions for loading cases of Figs. 13b and c. As shown in Ref 18, the stress  $\sigma_{zz}$  at  $z = 0$  obtained from the linear superposition agrees within 3 percent with that from the finite element solution for  $|x|/R > 1.1$ . For  $|x|/R = 1.0$ , the difference in stress  $\sigma_{zz}$  between the linear superposition solution and the finite element solution is 15 percent. Hence, it can be assumed that the stress distribution  $\sigma_{zz}$  along the  $x$ -axis for the loading case of Fig. 13a can be well represented by the superposition of  $\sigma_{zz}$  along the  $x$ -axis for the loading cases shown in Figs. 13b and c.

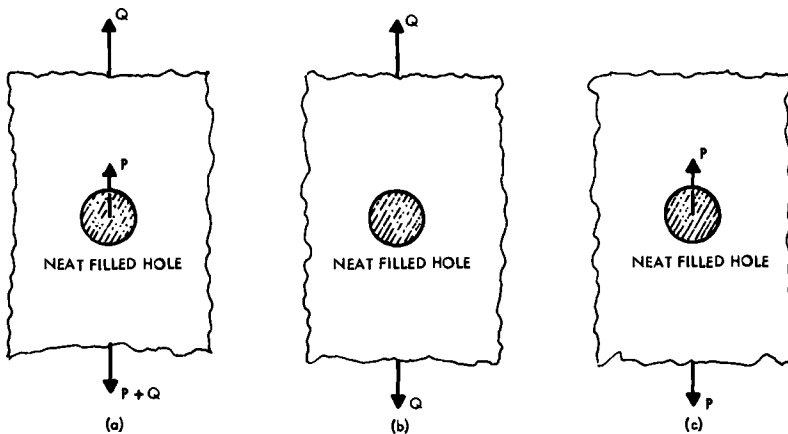


FIG. 13—A loaded neat filled hole in a plate subjected to remote tensile loading.

Since SIF's for cracks lying along the  $x$ -axis depend only on the stress  $\sigma_{zz}$  along the  $x$ -axis in an uncracked plate (infinite plate or solid), SIF's,  $K_{Ih}$ , for cracks emanating from a loaded neat filled hole in a plate subjected to remote loading (Fig. 13a) can be obtained by linearly superposing SIF's for cracks at a neat filled hole in a plate subjected to remote loading (Fig. 13b) and for cracks at a loaded neat filled hole (Fig. 13c). SIF's for the latter two cases were discussed before.

**Estimation of SIF's for Quarter-Elliptical Cracks in a Plate**

SIF's for one or two quarter-elliptical cracks originating at fastener holes (open, filled, loaded, or unloaded) in a finite thickness plate can be estimated from the previously derived solutions for SIF's for two semi-elliptical cracks in a solid and the appropriate correction factors for the stress free surfaces as indicated in Fig. 14. SIF's,  $K_{I2H}$ , for two quarter-elliptical cracks at a fastener hole in a semi-infinite solid (Fig. 14b) can be estimated by introducing a correction factor  $M_F(a/c, \beta)$  to account for the stress free front surface.

$$K_{I2H} = M_F(a/c, \beta)K_{Ih} \tag{24}$$

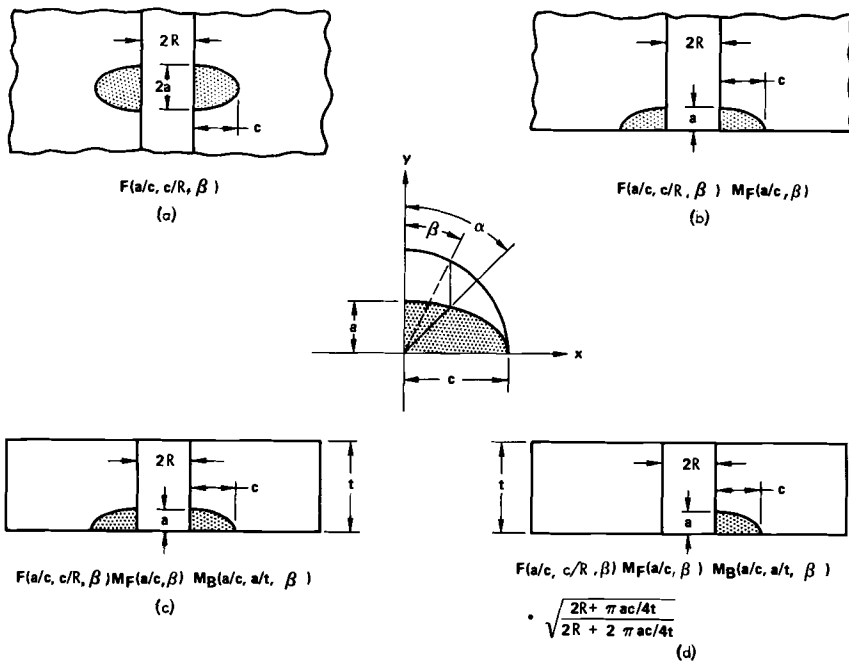


FIG. 14—Nondimensionalized stress intensity factors for quarter elliptical cracks at fastener holes.

where  $K_{1h}$  is the SIF for two semi-elliptical cracks at a fastener hole in an infinite solid (for the same conditions of fastener fit and loading).  $M_F(a/c, \beta)$  values are only available at the point of maximum depth ( $\beta = 0$  deg) for a semi-elliptical surface flaw in a uniform tension stress field given by Eq 25 [36]. At  $\beta = 90$  deg, the stress intensity solution for part-circular cracks shows that values of  $M_F(a/c, 90$  deg) vary from 1.1 to 1.23 [37]. At  $\beta = 90$  deg,  $M_F$  may then be assumed as 1.23. For estimating SIF  $K_{12H}$ ,  $M_F$  values may be assumed to be independent of  $\beta$  for  $0$  deg  $\leq \beta < 90$  deg, and to be given by Eq 25.

$$M_F(a/c, \beta) = 1.0 + 0.12(1 - a/2c)^2 \quad (25)$$

SIF's,  $K_{12P}$ , for two quarter elliptical cracks at a fastener hole in a finite thickness plate (Fig. 14c) can be estimated by introducing a second correction factor  $M_B(a/c, a/t, \beta)$  to account for the effects of the stress free back surface.

$$K_{12P} = M_F(a/c, \beta) \times M_B(a/c, a/t, \beta) \times K_{1h} \quad (26)$$

Back surface correction factors  $M_B$  are presently available only for an elliptical crack in a semi-infinite solid subjected to uniform tension [38,39], and these factors can be used to estimate  $K_{12P}$  in the foregoing equation.  $M_B$  values for various  $a/c$  ratios from 0.1 to 1.0,  $a/t$  ratios from 0.0 to 0.9, and  $\beta$  values from 0 to 90 deg are given in Ref 38.

SIF's,  $K_{11P}$ , for one-quarter elliptical crack in a finite thickness plate (Fig. 14d), can be estimated from  $K_{12P}$  for two-quarter elliptical cracks in a finite plate by introducing a factor similar to that given by Eq 2. A quarter elliptical crack having a depth  $a$  and length  $c$  has an area equal to that of a through crack of length  $\pi ac/4t$ . Thus, the stress intensity factor for one-quarter elliptical crack,  $K_{11P}$ , can be approximated by the following equation.

$$K_{11P} = M_F(a/c, \beta) \times M_B(a/c, a/t, \beta) \times \sqrt{\frac{2R + \pi ac/4t}{2R + 2\pi ac/4t}} \times K_{1h} \quad (27)$$

## Discussion

For quarter elliptical flaws of small  $a/c$  ratios ( $a/c$  less than or around 1.0) originating at fastener holes, calculated SIF's are maximum at the edge of the hole ( $\alpha = \beta = 0$  deg in Fig. 14). It is not expected that fracture would initiate at the edge of the hole due to the release of constraint to

crack tip deformation resulting from the stress free hole surface. Rather, fracture is expected to initiate some distance away from the hole surface after the crack tip deformations build up to a level equivalent to plane strain conditions. Eighteen specimens of 4340 steel containing one or two nearly quarter circular cracks originating at open holes or loaded filled holes were loaded to fracture [40]. Solutions derived in this paper were used to estimate SIF's. Results of these fracture tests indicated that fractures in these tests originated at a point about  $\alpha = 25$  deg (Fig. 14) away from the hole surface. SIF's derived in this paper were also used to predict fracture strengths and crack propagation lives for over 100 specimens made from 4340 steel, 9Ni-4Co-0.2C steel, 2219-T851 aluminum, and 6A1-4V (ELI) beta annealed titanium and containing through or quarter elliptical cracks originating at open holes and at loaded and unloaded filled holes [40]. Good agreement was obtained between experimental and calculated results. Experimental results [40] also confirm the analysis results that SIF's obtained for quarter elliptical cracks originating from open holes in a plate subjected to remote tension represent SIF's for quarter elliptical cracks originating at a close tolerance fastener filled hole in a plate subjected to the same loading.

### Conclusions

1. A simple procedure is formulated to derive approximate SIF's for both part-through and through-the-thickness cracks originating at open holes and holes containing either loaded or unloaded close tolerance fit fasteners. The procedure checks out with known solutions for SIF's of one or two through-the-thickness cracks emanating from an open hole in a plate subjected to uniaxial or biaxial loading.

2. SIF's for through cracks at loaded close tolerance fasteners in a plate, and for semi-elliptical cracks at open holes and at loaded and unloaded close tolerance fastener filled holes in a thick plate are then derived with this procedure. SIF's for part-through cracks are determined as a function of position around crack periphery, crack aspect ratio, and crack length to hole radius ratios.

3. SIF's are estimated for quarter-elliptical cracks originating at open holes and at loaded and unloaded close tolerance fastener filled holes in a finite thickness plate.

### Acknowledgment

The author wishes to express his appreciation to H. A. Wood of the U.S. Air Force Flight Dynamic Laboratory and J. N. Masters of Boeing Aerospace Company for their interest and support. Special thanks are due to A. S. Kobayashi for advice, discussions, and assistance and L. R. Hall for help in preparation of the manuscript.

## APPENDIX

### Estimation of Stress Intensity Factors for Two Semi-Elliptical Cracks at a Hole in a Solid

Consider a problem of two semi-elliptical cracks originating at a circular hole of radius  $R$  in a solid subjected to uniform uniaxial tension  $\sigma$ , as shown in Fig. 6. In order to derive SIF's for two semi-elliptical cracks at a hole, a solution for the SIF for an elliptical crack in an infinite solid subjected to a pressure distribution prescribed by Eq 4 is required. The most general solution available for the SIF of a pressurized elliptical crack is limited to the pressure distribution in the form of a third degree polynomial of  $X$  and  $Y$  defined by Eq 11 [16]. The formulation and the symmetry of the problem requires the use of only even power terms of  $X$ . Also, the stress distribution near the hole along the  $X$ -axis given by Eq 4 is a function of  $X$  only. Hence, the solution available for use here is limited to the pressure distribution given by the following equation.

$$p(X, Y) = A_{00} + A_{20}X^2 \tag{28}$$

It is not possible to fit exactly the stress distribution given by Eq 4 using Eq 28. For through-the-thickness cracks, however, it was believed that as long as the area under the fitted stress curve versus  $X$ ,  $A_f$ , is approximately the same as the area under the prescribed stress curve versus  $X$ ,  $A_p$ , and the trend of the fitted stress distribution is similar to the prescribed stress distribution, the SIF's calculated using the two different stress distributions would not differ greatly. This assumption is examined using the problem of two symmetrical through

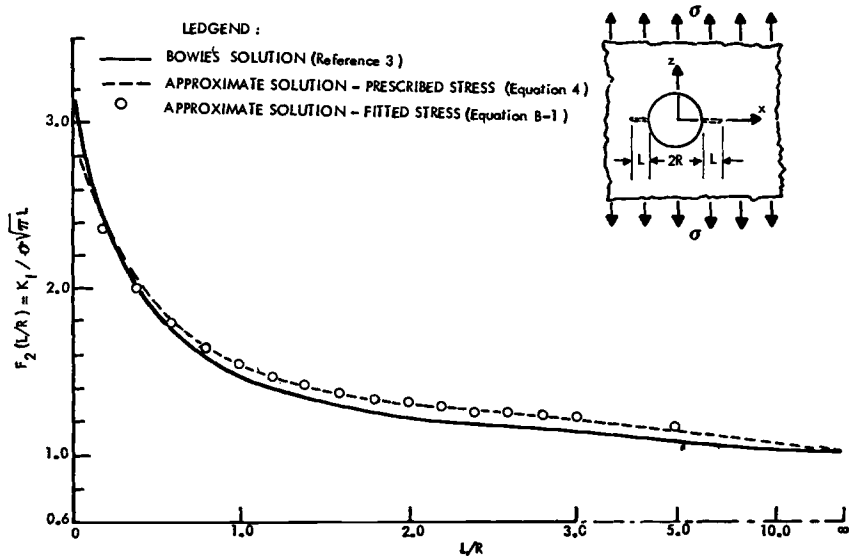


FIG. 15—Stress intensity factors for two through-the-thickness symmetrical cracks originating at a hole in a plate subjected to tension.

cracks, each of length  $L$ , originating at an open hole of radius  $R$ . The stresses prescribed by Eq 4 are least square fitted by Eq 28 for various values of  $L/R$  individually. The areas under the curves of the fitted stress and prescribed stress ( $A_f$  and  $A_p$ ) compare remarkably well for all  $L/r$  ratios and values of  $A_f/A_p$  range from 1.01 to 1.09 as values of  $L/r$  range from 0.1 to 6.0. The SIF's calculated using fitted stresses are plotted as open circles in Fig. 15 and agree within one percent with those computed from the prescribed stress of Eq 4 and using Eqs 5, 6, and 7. The maximum discrepancy between the SIF's computed from the fitted stress and those from Bowie's solution is less than 8 percent for  $0.1 \leq L/R < \infty$ . In view of the good agreement, fitted stresses are used to estimate the nondimensionalized SIF's for two semi-elliptical cracks at a hole in a solid, illustrated in Fig. 6, for various  $a/c$  ratios.

Initial estimates of SIF's for two semi-elliptical cracks at a hole in a thick plate are made by solving the equivalent problem of an embedded elliptical crack in a solid pressurized by the pressure distribution given by Eq 28. Similar to the

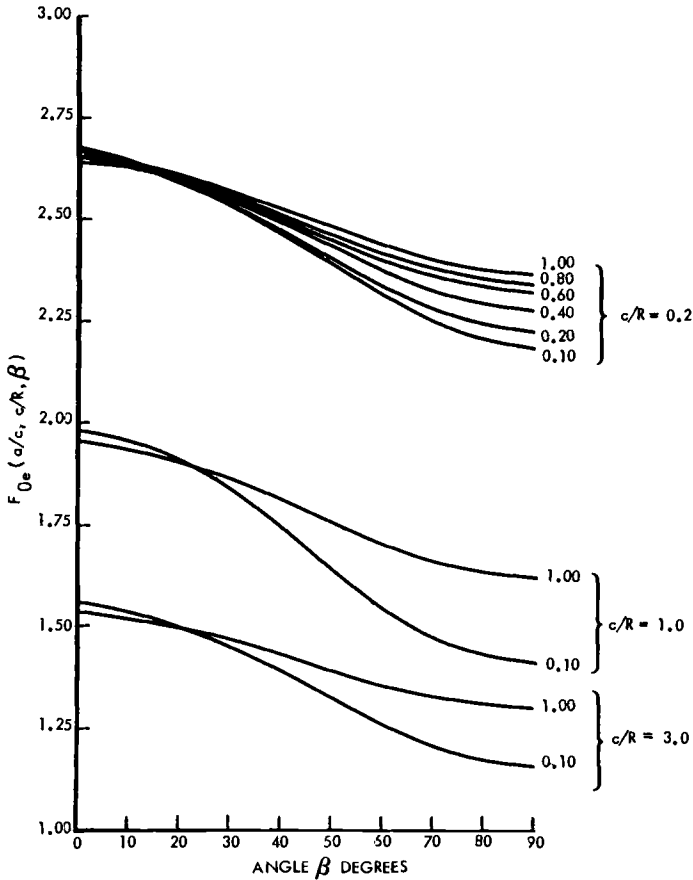


FIG. 16—Nondimensionalized stress intensity factors for two semi-elliptical cracks originating at a hole in a thick plate.

through-the-thickness crack problem, the constants  $A_{00}$  and  $A_{20}$  in Eq 28 are determined for every  $c/R$  ratio individually by least square fitting Eq 28 to Eq 4 for  $X/R$  equal to zero to the particular value of  $c/R$ . From Ref 16, the SIF  $K_{Ih}$  for the elliptical crack is then given by Eqs 17 and 21 of Ref 16. SIF's  $K_{Ih}$ , as anticipated, are dependent on the crack ratio  $a/c$ , crack length to hole radius ratio  $c/R$ , and the location of the crack periphery as designated by the angle  $\beta$ . The SIF  $K_{Ih}$  at any point on the crack periphery defined by angle  $\beta$  is normalized with respect to the SIF  $K_{Ie}$  for an elliptical crack of the same dimensions  $a$  and  $c$  in an infinite solid subjected to the applied tension  $\sigma$ . The nondimensionalized factor  $F_{oe}(a/c, c/R, \beta)$  and  $K_{Ie}$  are already defined by Eqs 15a and b or c. The nondimensionalized factors  $F_{oe}(a/c, c/R, \beta)$  for several  $a/c$  and three  $c/R$  values are shown in Fig. 16. In calculating  $F_{oe}$ ,  $\sigma_{ys}$  is assumed to be zero in Eqs 15 and 16. As seen from Fig. 16, values of  $F_{oe}$  are quite insensitive to the value of  $a/c$  for any given value of  $c/R$  and  $\beta$ . The maximum variation in  $F_{oe}$  occurs at  $\beta = 90$  deg and  $c/R = 1.0$  where the variation between  $F_{oe}$  at  $a/c = 0.1$  and at  $a/c = 1.0$  is less than 13 percent. For other ratios of  $c/R$  up to 10.0, the differences between  $F_{oe}$  at any particular angle  $\beta$  for any two  $a/c$  ratios is approximately the same or less percentagewise. In view of this result, it is concluded that  $F_{oe}(a/c, c/R, \beta)$  can be assumed to be independent of  $a/c$  for engineering estimates of SIF.

In summary, it is emphasized that the results of this appendix are only used to show that the nondimensionalized SIF's  $F_{oe}(a/c, c/R, \beta)$  derived for the prescribed stresses with the Green's function approach for  $a/c = 1.0$  can be used to estimate SIF's for any  $a/c$  value.

## References

- [1] Gran, R.J., Orazio, F. D., Paris, P. C., Irwin, G. R., and Hertzberg, R., "Investigation and Analysis Development of Early Life Aircraft Structural Failures," AFFDL-TR-70-1439, Air Force Flight Dynamics Laboratory, 1971.
- [2] *The Surface Crack: Physical Problems and Computational Solutions*, J. L. Swedlow, Ed., American Society of Mechanical Engineers, 1972.
- [3] Bowie, O. L., *Journal of Mathematics and Physics*, Vol. 35, 1956, pp. 60-71.
- [4] Newman, J. C., "An Improved Method of Collocation for the Stress Analysis of Cracked Plates with Various Shaped Boundaries," NASA TN D-6376, National Aeronautics and Space Administration, Washington, D.C., 1971.
- [5] Tweed, J. and Rooke, D. P., *International Journal of Engineering Science*, Vol. 11, 1973, pp. 1185-1195.
- [6] Grandt, A. F. and Gallagher, J. P. in *Fracture Toughness and Slow-Stable Cracking, Proceedings of the 1973 National Symposium on Fracture Mechanics, Part I, ASTM STP 559*, American Society for Testing and Materials, 1974, pp. 283-295.
- [7] Hall, L. R. and Finger, R. W. in *Proceedings of Air Force Conference on Fatigue and Fracture of Aircraft Structures and Materials*, AFFDL-TR-70-144, Air Force Flight Dynamics Laboratory, 1970, pp. 235-262.
- [8] Liu, A. F., *Engineering Fracture Mechanics*, Vol. 4, 1972, pp. 175-179.
- [9] Kobayashi, A. S. in *Significance of Defects in Welded Structures*, University of Tokyo Press, Tokyo, Japan, 1974, pp. 127-143.
- [10] Harris, H. G., Ojalvo, I. W., and Hudson, R. E., "Stress and Deflection Analysis of Mechanically Fastened Joints," AFFDL-TR-70-49, Air Force Flight Dynamics Laboratory, 1970.
- [11] Noble, M. and Hussain, M. A., *International Journal of Engineering Science*, Vol. 7, 1969, pp. 1149-1161.
- [12] Paris, P. C. and Sih, G. C. in *Fracture Toughness Testing and Its Applications, ASTM STP 381*, American Society for Testing and Materials, 1965, pp. 30-81.
- [13] Timoshenko, S. and Goodier, J. N., *Theory of Elasticity*, McGraw Hill, New York, 1951, pp. 78-81.

- [14] Grobner, W. and Hofreiter, N., *Integraltafel, Teil I, Unbestimmte Integrale*, Springer Verlag, Berlin, 1965.
- [15] Grobner, W. and Hofreiter, N., *Integraltafel, Teil I, Unbestimmte Integrale*, Springer Verlag, Berlin, 1966.
- [16] Shah, R. C. and Kobayashi, A. S., *Engineering Fracture Mechanics*, Vol. 3, 1971, pp. 71-96.
- [17] Smith, F. W., Kobayashi, A. S., and Emery, A. F. *Journal of Applied Mechanics*, Vol. 34, 1967, pp. 947-952.
- [18] Shah, R. C., "Stress Intensity Factors for Through and Part-Through Cracks at Unloaded and Loaded Open, Filled and Interference Fit Fastener Holes," Document D180-17951-1 Boeing Aerospace Company, 1974.
- [19] Davis, P. J. and Rabinowitz, P., *Numerical Integration*, Blaisdell Publishing Co., Waltham, Mass., 1967.
- [20] Irwin, G. R., *Journal of Applied Mechanics*, Vol. 29, 1962, pp. 651-654.
- [21] Gradshteyn, I. S. and Ryzhik, I. M., *Tables of Integrals, Series and Products*, Academic Press, New York, 1973.
- [22] *Handbook of Mathematical Functions*, M. Abramowitz and I. A. Stegun, Eds., Dover Publications, New York, 1965.
- [23] Stippes, M., Wilson, H. B., Jr., and Krull, F. N. in *Proceedings of the Fourth U.S. National Congress of Applied Mechanics*, American Society of Mechanical Engineers, 1962, pp. 799-806.
- [25] Noble, B. and Hussain, M. A. in *Proceedings of the Tenth Midwestern Conference of Applied Mechanics*, 1967, pp. 459-476.
- [26] Noble, B. and Hussain, M. A., *Journal of Institute of Mathematics and Its Applications*, Vol. 5, 1969, pp. 194-205.
- [27] Noble, B. and Hussain, M. A., *International Journal of Engineering Science*, Vol. 7, 1969, pp. 1149-1161.
- [28] Mohaghegh, M., "Biaxial Stress Analysis of a Plate with a Fastener," Document D6-24757 TN, the Boeing Company, 1971.
- [29] Bickley, W. G., *Philosophical Transactions of the Royal Society*, London, Series A, Vol. 227, 1928, pp. 383-415.
- [30] Knight, R. C., *Philosophical Magazine*, Series 7, Vol. 19, 1935, pp. 517-540.
- [31] Theocaris, P. S., *Journal of Applied Mechanics*, Vol. 23, 1956, pp. 85-90.
- [32] Sheremetev, M. P. in *Problems of Continuum Mechanics*, Society for Industrial and Applied Mathematics, 1961, pp. 419-439.
- [33] Green, A. E. and Zerna, W., *Theoretical Elasticity*, Oxford University Press, Oxford, England, 1954.
- [34] Coker, E. G. and Filon, L. N. G., *A Treatise on Photoelasticity*, University Press, Cambridge, England, 1931.
- [35] Frocht, M. M. and Hill, H. N., *Journal of Applied Mechanics*, Vol. 7, 1940, pp. A-5-A-9.
- [36] Kobayashi, A. S. and Moss, W. L., "Stress Intensity Magnification Factors for Surface-Flawed Tension Plate and Notched Round Tension Bar," *Proceedings of the Second International Conference on Fracture*, Brighton, England, 1969.
- [37] Thresher, R. W. and Smith, F. W., *Journal of Applied Mechanics*, Vol. 39, 1972, pp. 195-200.
- [38] Shah, R. C. and Kobayashi, A. S., *International Journal of Fracture*, Vol. 9, 1973, pp. 133-146.
- [39] Shah, R. C. and Kobayashi, A. S. in *The Surface Crack: Physical Problems and Computational Solutions*, American Society of Mechanical Engineers, 1972, pp. 79-124.
- [40] Hall, L. R., Shah, R. C. and Engstrom, W. L., "Fracture and Fatigue Crack Growth Behavior of Surface Flaws and Flaws Originating at Fastener Holes," AFFDL-TR-74-47, Air Force Flight Dynamics Laboratory, May 1974.

## Stress Intensity Factors for Deep Cracks Emanating from the Corner Formed by a Hole Intersecting a Plate Surface

---

**REFERENCE:** McGowan, J. J. and Smith, C. W., "Stress Intensity Factors for Deep Cracks Emanating from the Corner Formed by a Hole Intersecting a Plate Surface," *Mechanics of Crack Growth, ASTM STP 590*, American Society for Testing and Materials, 1976, pp. 460-476.

**ABSTRACT:** A technique consisting of a marriage between stress freezing photoelasticity and a numerical method was used to obtain stress intensity factors for natural cracks emanating from the corner at which a hole intersects a plate surface. Geometries studied were: crack depth to thickness ratios of approximately 0.2, 0.5, and 0.75; crack depth to crack length ratios of approximately 1.0 to 2.0; and crack length to hole radius ratios of about 0.5 to 2.0. All final crack geometries were grown under monotonic loading, and growth was not self similar, with most of the growth occurring through the thickness under remote extension. Stress intensity factors were determined at the intersection of the flaw border (1) with the plate surface ( $K_S$ ) and (2) with the edge of the hole ( $K_H$ ). Results showed that for the relatively shallow flaws  $K_H \approx 1.5 K_S$ , for the moderately deep flaws  $K_H \approx K_S$  and for the deep flaws  $K_H \approx 0.5 K_S$ , revealing a severe sensitivity of  $K$  to flaw geometry. Results were compared with the Bowie theory, and approximate criteria developed by Hall and Finger, and Hsu and Liu. These comparisons showed that these theories significantly overestimated the SIF for moderately deep flaws  $a/t \approx 0.5$  at both the plate surface and the hole, but, for shallow flaws, the Hall-Finger theory underestimated the SIF at the hole, and the Bowie theory underestimated the SIF at the surface for deep flaws.

**KEY WORDS:** crack propagation, stresses, residual stress, photoelasticity, stress analysis, stress intensity, fracture properties

### Nomenclature

$\sigma_{nm}, \sigma_{zz}, \tau_{nz}$  Stress components in plane normal to crack border  
(N/mm<sup>2</sup>)

<sup>1</sup> Assistant professor and professor, respectively, Department of Engineering Science and Mechanics, Virginia Polytechnic Institute and State University, Blacksburg, Va. 24061.

|                |   |
|----------------|---|
| $\sigma_0$     | Normal stress in direction of crack extension near crack tip (N/mm <sup>2</sup> ) |
| $\bar{\sigma}$ | Remote stress (N/mm <sup>2</sup> )  |
| $K_I$          | Mode I stress intensity factor (N/mm <sup>3/2</sup> )                             |
| $r, \theta$    | Polar coordinates (mm, rad)   |
| $a$            | Flaw depth (mm)   |
| $c$            | Flaw length (mm)  |
| $\check{r}$    | Hole radius (mm)  |
| $t$            | Plate thickness (mm)  |
| $N$            | Fringe order  |
| $f$            | Material fringe value (N/mm/order) ( $f_{\text{avg}} = 0.256$ )                   |
| $K_S$          | Mode I SIF at plate surface (N/mm <sup>3/2</sup> )                                |
| $K_H$          | Mode I SIF at hole surface (N/mm <sup>3/2</sup> )                                 |
| $K_{Ex}$       | Mode I SIF experimental (N/mm <sup>3/2</sup> )                                    |
| $K_{Ap}$       | Mode I SIF apparent (N/mm <sup>3/2</sup> )  |

A common cracked body problem in the aerospace industry consists of a corner crack emanating from the intersection edge between a plate surface and a hole. No analytical solution exists for this problem even as a near field solution only. Yet the designer is forced to design against this type of crack using very approximate methods [1].<sup>2</sup> Apparently, the first study undertaken of the problem was an experimental study by Hall and Finger [2]. They inserted artificial flaws by an electrical discharge machine (EDM) with depth/length less than unity and used fatigue loads to initiate cracks after which residual static strength tests were run. In evaluating their results, they assumed that a state of plane strain existed near the point of intersection of the flaw border and the boundary, but in their fracture criterion they had only one value for the stress intensity factor (SIF) and did not account for the variation of the SIF and constraint along the flaw border. As an alternate approach, they suggested modelling the corner flaw with an "equivalent" Bowie type [3] through crack. The latter approach was refined by Liu [4] for quarter circular cracks but still required the selection of an arbitrary equivalent crack length for the Bowie model. This approach has been recently expanded by Hsu and Liu [5], and, while this latter analysis contains some two dimensional approximations and takes no account of back surface effects, it constitutes the most recent effort at quantifying the problem.

Because of the technological importance of the foregoing problem and the approximate nature of existing analytical approaches necessitated by the intractability of the mathematical model of the complete problem, one is led to consider experimental techniques as an alternate approach.

<sup>2</sup> The italic numbers in brackets refer to the list of references appended to this paper.

Stress freezing photoelasticity is a well known technique for evaluating three dimensional stress distributions in the vicinity of stress raisers. A method for extracting the stress intensity factor from photoelastic data for two dimensional problems was proposed by Irwin [6] in 1953, and the method has been modified and refined substantially since that time. Recent studies by Kobayashi and his associates [7-10] have applied the method to dynamic photoelasticity, and the senior author and his associates [11-21] have refined the method for three dimensional problems.

It was the purpose of the present study to determine stress intensity factors at the end points of flaws emanating from the corner formed by the intersection of a plate with a hole using stress freezing photoelasticity and to compare the results with the studies just noted. The authors used a numerical technique known as the Taylor Series Correction Method (TSCM) [20] in order to extract the SIF values from the photoelastic data. Before describing the experiments, a brief review of the analytical background appears to be desirable.

### Analytical Considerations

Consider the Irwin two parameter near field equations for Mode I loading

$$\begin{aligned}\sigma_{nn} &= \frac{K_1}{(2\pi r)^{1/2}} \cos \frac{\theta}{2} \left( 1 - \sin \frac{\theta}{2} \sin \frac{3\theta}{2} \right) - \sigma_0 \\ \sigma_{zz} &= \frac{K_1}{(2\pi r)^{1/2}} \cos \frac{\theta}{2} \left( 1 + \sin \frac{\theta}{2} \sin \frac{3\theta}{2} \right) \\ \tau_{nz} &= \frac{K_1}{(2\pi r)^{1/2}} \sin \frac{\theta}{2} \left( \cos \frac{\theta}{2} \cos \frac{3\theta}{2} \right)\end{aligned}\quad (1)$$

where the notation, adapted to the problem at hand, is pictured in Fig. 1. Here  $\sigma_0$  is the part of the regular stress field which is independent of  $r$ . Although Eqs 1 were originally proposed for two dimensional problems, the singular parts have been shown to be valid for stresses in planes perpendicular to elliptically shaped crack borders [22] and are generally applied to arbitrary shaped plane crack borders as well. By substituting Eqs 1 into Eq 2

$$\tau_{\max} = \frac{1}{2} [(\sigma_{nn} - \sigma_{zz})^2 + 4\tau_{nz}^2]^{1/2} \quad (2)$$

and evaluating  $\tau_{\max}$  along  $\theta = \pi/2$ , one obtains

$$\tau_{\max} = \left[ \frac{K_1^2}{8\pi r} + \frac{K_1\sigma_0}{4(\pi r)^{1/2}} + \frac{\sigma_0^2}{4} \right]^{1/2} \quad (3)$$

which may be combined with the stress optic law

$$\tau_{\max} = \frac{Nf}{2t} \quad (4)$$

in order to obtain an expression of the form

$$K_1 = f(\sigma_0, N_i, r_i) \quad (5)$$

from which  $K_1$  may be evaluated from experimental data  $N_i, r_i$  along  $\theta = \pi/2$  (see Refs 16 and 17). The stresses are evaluated along  $\theta = \pi/2$  since the fringes spread out in approximately this direction and can be most accurately discriminated along this line. An alternate form of Eq 3 may be written as

$$\tau_{\max} = \frac{A'}{r^{1/2}} + B_0' + B_1'r^{1/2} \quad (6)$$

where

$$A' = \frac{K_1}{\sqrt{8\pi}} \text{ and } B_1' = B_1'(A', B_0')$$

When one accumulates photoelastic data along  $\theta = \pi/2$ , if the foregoing theory is to hold, the stresses in the data zone must be dominated by the singular stresses as given in Eqs 1. Experience with three dimensional problems has revealed that the singular zone is often severely constricted, and a part of the data may lie outside that zone. In order to account for this effect adequately, the authors have used a Taylor series expansion of the regular part of the maximum in plane shearing stress in the form

$$\tau_{\max} = \frac{A}{r^{1/2}} + \sum_{n=0}^m B_n r^{n/2} \quad (7)$$

where  $A = K_1/\sqrt{8\pi}$  as before.

If we ignore the dependence between the coefficients  $A'$ ,  $B_0'$ ,  $B_1'$  in Eq 6 we see that Eq 7 reduces to Eq 6 for a two degree of freedom system of equations to within truncation error. Moreover, Eq 7 corresponds to an application of the Williams stress function along  $\theta = \pi/2$  for two dimensional problems.

In order to apply Eq 7, one determines the coefficients  $A$ ,  $B_n$  from a least squares analysis of the experimental data using a truncated form of Eq 7. Normally the lowest order curve which best fits the experimental data is used. Details are described in Refs 17 and 21.

## Experiments

### Models

A series of stress freezing photoelastic experiments were designed for the purpose of obtaining estimates of the SIF near points  $S$  and  $H$  along the flaw border (Fig. 1) The specimens were made from PLM-4B, a stress freezing material manufactured by Photolastic, Inc., Malvern, Pa. and Hysol 4290 made by Hysol Corp., Olean, N. Y. using the following procedure:

1. Mill 0.762 mm from both surfaces of the plates.
2. Drill and ream holes.
3. Mount a razor blade in a special jig and tap in a quarter circular crack.
4. Mount test specimen in a stress freezing oven in a dead loading rig (Fig. 2) and heat to critical temperature.

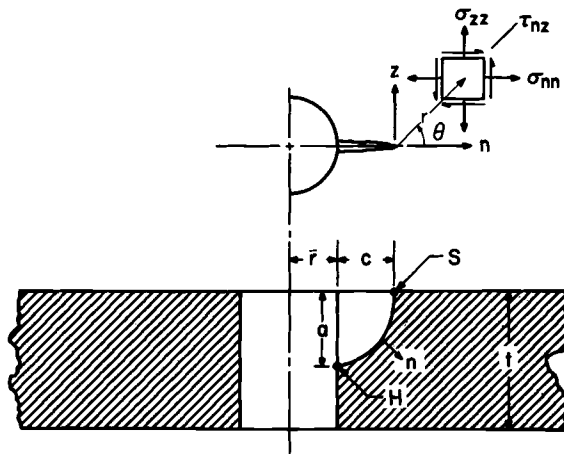


FIG. 1—Problem geometry and stress notation.

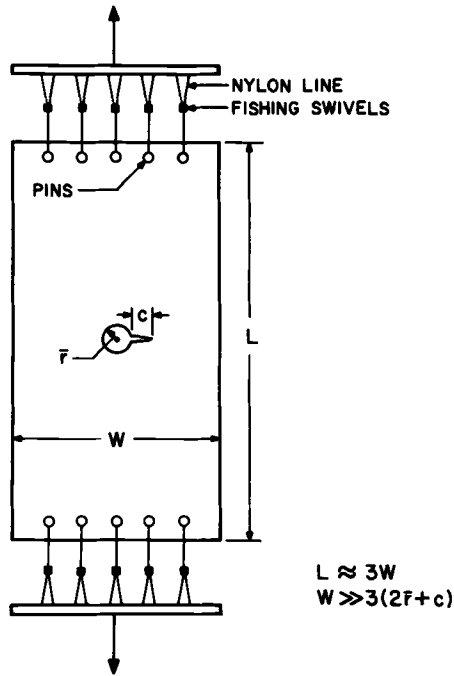


FIG. 2—Test setup.

5. Load with enough load to slowly extend flaw to its desired depth. Remove the load.

Test geometries studied are found in the upper part of Table 1. It was intended originally to attempt to duplicate the geometries of the Hall and Finger tests. However, since natural cracks were used, only one crack dimension could be controlled, and the other dimension grew to its "natural" companion value. This led to flaws for which  $a/c > 1.0$  and self similar flaw extension did not occur. Instead, most of the growth occurred in the depth direction. In one test, (Test 9) a crack with  $a/c < 1.0$  was produced by flexing the plate to enlarge the  $c$  dimension.

#### *Test Procedure*

After crack growth was completed, live loads below the threshold value to cause crack growth were applied above the critical temperature, and specimens were cooled under load, thus freezing in the fringes and deformations. Slices were then taken (*a*) parallel to the plate surface for use in determining the SIF at point *S* and (*b*) tangent to the hole for determining the SIF at point *H*. The latter slice was sanded on the hole surface to constant thickness. Slice locations are shown in Fig. 3. These

TABLE I—Data and results.

| Test Number  | Group I |       |       | Group II |       |       | Group III |       |       |
|--|---------|-------|-------|----------|-------|-------|-----------|-------|-------|
|  | 1       | 2     | 3     | 4        | 5     | 6     | 7         | 8     | 9     |
| Hole Radius ( $\bar{r}$ ) mm                       | 6.35    | 6.35  | 4.83  | 6.35     | 4.83  | 6.35  | 6.35      | 4.83  | 4.83  |
| Plate Depth ( $t$ ) mm                             | 14.7    | 23.6  | 19.3  | 14.5     | 19.8  | 13.7  | 13.5      | 19.8  | 19.8  |
| Crack Length ( $c$ ) mm                            | 2.79    | 3.56  | 9.65  | 6.35     | 7.62  | 4.06  | 5.08      | 7.37  | 25.91 |
| Crack Depth ( $a$ ) mm                             | 2.54    | 5.59  | 8.38  | 6.86     | 9.65  | 6.35  | 9.91      | 15.24 | 10.67 |
| Remote Stress ( $\bar{\sigma}$ ) N/mm <sup>2</sup> | 0.099   | 0.108 | 0.085 | 0.075    | 0.081 | 0.088 | 0.071     | 0.062 | 0.049 |
| $a/t$  | 0.18    | 0.24  | 0.43  | 0.48     | 0.49  | 0.46  | 0.74      | 0.78  | 0.55  |
| $a/c$  | 0.95    | 1.59  | 0.86  | 1.10     | 1.27  | 1.55  | 1.98      | 2.05  | 0.42  |
| $c/t$  | 0.43    | 0.56  | 2.02  | 0.98     | 1.60  | 0.63  | 0.79      | 1.56  | 5.44  |
| $2t/t$   | 0.87    | 0.54  | 0.49  | 0.88     | 0.48  | 0.94  | 0.95      | 1.48  | 1.48  |
| Stress Intensity Factors: Experimental Results     |         |       |       |          |       |       |           |       |       |
| Surface $K_{SEZ}$ N/mm <sup>3/2</sup>              | 0.327   | 0.446 | 0.308 | 0.311    | 0.383 | 0.382 | 0.424     | 0.305 | 0.239 |
| Hole $K_{HEZ}$ N/mm <sup>3/2</sup>                 | 0.482   | 0.634 | 0.323 | 0.307    | 0.248 | 0.365 | 0.262     | 0.166 | *     |
| Empirical Results                                  |         |       |       |          |       |       |           |       |       |
| Hall-Finger $K_{HF}$ N/mm <sup>3/2</sup>           | 0.376   | 0.471 | 0.392 | 0.367    | 0.360 | 0.414 | 0.355     | 0.306 | 0.286 |
| Bowie $K_B$ N/mm <sup>3/2</sup>                    | 0.528   | 0.600 | 0.495 | 0.454    | 0.457 | 0.500 | 0.416     | 0.347 | 0.351 |
| Hsu-Liu (Surface) $K_{HLS}$ N/mm <sup>3/2</sup>    | 0.423   | 0.564 | 0.400 | 0.383    | 0.415 | 0.465 | 0.408     | 0.339 | 0.193 |
| Hsu-Liu (Hole) $K_{HLH}$ N/mm <sup>3/2</sup>       | 0.592   | 0.696 | 0.965 | 0.672    | 0.796 | 0.612 | 0.524     | 0.571 | 0.838 |
| Subtable   |         |       |       |          |       |       |           |       |       |
| $K_{SEZ}/\bar{\sigma}c^{1/2}$                      | 2.0     | 2.2   | 1.2   | 1.7      | 1.8   | 2.2   | 2.7       | 1.8   | 1.0   |
| $K_B/\bar{\sigma}c^{1/2}$                          | 3.3     | 3.0   | 1.9   | 2.5      | 2.0   | 2.9   | 2.6       | 2.1   | 1.4   |
| $K_{HLS}/\bar{\sigma}c^{1/2}$                      | 2.6     | 2.8   | 1.5   | 2.1      | 1.9   | 2.6   | 2.6       | 2.0   | 0.8   |
| $K_{HF}/\bar{\sigma}a^{1/2}$                       | 3.0     | 2.5   | 1.3   | 1.6      | 1.0   | 1.7   | 1.2       | 0.7   | ...   |
| $K_{HF}/\bar{\sigma}a^{1/2}$                       | 2.4     | 1.9   | 1.6   | 1.9      | 1.4   | 1.9   | 1.6       | 1.2   | 1.8   |
| $K_{HLH}/\bar{\sigma}a^{1/2}$                      | 3.7     | 2.7   | 4.0   | 3.5      | 3.2   | 2.8   | 2.4       | 2.4   | 5.2   |

<sup>a</sup> Dropped due to data scatter.

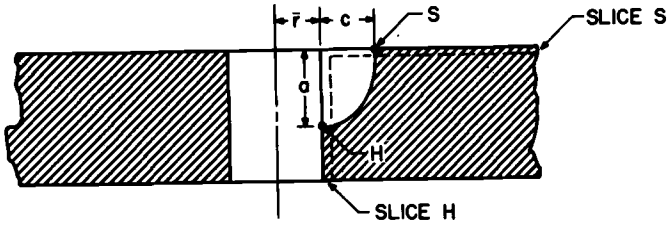


FIG. 3—Slice locations.

slices were placed in a tank of liquid of the same index of refraction as the model material and fringe patterns were obtained using partial mirror fringe multiplication and also by the Tardy method. A typical fringe pattern for the hole  $H$  is shown in Fig. 4. Slices were 0.51 to 1.78 mm thick.

The analytical status of the state of affairs at points where flaw borders intersect free boundaries is currently somewhat unsettled [22-24]. In the present study, since the slice thicknesses analyzed were at least two orders of magnitude thicker than the crack root radius, the SIF values obtained should be viewed only as average engineering estimates near the free surfaces and do not reflect boundary layer effects.

### Results

A typical set of data for regions  $S$  and  $H$  are shown in Fig. 5 together with the TSCM curves generated from the data. These curves may be regarded as typical of all of the tests analyzed. That is, for all tests, the surface slices revealed linear data which indicates a two degree of freedom system of equations while the slices along the hole revealed nonlinear data. For these cases, however, the Tardy method revealed that these data were also linear over a portion of the data zone nearer to the crack tip. Thus, instead of using a higher order curve to fit all of the data, the authors elected to use a two degree of freedom system on that portion of the data in the linear range as shown for the  $H$  curve in Fig. 5. The authors interpret the linear part of the curve to represent the singular zone and believe that extrapolation of the linear curve results in much less error than would be the case for a higher order curve. In order to verify this technique, a test was run where the corner crack was allowed to grow through the thickness of the plate so as to form a Bowie type crack on one side of the hole. The hole radius was 4.83 mm and the crack length was 29.21 mm. The resulting  $K_{Ex}$  was 2 percent higher than the result predicted by the Bowie analysis. The authors estimate, however, that experimental results generally can vary by 5 percent.

It is well to note that, in applying this technique to problems in which

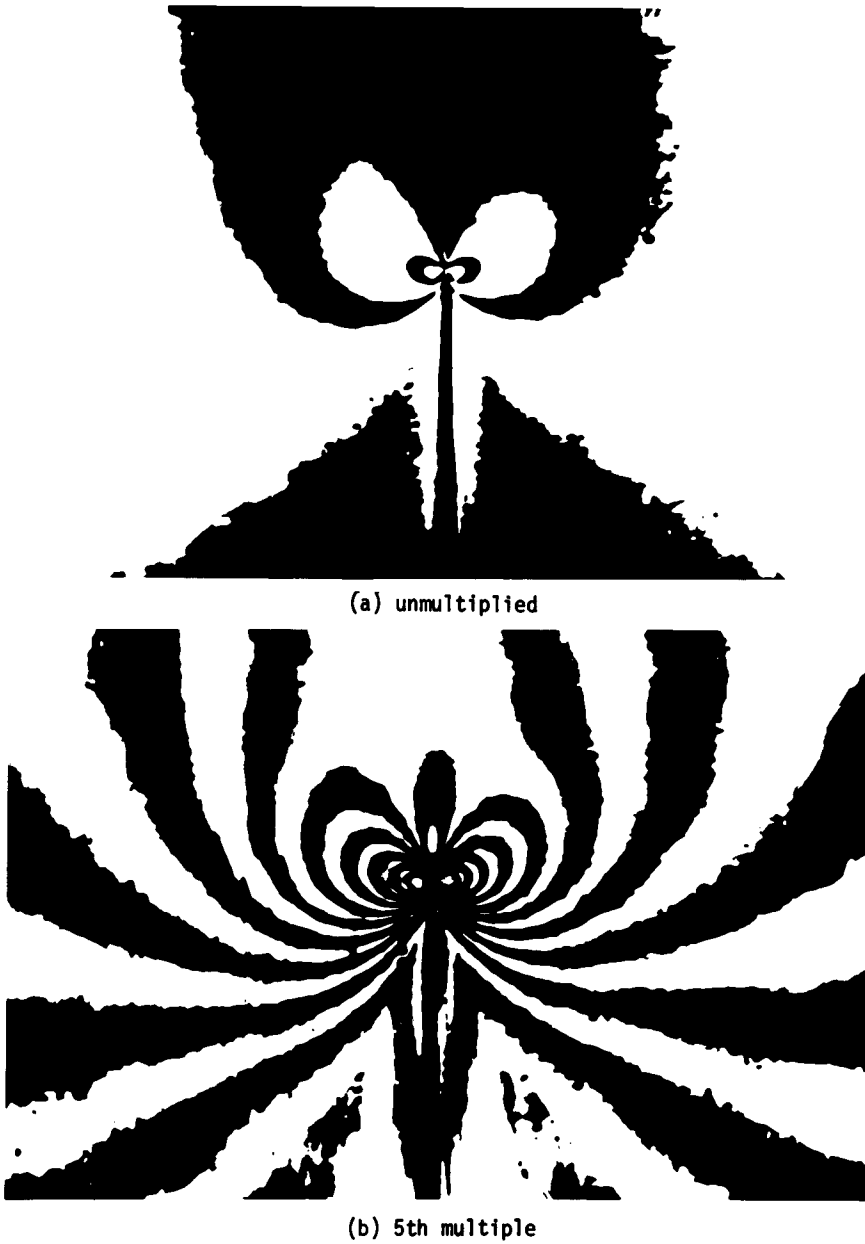


FIG. 4—Typical fringe patterns at H (a) unmultiplied and (b) fifth multiple (approximately X15).

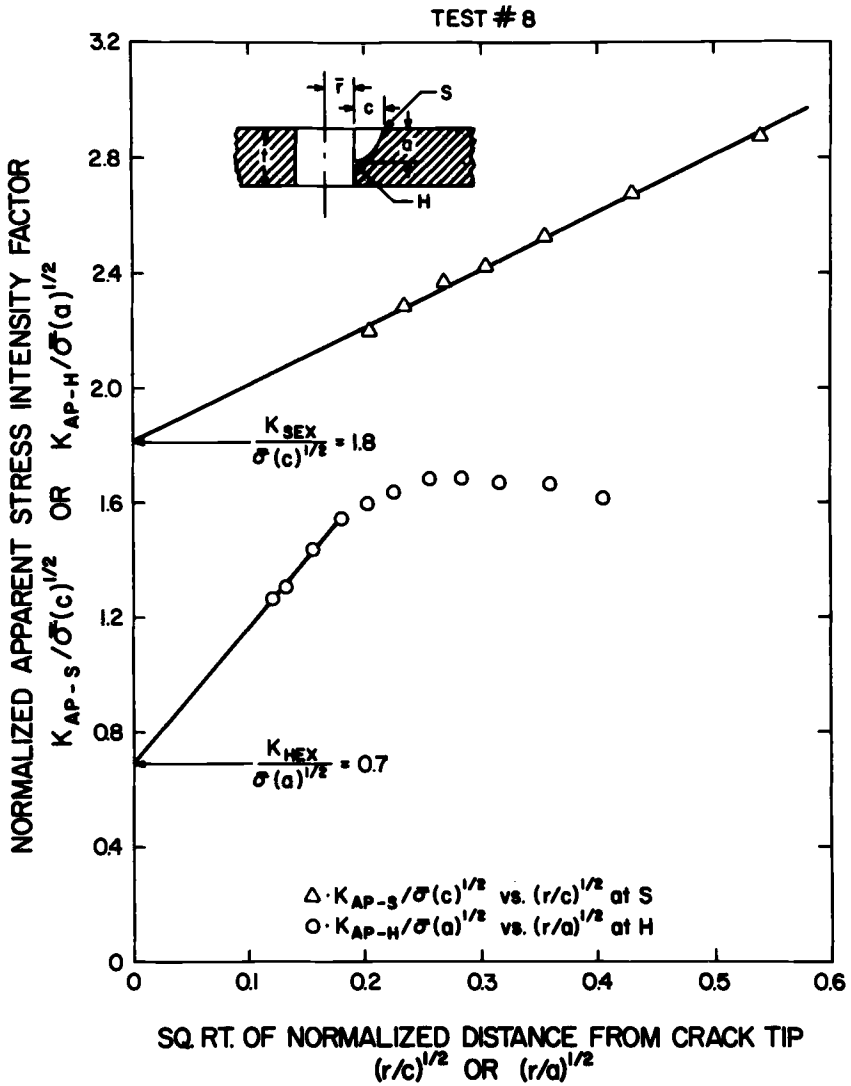


FIG. 5—Typical data and results.

the uncracked body geometry produces strong stress gradients, care must be exercised to keep both the distance of data points from the crack tip ( $r$ ) and the usable data range  $\Delta r$  small in comparison to the gross body geometrical dimensions.

Even after Tardy analysis, the slopes of the curves of normalized  $K_{Ap}$  versus  $(r/a)^{1/2}$  or  $(r/c)^{1/2}$  were, in some cases, sufficiently large to cause the authors some concern as to the accuracy of the  $K_{HEx}$  values. In general, the authors estimate that the values of  $K_{SEx}$  identified as Experimental Values in Table 1, are accurate to within 5 percent but values of  $K_{HEx}$  are, on the average, probably not better than about 15 percent. Thus, the authors feel that the results for  $K_{HEx}$  should be interpreted as trends rather than as exact values. In this context, the experimental results tabulated in Table 1 may be summarized as follows:

$$\text{For } \left\{ \begin{array}{l} a/t \approx 0.2 \\ a/c = 1.0 \text{ to } 1.5 \\ c/\bar{r} \approx 0.5 \\ 2\bar{r}/t = 0.5 \text{ to } 0.9 \end{array} \right\} K_{HEx} \approx 1.5 K_{SEx}$$

$$\text{For } \left\{ \begin{array}{l} a/t \approx 0.5 \\ a/c = 1.0 \text{ to } 1.5 \\ c/\bar{r} = 0.5 \text{ to } 2.0 \\ 2\bar{r}/t = 0.5 \text{ to } 0.9 \end{array} \right\} K_{HEx} \approx K_{SEx} \text{ (except Test 5)}$$

$$\text{For } \left\{ \begin{array}{l} a/t \approx 0.75 \\ a/c \approx 2.0 \\ c/\bar{r} = 0.8 \text{ to } 1.6 \\ 2\bar{r}/t = 0.5 \text{ to } 0.9 \end{array} \right\} K_{HEx} \approx 0.5 K_{SEx}$$

Moreover, except for the shallow flaws, for  $a/c > 1$ ,  $K_{SEx} > K_{HEx}$ . These results show that  $K_{HEx}$  drops off and  $K_{SEx}$  increases as the cracks grow deeper. This growth trend is believed to be due to a variation in constraint distribution and load. For the parametric ranges included in this study,  $a/t$  seems to be the dominant parameter but  $a/c$  is also seen to be important, especially for the larger values (that is,  $a/c \rightarrow 2.0$ ). For this reason, the tests are grouped according to  $a/t$  values, and within each group are ordered according to increasing values of  $a/c$ .

### Analytical Comparisons

In the middle of Table 1, values of the SIF are estimated for each case tested using the theories of Hall and Finger, Bowie, and Hsu and Liu (see

Appendix). These results are summarized in abbreviated normalized form in the Subtable at the bottom of Table 1 for purposes of comparison.

In Group II ( $a/t \approx 0.5$ ,  $a/c \approx 0.9$  to  $1.5$ ) all of the theories substantially overestimate the SIF both at the surface and at the hole. Although the overestimates range from 10 to 220 percent, they seem to average about 30 percent above the experimental result. These same trends are observed in Group I ( $a/t \approx 0.2$ ,  $a/c \approx 1$  to  $1.5$ ) at the surface and in Group III ( $a/t \approx 0.75$ ,  $a/c \approx 2.0$ ) at the hole. However, for Group I at the hole, the Hall-Finger solution underestimates the SIF by about 20 percent.

As noted earlier, there are many reasons why agreement should not be expected between the several theories and experiments. The Bowie solution is two dimensional and applies to a very different geometry than the cases studied here which are found to be highly geometry dependent. The Hall-Finger approach assumes that fracture initiates near the hole boundary under a state of plane strain constraint and obtains empirical functions from experimental data only for cases where  $a/c < 1.0$ . The Hsu-Liu theory provides a highly empirical modification of the Bowie solution for obtaining the SIF both at the surface and at the hole and neglects the back surface of the plate altogether. As noted earlier, the effect of increasing  $a/t$  was to decrease  $K_H$  and to increase  $K_S$ . The decrease of  $K_H$  with increase in  $a/t$  was also observed by Hall and Finger as an "unexpected result." The authors conjecture that this result may be due to the fact that, when the crack is deep, a substantial part of the load is transferred to the side of the hole opposite the crack due to the greater stiffness of this part of the plate. The remaining ligament between the crack and the back surface of the plate thus carries a reduced load, and this effect is in evidence in the results shown here. Values of  $a/c$  are low enough in Tests 1, 3, and 4 that some correlation might be expected with the Hall-Finger criterion. However, differences between that criterion and experimental results run as high as  $\pm 20$  percent, indicating that substantial three dimensional effects may be averaged out in the Hall-Finger approach.

### Problem Characterization and Conclusions

It is clear from the results of the Subtable under Table 1 that none of the theories studied here are (in their published form) suitable for dealing with deep flaws where  $a/c \approx 1.0$ . It is also clear that this problem is highly three dimensional and strongly geometry dependent. In order to assist the designer in converting these results into an interim design philosophy until further studies can be carried out, the following suggestions are made.

In Ref 1, the crack growth occurring in this type of problem through the thickness is estimated from the SIF for a quarter circular flaw emanating from the corner of a quarter infinite plate. It is clear from the value of

$K_{HEX}/\bar{\sigma}a^{1/2}$  from the tests in Group I that such a solution should be corrected to account for the stress raiser effect due to the hole and that this correction should be of the order of 2.0 to 2.5. Although difficult to justify on purely analytical grounds, the correction obtained from the Bowie solution as  $c \rightarrow 0$  by Hsu and Liu appears to be somewhat conservative but not unsuitable here. For Groups II and III, failure to correct for the presence of the hole is apparently more than offset by the load transfer mechanism mentioned earlier. A 20 percent or so decrease in the value of  $C$  in the Hall-Finger criterion would yield fairly accurate  $K_I$  estimates for  $K_H$ .

Once the crack has grown through the plate thickness, it forms a Bowie crack for which  $K_I$  (or  $K_S$ ) is predicted accurately by the Bowie theory. In fact, the use of the Bowie theory to predict  $K_S$  before the crack breaks through to the far side of the plate could be used (if  $K_B$  is decreased by about 40 percent) for Groups I and II (except Test 5). For Group III (and also Test 5), the Hsu-Liu correction would again be necessary.

The problem studied here is a complex, three dimensional problem, and the present study can only be expected to identify trends and point the way for future research. The trends and conclusions from the present study may be summarized as follows:

1. Extension of a crack emanating from a corner of intersection of a hole with a plate under monotonically increasing load is not self-similar. (In this work, most of the growth was through the thickness<sup>3</sup>). As the flaw depth increases  $K_H$  decreases and  $K_S$  increases.
2. Existing theories and design criteria significantly overestimate the SIF at both the hole and the surface except for shallow flaws at the hole and deep flaws at the surface.
3. As an interim design criterion for  $K_S$ , the Bowie theory with a coefficient of about six tenths yields results to within 10 percent for Groups I and II, (except Test 5) and, for Group III, a coefficient of unity is recommended. For  $K_H$  estimates, a Hall-Finger approach with adjusted coefficients and relationships is suggested.

The authors have extended the current study to other crack geometries [25] and are currently studying fastener effects.

#### *Acknowledgments*

The authors wish to acknowledge the studies of L. R. Hall, R. W. Finger, T. M. Hsu, A. F. Liu, and O. W. Bowie, upon whose work they have drawn. They are also indebted to J. C. Newman for his suggestions and to the staff and facilities of the Engineering Science and Mechanics Department of Virginia Polytechnic Institute and State University. This

<sup>3</sup> Test results on fatigue crack growth at U. S. Air Force Materials Laboratory show that, in some cases, significant growth may occur in the plate surface.

research was supported by NASA under NGR-47-004-076 with NASA Langley, Hampton, Virginia.

## APPENDIX

### Related Theoretical Solutions

Two approximate theories have been proposed for the problem described in the foregoing, and the two dimensional theory of Bowie was also used. These theories will be briefly described here and their limitations noted.

#### I. The Bowie Solution [3]

Bowie utilized conformal mapping in order to obtain a solution to the two dimensional problem of a through crack emanating from a hole under remote extension. The mapping function was constructed by considering separately the transformation between two upper half planes which carries the real axis of one into the real axis interrupted by branch cuts of finite length of the other, and the transformation which maps each of these half planes into circles and their exteriors. The mapping function used was the product transformation, and it was approximated by a polynomial. The resulting SIF for a single crack normal to a field of remote uniaxial tension may be expressed as

$$K_I = \bar{\sigma} \sqrt{\pi L} F \left( \frac{L}{\bar{r}} \right) \quad (8)$$

where

$\bar{\sigma}$  = remote tension normal to the crack,

$L$  = crack length,

$\bar{r}$  = hole radius, and

$F \left( \frac{L}{\bar{r}} \right)$  = numerically evaluated.

#### II. Hall and Finger [2]

These investigators prepared a series of test specimens in accordance with Table 2. Notches were inserted using an EDM, and specimens were fatigued to start the cracks. Residual static strength tests were then conducted. Hall and Finger then postulated that catastrophic fracture would originate near the intersection of the flaw border with the hole and that this region would be under a plane strain type of constraint. On the basis they proposed, as a fracture criterion

$$\bar{\sigma} \sqrt{a} f(a, c, \bar{r}, t) = K_{Ic} \quad (9)$$

Then, on the basis of parametric crossplots they refined Eq 9 into the form

$$C \bar{\sigma} \sqrt{a} F \left( \frac{c}{2\bar{r}} \right) \times G \left( \frac{a}{t} \right) \times H \left( \frac{\bar{r}}{t} \right) = K_{Ic} \quad (10)$$

TABLE 2—Test program for flaws originating at holes [2].

| Material             | $\frac{2F}{t}$ | $\frac{a}{t}$ | Number of Tests for $a/c =$ |      |      |
|----------------------|----------------|---------------|-----------------------------|------|------|
|                      |                |               | 0.25                        | 0.50 | 1.00 |
| 2219-T87<br>Aluminum | 1.0            | 0.2           | 2                           | 2    | 2    |
|                      |                | 0.5           | 2                           | 2    | 2    |
|                      |                | 0.8           | 2                           | 2    | 2    |
|                      | 0.5            | 0.2           | 2                           | 2    | 2    |
|                      |                | 0.5           | 2                           | 2    | 2    |
|                      |                | 0.8           | 2                           | 2    | 2    |
|                      | 1.0            | 0.2           | 2                           | 2    | 2    |
|                      |                | 0.5           | 2                           | 2    | 2    |
|                      |                | 0.8           | 2                           | 2    | 2    |
| Ti-5Al-2.5Sn         | 0.5            | 0.2           | 2                           | 2    | 2    |
|                      |                | 0.5           | 2                           | 2    | 2    |
|                      |                | 0.8           | 2                           | 2    | 2    |

NOTE—Test temperature -320°F.

where  $C = 1.1$ ,  $H(r/t) = 2\sqrt{r/t}$ , and  $F$  and  $G$  were obtained graphically from the test data. They obtained agreement with test data to within 10 percent. Two points however, should be noted:

1. Since  $C$ ,  $F$ ,  $G$ , and  $H$  were obtained from the test data, Eq 10 is limited necessarily to the range of test data which includes no  $a/c > 1.0$ .

2. While the assumption that plane strain constraint exists near the point where the flaw intersects the boundary is certainly the safe, logical assumption to make for a design criterion, and seems to yield reasonable results in their work, the complex variation in  $K_1$  and the constraint along the flaw boundary is masked by this assumption so that one would not be surprised to see deviations from this criterion for other geometries. Nevertheless, this study should be useful in establishing trends due to variations in test geometry.

III. Hsu and Liu [5]

These investigators modified the elliptic flaw solution to the form

$$K_1 = \frac{\bar{\sigma}\sqrt{\pi b} \times B \times M_1'}{\Phi} \tag{11}$$

$M_1' = M_1 \{ (b/b_1)^2 \sin^2\beta + \cos^2\beta \}^{1/4}$  where  $M_1$  is a front surface correction factor and  $\beta$  is measured from the minor axis to a point on the flaw border.

$$\Phi = \int_0^{\pi/2} \left\{ 1 - \left( \frac{b_1^2 - b^2}{b_1^2} \right) \sin^2\beta \right\}^{1/2} d\beta$$

where

$B$  = factor which corrects crack solution for the presence of the hole; it consists of  $F(L/\bar{r})$  in I,

$b_1$  = semi-major axis of ellipse, and

$b$  = semi-minor axis of ellipse.

Unfortunately, no attempt was made to account for the influence of the back surface of the plate upon the stress intensity factors. Moreover, the analytical basis for the  $B$  factor is two dimensional, and its variation along the flaw border is quite arbitrary and empirical.

In addition to the foregoing theories, a theory has been proposed by R. C. Shah and is presented elsewhere in this volume. A comprehensive evaluation of this theory against experiments is found in Ref 25.

## References

- [1] Wilhem, D. P., "Fracture Mechanics Guidelines for Aircraft Structural Applications," AFFDL-TR-69-111, U.S. Air Force Flight Dynamics Laboratory, Wright-Patterson Air Force Base, Ohio, Feb. 1970.
- [2] Hall, L. R. and Finger, R. W., "Fracture and Fatigue Growth of Partially Embedded Flaws," *Proceedings*, Air Force Conference on Fatigue and Fracture of Aircraft Structures and Materials, AFFDL-TR-70-144, U.S. Air Force Systems Command, Wright-Patterson Air Force Base, Ohio, Sept. 1970, pp. 235-262.
- [3] Bowie, O. L., *Journal of Mathematics and Physics*, Vol. 35, 1956, pp. 60-71.
- [4] Liu, A. F., *Journal of Engineering Fracture Mechanics*, Vol. 4, No. 1, March 1972, pp. 175-179.
- [5] Hsu, T. M. and Liu, A. F., "Stress Intensity Factors for Truncated Elliptical Cracks," Seventh National Symposium on Fracture Mechanics, College Park, Md., 27-29 Aug. 1973.
- [6] Irwin, G. R., discussion of the paper "The Dynamic Stress Distribution Surrounding a Running Crack — A Photoelastic Analysis," by A. A. Wells and D. Post, *Proceedings Society for Experimental Stress Analysis*, Vol. 16, No. 1, 1958, pp. 69-96.
- [7] Bradley, W. B. and Kobayashi, A. S., *Journal of Experimental Mechanics*, Vol. 10, No. 3, March 1970, pp. 106-113.
- [8] Bradley, W. B. and Kobayashi, A. S., *Journal of Engineering Fracture Mechanics*, Vol. 3, No. 3, Oct. 1971, p. 317-332.
- [9] Kobayashi, A. S., Wade, B. G., Bradley, W. B., and Chiu, S. T., "Crack Branching in Homalite — 100 Sheets," TR-13, Department of Mechanical Engineering, College of Engineering, University of Washington, Seattle, Wash., June 1972.
- [10] Kobayashi, A. S. and Wade, B. G., "Crack Propagation and Arrest in Impacted Plates," TR-14, Department of Mechanical Engineering, College of Engineering, University of Washington, Seattle, Wash., July 1972.
- [11] Smith, D. G. and Smith, C. W., *International Journal of Fracture Mechanics*, Vol. 6, No. 3, Sept. 1970, pp. 305-318.
- [12] Smith, D. G. and Smith, C. W., *Experimental Mechanics*, Vol. 11, No. 9, Sept. 1971, pp. 394-401.
- [13] Smith, D. G. and Smith, C. W., *Journal of Engineering Fracture Mechanics*, Vol. 4, No. 2, June 1972, pp. 357-366.
- [14] Marrs, G. R. and Smith, C. W., *Stress Analysis and Growth of Cracks, Proceedings of the 1971 National Symposium on Fracture Mechanics, Part I, ASTM STP 513*, American Society for Testing and Materials, Oct. 1972, pp. 22-36.
- [15] Schroedl, M. A., McGowan, J. J., and Smith, C. W., *Journal of Engineering Fracture Mechanics*, Vol. 4, No. 4, Dec. 1972, pp. 801-809.
- [16] Schroedl, M. A. and Smith C. W., *Progress in Flaw Growth and Fracture Toughness Testing, ASTM STP 536*, American Society for Testing and Materials, Oct. 1973, pp. 45-63.

- [17] Schroedl, M. A., McGowan, J. J., and Smith, C. W., *Journal of Experimental Mechanics*, Vol. 14, No. 10, Oct. 1974, pp. 392-399.
- [18] Harms, A. E. and Smith, C. W., "Stress Intensity Factors in Long Deep Surface Flaws in Plates Under Extensional Fields," VPI-E-73-6, Feb. 1973, Tenth Anniversary Meeting of Society for Engineering Science, Raleigh, N. C., Nov. 1973.
- [19] Schroedl, M. A. and Smith, C. W. in *Fracture Analysis, Proceedings of the 1973 National Symposium on Fracture Mechanics, Part II, ASTM STP 560*, American Society for Testing and Materials, 1975, pp. 69-80.
- [20] Smith, C. W. in *Proceedings of the Third International Congress on Experimental Mechanics*, 1974, pp. 287-292.
- [21] Schroedl, M. A., McGowan, J. J., and Smith, C. W., "Use of a Taylor Series Correction Method in Photoelastic Stress Intensity Determinations," VPI-E-73-34, Nov. 1973.
- [22] Sih, G. C. and Liebowitz, H., "Mathematical Theories of Brittle Fracture," *Fracture*, Vol. 2, H. Liebowitz, Ed., Academic Press, New York, 1968.
- [23] Sih, G. C., *International Journal of Fracture Mechanics*, Vol. 7, No. 1, March 1971, pp. 39-59.
- [24] Cruse, T. A. in *Proceedings of Symposium on Surface Flaws*, American Society of Mechanical Engineers, Nov. 1972, pp. 153-170.
- [25] Smith, C. W., McGowan, J. J., and Jolles, M., "Stress Intensities for Cracks Emanating from Holes in Finite Thickness Plates by a Modified, Computer-Assisted Photoelastic Method," *Proceedings of the Twelfth Annual Meeting of the Society for Engineering Science*, Austin, Tex., Oct. 1975, pp. 353-362.

A. S. Kobayashi<sup>1</sup> and A. N. Enetanya<sup>1</sup>

## Stress Intensity Factor of a Corner Crack

---

**REFERENCE:** Kobayashi, A. S. and Enetanya, A. N., "Stress Intensity Factor of a Corner Crack," *Mechanics of Crack Growth, ASTM STP 590*, American Society for Testing and Materials, 1976, pp. 477-495.

**ABSTRACT:** The alternating method for elliptical crack analysis, which is based on the combined use of a pressurized crack solution and a free surface solution, has been limited in its application due to convergence difficulties in the iteration process. By prescribing appropriate fictitious pressure on the elliptical crack surface, which protrudes into the free space, numerical convergence of the iteration was improved. As a result, the pressurized crack solution involving a third-order polynomial pressure distribution with limited use was extended to part-elliptical problems. The improved alternating procedure is then used to determine stress intensity factors in corner flaws with aspect ratios of  $a/b = 0.98$ , 0.4, and 0.2 and subjected to uniform or linearly varying pressure distributions.

**KEY WORDS:** crack propagation, stress analysis, mechanical properties, fracture properties

Published examples of actual failed parts [1]<sup>2</sup> show that failure often originates from surface flaws which are located in regions of high-stress concentrations which can be modeled by part-elliptical or part-circular cracks. Thus following the original paper by Irwin [2], substantial efforts have been mounted in the past to estimate the stress intensity factor of semi-elliptical cracks [3-7].

A step change in available analytical procedures for surface flaw problems was made in 1965 by Smith [8] who used the alternating technique in three-dimensional elasticity to determine the stress intensity factor of a semi-circular crack in a semi-infinite solid. This procedure was effectively used by Smith and his colleagues who then solved various embedded and surface flaw problems involving circular or part-circular

<sup>1</sup> Professor and formerly graduate student, respectively, Department of Mechanical Engineering, University of Washington, Seattle, Wash. 98195.

<sup>2</sup> The italic numbers in brackets refer to the list of references appended to this paper.

cracks [9-11]. Recently Hartranft and Sih introduced an improvement in this procedure by analyzing in detail the state of stress singularity in the region where the circular crack front penetrates the free surface [12].

Shah, on the other hand, considered the stress intensity factor of an elliptical crack which in some instances approximates better the geometries of actual cracks. A potential function of Segedin was used to represent a polynomial distribution of pressure on the elliptical crack surface and a series of problems involving embedded elliptical cracks were solved [13-17]. Mathematical complexity limited this polynomial distribution of pressure to third order terms which cannot readily represent the rapidly varying residual surface tractions on the elliptical crack surface in the alternating method of three-dimensional crack analysis. As a result, the surface problem was not analyzed directly in any of these problems. The stress intensity factor at the deepest penetration of a semi-elliptical crack, however, was approximated [16] by a product of Shah's back surface magnification factor [14] with Kobayashi's empirical front surface magnification factor [4]. Kobayashi recently found a procedure [18] with which the residual surface traction in the iteration process could be reduced significantly and thus extended the usefulness of the alternating technique which is based on the elliptical crack solution with a third-order polynomial of pressure distribution on the crack surface.

In addition to the semi-elliptical surface flaws just discussed, the problem of quarter-elliptical cracks has been of considerable interest to practitioners of fracture mechanics [1]. The first paper on this subject from the fracture mechanics viewpoint was presented in 1969 [19], and the increased interest since that time is evidenced by the two papers on corner flaws presented in this session [20,21].

In the following, a procedure which greatly accelerates the numerical convergence of the iteration procedure in the alternating method will be discussed. The procedure will then be used to determine the stress intensity factor in a corner flaw in a quarter-infinite solid.

### **Method of Approach**

The iterative procedure in the alternating technique for solving three-dimensional problems in fracture mechanics has been well documented in the papers by Smith and Shah and will not be repeated here. The necessary elasticity solution for the totally embedded elliptical crack, originally suggested by Segedin [22], and the half-space solution by Love [23,24], have also been repeatedly described in these papers. Thus, only the mathematical relations necessary for explaining the new procedure will be listed in the following.

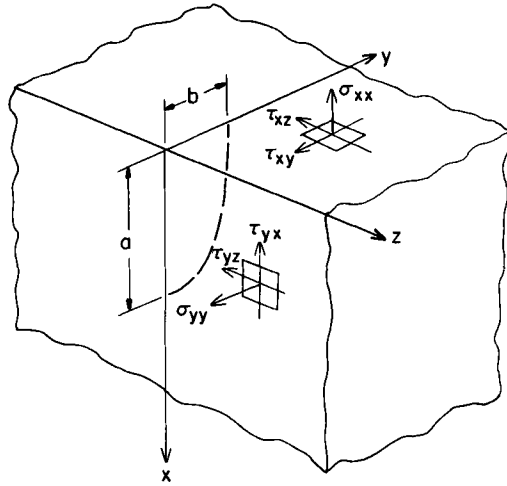


FIG. 1—Quarter elliptical crack in a quarter-infinite solid.

*Elliptical Crack in an Infinite Solid*

Consider an infinite elastic solid containing an elliptical crack which is located in the plane  $z = 0$  and is opened by applying an internal pressure  $p(x,y)$  symmetrically to both surfaces of the crack. The boundary conditions for this problem are <sup>3</sup> (see Fig. 1)

$$\sigma_{zz} = -p(x,y) \quad \left( \frac{x^2}{a^2} + \frac{y^2}{b^2} < 1, z = 0 \right) \quad (1a)$$

$$w = 0 \quad \left( \frac{x^2}{a^2} + \frac{y^2}{b^2} > 1, z = 0 \right) \quad (1b)$$

$$\tau_{xz} = \tau_{yz} = 0 \quad (z = 0) \quad (1c)$$

$$\sigma_{xx} = \sigma_{yy} = \sigma_{zz} = \tau_{xy} = \tau_{yz} = \tau_{zx} = 0 \text{ at infinity} \quad (1d)$$

<sup>3</sup> This problem is illustrated by quarter-infinite solid problem shown in Fig. 1.

For vanishing shear stresses on  $z = 0$  plane and in the absence of body forces, Navier's equations of equilibrium are satisfied by the harmonic function  $\Phi$ . Displacement perpendicular to the crack plane in terms of  $\Phi$  is

$$w = z \frac{\partial^2 \Phi}{\partial z^2} - 2(1 - \eta) \frac{\partial \Phi}{\partial z} \quad (2)$$

where  $\eta$  is the Poisson's ratio. Stress components necessary for solving the elliptical crack problem are given by

$$\sigma_{xx} = 2G \left[ z \frac{\partial^3 \Phi}{\partial x^2 \partial z} + \frac{\partial^2 \Phi}{\partial x^2} + 2\eta \frac{\partial^2 \Phi}{\partial y^2} \right] \quad (3a)$$

$$\sigma_{yy} = 2G \left[ z \frac{\partial^3 \Phi}{\partial y^2 \partial z} + \frac{\partial^2 \Phi}{\partial y^2} + 2\eta \frac{\partial^2 \Phi}{\partial x^2} \right] \quad (3b)$$

$$\sigma_{zz} = 2G \left[ z \frac{\partial^3 \Phi}{\partial z^3} - \frac{\partial^2 \Phi}{\partial z^2} \right] \quad (3c)$$

$$\tau_{xy} = 2G \left[ z \frac{\partial^3 \Phi}{\partial x \partial y \partial z} + (1 - 2\eta) \frac{\partial^2 \Phi}{\partial x \partial y} \right] \quad (3d)$$

$$\tau_{xz} = 2G z \frac{\partial^3 \Phi}{\partial x \partial z^2} \quad (3e)$$

$$\tau_{yz} = 2G z \frac{\partial^3 \Phi}{\partial y \partial z^2} \quad (3f)$$

where  $G$  is the shear modulus.

From Eqs 1, 2, and 3, the boundary conditions in the crack plane are given by

$$\frac{\partial^2 \Phi}{\partial z^2} = \frac{p(x,y)}{2G} \quad (4a)$$

on the elliptical crack surface, and

$$\frac{\partial \Phi}{\partial z} = 0 \tag{4b}$$

on the  $z = 0$  plane outside the elliptical crack surface.

Since neither  $x$  nor  $y$  plane symmetry exists in the problem of a quarter-elliptical crack in a quarter space, all ten terms of the polynomial pressure distribution [13],  $p(x,y)$ , must be used and thus

$$p(x,y) = \sum_{i,j=0}^3 A_{ij} x^i y^j \tag{5}$$

where  $i + j \leq 3$ .

Generally, the ten-term polynomial pressure distribution in Eq 5 cannot adequately fit a rapidly varying crack pressure distribution on the crack surface. Nevertheless, in order to best fit the pressure distribution to the residual crack surface tractions generated through the alternating technique described in the previous section, a least square method is used to determine the coefficients of  $A_{ij}$  in Eq 5. The large residues between the actual pressure and the fitted pressure distributions in 3-D crack problems involving part-elliptical crack were thus responsible for bad numerical convergence of the alternating technique.

The harmonic function related to the pressure distribution of Eq 5 was derived from Segedin potential function [22] and is represented as

$$\Phi(x,y,z) = \sum_{i,j=0}^3 \Phi_{ij} \tag{6a}$$

where  $i + j \leq 3$

$$\Phi_{ij} = C_{ij} \sum_{i,j=0}^3 \frac{\partial^{i+i}}{\partial x^i \partial y^j} \int_{\lambda}^{\infty} \frac{[\omega(s)]^{k+j+1}}{\sqrt{Q(s)}} ds \tag{6b}$$

$$Q(s) = [s(a^2 + s) (b^2 + s)] \tag{6c}$$

where  $\lambda$  is part of an elliptical coordinate system  $\lambda$ ,  $\mu$ , and  $\nu$  which are the roots of the following cubic equation

$$\omega(s) = 1 - \frac{x^2}{a^2 + s} - \frac{y^2}{b^2 + s} - \frac{z^2}{s} \quad (7a)$$

and

$$\infty > \lambda \geq 0 \geq \mu \geq -b^2 \geq \nu \geq -a^2 \quad (7b)$$

In the plane  $z = 0$ , the interior region of the elliptical crack is then represented by  $\lambda = 0$  and the exterior region is given by  $\mu = 0$ .

The harmonic function  $\Phi$  contains ten undetermined coefficients,  $C_{ij}$ , corresponding to each term, of  $x^i y^j$ . By substituting Eq 6 into Eq 4a and using Eq 5, the undetermined coefficients,  $C_{ij}$ , can be linearly related to the known coefficients  $A_{ij}$  of pressure distribution. Details of this procedure as well as the matrix equation which relates  $C_{ij}$  to  $A_{ij}$  are described in Ref 13.

The stress intensity factor, which can be obtained through a procedure described by Irwin [25] or Kassir and Sih [26], is

$$K_I = \sum_{i,j=0}^3 C_{ij} \frac{8G}{ab} \frac{\pi}{ab} (-1)^{i+j} 2^{i+j} (1+i+j)! \left(\frac{\cos\theta}{a}\right)^i \left(\frac{\sin\theta}{b}\right)^j \times [a^2 \sin^2\theta + b^2 \cos^2\theta]^{1/4} \quad (8)$$

where  $\theta$  is the angle in the parametric equations of ellipse. Thus, once the constants,  $C_{ij}$ , are known, the stress intensity factor for a prescribed pressure distribution of  $p(x,y)$  can be computed by the use of Eq 8.

The surface tractions acting on the free bounding planes, such as  $x = 0$  plane and  $y = 0$  planes in Fig 1, can also be computed by the use of Eq 3. Actual numerical computation of the six stress components, that is,  $\sigma_{xx}|_{x=0}$ ,  $\tau_{xz}|_{x=0}$ ,  $\tau_{xy}|_{x=0}$ ,  $\sigma_{yy}|_{y=0}$ ,  $\tau_{yx}|_{y=0}$ , and  $\tau_{yz}|_{y=0}$ , were accomplished by numerically differentiating the analytical expressions of  $\partial^2\Phi/\partial x^2$ ,  $\partial^2\Phi/\partial x\partial y$ ,  $\partial^2\Phi/\partial y^2$ , and  $\partial^2\Phi/\partial z^2$  in order to obtain the third partial derivatives of  $\Phi$  with respect to  $x$ ,  $y$ , and  $z$ . The purpose of such numerical differentiation is to reduce or eliminate the lengthy analytical derivations eventually as well as the complex computer programming of the higher order derivatives involved in the elliptical crack solution. Figure 2 shows a typical stress distribution computed by finite difference technique to evaluate the third derivatives of  $\Phi_{ij}$  from two second derivatives of  $\Phi_{ij}$  spaced 0.001 a distance apart.

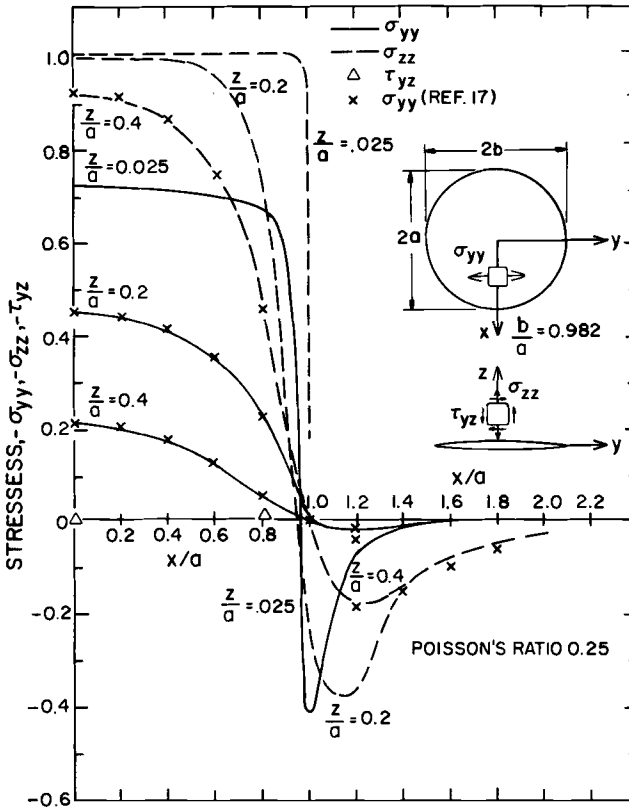


FIG. 2—Stresses obtained by numerical differentiation on  $y = 0$  plane of a nearly circular crack under uniform pressure.

Also shown by  $X$  marks are previously computed stresses [13, 14] which agree with the numerical results within third significant figures. Attempts were made to extend the numerical differentiation to second order finite differences where the stresses would be computed from  $\partial\Phi/\partial x$ ,  $\partial\Phi/\partial y$ , and  $\partial\Phi/\partial z$ . These numerically determined stresses agreed well with those from Refs 13 and 14 for an elliptical crack with uniform pressure. Stresses for elliptical cracks with nonuniform pressurization showed some deviations, and thus further numerical experimentation is necessary before the finite difference procedure can be extended to second order differentiation of  $\partial\Phi/\partial x$ ,  $\partial\Phi/\partial y$ , and  $\partial\Phi/\partial z$ .

*Surface Traction on the Plane of a Half Space*

The second step in the alternating technique is to eliminate the residual surface traction on the bounding free surfaces computed by the finite

difference procedure described in the previous section. Love's solution [23,24] for a half space with a uniform surface traction prescribed on a rectangle in the bounding free surface is used by all investigators for this computation. The total number of necessary rectangles for adequately erasing the residual surface tractions has been a subject of discussion in the past [12,18,27] and will thus not be repeated here. The criterion for maximum rectangle size set forth in Ref 18 was used to determine sizes of the rectangles on the two free bounding surfaces of a quarter-infinite space for quarter-elliptical cracks.

Briefly the foregoing criterion is based on the differences in resultant stresses in a half space due to: (1) a linearly varying normal or tangential stress distribution over the rectangle on the bounding plane; and (2) a uniform normal or tangential stress distribution, which is in equilibrium with the linearly varying stress distribution, over the rectangle. The maximum ratio in the two stresses generated by these two prescribed normal or tangential stresses is two at the point of load of application and diminishes rapidly at points short distances away from the regions of load application. These and other comparisons of the above two 2-D solutions indicated that the size of the rectangles in the half-space solution can be as large as its closest distance to the crack plane or to the other bounding surface for the case of a finite thickness solid. The numbers of necessary rectangles on the bounding free surfaces were then reduced systematically following this criterion.

Figure 3 shows a typical rectangular mesh on the two free bounding surfaces of a quarter-elliptical crack with an aspect ratio of  $b/a = 0.4$ . The number of rectangles in the  $y = 0$  plane has been reduced to 63 from the original 540 used by Smith in 1969 [8]. The numbers of rectangles in the  $x = 0$  plane are 63, 35, and 31 for crack aspect ratios of 0.98, 0.4, and 0.2, respectively.

#### *Fictitious Pressure Distribution on an Elliptical Crack*

As mentioned previously, the serious drawback in the elliptical crack solution lies in the third order polynomial in Eq 5 which cannot accurately match the rapidly varying residual tractions on the quarter-elliptical crack surface as well as in the uncertainty in continuing the pressure distribution in the other three quarters of the elliptical crack. A procedure of prescribing a pressure distribution on the fictitious elliptical crack surface which protrudes out of the bounded solid [18] led to a numerical experimentation to force the convergence of the alternating technique by a conveniently prescribed fictitious pressure distribution.

First, the two-dimensional edge crack problem as shown in Fig. 4 was considered as a counterpart of three-dimensional quarter-elliptical crack problem, and the four following distributions were studied

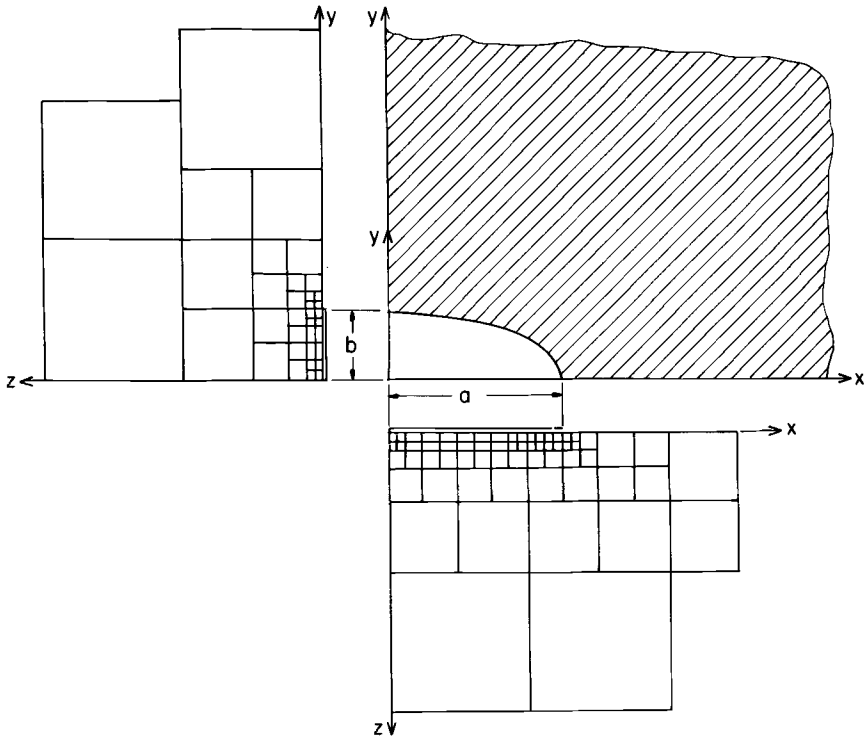


FIG. 3—Rectangles on the two bounding surfaces.

Constant pressure

$$p(y) = B_0 \tag{9a}$$

Linearly varying pressure

$$p(y) = B_1 \left(1 - \frac{y}{b}\right) \tag{9b}$$

Quadratically varying pressure

$$p(y) = B_2 \left(1 - \frac{y}{b}\right)^2 \tag{9c}$$

Cubically varying pressure

$$p(y) = B_3 \left(1 - \frac{y}{b}\right)^3 \tag{9d}$$

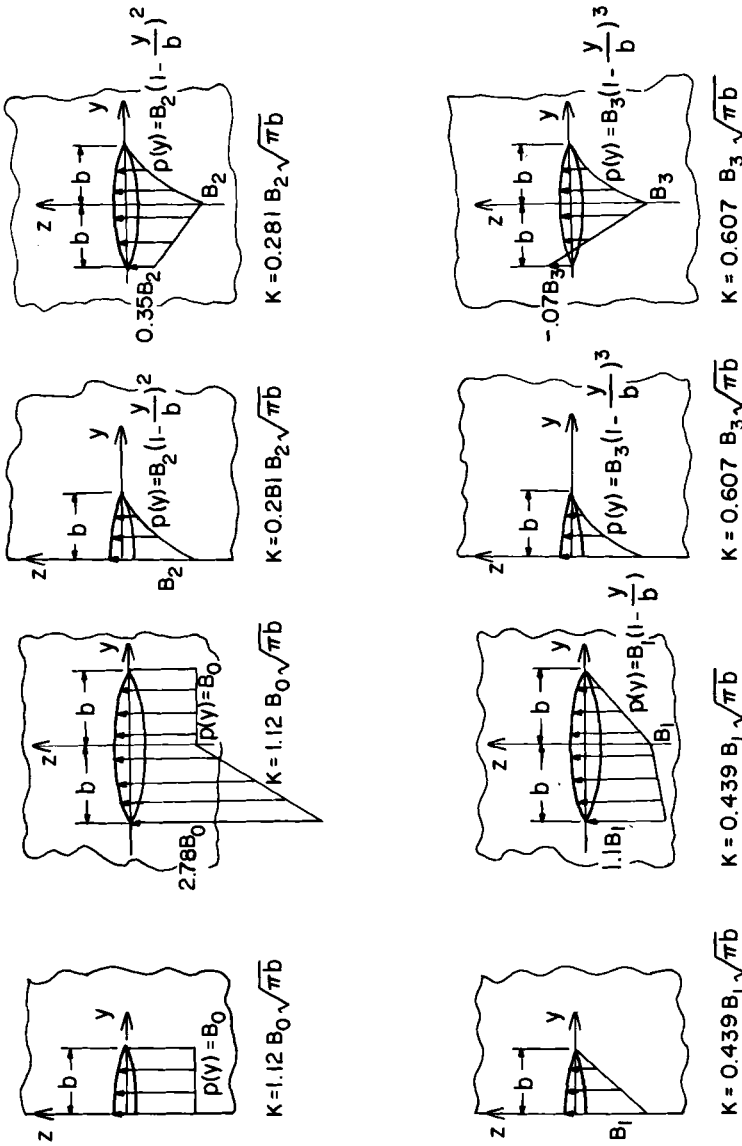


FIG. 4—Stress intensity factor for an edge crack subjected to variable pressure loadings.

The fictitious pressure in a totally embedded crack necessary to yield the correct edge-crack stress intensity factor was determined by the procedure described in Ref 18, and these results are summarized in Fig. 4.

In extending the above findings to a pressure distribution which varies with both  $x$  and  $y$ , in a quarter-elliptical crack shown in Fig. 5, the cross product terms of  $x$  and  $y$  in Eq 6 were discarded temporarily, and the remaining seven terms were used to determine the following fictitious pressure at discrete locations on the second and fourth quadrants of the elliptical crack surface. Fictitious pressure on the second quadrant of the elliptical crack in Fig. 5 for each  $y = \text{constant}$  line was represented as

$$p(x,y) = A_{00} + A_{10}x + A_{20}x^2 + A_{30}x^3 = \sigma \left[ B_{00} + B_{10} \left( 1 - \frac{x}{a'} \right) + B_{20} \left( 1 - \frac{x}{a'} \right)^2 + B_{30} \left( 1 - \frac{x}{a'} \right)^3 \right] \tag{10}$$

where  $a'$  is the half cord length at  $y = \text{constant}$ .

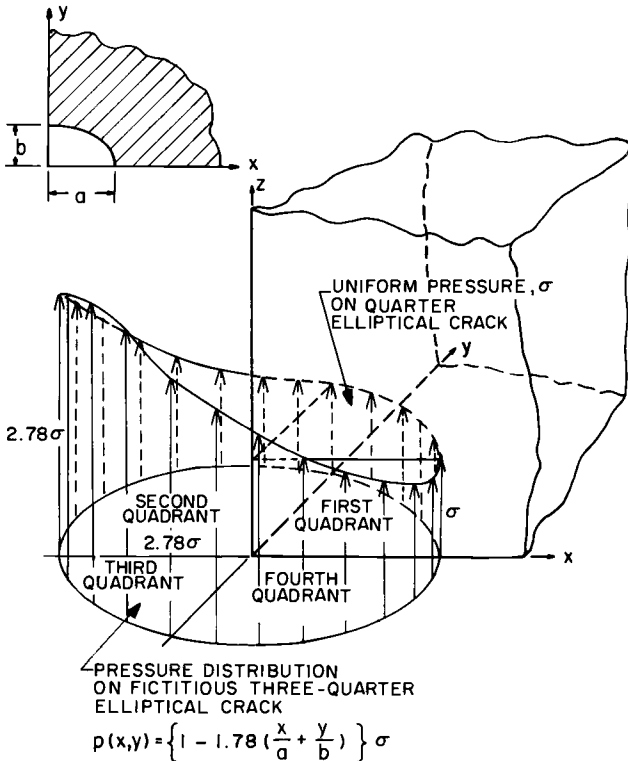


FIG. 5—Prescribed pressure distribution on elliptical crack.

Fictitious pressure on the fourth quadrant of the elliptical crack for each  $x = \text{constant}$  line was represented as

$$p(x,y) = A_{00} + A_{01}y + A_{02}y^2 + A_{03}y^3 = \sigma \left[ B_{00} + B_{01} \left( 1 - \frac{y}{b'} \right) + B_{02} \left( 1 - \frac{y}{b'} \right)^2 + B_{03} \left( 1 - \frac{y}{b'} \right)^3 \right] \quad (11)$$

where  $b'$  is the half cord length at  $x = \text{constant}$ .

Equations 10 and 11 were then used to solve for  $B_{ij}$  corresponding to the given  $x = \text{constant}$  or  $y = \text{constant}$  lines. Since each  $B_{ij}$  from Fig. 4, relates to a linearly varying fictitious pressure distribution, a linear superposition of these pressures yields the resultant fictitious pressure for each  $x = \text{constant}$  or  $y = \text{constant}$  line. By mapping the quarter-elliptical crack surface by such regularly spaced  $x = \text{constant}$  or  $y = \text{constant}$  lines, a fictitious pressure distribution throughout the second and fourth quadrants of the elliptical crack surface which protrudes into empty space can be established. The general polynomial expression of pressure represented by Eq 5 is then fitted to the residual pressures on the first quadrant as well as the fictitious pressures on the second and fourth quadrant of the elliptical crack to complete the first step of an iteration process in the alternating method.

The preceding procedure was not adhered to completely in prescribing the fictitious pressure in the first iteration process for a quarter-crack subjected to uniform pressure. Because of the steep gradients of the fictitious pressure distribution in regions where the crack front intersects the two free bounding planes, these regions were ignored in least square fitting Eq 5 to the prescribed and fictitious pressure distributions.

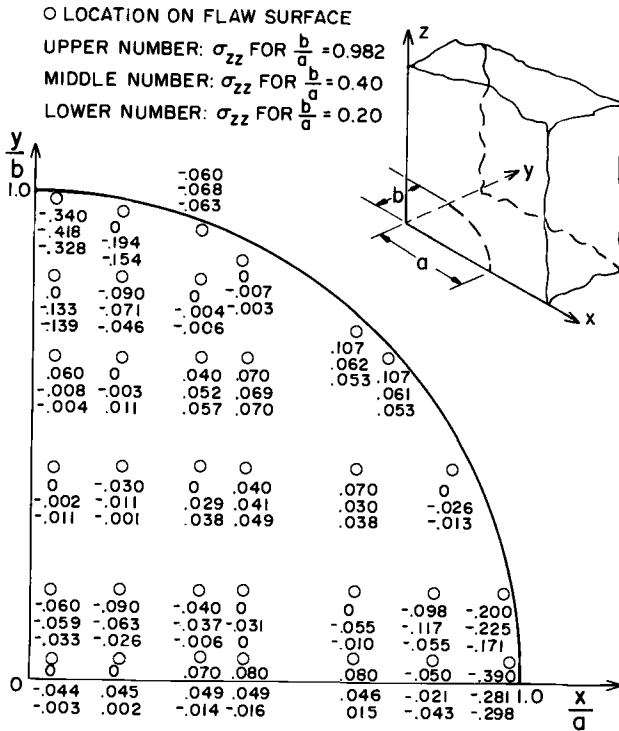
### Quarter-Elliptical Crack Within a Quarter-Infinite Solid

#### *Uniform Pressure on Crack Surface*

When the fictitious pressure shown in Fig. 5 for the first cycle of alternating method was used, the maximum residual surface traction on the quarter-elliptical crack at the end of the first iteration cycle, excluding the region where the crack front intersects the free surface, was less than  $0.2\sigma$ . This residual stress is less than one third of the maximum residual traction of an elliptical crack with prescribed constant pressure on all four quadrants of the crack surface [18]. The procedure of prescribing appropriate fictitious pressure distribution had thus accelerated the convergence of the iteration process in the alternating method.

Since the two bounding free surfaces interact with each other in this corner crack problem, running summations of the residual surface trac-

tions on each of the three surfaces, that is, the quarter-elliptical crack surface and the two free bounding surfaces, due to removal of residual surface tractions from any other two surfaces were maintained at all times. The current values of residual surface tractions were used at all times in the erasure process. The rectangle mesh spacing described previously together with 32 to 40 almost evenly spaced points on the embedded quarter-elliptical crack surface for least square fitting of  $p(x,y)$  were used in each iteration of the alternating technique. Three cycles of such iterations required central processing unit (CPU) time of 650, 703, and 783 s on the CDC 6400 computer for crack aspect ratios of  $b/a = 0.98, 0.4,$  and  $0.2,$  respectively. The residual tractions on the crack surface after these three iterations are shown in Fig. 6. The average residual surface tractions on the elliptical surface, with the exception of regions in the vicinity where the crack front intersected with the two free surfaces, decreased to less than 0.575, 0.893, and 0.45 percent of the



original uniform pressure for crack aspect ratios of 0.98, 0.4, and 0.2, respectively.

The isolated high local residual tractions, which are as high as 0.4 in the region where the crack front penetrates the free boundary surfaces as shown in Fig. 6, were then reduced by using the known solution of a penny-shaped crack subjected to equal and opposite concentrated load [28]. Reference 21, which can also be found in this proceedings, discusses sophisticated uses of this particular solution. The result of the preceding incomplete erasure is a definite trend of the stress intensity factor to decrease rapidly, as predicted by Hartranft and Sih [12], when the crack front approaches the free-bounding surface.

Similar erasure procedure was used in erasing the isolated high local residual tractions on the crack surface toward the midportion of the two free-bounding planes. As expected, these erasures contributed to less than 0.002 to the normalized stress intensity factors, and thus the effects of these residual tractions were ignored in subsequent computation.

The resultant normalized stress intensity factors for three elliptical cracks with aspect ratios of  $b/a = 0.98, 0.4,$  and  $0.2$  are shown in Fig. 7. Also shown in Fig. 7 is the finite element results for  $b/a = 1.0$  by Tracey [29]. The significant deviations between finite element results for  $b/a = 1.0$  and the results obtained by the alternating technique for  $b/a = 0.98$  could be attributed to the coarseness of the finite element breakdown.

#### *Linearly Varying Pressure on Crack Surface*

Similar analysis was conducted for a quarter-elliptical crack with a linearly decreasing pressure gradient in the direction of the minor axis of the ellipse or  $\sigma_{zz} = \sigma(1 - y/b)$ . The same procedure of prescribing fictitious pressure in the second and fourth quadrant of the elliptical crack was used to accelerate the convergence of the iteration procedure. Figure 8 shows the residual surface tractions on the crack surface after three iterations. These residual surface tractions are considerably less than those in Fig. 6 indicating, in retrospect, that the more moderate fictitious pressure distribution shown in Fig. 5 was relatively ineffective in accelerating the numerical convergence and was thus the primary cause of isolated high residual tractions in Fig. 6. Although the maximum residual surface tractions in Fig. 8 were significantly smaller than those in Fig. 6, the average residual tractions in the two problems were approximately the same. For the linearly varying pressure problem, the average residual surface tractions were 1.00, 0.833, and 0.3296 percent of the maximum value of the linearly varying pressures for crack aspect ratios of  $b/a = 0.98, 0.4,$  and  $0.2,$  respectively.

Since the residual tractions in the regions where the crack front intersects the free bounding surfaces were small, the procedure used to

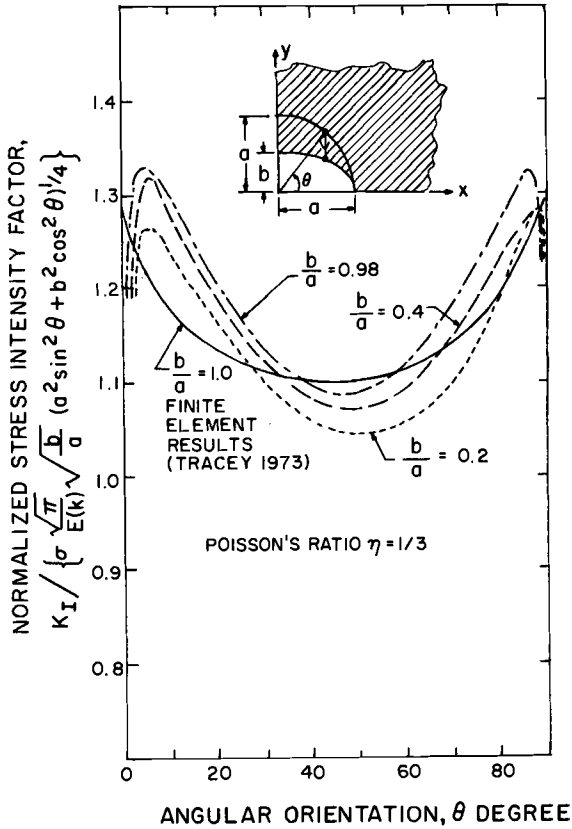


FIG. 7.—Stress intensity factor for a corner flaw in a quarter infinite solid subjected to uniaxial tension,  $\sigma_{zz} = \sigma$ .

erase isolated higher values of residual surface tractions did not show significant drop in the stress intensity factors as the crack front approached the two free bounding surfaces. The normalized stress intensity factors for quarter-elliptical cracks with aspect ratios of  $b/a = 0.98, 0.4,$  and  $0.2,$  shown in Fig. 9, do not show the rapid drops in stress intensity factors.

**Discussion**

As mentioned previously, the convergence in the iteration process in the uniform pressure problems could have been enhanced should the original procedure of prescribing fictitious pressure have been used. Severe restriction in computing funds did not allow the authors to rerun this set with the more appropriate fictitious pressure distribution. Since



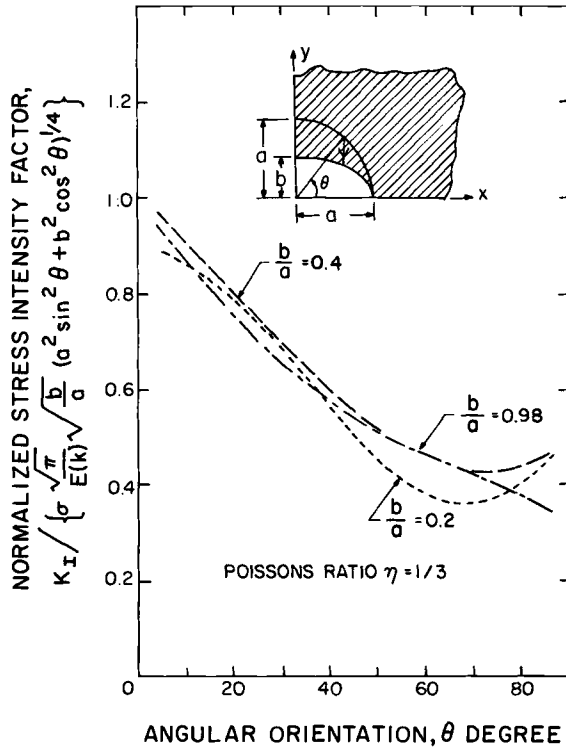


FIG. 9—Stress intensity factor for a corner flaw in a quarter infinite solid subjected to linear loading,  $\sigma_{zz} = (1 - y/b)\sigma$ .

finding substantiates the assumption made by Shah in estimating the stress intensity factors for various part-elliptical cracks using the accurately determined normalized stress intensity factors of semi-circular cracks [21].

*Acknowledgment*

The work reported here was supported by the U.S. Army Research Office—Durham. Some of the ideas for this work were conceived during the course of one of the authors' consulting engagement with The Boeing Company. The authors wish to express their appreciation to J. N. Masters, The Boeing Aerospace Company, for his support and particularly to R. C. Shah, The Boeing Aerospace Company, for his assistance on the many details of the theoretical and numerical analyses.

**References**

[1] *Fracture Mechanics of Aircraft Structures*, H. Liebowitz, Ed., AGARDograph No. 176, Advisory Group for Aeronautical Research and Development, 1974.

- [2] Irwin, G. R., *Journal of Applied Mechanics*, Vol. 29, *Transactions*, American Society of Mechanical Engineers, Vol. 84, 1962, pp. 651-654.
- [3] Kobayashi, A. S., "On the Magnification Factors of Deep Surface Flaws," Boeing Structural Research Memorandum, No. 16, the Boeing Aerospace Company, Dec. 1965.
- [4] Kobayashi, A. S. and Moss, W. L. in *Proceedings of the Second International Conference on Fracture*, Chapman and Hall Ltd., London, England, 1970, pp. 31-45.
- [5] Masters, J. N., Haese, W. P., and Finger, R. W., "Investigation of Deep Flaws in Thin Walled Tanks," NASA CR-72686, National Aeronautics and Space Administration, Washington, D.C., 1969.
- [6] Rice, J. R. and Levy, N., *Journal of Applied Mechanics*, Vol. 89, *Transactions*, American Society of Mechanical Engineers, Vol. 94, March 1972, pp. 185-194.
- [7] Newman, J. C., *Engineering Fracture Mechanics*, Vol. 5, No. 3, Sept. 1973, pp. 667-690.
- [8] Smith, F. W., Emery, A. F., and Kobayashi, A. S., *Journal of Applied Mechanics*, Vol. 34, *Transactions*, American Society of Mechanical Engineers, Vol. 89, 1967, pp. 953-959.
- [9] Smith, F. W. and Alavi, M. J., *Journal of Engineering Fracture Mechanics*, Vol. 3, Oct. 1971, pp. 241-254.
- [10] Smith, F. W. and Alavi, M. J., "Stress Intensity Factors for a Part-Circular Surface Flaw," *Proceedings of the First International Conference on Pressure Vessel Technology*, Delft, Holland, 1969.
- [11] Thresher, R. W. and Smith, F. W., *Journal of Applied Mechanics*, Vol. 39, *Transactions*, American Society of Mechanical Engineers, Vol. 95, March 1972, pp. 195-200.
- [12] Hartranft, R. J. and Sih, G. C. in *Mechanics of Fracture I—Methods of Analysis and Solutions of Crack Problems*, G. C. Sih, Ed., Noordhoff International Publishing, Leyden, The Netherlands, 1973, p. 179-23.
- [13] Shah, R. C. and Kobayashi, A. S., *Journal of Engineering Fracture Mechanics*, Vol. 3, No. 1, July 1971, pp. 71-96.
- [14] Shah, R. C. and Kobayashi, A. S., *International Journal of Fracture Mechanics*, Vol. 9, No. 2, June 1973, pp. 133-146.
- [15] Shah, R. C. and Kobayashi, A. S. in *Stress Analyses and Growth of Cracks, Proceedings of the 1971 National Symposium on Fracture Mechanics, Part I, ASTM STP 513*, American Society for Testing and Materials, 1972, pp. 3-21.
- [16] Shah, R. C. and Kobayashi, A. S. in *The Surface Crack: Physical Problems and Computational Solutions*, J. L. Swedlow, Ed., American Society of Mechanical Engineers, 1972, pp. 79-124.
- [17] Shah, R. C. and Kobayashi, A. S., *Journal of Pressure Vessel Technology, Transactions*, American Society of Mechanical Engineers, Vol. 96, Series J, No. 1, Feb. 1974, pp. 47-594.
- [18] Kobayashi, A. S., Enetanya, A. N., and Shah, R. C. in *Prospects of Fracture Mechanics*, G. C. Sih, H. C. van Elst, and D. Broek, Eds., Noordhoff International Publishing, Leyden, The Netherlands, 1975, p. 525-544.
- [19] Hall, L. R. and Finger, R. W. in *Proceedings of the Air Force Conference on Fatigue and Fracture of Aircraft Structures and Materials*, AFFDL TL-70-144, Air Force Flight Dynamics Laboratory, 1970, p. 235-264.
- [20] McGowan, J. J. and Smith, C. W., this publication, pp. 460-476.
- [21] Shah, R. C., this publication, pp. 429-459.
- [22] Segedin, C. M., *International Journal of Engineering Sciences*, Vol. 6, 1968, pp. 601-611.
- [23] Love, A. E. H., *Philosophical Transactions of the Royal Society*, Series A, Vol. 288, 1929, pp. 387-395.
- [24] Love, A. E. H., *A Treatise on the Mathematical Theory of Elasticity*, Dover Publications, New York, 1944, pp. 241-245.
- [25] Irwin, G. R., "Analytical Aspects of Crack Stress Field Problems," University of Illinois, Urbana, Ill., T and AM Report, No. 213, 1962.
- [26] Kassir, M. K. and Sih, G. C., *Journal of Applied Mechanics*, Vol. 33, *Transactions*, American Society of Mechanical Engineers, Vol. 89, Dec. 1966, pp. 601-611.

- [27] Smith, F. W., *The Surface Crack: Physical Problems and Computational Solutions*, J. L. Swedlow, Ed., American Society of Mechanical Engineers, 1972, pp. 125-152.
- [28] Tada, H., Paris, P., and Irwin, G., *The Stress Analysis of Cracks, Handbook*, Del Research Corporation, Hellertown, Pa., 1973, pp. 24.2.
- [29] Tracey, D. M., *International Journal of Fracture*, Vol. 9, 1973, pp. 340-343.
- [30] Kobayashi, A. S. in *Significance of Defects in Welded Structures: Proceedings of the US-Japan Seminar, 1973*, T. Kanazawa and A. S. Kobayashi, Eds., University of Tokyo Press, Tokyo, Japan, 1974, pp. 127-143.